10/7-18-95 (1)

LBL-37200
CONF-9503110--
UC-1240

Lawrence Berkeley Laboratory
UNIVERSITY OF CALIFORNIA

EARTH SCIENCES DIVISION

Proceedings of the TOUGH Workshop '95
Lawrence Berkeley Laboratory
Berkeley, California
March 20–22, 1995

K. Pruess, Editor

March 1995

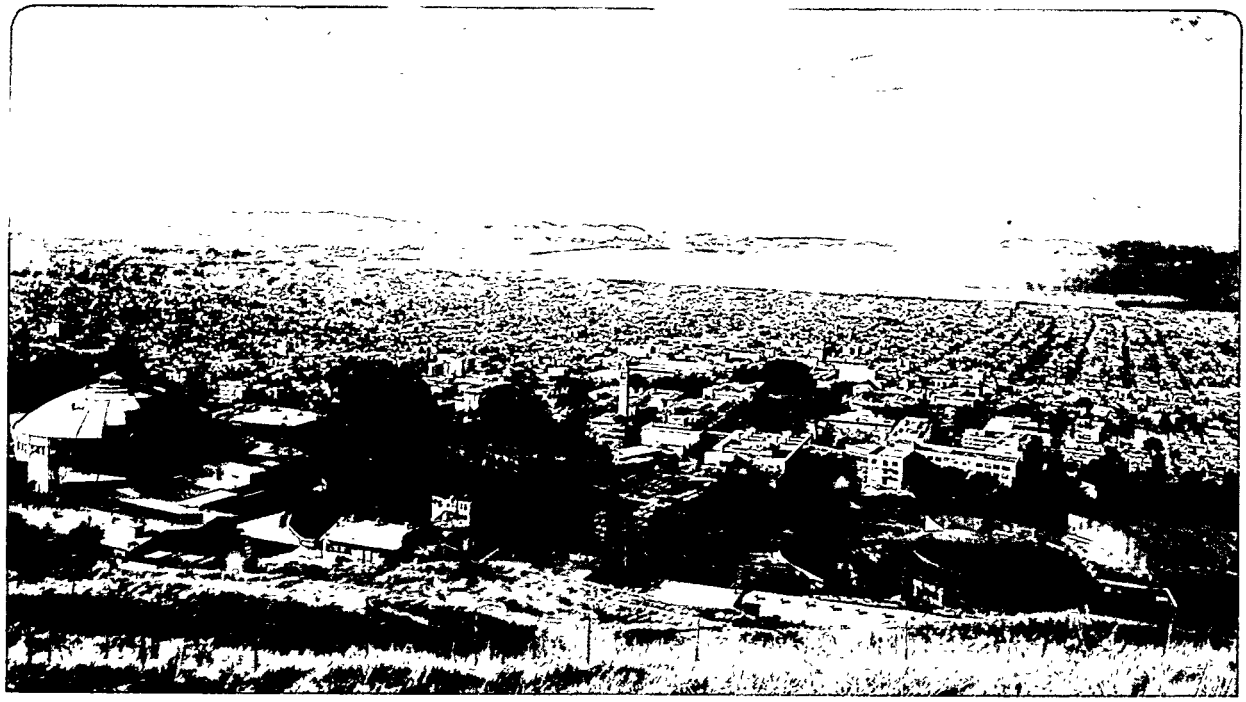

Prepared for the U.S. Department of Energy under Contract Number DE-AC03-76SF00098

LBL-37200
UC-1240
Conf.-9503110

PROCEEDINGS OF THE TOUGH WORKSHOP '95

LAWRENCE BERKELEY LABORATORY
BERKELEY, CALIFORNIA

MARCH 20 - 22, 1995

Karsten Pruess, Editor

Earth Sciences Division, Lawrence Berkeley Laboratory
University of California, Berkeley, California 94720

March 1995

This work was supported, in part, by the Director, Office of Civilian Radioactive Waste Management, Yucca Mountain Site Characterization Project Office, Regulatory and Site Evaluation Division, and by the Assistant Secretary for Energy Efficiency and Renewable Energy, Geothermal Division, of the U.S. Department of Energy under Contract No. DE-AC03-76SF00098.

ABSTRACT

The TOUGH Workshop '95 focused on applications and enhancements of the TOUGH/MULKOM family of numerical simulation programs for complex flows in permeable media, including multiphase, multicomponent, non-isothermal, and variable-density flows. There were about 100 participants from 10 countries in attendance. The topical areas covered included environmental remediation, nuclear waste isolation, geothermal and petroleum reservoir engineering, mining engineering, vadose zone hydrology, and simulation methods.

This volume features the extended summaries of papers that were presented at the workshop. The technical program and lists of authors and registered participants are included in appendices.

TABLE OF CONTENTS

Preface

A workshop on applications and enhancements of the TOUGH/MULKOM family of multiphase fluid and heat flow simulation programs was held at Lawrence Berkeley Laboratory on March 20 - 22, 1995. The workshop was organized as an open forum for information exchange among developers and users of the TOUGH/MULKOM codes, and was attended by approximately 100 participants from 10 countries. A unique aspect of the meeting was the strong diversity of subject matter, emphasizing the commonality of interest shared by different engineering disciplines in multiphase flows, and coupled fluid and heat flows. A total of 55 technical papers were presented in oral and poster sessions. Topics covered broad areas that involve complex flows in the subsurface, such as geothermal reservoir simulation, nuclear waste isolation, environmental remediation, and others.

The present volume includes extended summaries of the papers contributed to the TOUGH Workshop '95. In some cases these were slightly revised by the authors after the workshop, but no editing was performed by Lawrence Berkeley Laboratory. Regrettably, the Mexican authors were unable to attend, but their contributions are included in this report.

It is perhaps appropriate to preface these proceedings with some remarks about past development and future trends of the TOUGH/MULKOM family of numerical simulation programs. The basic concepts and first "ancestral" code implementations date from the early eighties, and were developed in the context of LBL's geothermal reservoir engineering program. Robust numerical techniques were devised for modeling two-phase flow af water and vapor with strong coupling to heat flow. The strong non-linearities and inherent diversity of geothermal flow problems were addressed by techniques that included fully implicit time differencing, flexible space discretization by means of integral finite differences, upstream weighting of mobilities, variable switching during phase transitions, a residual-based strictly mass-and-energy conservative formulation of discretized equations, Newton-Raphson iteration, assembly of the Jacobian matrix by numerical differentiation, and provisions for automatic time stepping.

It was realized early on that the equations governing multiphase fluid and heat flows have the same mathematical form, regardless of the number and nature of fluid phases and components present. Thus, flow problems arising in geothermal reservoirs, oil and gas production and storage, geologic disposal of nuclear waste, and environmental remediation are very similar from a mathematical point of view. Differences arise only because of different thermophysical properties of the fluids, giving rise to different numerical values of the parameters in the governing equations.

Accordingly, the MULKOM code was set up as a general-purpose flow and transport simulator, for an arbitrary number of fluid phases and components. This architecture provided a great deal of flexibility, which is very desirable and convenient for a research-oriented environment. Application of MULKOM to a specific flow problem required interfacing of the general flow-and-transport module with an appropriate fluid property module. From the early to the mid-eighties a number of fluid property modules were developed, primarily for applications in geothermal reservoir engineering, but also for oil and gas production and storage, and for nuclear waste disposal applications. These simulation modules were research tools, whose development was driven by the desire to understand flow behavior in various kinds of subsurface systems and to develop engineering approaches for these systems. The modules were usually only partially documented, and were frequently modified as dictated by the needs of evolving research

programs in LBL's Earth Sciences Division. They were often not mutually compatible, and use outside of LBL was limited to a few research collaborations.

The demands of nuclear-waste related applications for a stable and fully documented simulation program led to the development and release of the TOUGH code in 1987. The acronym "TOUGH" stands for **T**ransport **O**f **U**nsaturated **G**roundwater and **H**eat, which is an allusion to the types of flow problems encountered in the partially saturated tuff formations at Yucca Mountain, Nevada, currently (and then) under investigation by the U.S. Department of Energy as a potential host rock for a civilian nuclear waste repository. The TOUGH code was simply a stripped-down version of MULKOM, specialized for the problem of two-phase two-component flow of water and air.

In 1991 we released a successor code to TOUGH known as "TOUGH2." TOUGH2 features the fully flexible MULKOM-architecture for flows with an arbitrary number of fluid components and phases, although the 1991 release included only a limited selection of the "core" geothermal and nuclear-waste related fluid property modules. TOUGH2 supersedes TOUGH in the sense that it includes all the capabilities of TOUGH, and offers additional features and capabilities in an upwardly compatible manner. In an effort to satisfy nuclear-waste related demands on referenceability of code applications, while maintaining the openness and flexibility of an evolving research tool, an internal version control system was implemented in TOUGH2. The development of TOUGH2 is ongoing. Some of the recent enhancements developed by the LBL group include (i) a preconditioned conjugate gradient module 'T2CG1' for efficient solution of large 2-D and 3-D problems, (ii) a module 'T2VOC' for 3-phase 3-component flow of water, air, and a volatile organic compound (VOC), (iii) a module 'M2NOTS' for 3-phase flow of water, air, and a multicomponent mixture of nonaqueous-phase liquids (NAPLs), (iv) ITOUGH2, an inverse module for automatic calibration, history matching, and optimization of TOUGH2-flow problems, and (v) T2DM, a module for strongly coupled flow and transport of fluids with variable salinity, including full hydrodynamic dispersion. The TOUGH and TOUGH2 codes, and most of these recent enhancements, including special code versions for installation on PCs, are available to the public through DOE's Energy Science and Technology Software Center (ESTSC).† In addition, very considerable enhancements of simulation capabilities for the TOUGH/MULKOM codes have been and are being developed outside LBL, by academic and public research institutions as well as by private companies. Many new modules are described in papers included in this volume; interested parties should directly contact the developers regarding status and availability of these codes.

The trend with ongoing code enhancements is for "self-documenting" and "plug-compatible" modules. Ideally, such modules can be linked with "standard-TOUGH2" to produce a functioning code. They come with `READ.ME` files and sample inputs that include comments for describing input data and formats, and they produce informative output to document code features and capabilities when executed. The LBL group does not presume to "set policy" with respect to format and architecture of code enhancements. We see our role as anchors and facilitators of TOUGH/MULKOM applications and enhancements. Our code developments and releases are configured with the intent to provide a framework that developers outside LBL will find easy to use and to adopt as they develop code enhancements for their own applications. It is hoped that in this way compatibility among different code enhancements can be maintained, so that codes can be easily shared for maximum benefit to the entire user community.

---

† Energy Science and Technology Software Center, P.O. Box 1020, Oak Ridge, TN 37831-1020; phone (615) 576-2606, fax (615) 576-2865; Internet: estsc @ adonis.osti.gov

The organization of the workshop was greatly aided by an international advisory committee, which included Adeyinka E. Adenekan, Houston (Texas), USA, Alfredo Battistelli, San Lorenzo in Campo, ITALY, Ronald W. Falta, Clemson (South Carolina), USA, Rainer Helmig, Stuttgart, GERMANY, Edwin M. Kidd, Oak Ridge (Tennessee), USA, Tony Menzies, Richmond (California), USA, George Moridis, Berkeley (California), USA, Michael O'Sullivan, Auckland, NEW ZEALAND, and Steve Webb, Albuquerque (New Mexico), USA. I am deeply grateful to these individuals for their support and good suggestions, which were crucial in putting together a productive meeting.

Special thanks are due to John Bredehoeft, who added a unique highlight to the meeting with his banquet address, reminding us of the basic foundations and limitations of numerical modeling as just one tool among many that must be brought to bear if we are to make sense of subsurface flow systems.

I would also like to take this opportunity to thank the various agencies and offices that have supported our efforts in development and application of the TOUGH/MULKOM codes over the years. These include the Geothermal Division and the Office of Basic Energy Sciences of the Department of Energy, the Nuclear Regulatory Commission, the Gas Research Institute, DOE's Yucca Mountain Site Characterization Project (originally through Sandia's Nevada Nuclear Waste Storage Investigations Project, and more recently through the Las Vegas project office), and Sandia's WIPP project.

Last but not least I want to thank the many colleagues, at LBL and elsewhere, whose continued interest and support has made it possible to develop flow modeling capabilities that are sophisticated, yet robust enough to be practically useful for a wide range of engineering applications.

Berkeley, California, March 1995

Karsten Pruess

Analysis of Nuclide Transport under Natural Convection and Time Dependent Boundary Condition using TOUGH2

V. Javeri
Gesellschaft für Anlagen- und Reaktorsicherheit (GRS) mbH,
Schwertnergasse 1, 50667 Köln, Germany

1 Introduction

After implementation of TOUGH2 at GRS in summer 91, it was first used to analyse the gas transport in a repository for the nuclear waste with negligible heat generation and to verify the results obtained with ECLIPSE /JAV 92/. Since the original version of TOUGH2 does not directly simulate the decay of radionuclide and the time dependent boundary conditions, it is not a appropriate tool to study the nuclide transport in a porous medium /PRU 87, PRU 91/. Hence, in this paper some modifications are proposed to study the nuclide transport under combined influence of natural convection, diffusion, dispersion and time dependent boundary condition. Here, a single phase fluid with two liquid components is considered as in equation of state model for water and brine /PRU 91A/.

2 Modification of TOUGH2 Models

TOUGH2 assumes a constant permeability and does not directly simulate the convergence of a salt rock. Hence, the calculation of porosity ϕ and permeability k is modified:

$\phi = \phi$ (p, T, t) > $\phi_{min} = \phi_{min}$ (material domain): input parameter,

k = k (ϕ, material domain): input function, $\phi_p = (1/\phi)\ (\partial\phi/\partial p)$: input parameter,

$\phi_T = (1/\phi)\ (\partial\phi/\partial T)$: input parameter, $\phi_t = (1/\phi)\ (\partial\phi/\partial t)$: input parameter,

p: pressure, T = temperature, t: time,

$(1/\phi)\ (d\phi/dt) = \phi_p\ (\partial p/\partial t) + \phi_T\ (\partial T/\partial t) + \phi_t$.

In the original version of TOUGH2, only the first two terms on the right side of the above equation are included. Employing input parameters and user specified function for k, time dependent porosity and permebility can be determined. Within the original version of TOUGH2, a simulation of time dependent boundary conditions is troublesome. Therefore, user specified functions are introduced to model them:

$p = p\ (t, j_i)$, $T = T\ (t, j_i)$, $X_2 = X_2\ (t, j_i)$,

X_2 : mass fraction of secondary component (brine), j_i : index of a inactive element.

To simulate the decay of a nuclide, which can be represented by the secondary component (brine), following equations are inserted into original version:

$\Delta X_2 = \text{abs}\,(\lambda X_2 \Delta t)$, $X'_2 = X_2 - \Delta X_2$, $X'_1 = X_1 + \Delta X_2$,

X_1 : mass fraction of primary component (water),

λ : decay constant for the secondary component, ' : initial value for the next time step.

In extension to the original version /PRU 87, PRU 91/, a dispersion model for two liquid components (water/brine) is developed by /PRU 93/. Since this dispersion model assumes a full two dimensional configuration, it is inexpedient to analyse a configuration, which consists of drifts and shafts mainly. Therefore, the original version /PRU 87, PRU 91/ is extended to simulate dispersive and diffusive flux G at the interface of two elements:

$\mathbf{G}_{i,\text{diff}} = -\rho_F \phi f \,\text{grad}\,(X_i)$, $\mathbf{G}_{i,\text{disp}} = -\rho_F \beta \,\text{abs}\,(u)\,\text{grad}\,(X_i)$,

f = f (direction, material domain) : molecular diffusion coefficient, input parameter,

β = β (direction, material domain) : dispersion length, input parameter,

u : darcy velocity, ρ : density, index F : fluid; i : component 1 or 2.

The determination of flux G is very similar to flux F in the dispersion model of /PRU 93/. However, this model modification does not assume a full two dimensional configuration as in /PRU 93/ and can easily be applied to a three dimensional configuration containing drifts and shafts and, as shown below, it can save computation time significantly compared to the sophisticated model of /PRU 93/.

To implement all the modifications mentioned above, only two subroutines MULTI and CONVER of the original version are extended. At present, these modifications are implemented in a separate package containing only these two subroutines and are used only with the original version /PRU 91/ and the module EOS-7 for water and brine. In following, both liquid components are treated as water.

3 Results

To verify the modifications explained above, several one dimensional examples are treated in GRS reports /JAV 94, JAV 95/ to estimate the individual impact of discretization, hydrodynamic dispersion, molecular diffusion, time dependent boundary condition and radioactive decay. They also contain various examples on natural convection to verify the original models of TOUGH2. A few of them are summarized below:

Case WL3: Heat conduction under time dependent boundary temperature. On one boundary of a one dimensional configuration, temperature as a linear function of time is imposed; no heat flux is assumed at other boundaries. The analytical solution and the results obtained with the modifications above shows a very good agreement.

Case NH2: Natural convection in a long drift (H << L) with a horizontal temperature gradient. For the steady state with constant material proporties, an analytical solution gives a linear valocity profile over the height H with zero at the center line and maximum magnitude at the drift walls. For H/L = 4/700, the deviation between the maximum Darcy velocity from the analytical solution and TOUGH2-value accounts to be less than 5 %, which is acceptable.

Case NV2: Natural convection in a shaft with a vertical temperature gradient. In this case, a natural convection in the full height occurs, if the Rayleigh number Ra > Ra_{crit}, which depends on the ratio heigth/width. TOUGH2 calculations with different Rayleigh numbers showed a proper tendency for the occuring of natural convection.

Case ZH20: Mass transport without dispersion in a one dimensional horizontal drift. In a case of a long drift with a constant tracer mass fraction at the entrance, a constant tracer profile moving with the pore velocity is to be expected. TOUGH2 shows a noticeable deviation due to numerical mixing, which decreases slowly with a finer grid (Fig. 1).

Case ZH21: Mass transport with dispersion. This case is like ZH20 but with a horizontal dispersion length of 10 m. A similar case is considered in /PRU 93/. In Fig. 2, the TOUGH2 results, which are obtained by using the complicated model of /PRU 93/, are compared with the analytical solution. As expected, the case ZH21 is closer to the analytical solution than case ZH20. But, the effect of numerical mixing is so significant that, even if physical dispersion is not included in a numerical model, one might meet the analytical solution with dispersion reasonably well by an appropriate choice of grid. Hence, it is concluded, if a numerical analysis shows an acceptable agrrement with an analytical solution, it does not necessarily mean that the numerical solution reproduces physical effects reasonably well. This case was also repeated with the original version /PRU 91/ and employing the modifications regarding the dispersive flux G in section 2 and not with the complicated dispersion model of /PRU 93/. Both calculations yield practicaly the same results. Hence it is concluded, the modifications are implemented correctly. The computation with model /PRU 93/ was about 4 times slower.

Case ZH22: Nuclide transport without dispersion. This case is same as ZH20 but with a tracer decay constant of 0.001 1/day within drift only and in case ZH23 also at the drift entrance. These cases are selected to verifiy the decay modifications of section 2. The agreement between the analytical solution /JAV 84/ and TOUGH2 results is satisfactory, whereas the deviation is mainly due to numerical mixing (Fig. 3).

All above cases are selected as basic examples to verify TOUGH2. Now, an additional case of nuclide transport under combined influence of natural convection, dispersion and decay in a simple network is considered (Fig. 4). The network with a initial vertical temperature gradient of 0.024 °C/m and with a heat generating waste located at the right end of the drift is discretized with 768 active elements and is analysed with original version of TOUGH2 including modifications of section 2 without employing the complicated dispersion module of /PRU 93/. As the module /PRU 93/ requires a

complete two dimensional model including insignificant elements located outside drifts and shafts, it is inexpedient and very time consuming for the present case. Figure 5 shows the tracer distribution at t = 20 years for three different cases. The tracer enters into the drift from the right side and is transported mainly through natural convection. As expected, in case NZ1 tracer mass fraction is far higher than in case NZ2 or NZ3, in which temperature and the tracer mass fraction decay at the drift entrance x = 1396 m with a half life period of 10 years. In present case, the dispersion influences the tracer distribution very insignificantly. In case NZ2 or NZ3, the tracer distribution shows a relative minimum around x = 1270 m, which is due to the time dependent boundary conditions at the drift entrance (see similar example TZ4 in /JAV 95/). Figure 6 shows the distribution of tracer mass fraction of case NZ2 at t = 20 years. Since no other tool is used to check the TOUGH2 results for the cases NZ1 to NZ3, it is difficult to access their accurancy. However, after analyzing various one and two dimensional basic examples, the results of NZ1 to NZ3 seem to be reliable.

4 Conclusions

Several modifications are introudced to simulate time dependent porosity, permeability and boundary conditions and radioactive decay of the secondary liquid component as well as to compute faster the diffusive and dispersive flux mainly for a network consisting of drifts and shafts. After treating various one and two dimensional basic examples to verify TOUGH2 with modifications, it is concluded that a qualified application of TOUGH2 can lead to reasonable results, however the effect of numerical mixing should not be underestimated.

References

/JAV 84/ Javandel, I. et al.: Groundwater Transport, American Geophysical Union, Washington, USA (1984)

/JAV 92/ Javeri, V.: Orientierende Analysen zur Gasausbreitung im Gebirge des Endlagers Konrad, GRS-A-1925 (Mai 1992)

/JAV 94/ Javeri, V.: Orientierende Analysen zur Naturkonvektion und Dispersion in porösen Medien, GRS-A-2159 (Aug. 1994)

/JAV 95/ Javeri, V.: Orientierende Analysen zum Nuklidtransport durch Naturkonvektion und Diffusion in porösen Medien, GRS-A-2190 (Jan. 1995)

/PRU 87/ Pruess, K.: TOUGH User's Guide, LBL-20700 (June 1987)

/PRU 91/ Pruess, K.: TOUGH2, LBL-29400 (May 1991)

/PRU 91A/ Pruess, K.: EOS7 module, LBL-31114 (Aug. 1991)

/PRU 93/ Pruess, K.: Dispersion module for TOUGH2, LBL-32505 (Sept. 1993)

Figure 1

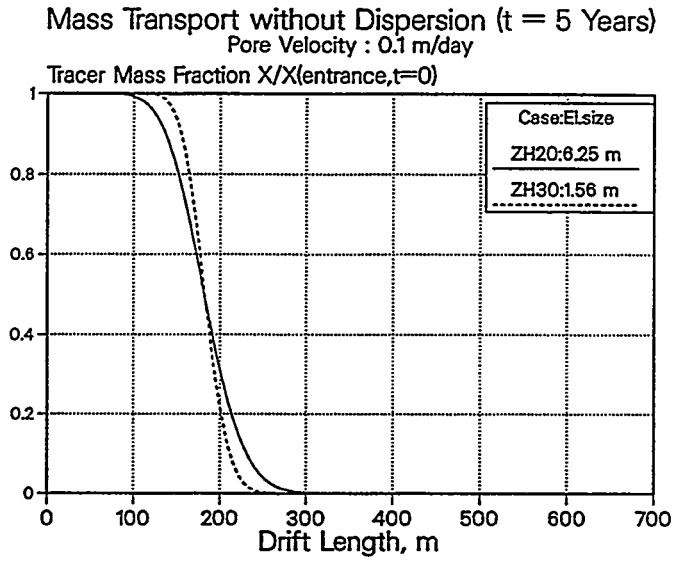

Figure 2

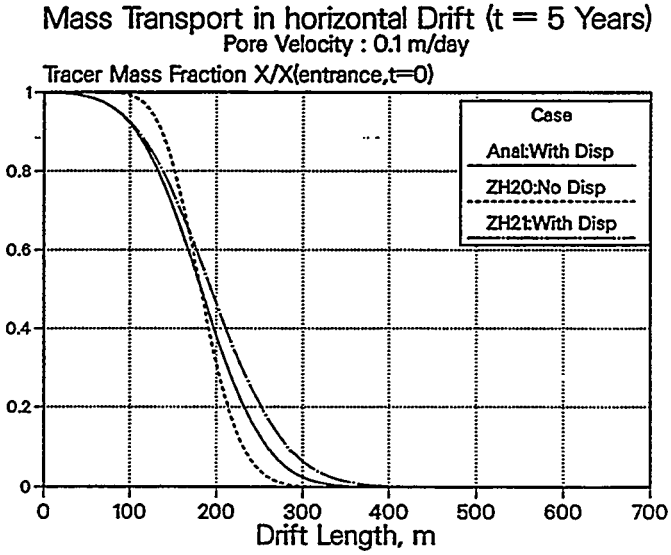

Figure 3

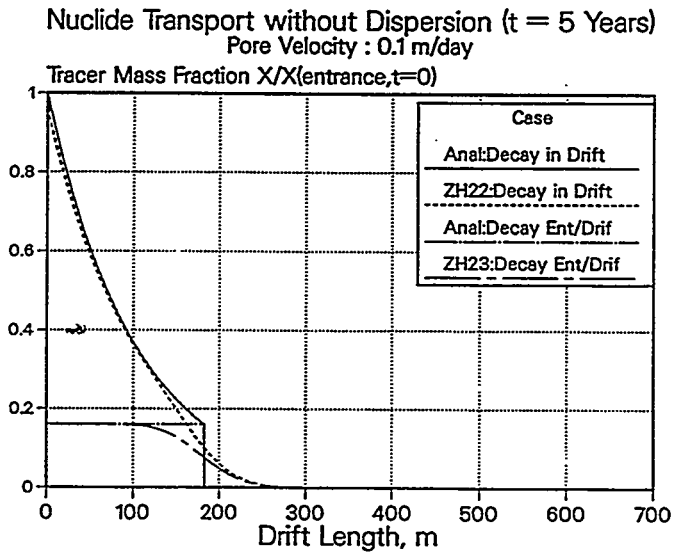

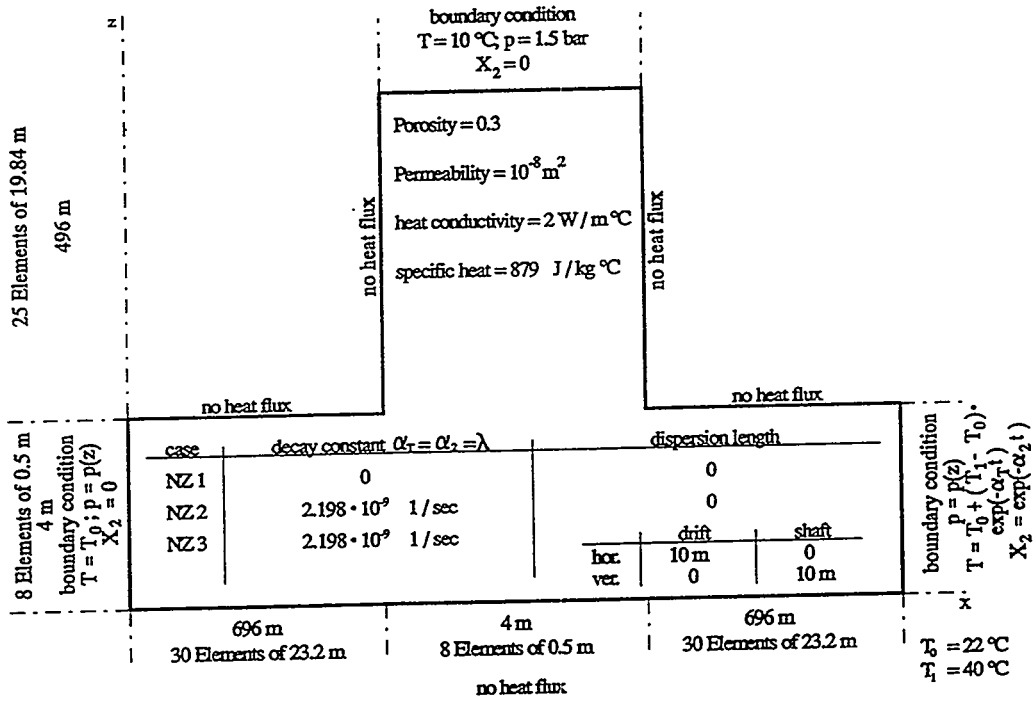

Figure 4: Model of nuclide transport in a simple network

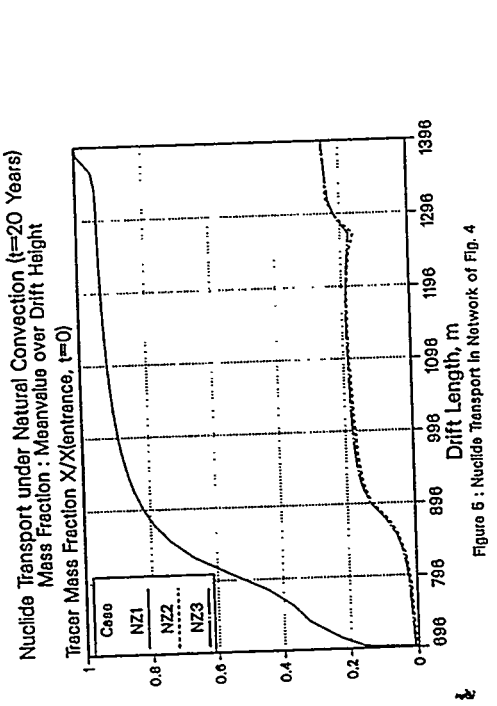

Figure 5 : Nuclide Transport in Network of Fig. 4

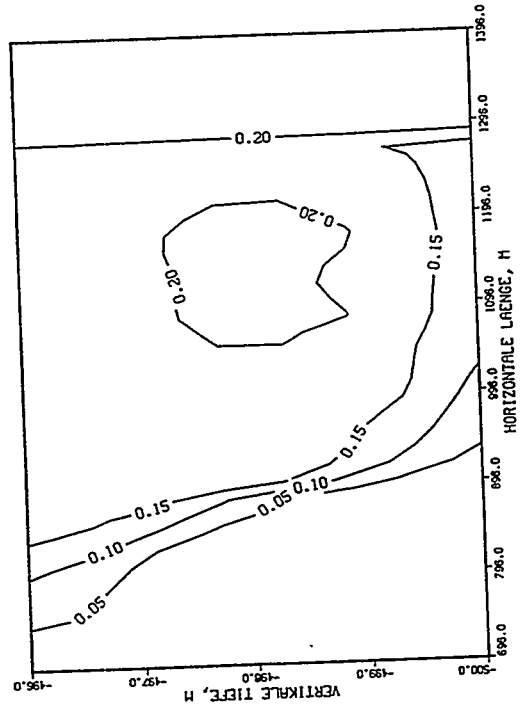

Figure 6 : Tracer Mass Fraction, Case NZ2, t = 20 Years

Investigation of Potential Water Inflow into a Ventilated Tunnel of the Proposed Low/Intermediate-Level Waste Repository in Switzerland

Stefan M. Eugster
Laboratory of Hydraulics, Hydrology and Glaciology, Swiss Federal Institute of Technology Zurich, Switzerland

Rainer K. Senger
INTERA Inc., Austin, Texas 78731, USA

Abstract

Design calculations of two-phase flow phenomena associated with the construction and ventilation of a tunnel were investigated to estimate the potential water inflow through discrete water-conducting features (WCFs) into the tunnel. The physical processes that were considered in numerical simulations include the transient propagation of the pressure decline into the formation (Valanginian Marl, initially fully saturated, no dissolved gas) as a result of the tunnel construction. Ventilation of the tunnel results in a reduction in relative humidity of the tunnel air which, in turn, causes evaporation of water at the tunnel wall and the potential development of an unsaturated zone into the formation. The objective of this study is to investigate under what conditions the tunnel wall appears wet or dry, i.e. whether WCFs can be identified in a ventilated tunnel by mapping water inflow patterns.
The simulation results indicate that inflow to the tunnel decreases with time approaching steady state flow rates under single-phase flow conditions, which is lower than the evaporation rate. The water inflow rate decreased more rapidly for a first model scenario (WCF parallel to the tunnel axis), caused by linear flow through the WCF, than for a second model scenario (WCF perpendicular to the tunnel axis), characterized by radial flow toward the tunnel. Similarly, the desaturation zone extends farther into the WCF under linear flow than under radial flow.

1. Introduction

The following study is in connection with the safety assessment for the proposed repository for low/intermediate level (L/ILW) radioactive wastes at Wellenberg, Switzerland. The design of the proposed subsurface repository consists of a horizontally accessable cavern system in the low-permeability unit of the Valanginian Marl.
The access tunnel will yield hydrogeologic information on the host rock which is important for the safety assessment of the proposed repository. The objective of the numerical simulations are to assess if a WCF with a transmissivity of 1.E-9 m^2s^{-1} can be identified as a wet area on the tunnel wall. For this purpose, the following physical processes were simulated.

(i) The construction of the tunnel creates a transient pressure perturbation, which propagates into the formation.

(ii) Ventilation reduces the relative humidity in the tunnel air, resulting in a significant capillary suction pressure at the tunnel wall, thereby increasing the hydraulic gradient for water flow toward the tunnel.

(iii) The reduced air humidity in the tunnel results in the evaporation of inflowing water from the formation at the tunnel wall. The equivalent capillary suction pressure associated with the reduced air humidity causes a desaturation front to propagate into the formation creating two-phase flow conditions near the tunnel.

An illustration of the physical processes associated with the construction and ventilation of a tunnel is shown in Fig. 1.

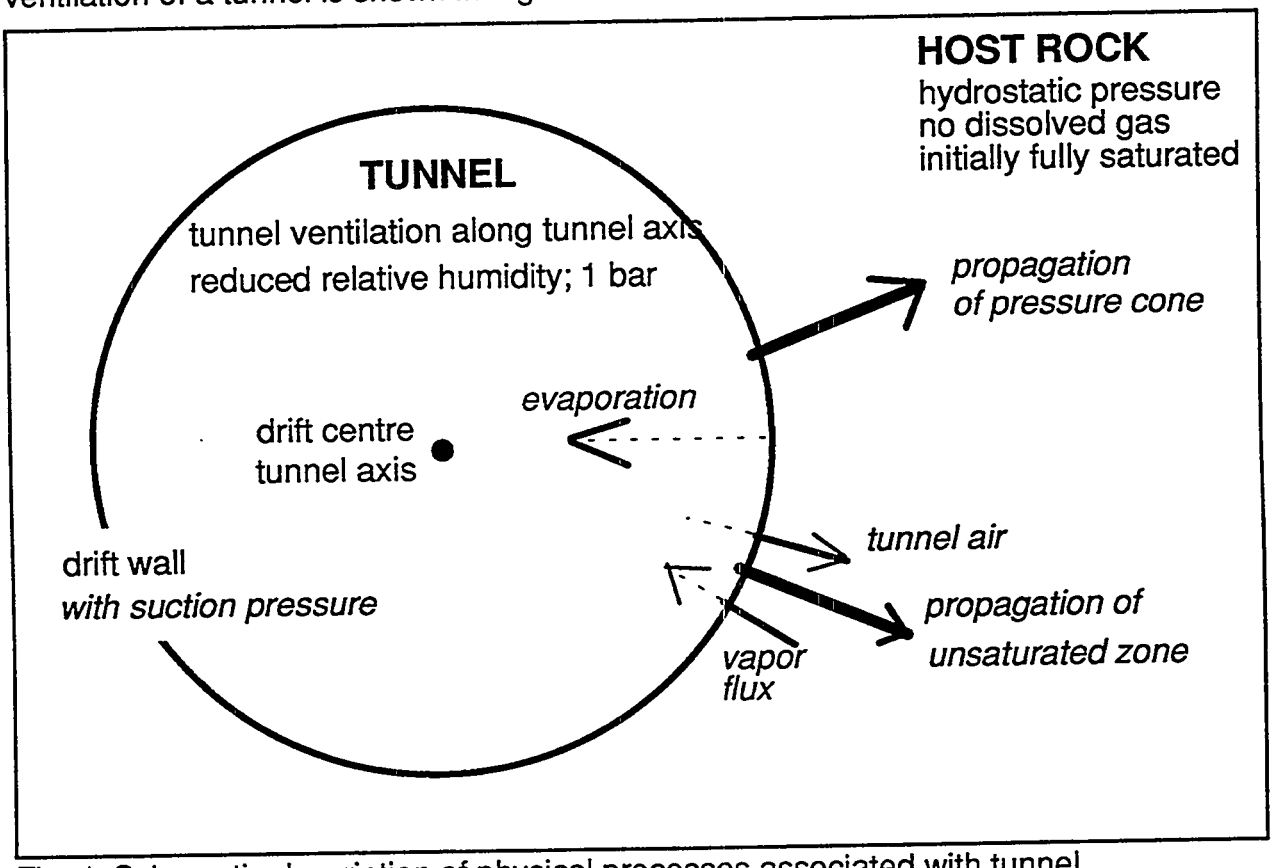

Fig. 1: Schematic description of physical processes associated with tunnel construction and ventilation

To determine whether the tunnel wall will appear wet or dry, the simulated water flow into the tunnel is compared to the potential evaporation rate that is computed as a function of reduced humidity and air velocity.

2. Model Geometry

A 2-D cross-sectional model perpendicular to the tunnel axis was used for the numerical simulations. In the first model scenario the WCF is parallel (type P) to the tunnel axis, represented by a 45 degree inclined, 1-m wide and about 400-m long zone (linear flow model) having at least two orders of magnitude higher permeability than the adjacent matrix. In the second model scenario (type Q), the plane of the WCF is perpendicular to the tunnel axis involving radial flow through the WCF toward the tunnel.

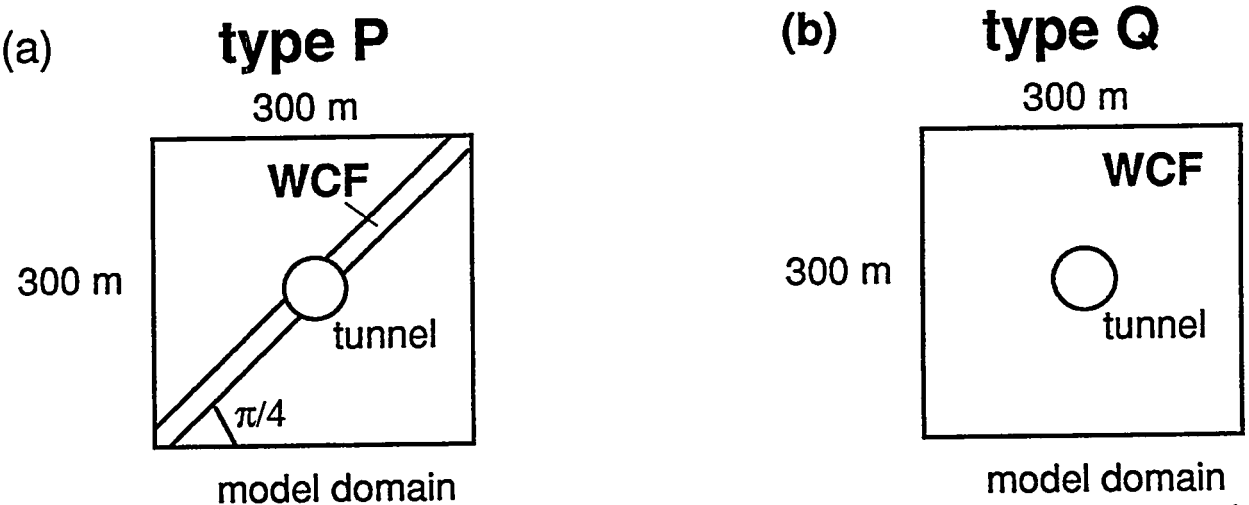

Fig. 2: Schematic representation of the model scenarios (a) WCF parallel to the tunnel axis (linear flow model) and (b) WCF perpendicular to the tunnel axis (radial flow model)

Initially hydrostatic pressures were assumed in the host rock and atmospheric pressure conditions in the tunnel. Transient water inflow into the tunnel was simulated with prescribed suction pressures at the tunnel wall as a function of the relative humidity and for a range of permeabilities of the WCF (sensitivity study). The simulated water inflow was compared with the potential evaporation rates that were analytically estimated from the relative humidity and wind velocity in the tunnel to determine, if and how long after tunnel excavation the tunnel wall appears wet or dry.

The following two analytical solutions are used to estimate the evaporation rate in the tunnel according to SVEDRUP (ref. in DRACOS, 1980)

$$E_v = 0.622 \cdot \frac{\rho_a}{p_a} \cdot \kappa^2 \cdot u \cdot (e1 - e2) \cdot \ln\left(\frac{z}{k}\right)^{-2} \qquad (1)$$

and (WATANABE & BOSSART, 1992)

$$E_v = \frac{\Delta Q}{\Delta t} = -\frac{D}{\Delta x \cdot R} \cdot \left(\frac{p_{sb} \cdot h_b}{T_b} - \frac{p_{sa} \cdot h_a}{T_a}\right) \qquad (2)$$

For more detailed information on the analytical and technical aspects of determination potential evaporation rates, the reader is referred to DRACOS (1980), WATANABE & BOSSART (1992) and EUGSTER & SENGER (1994).

Estimation of the evaporation rate is based on the assumption of a constant relative humidity in the tunnel and a linear decrease of humidity from 100% to a constant value within the first few centimeters away from the wall.

Tunnel ventilation is implemented in the numerical model as a prescribed boundary condition at the tunnel wall. This boundary condition is defined as an equivalent capillary suction pressure, corresponding to the reduced humidity according to the Kelvin equation (3) (EDLEFSON & ANDERSON, 1943). The capillary suction pressure increases the gradient of liquid flow toward the tunnel.

$$\phi_{suc} = \ln(h) \cdot \rho \cdot \frac{RT}{M_w} \qquad (3)$$

3. Results

In order to answer the main question "wet or dry?" the results concerning water inflow vs. evaporation are illustrated in Fig. 3 and Fig. 4 for the base cases and in Tab. 1 for all simulated cases.

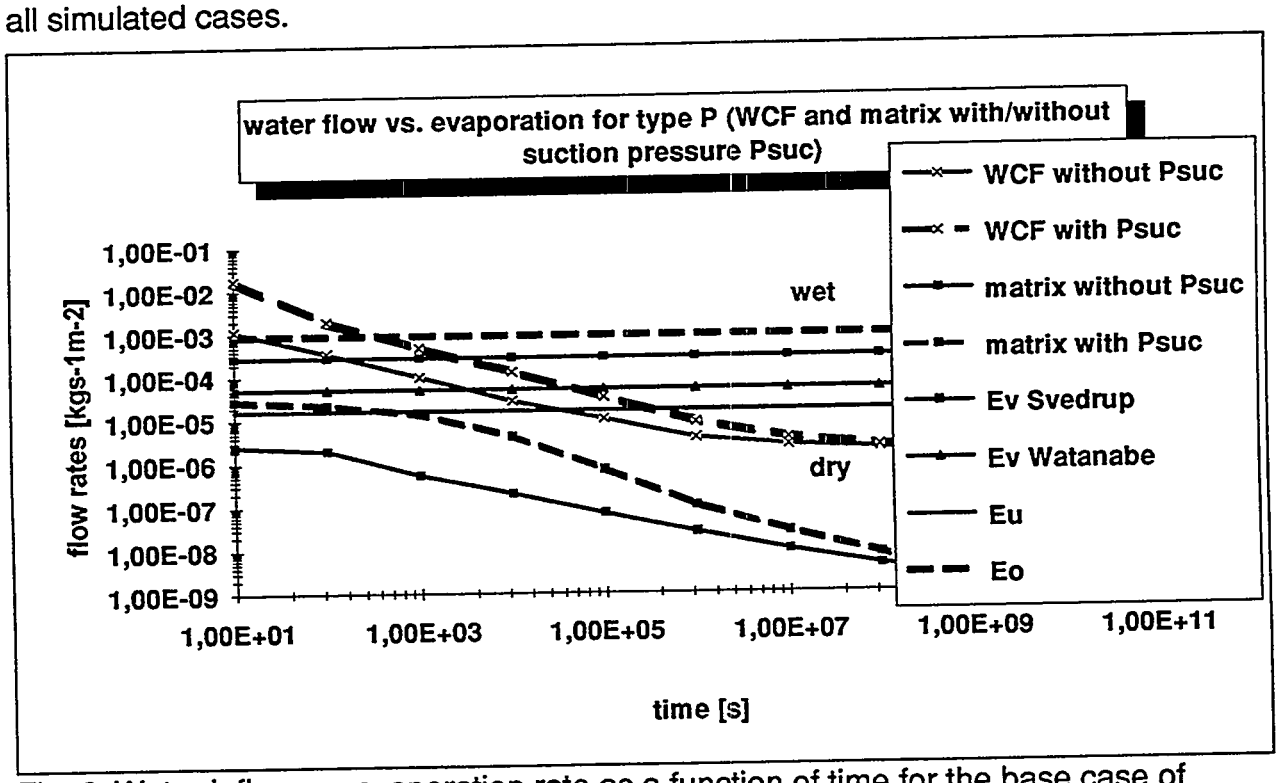

Fig. 3: Water inflow vs. evaporation rate as a function of time for the base case of type P (matrix and WCF)

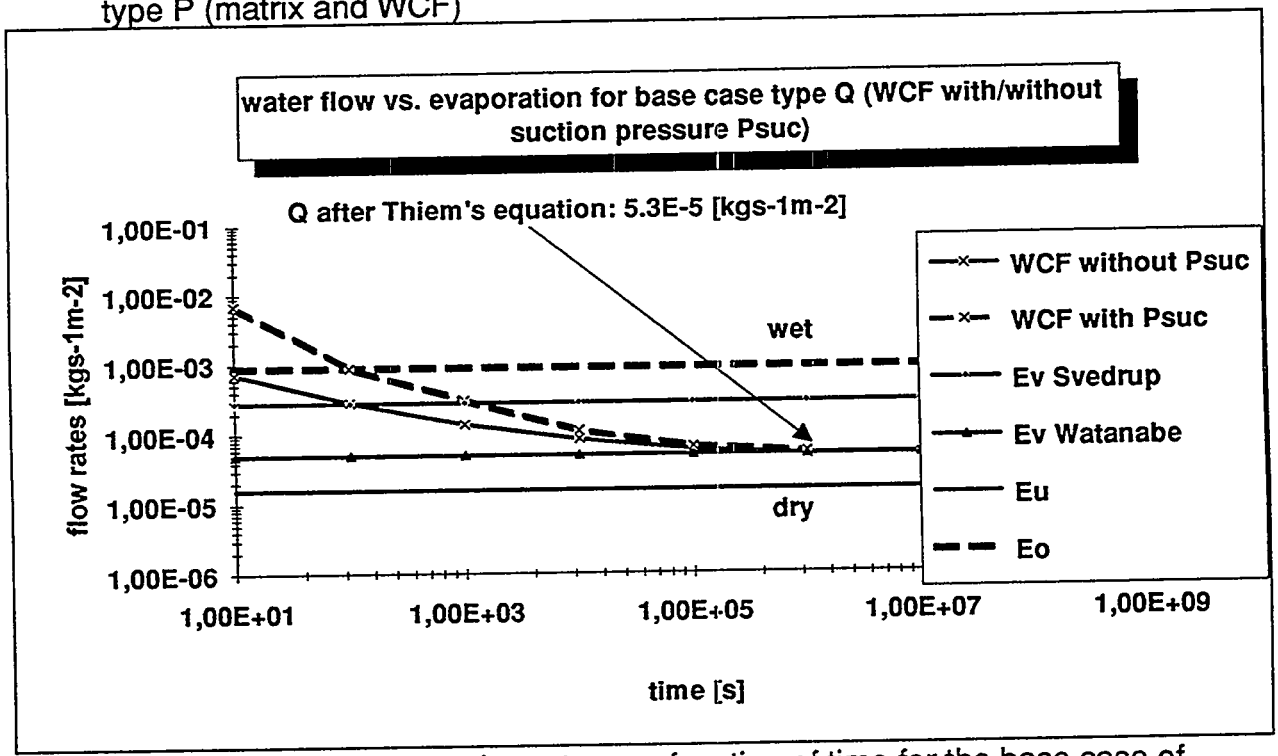

Fig. 4: Water inflow vs. evaporation rate as a function of time for the base case of type Q

The results indicate that inflow to the tunnel decreases with time approaching steady state flow rates under single-phase flow conditions, which is below the evaporation rates in the tunnel for type P (linear flow model) and about the evaporation rates for type Q (radial flow model). The equivalent suction pressure increases the water flow rate. A dry WCF can be observed if the evaporation rate (lower confidence bound Eu) is greater than the flow rate; this is reached after about 4 days in the example of Fig. 3. The flow behavior for the matrix also illustrated in Fig. 3 indicates dry conditions after a short time. Fig. 4 shows a steady state liquid flow rate that is about equal to the evaporation rate. In this case (type Q) it is not clear if the WCF is wet or dry at the tunnel wall.
The results of Table 1 indicate that for the linear flow model (type P), the WCF appears dry after a relatively short time for typical values of permeability and relative humidity. The WCF therefore cannot be identified at the tunnel wall. On the other hand, the results for the radial flow model (type Q) show a somewhat higher inflow. Therefore, it is not clear, whether the WCF can be identified or not. The desaturation zone extends farther into the WCF under linear flow than under radial flow (not illustrated).

Tab.1: A qualitative summary of all modeled cases for both scenarios type P and Q

evapo-ration rates h T	ESv: 4.67E-04 EWa: 8.38E-05 Eu: 2.65E-05 Eo: 1.48E-03 **50%**	ESv: 2.80E-04 EWa: 5.03E-05 Eu: 1.59E-05 Eo: 8.85E-04 **70%**	ESv: 0.93E-04 EWa: 1.68E-05 Eu: 5.31E-06 Eo: 2.94E-04 **90%**
1.E-8	**P dry after about 11 days** **Q never dry**	**P never dry** **Q never dry**	**P never dry** **Q never dry**
1.E-9	**P dry after about 1.5 days** **Q never dry**	**P dry after about 4 days** **Q never dry (see also Fig. 3 and 4)**	**P dry after about 25 days** **Q never dry**
1.E-10	**P dry after about 0.3 days** **Q dry after about 0.2 days**	**P dry after about 1 day** **Q dry after about 0.7 days**	**P dry after about 4.5 days** **Q dry after about 1 year**

ESv evaporation rate after SVEDRUP [$kgs^{-1}m^{-2}$]
EWa evaporation after WATANABE [$kgs^{-1}m^{-2}$]
Eu lower confidence bound of evap. [$kgs^{-1}m^{-2}$]
Eo upper confidence bound of evap.[$kgs^{-1}m^{-2}$]
T transmissivity of WCF [m^2s^{-1}]
h relative humidity in tunnel [-]

4. Discussion

Some points concerning the results have to be mentioned:

(i) The pressure decline due to tunnel construction was considered instantaneous. This leads, specially in the beginning, to an overestimation of water inflow.

(ii) No dissolved gas in the formation water was modeled. Potential degassing due to the induced pressure decline would lead to a smaller relative permeability for water. Neglecting this effect leads to an overestimation of water inflow.

(iii) "Enhanced binary diffusion" and "vapor pressure lowering" didn't have a significant influence on the water flow. A certain influence was observed for vapor and air flow which were not relevant in this study.

(iv) The linear flow model (type P) shows a preferential propagation of the unsaturated zone along the WCF. An unsaturated zone is developping from the desaturated part of the WCF into the matrix.

5. Summary

The results of the linear flow model (type P) show for typical values of permeability (WCF) and humidity (tunnel air) a dry surface for the WCF at the tunnel wall after a reasonable short time of about 1 week. For the radial flow model (type Q) it is not possible to predict whether the WCF is wet or dry at the tunnel surface. The extent of the unsaturated zone is larger for type P than for type Q.

Acknowledgments

This work was carried out for the Swiss National Cooparation for the Disposal of radioactive Waste (Nagra). We are especially grateful to P. Vinard (Nagra) for his support.

References

BAER, T., BAERTSCHI, P., BOSSART, P., GIMMI, T., FLUEHLER, H., LANG, J., LAESER, H.P., MALIKI, M., MEIER, E., RAZ, U., SCHNEEBELI, U., WALCZAK, R., WYDLER, H. 1994: Nearfield 2-Phase Phenomena. In: FRIEG, B. & VOMVORIS, S., (eds.): GTS Investigation of Hydraulic Parameters in the Saturated and Unsaturated Zone of the Ventilation Drift, Chapter 2, NAGRA Technical Report NTB 93-10, Wettingen, Switzerland

BEAR, J. 1979: Hydraulics of Groundwater, McGraw-Hill, p.306

BROOKS, R., COREY, A. 1964: Hydraulic properties of porous media, Hydrology Paper No.3, Colorado State University

DRACOS, TH. 1980: Hydrologie, Springer Verlag, Wien, p.44 ff.

EDLEFSEN, N. E., ANDERSON, A. B. C. 1943: Thermodynamics of soil moisture, Hilgardia, 15(2), 31-298

EUGSTER, S.M., SENGER, R.K. 1994: Nachweisgrenze von Transmissivität eines transmissiven Elementes (TE) an der ventilierten Stollenwand, NAGRA Interner Bericht NIB 94-59, Wettingen

FINSTERLE, S. 1993: Inverse Modellierung zur Bestimmung hydrogeologischer Parameter eines Zweiphasensystems, VAW Mitteilungen 121, Zürich

FINSTERLE, S., PRUESS, K. 1993a: Design Calculation for a Combined Ventilation and Brine Injection Experiment at the Grimsel Rock Laboratory, NAGRA Internal Report NIB 93-122, Wettingen, Switzerland

FINSTERLE, S., PRUESS, K. 1993b: Solving the Estimation-Identification Problem in Two-Phase flow Modeling, Lawrence Berkeley Laboratory report LBL-34853, Berkeley, CA

FINSTERLE, S., VOMVORIS, S. 1991: Inflow to Stripa Validation Drift under Two-Phase Conditions: Scoping Calculations, NAGRA Internal Report NIB 91-40, Wettingen, Switzerland

FLUEHLER, H., SCHULIN, R., BUCHTER, B., ROTH, K. 1990: Methoden und Konzepte der Bodenphysik, Teil B, Modellierung des Stofftransportes im Boden, S. 33 ff., Zürich

HÖLTING, B. 1992: Hydrogeologie, Enke Verlag, Stuttgart, S. 123 ff.

MARSILY, G. DE 1986: Quantitative Hydrology, Academic Press Inc., San Diego, CA, S. 165 f.

PRUESS, K. 1991: TOUGH2 - A general-purpose numerical simulator for multiphase fluid and heat flow, Lawrence Berkeley Laboratory report LBL-29400, Berkeley, CA

PRUESS, K. 1987: TOUGH user's guide, NURE/CR-4645, SANDIA-7104, LBL-20700, Berkeley, CA

VAN GENUCHTEN, M. TH. 1980: A closed form equation for predicting the hydraulic conductivity of unsaturated soils, Soil Sci. Am. J., 44(5), 892-898

WATANABE, K., BOSSART P. 1992: Complementary Methods for Measuring Water Inflow into the Ventilation Drift. In: VOMVORIS, S. & FRIEG, B., (eds): GTS Overview of NAGRA Field and Modeling Activities in the Ventilation Drift (1988 - 1990), Chapter 3, NAGRA Technical Report NTB 91-34, Wettingen, Switzerland

THE USE OF TOUGH2 FOR THE LBL/USGS 3-DIMENSIONAL SITE-SCALE MODEL OF YUCCA MOUNTAIN, NEVADA

Gudmundur Bodvarsson
Lawrence Berkeley Laboratory
1 Cyclotron Rd., Mail Stop 50E
Berkeley, CA 94720
510-486-4789

Gang Chen
Lawrence Berkeley Laboratory
1 Cyclotron Rd., Mail Stop 50E
Berkeley, CA 94720
510-486-7107

Charles Haukwa
Lawrence Berkeley Laboratory
1 Cyclotron Rd., Mail Stop 50E
Berkeley, CA 94720
510-486-4160

Edward Kwicklis
U.S. Geological Survey
Box 25046, Mail Stop 421
Denver Federal Center
Denver, CO 80225-0046
303-236-6228

INTRODUCTION

The three-dimensional site-scale numerical model of the unsaturated zone at Yucca Mountain is under continuous development and calibration through a collaborative effort between Lawrence Berkeley Laboratory (LBL) and the United States Geological Survey (USGS). The site-scale model covers an area of about 30 km^2 and is bounded by major fault zones to the west (Solitario Canyon Fault), east (Bow Ridge Fault) and perhaps to the north by an unconfirmed fault (Yucca Wash Fault). The model consists of about 5,000 grid blocks (elements) with nearly 20,000 connections between them; the grid was designed to represent the most prevalent geological and hydro-geological features of the site including major faults, and layering and bedding of the hydro-geological units. Further information about the three-dimensional site-scale model is given by Wittwer et al. (1992, 1993, 1994) and Bodvarsson et al. (1994, 1995).

The general approach used in the development of the current site-scale model is to start with a detailed three-dimensional representation of the geology and hydro-geology of the site and to incorporate the different important processes and components (e.g., water, gas, heat) in stages. The model is designed to readily accommodate future requirements and complexities as additional data are collected, and as important features of the basic underlying conceptual model are identified or changed. Submodels are used to investigate specific hypotheses and their importance before incorporation into the three-dimensional site-scale model. The primary objectives of the three-dimensional site-scale model are to:

(1) quantify moisture, gas and heat flows in the ambient conditions at Yucca Mountain,

(2) help in guiding the site-characterization effort (primarily by USGS) in terms of additional data needs and to identify regions of the mountain where sufficient data have been collected, and

(3) provide a reliable model of Yucca Mountain that is validated by repeated predictions of conditions in new boreholes and the ESF and has therefore the confidence of the public and scientific community.

The computer code TOUGH2 developed by K. Pruess (1990) at LBL was used along with the three-dimensional site-scale model to generate these results. We have also incorporated gas flow and the geothermal gradient into the site-scale model. In this paper, we also describe the three-dimensional site-scale model emphasizing the numerical grid development, and then show some results in terms of moisture, gas and heat flow.

THE SITE-SCALE MODEL AND ITS PARAMETERS

Figure 1 shows the horizontal grid used in the three-dimensional site-scale model; the grid was designed based on locations of existing and proposed boreholes, traces of selected major faults and spatial distributions of infiltration zones and outcrops (Wittwer et al., 1992). The major faults explicitly considered in the model include the Ghost Dance Fault, the Abandoned Wash Fault and the Dune Wash Fault. These three faults have large offsets and may therefore greatly affect the three-dimensional moisture flow within the mountain. The subsurface formation consists of a series of fractured welded ashflow tuffs (Tiva Canyon, Topopah Spring tuffs) and porous non-welded ashflow and ashflow tuffs (Yucca Mountain-, Pah Canyon, Calico Hills, Prow Pass, Bullfrog tuffs, bedded tuffs). Isopach maps of these

most important hydro-geological units were prepared by Wittwer et al. (1992) based on all available borehole data at the time and these are used in the model with appropriate modifications as new data became available.

For the numerical simulations one requires hydrological property values for the rock matrix blocks and the fractures for each gridblock. The most important hydrological parameters include formation porosities, permeabilities and characteristic curves (relationships between saturations, capillary pressures and relative permeabilities). In this work we use hydrological parameter values similar to those employed in earlier work (Wittwer et al., 1994). Fourteen different hydrological properties are used for the seventeen model layers with two sets of values representing the Tiva Canyon unit, three for the bedded non-welded tuffs (Paintbrush), five for the Topopah Spring welded unit and four sets representing the vitric and zeolitic portions of the Calico Hills formation. In general, rock matrix permeabilities of the welded units, the Tiva Canyon and Topopah Spring formations are low or on the order of 10^{-18} m^2, whereas higher permeabilities are used for the non-welded tuffs of the Paintbrush unit (~ 10^{-13}m^2) and the Calico Hills (10^{-13}m^2 for the vitric part and 10^{-16} m^2 for the zeolitic part). Matrix porosities also vary greatly among and within the different formations.

The fracture medium properties were developed using the equivalent continuum approximation developed by Klavetter and Peters (1986), which assumes capillary equilibrium between the fractures and the adjacent rock matrix blocks.

Due to lack of hydrological information on fault properties at Yucca Mountain, we have taken the approach of assuming extreme hydrological properties in order to understand the importance of the faults and their properties. Three different assumptions regarding the hydrological behavior of the faults are made as follows:

(1) the faults are capillary barriers,
(2) the faults are impermeable, and
(3) the faults are permeable and have characteristic curves similar to the bedded tuffs of the Paintbrush units.

NUMERICAL GRID

The TOUGH2 computer code used in the site scale model study is based on the integrated finite-difference method and therefore, allows to create irregular gridblocks. The grid was designed in order to accommodate the spatial distribution of main hydrogeological units, the effects of major structural features, the sharp thermodynamic gradients at the boundaries between hydrogeological units, and relevant surficial information.

The three-dimensionnal numerical grid consisting of about 5000 elements and 20000 connections was designed in two steps. First, all available surficial information was used to create an horizontal two-dimensional grid. Then, data from isopach maps of hydrogeological units were integrated to vertically develop the horizontal grid between the ground-surface and the water table, thus creating the 3D grid. This step of grid generation required a lot of manual

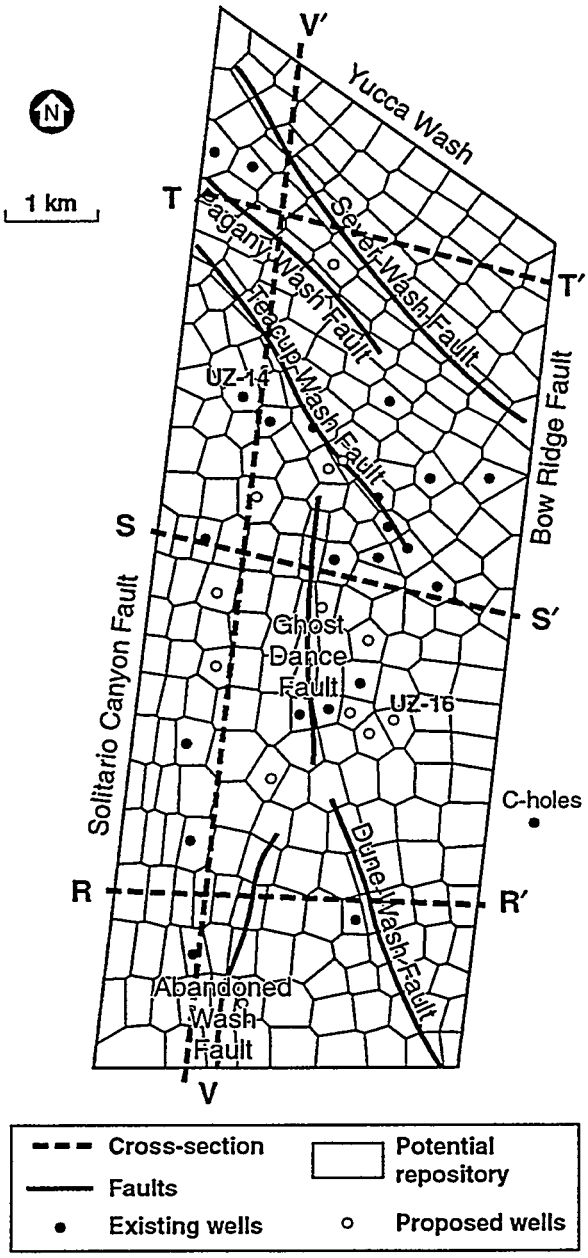

Figure 1. Areal extent and horizontal grid of the 3-D site-scale model. Also shown are some of the major faults in the area.

manipulation in order to handle small elements at interfaces and the fault offsets.

Horizontal Grid

The locations of the nodal points for the horizontal two-dimensional grid were determined based on different data. They are the locations of existing or proposed boreholes, the major faults, such as the Ghost Dance fault, Dune Wash fault and Abandoned Wash fault, the distribution of the different infiltration zones properties and rate, and different exposed rock types. The grid blocks are also designed to have gradual changes in element sizes in order to minimize errors in representing gradients in thermodynamic conditions, hence minimizing model inaccuracies.

After all the nodal points were located, an automatic numerical grid generator was used to develop the horizontal grid. Later (1994) this 2D horizontal grid was modified to include the trace of the ESF by aligning elements along it.

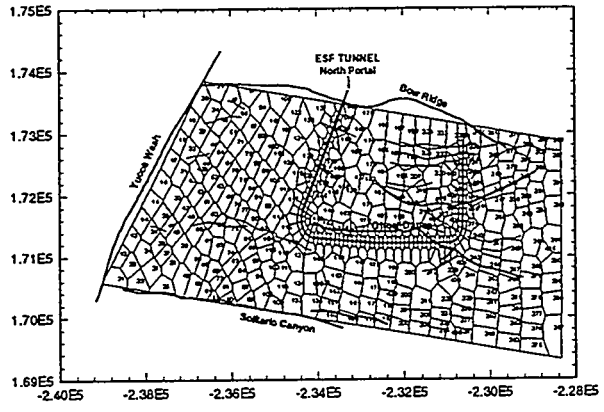

Figure 2. Horizontal grid for the site-scale model including the trace of the ESF tunnel.

Vertical Grid

The vertical grid (Fig. 3) has seventeen layers of gridblocks which represent, as closely as possible, the lithological variations within the main units. The offsets along the three fault zones (Ghost Dance-, Abandoned Wash-, and Dune Wash faults) were explicitly represented within the three-dimensional grid. The grid blocks along the fault horizontally connect the sublayers on each side of the faults through a double number of gridblocks. This model geometry is consistent with the complex geology of this heavily faulted region.

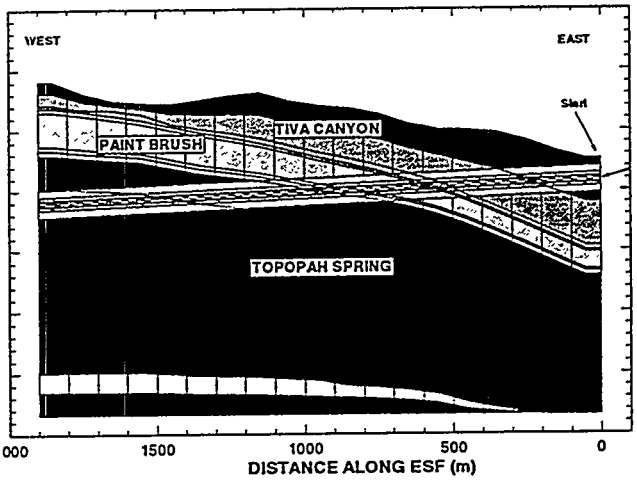

Fig. 3. Vertical cross section including the ESF Tunnel.

Gridblocks with Offsets

A major problem for gridblocks along the fault traces was the proper way to connect the sharp offsets of the units on two sides of the fault through the fault itself.

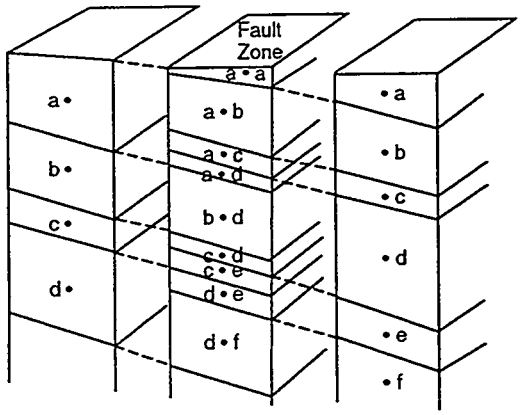

Figure 4. Example of grid design by fault zones.

This was solved by creating a double number of sublayers for the fault-gridblocks, and modifying the mesh generator to connect them by their common interfaces to the adjacent gridblocks. A schematic representation of this grid design is given in Figure 4. To obtain the right volumes and interfaces, dummy elements were introduced in the faults and in the columns adjacent to fault columns. These dummy elements helped generate the proper connections and maintain the observed fault offsets.

New 3D Grid Generator

We are developing a new flexible grid generator with arbitrary 3D grids and fault offsets (Fuller et al., 1995). The

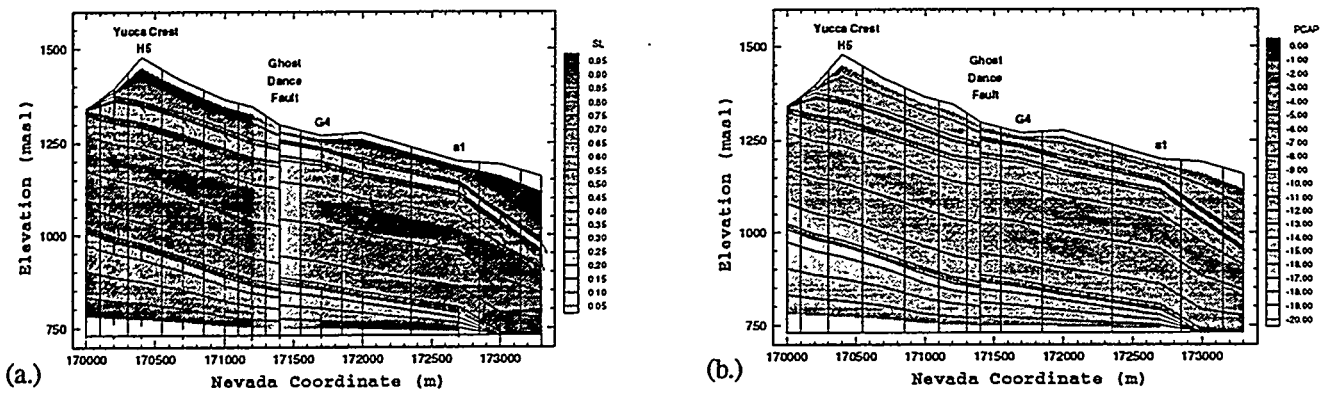

Figure 5. Two-dimensional cross section S-S' showing calculated distributions of liquid saturation (2a) and capillary pressure (2b).

data input for the generator will be a combination of the following:

(1) Surface and subsurface location of wells and tunnels. Location, dip, strike and offset of faults as well as the thickness of fault zones.
(2) Description of each layer or horizon (hydrogeologic) unit: depth to each unit (isopach), dip of layers, thickness of layers, elevation of layers.

Given the combination of the above data of a flexible 3-D finite element mesh, element and connections information is generated for input to a numerical simulation routine e.g. TOUGH2. We require for all the elements (including the fault and boundary elements), the interface areas, the interface distances, the element volume at each xyz coordinate.

The grid generator is now completed to the point that the site-scale model grid can be automatically generated in less than a minute using several input files containing the data listed above. New faults can readily be added to the model with arbitrary offsets.The grid generator is now being extended to the explicit modeling of tunnels and wells in which transition from radial to rectangular geometry is desired.

MOISTURE FLOW SIMULATIONS

We have conducted a series of three-dimensional moisture flow simulations in order to investigate possible patterns of moisture flow within Yucca Mountain. The approach used is to assume a given average infiltration rate (usually 0.1mm/year, although there is no definite evidence for this value), then assume an infiltration distribution (either uniform or spatially variable), and finally use the three-dimensional site-scale model to compute the moisture flow within the mountain for assumed hydrological characteristics of the major faults. All of these assumptions have to be made in the current work because the site-characterization effort has only recently started and the various model input parameters, such as the effective infiltration rates and distributions, hydrological fault property values, etc., are poorly known at best, but will be much better quantified as the site-characterization effort progresses.

A. Uniform Infiltration Rate

A series of simulations were conducted using the three-dimensional site-scale model assuming an uniform (areally) infiltration rate. In these simulations the faults were modeled assuming either "capillary barrier" behavior or "permeable fault" behavior. Figure 5 shows typical results of the simulations in terms of two-dimensional cross-section S-S', which location is shown in Figure 1. Cross section S-S' extends across Yucca Mountain from west to east through wells H5, G4 and a1, and intersects the Ghost Dance fault. An average uniform infiltration rate of 0.1 mm/year is used. Typically steady-state results, with insignificant changes in saturation (<0.001) are reached after about 1016 to 1017 seconds (3x108 years) of simulation time.

The results shown in Figure 5 illustrate low saturation in the Ghost Dance fault, which is to be expected because of the assumed "capillary barrier" nature of the fault. Low liquid saturations, on the order of 40% or so, are found in the Paintbrush unit and in the vitric portion of Calico Hills formation. On the other hand, the welded tuff such as Tiva Canyon and the Topopah Spring units show liquid saturation exceeding 80% for almost the entire formation, again reflecting the relatively low matrix permeabilities of these units. In general, the dipping of the formations in the model leads to significant lateral flow in the Paintbrush unit and various sub-units of the Topopah Spring formation. Capillary pressures are mostly above -10 bars for most of the layers except the bottom part of Topopah Springs and the top part of Calico Hills vitric, near the western boundary of the model (Figure 5b).

Figure 6 shows four nearly horizontal slices of normalized vertical moisture flow within the mountain. Here we

define the normalized vertical moisture flow as the vertical moisture flow at any location (x, y, z) normatized (divided) by the assumed average infiltration rate at the ground surface (in this case, 0.1mm/year). These horizontal slices are shown for locations above the Paintbrush non-welded units (bottom of Tiva Canyon), right below the bedded units (top of Topopah Spring), bottom of Topopah Spring, and at the water table. Figure 6a shows that the moisture flow in the Tiva Canyon unit is near vertical with almost no variation in normatized vertical flux (everywhere about 100% of the net infiltration-rate at the ground surface). Figure 6b, which represents a location below the Paintbrush unit, shows the large degree of variations due to lateral flow within that unit when compared to Figure 6a. In general, lateral flow occurs towards the east due to the dipping of the layers, with moisture accumulation close to major faults (assumed to be capillary barriers in this case) and model boundaries (e.g., Bow Ridge Fault is assumed to be an impermeable boundary in the model). In the horizontal slice representing the bottom of the Topopah Spring units (Figure 6c), additional lateral flow is evident with drying of regions west of major faults and moisture accumulation near the faults. This trend is further enhanced at the water table (Figure 6d).

Several important conclusions can be drawn from these results keeping in mind the underlying assumptions of uniform infiltration of 0.1mm/year and faults acting as "capillary barriers":

(1) Most of the lateral moisture flow occurs in the Paintbrush non-welded units;
(2) There is considerably more lateral flow in the southern part of Yucca Mountain than the northern part, mostly because of steeper dipping layers in the southern part. In

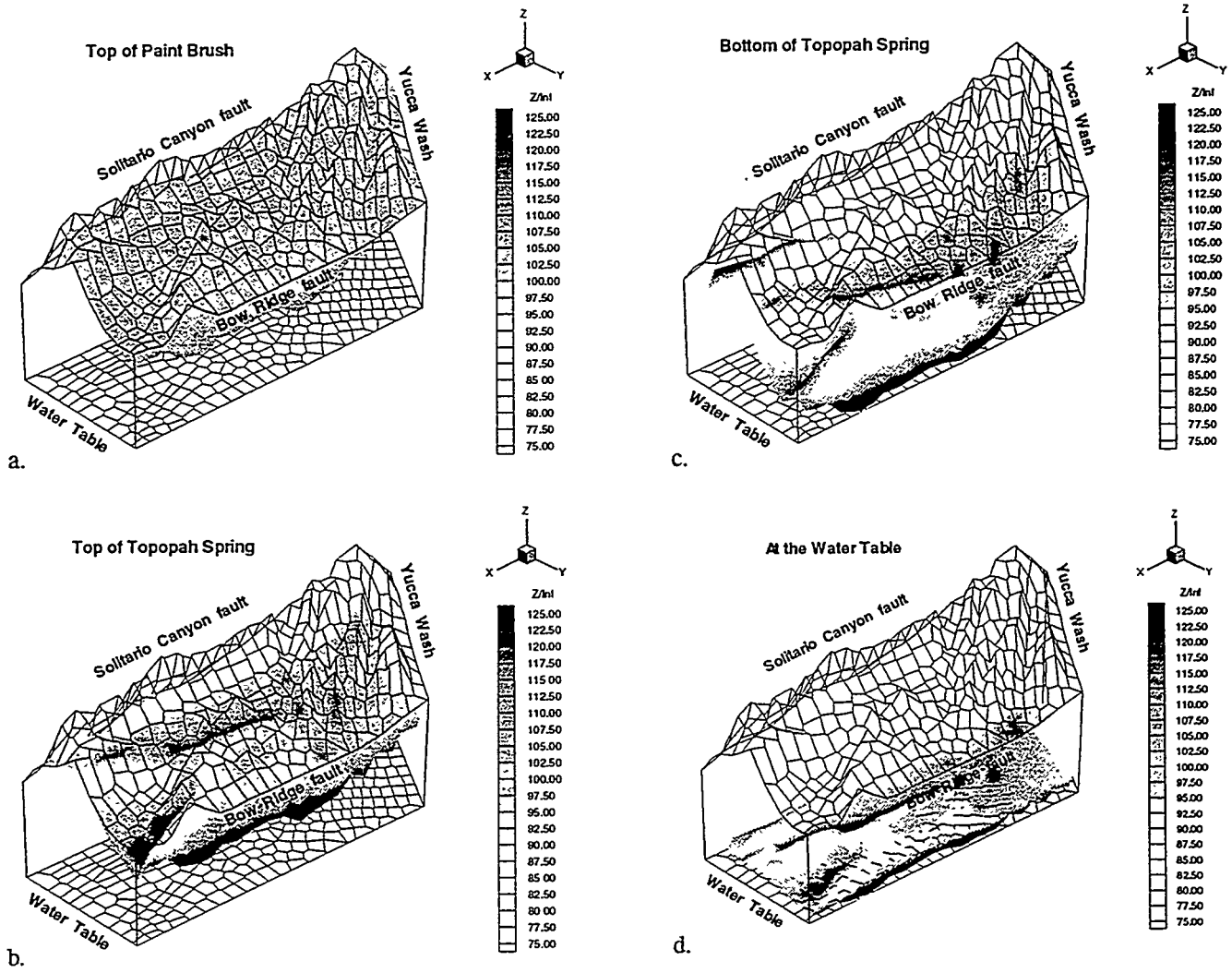

Figure 6. Calculated normalized vertical moisture fluxes (% of infiltration at ground surface) at different depths in the site-scale model for the case of "capillary barrier" faults, and an uniform areal infiltration rate of 0.1 mm/year.

some regions north of Ghost Dance Fault near one-dimensional vertical moisture flow is exhibited from these model calculations.

(3) Large vertical flow is found near major faults due to lateral flow and moisture accumulation near the faults because of their "capillary barrier" nature in these simulations. Hence, measurements of saturations and capillary pressures in rock matrix blocks near faults may give as much information about flow characteristics of the faults, as measurements of these quantities in the faults themselves.

A series of numerical simulations were also performed assuming non-uniform distribution of infiltration at the ground surface. Due to space limitations, these simulations are not described here, but the reader is referred to Bodvarsson et al. (1994).

MODEL EFFICIENCY

In order to investigate the model efficiency, we performed 1-D, 2-D, and 3-D simulations using the TOUGH2 standard version as well as a decoupled version which only solves for moisture flow. We used a 0.1mm/year uniform moisture infiltration at the top for all of these runs. An additional layer was put on the top of the mountain to simulate the atmospheric condition for the fully coupled runs. The observed temperature gradient of Yucca Mountain was prescribed in the simulations.

For all of the cases considered, the problem was simulated to steady state conditions. In general, steady state conditions were considered to be reached after the outflow of water at the water table equalled within a fraction of a percent the total infiltration prescribed at the ground surface. For cases with gas flow, similar mass balance was performed for this component. In most cases, steady state conditions were reached after 10^{13} seconds (3×10^6 years). As expected, this was the case independent of the dimensionality of the model (1-D, 2-D and 3-D). The computer execution time (CPU time) to reach steady state varied from less than a minute for the 1-D runs, typically 30 minutes for the 2-D runs and 2 to 15 hours for the 3-D runs. These runs were made on a Pentium (90MHz) personal computer.

The single component moisture flow runs reach steady state in around one hour, whereas the fully coupled gas, moisture and heat flow runs take 10-20 hours of CPU time to reach steady state. It should be noted that one must be very careful in prescribing boundary conditions in order to get meaningful simulation results.

SUMMARY

The development of the three-dimensional site-scale model of Yucca Mountain continues with the purpose of guiding the site characterization effort. A large effort has been devoted to the development of an automatic grid generation for complex geological settings such as Yucca Mountain. Various three-dimensional moisture flow simulations have been carried out by assuming different infiltration patterns, and using various assumptions regarding hydrological characteristics of major faults. The model has been modified to include the Exploratory Studies Facility (ESF) and is being extended in all directions to include more wells.

ACKNOWLEDGMENTS

This work was prepared under U.S. Department of Energy contract no. DE-AC03-76SF00098, and DE-A108-78ET44802 administered by the Nevada Operations Office in cooperation with the U.S. Geological Survey, Denver. Review of this paper by J. Wang and Y. Tsang of LBL, is greatly appreciated. The authors also appreciate the contributions of M. Chornak, A. Flint, L. Flint, and R. Spengler from the U.S. Geological Survey.

REFERENCES

G.S.Bodvarsson, G. Chen and C. Wittwer, "Preliminary analysis of three-dimensional moisture flow within Yucca Mountain, Nevada," proceeding of Fifth International High Level Nuclear Waste Conference, 1038-2047 pp., 1994.

G.S. Bodvarsson, Z. Aunzo, G. Chen, C. Haukwa, A. Flint, L. Flint, E. Kwicklis, "Recent development of the LBL/USGS site-scale model of Yucca Mountain, Nevada," International High Level Nuclear Waste Conference, proceedings of sixth workshop, 1995.

P. Fuller, C. Haukwa and G.S. Bodvarsson, "USERS MANUAL: A 3-D grid generator for LBL's flow and transport numerical codes," Lawrence Berkeley Laboratory Report (in preparation).

E.A. Klavetter and R.R. Peters, "Estimation of hydrologic properties of an unsaturated fractured rock mass," SAND84-2642, Sandia National Laboratories, 1986.

K. Pruess, "TOUGH2-A General-purpose Numerical Simulator for Multiphase Fluid and Heat Flow," LBL-29400, Lawrence Berkeley Laboratory, 103 pp., Berkeley, 1990.

C.S. Wittwer, G.S. Bodvarsson, M.P. Chornak, A.L. Flint, L.E. Flint, B.D. Lewis, R.W. Spengler, and C.A. Rautman, "Design of a three-dimensional site-scale

model for the unsaturated zone at Yucca Mountain, Nevada," High Level Radioactive Waste Management, Proceedings of the Third Annual International Conference, 263-271, Las Vegas, 1992.

C.S. Wittwer, G.S. Bodvarsson, M.P. Chornak, A.L. Flint, L.E. Flint, B.D. Lewis, R.W. Spengler, and C.A. Rautman, "Development of a three-dimensional site-scale model for the unsaturated zone at Yucca Mountain, Nevada," Journal of Radioactive Waste Management and Environmental Restoration, Vol. 19, #1-3, 147-164 pp., 1994.

C.S. Wittwer, G. Chen, and G.S. Bodvarsson, "Studies of the role of fault zones on fluid flow using the site-scale numerical model of Yucca Mountain," High Level Radioactive Waste Management, Proceedings of the Fourth Annual International Conference, 667-674, American Nuclear Society, La Grange Park, Ill., 1993.

DRIFT-SCALE THERMO-HYDROLOGIC ANALYSES FOR THE PROPOSED REPOSITORY AT YUCCA MOUNTAIN, NV

Mark Reeves and Suresh Lingineni *
M&O / Intera, Inc.
101 Convention Center Dr., Suite P-110
Las Vegas, NV 89109

Focusing on the near field of a waste package, this paper presents results obtained from a thermo-hydrologic model. Vertically, the conceptual model extends from ground surface to a depth of 1000 m below the water table. Horizontally, it is bounded by the centerlines of two pillars. Inside an assumed circular drift, an invert (backfill) surrounds the waste package. Here, a coarse-grained crushed tuff is assumed to provide a capillary barrier against infiltrating ground water. For comparison, the invert is replaced by intact tuff, corresponding to borehole emplacement.

In further examining the near-field thermo-hydrology of a waste package, the study considers several values of the areal power density together with both nonenhanced and enhanced levels of vapor diffusivity. In order to characterize drift resaturation effects deriving from the latter, the calculations extend to 100,000 years.

The clarity of the coding present in LBL's integrated finite-difference model TOUGH2 has permitted us to make several code changes. For the most part, they expedite convergence on difficult applications. The paper briefly discusses these changes.

* The authors regret that, due to heavy prior commitments, they were unable to complete an extended abstract in time for inclusion in this volume.

Presented at the TOUGH '95 Workshop, Lawrence Berkeley Laboratory, Berkeley, CA, March 20-22, 1995.

SAND95-0565C
The Effect of Stratigraphic Dip on Multiphase Flow at the Waste Isolation Pilot Plant

Stephen W. Webb and Kurt W. Larson
Sandia National Laboratories
Albuquerque, NM

Introduction

The Waste Isolation Pilot Plant (WIPP) is a U.S. Department of Energy research and development facility for the underground disposal of transuranic waste from U.S. defense-related activities. The WIPP repository is located within the Salado Formation, which is comprised of beds of pure and impure halite with thin interbeds of anhydrite and related clay seams. This formation is brine saturated with a pore pressure of approximately 12.5 MPa at the repository horizon. The Salado Formation dips gently southeast, on the average approximately 1°, with steeper dips locally. Elevated repository pressures, caused by gas generated as emplaced waste corrodes and degrades, may drive brine and gas out of the repository into the surrounding formation. Stratigraphic dip may cause increased brine inflow to the repository through countercurrent flow in the interbeds and enhanced gas migration distances in the updip direction due to buoyancy. Additional results are given by Webb and Larson (in press).

Overview of Two-Phase Flow Considerations

Stratigraphic dip can affect the fluid flow behavior along a flow path. Two flow conditions are possible, cocurrent flow in which both fluids (brine and gas) flow in the same direction and countercurrent flow in which the fluids flow in opposite directions. If only cocurrent flow is possible, brine inflow into the repository will stop when gas migrates from the room into the Salado Formation, reducing the amount of brine that flows into the repository and possibly limiting the amount of gas generated. If countercurrent flow occurs, brine will continue to flow into the repository while gas migration occurs, possibly increasing the amount of gas generated. In addition to affecting brine inflow, stratigraphic dip will impact gas migration behavior. Gas will preferentially migrate updip because the far-field pressure decreases with distance. In the updip direction, brine may flow into the repository, decreasing the flow resistance for gas migration. Similarly, gas migration downdip is much more difficult since the far-field pore pressure increases with distance.

Cocurrent and Countercurrent Flow

As detailed in Webb (in preparation), cocurrent and countercurrent flow regimes can be characterized by the Darcy velocities of the phases. Note that Darcy's Law predicts separate wetting (brine) and nonwetting (gas) phase velocities for a single flow path. Transition between cocurrent and countercurrent flow occurs when a phase velocity is zero, discounting the case where one or both of the fluids are immobile. Two transitions are possible, each involving a change in direction of one of the two fluids. Figure 1 shows the cocurrent and countercurrent flow regions along with a possible path of fluid velocities for the brine-inflow/gas-migration scenario in the updip direction, where the positive sign indicates flow towards the repository.

Starting from the left of the velocity path (Point A), gas (if present in the formation) and brine are flowing towards the repository. As the repository gas pressure increases, gas and brine flow towards the repository decrease, and the position on the velocity path moves upward and to the right. Eventually, the repository pressure increases sufficiently such that gas flow will be zero while some brine continues to flow slowly towards the repository (Point B). Moving yet further upward and to the right on the velocity path, gas pressure increases further such that gas flows away from the repository, while brine flow is zero (Point C). Between Points B and C, countercurrent flow will occur such that brine flows towards the repository while gas flows away. Continuing to the right, any additional increase in the gas pressure produces both brine and gas flow away from the repository.

Gas Migration

Consider a static column of water tilted at an angle θ as depicted in Figure 2a. Relative to location x=0, the water pressure changes with depth due to hydrostatic pressure. For illustration purposes, assume that the water pressure at 0 is 12.5 MPa. Also at location 0, suppose that gas is introduced at 12.6 MPa, and assume negligible capillary pressure. Because the gas is at a higher pressure, it will flow updip and downdip from location 0. Figure 2b shows the pressure variation for each fluid neglecting pressure drop due to flow. Since the gas has a lower density than water (or brine), the hydrostatic gradient is smaller. Gas will flow downdip a relatively short distance until the gas pressure is equal to the liquid pressure, which occurs at point a. Updip, however, the pressures never equalize, and the pressure difference between the gas phase and liquid phase continuously increases. While the distance is limited downdip, there is no limit to gas migration updip.

WIPP Simulations

Brine Inflow

Two-dimensional simulations of an isolated WIPP repository room have been performed using TOUGH2 for horizontal and 1° dipping stratigraphy similar to the geometry used in previous studies (Figure 3). The volume of the room changes with time due to salt creep through the pressure-time-porosity approach as described in Freeze et al. (1995). The room was located approximately midway between the top and bottom of the mesh. Two interbeds are in the model domain that extends laterally away from the room and are the preferential gas and brine flow paths away from the room. A simplified model for approximating the formation and propagation of fractures in the anhydrite interbeds due to high pore pressures was used. The simplified fracture model assumed that the anhydrite interbeds fracture when fluid pressures exceed the far-field fluid pressure by a specified amount, increasing interbed porosity and permeability. Increased interbed permeability decreased the resistance to brine and gas flow between the room and the interbeds, increasing flow away from the room and reducing the maximum room pressure. In addition, as discussed by Webb and Larson (in press), increased permeability increases the effect of countercurrent flow.

In both the dipping and horizontal simulations, fractures formed at about 300 years in the Upper Composite Interbed and in Marker Bed 139. The porosity and permeability of the interbeds

increased significantly due to fracturing, creating more storage volume for gas and increasing lateral transmissivity. Before interbed fracturing, the amount of brine which flowed into the room was similar with and without dip. However, with dip, a second period of brine-inflow, due to countercurrent flow, occurred after fractures formed. This brine inflow was driven by the formation of a cell of countercurrent brine and gas that formed about 325 years after the start of the simulation (Figure 4a-4c) and continued until the end of the simulation. In that cell, gas flows up dip and away from the room, while brine flows down dip and towards the room. The volume of brine inflow due to countercurrent flow is of similar magnitude to the brine inflow occurring during room consolidation and pressurization as shown in Figure 4d. This countercurrent flow cell is associated with the leading edge of the zone of fractured rock in the Upper Composite Interbed. As the fractures propagate outward, the countercurrent flow cell follows. In these simulations, the cell has a maximum length of about 1500 m. The countercurrent flow cell appears to be a mechanism for redistribution of brine within the Upper Composite Interbed, that, when it is in close proximity to the room, provides brine inflow at a relatively high rate. The brine inflow rate due to countercurrent flow decreases as the countercurrent flow cell moves away from the room.

Gas Migration Distance

With the addition of dip and buoyancy effects, gas migration becomes a fully three-dimensional process. Except for geometry, the three-dimensional simulations used the same parameters as the two-dimensional simulations. Simulations were run to investigate gas migration in three dimensions with and without dip using mixed Brooks and Corey (Brooks and Corey, 1964) and van Genuchten/Parker (van Genuchten, 1980; Parker et al., 1987) two-phase characteristic curves as given in Webb (in press).

Figure 5 shows the gas-migration plumes and gas-saturation contours at 10,000 years. Figures 5a and 5b depict the effect of 1° dip using the mixed Brooks and Corey curves, while Figures 5c and 5d show the dip effect for van Genuchten/Parker. Without dip, the gas-migration plumes are approximately circular in shape and symmetrical about the room in both the upper and lower interbeds for both sets of two-phase curves. Deviations from a circular shape are due to the relatively crude nodalization employed. For mixed Brooks and Corey, the impact of stratigraphic dip is relatively small. In contrast, for van Genuchten/Parker, the shape of the plume of migrating gas is significantly different for 1° dip than for 0° dip. A teardrop shape forms in both interbeds, with significantly larger gas migration updip than downdip. Gas migrates three times as far for 1° dip than for 0° dip for van Genuchten/Parker.

Summary and Conclusions

The impact of dip on multiphase flow at the WIPP may be significant. With dip, an additional mechanism for brine inflow may occur, namely the formation of a cell of countercurrent brine and gas flow in the interbeds. The additional volume of brine inflow resulting from the countercurrent flow cell may be of similar magnitude to brine inflow without dip. Therefore, dip must be included in any repository model to include the countercurrent brine inflow mechanism. Gas migration may also be significantly influenced due to dip. Gas migration distances may increase dramatically with preferential migration updip.

Acknowledgment

This work was supported by the United States Department of Energy under Contract DE-AC04-94AL85000.

References

Brooks, R.H., and A.T. Corey (1964), "Hydraulic Properties of Porous Media," Hydrology Papers, No. 3, Colorado State University, March 1964.

Freeze, G.A., K.W. Larson, P.B. Davies, and S.W. Webb (1995), "Using a Multiphase Flow Code to Model the Coupled Effects of Repository Consolidation and Multiphase Brine and Gas Flow at the Waste Isolation Pilot Plant," *TOUGH '95 Workshop Proceedings*.

Parker, J.C., R.J. Lenhard, and T. Kuppusamy (1987), "A Parametric Model for Constitutive Properties Regarding Multiphase Flow in Porous Media," *Water Resour. Res.*, Vol. 23, No. 4, pp. 618-624, 1987.

van Genuchten, M.Th. (1980), "A Closed-form Equation for Predicting the Hydraulic Conductivity of Unsaturated Soils," *Soil Sci. Soc. Am. J.*, Vol. 44, pp. 892-898, 1980.

Webb, S.W. (in preparation), *Cocurrent and Countercurrent Flow in Porous Media As Implied by Darcy's Law for Unsaturated Flow.*

Webb, S.W. (in press), *Review of Two-Phase Characteristic Curves for Porous Media and Application to the WIPP*, SAND93-3912, Sandia National Laboratories.

Webb, S.W. and K.W. Larson (in press), *The Effect of Stratigraphic Dip on Brine Inflow and Gas Migration at the Waste Isolation Pilot Plant*, SAND94-0932, Sandia National Laboratories.

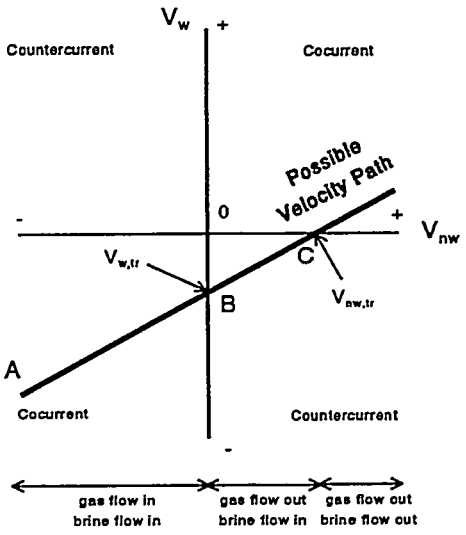

Figure 1
Two-Phase Flow Map

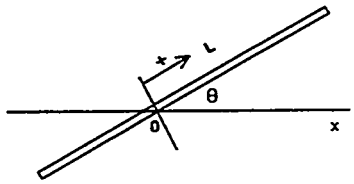

Figure 2a
Tilted Water Column

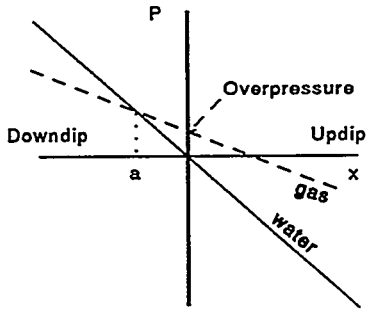

Figure 2b
Water and Gas Pressure Variation

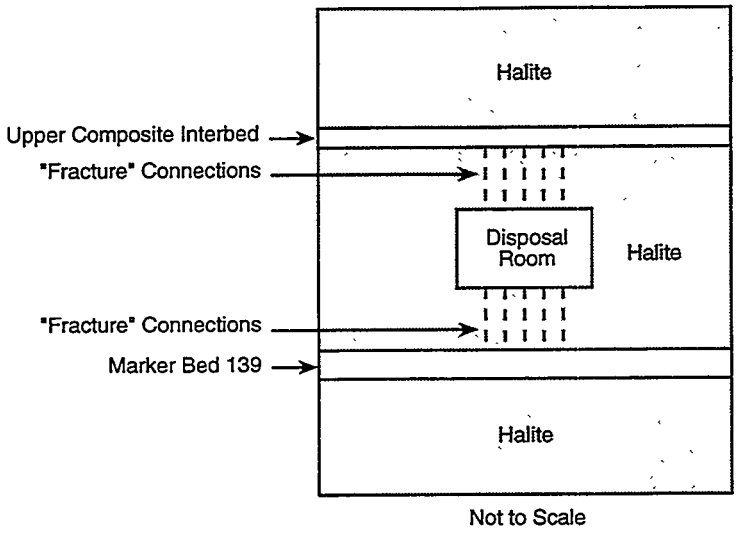

Figure 3
Conceptual Model

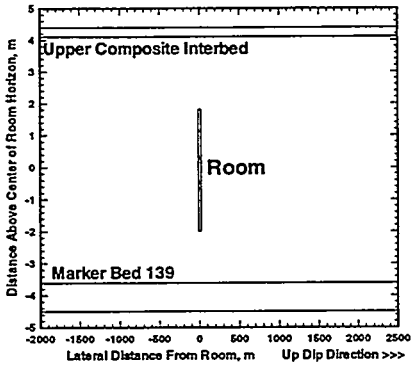

a) Flow Conditions at 75 Years with Dip
(Brine Inflow, Gas Inflow)

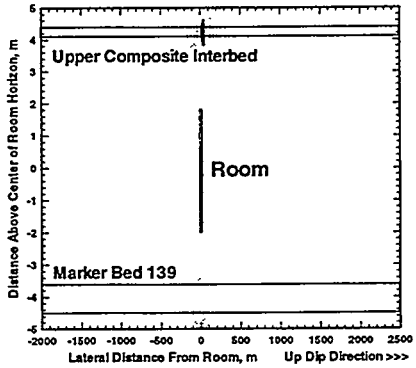

b) Flow Conditions at 325 Years with Dip
(Small Brine Inflow, Gas Outflow)

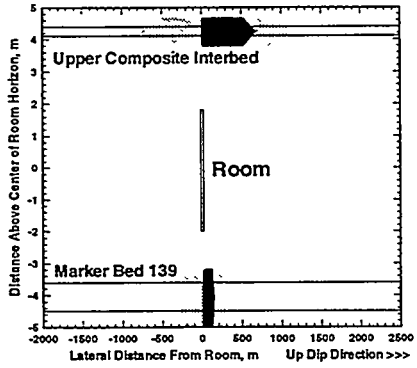

c) Flow Conditions at 500 Years with Dip
(Fracturing Stimulates Countercurrent Flow)

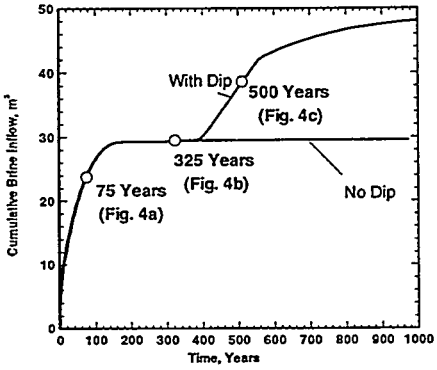

d) Brine Inflow With and Without Dip

Figure 4
Effect of Dip on Brine Flow Mechanisms

Black - countercurrent flow
Grey - cocurrent flow
White - gas immobile

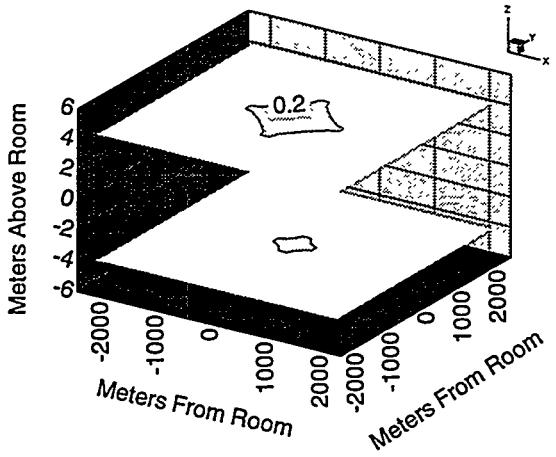

a) Brooks and Corey - No Dip

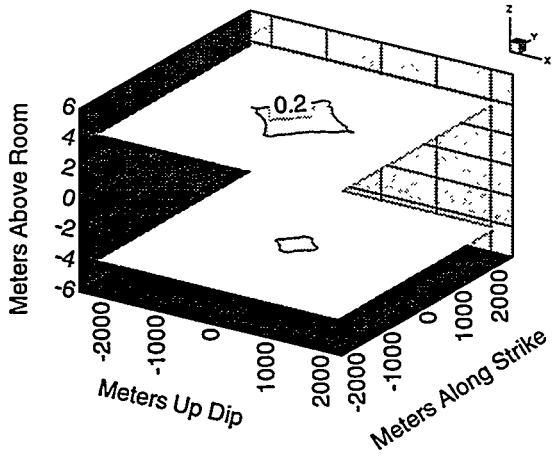

b) Brooks and Corey - 1 degree dip

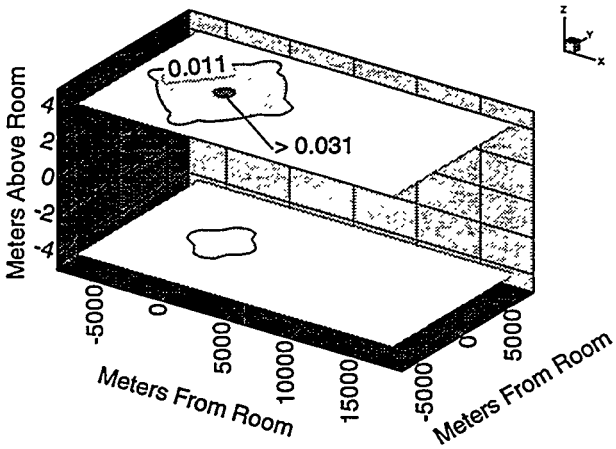

c) van Genuchten/Parker - No Dip

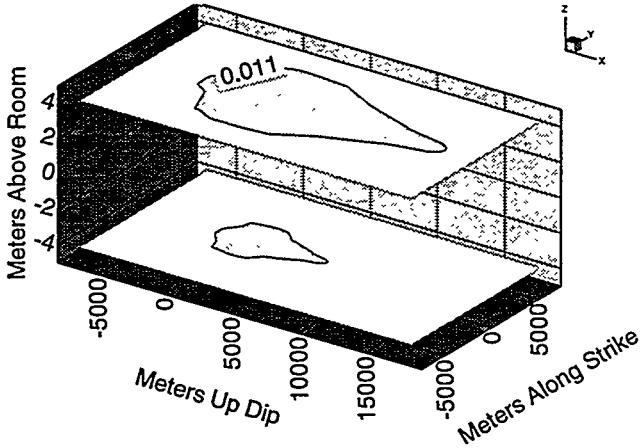

d) van Genchten/Parker - 1 degree dip

Figure 5
Effect of Dip on Gas-Migration Plumes and Gas-Saturation Contours

Presented at the TOUGH '95 Workshop, Lawrence Berkeley Laboratory, Berkeley, CA, March 20-22, 1995.

SAND95-0568C

Modification and Application of TOUGH2 as a Variable-Density, Saturated-Flow Code and Comparison to SWIFT II Results

Tracy L. Christian-Frear[1] and Stephen W. Webb[2]

1.0 Introduction

Human intrusion scenarios at the Waste Isolation Pilot Plant (WIPP) involve penetration of the repository and an underlying brine reservoir by a future borehole. Brine and gas from the brine reservoir and the repository may flow up the borehole and into the overlying Culebra formation, which is saturated with water containing different amounts of dissolved solids resulting in a spatially varying density. Current modeling approaches involve perturbing a steady-state Culebra flow field by inflow of gas and/or brine from a breach borehole that has passed through the repository. Previous studies simulating steady-state flow in the Culebra have been done. One specific study by LaVenue et al. (1990) used the SWIFT II code (Reeves et al., 1986), a single-phase flow and transport code, to develop the steady-state flow field. Because gas may also be present in the fluids from the intrusion borehole, a two-phase code such as TOUGH2 can be used to determine the effect that emitted fluids may have on the steady-state Culebra flow field. Thus a comparison between TOUGH2 and SWIFT II was prompted.

In order to compare the two codes and to evaluate the influence of gas on flow in the Culebra, modifications were made to TOUGH2. Modifications were performed by the authors to allow for element-specific values of permeability, porosity, and elevation. The analysis also used a new equation of state module for a water-brine-air mixture, EOS7 (Pruess, 1991), which was developed to simulate variable water densities by assuming a miscibile mixture of water and brine phases and allows for element-specific brine concentration in the INCON file.

2.0 Code Modifications

Comparison between SWIFT II and TOUGH2 numerical models of the Culebra Dolomite prompted changes to be made in TOUGH2. SWIFT II allows the analyst to enter element-specific formation properties; TOUGH2 did not. Thus changes were required in TOUGH2 to be able to enter element-specific formation properties such as permeability, porosity, and elevation. These properties needed to be varied at each grid-cell center. Additional changes were made in the TOUGH2 code so that portions of a SWIFT II input deck could be read and the information utilized by TOUGH2. An outline of the general changes made to the code is shown in Figure 1.

Three new subroutines were added to TOUGH2: HETERO, HINCON and EL2BETA. Three input files that hold the general information, the initial conditions and the boundary conditions are read to provide the heterogeneous formation parameters. All the heterogeneous parameters are output to the file *INCON* and subsequently read in RFILE. Changes to the format of *INCON* include addition of the permeability vectors and elevation on the same line as the "elem" and porosity values. Changes were made to the *SAVE* file format to mimic *INCON*.

HETERO is called by the main program. It reads the heterogeneous formation parameters from three input files and stores the information in specified matrices. The three input files are *HETERO.INP*, *HETIC.INP* and *HETBC.INP*. HETERO also converts hydraulic conductivity values to permeability if so requested.

1 RE/SPEC Inc., 4775 Indian School Rd., Albuquerque, NM 87110
2 Sandia National Laboratories, Albuquerque, NM 87185

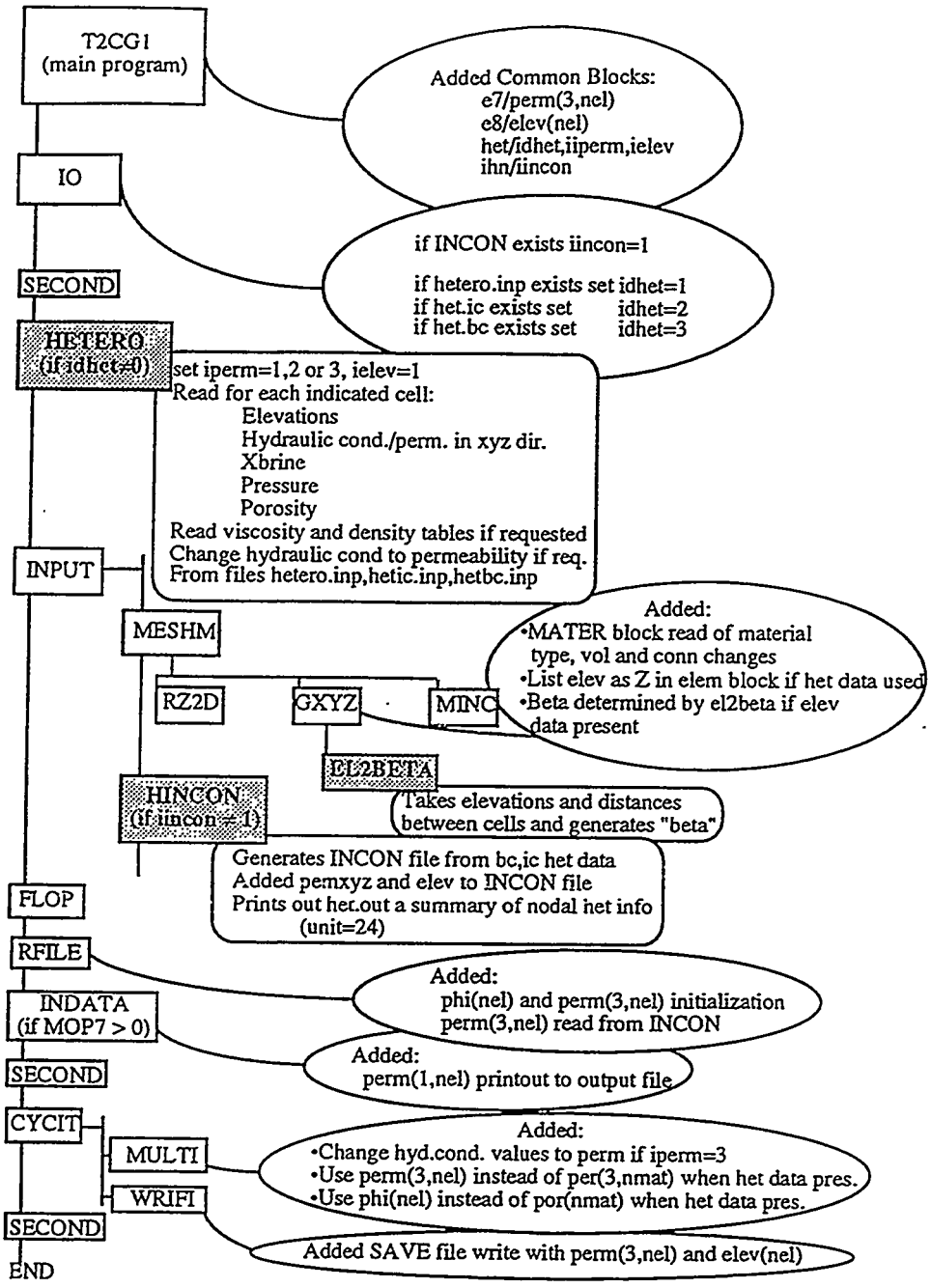

Figure 1. Flow diagram of general heterogeneous material properties changes made to TOUGH2.

HINCON is called by the subroutine INPUT. HINCON writes out the file *INCON* with the appropriate information. Additions to the *INCON* file include the values of the permeability vectors and elevation data for each node on the same line that the "elem" and porosity data are stored. HINCON also prints out *HET.OUT* a summary of the values that were processed by HETERO.

EL2BETA is called by subroutine GXYZ in MESHM. EL2BETA uses elevation data to determine the "betax" parameter (between two elements) of the CONNE.1 card. Betax is the cosine of the angle between the gravitational acceleration vector and the line between the center of the two elements (the

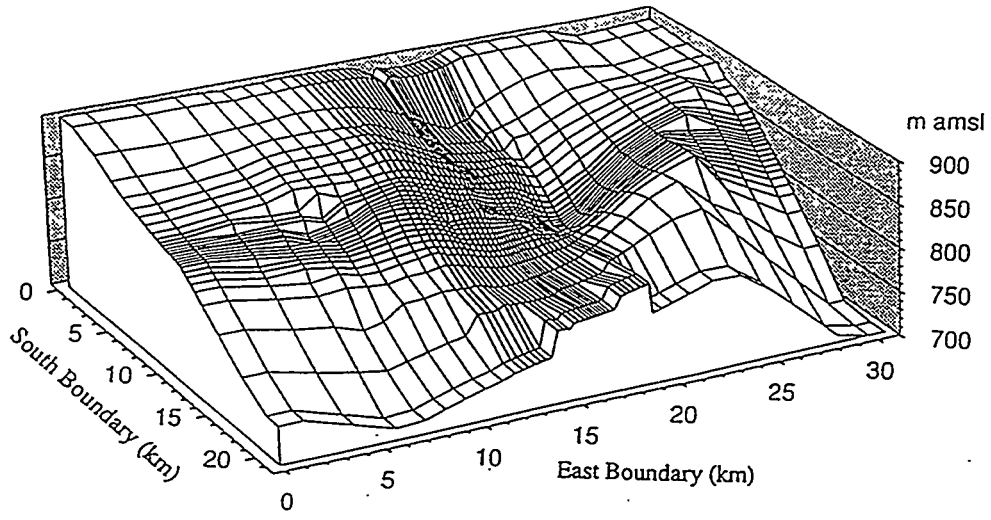

Figure 2. Surface plot of the Culebra model region mesh mid-point elevations.

hypotenuse of the triangle). EL2BETA uses the elevation data (elev1 and elev2) and the distances from the element centroids to their common interface (x1 and x2) to determine betax. MULTI uses betax in conjunction with the gravity vector value to determine density pressure changes due to height differences.

3.0 Culebra Steady-State Flow Field Results

The Culebra Dolomite is generally considered to be the principal groundwater-transport pathway for radionuclides to the accessible environment if a human-intrusion breach in the repository should occur. The Culebra is the most permeable and laterally continuous hydrostratigraphic unit above the repository. It is a fractured, finely crystalline, vuggy dolomite. The transmissivity of the Culebra varies by more than six orders of magnitude in the vicinity of the WIPP (Sandia WIPP Project, 1992). Transmissivity is controlled by the extent of fracturing and the degree to which the fractures are filled by evaporite minerals.

The region of Culebra Dolomite chosen for simulation coincides exactly with the model of LaVenue et al. (1990), who used the SWIFT II code (Reeves et al., 1986). The spatial scale of the model, which includes the WIPP-site boundary, is 21.3 km in the east-west direction by 30.6 km in the north-south direction, for a total area of 651.8 km^2. The model geometry consists of a two-dimensional model of the Culebra as is shown in Figure 2. The Culebra varies in elevation almost 200 meters, from approximately 700 to 900 meters above mean sea level (m amsl). The thickness of the Culebra is 7.7 meters, the median thickness reported for this unit. The permeability distribution for the modeled region is shown in Figure 3. The brine-water density distribution is shown in Figure 4.

Results of the saturated, steady-state pressure and flow fields calculated from the modified version of TOUGH2/EOS7 are essentially the same as those produced by SWIFT II. Figure 5 shows the comparison of the TOUGH2 pressure field to that of the comparable steady-state model of LaVenue et al. (1990). The results show that the pressures trend primarily from east to west, with the higher pressures in the east. The velocity distributions indicate that the largest flux of groundwater occurs along the western portion of the model, where permeabilities are highest. Within the WIPP site boundary the velocities range from 5.0×10^{-8} m/s in the northwestern corner to 1.3×10^{-10} m/s on the southeastern boundary.

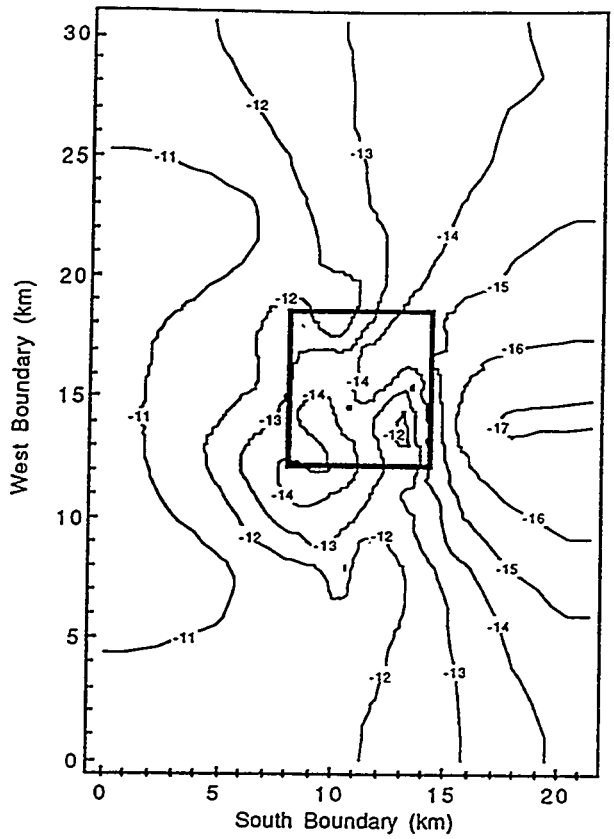

Figure 3. Culebra permeability distribution (log m^2). Box in the center indicates WIPP site boundary.

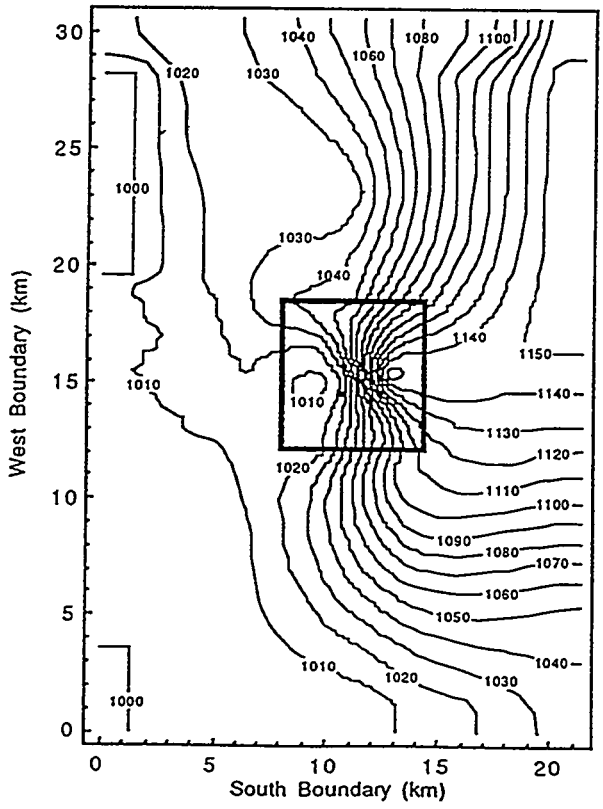

Figure 4. Culebra brine-water density (kg/m^3) distribution. Box in the center indicates WIPP site boundary.

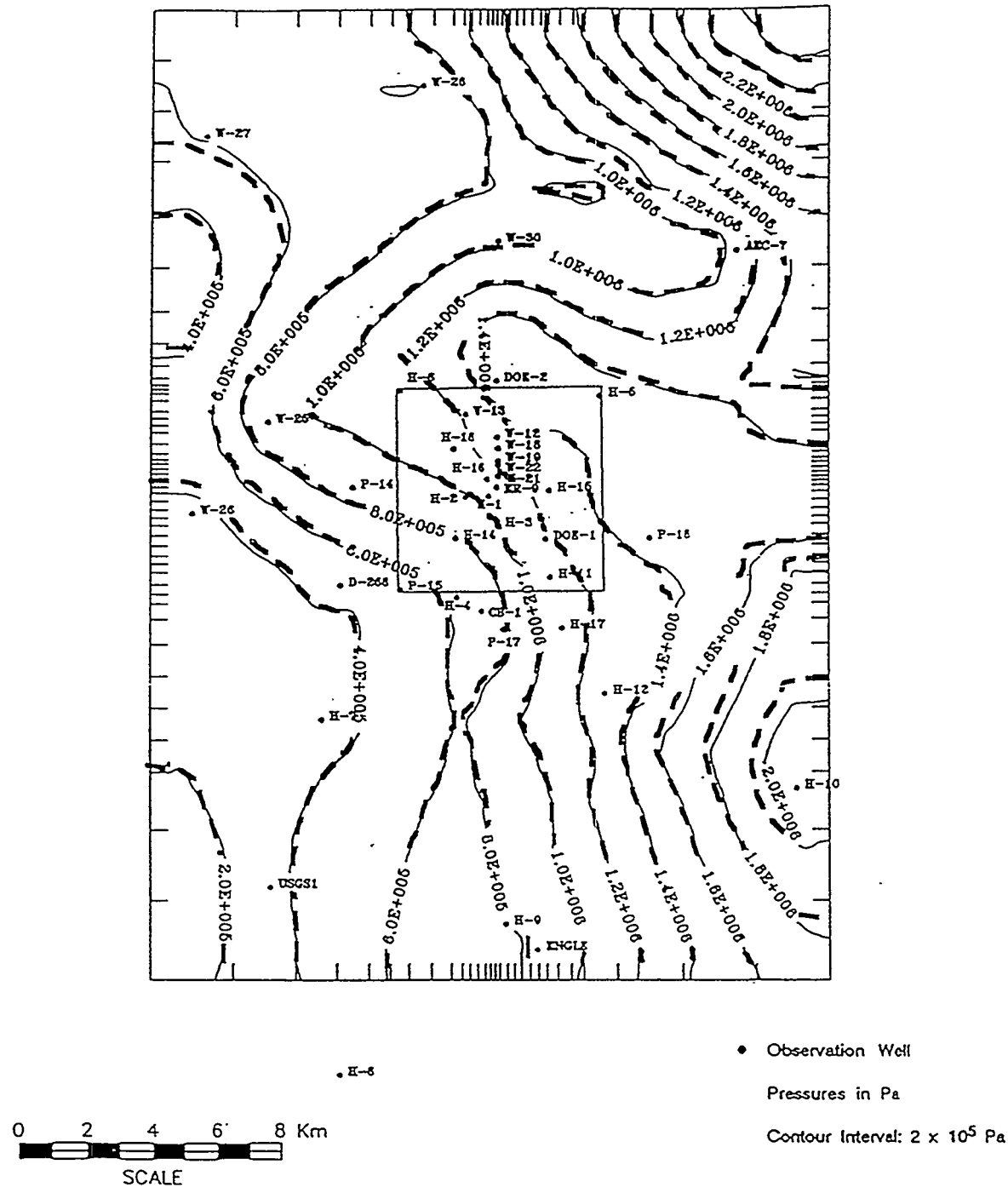

Figure 5. Comparison of steady-state pressure fields of LaVenue et al. (1990) (solid lines) to modified TOUGH2/EOS7 (dashed lines). Box in the center indicates WIPP site boundary.

4.0 Conclusions

Steady-state simulations of a Culebra Dolomite in the region surrounding the WIPP site were made. The resulting steady-state pressure and flow fields produced from these simulations are essentially the same as those produced by LaVenue et al. [1990]. This model comparison provides a useful benchmark of the newly developed EOS7 module for the TOUGH2 code, illustrating application of TOUGH2 to a variable-density regional groundwater flow problem.

Acknowledgments

The authors thank Karsten Pruess for his development of EOS7 for TOUGH2. This work was supported by the United Sates Department of Energy under Contract DE-AC04-94AL85000.

References

LaVenue, A. M., T. L. Cauffman, and J. F. Pickens, 1990. *Ground-Water Flow Modeling of the Culebra Dolomite Volume 1: Model Calibration,* Contractor Report SAND89-7068/1, Sandia National Laboratories, Albuquerque, NM.

Pruess, K., 1991. "EOS7, An Equation-of-State Module for the TOUGH2 Simulator for Two-Phase Flow of Saline Water and Air," *Lawrence Berkeley Laboratory LBL-31114,* August 1991.

Reeves, M., D. S. Ward, N. D. Johns, and R. M. Cranwell, 1986. *Theory and Implementation for SWIFT II, the Sandia Waste-Isolation Flow and Transport Model, Release 4.84,* SAND83-1159, Sandia National Laboratories, Albuquerque, NM.

Cauffman, T.L., A.M. LaVenue, and J.P. McCord, 1990. *Ground-Water Flow Modeling of the Culebra DolomiteVolume II: Data Base,* Contractor Report SAND89-7068/2, Sandia National Laboratories, Albuquerque, NM.

Presented at the TOUGH'95 Workshop, Lawrence Berkeley Laboratory, Berkeley, CA, March 20-22, 1995.

SAND95-0564C
Using TOUGH2 to Model the Coupled Effects of Gas Generation, Repository Consolidation, and Multiphase Brine and Gas Flow at the Waste Isolation Pilot Plant

G.A. Freeze[1], K.W. Larson[2], P.B. Davies[2], and S.W. Webb[2]

[1] INTERA Inc., 1650 University Blvd., Albuquerque NM 87102
[2] Sandia National Laboratories, Albuquerque NM 87185

Introduction

The Waste Isolation Pilot Plant (WIPP) is a U.S. Department of Energy facility designed to demonstrate the safe underground disposal of transuranic waste. The WIPP repository lies within the Salado Formation, a thick sequence of bedded pure and impure halite with thin, laterally continuous interbeds of anhydrite. The underground waste storage area is designed to have eight waste disposal panels, each of which will contain seven waste disposal rooms. Each disposal room, approximately 4 m high, 10 m wide, and 91 m long, is to be filled with steel drums containing contact-handled (CH) transuranic (TRU) waste. Following waste emplacement, each room will be backfilled with crushed salt. Due to deviatoric stress introduced by excavation, the walls of the waste disposal rooms in the repository will deform over time, consolidating waste containers and salt backfill, thereby decreasing the void volume of the repository.

Gas may be generated from the emplaced waste by anoxic corrosion reactions between steel and brine, and by microbial degradation. Gas generation could produce elevated pressures within the disposal rooms. If repository pressures approach lithostatic, backstress on the room walls will force room expansion and/or Salado fracturing, mitigating further pressure increases. Elevated pressures could drive gas release from the repository and enhance contaminant movement towards regulatory boundaries. Gas pressure in the disposal rooms is strongly influenced not only by the gas-generation rate, but also by changes in gas-storage volume caused by creep closure and/or expansion of the rooms, and by gas release from the rooms into the surrounding rock. Long-term repository assessment must consider the processes of gas generation, room closure and expansion due to salt creep, and multiphase (brine and gas) fluid flow, as well as the complex coupling between these three processes.

Stone (1992) used the mechanical creep closure code SANCHO (Stone et al., 1985) to simulate the closure of a single, perfectly sealed disposal room filled with waste and backfill. SANCHO uses constitutive models to describe salt creep, waste consolidation, and backfill consolidation. Five different gas-generation rate histories were simulated (Figure 1a), differentiated by a rate multiplier, f, which ranged from 0.0 (no gas generation) to 1.0 (expected gas generation under brine-dominated conditions). The results of the SANCHO f-series simulations provide a relationship between gas generation, room closure (Figure 1b), and room pressure (Figure 1c) for a perfectly sealed room. Several methods for coupling this relationship with multiphase fluid flow into and out of a room were examined by Freeze et al. (in press a). Two of the methods are described below.

Model Development

TOUGH2 was employed to couple the processes of gas generation, room closure/consolidation, and multiphase brine and gas flow. Two empirically-based methods for approximating salt creep and room consolidation were implemented in TOUGH2: the pressure-time-porosity line interpolation approach and the fluid-phase-salt approach. Both approaches utilized links to the SANCHO f-series simulation results to calculate room-void-volume changes with time during a simulation.

The Salado Formation was conceptualized as a homogeneous halite containing single anhydrite interbeds above and below the disposal room (Figure 2). A single, isolated, half-width disposal room (with symmetry across the centerline assumed) was simulated. Each of the four regions (disposal room, halite, upper interbed, and lower interbed) in the fluid-flow continuum was defined by a different set of physical properties. The interbeds provide the preferred path for gas release from the room because of a low threshold (gas-entry) pressure and a high intrinsic permeability relative to the halite. Direct connections between interbed elements and elements on the edge of the disposal room were specified (Figure 2). These connections had large transmissivities, representative of fracture-like connections. Gas generation was simulated by placing a number of gas sources within the modeled disposal room.

Pressure-Time-Porosity Line Interpolation Approach

The room porosity vs. time and room pressure vs. time results from the five SANCHO f-series simulations (Figures 1b and 1c, respectively) were used to calculate a set of three-dimensional pressure-time-porosity lines (functions). One pressure-time-porosity line corresponds to each of the five SANCHO simulations. At each TOUGH2/EOS8 time step, a room porosity value is obtained by linear interpolation between the two pressure-time-porosity lines which bound the current simulated time and room gas pressure conditions. The simulated room porosity is then adjusted to the value determined from the interpolation. With this pressure-time-porosity line interpolation process (also referred to as the pressure lines method), the SANCHO-simulated relationship between room porosity (closure), pressure, and time, was transferred to TOUGH2/EOS8 where it was simulated in conjunction with multiphase fluid flow.

Fluid-Phase-Salt Approach

The fluid-phase-salt approach uses the Darcy flow of a highly-viscous fluid phase to represent salt creep. To implement this approach, a three-phase, three-component equation-of-state module, EOS8 (brine, hydrogen, "dead" oil) was created by Karsten Pruess at Lawrence Berkeley Laboratories. The "dead" oil phase was used to represent "fluid" salt. In TOUGH2/EOS8, the flow properties of the fluid-salt phase are selected such that the flow of salt into the disposal room approximates room closure. The fluid-phase-salt approach requires a dual continuum conceptualization in which salt-phase flow is confined to a separate salt-flow continuum (Figure 3) to avoid interference with gas and brine flow. The salt-flow continuum contains only two regions: disposal room and halite matrix. Multiphase brine and gas flow is confined to the same fluid-flow continuum (Figure 2) used with the pressure lines method. The interbeds are not included in the salt-flow continuum because they are not considered to have a significant impact on the physical process of room closure due to salt creep. With this approach, only the disposal room is common to both continuums. As a result, any impact of salt flow on multiphase brine and gas flow occurs through the pressure relationships within the disposal room.

The theoretical relationship between fluid (salt) flow and salt deformation, which governs the fluid-phase-salt approach, assumes that a pressure-controlled backstress opposes creep. This relationship fails to account for the additional backstress opposing room closure that is caused by the consolidation of the room contents, and consequently, does not accurately predict room closure when there is significant room consolidation. To overcome this difficulty, a method to approximate the consolidation-induced backstress was implemented in TOUGH2/EOS8. Using an artificial boundary, the disposal room is divided into two regions (Figure 3). The salt-accessible room region, which is connected to the salt-flow continuum, initially contains all three phases (salt, gas, and brine). The salt-inaccessible room region, which is connected to the fluid-flow continuum, contains only gas and brine. Salt flow into the disposal room, which comes only from the salt-flow continuum, is restricted by the artificial boundary to the salt-accessible region. Brine inflow, which comes only from the fluid-flow continuum, flows into the salt-inaccessible region of the room. Brine and gas can flow across the artificial boundary, making the entire room void volume available to brine and gas. However, brine and gas release from the room goes only to the fluid-flow continuum, brine and gas are not permitted to flow into the salt-flow continuum.

The model geometry and gas generation scheme are designed so that a pressure gradient from the salt-accessible region to the salt-inaccessible region is maintained during room closure. The resulting flow of gas from the salt-accessible region to the salt-inaccessible region is limited by a flow restriction (low transmissivity) specified across the artificial boundary. This flow restriction results in increased pressurization of the salt-accessible region as salt flows in, which in turn produces increased resistance to salt inflow. The additional resistance to salt inflow is analogous to the additional backstress caused by consolidation of the waste and backfill.

A calibration process was undertaken with TOUGH2/EOS8 to determine the combination of parameters controlling (1) salt-phase flow (i.e., salt viscosity) and (2) gas flow across the artificial boundary (i.e., transmissivity), that produced the best match with room closure and room pressure history results from the SANCHO f-series simulations. With the calibrated parameters, the fluid-phase-salt method slightly underestimated room pressure at high gas-generation rates ($f \geq 0.6$) and slightly overestimated room pressure at low rates ($f \leq 0.2$). However, the method captured a wide range of room closure and pressure behavior ($f=0.0$ to 1.0) with a single set of calibrated parameters. Qualitatively, the additional resistance to closure is similar to the resistance to closure provided by the compression of the waste and backfill in that it is more significant when there is greater room closure.

Simulation Results

Two sets of TOUGH2/EOS8 simulations are discussed here: (1) sealed-room closure (no fluid flow into/out of room); and (2) fully coupled flow and closure. Results from numerous other simulations are described in Freeze et al. (in press b).

Sealed-Room Closure

A sealed room simulation, similar to the SANCHO conceptualization in that there was no fluid flow in or out of the room, was performed with gas-generation rate history (Figure 3a) that was quite different from the SANCHO f-series rate histories (Figure 1a). This non-f-series rate history was selected because actual gas generation in the repository could be quite different from the f-series rate history. The non-f-series rate history had gas-generation rates that did not always decrease with time and the specified times for rate switches were different from the f-series simulations. The total mass of gas generated was the same as for the f=1.0 case.

Non-f-series simulation results for both closure coupling methods are shown in Figure 4. The two methods produced significantly different responses. Differences in the respective responses were particularly evident at 750 years, 1,050 years, and 1,200 years. At 750 years, following a decrease to zero gas generation, the rate of room expansion slowed with the fluid-phase-salt method (Figure 4b) and gas pressure in the room decreased (Figure 4c) in response to the continued room expansion. With the pressure lines method, room expansion immediately reversed at 750 years (Figure 4b) and room pressure continued to increase (Figure 4c), albeit at a slower rate than during the first 750 years. It is reasonable to assume that effect of a decrease to zero gas generation in the room would gradually impact salt creep behavior as the salt approached a new equilibrium with the room pressure and the room void volume. This gradual response was correctly predicted by the fluid-phase-salt method. The pressure lines method response at 750 years was an artifact of the structure of the pressure-time-porosity lines. In the SANCHO simulations used to create the pressure-time-porosity lines, room pressure was relatively constant between 550 and 1,050 years (Figure 1c). This pressure trend is evident in the non f-series pressure lines method response between 750 and 1,050 years (Figure 4c).

At 1,050 years the pressure lines method predicted a change in room closure and room pressure response despite the fact that there was no change in gas-generation rate. The declining room pressure again appears to be an artifact of the SANCHO simulations, in which gas generation ended at 1,050 years. At 1,200 years, following an increase in gas-generation rate, the rate of room expansion increased with both methods. However, the room gas pressure increased for the fluid-phase-salt method and decreased for the pressure lines method. It is reasonable to assume that the resumption of gas-generation would increase room pressure which, in turn, would increase the rate of room expansion. However, the pressure lines method response again appears to be adversely influenced by the structure of the SANCHO-generated pressure lines.

These non f-series rate history simulations demonstrate that the use of the pressure-time-porosity line interpolation method skews results towards the SANCHO f-series results because time is used as one of the interpolation axes. The time axis indirectly contains information about the history of salt creep and backstress on the room walls. Thus, the backstress and room closure history described by each pressure-time-porosity line are specific to the SANCHO-simulated gas-generation rate history.

Coupled Flow and Closure

To examine the behavior of the fluid-phase-salt and pressure-time-porosity line interpolation methods under coupled flow and closure conditions, simulations were performed with the f=1.0 gas-generation rate history. Simulations were extended to 10,000 years to allow the comparison to encompass the complete period of gas release and migration. Simulation results for both coupling methods are shown in Figure 5. System behavior differs from the sealed room simulations in that after gas generation ends at 1,050 years, gas is being expelled from the room (Figure 5c) and the room void volume starts to decline again (re-closure of the room) (Figure 5a). As with the sealed room simulations, the two different coupling methods produced differences in simulation results. The differences are attributable to: (1) room closure calibration effects with the fluid-phase-salt method; and (2) different room conceptualizations for coupling of room closure with multiphase flow.

As noted previously, the fluid-phase-salt calibration process resulted in a slight underestimation of room pressure for high gas-generation rates and a slight overestimation of room pressure for low gas-generation rates. For the f=1.0 rate history, this calibration effect caused the fluid-phase-salt method to produce

lower room pressures than the pressure lines method (Figure 5b). The lower room pressure translated to less gas expulsion (Figure 5c) and a larger room void volume (Figure 5a).

Differences between the coupling methods are also due to the different ways each method conceptualizes the disposal room. Multiphase flow is controlled by the gas- and brine-phase saturations within the room. These phase saturations impact both brine and gas expulsion through relative permeability relationships. For example, in simulations using the fluid-phase-salt method, brine inflow is typically confined to the small salt-inaccessible room region, producing high brine saturations and high relative permeability to brine. As a result, the fluid-phase-salt method produces more brine expulsion than does the pressure lines method. Additional simulations have shown that brine and gas expulsion under both the fluid-phase-salt and pressure lines methods is similar to brine expulsion from a fixed room, which is free of any closure coupling effects.

Conclusions

Two methods for coupling gas generation, disposal room closure/consolidation, and multiphase brine and gas flow at WIPP were examined using the TOUGH2/EOS8 code. Both methods incorporated links to the SANCHO f-series simulations (Stone, 1992), which coupled gas-generation rate with the mechanical creep closure of a room.

The pressure-time-porosity line interpolation method was useful for simulations with low gas-generation rates ($f \leq 0.2$) or with gas-generation rate histories similar to the SANCHO f-series. However, this method showed a tendency to introduce errors when the simulated gas-generation rate history involved high rates ($f > 0.4$) in a significantly different sequence than the f-series rate histories from which the pressure-time-porosity lines were derived. Under these conditions, the pressure lines method results tend to be skewed towards the SANCHO results.

The fluid-phase-salt method worked reasonably well under both f-series and non-f-series gas-generation rate histories. The dual room region conceptualization appeared not to adversely impact brine flow or gas release to the Salado Formation. The fluid-phase-salt method was calibrated in a manner such that it was accurate over the range of SANCHO f-series rate histories. It is uncertain whether the empirical calibration relationships can be extrapolated to gas-generation and room-closure conditions that are significantly outside the SANCHO f-series conditions.

The fluid-phase-salt method is thought to be a more reliable indicator of system behavior because it treats salt deformation as a viscous process and has a theoretical basis. However, it is a complex method that requires detailed calibration and may be difficult to implement in more complex repository geometries. The pressure lines method is thought to be less reliable due to the potential skewing of results towards SANCHO f-series results. However, due to its relative simplicity, the pressure lines method is easier to implement in multiphase flow codes, and pressure lines simulations run significantly faster (10 to 20 times) than fluid-phase-salt simulations.

References

Freeze, G.A., Larson, K.W., and P.B. Davies. in press a. *A Summary of Methods for Approximating Salt Creep and Disposal Room Closure in Numerical Models of Multiphase Flow.* SAND94-0251. Albuquerque, NM: Sandia National Laboratories.

Freeze, G.A., Larson, K.W., and P.B. Davies. in press b. *Coupled Multiphase Flow and Closure Analysis of Repository Response to Waste-Generated Gas at the Waste Isolation Pilot Plant (WIPP).* SAND93-1986. Albuquerque, NM: Sandia National Laboratories.

Stone, C.M. 1992. "Creep Closure Behavior of Waste Disposal Rooms in Bedded Salt Due to Gas Generation Produced by Several Alternatives of the Engineered Alternatives Task Force," memorandum to B.M. Butcher (October 6). Albuquerque, NM: Sandia National Laboratories.

Stone, C.M., R.D. Krieg, and Z.E. Beisinger. 1985. *SANCHO, A Finite Element Computer Program for the Quasistatic, Large Deformation, Inelastic Response of Two-Dimensional Solids.* SAND84-2618. Albuquerque, NM: Sandia National Laboratories.

Acknowledgements

This work was supported by the United States Department of Energy under Contract DE-AC04-94AL85000. The authors wish to recognize Karsten Pruess and George Moridis for their support of the TOUGH2 and TOUGH2/EOS8 codes, Mark Reeves for his theoretical insights into fluid flow and salt creep coupling, and Toya Jones for running numerical experiments with various flow and closure coupling schemes.

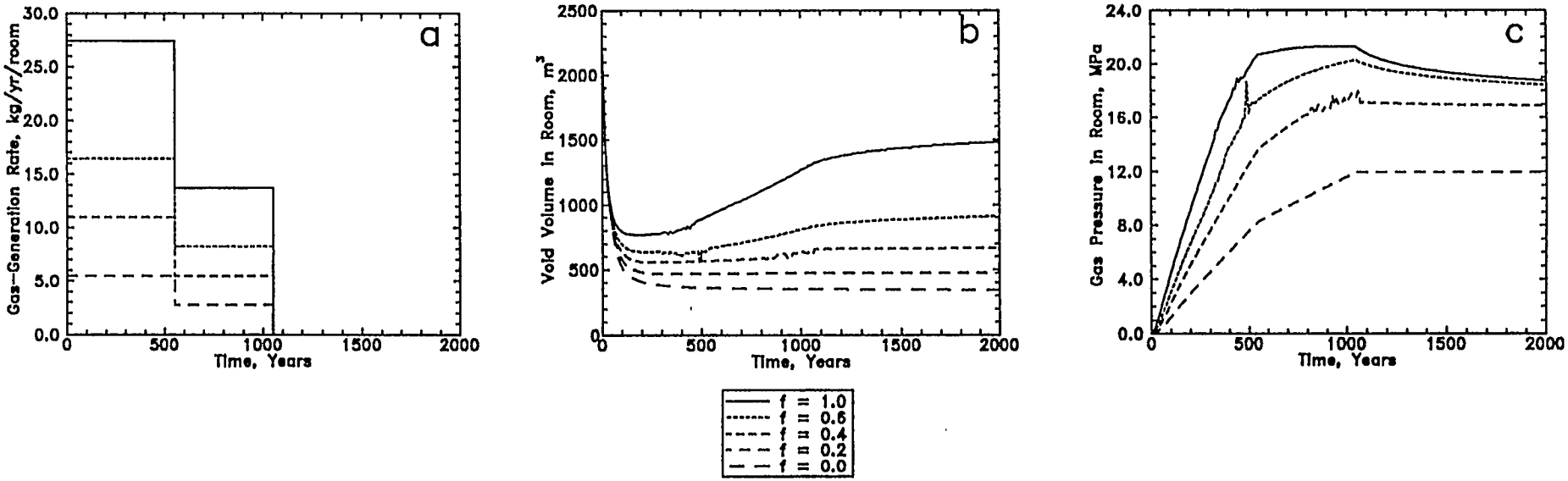

Figure 1. Gas-generation rate histories and SANCHO simulation results from Stone (1992).

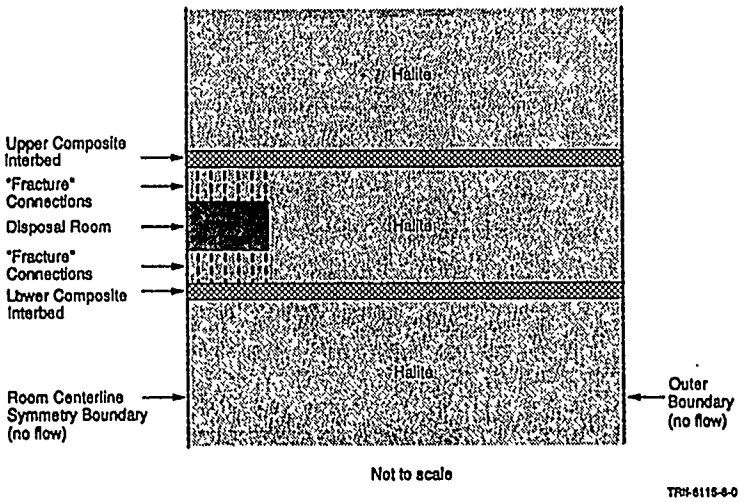

Figure 2. Schematic representation of the fluid-flow continuum.

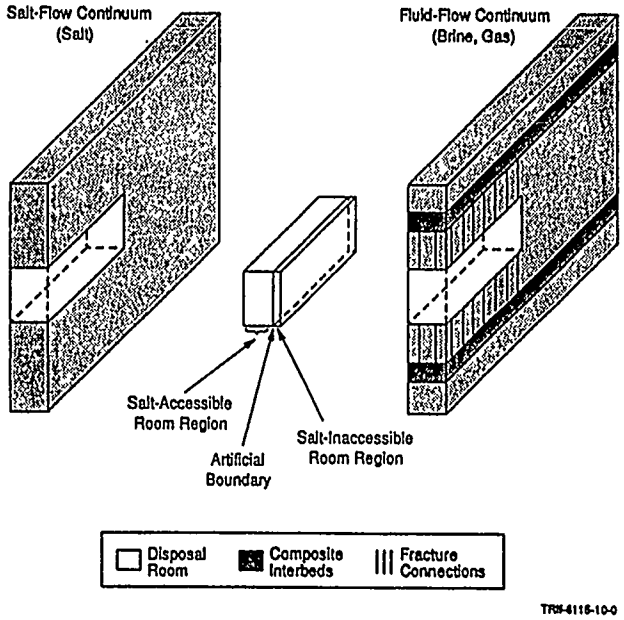

Figure 3. System conceptualization with the fluid-phase-salt method.

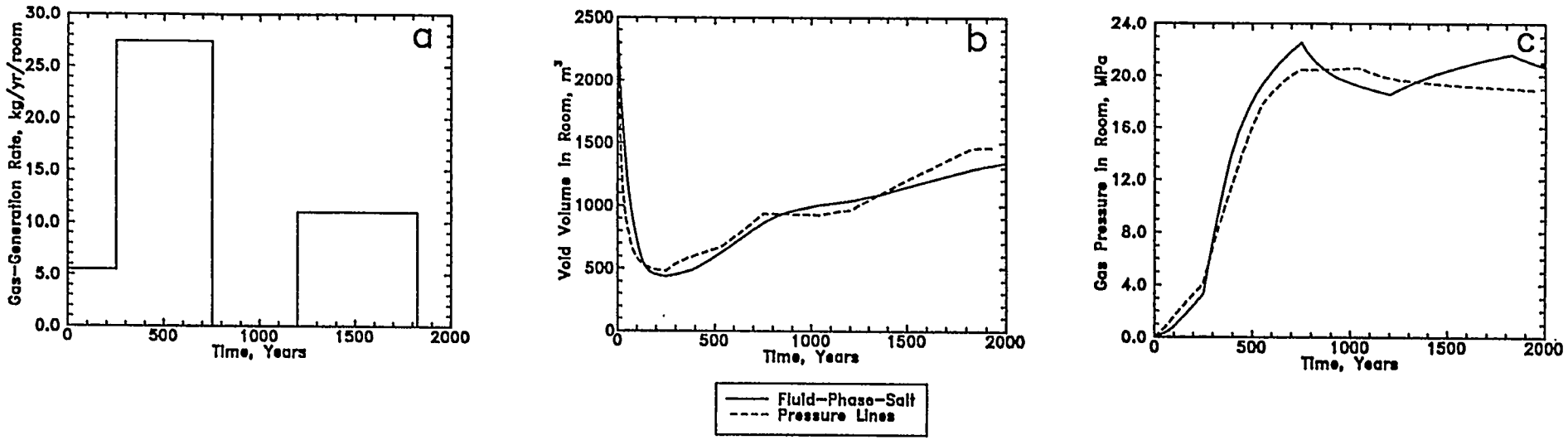

Figure 4. Gas-generation rate history and simulation results from TOUGH2/EOS8 sealed room simulation.

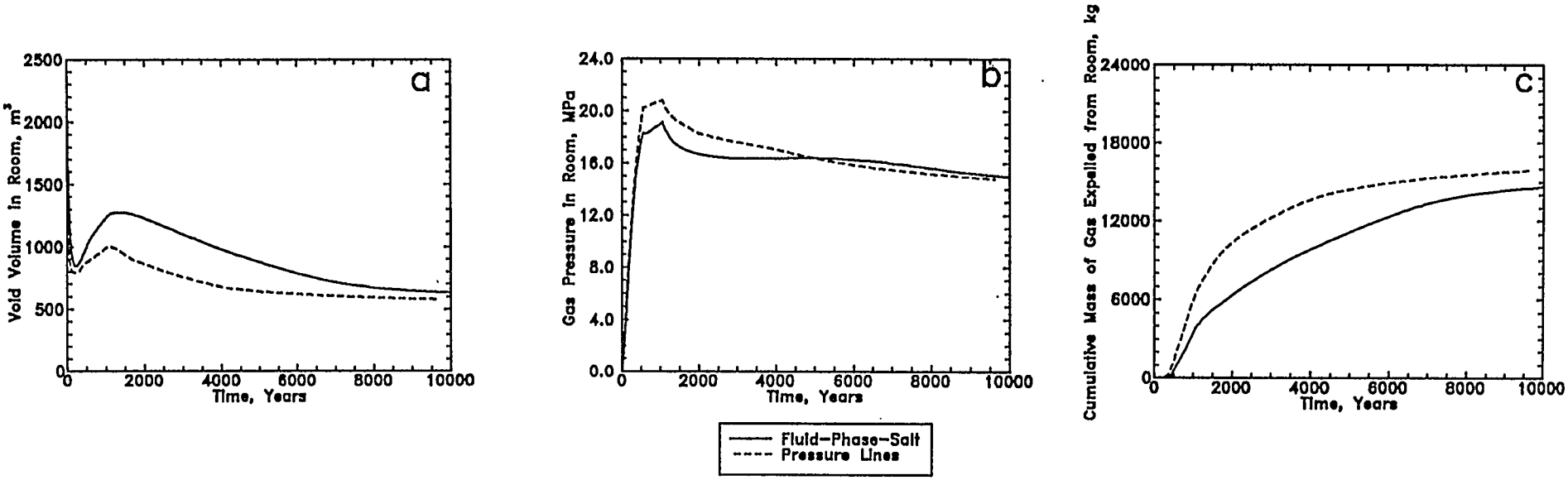

Figure 5. Simulation results from TOUGH2/EOS8 fully coupled flow and closure simulation with an f=1.0 gas-generation rate history.

PRELIMINARY ANALYSIS OF TANK 241-C-106 DRYOUT DUE TO LARGE POSTULATED LEAK AND VAPORIZATION

Mel G. Piepho[a]
Westinghouse Hanford Co.

a) Currently with Daniel B. Stephens & Associates, Inc., Pacific Northwest Branch Office, 1845 Terminal Dr., Suite 200, Richland, WA 99352

INTRODUCTION

At the Hanford site in SE Washington, there are 149 single-shell tanks containing radionuclide wastes in the form of liquids, sludges and salt cakes. One of the tanks, tank 241-C-106, is heated to the boiling point due to radionuclide decay (primarily Sr-90). Water is added to the tank, which is ventilated, in order to cool the tank. This analysis assumes that there is a hypothetical large leak at the bottom of Tank 241-C-106 which initiates the dryout of the tank. The time required for a tank to dryout after a leak is of interest for safety reasons. As a tank dries outs, its temperature is expected to greatly increase, which could affect the structural integrity of the concrete tank dome. Hence, it is of interest to know how fast the temperature in a leaky tank increases, so that mitigation procedures can be planned and implemented in a timely manner.

The objective of the study was to determine how long it would take for tank 241-C-106 to reach 350 degrees Fahrenheit (about 177 degrees Centigrade) after a postulated large leak develops at the bottom center of the tank.

CONCEPTUAL MODEL

The scenario used in this analysis is that a large hole (1-m radius) is postulated to open in the bottom center of the tank. This large hole is unrealistic, but it does provide a conservatively rapid loss of drainable liquid. Some of the fluid, which is assumed to be water, in the tank sludge then drains out of the large hole into the soil below the hole. The ventilation system for the tank is assumed to be turned off.

The conceptual model assumes azimuthal symmetry (radius and height are the only spatial variables) and is shown graphically in Figure 1. Since actual tank waste prperties are not known, this pseudo-3D analysis assumes two types of porous media for the sludge in Tank 241-C-106: 1) a backfill soil that is fairly permeable (3.E-11 m^2) and represents a worst-case choice of medium, and 2) the middle Ringold geologic formation (cemented sand, gravel and cobbles) at Hanford. The Ringold formation is more impermeable (2.4E-15 m^2) than backfill soil, but more permeable than clay (1.E-18 to 1.E-16 m^2), and exists in the soil stratigraphy, above the basalt layers, at the Hanford site. These two media are hydraulically well characterized and are described in many reports (Piepho 1994).

Since the air space above the sludge in the tank is important for holding vapor emitted from the hot sludge, it was included in the model as a large-porosity (99%) gravel. The porous-media computer code that was used for the analysis, needs porous-media properties for all spatial regions of the model even if the spatial region is an air space. Gravel properties will permit high velocities to take place and moisture retention capability is almost non-existent; hence, the gravel hydraulic properties are closer to pure air properties than those of other porous media. The large porosity of 0.99 essentially makes this gravel almost all air.

FIGURE 1 Conceptual Model

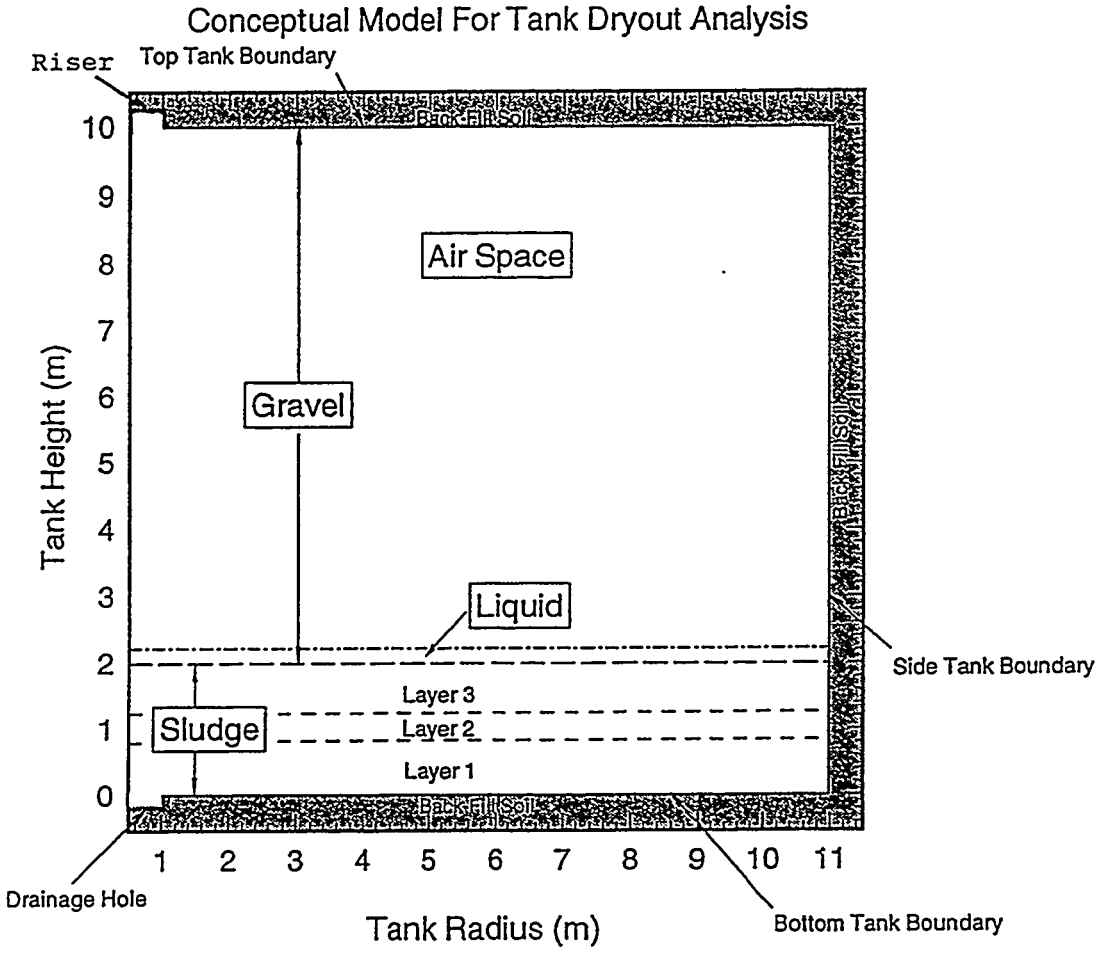

The boundary surrounding the sludge was given a zero permeability, creating a no-flow situation, in order to represent the impermeable steel shell between the sludge and the concrete. The boundary cells are not drawn to scale in Figure 1 and are actually 10-m thick in the model. The boundary cell below the hole in the tank is actually much larger in volume. With an extremely large-volume drainage cell, all of the fluid in the tank can easily be held in that cell without changing the moisture-retention properties of the cell. This is conservative, since the unsaturated drainage cell will continue to draw the liquid out more than a saturated cell. To check this conservative

model feature, another much larger grid was made which included the backfill soil down to the water table (about 70 m).

MATHEMATICAL/NUMERICAL MODEL

The mathematical model consists of the mass- and energy-balance equations required for nonisothermal multiphase flow. These equations are solved numerically by the TOUGH2 code (Pruess 1991). The primary multiphase thermodynamic variables are gas (both air and vapor) pressure, gas saturation, and temperature. The fourth equation-of-state (EOS4) module was chosen from the TOUGH2 suite of modules. The EOS4 module provides the equations of state for a water-air system with vapor pressure-lowering effects (Pruess 1991). The vapor pressure-lowering effects are a result of very dry conditions. For very dry conditions, the vapor pressure is lower than predictions derived from the ideal gas law, and the EOS4 module modifies the vapor pressure calculation according to Kelvin's equation, which lowers the vapor pressure.

The hydraulic and thermal data are given in an earlier report (Piepho 1995). The heat generation rates, one for each of the three sludge layers, correspond to a total heat load of 110,000 BTUs per hour (32,240 Watts). The spatial heat generation distribution, which is highest in the middle sludge layer (68.7 W/m^3) and lowest (17.2 W/m^3) in the top sludge layer (52.2 W/m^3 in the bottom sludge layer), was determined by Bander (1993).

The thermal conductivities came from Bouse (1975) as he performed real measurements on both wet and dry sludge. The thermal conductivity of fully-wet gravel (99% water) representing the tank air space is basically that of water (0.6 W/m/C), and the thermal conductivity of dry gravel (99% air) is that of air (0.027 W/m/C). The wet sludge's thermal conductivity was taken to be 0.8 W/m/C, and the dry sludge's thermal conductivity was 0.16 W/m/C.

RESULTS AND CONCLUSIONS

Seven simulated cases are reported. Many more cases were run, but the results from these seven cases are considered to summarize and bound the analysis. The Ringold hydraulic properties were used for the sludge properties for four cases with three different permeabilities and the Klinkenburg effect. The backfill soil properties were used for sludge properties for the three cases with a much smaller leakage hole (10% of the original hole area) and much larger grid which included the entire soil from the ground surface to the aquifer.

The maximum temperature in the tank for all times up to one year, is shown graphically in Figure 2 for all seven cases. The maximum temperature is not constrained to any one cell; in fact, the cell with the maximum temperature does change over time in most of the simulations.

The worst-case scenario (Case 5 with backfill soil properties for sludge), shows that it would take about four months after the tank starts leaking before the maximum tank temperature reaches 350 degrees Fahrenheit. Even if the hole size (1-m radius) is reduced by 10% in area (Case 6), the 350 deg F temperature is reached only about eight days later than the Case 1 with the original large hole. Basically, the backfill soil, with its capillary forces,

is controlling the leak rate more than the hole size. When the more realistic large grid is used (Case 7), the time to reach 350 deg F is extended to 157 days or about a month longer than Case 1. This indicates that the peak tempertatures are more conservative or higher when the smaller grid is used.

FIGURE 2 Maximum Tank Temperatures for the Seven Simulated Cases

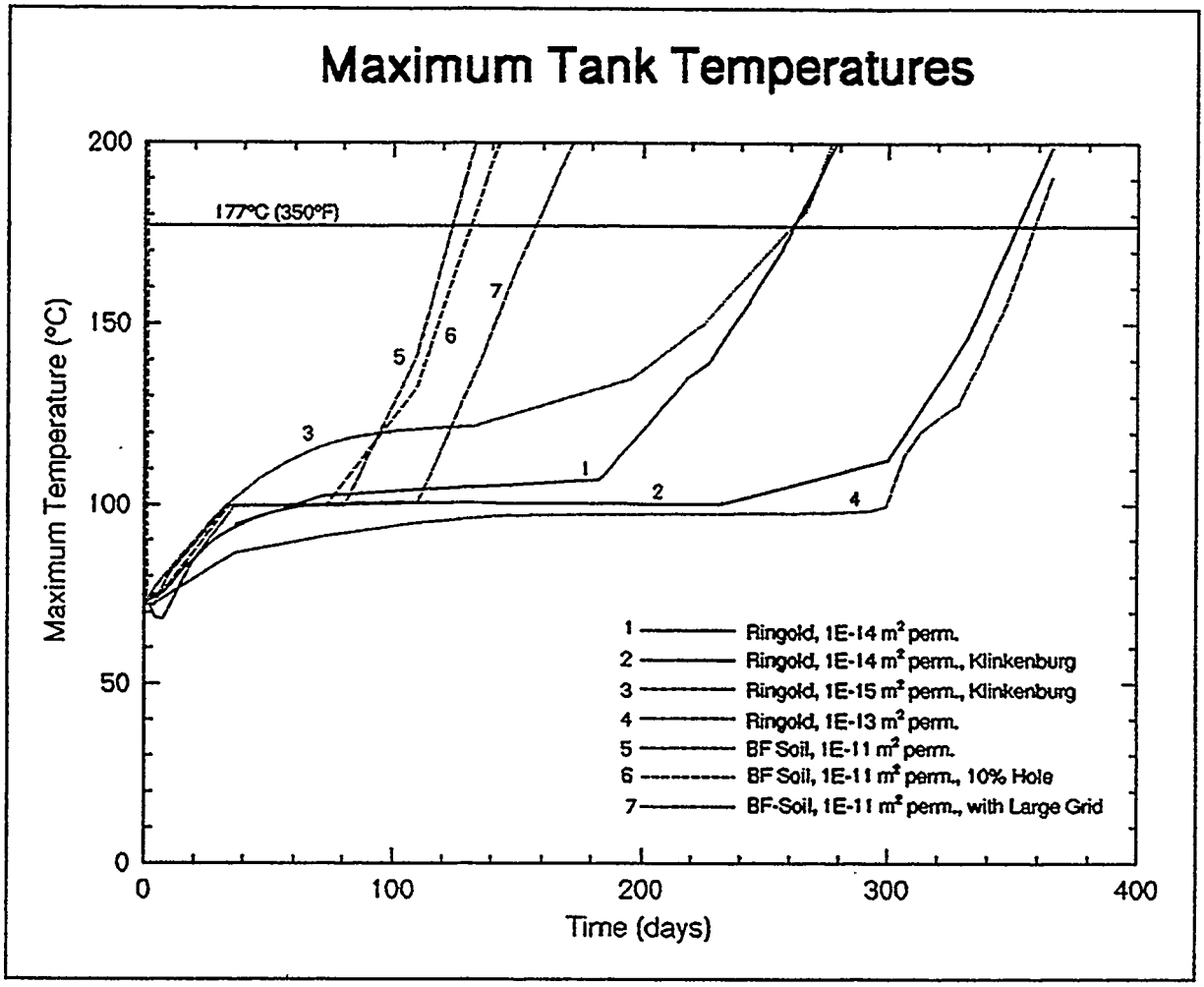

The sludge permeability is probably closer to the Ringold permeability which is more impermeable than backfill soil, but still more permeable than most clays by one to three orders of magnitude. With Ringold moisture-retention properties and its permeability increased by 10 (Case 1), the maximum tank temperature reaches 350 degrees Fahrenheit in 260 days. With the Klinkenburg effect, the gas in the sludge has a higher permeability, which is pressure dependent, than the liquid (Case 2), and the time to reach 350 deg Fahrenheit is now 350 days. The difference between cases 1 and 2 indicate that the gas is pushing out the liquid from the sludge and keeps the liquid from entering the sludge. With the Klinkenburg effect, the gas can escape the sludge more easily, due to a larger gas permeability, and leave more of the liquid in the sludge. The effect of the gas (gas is air plus vapor here) is clearly shown in Figure 3 for Case 1 at 182 days after the leak.

FIGURE 3 Liquid and Gas (Air+Vapor) Mass Flows for Case 1 at 182 Days

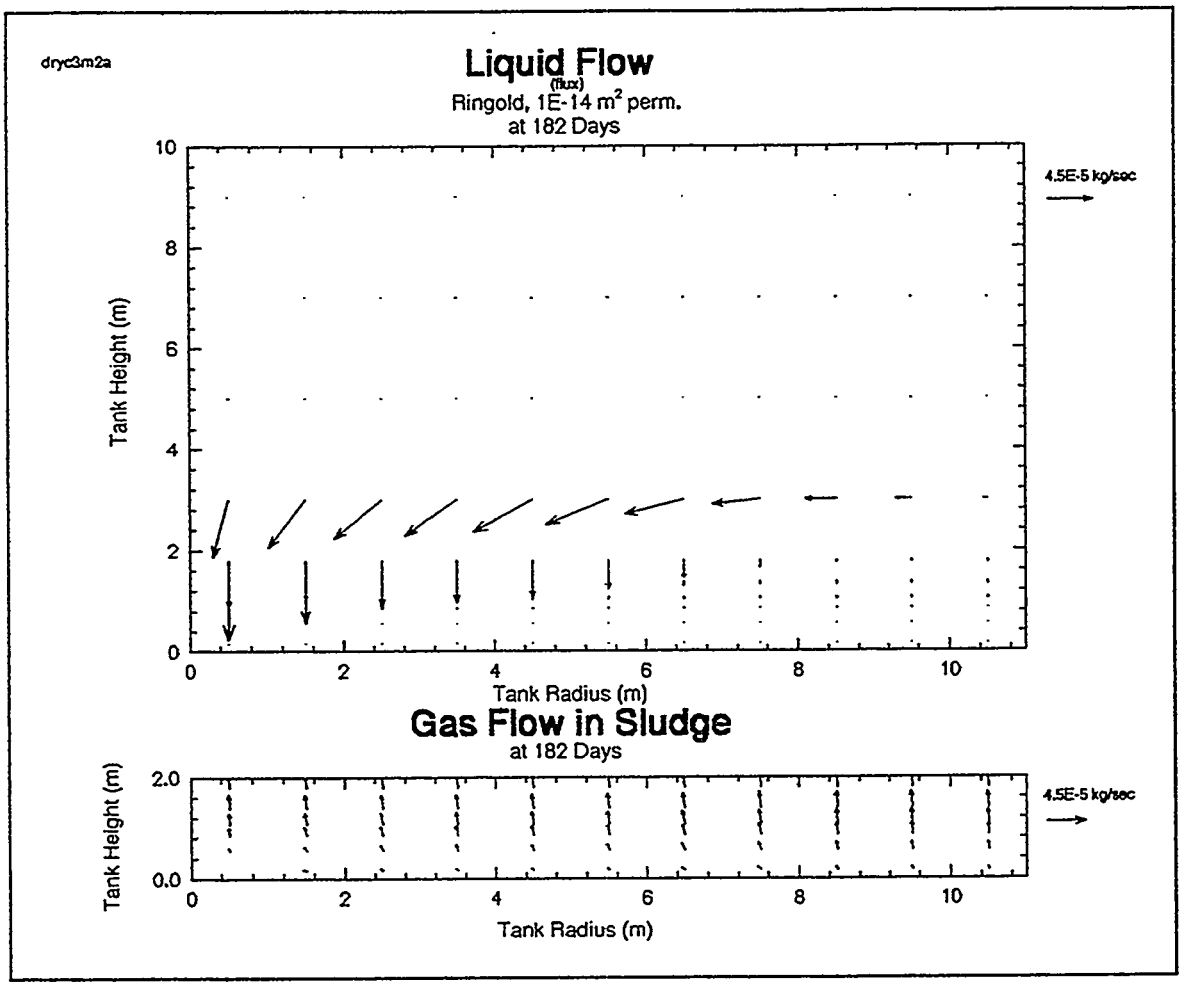

The liquid mass flow shows a horizontal movement just above the sludge, which occupies the bottom 2 m of tank. The vertical liquid movement into the sludge eventually stops, sooner on the right side and middle, with no horizontal liquid movement resulting. This is explained by the gas mass flow moving up and canceling the liquid flow. On the far right, the gas or vapor actually bubbles up into the air space where it condenses and contributes to the liquid flow again.

Going back to the maximum temperatures in Figure 2, one can see that Case 4 is the same as Case 1 except that the permeability has been decreased an order of magnitude to 2.4E-13 m^2. With the higher permeability, the gas can escape the sludge more easily without pushing the liquid out of the sludge and the time to reach 350 deg F is extended to 360 days.

Another reason, in addition to smaller permeabilities and higher capillary forces, that the Ringold-type sludge takes longer to heat up than the backfill-soil-type sludge is that the Ringold porosity is larger than the backfill-soil porosity. Hence, the Ringold-type sludge contains more liquid initially and takes longer to heat up and dryout.

Case 3 is the same as Case 2 except that the permeability has been decreased an order of magnitude to 2.4E-15 m^2, which is the true permeability of the Ringold Formation. This permeability is one to three orders of magnitude larger than most clay permeabilities. With this smaller permeability, the pressures are greater in the sludge, resulting in higher temperatures for early times after the leak (i.e., the pressure cooker effect). Even with the Klinkenburg effect, the gas still cannot easily escape the sludge and has a harder time pushing the fluid out, resulting in higher pressures and temperatures. The time to reach 350 deg F is 260 days, the same as Case 1 which has a higher permeability and no Klinkenburg effect. Hence, for Case 3, the smaller permeability is enough to more than offset any increase in air permeability that the Klinkenburg effect causes.

RECOMMENDATIONS

Since this analysis was preliminary, several improvements can be recommended. Obtaining specific hydraulic and thermal data for the sludge in Tank 241-C-106 or a very similar tank would certainly be more reliable than assuming the values. Sludge properties can vary widely from tank to tank. Also, the sludge properties may have a spatial distribution of hydraulic properties with the bottom sludge being more impermeable than the top sludge. Furthermore, the thermal conductivities could easily be higher, which will conduct more heat out of the tank faster, than those used here. The size of the leaking hole appears not to be very important as the porous-media moisture-retention properties of the sludge appear to dominate. In summary, the most important sludge properties are the following: 1) permeability, 2) porosity, 3) moisture-retention relationship, and 4) thermal conductivities.

The main recommended items for future work are summarized below: 1) cracks, 2) air ventilation and air chiller, 3) water sprays, 4) location of leak, 5) specific thermal/hydraulic data for sludge, and 6) better initial conditions.

REFERENCES

Bander, T. J., 1993. Revised Thermal History of Tank 241-C-106, WHC-SD-WM-ER-200, Rev. 0, Westinghouse Hanford Company, Richland, Washington.

Bouse, D. G., 1975. Thermal Conductivity of Hanford Waste Tank Solids and SX Farm Soil Samples, ARH-CD-378, Atlantic Richfield Company, Richland, WA.

Handy, L. L., 1975. Flow Properties of Salt Cake for Interstitial Liquid Removal/Immobilization Development Program, ARH-C-6, Atlantic Richfield Company, Richland, Washington.

Piepho, M. G., 1994. Grout Performance Assessment Results of Benchmark, Base, Sensitivity and Degradation Cases, WHC-SD-WM-TI-561, Rev. 0, Westinghouse Hanford Company, Richland, Washington.

Piepho, M. G., 1995. Preliminary Analysis Of Tank 241-C-106 Dryout Due To Large Postulated Leak And Vaporization, WHC-EP-083, Rev. 1, Westinghouse Hanford Company, Richland, Washington.

Pruess, K., 1991. TOUGH2: A General-Purpose Numerical Simulator for Multiphase Fluid and Heat Flow, LBL-29400, Lawrence Berkeley Laboratory, Berkeley, California.

Presented at the TOUGH '95 Workshop, Lawrence Berkeley Laboratory, Berkeley, CA, March 20-22, 1995.

SAND95-0587C
Summary of Applications of TOUGH2 to the Evaluation of Multiphase Flow Processes at the WIPP

Stephen W. Webb, Kurt W. Larson, Geoff A. Freeze[1], and Tracy L. Christian-Frear
Sandia National Laboratories
Albuquerque, NM 87185

Introduction

The Waste Isolation Pilot Plant (WIPP) is a U.S. Department of Energy (DOE) research and development facility for the underground disposal of transuranic waste in southeastern New Mexico. The WIPP repository is located 655 m below the land surface in the lower portion of the Salado Formation, which is comprised of beds of pure and impure halite with thin interbeds of anhydrite and related clay seams. The regional dip of the Salado Formation is approximately 1° southeast in the vicinity of the repository. The proposed waste storage area has eight waste disposal panels, each of which will contain seven rooms (Figure 1). The repository is designed to follow a single stratigraphic horizon. Due to the dip, the north end of the panels will be about 8 meters higher than the south end.

Waste that is emplaced in the disposal rooms will generate gas due to microbial degradation, anoxic corrosion, and radiolysis. Brine inflow to the rooms from the surrounding Salado Formation may significantly influence the gas generation rate and the total amount of gas generated. The salt surrounding the repository will creep in response to the excavation, reducing the room volume. Gas generation in the room may increase the pressure sufficiently to drive brine and gas into the surrounding Salado Formation. Migration of gas and brine in the Salado is an important factor in evaluating the performance of the repository.

The studies summarized in this paper have been performed to evaluate brine and gas flow processes in the WIPP disposal system and to identify some of the important processes. These studies are done in support of, but are not part of, the formal Performance Assessment (PA) effort. Because of probabilistic and system-scale requirements, the PA effort uses the Sandia-developed BRAGFLO (BRine And Gas FLOw) code for multiphase flow calculations.

Repository Modeling Studies

Our studies to date have generally been limited to two-dimensional modeling of a single room, although some three-dimensional modeling has been performed and more is planned. Early studies of brine inflow and gas migration used the ECLIPSE code. While this code was adequate for early analyses, TOUGH2 was selected for current use due to the availability of the source code and its use on the Yucca Mountain Project.

Most early studies of the response of the repository assumed a constant volume room (Webb, 1992a) for simplicity. However, time-dependent creep closure and pressure-induced re-inflation of the repository could have a significant impact on repository performance. Attempts to model salt creep and repository closure through the flow of a highly-viscous fluid (salt) were performed

[1] INTERA, Inc., Albuquerque, NM

using ECLIPSE (Davies et al., 1992). As the transition was made to TOUGH2, similar modifications were made resulting in a special air-water-oil equation of state, EOS8, in which the flow of the oil phase simulates salt creep as given by Freeze, et al. (1995).

While this approach was an improvement over a constant room volume calculation, questions about the applicability of the approach in general have led to the development of PHENIX, which crudely couples TOUGH2 and a rock mechanics code, SANTOS (Stone, in preparation). The PHENIX code simply passes appropriate parameters between TOUGH2 and SANTOS every few time steps. While this coupling is crude, it is an improvement over the EOS8 module.

A number of other studies have been performed to evaluate assumptions made in the development of the Performance Assessment (PA) model. Due to computational constraints related to the large number of Monte Carlo simulations and the need to model the repository - geosphere system, PA uses a highly simplified repository and Salado Formation model. For example, due to the relatively small dip of the formation ($\sim 1°$), a horizontal configuration has been assumed. In addition, the number of stratigraphic layers represented in the Salado Formation is limited. The PA model is also a hybrid 2D/3D model assuming radial symmetry. The room/panel/repository model is extremely simplified even though waste properties such as permeability vary orders of magnitude. These and other assumptions have been or are planned to be evaluated using more detailed TOUGH2 modeling.

The regional dip of the Salado, even though only about 1°, has the potential to significantly alter some of the two-phase flow behavior. If a horizontal configuration is assumed, only cocurrent two-phase flow is likely. If the configuration is not horizontal, countercurrent two-phase flow is possible. In the case of the WIPP repository, the inclusion of this 1° dip may increase brine inflow by about 50 percent due to counterflow in the anhydrite interbeds. In addition, due to buoyancy forces, gas migration distances may be dramatically increased when dip is included as shown by Webb and Larson (1995).

There are about 40 distinctive stratigraphic layers within 10 meters vertically of the repository, consisting of units of anhydrite, argillaceous halite, polyhalitic halite, and pure halite. The present PA model lumps two of the anhydrite layers together, and represents all the non-anhydrite layers by a single composite impure halite material. The difference in the layering detail is shown in Figure 2, where LAY and PAL refer to the detailed and PA schemes, respectively. A room model using both layering schemes has been examined by Christian-Frear and Webb (in review) to evaluate the performance differences between the two representations.

Figure 3 compares a variety of cases with the two layering schemes. For any one variation, such as the base case or interbed fracture, the results are similar. Differences in repository pressurization and brine inflow due to the two layering schemes are quite small, while gas migration distances show a moderate influence of the layering detail. Based on these results, explicit representation of the individual layers is probably not warranted in the PA model, especially when repository pressure and brine inflow are the main performance measures. If gas migration distance is the main issue, additional stratigraphic layering detail may be necessary.

Additional studies planned include development of a full three-dimensional model of the repository. The TOUGH2 integrated finite difference method offers significant advantages over standard finite difference meshes in that detail in certain regions can be included without altering the entire model domain. For example, one of the panels may be broken up into separate rooms, while the other panels use a lumped representation. Unlike the traditional finite difference approach, this added detail will not affect other parts of the mesh.

Fracturing of the anhydrite interbeds may occur if the repository pressure approaches lithostatic. Development of a dual permeability and/or dual porosity model of fractured interbeds is another planned activity. The dual continuum capability of TOUGH2 will be used to evaluate the simplified porous medium representation currently used by PA.

Finally, development of a detailed model of a room is planned. Each room will contain waste with widely varying porosity and permeability. If the repository pressurizes, gas and brine will tend to move out of the repository and into the interbeds. Due to the variation of physical properties and the stratigraphic dip, significant nonuniform behavior is possible, and large regions of brine may be left behind that may continue to generate gas. A detailed room model is planned to address heterogeneity issues in the room.

Salado Data Interpretation Studies

In addition to the modeling studies described above, TOUGH2 has been used as a data interpretation and sensitivity analysis tool. Brine inflow is an important parameter for the WIPP. As part of the evaluation of brine inflow data into open boreholes, Webb (1992b) and Christian-Frear (1993) performed one- and two-dimensional sensitivity studies considering such factors as dissolved gas exsolution, free gas, multiple boreholes, the effect of a room on brine inflow to a borehole, and stratigraphic layering. Brine inflow data are also being collected in Room Q, a large 9.5-ft diameter 300-ft long circular room which has been sealed off in order to collect brine inflow data. Interpretation of the brine inflow and surrounding pore pressure data with TOUGH2 and ITOUGH is planned.

As part of the Salado testing program, packed-off sections of boreholes are tested to evaluate formation parameters in different units at various distances from the repository. Some threshold pressure tests were conducted in a packed-off borehole to try to estimate the threshold pressure of an anhydrite layer. These data were interpreted using TOUGH2 to evaluate different sets of two-phase characteristic curves.

Non-Salado Studies

In some WIPP human intrusion scenarios, brine from pressurized brine reservoirs in the Castile Formation below the Salado is assumed to flow into the repository through a borehole, and repository fluids (gas and brine) are released into the overlying Culebra Formation. Currently, flow in the Culebra has only been analyzed as a variable density brine, neglecting the effect of the gas. To address this concern, an air-water-brine equation of state, EOS7, was developed in which the brine and water were miscible. EOS7 was tested by comparison to the variable

density brine analysis done with SWIFT II as summarized by Christian-Frear and Webb (1995). Extension to brine and gas flow in the Culebra is possible in the near future.

Conclusions

TOUGH2 has been shown to be a powerful and versatile multiphase analysis tool for the WIPP, useful for repository modeling, data interpretation, and PA model evaluation. It has shown where PA model simplifications have significant impact on the results, such as in ignoring dip, and has indicated where existing PA models are sufficient, such as in the stratigraphic layering detail. Additional studies evaluating other features of the PA model are planned.

Acknowledgment

This work was supported by the United States Department of Energy under Contract DE-AC04-94AL85000.

References

Christian-Frear, T.L. (1993), *Simulations of Brine Inflow into a Waste Isolation Pilot Plant Borehole: Results of Two-Dimensional Numerical Sensitivity Studies*, Topical Report RSI/ALO 1993-470, RE/SPEC, Inc., Albuquerque, NM.

Christian-Frear, T.L., and S.W. Webb (in review), *The Effect of Explicit Representation of the Stratigraphy on Brine and Gas Flow at the Waste Isolation Pilot Plant*, SAND94-3173, Sandia National Laboratories.

Christian-Frear, T.L., and S.W. Webb (1995), "Modification and Application of TOUGH2 as a Saturated Flow Code and Comparison to SWIFT Results," *TOUGH '95 Workshop Proceedings.*

Davies, P.B., L.H. Brush, and F.T. Mendenhall (1992), "Assessing the Impact of Waste-Generated Gas From the Degradation of Transuranic Waste at the Waste Isolation Pilot Plant (WIPP): An Overview of Strongly Coupled Chemical, Hydrological, and Structural Processes," *Gas Generation and Release from Radioactive Waste Repositories*, Aix-en-Provence, France, Nuclear Energy Agency, OECD, pp. 55-74.

Freeze, G.A., K.W. Larson, P.B. Davies, and S.W. Webb (1995), "Using a Multiphase Flow Code to Model the Coupled Effects of Repository Consolidation and Multiphase Brine and Gas Flow at the Waste Isolation Pilot Plant," *TOUGH '95 Workshop Proceedings.*

Stone, C.M. (in preparation), "SANTOS - A Two-Dimensional Finite Element Program for the Quasistatic, Large Deformation, Inelastic Response of Solids," SAND90-0543, Sandia National Laboratories.

Webb, S.W. (1992a), "Sensitivity Studies for Gas Release From the Waste Isolation Pilot Plant (WIPP)," *Gas Generation and Release from Radioactive Waste Repositories*, Aix-en-Provence, France, Nuclear Energy Agency, OECD, pp.310-326.

Webb, S.W. (1992b), *Brine Inflow Sensitivity Study for Waste Isolation Pilot Plant Boreholes: Results of One-Dimensional Simulations*, SAND91-2296, Sandia National Laboratories.

Webb, S.W., and K.W. Larson (1995), "The Effect of Stratigraphic Dip on Multiphase Flow at the Waste Isolation Pilot Plant," *TOUGH '95 Workshop Proceedings.*

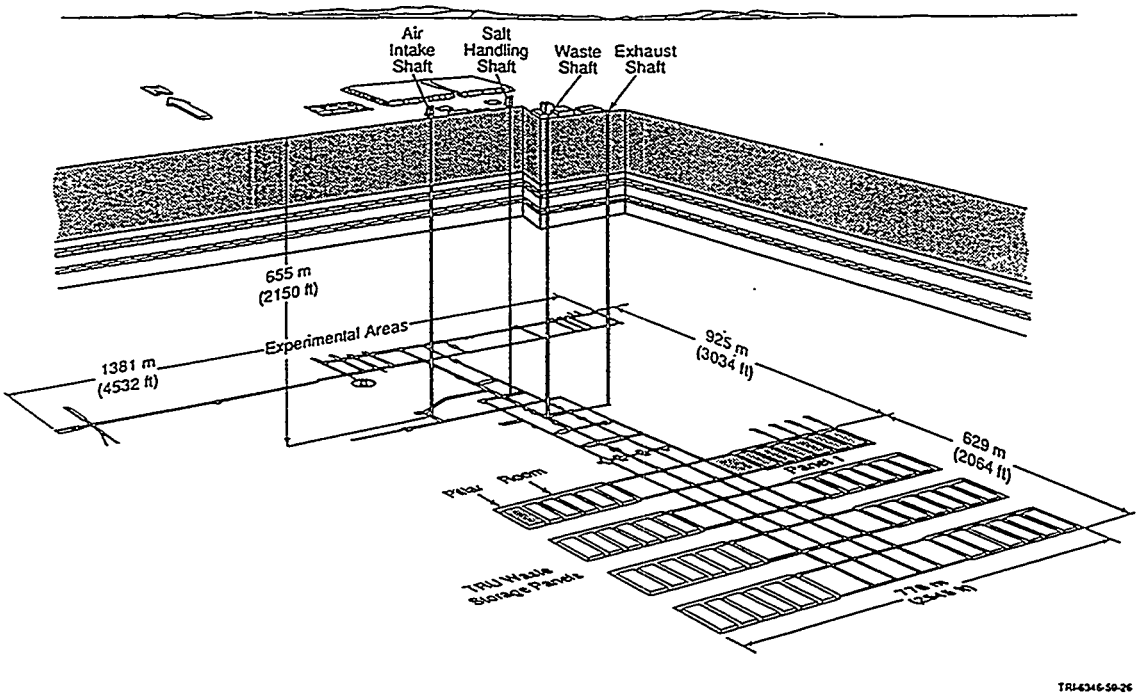

Figure 1 Underground configuration of the Waste Isolation Pilot Plant.

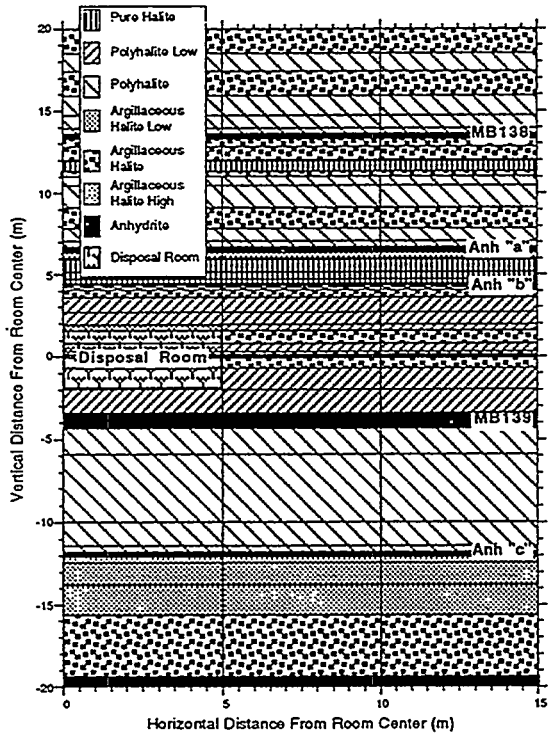

Figure 2a. A partial representation of the LAY model mesh near the disposal room with the location of the modeled anhydrite beds.

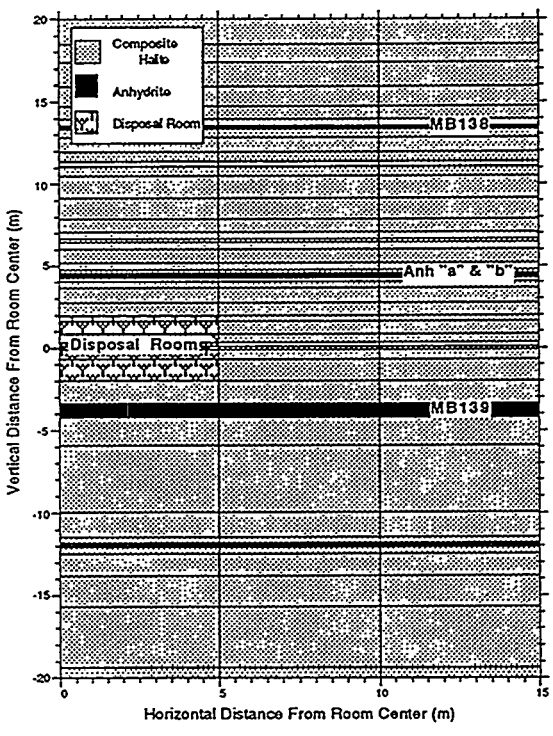

Figure 2b. A partial representation of the PAL model mesh near the disposal room with the location of the modeled anhydrite beds.

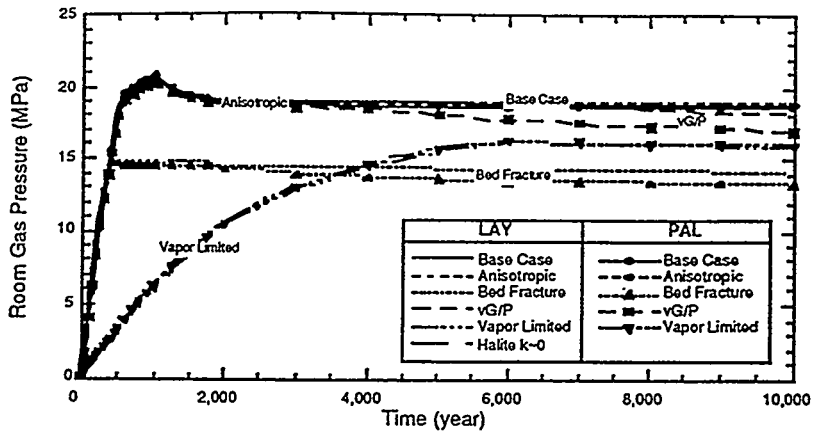

3a. Repository pressure.

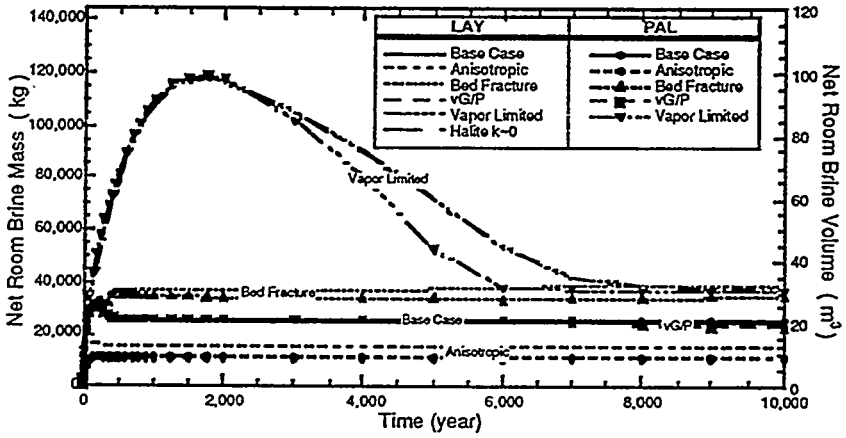

3b. Brine inflow into the repository

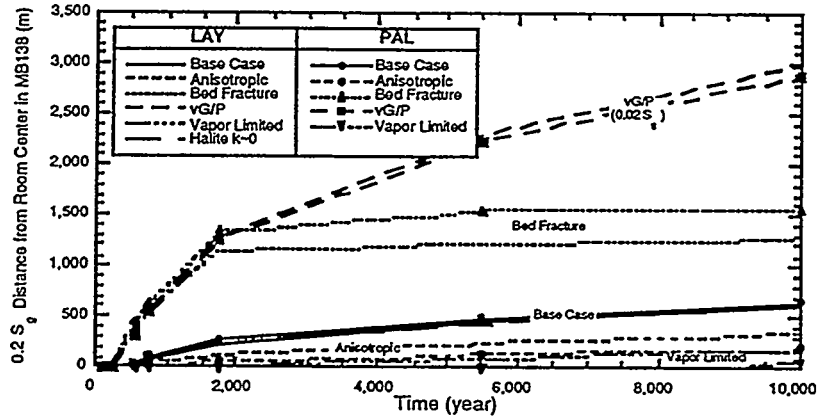

3c. Gas migration distance.

Figure 3. Effect of stratigraphic layering detail.

Requirements on Sealing Measures Due to Gas Production

March 1995

G. Arens, L. Höglund, M. Wiborgh

Summary

Since 1981 the former rock salt mine Bartensleben near Morsleben (former GDR) ERAM has been in operation as a repository for low and intermediate level radioactive waste. As a result of the reunification and the changed licensing situation a new closure concept for the repository has to be developed.

During the post-opertional phase of a repository for radioactive waste gas may be produced by corrosion of metals, microbial degradation and radiolytic decomposition. In the process of developing the concept to be used for backfilling and sealing in ERAM it is important that gas formed in the repository will not disrupt the barrier against radionuclide escape or enhance the radionuclide release. To evaluate the performance and the properties for a bentonite plug as the main element of the sealings gas transport modelling with THOUGH were performed.

Due to the lack of site-specific data literature data were used. Consequently, large uncertainties in data remain at present, which were taken into account by a great number of parameter variations. To handle this a course discretisation for the calculations were developed. Started with a two-dimensional grid at the end the calculations were performed with a coarse one-dimensional grid.

The primary question to answer in these calculations is if there is a risk for excessive pressurization of the repository caverns as a result of gas generation. In the reference case a maximum pressure of approximatley 10 Mpa inside a cavern is reached after 1000 years which seems not to jeopardize the integritiy of the repository.

1. Gas production in the repository

The Federal Office for Radiation Protection in Germany (BfS) is required to submit before 1997 the basis for the legal procedure of authorising the plans for the operation of the repository for low-level radioactive waste at Morsleben, ERAM, in the German state of Saxony-Anhalt after the year 2000. The description of the planned backfilling and sealing measures forms the most important part of the documentation to be prepared and a basis for the long-time safety analyses.

During the post-operational phase gas will be produced inside the waste caverns by corrosion of metals, microbial degradation and radiolytic decomposition. This could impact the safety of the repository in different ways. Gas production could act as a driving force for brine flow, could enable radionuclide transport in the gaseous phase and could jeopardize the integrity of sealing measures.

To study the impact of gas production on sealing measures THOUGH gas transport calculations were performed for the actual most

important waste cavern. The so-called Westfeld has an excavated volume of approximately 40 000 m^3 with a capacity to store approximately 16 500 m^3 waste. The assumed average composition of the mixed waste and mixed solids is described in Table 1.

Waste:	Vol- %
Metal (Fe)	20
Laboratory waste	5
Stabilized waste	10
$CaSO_4$-stabilized waste	10
Cemented waste	25
PVC and other plastics	3
Activated carbon	2
Epoxy resin	2
Wood	1
Pulp, paper, cellulose	2
Filters	15
Bitumen	2
Textile	3

Tab. 1: average composition of the mixed waste

Considering the waste content and waste acitivity wich is limited to $4 \cdot 10^{10}$ Bq/m^3 β/γ-radiation hydrogen production by anaerobic corrosion of steel as the most important gas producer was pointed out.

While the potential of the total amount of hydrogen is easily determined by the total amount of stored steel the gas production is strongly dependent on the szenario for the chemical and physical conditions during the post-operational phase. Due to the lack of site-specific data reported corrosion rates have been compiled. Figure 1 shows compiled corrosion rates for the relevant temperature range from 0 - 60 °C.

2. Basic scenario

In the performed gas transport calculations a basic scenario has been assumed for the post-operational phase of the repository. Once the waste is stored in the repository, the void between the waste packages is backfilled with crushed salt or lignite fly-ash. After completed operation the Westfeld is sealed with a bentonite plug. The initial water saturation is only 2 % of the porosity. During the post-operational phase slight amounts of water may however enter by leakage through the host rock, enough to support a corrosion rate of 1 µm/a of steel wich consumes approximately 2 m^3/year water. The shafts have been assumed to be rapidly filled by saline groundwater, thereby establishing a hydrostatic pressure of 5 MPa on the outside of the bentonite plug.

Fig. 2 shows the annual amounts of hydrogen gas produced as a function of time for variations in the corrosion rate. In the reference case a total metal load of approximately 14 000 Mg is assumed.

3. Model implementation

The overall objective of the investigation was to determine the pressurization of the repository versus time, and the overall behaviour of the plug with respect to intrusion and discharge of brine. The exact definition of dimensions and properties of the plug are not finally decided so the geometrical representation of the Westfeld has greatly been simplified. A two-dimensional mesh, a coarse one-dimensional mesh and a detailed fine one-dimensional mesh have been used in the calculation. Figure 3 shows the layout of the model.

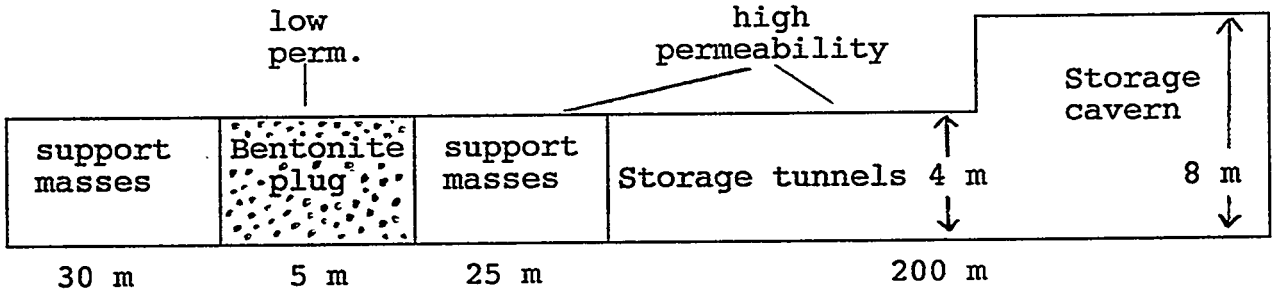

Fig. 3: layout of the numerical model

The THOUGH version 1 code was used on several 486 DX/50MHz PCs for the calculations. Different grids where tested for numerical convergence and precision. But for the essentially one-dimensional nature of the problem no differences were found between grids with 10 elements or 100 elements and one- or two-dimensional grids. For transient calculations from 0 to 10000 years the effective run times varied within the order of 1 hour for favourable cases and more than two weeks for combinations of high permeability and high capillary pressures.

4. Results

The calculations show that a total of 8 million m^3 of gas can be formed over a period of 5000 years. The maximum gas formation rate is estimated for 2400 m^3/year during the first 900 years.

For a plug permeability of 10^{-18} m^2 in the reference case the maximum pressure of 10,5 MPa, 5,5 Mpa in excess of the hydrostatic pressure is reached after 1000 years. An equilibrium between gas production and outflow exists between 2000 and 5000 years after closure. The maximum pressure of 6,5 MPa, 1,5 MPa in excess of hydrostatic pressure is in agreement with the critical gas pressure for the bentonite plug (see fig. 4).

With respect to more than 40 performed parameter variations pressurization of the Westfeld in excess of the lithostatic pressure has not to be expected for favourable cases.

Of particular interest is information on the amount of brine which at any point in time tends to be expelled form the repository by the gas. The expelled brine may be contaminated by radionuclides and therby contribute to the escape of radionuclides from the repository. From figure 5 it is clear that, for a permeability less 10^{-17} m^2, brine will not be pressed out of the repository at any time.

5. Conclusions and outlook

The issue of gas formation in a deep repository need to be seriously considered in an early stage of the conceptual work for the sealing measures.

The relative importance of the gas formation rate and the time for onset of full gas formation rate cannot be evaluated in a simple way. Large uncertainties are connected with the selection of the long-term corrosion rates. This is due to less well defined repository conditions in the post-operational phase and limited amount of data concerning corrosion rates measured under saline conditions. The uncertainties concerning the repository conditions include temperature, pH, as well as availability and quality of water. To reduce data uncertainties in the gas formation rates site-specific experiments have been set up.

The calculations need to be performed for a span of data to estimate the consequences of various parameter combinations. The calculations performed using a fully coupled brine and gas transport model show the need for a simplified model to be able to make calculations for a broad span of data. The use of a simple analytical model with the capability of handling the parameter combinations with a probabilistic approach is planned.

Due to the dry conditions in the waste caverns and the low iron content in the waste a low gas production is expected. Therefore closure of the waste caverns by tight sealings will not jeopardize the integrity of the repository by pressurization. The calculations as well indicate that brine will only flow into the repository, at least during the first 10000 years. The gas formation would not enhance the radionuclide release rate from the repository by expelling contaminated brine.

6. Literature

Müller W., Morlock G. and Gronemeyer C., Produktion und Verbleib von Gasen im Grubengebäude eines salinaren Endlagers, GSF-Bericht 3/92, 1992

Pusch R., Hökmark H. and Börgesson L., Outline of models of water and gas flow through smectite clay buffers, SKB Technical Report 87-10, Swedish Nuclear Fuel and Waste Management Co., June 1987

Pusch R. and T. Forsberg, Gas migration through bentonite clay, SKBF/KBS Technical Report 83-71, Swedish Nuclear Fuel and Waste Management Co., Dec. 1983

Pruess K., THOUGH User's Guide, Lawrence Berkeley Laboratory, LBL-20700, June 1987

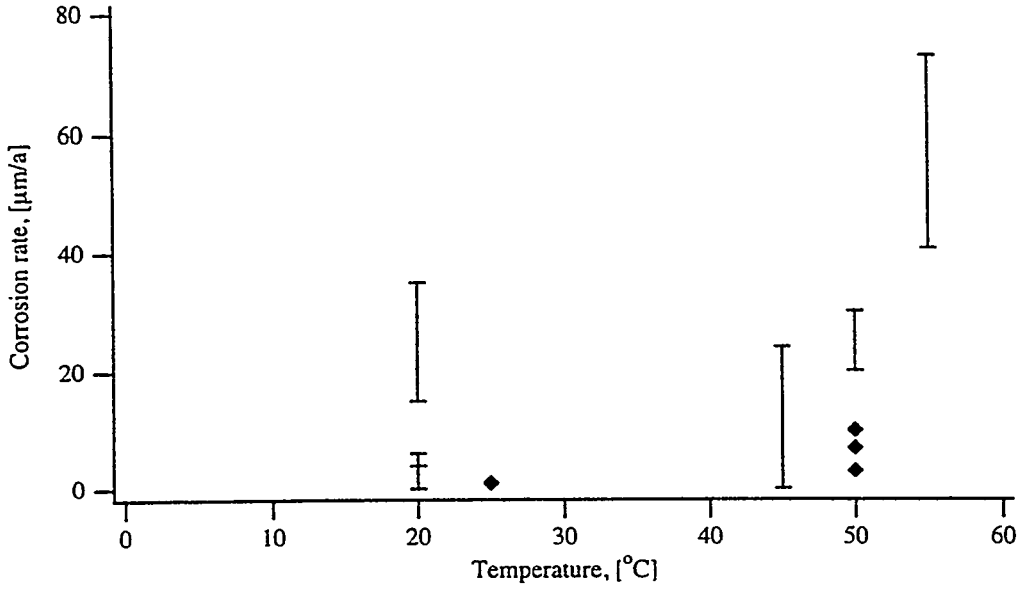

Fig. 1: corrosion rates for 0 - 60 °C

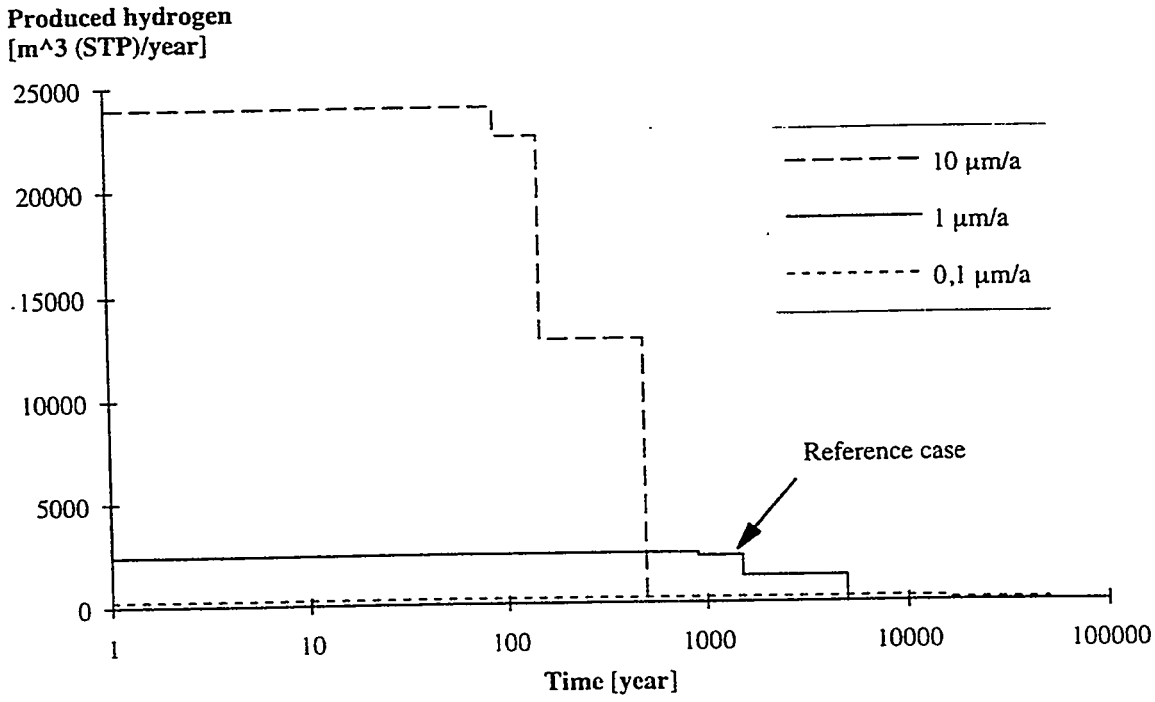

Fig. 2: amounts of hydrogen gas produced in the Westfeld as a function of time

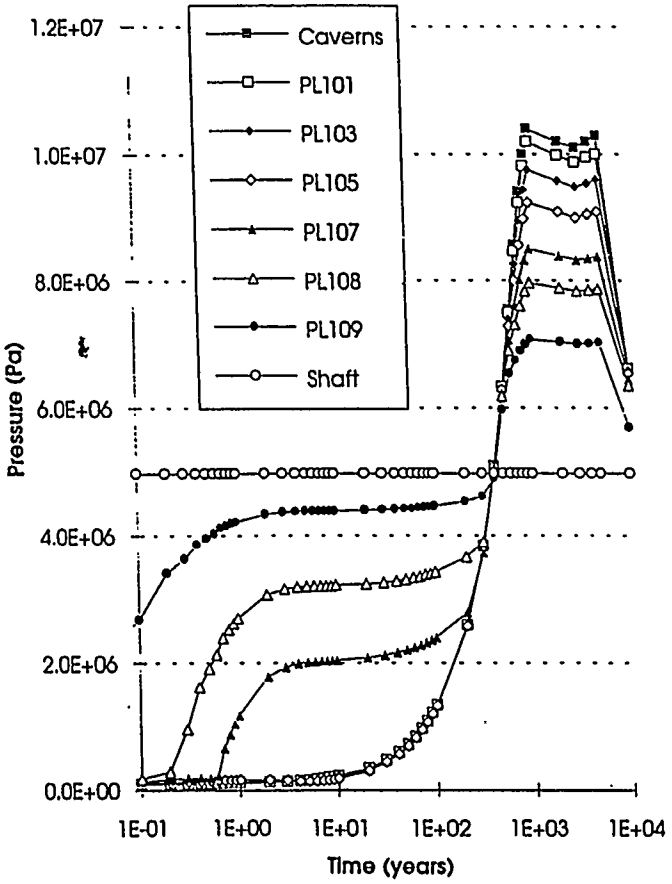

Fig. 4: prssure versus time in different elements

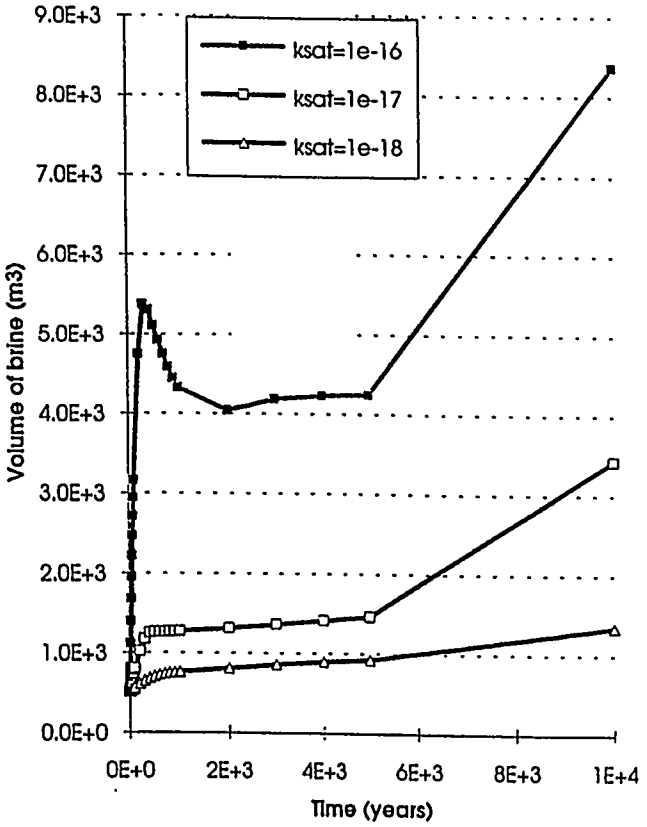

Fig. 5: variation of brine volume in the cavern versus time

Parametric Analysis of a TOUGH2 Model for the Unsaturated Zone at Yucca Mountain

Yanyong Xiang, Srikanta Mishra and Bryan Dunlap
CRWMS M&O/INTERA, Inc.
101 Convention Center Drive, Suite P110
Las Vegas, NV 89109

1. BACKGROUND AND SCOPE

Yucca Mountain in Nevada is currently being investigated for suitability as a potential site for the disposal of high-level radioactive waste and spent nuclear fuel. As the most important natural barrier against radionuclide migration to the accessible environment, the unsaturated zone at Yucca mountain is a key constituent in assessing the ambient geohydrology. A three-dimensional site-scale TOUGH2 model of the unsaturated zone is currently under development by Lawrence Berkeley Laboratory (LBL) and the United States Geological Survey (USGS) (*Wittwer et al.*, 1993; *Bodvarsson et al.*, 1994). The model covers an area of about 30 km^2 (**Figure 1**), and consists of six hydrogeologic units - TCw (Tiva Canyon welded), PTn (Paintbrush nonwelded), TSw (Topopah Spring welded), TSv (Topopah Spring welded-vitrophyre), CHnv (Calico Hills nonwelded-vitric), and CHnz (Calico Hills nonwelded-zeolitic), which are further subdivided into seventeen layers to represent additional lithologic detail (**Table I, Figure 2**). Based on the work of *Klavetter and Peters* (1986), the fractured units TCw and TSw are treated as equivalent continua with specified threshold saturations for triggering fracture flow.

Using two northwest to southeast cross sections (one including the Ghost Dance fault, and the other including the Abandoned Wash and Dune Wash faults), *Wittwer et al.* (1993) investigated the impacts of two extreme (high, low) fault permeabilities on moisture flow patterns. Their analyses indicated that steady-state moisture flow is dominantly vertical, whereas marginal lateral flow occurs only in some localized regions where prominent dipping stratigraphy and contrasting permeabilities exist. The three-dimensional analyses by *Bodvarsson et al.* (1994), who assumed three hydrological representations of the faults, i.e., capillary barrier, low permeability, and high permeability, indicated complex lateral as well as vertical flow patterns.

Further evaluation of the effects of input uncertainty (i.e., hydrologic representation of rock units and infiltration rate/pattern imposed at the ground surface) on predictions of the site-scale model are presented in this paper. These simulations are intended to help understand the range of expected system response subject to various uncertainties, and as such provide the bases for developing the abstractions of the ambient unsaturated flow regime for incorporation in total system performance assessment models. An associated objective is to examine the geometry of flow paths predicted by multidimensional models in order to substantiate the assumption of one-dimensional flow paths conventionally used in total system models.

2. MODEL DESCRIPTION

2.1 Geometry and Boundary Conditions

The simulations discussed herein are based on a northwest-southeast cross-section of Yucca Mountain (**Figure 2**) which is extracted from the LBL-USGS 3-D site-scale model. The cross-section passes through the potential repository area and includes the Ghost Dance Fault. The left and right boundaries are assumed to be of the no-flow type. The top boundary (ground surface) is treated as a constant pressure/temperature single-phase air surface. The bottom boundary (water table) is treated as essentially a single-phase liquid surface (a liquid saturation of 0.999) at constant pressure and temperature. Both top and bottom boundary conditions are imposed via fictitious grid blocks of large volumes with their nodal points placed on the physical boundaries. Infiltration at the ground surface is simulated as liquid sources located at the nodal points of the top layer grid blocks. Note that the constant pure-air condition at the ground surface precludes any possibility of moisture flow above the mountain, and that the water table boundary condition implies that the saturated zone acts as a sink of infinite capacity.

2.2 Parametrization

The original LBL-USGS site-scale model uses a 'best-guess' hydrologic parameter set (*Wittwer et al.*, 1993). An alternative set of material properties has been presented as part of a Performance Assessment Data Base developed at Sandia National Laboratories (*Wilson et al.*, 1994). This data set includes ranges and summary statistics associated with each hydraulic property (porosity, saturated permeability, and Van Genuchten parameters) for all hydrogeologic units, and as such, is more amenable to uncertainty propagation studies. Note that the SNL data are organized with respect to the six major hydrogeologic units, whereas the LBL data correspond to a more detailed stratigraphy to represent modest intra-unit changes in hydrogeologic properties. To examine the impacts of such a detailed representation of rock units (or the lack thereof) on the hydrologic behavior of the system, the original 17-layer LBL data were reduced to a 6-layer parameter set by averaging the various parameters within each of the six major units. Geometric averaging was used for saturated permeability and the Van Genuchten air-entry scaling parameter, and arithmetic averaging was used for porosity and the Van Genuchten pore-size distribution parameter. Table I presents a comparison of the original LBL data, the averaged LBL data, and the SNL data. Note that both matrix and fracture residual saturations are assumed to be zero in LBL data, and are assumed to take the following values in the SNL data: TCw - 0.021, PTn - 0.154, TSw - 0.045, TSv - 0.118, CHnv - 0.097, and CHnz - 0.121.

3. RESULTS AND DISCUSSION

3.1 Sensitivity to Matrix Properties

Figure 2 shows the model discretization along with a color image of the liquid saturation distribution for a constant infiltration rate of 0.1 mm/yr with the original LBL parameters. Picking column 153 as a representative column of the two-dimensional system within the proposed repository region, Corresponding to the infiltration rates of 0.0 mm/yr and 0.1 mm/yr, respectively, **Figures 3** and **4** show liquid saturation profiles for the LBL and SNL data sets. As

expected, the average LBL property case is a more smeared version of the response obtained with the original LBL data set. Both the original and the averaged LBL data sets produce liquid saturations in the nonwelded (PTn and CHnv) units much higher than those from the SNL data, although the predicted saturations agree much better for the welded (TCw, TSw and TSv) units. The liquid distribution patterns shown in **Figure 3** primarily reflect differences in capillary properties of the different units as defined in the various data sets. Note that increasing the infiltration rate reduces the differences between the three data sets in predictions of liquid saturations in the welded units. **Figures 5** and **6** are plots of liquid-phase velocity fields and streamlines corresponding to the original LBL and the averaged LBL data, respectively. Lateral flow is seen to occur along the interfaces between TCw and PTn, and between TSv and CHnv, which coincide with sharp permeability contrasts. The lateral flow is also enhanced, due to gravity, by the eastward dipping stratigraphy of all units. The lateral flow for the averaged LBL data is of a much smaller extent than for the original LBL data.

Figure 7 describes vertical linear liquid velocity distributions along column 153. Note that all three different hydrologic descriptions assume essentially the same velocity distribution pattern, although abrupt velocity variations occur at unit interfaces. **Figure 8** plots the liquid-phase particle travel times from ground surface to the water table, as a function of infiltration rate, assuming vertical flow only along columns 153, 157, and the Ghost Dance Fault. It indicates that the fault of distinctively higher permeability is the fastest travel path, and that the three columns resemble one another in travel time as a function of infiltration rate. The finite velocities observed for the zero infiltration case are an artifact of the vertical liquid-vapor counterflow induced by the geothermal gradient and by the fixed pure-air assumption for the top boundary.

3.2 Sensitivity to Fracture Properties

As described in *Klavetter and Peters* (1986) and *Wittwer et al.* (1993), a threshold saturation has been used as the pivoting parameter above which fluid flow occurs in the fracture as well as in the matrix. In the simulations described above, such composite fracture-matrix models have been used to represent the fluid transmitting properties of the welded units, assuming a fracture porosity of 0.001. To examine the sensitivity of liquid saturation distributions to the assumptions regarding the composite model fracture porosity values, simulations are conducted using different fluid transmission models and fracture porosities. **Figure 9** indicates that for all the three data sets, the liquid saturations for the composite model are only fractionally smaller than those for the matrix-only model in the welded units, whereas no difference exist in other units. **Figure 10** describes the liquid distributions along column 153 using the composite matrix-fracture model with different fracture porosity values. The liquid saturations in the welded units for the 0.005 fracture porosity case are apparently smaller, but still by insignificant magnitudes.

3.3 Sensitivity to Imposed Patterns of Infiltration

Another source of uncertainty is related to the specification of infiltration patterns and intensities at the ground surface, which are dependent upon the moisture transmitting properties of the surfacial materials and climatic conditions. It is also necessary to estimate the depth at which seasonal fluctuations diminish and steady-state downward flux conditions are likely to occur. By assuming exclusive matrix flow and relating infiltration to the estimated hydraulic properties of the surfacial materials, *Flint and Flint* (1994) proposed a distributed infiltration map for the LBL

three-dimensional unsaturated zone model, ranging from 0.02 mm/yr for TCw to 13.4 mm/yr for PTn. **Figure 11** shows the liquid-phase velocity field and the streamlines corresponding to a 10.0 mm/yr infiltration rate for the PTn outcrop at the top-left corner and a 0.1 mm/yr rate for other areas. Comparing **Figure 11** with **Figure 5**, and examining **Figure 12**, it can be observed that the higher infiltration only has appreciable effects localized in the vicinity of the PTn outcrop.

4. CONCLUDING REMARKS

The hydrologic effects of different matrix/fracture properties and infiltration patterns on ambient (steady-state) unsaturated flow at Yucca Mountain have been examined using a series of two-dimensional cross-sectional simulations. The major findings can be summarized as follows:

(1) The SNL data set produces much lower liquid saturations than the LBL data sets for the non-welded units. Averaging of the original LBL data has smearing effects on liquid distributions and reduces the extent of lateral flow. At higher infiltration rates, the differences in liquid distributions in the welded units between the three data sets diminish.
(2) Liquid flow is vertically dominant in most regions, while lateral liquid flow is of much smaller magnitude and induced mainly by the nonwelded units due to their distinctively higher permeabilities, and by the eastward dipping stratigraphy.
(3) Vertical continuity of liquid along a column can be assumed without inducing significant errors in estimating liquid-phase particle travel times.
(4) Saturations predicted for the welded units by the composite-porosity model, with a fracture porosity of 0.001, are only marginally smaller than those for a matrix-only flow model. Increasing the fracture porosity by a factor of five produces only a small decrease in saturation for the welded units.
(5) Locally focussed infiltration can enhance lateral flow, but such effects diminish for more distant regions.

The results presented in this paper were derived from simulations based on various simplifications and assumptions. Future work should be directed toward describing the ambient unsaturated zone hydrology in greater detail, e.g., better representation of the interfaces between the unsaturated zone and the water table/atmosphere, consideration of the variabilities in material properties and their most probable combinations, incorporation of alternate conceptual models for non-equilibrium fracture-matrix interaction.

5. REFERENCES

Bodvarsson, G., et al., Preliminary analysis of three-dimensional moisture flow within Yucca Mountain, Nevada, *High Level Radioactive Waste Management, Proceedings of the Fifth Annual International Conference, Las Vegas, 2038-2047, 1994*

Flint, A., and L. E. Flint, Spatial distribution of potential near surface moisture flux at Yucca Mountain, *High Level Radioactive Waste Management, Proceedings of the Fifth Annual International Conference, Las Vegas, 2352-2358, 1994*

Klavetter, E. A., and R. R. Peters, Estimation of hydrologic properties of an unsaturated fractured rock mass, SAND84-2642, Sandia National Laboratories, 1986.

Wilson M. L. et al., Total-system performance assessment for Yucca Mountain-SNL second iteration (TSPA-1993), SAND93-2675, 1994.

Wittwer, C. S., et al., Studies of the role of fault zones on fluid flow using the site-scale numerical model of Yucca Mountain, *High Level Radioactive Waste Management, Proceedings of the Fourth Annual International Conference, Las Vegas, 667-674, 1993.*

Table I. Stratigraphy and Hydrologic Properties
(LBL—original LBL data, AVE.—averaged LBL data, SNL—SNL data)

Unit	Layer	Porosity (%)			Permeability (m^2)			VG α (10^{-5} Pa^{-1})			VG β		
		LBL	AVE.	SNL	LBL	AVE.	SNL	LBL	AVE.	SNL	LBL	AVE.	SNL
TCw	11	17	13	9	1e-18	1.0e-18	1.3e-18	0.067	0.067	0.081	1.33	1.333	1.608
	12	17			2e-18			0.067			1.33		
	13	6			1e-18			0.067			1.33		
PTn	21	33	34	42	1e-13	7.9e-14	1.1e-15	1.67	3.5	0.74	1.20	1.186	2.222
	22	37			5e-14			6.0			1.19		
	23	32			1e-13			4.33			1.17		
TSv	31	6	6	7	1e-18	1.0e-18	1.0e-18	0.067	0.067	0.024	1.41	1.408	2.232
TSw	32	15	14	14	4e-16	1.4e-17	2.0e-18	0.125	0.12	0.13	1.22	1.290	1.709
	33	13			4e-18			0.2			1.28		
	34	14			5e-18			0.133			1.33		
	35	12			5e-18			0.067			1.33		
TSv	36	5	6	7	1e-18	1.0e-18	1.0e-18	0.067	0.067	0.024	1.41	1.408	2.232
CHnv	51	35	34	33	2e-13	2.6e-13	1.0e-16	2.0	2.0	0.23	1.15	1.140	2.358
	52	28			3e-13			2.0			1.14		
	53	39			3e-13			2.0			1.14		
CHnz	54	25	25	31	1e-16	1.0e-16	1.6e-18	0.1	0.1	0.054	1.23	1.235	1.672
	55	25			1e-16			0.1			1.23		

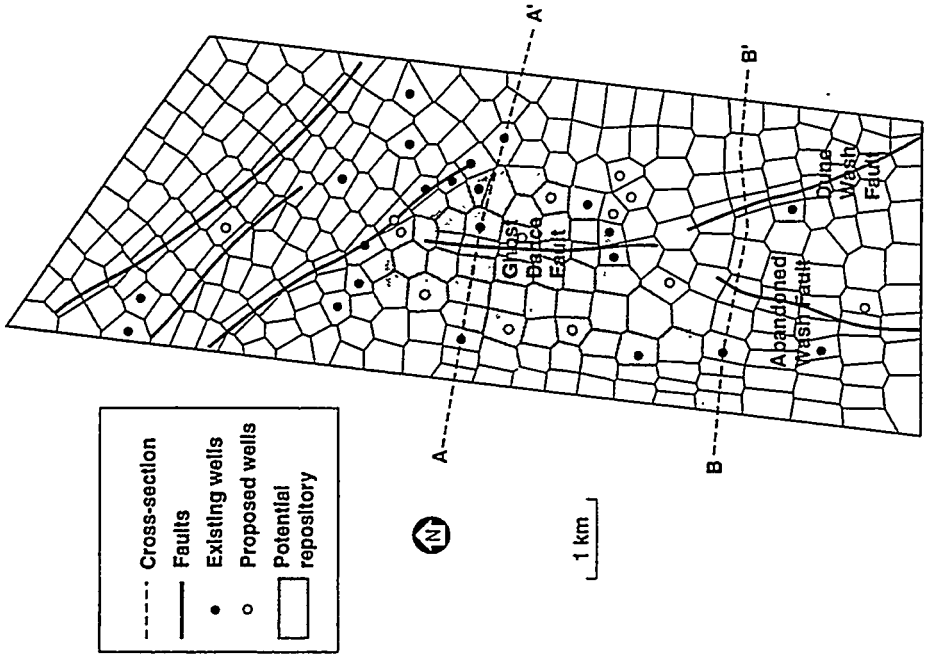

Figure 1: Horizontal grid of the LBL-USGS model, showing locations of the two cross sections.

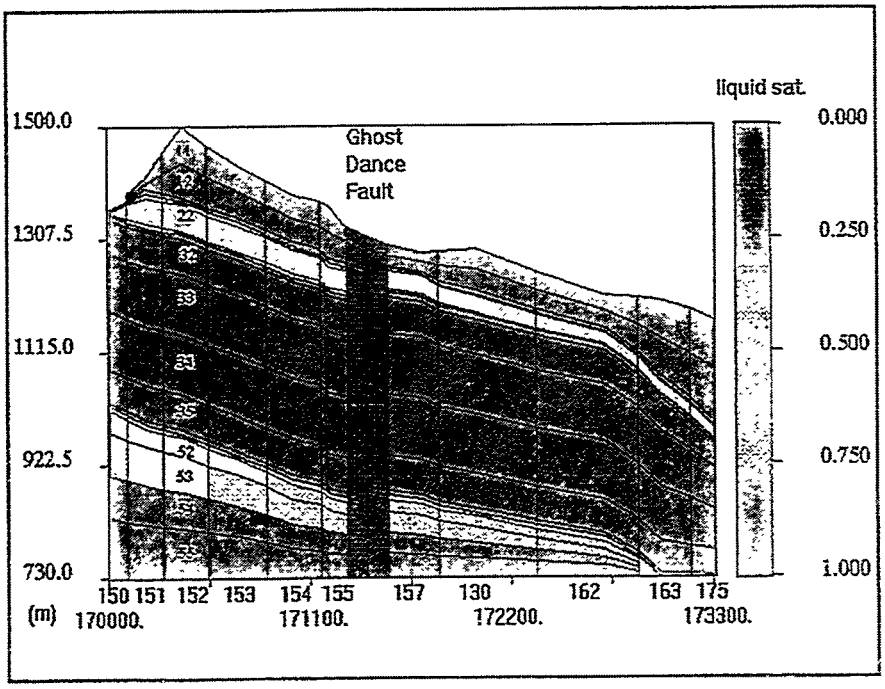

Figure 2: Discretization and stratigraphy of the cross section A-A', with the color image representing the liquid distribution under the original LBL description and a uniform infiltration of 0.1 mm/year.

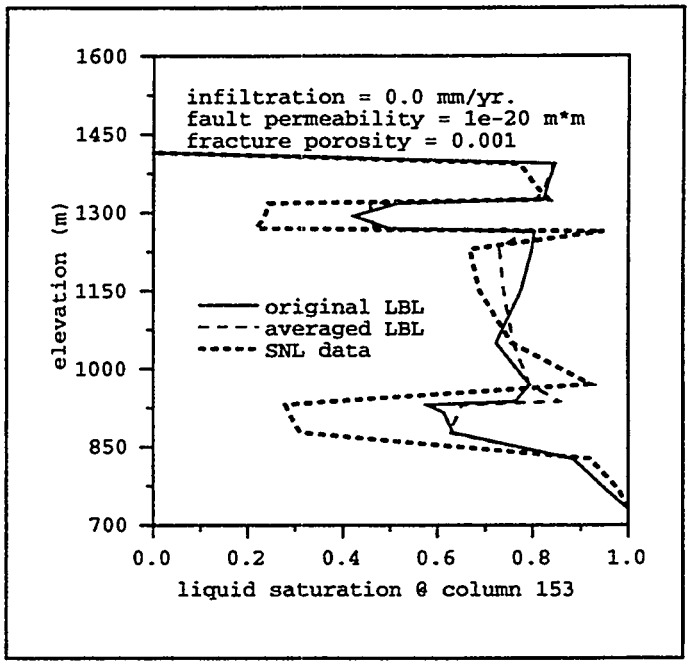

Figure 3: Liquid distributions along column 153 under an infiltration rate of 0.0 mm/year.

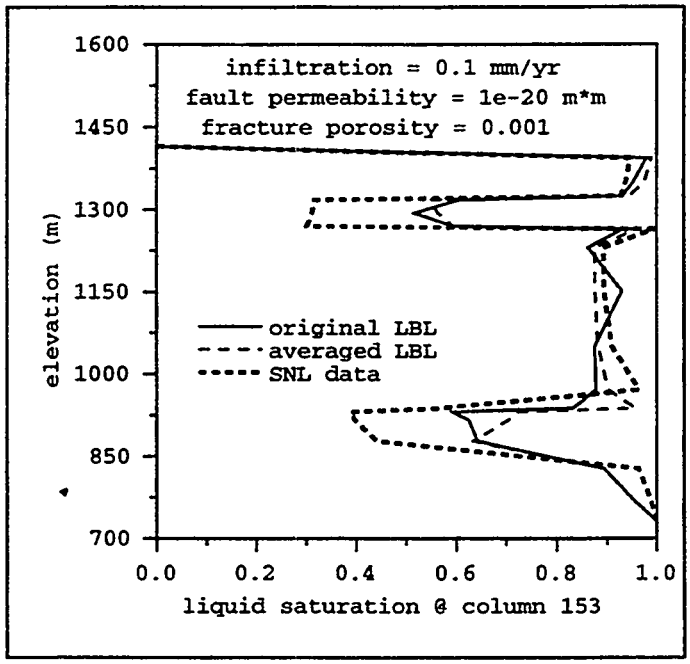

Figure 4: Liquid distributions along column 153 under an infiltration rate of 0.1 mm/year.

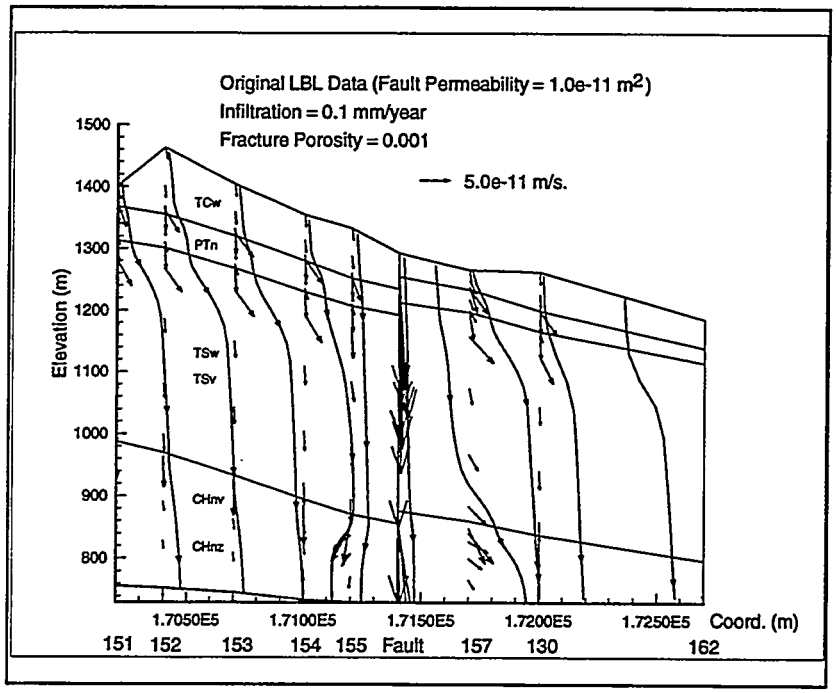

Figure 5: Liquid phase velocity field and streamlines under the original LBL description and a uniform infiltration of 0.1 mm/year.

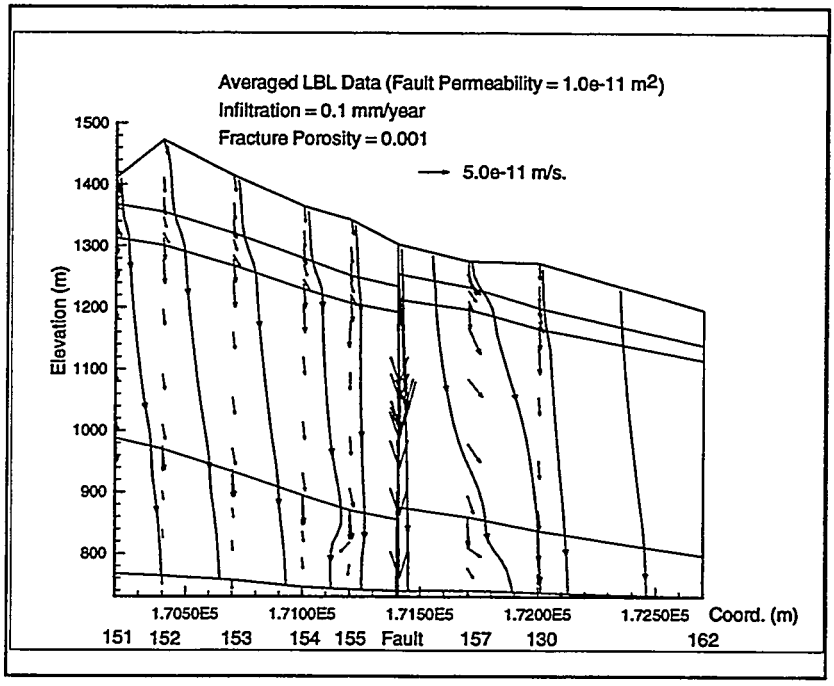

Figure 6: Liquid phase velocity field and streamlines under the averaged LBL description and a uniform infiltration of 0.1 mm/year.

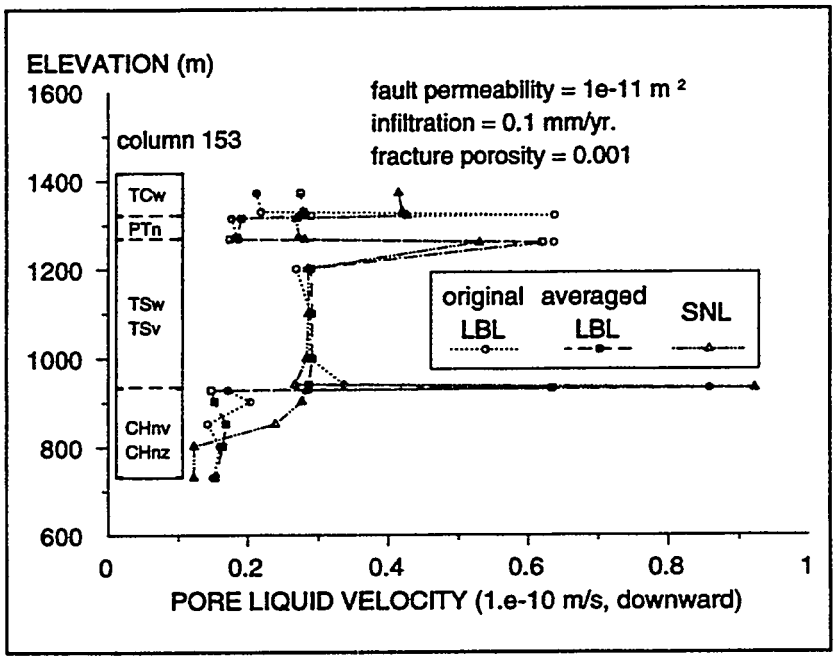

Figure 7: Vertical liquid phase linear velocity ditributions along cloumn 153.

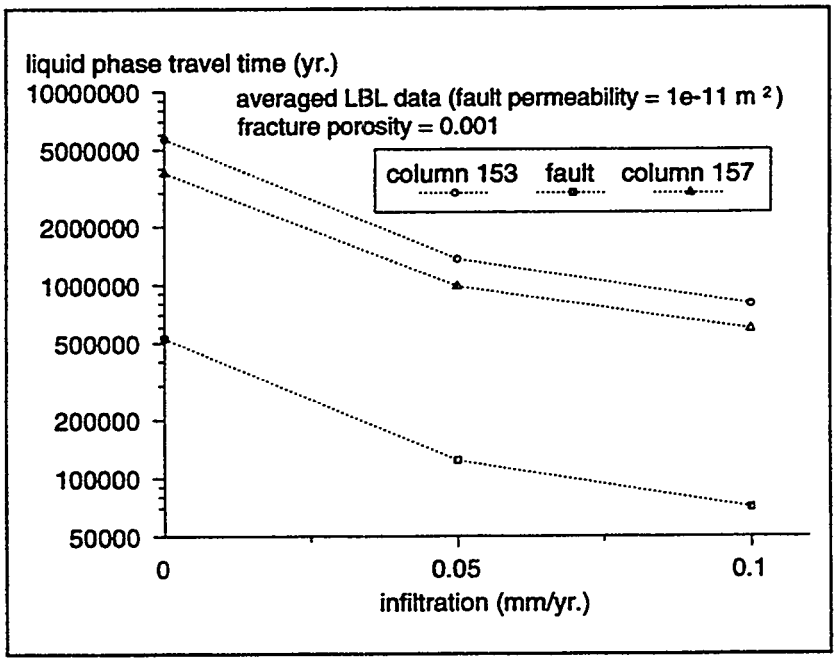

Figure 8: Estimated particle travel time in liquid phase as a funtion of infiltration rate,

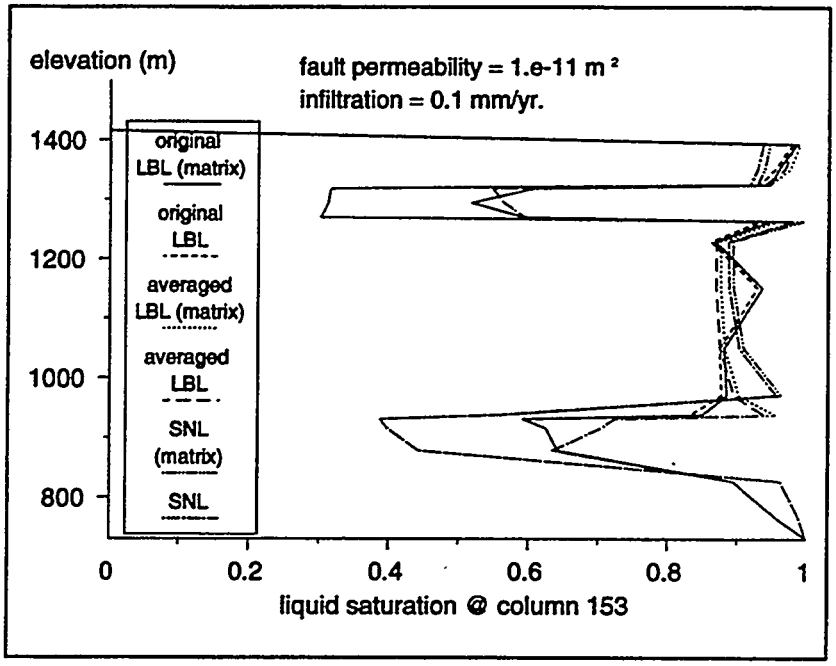

Figure 9: Liquid distributions along column 153 for matrix-only and composite matrix-fracture flow models.

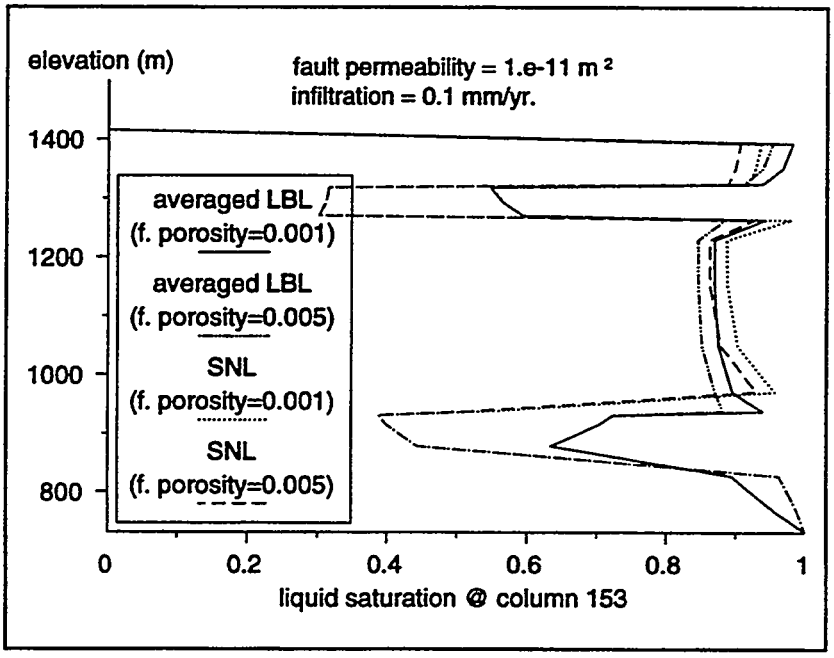

Figure 10: Liquid distributions along column 153 for different fracture porosity values.

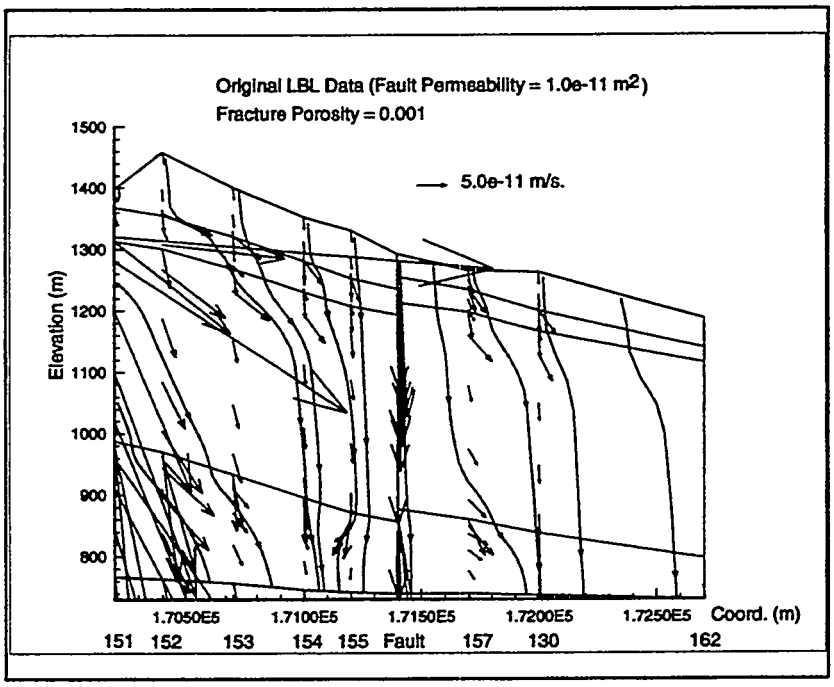

Figure 11: Liquid Phase velocity field and streamlines under the original LBL description and infiltration of 10.0 mm/year for the PTn outcrop and 0.1 mm/year for other areas.

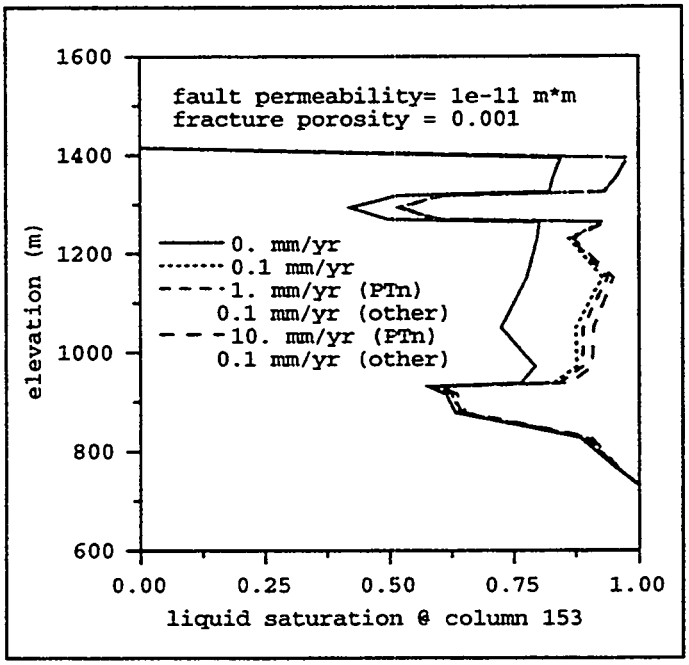

Figure 12: Liquid distributions along column 153 under the original LBL description and various infiltrations.

Presented at TOUGH Workshop '95, Lawrence Berkeley Laboratory, Berkeley, CA 94720, March 20-22, 1995

LBL-36872

APPLICATIONS OF TOUGH2 TO INFILTRATION OF LIQUIDS IN MEDIA WITH STRONG HETEROGENEITY

Karsten Pruess and Emilio Antunez

Earth Sciences Division, Lawrence Berkeley Laboratory
University of California, Berkeley, California 94720

Introduction

Much hydrogeological research during the last decade has focused on the heterogeneity of natural geologic media on different scales. Most of this work has dealt with flow and transport in single-phase, isothermal conditions. The present paper is concerned with multiphase and nonisothermal flows in strongly heterogeneous media. A primary driver of our studies is the hydrogeological system at Yucca Mountain, which is currently being evaluated by the Department of Energy for its suitability as the site of the first geologic repository for civilian high-level nuclear wastes in the U.S. Yucca Mountain is located in the arid Southwest, near the Nevada-California border. Going from large scale to small, formation heterogeneities at Yucca Mountain include (i) alternating tilting layers of welded and non-welded tuffs with different matrix permeability and variable degree of fracturing, (ii) major fault systems, (iii) well-connected and permeable fracture networks in low-permeability rocks, and (iv) individual fractures with highly variable apertures.

The potential repository horizon at Yucca Mountain is approximately 375 m beneath the land surface, in partially saturated, fractured rock; the water table is at a depth of approximately 600 m. Under present climatic conditions, rates of water infiltration at Yucca Mountain are small. There would be little concern about migration of water-soluble radionuclides if water flow proceeded in a uniform, volume-averaged manner. Concerns for site suitability and repository performance arise from potentially highly non-uniform water distribution and flow, which may be induced by the strong heterogeneities, especially fractures (Chesnut, 1994). Key issues involve the possible development of fast preferential flow paths, flow focusing, and localized water ponding. Numerical simulation experiments in computer-generated heterogeneous media are being used as a means to learn about water flow under partially saturated conditions with strong multi-scale heterogeneity.

Additional motivations for studying gravity-driven seepage of liquids in heterogeneous media arise in the context of water injection into depleted vapor-dominated geothermal reservoirs, and in environmental contamination problems involving non-aqueous phase liquids (NAPLs).

Heterogeneous Media

Numerical simulation of a variety of fluid flow and heat transfer processes has been performed in media with different styles of heterogeneity (Figs. 1 - 3). Figure 1 shows a random distribution of low-permeability features in an otherwise homogeneous two-dimensional medium. This may represent a vertical section with silt bodies in a sandstone, or clay lenses in a soil. Figure 2 shows a layered medium, generated by means of the turning bands method (Tompson, 1989; Antunez and Pruess, 1994), with larger horizontal than vertical spatial correlation length. This style of heterogeneity is typical for sedimentary systems, such as clayey soils. For "small" fractures in hard rocks, essential features of aperture heterogeneity include (i) the presence of numerous asperity contacts between the fracture walls, (ii) a more or less gradual change from small apertures near the asperities to larger apertures away from the asperities, and (iii) significant local aperture variations due to wall roughness. A two-dimensional heterogeneous medium which may represent such fractures is shown in Fig. 3. It was also generated by means of the turning bands method, but specifying spatial correlation to be short-range. To obtain asperity contacts with zero apertures, the

log-normal aperture distribution used in the turning bands method was subjected to a linear shift, b $\rightarrow$ b' = b - Δ, and all b' < 0 were reset to 0. The resulting distribution of asperities, idealized as regions of zero permeability, is shown in Fig. 4.

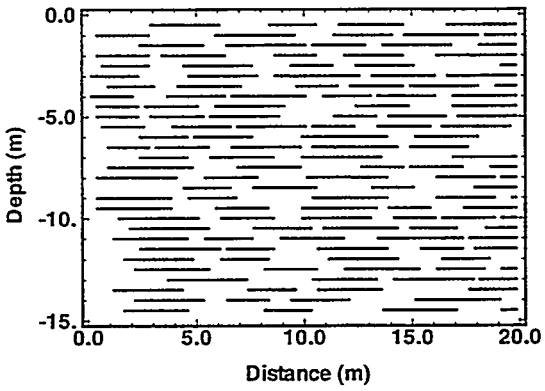

Figure 1. A heterogeneous medium, generated by random placement of horizontal impermeable obstacles, with lengths uniformly distributed in the range of 2 - 4 m.

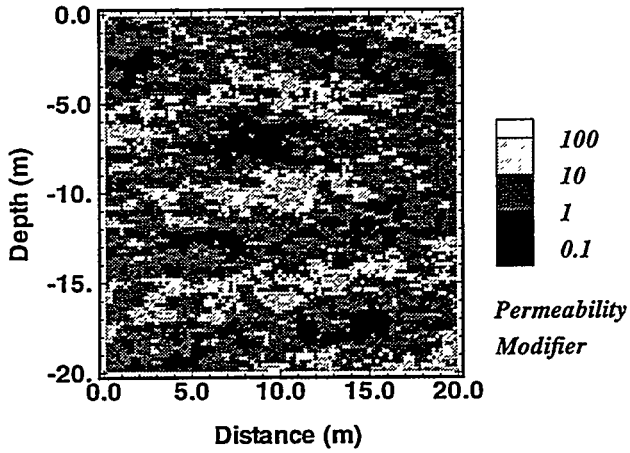

Figure 2. Log normally distributed permeability field, with spatial correlation lengths of λ_X = 0.8 m, λ_Z = 0.4 m.

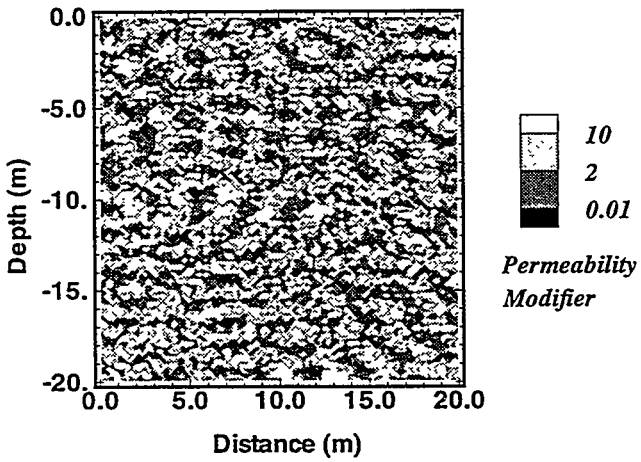

Figure 3. Stochastic permeability field, with correlation lengths of λ_X = 0.2 m, λ_Z = 0.1 m.

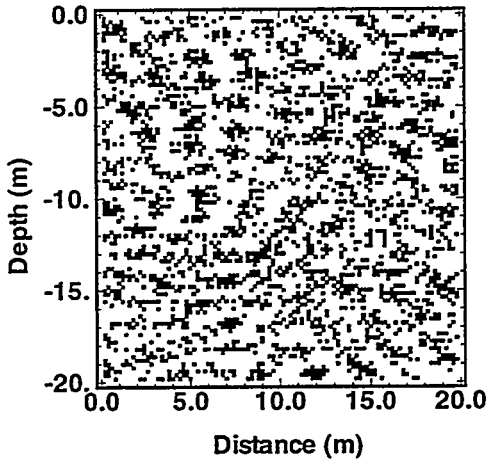

Figure 4. Distribution of asperity contacts in the permeability field of Fig. 3.

Code Enhancements

Detailed resolution of small-scale heterogeneity requires thousands of grid blocks and leads to very demanding flow simulations. Using the recently developed preconditioned conjugate gradient module, TOUGH2 can handle systems with of the order of 10,000 grid blocks on workstations and PCs (Moridis and Pruess, 1995; Antunez et al., 1994). The code can model flow in heterogeneous media "as is;" all that is required is specification of an appropriate (large) number of domains with different properties in data block 'ROCKS'. However, specification of thousands

of different flow domains would be quite inconvenient as far as preparation of input data is concerned. Therefore, we have made some modifications in TOUGH2 to more conveniently deal with "strong" (grid-block-by-grid-block) heterogeneity. Additional revisions were made to address some new features in flow behavior that arise in strongly heterogeneous systems.

For flow systems with 10,000 or more grid blocks it is necessary to accommodate 5-digit element identification numbers. This requires changing the `1505 FORMAT(20I4)` statements in subroutines INPUT and RFILE, file t2f.f, to `(16I5)`. To avoid having to specify large numbers of flow domains in problems with block-to-block permeability variation, we introduced an array of "permeability modifiers," `PM`. Externally generated `PM`-data, representing e.g. geostatistical realizations of spatially-correlated fields, can be conveniently fed into TOUGH2 as a floating point variable for each element through previously unused and available columns 41-50 in the 'ELEME' data block. We also coded provisions to optionally generate stochastic permeability modifiers internally. These modifiers are applied in subroutine MULTI as multiplicative factors to the permeabilities defined in block 'ROCKS'. This way, point-by-point permeability variation can be realized by specifying only one single set of domain data, which serves as a reference material. In addition to scaling absolute permeabilities according to $k \rightarrow k' = k * PM$, we simultaneously apply a consistent scaling of capillary pressures according to $P_{cap} \rightarrow P_{cap}' = P_{cap}/SQRT(PM)$ (Leverett, 1941).

Flow simulations with strong (block-by-block) heterogeneity pose some difficulties that are not usually encountered when simulating the same fluid and heat flow processes in homogeneous media, or in media with only a few different domains. The variations in absolute permeability and strength of capillary pressure make intrinsic response times highly spatially variable. This complicates and lengthens the approach to steady states which are often desired as initial conditions for flow simulations. Potentially more serious problems may arise when in the course of a simulation certain grid blocks come very close to phase boundaries, and remain there for extended time periods. This can severely limit attainable time step sizes. Such occurrences are of course possible in much simpler, less heterogeneous systems. However, in systems with block-by-block variation of permeability fields these effects can be so frequent and persistent that some code revision may be necessary, to prevent time steps from being reduced to impractical levels. A more robust behavior can be achieved by broadening the phase change criterion from a "sharp" line to a finite-size window. For example, in the EOS4 fluid property module a transition from single-phase liquid to two-phase conditions is normally made when $P < P_{gas}$ is encountered, where P_{gas} is the "bubbling" pressure. For some simulations of highly heterogeneous systems, we have revised this condition to $P < P_{gas} * (1.-1.e-4)$, i.e., we require pressure to drop below P_{gas} by a finite amount before allowing a gas phase to evolve.

Numerical Experiments

Gravity-driven infiltration of water in the media shown in Figs. 1 - 3 was simulated with a new equation-of-state module, EOS9. This implements a Richards' equation-type approximation to saturated/unsaturated flow, which treats only single-component aqueous-phase flow, while the gas phase is treated as a passive bystander at constant pressure. Simulation parameters used are variations of a reference medium as given in Table 1; results are shown in Figs. 5 - 9.

Medium with Random Horizontal Obstacles

Infiltration of an initially rectangular water plume in the medium of Fig. 1 shows a dendritic pattern of liquid migration when capillary pressures are neglected (Fig. 5). The impermeable obstacles divert flow sideways, causing the plume to broaden as it descends. A detailed analysis shows that plume broadening proceeds in analogy to Fickian diffusion, i.e., mean square plume size grows proportional to vertical distance traveled by the center-of-mass of the plume (Pruess, 1994). The heterogeneous medium behaves as an anisotropic dispersive medium; effective volume-averaged properties are found to be $k_h = 7.5$ darcy, $k_v = 1.2$ darcy, anisotropy ratio $k_h/k_v = 6.3$, and transverse dispersivity $\alpha_T = 1.2$ m.

Table 1. Parameters for test problems with detailed explicit heterogeneity.

Reference permeability Porosity	$k = 10^{-11}$ m^2 (10 darcy) $\phi = 0.35$
Relative Permeability	
van Genuchten function for liquid (1980) $k_{rl} = \sqrt{S^*}\left\{1-\left(1-\left[S^*\right]^{1/\lambda}\right)^{\lambda}\right\}^2$	$S^* = (S_l - S_{lr})/(1 - S_{lr})$
Corey-curve for gas† $k_{rg} = (1-\hat{S})^2\left(1-\left[\hat{S}\right]^2\right)$	$\hat{S} = (S_l - S_{lr})/(1 - S_{lr} - S_{gr})$
irreducible water saturation irreducible gas saturation exponent	$S_{lr} = 0.15$ $S_{gr} = 0.05$ $\lambda = 0.457$
Capillary Pressure	
van Genuchten function (1980) $P_{cap} = -(\rho_w g/a)\left(\left[S^*\right]^{-1/\lambda} - 1\right)^{1-\lambda}$	$S^* = (S_l - S_{lr})/(1 - S_{lr})$
irreducible water saturation exponent strength coefficient	$S_{lr} = 0.0$ or 0.15 $\lambda = 0.457$ $a = 5$ m^{-1}

† used only when both liquid and gas phases are active

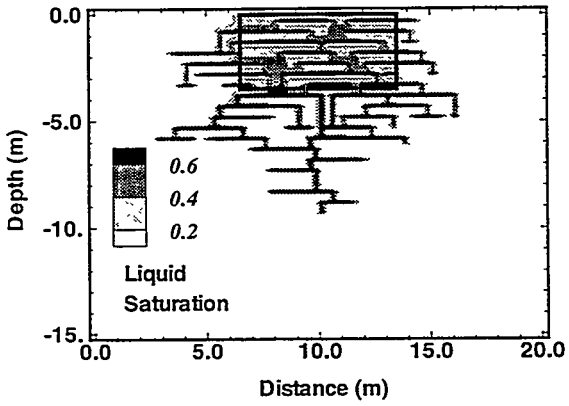

Figure 5. Water infiltration in the medium of Fig. 1, capillary pressures neglected. Initial water saturation is at irreducible level of $S_l = 0.15$ throughout, except for the region outlined by the black rectangle where $S_l = 0.99$. Shading indicates water saturations after 2×10^5 seconds.

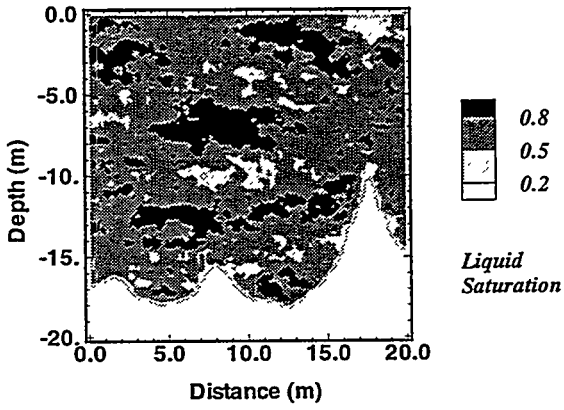

Figure 6. Water saturation in the medium of Fig. 2 after 6×10^5 seconds of uniform infiltration applied at the top.

Layered Medium

To study water infiltration in the layered medium of Fig. 2, we place a grid block with reference domain assignments (permeability modifier = 1) across the entire top of the domain. Water is injected into this block at a rate of 0.1 kg/s, which is approximately 6 % of the maximum unsaturated vertical water flow rate under unit head gradient. Water saturations after 6.9 days of infiltration, shown in Fig. 6, reflect the layering of the medium, with higher water saturations encountered in the less permeable layers where capillary effects are stronger. Capillary pressures at the injection boundary quickly reach a quasi-steady value of P_{cap} = - 1830 Pa. This capillary pressure is sufficiently negative to largely prevent water from entering the more highly permeable region that extends from 16.5 to 18.5 m distance at the top of the flow domain. The diminished infiltration over a portion of the boundary is seen to cast a "shadow" of diminished water saturations all the way down to the infiltration front.

Small Fracture in Hard Rock

The heterogeneous medium shown in Fig. 3 serves as a model of a small fracture in hard rock, such as may be encountered in the tuff formations at Yucca Mountain. To study the behavior of liquid infiltration plumes, the entire flow domain is initialized with a uniform initial water saturation at the irreducible level of $S_l = 0.15$, except for a square region at the top (extending from 6 to 14 m distance, and from 0 to - 8 m depth) which is initialized as $S_l = 0.99$. Fig. 7 shows the liquid saturation distribution after the initially square plume has evolved for a period of 4.6 days in response to gravity, capillary, and pressure forces. This simulation shows features that are reminiscent of field observations at Rainier Mesa, a possible analog to the Yucca Mountain site (Wang et al., 1993). In particular, we note the development of preferential, fingering flow, with significant ponding and bypassing. Fig. 8 shows an infiltration plume in the same fracture, which evolved from applying constant-rate injection at the top in the distance interval from 6 m to 14 m. The injection rate was specified in such a way that at the time of 4.6 days the fluid content of the plume in Fig. 8 is equal to that of Fig. 7. The infiltration patterns are quite different, indicating the sensitivity to boundary conditions in this highly gravitationally-unstable problem.

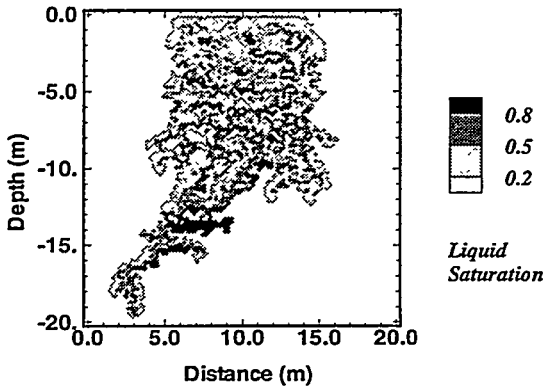

Figure 7. Water saturations in the medium of Fig. 3, shown 4.6 days after releasing a square plume of 8 x 8 m^2 size from the top, center of the domain.

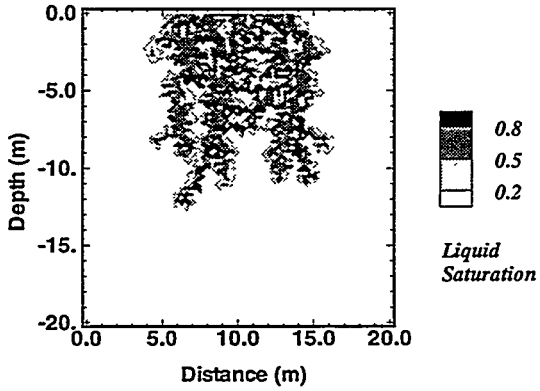

Figure 8. Same as Fig. 7, except here water was injected uniformly for 4.6 days at the top in the interval 6 m $\leq x \leq$ 14 m. Total water mass is equal to that in the plume in Fig. 7.

Water Seepage through a Hot Fracture

The final study presented here was designed to explore thermo-hydrologic processes that would be encountered near the hot repository horizon at Yucca Mountain. A key issue is whether or not water seeping downward along sub-vertical fractures would fully vaporize as it traverses regions with temperatures above the nominal boiling point (96 °C at the repository elevation). The

basic flow system involves the heterogeneous vertical fracture shown in Fig. 3, with a reference permeability of 10^{-10} m^2 over the assumed thickness of the 2-D section of 1 cm. The EOS4 fluid property module is used to represent vapor pressure lowering effects which can be very strong in processes involving (partial) dry-out. The fracture is initialized at a temperature of 110 °C, and is assumed to contain vapor (no air) in gravity equilibrium with an average pressure of 88.74 kPa. Even though vapor pressures are considerably below the saturated vapor pressure of 143.27 kPa at T = 110 °C, a small liquid saturation of approximately .013 % is present in the fracture due to strong vapor pressure lowering effects. The fracture walls are modeled as semi-infinite impermeable halfspaces, also initialized at a uniform above-boiling temperature of 110 °C. Water at a temperature of approximately 24 °C is then injected at the top of the fracture at a rate of 273.8 kg per day, and constant-pressure boundary conditions are maintained at the right edge of the fracture. The essential mechanism determining the fate of the injected water is heat exchange between the fracture and the wall rock, which is modeled here by means of the semi-analytical technique provided in TOUGH2.

The evolution of the liquid plume shows strong similarities to the behavior of water injection plumes in depleted zones of vapor-dominated geothermal reservoirs (Pruess, 1991; Pruess and Enedy, 1993; Pruess, 1995). Water descending in the fracture by gravitational force is partially vaporized from heat that is supplied conductively from the wall rock. Complex two-phase fluid flow and heat transfer processes develop, including vapor-liquid counterflows that provide a very efficient heat transfer mechanism akin to a heat pipe. Water boils throughout the hotter portions of the plume, while vapor condensation occurs in cooler regions. The general direction of vapor flow is towards the right constant-pressure boundary. The vapor pressure gradients associated with this flow cause the descending liquid plume to deviate from the predominant vertical direction and veer to the right (see Fig. 9).

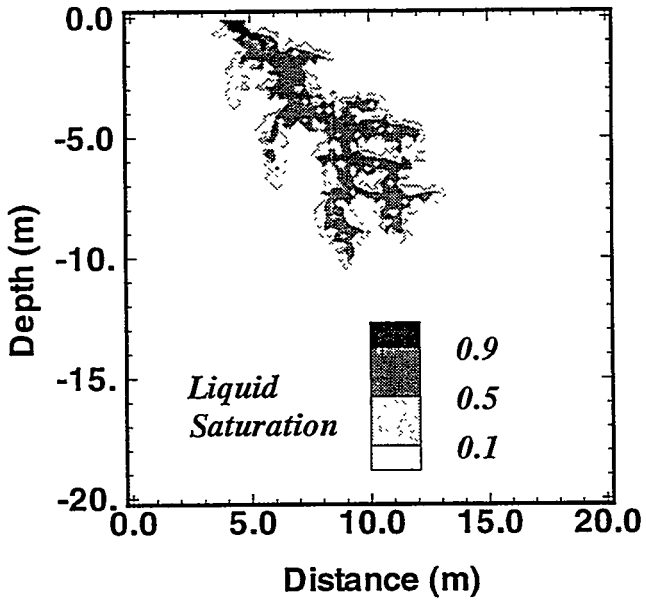

Figure 9. Boiling infiltration plume after 11.63 hours of water injection into a highly heterogeneous, hot fracture (initial temperature 110 °C).

Of the total liquid mass of 132.7 kg injected over an 11.63 hour period, an amount of 60.4 kg or 45.5 % has escaped vaporization, and has seeped over more than 10 m vertical distance through the hot fracture. Additional numerical experiments have shown that the fraction of water escaping vaporization increases with injection rate, as expected, reflecting limitations of conductive heat transfer from the wall rocks. Additional fully three-dimensional calculations have been initiated to include effects of water being imbibed by wall rocks of low but finite permeability.

Discussion and Conclusions

The recently developed package of preconditioned conjugate gradient solvers for TOUGH2 makes possible the simulation of complex multi-phase fluid and heat flow processes in highly heterogeneous media. For most of the flow problems presented here the Lanczos-type bi-conjugate gradient square solver (DSLUCS) provided a stable and efficient solution. However, the problem of water seepage through a hot fracture could only be solved with the bi-conjugate gradient method (DSLUBC), while DSLUCS as well as the generalized minimum residual method (DSLUGM) performed poorly.

Heterogeneity at different scales may be the key to understanding water flow, thermal loading effects, and radionuclide transport at Yucca Mountain. Using flow systems with of the order of 10,000 grid blocks we have been able to achieve a detailed resolution of spatially-correlated heterogeneities down to the decimeter scale. Numerical experiments of gravitationally unstable liquid infiltration in such media have revealed complex phenomenology, including fingering, ponding, and bypassing. Simulation capabilities have now reached a sophistication where detailed mechanistic models can be constructed to study issues that are critical to nuclear waste containment, such as fast preferential water flow in fractures.

Acknowledgement

The authors appreciate helpful discussions with George Moridis. Thanks are due to Curt Oldenburg and Stefan Finsterle for a careful review of the manuscript. This work was carried out under U.S. Department of Energy Contract No. DE-AC03-76SF00098 for the Director, Office of Civilian Radioactive Waste Management, Yucca Mountain Site Characterization Project Office, and Office of External Relations, administered by the Nevada Operations Office, U.S. Department of Energy, in cooperation with the Swiss National Cooperative for the Disposal of Radioactive Waste (NAGRA).

References

Antunez, E. and K. Pruess. The Use of the Turning Bands Method (TBM) to Generate Stochastic Aperture Distributions in Heterogeneous Fractures. Lawrence Berkeley Laboratory Report LBL-35581, May 1994.

Antunez, A., G. Moridis and K. Pruess. Large-Scale Geothermal Reservoir Simulation on PCs, Lawrence Berkeley Laboratory Report LBL-35192, presented at 19th Workshop on Geothermal Reservoir Engineering, Stanford University, Stanford, CA, January 1994.

Chesnut, D.A. Dispersivity in Heterogeneous Permeable Media, Proceedings, Fifth Annual International High-Level Radioactive Waste Management Conference, Las Vegas, NV, Vol. 4, pp. 1822 - 1841, American Nuclear Society, La Grange Park, IL, May 1994.

Leverett, M. C., Capillary Behavior in Porous Solids, *Trans. Soc. Pet. Eng. AIME*, 142, 152-169, 1941.

Moridis, G. and K. Pruess. T2CG1: A Package of Preconditioned Conjugate Gradient Solvers for the TOUGH2 Family of Codes, Lawrence Berkeley Laboratory Report LBL-36235, Lawrence Berkeley Laboratory, Berkeley, CA, 1995.

Pruess, K. Numerical Simulation of Water Injection into Vapor-Dominated Reservoirs. Paper accepted for presentation at World Geothermal Congress, Florence, Italy, May 1995.

Pruess, K. On the Validity of a Fickian Diffusion Model for the Spreading of Liquid Infiltration Plumes in Partially Saturated Heterogeneous Media. Invited Paper, in: *Computational*

Methods in Water Resources X, Vol. 1, pp. 537 - 544, Kluwer Academic Publishers, Dordrecht, Boston, London, 1994.

Pruess, K. and S. Enedy. Numerical Modeling of Injection Experiments at The Geysers, Lawrence Berkeley Laboratory Report LBL-33423, presented at 18th Workshop on Geothermal Reservoir Engineering, Stanford University, Stanford, CA, January 26-28, 1993.

Pruess, K. Grid Orientation and Capillary Pressure Effects in the Simulation of Water Injection into Depleted Vapor Zones, *Geothermics*, 20 (5/6), 257-277, 1991.

Tompson, A.F.B. Implementation of the Three-Dimensional Turning Bands Random Field Generator, *Water Resources Res.*, Vol. 25, No. 10, pp. 2227 - 2243, 1989.

van Genuchten, M. Th. A Closed-Form Equation for Predicting the Hydraulic Conductivity of Unsaturated Soils, *Soil Sci. Soc. Am. J.*, Vol. 44, pp. 892-898, 1980.

Wang, J.S.Y., N.G.W. Cook, H.A. Wollenberg, C.L. Carnahan, I. Javandel, and C.F. Tsang. Geohydrologic Data and Models of Rainier Mesa and Their Implications to Yucca Mountain, Proceedings, Fourth Annual International High-Level Radioactive Waste Management Conference, Las Vegas, NV, Vol. 1, pp. 675 - 681, American Nuclear Society, La Grange Park, IL, April 1993.

VAPOR PRESSURE LOWERING EFFECTS DUE TO SALINITY AND SUCTION PRESSURE IN THE DEPLETION OF VAPOR-DOMINATED GEOTHERMAL RESERVOIRS

Alfredo Battistelli (+), Claudio Calore (*) and Karsten Pruess (&)

(+) Aquater S.p.A., Via Miralbello 53, 61047 S. Lorenzo in Campo (PS), Italy.
(*) Istituto Internazionale per le Ricerche Geotermiche - CNR, Piazza Solferino 2, 56126 Pisa, Italy.
(&) Earth Sciences Division, Lawrence Berkeley Laboratory, 1 Cyclotron Road, Berkeley, CA 94720, USA.

Key words: numerical simulation, suction pressure, salt effects, permeability reduction, fractured reservoirs.

ABSTRACT

The equation-of-state module able to handle saline brines with non-condensible gas, developed for the TOUGH2 simulator, has been improved to include vapor pressure lowering (VPL) due to suction pressure as represented by Kelvin's equation. In this equation the effects of salt are considered whereas those of non-condensible gas have currently been neglected.

Numerical simulations of fluid production from tight matrix blocks have been performed to evaluate the impact of VPL effects due to salinity and suction pressure on the depletion behaviour of vapor-dominated geothermal reservoirs.

Previous studies performed neglecting VPL due to suction pressure showed that for initial NaCl mass fractions above threshold values, "sealing" of the block occurs and large amounts of liquid fluid may not be recovered. On the other hand, below the threshold value the matrix block dries out due to fluid production.

The inclusion of VPL due to suction pressure does not allow complete vaporization of the liquid phase. As a result, the threshold NaCl concentration above which sealing of the matrix block occurs is increased. Above the 'critical' NaCl concentration, block depletion behaviour with and without the VPL due to suction pressure is almost identical, as liquid phase saturation remains high even after long production times.

As the VPL due to suction pressure depends mainly on capillary pressure, the shape of capillary pressure functions used in numerical simulations is important in determining VPL effects on block depletion.

INTRODUCTION

An equation-of-state (EOS) module, here referred to as EWASG, able to handle saline brines with non-condensible gas (NCG), was developed by Battistelli et al. (1993) for the TOUGH2 simulator. Vapor pressure lowering phenomena due to salinity only were considered in that EOS module version.

Capillary pressure and vapor adsorption effects, here referred to as suction pressure effects, and associated VPL phenomena are believed to have a large importance in determining the in-place and extractable fluid reserves of a geothermal reservoir (Nghiem and Ramey, 1991).

Modeling studies of the effects of capillarity and vapor adsorption on the depletion of vapor-dominated geothermal reservoirs have been performed by Pruess and O'Sullivan (1992) considering pure water. The VPL due to suction pressure has now been implemented in the EWASG module.

This paper illustrates the method used to model the VPL due to suction pressure in the presence of saline brines. We also present and discuss preliminary results of numerical simulations performed to evaluate the impact of these effects on the depletion of geothermal reservoirs containing saline brines. In these simulation studies the presence of NCG has not been accounted for.

MODELLING APPROACH

In the EWASG formulation the multiphase mixture is assumed to be composed of three mass components: water, sodium chloride and NCG. While water and NCG components may be present only in the liquid and gas phases, the salt component could be present dissolved in the liquid phase or precipitated to form a solid salt phase. The small solubility of NaCl in the gas phase is disregarded.

The reduction of rock porosity owing to salt precipitation is taken into account, as well as the related decrease of formation permeability according to the Verma and Pruess model (1988).

The dependence of brine enthalpy, density, viscosity and vapor pressure on salt concentration has been accounted for, as well as the effect on NCG solubility and heat of solution in the brine. Transport of the mass components occurs by advection in liquid and gas phases; binary diffusion in the gas phase for steam and the NCG is accounted for. Dispersive processes

in the liquid and gas phases are not included in the present formulation. It is assumed that the three phases (gas, liquid, and solid salt) are in local chemical and thermal equilibrium and that no chemical reactions take place other than interphase mass transfer.

In the integral finite differences formulation used by TOUGH2, the mass balance equations are written in the following general form (Pruess, 1991):

$$\frac{d}{dt}\int_{V_n} M^{(k)}\,dV = \int_{\Gamma_n} F^{(k)}\cdot n\,d\Gamma + \int_{V_n} Q^{(k)}\,dV \qquad (1)$$

where k=1,2,3 in EWASG indicates water, NaCl and NCG components, respectively. A complete description of the nomenclature used is given at the end of the paper. The accumulation and mass flux terms for the NaCl component (k=2) are written as follows:

$$M^{(2)} = \phi S_s \rho_s + \phi S_l \rho_l X_l^{(2)} \qquad (2)$$

$$F^{(2)} = -k\frac{k_{rl}}{\mu_l}\rho_l X_l^{(2)}(\mathrm{grad}P_l - \rho_l g) \qquad (3)$$

where S_s is the "solid saturation", defined as the fraction of pore volume occupied by solid salt.

The vapor pressure as affected by suction pressure and salinity effects is given by:

$$P_v(T, S_{la}, X_l^{(2)}) = f_{VPL}(T, S_{la}, X_l^{(2)})\; P_{b\,sat}(T, X_l^{(2)}) \qquad (4)$$

where $P_{b\,sat}$ is the saturated vapor pressure of brine with dissolved salt mass fraction $X_l^{(2)}$ at temperature T, and f_{VPL} is the vapor pressure lowering factor given by Kelvin's equation:

$$f_{VPL} = \left[\frac{W^{(1)} P_c(S_{la})}{\rho_l(P_l, T, X_l^{(2)})\, R\,(T+273.15)}\right] \qquad (5)$$

The capillary pressure is evaluated considering the 'active liquid phase' S_{la}. Active saturation of flowing phases is defined as:

$$S_{\beta a} = S_\beta / (1 - S_s) \qquad (6)$$

where β=l,g and:

$$S_{la} + S_{ga} = 1 \qquad (7)$$

The VPL implementation on EWASG differs from that available on the EOS4 module for water-air mixtures (Pruess, 1991), depending also on the choice of primary variables set. In EWASG the primary variables used for single phase conditions are total pressure of reference phase, P, salt mass fraction, $X^{(2)}$, NCG mass fraction, $X^{(3)}$, and temperature, T. If solid salt is present, the second primary variable is switched to solid saturation S_s. In two-phase conditions the third primary variable is switched from NCG mass fraction to gas phase saturation S_g.
The same primary variables set is used in EWASG with VPL capabilities in order to allow full compatibility with the previous version. VPL capabilities can be invoked simply by setting on/off a switch from the input deck.

In the presence of VPL effects due to suction pressure, the liquid phase can be present under conditions where vapor partial pressure and the gas phase total pressure are less than the brine saturation pressure. The thermophysical properties of liquid phase are calculated in these conditions considering the liquid phase pressure used by Pruess (1991):

$$P_l = \max(P_g, P_{b\,sat}) \qquad (8)$$

The liquid phase pressure determined with the above condition is also used to calculate the brine density for the Kelvin's equation.

CAPILLARY PRESSURE FUNCTION

Different geologic media show a great diversity of VPL and suction pressure relationships. Pruess and O'Sullivan (1992) presented a compilation of published experimental data with a description of available experimental methods.

Among the equations used to fit experimental data, Pruess and O'Sullivan considered for their numerical simulation study the equation suggested by van Genuchten (1980):

$$P_c = -Po\,(S_{ef}^{-1/\lambda} - 1)^{1/\lambda} \qquad (9)$$

where:

$$S_{ef} = \frac{S_{la} - S_{lr}}{1 - S_{lr}} \qquad (10)$$

Po, and λ are fitting parameters, whereas S_{la} is the active liquid saturation and S_{lr} is the liquid residual saturation. We used for our numerical studies the same capillary pressure curve used by Pruess and O'Sullivan with the following parameters obtained by Peters et al. (1984) through the fitting of experimental data obtained on tuff samples from Yucca Mountain:

S_{lr} = 0.0801

λ= 0.4438

Po = 1.727 MPa

Although the van Genuchten model allows consistent formulation for both capillary pressure and relative permeability functions, it presents the drawback that P_c goes to infinity as the liquid saturation approaches the residual value. The capillary pressure corresponding to the above parameters, is plotted vs the liquid phase saturation in Fig. 1. The figure also shows the VPL factor and the total pressure vs liquid saturation for a two-phase system at constant temperature of 220°C, for both pure water and a brine with a salt mass fraction of 20%.

As shown in Fig. 1, a maximum value of 500 MPa has been considered to avoid the infinity in the capillary pressure. Due to rapid increase of P_c at liquid saturation approaching the residual value, the VPL factor decreases from about 0.9 at S_l=0.2 to approx 0.1 at liquid saturation of 0.09. The effect of salt on VPL factor is limited: due to the higher liquid phase density, the VPL factor is slightly higher in the presence of saline brine. On the other hand, the total pressure is lower as the effect of VPL due to salinity prevails.

Fig. 1 suggests that, at least for selected capillary pressure curve, the effects of VPL due to suction will be important only at low liquid saturation values (Pruess and O'Sullivan, 1992).

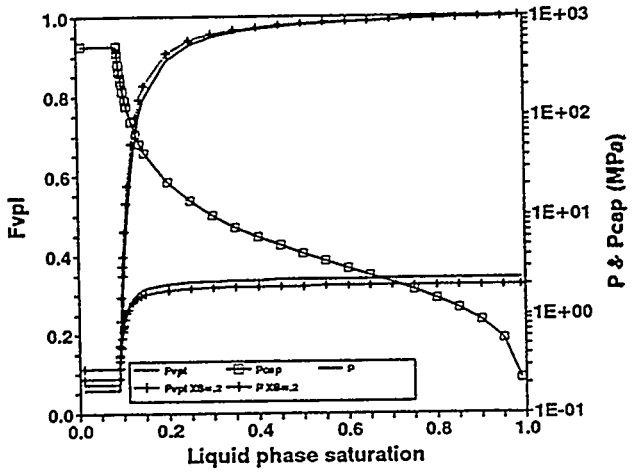

Fig.1 Capillary pressure, VPL factor and total pressure as a function of liquid saturation at a constant temperature of 220°C, for pure water and brine with 20% salt content.

DEPLETION OF TIGHT MATRIX BLOCKS

Most of the fluid reserves in vapor-dominated reservoirs are stored in tight matrix blocks with permeability in the order of microdarcy. Fracture systems are believed to contribute little to fluid storage, mainly providing large-scale permeability. The effect of VPL due to suction pressure is to generate an additional pressure decline as the block dries out, thus slowing down the recovery of fluid reserves.

Previous studies (Pruess and O'Sullivan, 1992) have analysed the effects of suction pressure on the depletion behaviour of tight matrix blocks, under conditions considered representative of vapor dominated systems. Battistelli et al. (1995) have examined the effects of salt content on depletion behaviour neglecting the VPL due to suction pressure. This paper presents simulations studies on the combined effects of permeability reduction and VPL due to salinity and suction pressure.

A model similar to that described by Pruess and O'Sullivan (1992) has been employed. It consists of a single block of rock matrix in the shape of a cube with side length of 50 m, which is to be viewed as a subdomain of a large reservoir volume. The block is surrounded by fractures with a small fractional volume of 10^{-4}. The matrix block is discretized according to the MINC method (Pruess and Narasimhan, 1985) with 15 nested cubes of 0.5%, 1%, 2%, 3%, 4%, 5%, 6%, 7%, 8%, 9%, 10%, 10%, 11%, 11%, and 12.5% volume fractions, as used by Battistelli et al. (1995). Matrix permeability, porosity density, specific heat and thermal conductivity are $5x10^{-18}$ m^2, 5%, 2600 kg/m^3, 920 J/kg°C and 2.51 W/m°C, respectively.

The system is initially in two-phase conditions at temperature of 240 °C, with liquid saturation of 80% in the matrix block, and 1% in the fractures. Liquid relative permeability and capillary pressure are assumed in the van Genuchten form as used by Pruess and O'Sullivan (1992). Gas relative permeability is given by $k_{rg}=1-k_{rl}$. Block depletion occurs by a "well on deliverability" placed in the fractures with a prescribed wellbore pressure of 1 MPa, and a productivity index of $1.788x10^{-13}$ m^3.

We modelled the permeability reduction using the series model for tubular flow with fractional length=0.8 and critical porosity fraction= 0.8. The equations employed have been presented by Battistelli et al. (1995) whereas a complete model description is given by Verma and Pruess (1988).
Six cases are presented with different initial salt content. The effects of salt content and VPL on initial pressure and fluid reserves are summarized in Table 1.

Battistelli et al. (1995) found that in the depletion of low matrix permeability blocks persistent boiling near the block

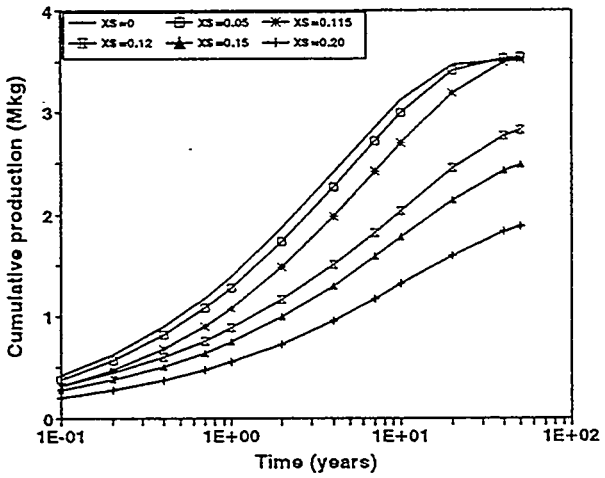

Fig.2 Cumulative fluid recovery as a function of time for cases 1 to 6.

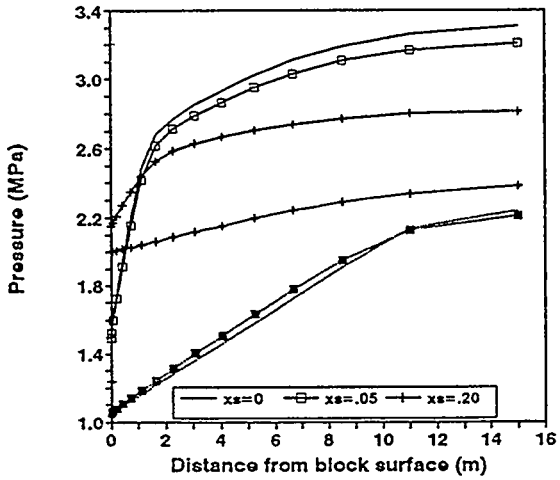

Fig.3 Pressure distribution vs distance from block surface after 0.4 and 10 years for cases 1, 2 and 6.

Case	Salinity (%)	Pressure (MPa)	Psat (MPa)	Mass in place (Mkg)	Water (Mkg)
1	0	3.323	3.348	4.088	4.088
2	5	3.221	3.244	4.306	4.092
3	11.5	3.066	3.086	4.585	4.060
4	12	3.052	3.073	4.607	4.056
5	15	2.970	2.989	4.736	4.028
6	20	2.821	2.839	4.948	3.962

Table 1. Initial pressure, saturation pressure and fluid reserves for different salt contents.

surfaces leads to concentration and, ultimately, precipitation of solids. They found that when the initial salt content is above a threshold value, the salt precipitation causes a severe loss in permeability so that the rate at which the fluid reserves are recovered is considerably lowered. For the same model used in this paper, neglecting the VPL due to suction pressure, the 'critical' salt mass fraction is between 0.08 and 0.085.

The effects of permeability reduction as a function of initial salt content in the presence of VPL effects due to suction pressure are presented in Fig. 2, which shows the cumulative mass production vs time for the 6 cases. It is interesting to note that the 'critical' initial salt mass fraction is increased to a value between 0.115 to 0.12. This increase is due to the fact that, avoiding complete vaporization of liquid phase inside the block, a higher value of salt mass fraction is necessary in order to reach the conditions for the sealing of block surfaces.

The change in behaviour below and above the threshold value is high-lighted in Fig. 3 showing the pressure distribution in the matrix block after 0.4 and 10 years.

At early times, 0.4 years, a high pressure decrease occurs near the block surface due to low matrix permeability, producing strong vaporization. Since from the beginning no liquid phase is discharged from the block to the fractures being held by capillary forces, in the first matrix element salt accumulates owing to vaporization of brine flowing towards the block surface from the interior until salt precipitation takes place.

For initial salt content lower than the threshold value, the first matrix element vaporizes until the minimum value allowed by the VPL effects is approached, and the precipitation of solid salt starts in the second matrix element. Then vaporization takes place progressively in the interior of the block with precipitation of solid salt distributed in all the elements.

For initial salt content higher than the threshold value, the accumulation of salt in the first element is so fast that further boiling in this element is prevented. In fact the permeability reduction reduces the extracted mass rate and slows down the depletion associated processes. Consequently, all the matrix elements remain in two-phase conditions.

Fig.4 shows liquid saturation as a function of distance from block surface at 10 years for cases 1, 2 and 6. Curves obtained with and without VPL due to suction pressure are compared. Below the threshold value (cases 1 and 2), the introduction of VPL avoids complete vaporization of the liquid phase. The liquid saturation close to block surfaces approaches the minimum value allowed by the capillary pressure curve chosen. Above the threshold value, the S_l distribution is almost identical, as for $S_l > 0.5$ the effect of VPL is very limited, as shown in Fig. 1 for the f_{VPL} factor as a function of liquid saturation.

As observed when VPL effects due to suction pressure are

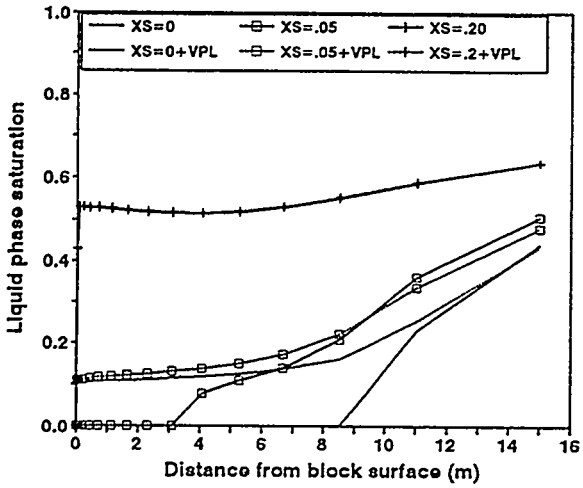

Fig.4 Liquid saturation distribution vs distance from block surface after 10 years for cases 1, 2 and 6 with and without VPL due to suction pressure.

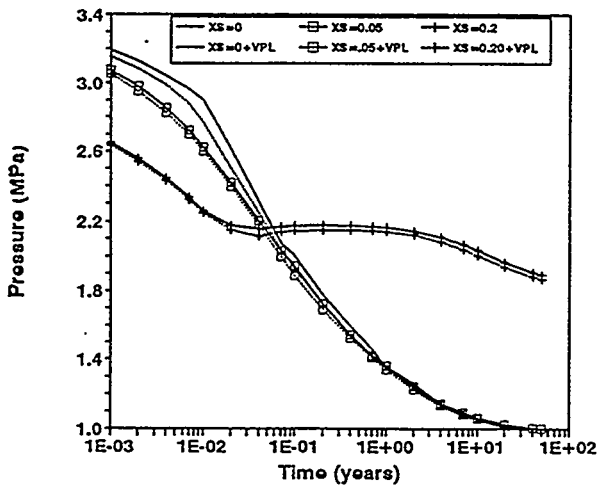

Fig.5 Pressure history in the first matrix element for cases 1 to 6.

disregarded, two factors mainly control the depletion behaviour: boiling of theliquid phase with progressive drying out of matrix elements, and permeability reduction due to solid salt precipitation.

The change between the two observed behaviors depends on which factor prevails: at low salt content the first matrix element reaches the minimum liquid saturation value before the salt precipitation seals the matrix block surface.

To show how this process works, the pressure in the first matrix element is plotted as a function of time for all 6 cases in Fig. 5. At early time, the liquid saturation decreases faster for lower initial salt content because of higher extraction rate. For higher initial salt content the deposition of solid salt starts earlier and reduces the rate of pressure decline. When solid saturation approaches 0.20, the reduction of permeability is so high that production is strongly reduced and consequently the pressure becomes almost constant due to fluid redistribution in the interior of the block. For the cases shown, characterized by initial salt content far from the threshold value, the pressure history of first element with and without VPL effects due to suction is almost identical for the different cases. Total pressure is, of course, slightly smaller due to VPL effects.

The liquid saturation as a function of time is shown in Fig. 6 for the same cases with and without VPL effects. Whereas for XS=0.20 the history is almost identical, for cases below the threshold value the first element never vaporizes completely and a lower limit seems to be approached independently from the initial salt content.

The reasons for the convergence of liquid saturation at late

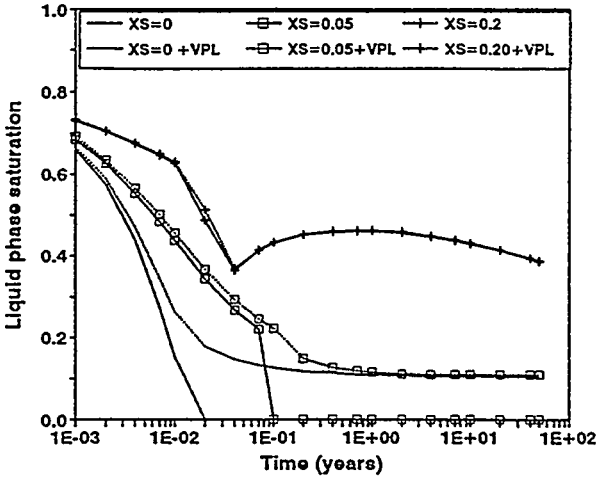

Fig.6 Liquid phase saturation history in the first matrix element for cases 1, 2 and 6 with and without VPL due to suction pressure.

time towards a finite value independently from initial salt content lower than the threshold value, is due mainly to the shape of the adopted capillary pressure curve.
As the van Genuchten equation gives capillary pressure tending to infinity when the irreducible liquid saturation is approached, in our simulation the VPL factor decreases sharply when liquid saturation is lower than approximately 0.20. The well on deliverability option chosen for fluid extraction determines the minimum value for the pressure inside the block. At late time, close to 50 years, the pressure inside the block is almost 1 MPa everywhere for initial salt contents lower than the threshold value. Fig. 1 shows that the effect of salt on VPL due to suction pressure is very limited. Thus the total pressure of 1 MPa is reached at comparable S_l values regardless of the initial salt content.

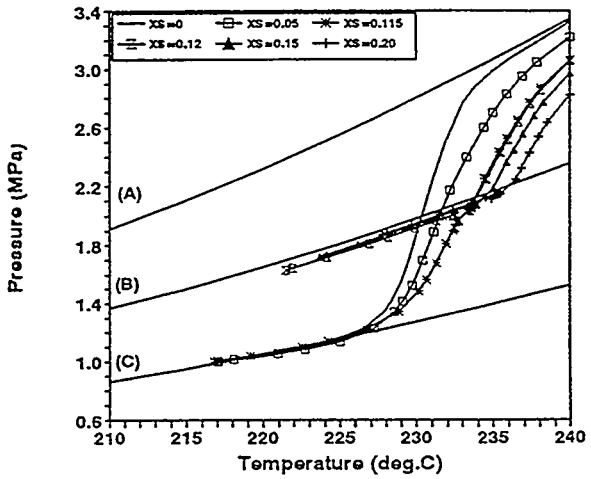

Fig.7 Thermodynamic path followed by the first matrix element during block depletion for cases & to è.

This behaviour does not change if a different value of irreducibleliquid saturation is considered. Simulation runs for pure water utilising S_{lr} values of 0, 0.04 and 0.30 gave similar results. Different choices will naturally affect the threshold value at which the transition between the two different depletion behaviours occurs.

Similar results have also been obtained by using the same S_{lr} value and different Po values equal to 50% and 200% of the value used in the base case. In this way the capillary pressure has the asymptotic behavior at the same S_l value and the curve is shifted down or up according to the increase or decrease of Po parameter. The total pressure as a function of time changes, of course, according to the increase or decrease of VPL effects, but the depletion behaviour is almost identical.

The bottomhole pressure has also been changed from 1 MPa to 0.5 MPa. The recovery of fluid reserves was of course faster because of the higher pressure gradient, but it is interesting to note that the cumulative production after 50 years was only slightly higher. In fact, apart from the effects of minor differences in final block temperature, in order to reduce the total pressure to 0.5 MPa, a value of f_{VPL} equal to 50% of that of base case is necessary. For pure water, the final liquid saturation is about 9.6% instead of 10.6%. Thus the production increase, lowering bottomhole pressure to 50% of the initial base case value, corresponds to only 1% of liquid saturation.

Fig. 7 shows the thermodynamic path followed by the first matrix element during block depletion in terms of pressure vs temperature for all six cases. The saturation curve of pure water (A), that of NaCl saturated brine (B) and the saturation curve of pure water with VPL due to suction at a constant liquid saturation of 0.106 (C) are also shown. It is evident that for cases 1, 2 and 3 (with initial salt content below thethreshold value) the saturation curve of pure water with VPL effects at 10.6% liquid saturation is followed. The effects of salt on the VPL due to suction are limited.

On the other hand, the cases with an initial salt content above the threshold value (cases 4, 5 and 6) follow the shape of the brine saturation curve with NaCl concentration at saturation values.

CONCLUSIONS

The EWASG module including VPL due to salinity only and permeability reduction from the precipitation of salt, i.e. the EOS module for H_2O-NaCl-NCG mixtures developed for the TOUGH2 simulator by Battistelli et al. (1993, 1995), has been improved implementing the VPL due to suction pressure effects.

Simulation studies of fluid production from tight matrix blocks have been performed to evaluate the effects of VPL due to suction pressure on the depletion of fractured vapor-dominated reservoirs containing brines.

For the model and parameters investigated, previous simulations carried out using the EWASG module, showed a different depletion behavior depending on the initial NaCl concentration being higher or lower than a threshold value because of salt precipitation and related permeability reduction. The existence of these threshold values has been confirmed by simulation with VPL due to suction pressure effects included, but the change in the depletion behavior occurs at higher threshold values.

VPL due to suction pressure prevents complete dry-out of matrix block. Even for initial salt concentrations below the threshold value and after long production times, the block is in two-phase conditions and for the parameters used here, about 10% of initial water reserves are not produced.

Above the threshold value, persistent boiling near the surfaces of matrix blocks produces a severe loss in permeability, and considerably slows down the rates at which fluid reserves can be recovered. As liquid saturation remains at high values throughout the block, the VPL due to suction pressure does not produce remarkably effects.

Due to the strong dependence of the VPL factor from the relationship between suction pressure and liquid saturation, the results obtained are dependent upon the shape of capillary pressure function characteristics of different geologic media.

ACKNOWLEDGEMENTS

This work was supported by Aquater S.p.A. of the Italian National Hydrocarbons Agency (ENI), by the International Institute for Geothermal Research of the Italian National Research Council (CNR), and by the Assistant Secretary for Conservation and Renewable Energy, Geothermal Division, of the U.S. Department of Energy under contract No DE-AC03-76SF00098.

NOMENCLATURE

F(k) mass flux of component k, kg/(s m^2)
f_{VPL} vapor pressure lowering factor, dimensionless
g acceleration of gravity, m^2/s
k intrinsic permeability, m^2
$k_{r\beta}$ relative permeability to β phase
$M^{(k)}$ accumulation term of component k, kg/m^3
n unit normal vector
P pressure, Pa
P_c capillary pressure, Pa
Po fitting parameter in the van Genuchten's equation
$Q^{(k)}$ source term for component k, kg/(s m^3)
R universal gas constant, 8,314 J/°C mole
S_β saturation of phase β
T temperature, °C
Vn volume of grid element n, m^3
$X^{(k)}$ mass fraction of component k
$W^{(k)}$ molecular weight of component k, kg/mole
Γn surface area of grid element n, m^2
ø porosity
λ fitting parameter in the van Genuchten's equation
μ dynamic viscosity, Pa s
ρ density, kg/m^3

Subscripts and Superscripts

a active
b brine
g gas phase
l liquid phase
r residual
s solid salt phase
sat vapor-saturated
1 water component, H_2O
2 salt component, NaCl
3 gas component, NCG
β phase index

REFERENCES

Battistelli, A., Calore, C. and Pruess, K. (1993). *A Fluid Property Module for the TOUGH2 Simulator for Saline Brines with Non-Condensible Gas.* Proc. 18th Workshop on Geoth. Res. Eng., Stanford University.

Battistelli, A., Calore, C. and Pruess, K. (1995). *Analysis of Salt Effects on the Depletion of Fractured Reservoir Blocks.* Proc. World Geoth. Congress, Florence, May 18-30, in press.

Nghiem, C. P., and Ramey, H. J. Jr. (1991). *One-Dimensional Steam Flow in Porous Media under Desorption.* 16th Workshop on Geoth. Res. Eng., Stanford University.

Peters, R. R., Klavetter, E. A., Hall, I. J., Blair, S. C., Heller, P. R., and Gee, G. W. (1984). *Fracture and Matrix Hydrologic Characteristics of Tuffaceous Materials from Yucca Mountain, Nye County, Nevada.* Sandia Ntl. Lab., Report SAND84-1472.

Pruess, K. and Narashiman, T. N. (1985). *A Practical Method for Modeling Fluid and Heat Flow in Fractured Porous Media.* Soc. Pet. Eng. J., Vol. 25(1), pp. 14-26.

Pruess, K. (1991). TOUGH2 - *A General-Purpose Numerical Simulator for Multi-phase Fluid and Heat Flow.* Earth Sci. Div., Lawrence Berkeley Laboratory Report LBL-29400.

Pruess, K. and O'Sullivan, M. (1992). *Effects of Capillarity and Vapor Adsorption in the Depletion of Vapor-Dominated Geothermal Reservoirs.* Proc. 17th Workshop on Geoth. Res. Eng., Stanford University.

Verma, A. and Pruess, K. (1988). *Thermohydrological Conditions and Silica Redistribution Near High-Level Nuclear Wastes Emplaced in Saturated Geological Formations.* J. of Geophys. Res., Vol. 93(B2), pp. 1159-1173.

Coupling of the Reservoir Simulator TOUGH and the Wellbore Simulator WFSA

Teklu Hadgu, Robert W. Zimmerman, and Gudmundur S. Bodvarsson

Earth Sciences Division
Lawrence Berkeley Laboratory
University of California
Berkeley, Calif. 94720 U.S.A.

ABSTRACT: The reservoir simulator TOUGH and the wellbore simulator WFSA have been coupled, so as to allow simultaneous modeling of the flow of geothermal brine in the reservoir as well as in the wellbore. A new module, COUPLE, allows WFSA to be called as a subroutine by TOUGH. The mass flowrate computed by WFSA now serves as a source/sink term for the TOUGH wellblocks. Sample problems are given to illustrate the use of the coupled codes. One of these problems compares the results of the new simulation method to those obtained using the deliverability option in TOUGH. The coupled computing procedure is shown to simulate more accurately the behavior of a geothermal reservoir under exploitation.

INTRODUCTION

Several reservoir simulators currently exist that model flow processes occurring in the subsurface (e.g., PT, Bodvarsson, 1982; TOUGH, Pruess, 1987; TETRAD, Vinsome, 1991; STAR, Pritchett, 1994). These models typically ignore the details of flow in the wellbore, and treat the well in a very simplified manner. Likewise, several wellbore flow simulators exist which model the internal flow in the wellbore, with varying degrees of accuracy and sophistication (e.g., WF2, Ortíz-Ramírez, 1983; GEOTEMP2, Mondy and Duda; 1984; WELF, Miller, 1984; HOLA, Bjornsson and Bodvarsson, 1987; WFSA and WFSB, Hadgu and Freeston, 1990). These codes usually take as their input some parameters, such as flowrates and enthalpies, that would be found as output of a reservoir simulator. Several previous attempts have been made at coupling wellbore and reservoir simulators. For example, Miller (1980) developed a simplified transient-wellbore code to model wellbore storage effects. Recently, Murray and Gunn (1993) used lookup tables generated by the wellbore simulator WELLSIM to be used as input to the reservoir simulator TETRAD. We have written a computational module called COUPLE that allows the wellbore simulator WFSA to serve as a subroutine for TOUGH. The resulting coupled reservoir-wellbore simulation capability allows more accurate and integrated modeling of the exploitation of geothermal systems.

TOUGH RESERVOIR SIMULATOR

TOUGH (Pruess, 1987) is a numerical code designed to simulate the coupled transport of fluid, heat and chemical species for multi-phase flow in porous as well as fractured media. TOUGH is a three-dimensional code which solves the equations of mass and energy conservation by discretizing them in space using the "integral finite difference" method. Time is discretized in a fully implicit manner, as a first-order finite difference. Darcy's law is used to describe single-phase and two-phase flow with interference between phases represented by relative permeability functions. Thermodynamic and transport properties of water are obtained from steam table equations. Heat flow is represented by conduction, convection and gaseous phase diffusion.

At each time step, TOUGH solves mass balance and an energy balance equations for each computational gridblock. TOUGH equates the net flux into each gridblock, including source/sink terms, with the change in the stored amount of that component in the block. The difference between the change in storage and the net influx, which is called the residual, is set to zero. These balance equations are nonlinear, due to the dependence of the thermodynamic and

transport properties on the independent variables pressure, temperature and saturation. An iterative Newton-Raphson method is used to solve these equations, which results in a set of linear algebraic equations at each iteration step, which are then solved using sparse matrix solvers.

TOUGH has options for describing fluid/heat injection or withdrawal from the reservoir, treated as source/sink terms. One particular type of source/sink is the "deliverability" option, in which well output is calculated based on a specified bottomhole pressure and productivity index through the equation

$$W = \nu PI(Pr - Pwb), \tag{1}$$

$$\nu = \frac{krl\rho l}{\mu l} + \frac{krg\rho g}{\mu g}, \tag{2}$$

where the subscript l denotes liquid, the subscript g denotes vapor, Pwb is the wellbottom pressure, Pr is the reservoir pressure in the gridblock containing the well, and ν is the effective kinematic viscosity of the flowing two-phase mixture. When using the deliverability option, Pwb must be specified in advance at some constant value. In most production scenarios, however, Pwb will vary with time. This variation can only be found by simultaneously solving for the flowfields in the reservoir and the wellbore.

PRODUCTIVITY INDEX

In order to use the deliverability option, a productivity index (PI) must be specified, in order for TOUGH to calculate the flowrate from the wellblock into the wellbore. In many instances, PI would be found by performing a history match. In principle, however, the productivity index can be found through the following analysis.

If we ignore the possibility of turbulent flow occurring near the borehole (see Kjaran and Eliasson, 1983, for a discussion of turbulent flow to geothermal boreholes), the mass flowrate would be described by the two-phase version of Darcy's law:

$$\frac{dP}{dR} = \frac{W\nu}{2\pi kHR}. \tag{3}$$

Coats (1977) showed that this equation could be numerically integrated from R = R* to R = Rw, where R* is the effective radius of the gridblock containing the wellbore, and Rw is the radius of the wellbore. However, if the pressure drop in the wellblock is small enough that flashing does not occur, we can evaluate all properties appearing in eq. (3) at reservoir conditions, and solve directly for the flowrate. Including a skin factor to account for the added pressure drop due to an altered zone around the wellbore, we find

$$W = \frac{2\pi kH}{\nu[\ln(R^*/Rw) + s]}(Pr - Pwb). \tag{4}$$

To find a numerical value for PI, we need to know the effective wellblock radius, R*. If a single well test is being modeled, a fine-meshed radial grid would typically be used around the wellbore. One common type of radial grid is one in which the outer radius of the ith gridblock, Ri, is defined by

$$Ri+1 = cRi, \tag{5}$$

where c > 1 is a constant. For this type of grid, the effective wellblock radius will be (Aziz and Settari, 1979, p. 88)

$$R^* = \frac{\ln(c)}{(c-1)} R1. \tag{6}$$

The productivity index can then be found by equating (1) and (4):

$$PI = \frac{2\pi kH}{\ln(R^*/R1) + s}, \tag{7}$$

where R* defined by eq. (6). A similar analysis for a rectangular grid is presented in Hadgu et al. (1995).

The deliverability equation (1) was derived for steady-state cases. To test the validity of this assumption, Hadgu et al. (1995) compared the deliverability method with the analytical solution for flow from a constant-pressure wellbore, and the output from a TOUGH simulation in which the wellblock is discretized into a fine mesh. They found that the deliverability method agreed with the analytical and fine-mesh numerical solutions for sufficiently large times. The time needed for the quasi-steady-state approximation to become accurate agreed reasonably well with the value estimated by Pritchett and Garg (1980), which was $4\phi c\mu R1^2/k$, where R1 is the radius of the gridblock.

WELLBORE SIMULATOR WFSA

The presence of liquid water, steam, dissolved solids and non-condensable gases in the geothermal fluid renders wellbore flow a complex multi-phase flow problem. Because of these complexities, many researchers have used empirical methods to simulate the fluid flow. Unfortunately, most existing empirical correlations were derived under conditions very different from those found in geothermal wellbores, i.e., air and water as the two phases, instead of air and steam, diameters of only a few inches, etc.

The wellbore simulators WFSA and WFSB attempt to model the two-phase flow in the wellbore by actually solving a one-dimensional version of the Navier-Stokes equations. These simulators were developed at Auckland University, New Zealand (see Hadgu and Freeston, 1990). These codes include features such as presence of dissolved solids, presence of non-condensible gases, multiple feed zones, and fluid-rock heat exchange. A related code, STFLOW, was developed to handle wells in vapor-dominated fields, and can treat superheated steam. These three codes (WFSA, WFSB and STFLOW) were later combined into a single simulator with all the features, WELLSIM Version 1.0 (Gunn and Freeston, 1991). We have used WFSA in our work.

WFSA assumes that the flow is steady and one-dimensional, the phases are in thermodynamic equilibrium, and dissolved solids can be represented by NaCl. In the case of wells with multiple feedzones, the mass flowrate and enthalpy (or reservoir pressure, drawdown factor and enthalpy) are needed as input for each feed point. WFSA uses finite differences to solve the equations of mass, momentum and energy conservation along the length of the wellbore. There is no restriction on the geometry or variation of well diameter with depth, and any number of feed points can be included, provided that the mass flowrate, pressure and enthalpy of the fluid are prescribed.

COUPLING OF TOUGH AND WFSA

For a well with multiple-layer completion (i.e., multiple feedzones), TOUGH's deliverabiliy option requires a productivity index for each of the layers and a constant wellbore pressure for the uppermost one. The code then calculates wellbore pressures for the other layers based on that specified wellbore pressure. The assumption is made that wellbore pressures in other layers can be obtained approximately by accounting for gravity effects.

For the reservoir-wellbore coupling (see Fig. 1), the above procedure has been changed. The wellbore pressure of the uppermost layer is no longer required, but wellhead pressure needs to be specified instead. The deliverability option in TOUGH is used, but the calculations are performed in the separate subroutine COUPLE that couples TOUGH and WFSA. The deliverability equation (1), which connects the reservoir and the wellbore is applied at each feedzone.

An iterative procedure is utilized between COUPLE and WFSA to evaluate mass flowrates and wellbore pressures at each feedzone. The iterative methods are encoded in subroutine COUPLE, using a 4th-order Runge-Kutta method. To initiate the iteration, the first guess for Pwb in the bottom-most feedzone is taken to be slightly less than the pressure in the reservoir. Based on this initial Pwb, the mass flowrate is calculated using eq. (1). WFSA then computes fluid parameters up the wellbore until the next feedzone is encountered. Applying mass and heat balance at this feedzone yields new parameters required to continue computation up the wellbore. The procedure is repeated at each feedzone until the wellhead is reached. If the computed wellhead pressure differs from the specified wellhead pressure by more than some specified tolerance, the computation is repeated, starting from bottomhole.

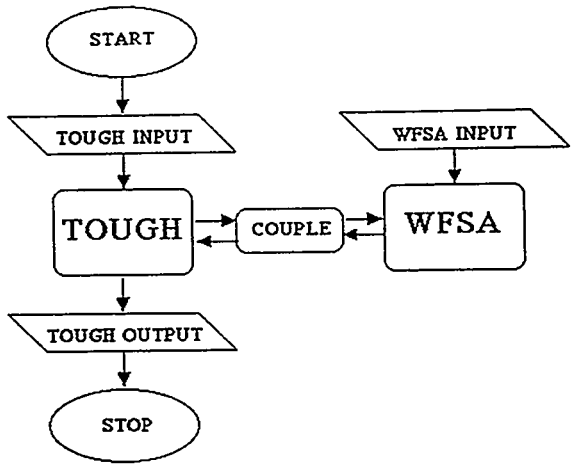

Fig. 1. Schematic diagram of the coupling procedure.

SAMPLE SIMULATIONS

Following are some sample calculations to demonstrate the use of the coupled simulation procedure; further examples can be found in Hadgu et al. (1995). We consider a single well having an inside diameter of 0.2 m, and a depth of 1000 m, located in an infinite, radially-symmetric reservoir. The reservoir has a thickness of 500 m and is overlain by a 750 m-thick caprock. The reservoir is taken to have a permeability of 0.1 D, a porosity of 0.1, a rock density of 2600 kg/m^3, and a rock specific heat of 1 kJ/kg°C. The initial conditions in the reservoir are taken to be a pressure of 60 bars, a temperature of 275.6°C, and a gas saturation of 0.1. A radial mesh was used according to eq. (5), with a wellblock radius of 100 m, and a mesh-amplification factor of c = 1.29. Using eqs. (6) and (7), and assuming no skin effect, the nodal distance for the wellblock and the productivity index were calculated to be 87.8 m and 4.64 x 10^{-11} m^3, respectively.

First, we compare the output of the coupled codes with that obtained by running TOUGH using the deliverability option. The above set of data is common for the two simulation approaches. The difference is that the coupled codes use a constant wellhead pressure, while TOUGH's deliverability option uses a constant bottomhole pressure. In order to find the best estimate for Pwb, the coupled codes were run first. The selected wellhead pressure was 7 bars. The initial calculated bottomhole pressure from the coupled codes, which was Pwb = 57.4 bars, was then used as the input to TOUGH.

The wellbore pressure is predicted to remain constant when using TOUGH's deliverability method, whereas the coupled codes predicted a drawdown (Fig. 2). The decrease in wellbore pressure is accompanied by a drop in reservoir pressure which is larger than that predicted using TOUGH's deliverability option. The larger drawdown given by the coupled codes results in a higher rise in vapor saturation, and a higher discharge rate (Fig. 3). Consequently, the initial rise in flowing enthalpy predicted by the coupled codes is also greater (Fig. 4).

We have also used the coupled simulation procedure to examine the power output of a well operating under different wellhead pressures. All parameters are taken as before, except that the initial gas saturation in the reservoir is assumed to be 0.2. Fig. 5 shows the prediction of mass flowrate at different wellhead pressures. The curves indicate an increase in mass flowrate with a decrease in wellhead pressure, which agrees with typical output curves of large-diameter production wells. The mass flowrate slowly declines with time, except for the two cases with the highest wellhead pressures. For times greater than those given in the figure, all curves show a decline in flowrate, as reservoir pressure in the wellblock declines further. Predicted flowing enthalpies consistently show a rise, with enthalpy decreasing slightly as wellhead pressure increases (Fig. 6). The mass flowrates were found to change significantly with wellhead pressure, whereas the changes in enthalpy were not as substantial (not shown; see Hadgu et al., 1995).

Electrical power output and steam consumption predictions were made using the computed mass flowrates, enthalpies and wellhead pressures, assuming that the wellhead pressure represents the turbine inlet pressure. The turbine exhaust pressure was taken to be 0.8 bars. At low wellhead pressures the mass flowrates are high, but the change in enthalpy between turbine inlet and exhaust is low; at high wellhead pressures the reverse occurs (Fig. 7). As a result, the curve for electrical power output shows a peak at intermediate pressures.

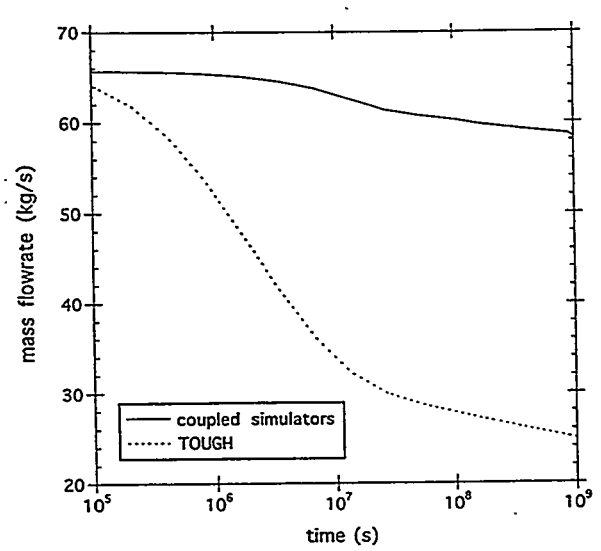

Fig. 2. Predicted reservoir pressure, Pr, and wellbottom pressure, Pwb, according to the deliverability method, and the coupled simulation procedure.

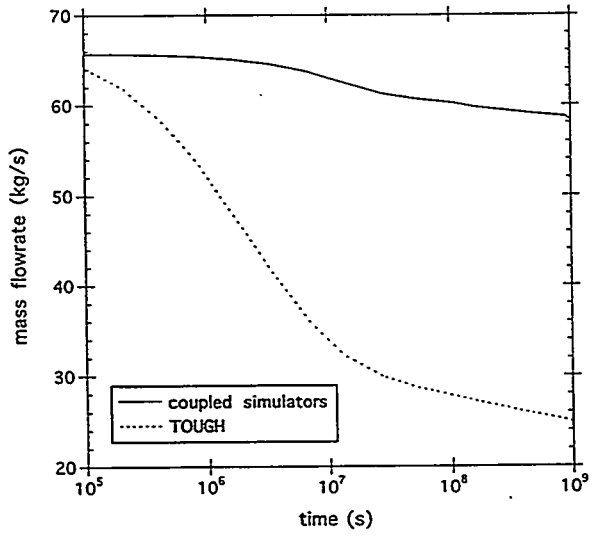

Fig. 3. Predicted discharge rates for problem discussed in text. For deliverability method, Pwb = 57.5 bars; for coupled simulation procedure, Pwh = 7 bars.

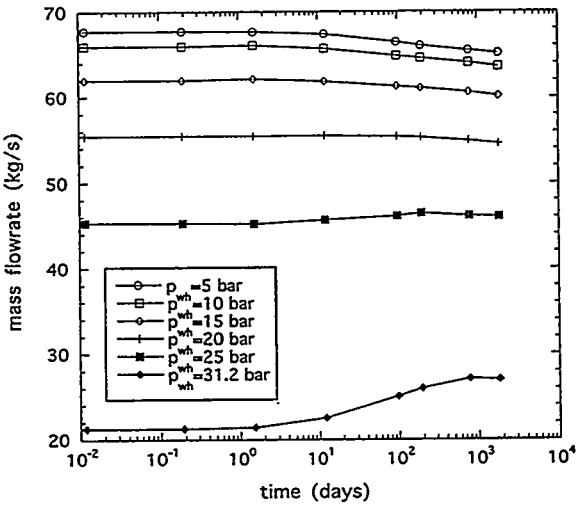

Fig. 5. Well discharge rate predicted by the coupled simulation procedure, for different wellhead pressures.

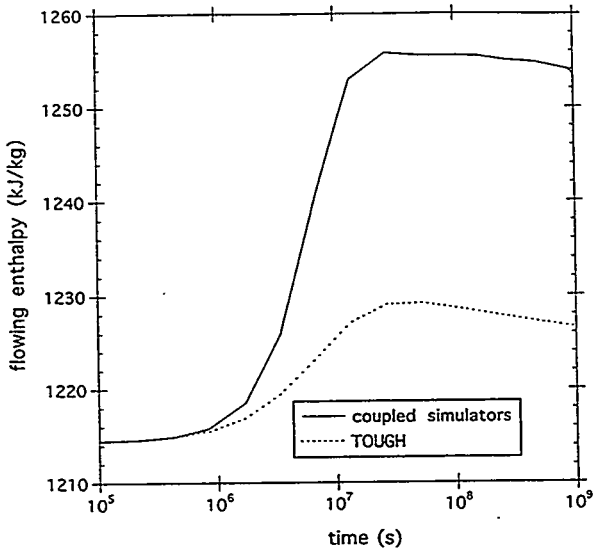

Fig. 4. Predicted flowing enthalpy; same problem as shown in Figs. 2 and 3.

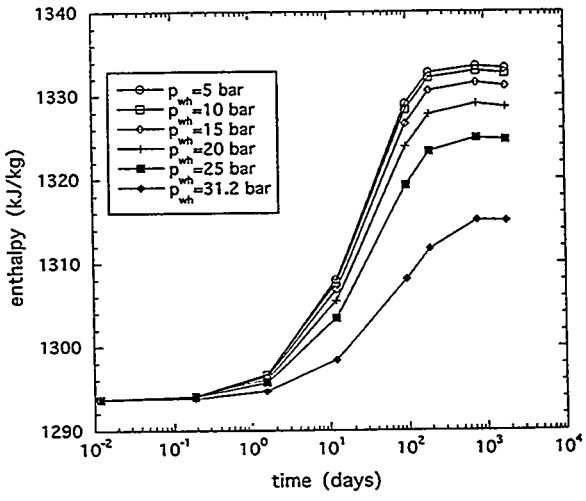

Fig. 6. Flowing enthalpies predicted by the coupled simulation procedure, for different wellhead pressures.

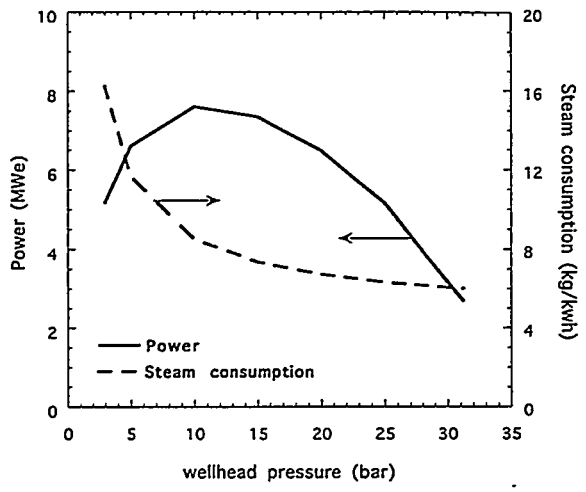

Fig. 7. Electrical power output and steam consumption, after five years of production.

SUMMARY

A module "COUPLE" has been developed to act as an interface between the reservoir simulator TOUGH and the wellbore simulator WFSA. This allows coupled, simultaneous simulation of flow in the wellbore and the reservoir. Some sample simulations were conducted to compare outputs of the coupled codes with that of TOUGH's deliverability method, and also to demonstrate possible applications of the coupled simulation procedure. The coupled simulation procedure is expected to be useful in simulating the behavior of geothermal reservoirs.

Acknowledgments - The work described in this paper has benefited from the comments and suggestions of Emilio Antunez, Christine Doughty, Roland Horne, Marcelo Lippmann, Jim Lovekin, Manuel Nathenson and Karsten Pruess. This work was supported by the Assistant Secretary for Energy Efficiency and Renewable Energy, Geothermal Division, of the U.S. Department of Energy under Contract No. DE-AC03-76SF00098.

REFERENCES

Aziz K. and Settari, A. (1979) *Petroleum Reservoir Simulation*, Elsevier Applied Science Publishers, London, U.K.

Bjornsson, G. and Bodvarsson, G. S. (1987) A multi-feedzone wellbore simulator, *Geoth. Resour. Counc. Trans.*, v. 11, pp. 503-507.

Bodvarsson, G. S. (1982) Mathematical modeling of the behavior of geothermal systems under exploitation, Report LBL-13937, Lawrence Berkeley Laboratory, Berkeley, Calif., U.S.A.

Coats, K. H. (1977) Geothermal reservoir modelling, Paper SPE 6892, presented at the 1977 SPE Technical Conference and Exhibition, Sept. 9-12, Denver, Colo., U.S.A.

Gunn, C. I. M. and Freeston, D. H. (1991) An integrated steady-state wellbore simulation and analysis package, *Proc. 13th New Zealand Geothermal Workshop*, Auckland, N.Z., pp. 161-166.

Hadgu, T. and Freeston, D.H. (1990) A multi-purpose wellbore simulator, *Geoth. Resour. Counc. Trans.*, v. 14, pp. 1279-1286.

Hadgu, T., Zimmerman, R. W. and Bodvarsson, G. S. (1995) Coupled reservoir-wellbore simulation of geothermal reservoir behavior, *Geothermics*, v. 24, pp. 000-000.

Kjaran, S. P. and Eliasson, J. (1983) Geothermal Reservoir Engineering Lecture Notes, Report 1983-2, United Nations University Geothermal Training, Reykjavik, Iceland.

Miller, C. W. (1980) Wellbore users manual, Report LBL-10910, Lawrence Berkeley Laboratory, Berkeley, Calif., U.S.A.

Miller, C. W. (1984) User guide for WELF, BG Software, Berkeley, Calif., U.S.A.

Mondy, L. A. and Duda, L. E. (1984) Advanced wellbore thermal simulator GEOTEMP2, user manual, Report SAND84-0857, Sandia National Laboratories, Albuquerque, N.M., U.S.A.

Murray, L. and Gunn, C. (1993) Toward integrating geothermal reservoir and wellbore simulation: Tetrad and Wellsim, *Proc. 15th New Zealand Geothermal Workshop*, Auckland, N.Z., pp. 279-284.

Ortíz-Ramírez, J. (1983) Two-phase flow in geothermal wells: Development and uses of a computer code, Report SGP-TR-66, Stanford Univ., Stanford, Calif., U.S.A.

Pritchett, J. W. (1994) STAR - A general purpose geothermal reservoir simulator, *Geoth. Resour. Counc. Bull.*, v. 23, pp. 139-141.

Pritchett, J. W. and Garg, S. K. (1980) Determination of effective wellblock radii for numerical reservoirs simulations, *Water Resour. Res.*, v. 16, pp. 665-674.

Pruess, K. (1987) TOUGH user's guide, Report LBL-20700, Lawrence Berkeley Laboratory, Berkeley, Calif., U.S.A.

Pruess, K. (1988) SHAFT, MULKOM, TOUGH, *Geotermia Rev. Mex. Geoenergía*, v. 4, pp. 185-202.

Vinsome, P. K. W. (1991) TETRAD Users Manual, Vers. 9.4, Dyad Engineering, Calgary, Can.

A Graphical Interface to the TOUGH Family of Flow Simulators

M.J.O'Sullivan and D.P.Bullivant
Department of Engineering Science
University of Auckland
New Zealand

Abstract
A graphical interface for the TOUGH family of simulators is presented. The interface allows the user to graphically create or modify a computer model and then to graphically examine the simulation results. The package uses the X Window System, enabling it to be used on many computer platforms.

1. Introduction

The development of the MULKOM/TOUGH codes has enabled the modelling of a number of different complex problems involving multi-component, multi-phase flows in a porous medium. Often the models set up involve large complicated three dimensional block structures and it is almost essential to use graphical methods for setting up and checking input data files and for displaying simulation results. These pre-processing and post-processing tasks have received considerable attention from finite element code developers but the software products developed are expensive and mostly customised for one particular modelling package. Some general purpose 3-D graphics packages can be used for assisting with the pre-processing and post-processing of input and output data from codes such as MULKOM/TOUGH (see Kissling,1994, for example) but it is difficult to set them up as general purpose and user friendly modelling tools.

The present paper describes a geothermal modelling graphical interface (called MULGRAPH) developed at the University of Auckland . It can be used to create input files, check and edit input data files and plot results contained in output files. The package was originally based on the low level GKS graphical library but it has recently been modified to use the X Window System enabling it to run on many computer platforms.

A relatively simple 3-D model of the Wairakei geothermal field is used here to demonstrate some of the features of MULGRAPH.

2. Model Geometry

The finite volume approach used in the MULKOM/TOUGH codes (Narasimhan and Witherspoon, 1976, Pruess, 1988) allows very general types of grid or block structures to be used. This is one of the many advantages of these codes but it also means that it is difficult to anticipate all the types of block structures which might be used with MULKOM/TOUGH. It was decided by the authors, in the first stage of the development of MULGRAPH, to limit the type of block structures to that commonly used in their models of geothermal fields such as

Wairakei and Broadlands. These models involve a number of horizontal layers, each of constant thickness and with the same block structure in plan view. Some variations of this general system are possible with MULGRAPH and some further modifications are being considered (discussed below).

The geometric data used by MULKOM/TOUGH are the block volumes, the block interface areas and the distance from block interfaces to block centres. These data are all that are required to solve the mass, energy and chemical balances equations which together with Darcy's law are solved numerically by MULKOM/TOUGH. However these data do not allow the reconstruction of the actual geometric shape of the model and an additional geometry file is required for graphical pre-processing and post-processing of MULKOM/TOUGH data.

Therefore the first stage of a new modelling investigation using MULKOM/TOUGH is to set up the geometry file. This can be done manually or by using a separate graphics package (MULGEOM) developed by the authors. MULGEOM allows the user to set up a plan view of the block structures, with each block consisting of nodes or vertices connected by lines. A digitised map of the region of interest can be displayed as background to the grid structure. Extensive editing is possible. For example, nodes and lines can be added, deleted or moved.

Table 1 Data structure for a MULGRAPH geometry file

Module name	Data
VERTIces	Node number and node coordinates
GRID	Block number, number of nodes in the block and their numbers.
CONNEctions	Blocks connected together (two for each connection)
LAYERs	Elevation of midpoint and bottom of each layer (starting with atmosphere).
SURFAce	Elevation of the water level in each block in the top layer
WELLS	Coordinates x,y,z for feed zones of each well.

The geometry file is written in modular form, similar to the style of data for MULKOM/TOUGH. The module names and the data they contain are listed above in Table 1. The purpose of the SURFA module is to allow the top layer on the model to have a variable thickness (in order to represent the estimated elevation of the water table). The WELLS module provides the required information so that the location of the production wells and reinjection wells can be shown on the same plots.

3. Creation of Input data

Once the geometry file has been constructed, either manually or by using MULGEOM, the modelling interface MULGRAPH can be used to create an input file for MULKOM/TOUGH. The main menu in MULGRAPH presents the user with several choices. Usually the "check grid" option is selected first and either layers or vertical slices through the model can be

displayed (and printed out if desired). Once the geometry file is satisfactory the "create grid" option can be selected and the user is taken through the procedure for setting up a MULKOM/TOUGH input file. All the tedious calculations of volumes, areas and distances are carried out by MULGRAPH. One of the most time consuming parts of the data creation task is the assignment of rock types to blocks. This is done graphically by pointing and clicking with the mouse. The modification of rock types is probably the most commonly used part of the "edit file" option (discussed in more later). Some parts of setting up a MULKOM/TOUGH file are still more conveniently carried out with an ordinary file editor and usually the authors do not use all the features available in MULGRAPH. For example in MULGRAPH it is possible to set up a complete set of initial data for a modelling run with a different pressure and temperature specified in every block, but this is seldom done. Instead very approximate initial conditions are set up and a natural state is calculated from these. This natural state is then used as the initial data for production runs. Similarly a complex table of production rates and times required for a simulation of production from a geothermal field could be set up using MULGRAPH but usually some alternative procedure is used.

4. Checking an input file

To make use of this option in MULGRAPH a geometry file and a MULKOM/TOUGH input file are required. The geometric data are checked (volumes, areas and distances) and various views of the model can be displayed to check that the desired rock-type structure has been set up. MULGRAPH also checks for missing blocks and connections. The authors have sometimes found such checks of MULKOM/TOUGH input files, previously prepared by hand for large complex models, rather embarrassing.

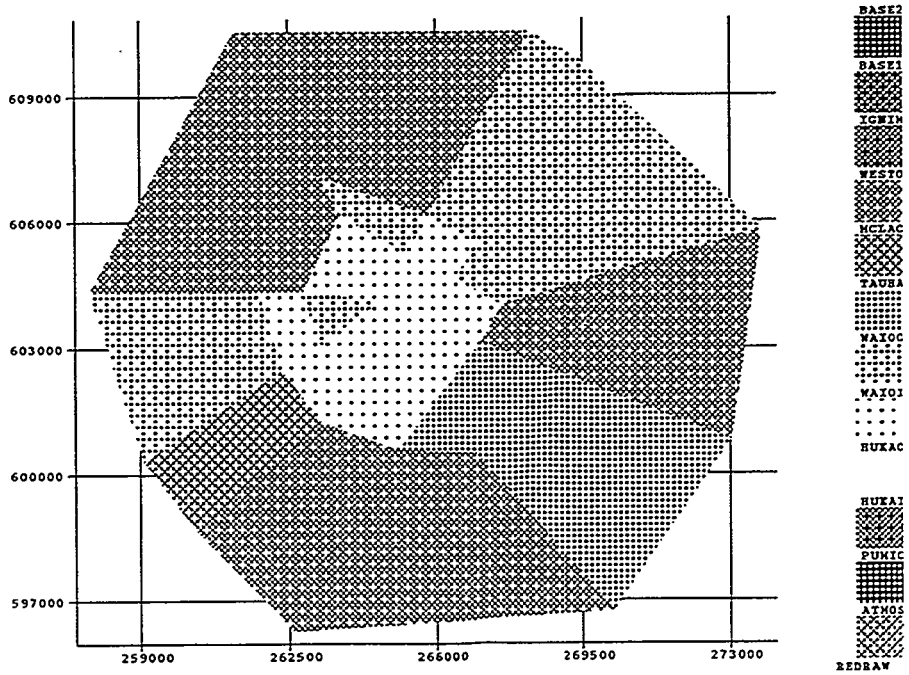

Figure 1. The MULGRAPH window while editing the rock-type assignment

5. Editing an input file

As mentioned above, the most common use of this option is for graphical editing of the rock-type distribution in a model. Other parameters can also be changed but often it is just as convenient to do so with a file editor. For example the authors would not normally use MULGRAPH to change permeability values within the ROCKS module of a MULKOM/TOUGH input file. A typical plot, for the Wairakei model, showing the shaded plot of rock-types and a legend is shown in Fig. 1.

6. Plotting Results

Once a MULKOM/TOUGH input file has been set up and a simulation run carried out the "plot results" option in the main menu of MULGRAPH can be selected. For this option MULGRAPH requires three files: the geometry file, a MULKOM/TOUGH input file and a MULKOM/TOUGH output file. A variety of plots of block parameters (pressure, temperature, saturation, etc.) can be produced. Two dimensional plots can be produced on layers or vertical slices, either showing numerical values or appropriately shaded. A typical example is shown in Fig. 2.

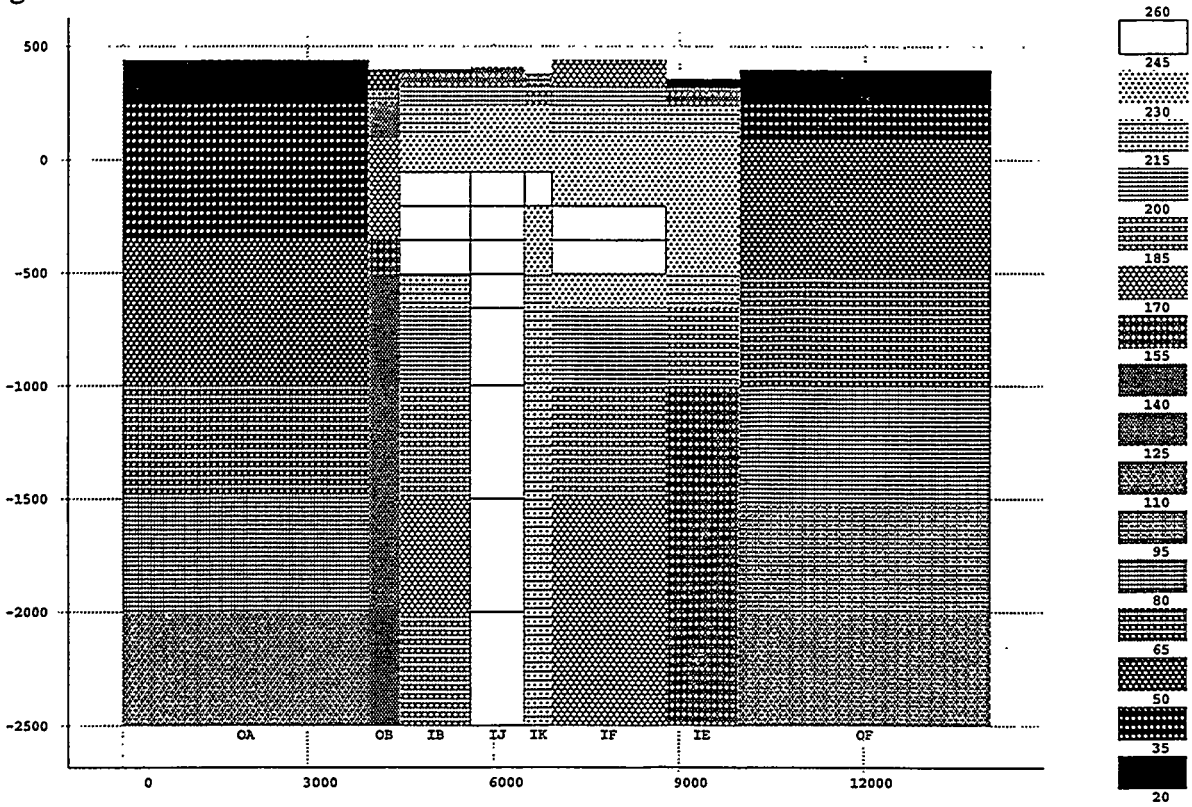

Figure 2. A vertical slice showing the temperature distribution for the Wairakei model.

Two-dimensional plots of flows across connections show arrows, proportional in size to the magnitude of the flows, located at the centre of the connections. Plots of flows through the tops of layers show the numerical values of the flows.

One dimensional plots showing variation of block parameters with depth can also be produced. Field data can be superimposed as shown in Fig. 3.

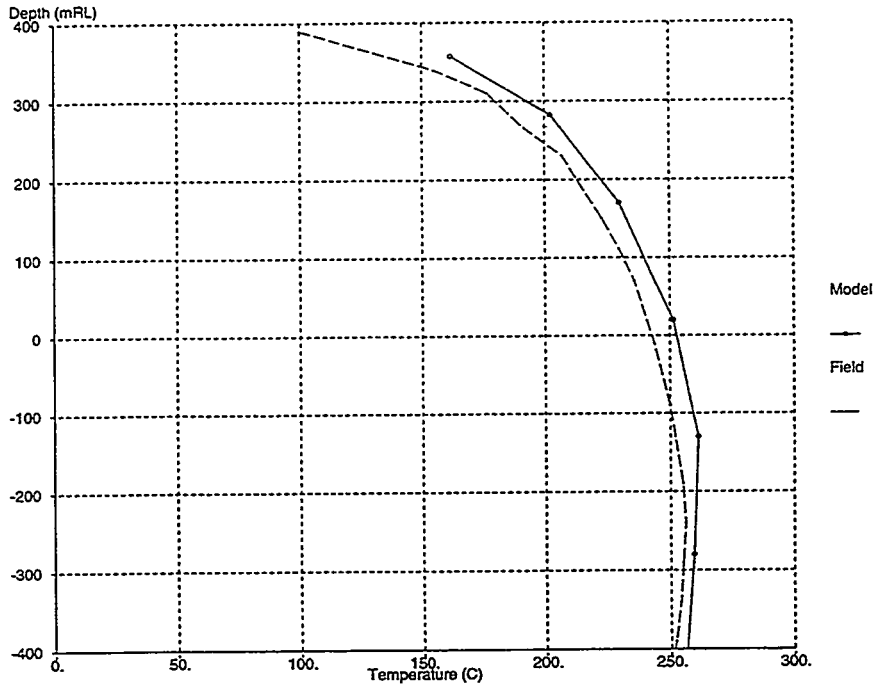

Figure 3. Comparison of natural state temperature profiles in the Wairakei model.

Plots of various quantities as functions of time can be produced. A typical example from the Wairakei model is shown in Fig. 4. In order to be able to produce these time plots some modification of the standard MULKOM/TOUGH output was required. In the standard version of MULKOM/TOUGH two levels of output are possible: either a complete output for all blocks or output for one block. We have set up an intermediate option where output for a few selected blocks, connections and wells can be included in the output file. An extra module with the heading SHORT is added to the input file. It lists the selected blocks, connections and wells.

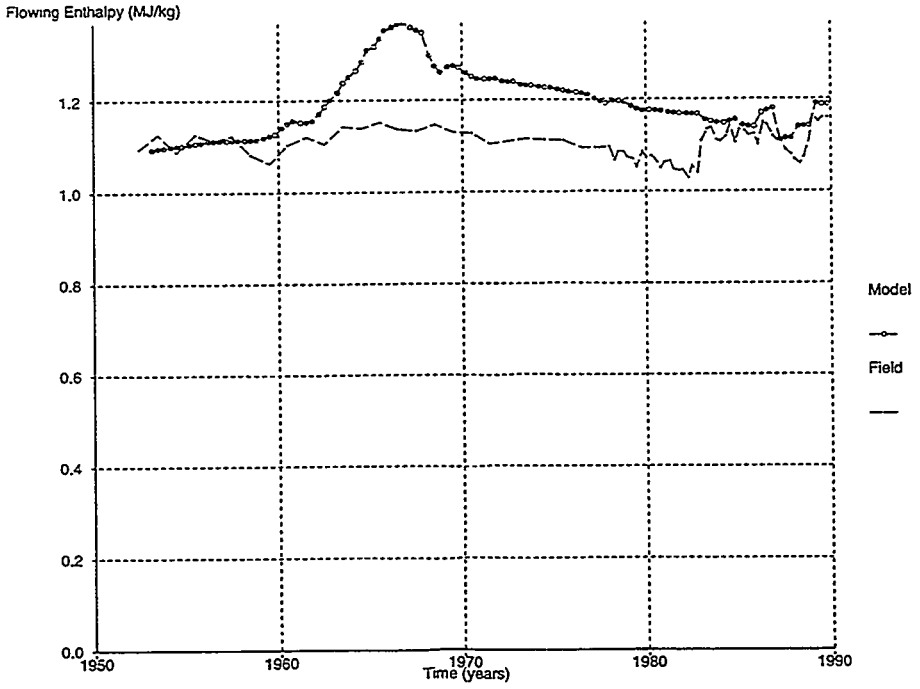

Figure 4. Average production enthalpy from the Wairakei model

7. Graphics

The interface uses simple graphical techniques for output (line, point, filled area and text) and input (string, locate and menu). Initially, these were provided by the Graphical Kernel System (GKS) library. To make the interface available on a wider array of computer platforms, the calls to GKS were separated into a set of graphics routines within the interface and these internal graphics routines were implemented using the X Window System and Motif. The interface could be ported to a computer with a graphics system different from GKS or X, by rewriting the internal graphics routines using the new graphics system. An alternative would be to install an X server (available for personal computers) and use the X version of the interface.

8. General Comments

(i) The MULGRAPH package has been designed to interface to the MULKOM/TOUGH code, but could easily be adapted to read input and output files for other 3-D modelling packages.

(ii) The particular style of model on which MULGRAPH is based, with the layered structure, does limit its usefulness. However it is possible to have a complex vertical structure by arranging the "layers" to be vertical. MULGRAPH allows the orientation of the layers relative to the vertical direction to be selected. We are currently working on an option to allow some local subdivision of blocks.

(iii) Other plotting options such as contours on 2-D plots, 3-D plots and animation are being investigated.

(iv) MULGRAPH does not provide a complete graphical output capability. More sophisticated packages are required to provide genuine 3-D plots with zooming and rotation as options. However MULGRAPH does provide most graphical options which are required for modelling projects. The authors have found MULGRAPH to be an essential tool for geothermal modelling.

(v) MULGRAPH has been extensively used by graduate students and students attending short courses on reservoir engineering at the University of Auckland. It seems to be user friendly and relatively easy to learn to use.

References

Kissling, W., Visualisation of geothermal reservoir models, presented at the 16th New Zealand Geothermal Workshop, University of Auckland (1994).

Narasimhan, T.N. and Witherspoon, P.A., An integrated finite difference method for analyzing fluid flow in porous media, *Water Resour. Res.*, **12**, 57-64 (1976).

Pruess, K., SHAFT, MULKOM, TOUGH: a set of numerical simulators for multiphase fluid and heat flow, *Geotermia, Rev. Mex. Geoenergia*, 4(1), 185-202 (1988).

PROGNOSTIC SIMULATION OF REINJECTION - RESEARCH PROJECT GEOTHERMAL SITE NEUSTADT-GLEWE / GERMANY

Joachim Poppei, Dirk Fischer

Geothermie Neubrandenburg GmbH

Germany

Introduction

For the first time after political and economical changes in Germany a hydrothermal site was put into operation in December 1994.

Due to prevailing conditions extraordinary in Central Europe (reservoir temperature 99°C; 220 g/l salinity) the project Neustadt-Glewe is supported by a comprehensive research program. The wells concerned (a doublet with an internal distance of 1.400 m) open the porous sandstone aquifer with an average thickness of about 53 m in a depth of 2.240 m.

One point of interest was the pressure and temperature behavior over a period of 10 years considering the fluid viscosity changes due to variable injection temperature. For means of reservoir simulation and prognosing the injection behavior the simulator code TOUGH2 was used.

Long-term behavior of injection

Far field simulation is important in long-term operation. Transient and non-isothermal effects are the reservoir temperature and viscosity change and their influence on the well head pressure. For means of reservoir simulation a three-dimensional model was used. The aquifer is totally characterized by 6 horizontal layers. For consideration of the heat transfer with caprocks the full three-dimensional characterization as well as the semi-analytical solution were investigated. Due to symmetry only the half of the basic pattern has to be considered. The model made use of 2640 elements, 7246 connections and 12 time depending sinks and sources. The time steps are variable.

The initial conditions of temperature and pressure within the layers are determined by the geothermal gradient of 0.04 K/m and gravitation.

Figure 1 illustrates the time varying flow rate due to the transient heat demand. Additional, after five years operating, the regime of exploitation will be changed due to provided enlargement of district heating demand.

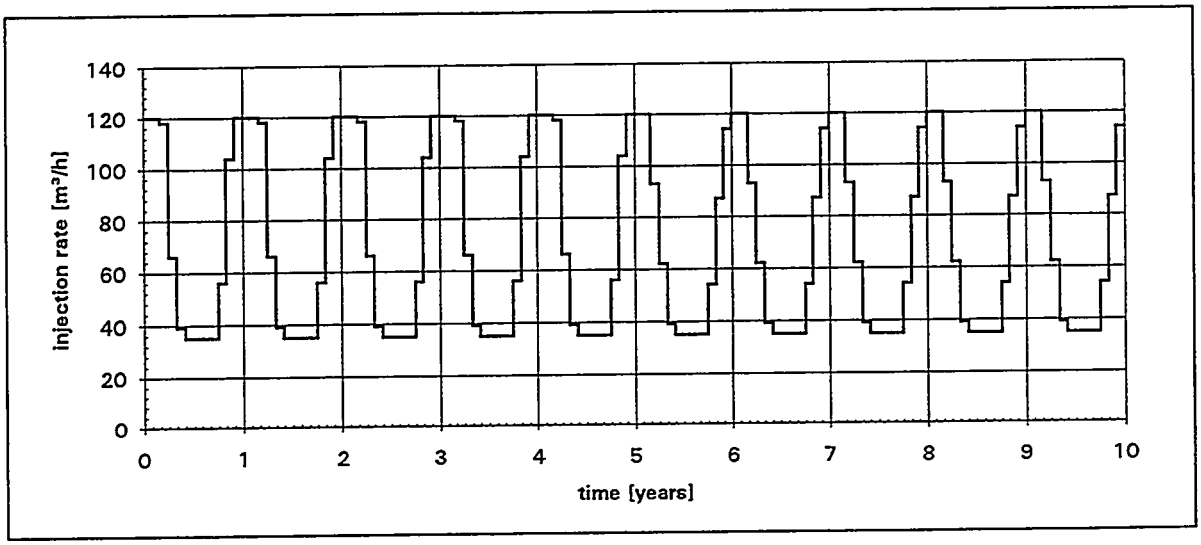

Fig. 1: Provided injection flow rate over a 10 years period

Figure 2 illustrates the time varying injection and sandface temperatures. The dash line characterizes the injection temperature. The sandface temperature line calculated is slightly smoothed due to numerical effects. Wellbore storage effects had been neglected.

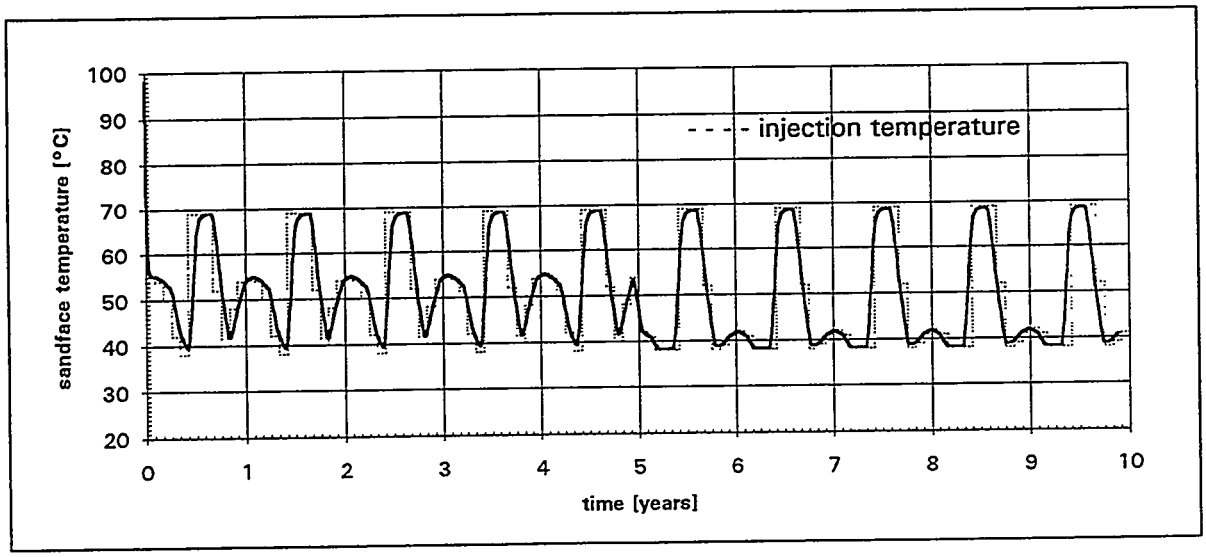

Fig. 2: Injection and calculated sandface temperature in the injection well

The calculated pressure response over this period is given in figure 3. The pressure increase due to reservoir cooling was proved to be controllable.

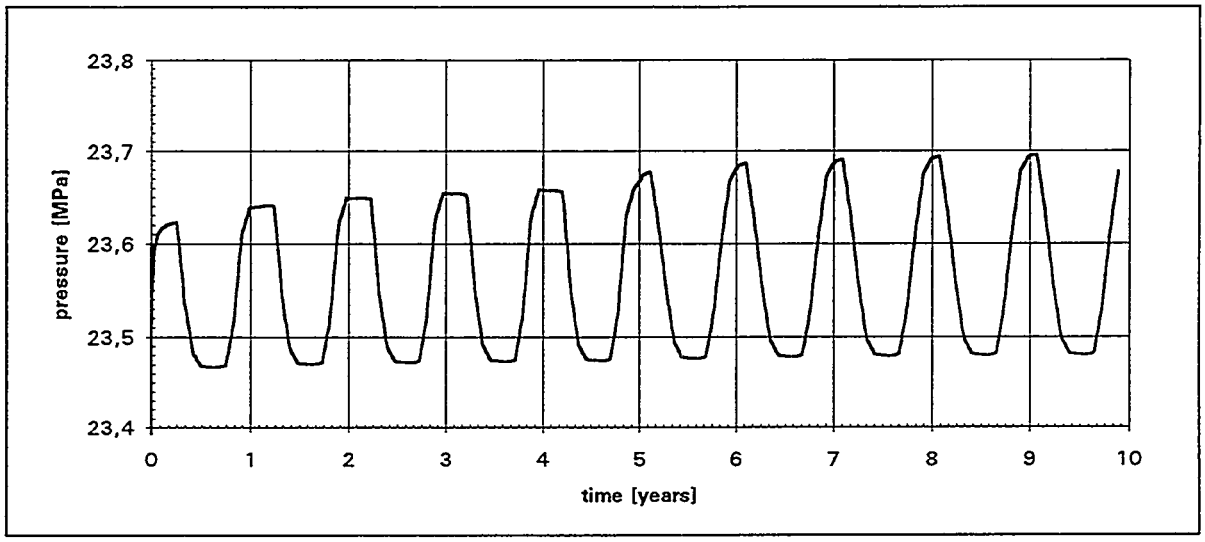

Fig. 3: Calculated pressure response over 10 years period

The results calculated were compared to results given by the simulator code CFEST (Gupta et. al /1/). The pressure behavior is similar, although the absolute values cannot be compared due to neglecting the salinity in the TOUGH simulation.

Consideration of salinity

With the help of the EOS7-module /2/ it became possible to consider the salinity of thermal water. The clipping of the input-file *NGbrine* for TOUGH-simulation neglecting the complete time-control-description is given in figure 4.

```
*NG06brine* Research project geothermal site
ROCKS----1----*----2----*----3----*----4----*----5----*----6----*----7----*----8
POMED          2650.       .22    9.E-13    9.E-13    9.E-13       2.2      905.7
MATRX          2650.       .01    9.E-18    9.E-18    9.E-18       2:0      707.5

SELEC----1----*----2----*----3----*----4----*----5----*----6----*----7----*----8
    2
     0.1E6       20.     1150.

MULTI----1----*----2----*----3----*----4----*----5----*----6----*----7----*----8
    2    3    2    6
START----1----*----2----*----3----*----4----*----5----*----6----*----7----*----8
PARAM----1----*----2----*----3----*----4----*----5----*----6----*----7----*----8
   4 999      9910000000000002 47
       0.0 3.12000E8       -3.     2.6E5A2113           9.81
    1.E-2      2.E-2     3.E-2     4.E-2     5.E-2     6.E-2     7.E-2    2.2E-1
    5.E-1       9.E0      9.E1      1.E2      1.E2      7.E2      9.E3      2.E4
     2.E4       5.E4      6.E4      1.E5     2.6E5     2.6E5     2.6E5     2.6E5
    1.E-4
             23.60E6                 1.                98.
TIMES----1----*----2----*----3----*----4----*----5----*----6----*----7----*----8
    1    1
   1.560E8
GENER----1----*----2----*----3----*----4----*----5----*----6----*----7----*----8
A2113BRI 1                126     COM22
0.0                    1.E0        1.E1        1.E2
           *
           *
       1.6595            0.1      1.6595         0.1
           *
           *
       2.50E5         2.50E5      2.50E5      2.50E5
           *
           *
A7129BRI 6                126     COM2
0.0                    1.E0        1.E1        1.E2
           *
           *
      -1.6595           -0.1     -1.6595        -0.1
           *
           *

INCON----1----*----2----*----3----*----4----*----5----*----6----*----7----*----8

ENDCY----1----*----2----*----3----*----4----*----5----*----6----*----7----*----8
MESHMAKER1----*----2----*----3----*----4----*----5----*----6----*----7----*----8
XYZ
        0.
NX      33
  5000000.    50000.      100.      100.      100.      100.      100.      100.
      100.      100.       50.       49.        2.       49.       50.      100.
      100.      100.      100.      100.      100.      100.      100.      100.
      100.      100.      100.       49.        2.       49.      100.    50000.
  5000000.
NY      10
       50.      100.      100.      100.      100.      100.      100.      100.
    50000.   5000000.
NZ       8
      100.       4.5        9.        9.        9.        9.       4.5      100.


ENDCY----1----*----2----*----3----*----4----*----5----*----6----*----7----*----8
```

Fig. 4: Input-file for EOS7-simulation

In figure 5 the results of calculated pressure response for pure and mineralized water over an one-year-period are compared. The calculated pressures are proved to be in agreement with test- and first operation-results.

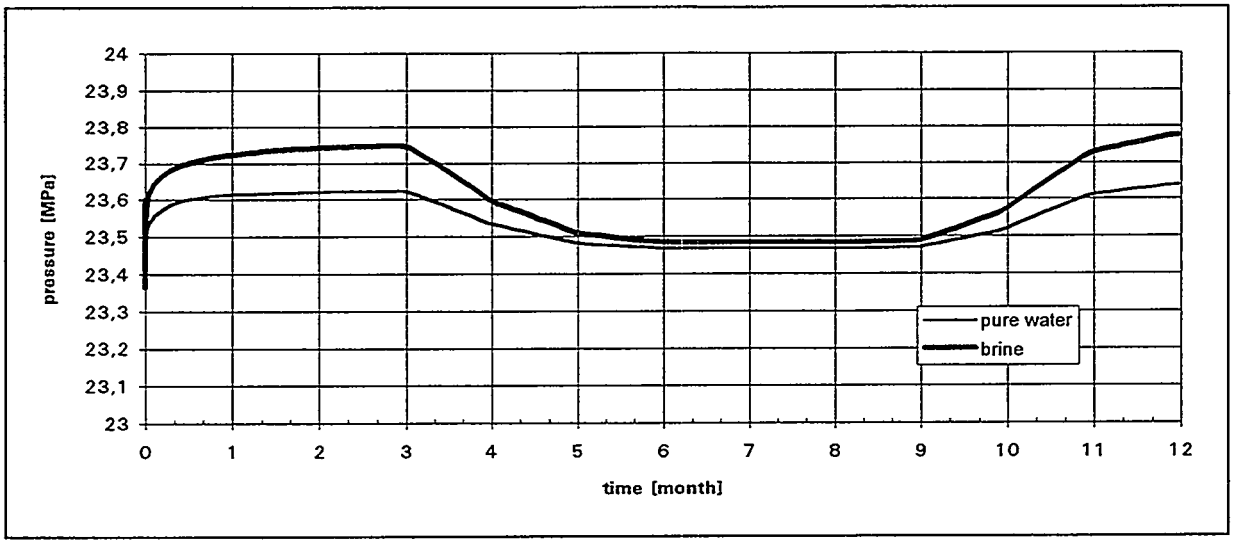

Fig. 5: Comparison of calculated pressure response for pure and mineralized water

Conclusion

In German geothermal activities pressure responses due the reservoir cooling in long-time reinjection prognosis were neglected in the past.

The TOUGH2-code is proved to be fairly suitable to consider the viscosity-density-change in injection wells for prognostic simulation of long-term-behavior of reinjection.

References

/1/ Gupta, S.K. et al.: Coupled Fluid, Energy, and Solute Transport (CFEST) Model: Formulation and User´s Manual
Technical Report BMI/ONWI-660, Office of Nuclear Waste Isolation, Battelle Memorial Institute,Columbus, OH 1987

/2/ Pruess, K.: EOS7, An Equation-of-state Module for the TOUGH2 Simulator for Two-Phase Flow of Saline Water and Air, LBL-31114

Extended abstract submitted to the TOUGH Workshop '95
Lawrence Berkeley Laboratory, Berkeley, CA, March 20-22, 1995

SIMULATION OF THE HEBER GEOTHERMAL FIELD, A TOUGH2/PC APPLICATION

Emilio Antúnez[1], Marcelo Lippmann[1], M. Ali Khan[2], and Timothy Boardman[3]

[1] Lawrence Berkeley Laboratory, Berkeley, CA
[2] California Department of Conservation, Division of Oil, Gas, and Geothermal Resources, Santa Rosa, CA
[3] California Department of Conservation, Division of Oil, Gas, and Geothermal Resources, El Centro, CA

ABSTRACT

A numerical simulation model for the Heber geothermal field in southern California is being developed under a technology transfer agreement between the Department of Energy/LBL and the California Department of Conservation, Division of Oil, Gas, and Geothermal Resources (Division). The two objectives of the cooperation are: (1) to train Division personnel in the use of the TOUGH2/PC computer code; and (2) to develop a module compatible with TOUGH2 to investigate the effects of production/injection operations on the ground surface subsidence-rebound phenomenon observed in the field. The compaction of the rock formation will be handled assuming an elastic behavior of the rock-fluid system. Considered will be changes in pore volume and in-grid block dimensions, as well as, the process by which the change in formation volume is transmitted to the surface (vertical deformation; subsidence and rebound).

Introduction

The Division has among its diverse functions: (1) the supervision of oil, gas, and geothermal fields; (2) the gathering of production/injection data; and (3) forecasting the behavior of fields including the amount of ground surface subsidence and rebound caused by exploitation. So far, the Division's forecast of fluid production/injection has been based on modeling data provided by the field operators. When these data are not

available, the Division has used first-order methods for its forecasts. At times, these methods may be inappropriate for the task. For this reason, the Division requested the assistance of the U.S. Department of Energy (DOE) in training of its personnel on the use of TOUGH2 (Pruess, 1991).

The Division and LBL collaboration began in early 1994 with funding from DOE's Geothermal Division. So far, the Division's personnel have received introductory training on the use of TOUGH2, have been instructed on the kind of field data relevant to reservoir behavior prediction, and asked to choose a geothermal field to built a numerical model using actual data. The Heber geothermal field in southern California was selected.

A numerical model of Heber is under development. The field has experienced up to six inches of subsidence at the center of the production area and shown up to seven inches of ground surface rebound due to injection (Fig. 1). Therefore, there are plans to write and include a new module to TOUGH2 to account for subsidence and rebound; this adds research significance to the collaborative work.

The training will continue with discussions on the calibration of a numerical model using the TOUGH2/PC simulation code (Antúnez *et al.,* 1994) and on the use of the model as a predictive tool. This training will undoubtedly benefit the Division's regulatory activities. Through this collaboration, LBL is helping to transfer the technology developed under DOE-funded programs.

Objectives

LBL will:

1. train two Division engineers in the use of LBL's general purpose simulator TOUGH2/PC;

2. develop a TOUGH2 compatible computer code module that will help to analyze the ground surface subsidence and rebound in the Heber geothermal field. The module will include elastic changes in pore volume and in grid-block dimensions in response

to the changes in the compressibility of the rock-fluid system. The process by which the lost (compacted) volume is transmitted to the surface (subsidence) will also be considered;

3. test and verify the new module using synthetic and field data;

4. train the Division engineers on how to construct a numerical model using the Heber field data as an example, how to calibrate it, and use it in field development and monitoring; and

5. conduct simulation runs with the modified version of TOUGH2/PC to develop guidelines to control or minimize changes in ground surface elevation.

So far, all the Heber data gathered by the Division has been reviewed and inventoried. After reviewing the data, a decision was made that a N-S grid orientation was adequate for the Heber model (see Fig. 1). Dimensions of the model were set at 14 km (N-S) by 13 km (E-W), and a thickness of 3 km (10,000 ft) with the thermal anomaly approximately at the center of the grid.

Considering the available data, discussions with the Division engineers, and a paper by E.D. James et al. (1987), it was decided to subdivide the model in eight horizontal layers. Eight maps showing isotherms at 150, 425, 700, 1050, 1450, 1829, 3000, 3048 m (490, 1390, 2300, 3440, 4760, 6000, 9840, and 10,000 ft respectively) below sea level were sketched. The first seven elevations correspond to the middle of each layer; the last one to the bottom of the model. The isotherms at 1829 m (6000 ft) below sea level are shown in Figure 2.

Currently, the gridding for each layer is in progress; this requires the exact location of the completion intervals from all wells. The intervals are available but are reported in terms of measured depth. A correction is required to obtain their true vertical depth and location in California coordinates. LBL wrote the program to make these corrections and the Division staff is presently processing the well directional surveys.

Simultaneous to the previous task, LBL and the Division are collecting information on the physical properties of rock types present in Heber's lithological column (clays, sandstones and indurated sediments).

ACKNOWLEDGMENTS

The authors want to express their gratitude to Karsten Pruess and Curt Oldenburg of LBL for reviewing this manuscript and for all their helpful suggestions. This work was supported by the Assistant Secretary for Energy Efficiency and Renewable Energy, Geothermal Division, of the U.S. Department of Energy under contract No. DE-AC03-76SF00098.

References

Antúnez, E., Moridis, G., and Pruess, K. (1994) Large-Scale Three-Dimensional Geothermal Reservoir Simulation on PCs, Proc. Nineteenth Workshop on Geothermal Reservoir Engineering, Stanford University, pp. 94-106.

James, E.D., Hoang, V.T., and Epperson, I.J. (1987) Structure, Permeability, and Production Characteristics of the Heber, California Geothermal Field, Proc. Twelfth Workshop on Geothermal Reservoir Engineering, Stanford University, pp. 267-271.

Pruess, K. (1991) *TOUGH2* - A General-Purpose Numerical Simulator for Multiphase Fluid and Heat Flow, Lawrence Berkeley Laboratory report LBL-29400.

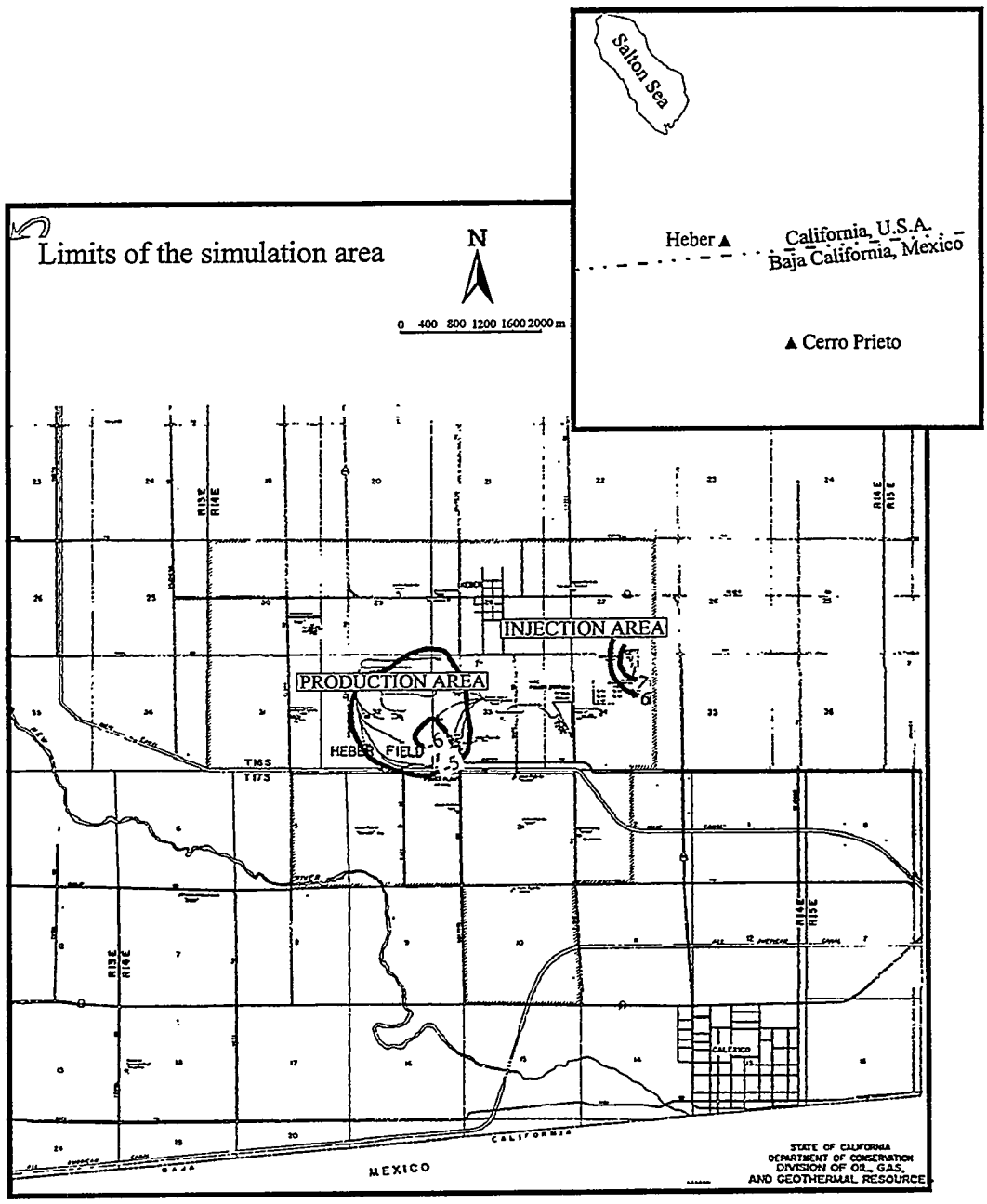

Fig. 1: Base map of the Heber geothermal field, showing subsidence in the production area, rebound in the injection zone, and limits of the simulation area.

Isotherms at 1,829 m (6,000 ft) below sea level

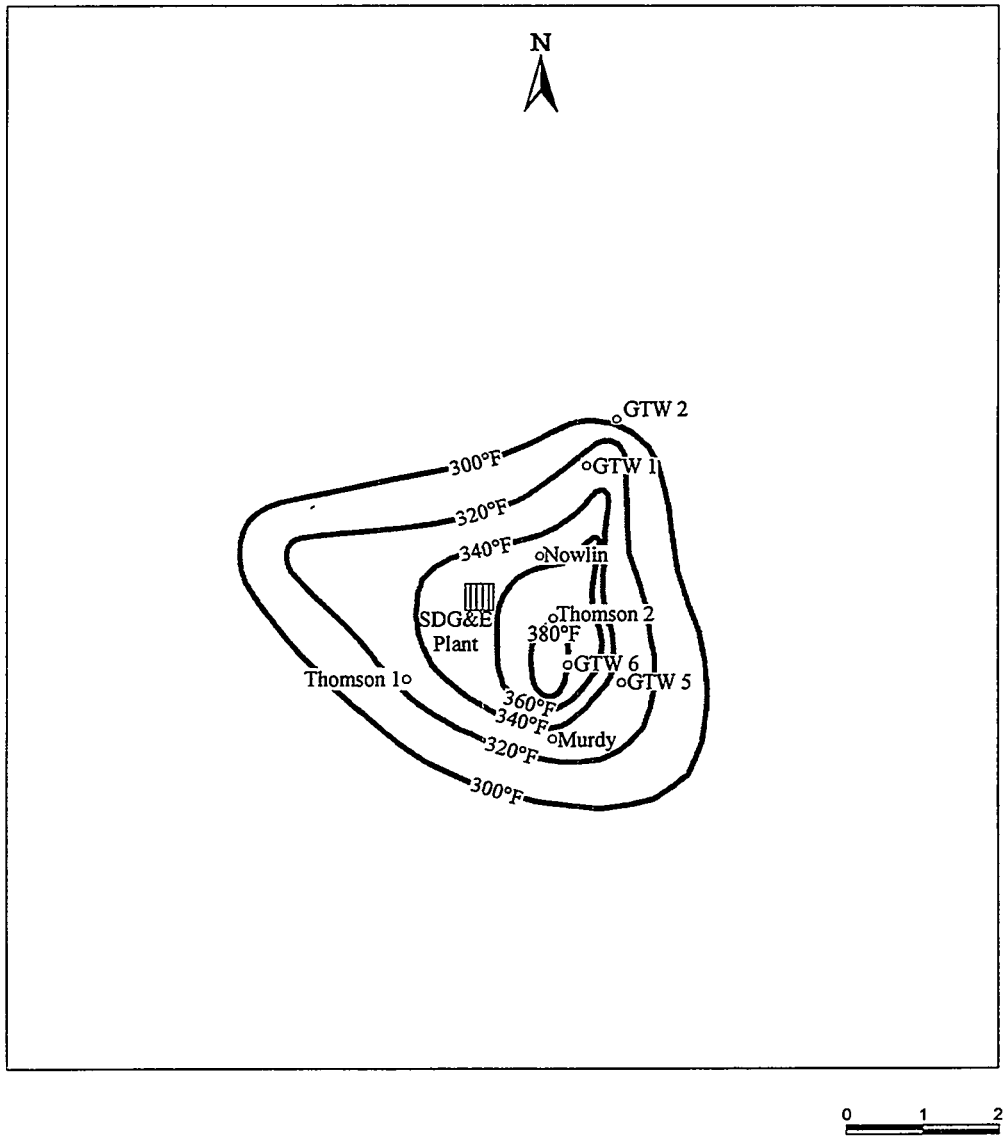

Fig. 2: Heber geothermal field, limits of the simulation area, and inferred isotherms at 1,829 m (6,000 ft) below sea level

MODELING OF HYDROTHERMAL CIRCULATION APPLIED TO ACTIVE VOLCANIC AREAS. THE CASE OF VULCANO (ITALY)

Micol Todesco
Dip. Scienze della Terra, via S. Maria, 53, 56126 Pisa, Italy
e-mail: todesco@dst.unipi.it - Fax: 39 (50) 500 675

1. Introduction

Modeling of fluid and heat flows through porous media has been diffusely applied up to date to the study of geothermal reservoirs (Pruess, 1990). Much less has been done to apply the same methodology to the study of active volcanoes and of the associated volcanic hazard. Hydrothermal systems provide direct information on dormant eruptive centers and significant insights on their state of activity and current evolution. For this reason, the evaluation of volcanic hazard is also based on monitoring of hydrothermal activity. Such monitoring, however, provides measurements of surface parameters, such as fluid temperature or composition, that often are only representative of the shallower portion of the system. The interpretation of these data in terms of global functioning of the hydrothermal circulation can therefore be highly misleading. Numerical modeling of hydrothermal activity provides a physical approach to the description of fluid circulation and can contribute to its understanding and to the interpretation of monitoring data. In this work, the TOUGH2 simulator (Pruess, 1991) has been applied to study the hydrothermal activity at Vulcano (Italy). Simulations involved an axisymmetric domain heated from below, and focused on the effects of permeability distribution and carbon dioxide. Results are consistent with the present knowledge of the volcanic system and suggest that permeability distribution plays a major role in the evolution of fluid circulation. This parameter should be considered in the interpretation of monitoring data and in the evaluation of volcanic hazard at Vulcano.

2. Geological Setting

Vulcano is an active volcanic center in Southern Italy (Fig.1), whose last explosive eruption took place at the end of last century (1888-1890). Since then, the island has experienced a continuous fumarolic activity, both at the crater rim, where the highest temperatures are observed, and near the Baia di Levante beach (Todesco, 1994 and ref. therein). The intensity of fumarolic activity varied with time, and periodic system crises have been evidenced by changes in gas temperature, composition and emission rate. These crises are often accompanied by shallow seismic activity, related to fluid motion, and ground deformations within the area of the active cone. Gases emitted at the crater fumaroles mainly consist of water and carbon dioxide, with sulphur compounds, HCl, HF, B, and Br being minor components. Gas emission at the crater fumaroles can reach 1100 ton/ day. Higher mass flow rates are usually associated with higher temperatures, higher carbon dioxide contents, and gas/steam ratios. Gas temperature changes with time and at different vents, ranging from 200°C to about 700°C. Fumaroles at the Baia di Levante beach show constant gas temperature of 100°C and are characterized by the loss of reactive components with respect to gas composition at the crater. Changes in mass flow rate and in gas composition affect simultaneously crater and beach fumaroles (Martini *et al.*, 1989; Chiodini *et al.*, 1991a). Thermal waters, with temperatures up to 60°C (Panichi & Noto, 1992; Capasso *et al.*, 1993) and diffuse gas emanations from the soil (Badalamenti *et al.*, 1984; Carapezza & Diliberto, 1993) are among other surface manifestation of the hydrothermal activity at Vulcano and characterize the area around the La Fossa cone.

More information derives from the geothermal wells (Fig.1) drilled on the island during the '50s (VU2bis) and '80s (IV1 and VP1). In-hole temperature distributions are showed in Table 1. The VU2bis well reached the depth of 200 m and produced wet-steam for two years, attesting the presence of a boiling aquifer feeding the beach fumaroles (Sommaruga, 1984). The other wells, IV1 and VP1, reached greater depths (1000 m and 2000 m, respectively), but were never productive. The study of cuttings and core samples evidenced low permeability and the presence

of enhanced hydrothermal alteration at shallow levels, both recent and fossil (Faraone *et al.*, 1988; Barberi *et al.*, 1989; Gioncada & Sbrana, 1991).

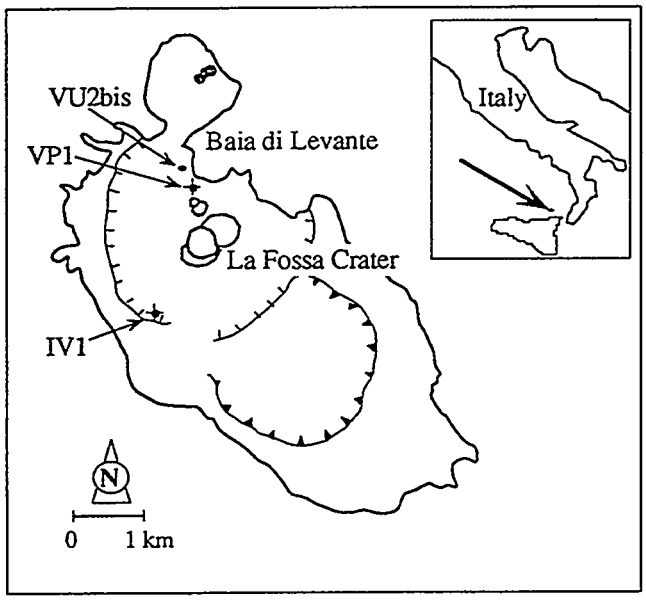

Figure 1. The Island of Vulcano (Aeolian Islands, Italy). The active crater and the position of the main geothermal wells are indicated.

Table 1. Temperature distribution in the geothermal wells.

VU2bis		IV1		VP1	
m	°C	m	°C	m	°C
15	101	200	60	600	60
100	136	650	75.6	1000	168
236	198	770	76.5		
		1160	112		
		1500	180		
		2000	419		

During the last twenty years, gas temperature and emission rates increased significantly and synchronous variations of gas composition were observed. The areal extent of fumaroles increased and new fractures opened at the crater rim (Barberi *et al.* 1991). These phenomena and the associated seismic activity created some concern among the population (15,000 people during summer times) living at the base of the active cone. The interpretation of the observed changes plays a major role in hazard evaluation, as they may arise either from changes within the magma chamber (and could therefore prelude to new magmatic activity) or from variations within the hydrothermal system. In this latter case, more attention should be paid to hazards associated with fluid circulation, such as toxic gas emissions or phreatic explosions. The understanding of fluid circulation at Vulcano is therefore necessary to achieve a satisfactory hazard mitigation on the island.

3. Physical Modeling

The simulations presented here were carried out to investigate the effects of permeability distribution, and carbon dioxide on the evolution of the hydrothermal system. The TOUGH2 numerical simulator (Pruess, 1991) was used with the EOS1 and EOS2 modules, to describe the coupled multiphase and multicomponent fluid and heat flows. The simulations were carried out on a cylindrical domain with a radius of 500 m and depth of 1500 m, heated from below by fixing the bottom temperature at 300°C. The computational mesh is formed by 480 elements (48 layers of 10 elements each), with a constant radial size of 50 m, and variable vertical dimension ranging from 5 m (near the top and bottom boundaries) to 50 m. Initial and boundary conditions are listed in Table 2, and the rock physical parameters are showed in Table 3.

The effect of porosity and permeability was investigated by running some simulations with pure water on a uniform domain, with porosity of 0.25 and 0.35 and permeability ranging from 10^{-21} to 10^{-9} m^2. These simulations showed that the onset of fluid circulation is strongly dependent on the average value of rock permeability. Narrow plumes develop when rock permeability is higher than 10^{-18} m^2, and fluid convection enhances the system heating also at shallow levels. A two-

phase region forms after a time span that depends on the given permeability (k), and may range from few days (if $k=10^{-9}$ m^2), to few years (if $k=10^{-12}$ m^2), to thousands of years (if $k=10^{-15}$ m^2). For permeability lower than 10^{-18} m^2, heating of the system is much less efficient due to the scarce fluid mobility, and the resulting temperature and pressure distribution are not consistent with the development of a vapor phase. Higher rock porosity slightly enhances the development of rising plumes, leading to a faster heating and to an earlier development of the two-phase zone.

Table 2. Initial and Boundary Conditions.

Initial Temperature Initial Pressure	30°C everywhere Hydrostatic Pressure
Top Boundary	Fixed T=30°C Fixed P=1.0132×10^5Pa
Bottom Boundary	Fixed T=300°C Fixed P=0.14×10^8Pa
Vertical Boundary	No Flow

Table 3. Rock Physical Properties.

Density	2800 kg/ m^3
Specific Heat	800 J/ kg°K
Heat Conductivity	2.5 W/ m °K

Table 4. Performed Simulations.

	Permeability (m^2)	Fluid
1	10^{-12} z=0-1500m	H_2O
2	10^{-18} z<5m 10^{-12} z>5m	H_2O
3	10^{-12} z<600m 10^{-18} z>600m	H_2O
4	10^{-12} z=0-1500m	H_2O+ CO_2
5	10^{-12} z<600m 10^{-18} z>600m	H_2O+ CO_2

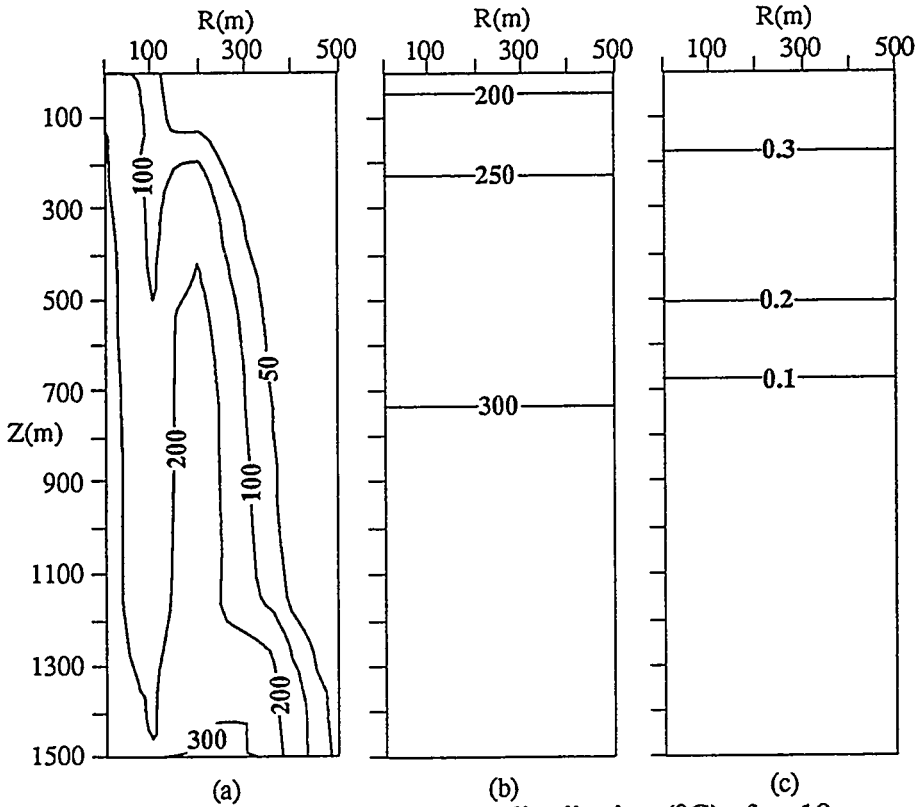

Figure 2. Simulation 1. Temperature distribution (°C) after 10 years (a) and 100 years (b) from the beginning of the simulation; gas volumetric fraction after 100 years (c).

The simulation with permeability of 10^{-12} m^2 and porosity of 0.35 was then chosen as reference case for the following work devoted to the study of non-uniform permeability distribution and of two-component fluid. A list of the simulations described below is given in Table 4.

4. Results

The evolution of a system with uniform permeability is given in Figure 2 for the case of $k=10^{-12}$ m^2 (Simulation 1). After 10 years form the beginning of the simulation, hot rising plumes reach the surface (Fig. 2a) and after 100 years the system is uniformly heated (Fig.2b) and a broad two-phase region with maximum gas saturation of about 0.4 extends to the depth of 700 m (Fig. 2c). Simulations 2 and 3 investigated different permeability distributions. In Simulation 2, low permeability (10^{-18} m^2) was assigned to the first 5 m depth, to verify the effects of a partially sealed cap. Temperature field and gas saturation are shown in Figure 3. The heat flow at the surface is reduced by the low permeability cap that limits the discharge of the warm fluid through the top of the domain. As a consequence, the system is heated more efficiently, as it appears from a comparison between Figure 2 and 3. Since the surface fluid discharge is inhibited, a narrow zone of fluid downflow develops and separates the larger rising plumes (Fig. 3a). The shape of the two-phase zone and the temperature distribution after 100 years (Fig. 3b,c) also reflect the presence of downflow regions. Pressure distribution is also affected by the low-permeability at the top, that induces a steeper pressure gradient. Figure 4a shows that the pressure at the top after 100 years is about 40 times higher than the atmospheric value. The pressure distribution for Simulation 1 is also shown for a comparison.

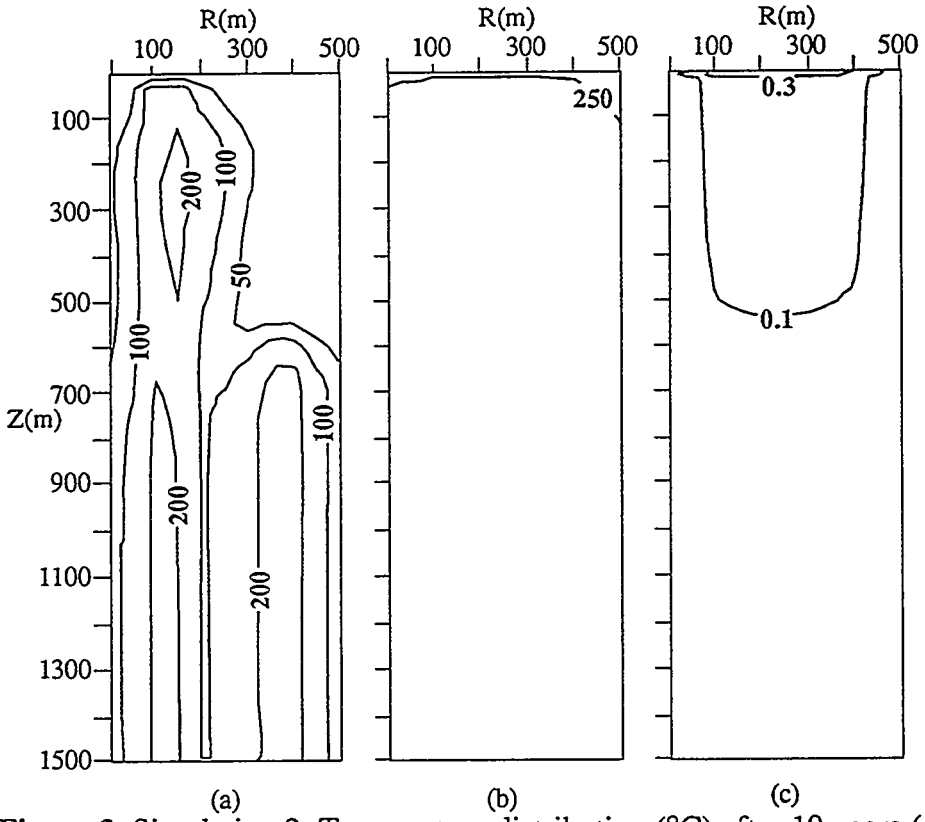

Figure 3. Simulation 2. Temperature distribution (°C) after 10 years (a) and 100 years (b) from the beginning of the simulation; gas volumetric fraction after 100 years (c).

In Simulation 3, low permeability was imposed to the bottom region, at depths greater than 600 m, and resulted in a much slower system evolution. As the thermal perturbation reaches the more permeable region, a convective cell develops and provides a continuos recharge of cold fluid from the top of the domain. Low uniform temperatures from 50 to 60°C characterize the shallow region (Todesco, 1995). This temperature distribution is consistent with the data from the geothermal wells, and it does not allow a vapor phase to develop.
Two more simulations were carried out to evaluate the effects of the presence of carbon dioxide on the system evolution. The carbon dioxide partial pressure was initially taken at the atmospheric value (about 33 Pa), and a partial pressure of 0.15×10^7 Pa was imposed at the bottom of the domain. A first case (Simulation 4) was run with the same uniform permeability distribution of Simulation 1. Figure 4b,c shows the temperature and gas volumetric fraction after 100 years from the beginning of the simulation. A comparison between Figures 2b,c and 4b,c shows that carbon dioxide tends to enlarge the two-phase region to the depth of 800 m and to slightly reduce temperature. The following Simulation 5 was run with the same initial and boundary conditions as Simulation 4, but with a layered permeability distribution, as in Simulation 3. Under these conditions, the two-phase zone does not develop and the carbon dioxide is completely dissolved in water. In this case, the presence of carbon dioxide does not affect significantly the pressure and temperature distribution in the system.

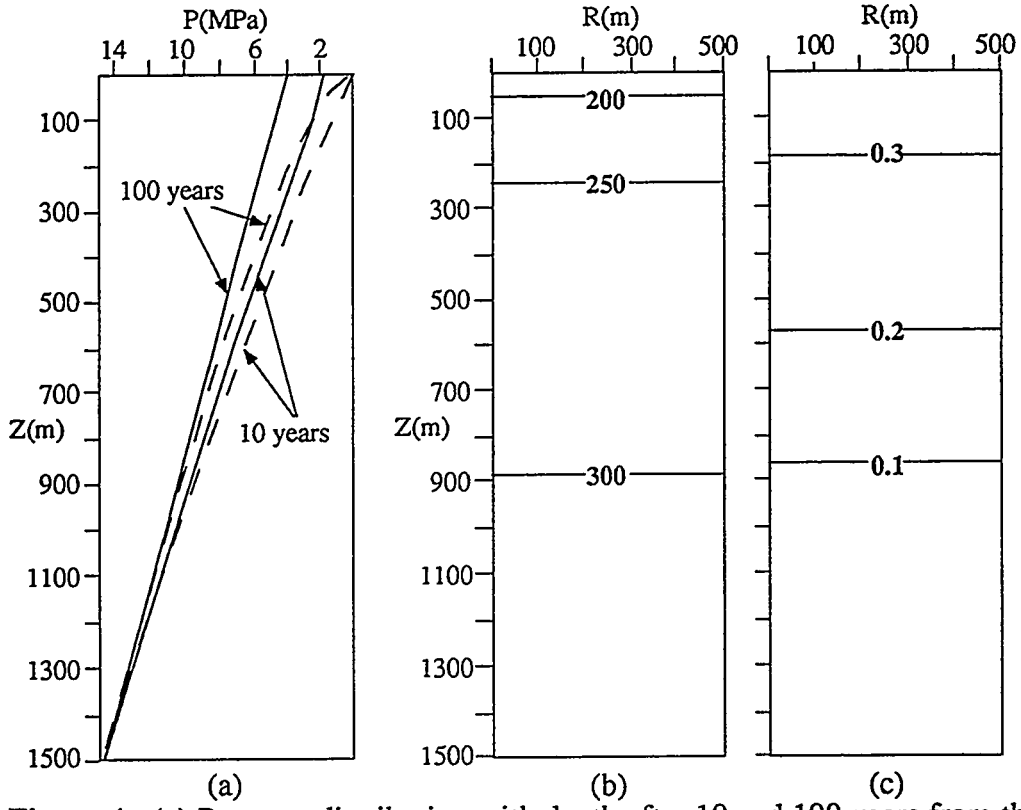

Figure 4. (a) Pressure distribution with depth after 10 and 100 years from the beginning of the simulation for Simulation 1 (dashed lines) and Simulation 2 (solid lines). (b) Temperature distribution (°C) and (c) gas volumetric fraction after 100 years (Simulation 4).

5. Conclusions

Modeling of two-phase, two-component fluid and heat circulation was carried out to simulate the hydrothermal activity at Vulcano (Italy). Results showed that temperature and pressure distributions within the system are highly dependent on the overall rock permeability. The evolution of a system can be strongly modified by changes in the permeability distribution even

if boundary conditions remain unchanged. High rock permeability throughout the domain allows a rapid temperature increase and an early development of a liquid-dominated two-phase zone. Rock permeability lower than 10^{-18} m^2 induces a much slower heating and the resulting temperature distribution is not consistent with the development of a vapor phase, both in the case of uniform and layered permeability structure. The presence of a low-permeability cap at the top of the domain reduces the heat and fluid outflow at the surface. As a consequence, the system undergoes a faster heating and a significative pressure increase at shallow levels. Results also show that the presence of carbon dioxide can increase the size of the two-phase region by enhancing the development of the gas phase.
Some insight on the hazard evaluation at Vulcano can derive from the performed simulations. Results show that higher permeability is responsible for higher temperature and mass discharge rates at the surface. This suggests that the observed variations at the fumarolic fields could derive from changes in rock permeability, even in absence of significative modification of the magmatic source. Processes leading to variation in rock permeability should be emphasized in the interpretation of monitoring data. In particular, self-sealing processes at shallow levels should be monitored due to the potential risk of phreatic explosion triggered by overpressure.

6. References

Badalamenti B., Gurrieri S., Hauser S., Tonani F. & Valenza M. (1984) - *Considerazioni sulla concentrazione e sulla composizione isotopica della CO_2 presente nelle manifestazioni naturali e nell'atmosfera dell'isola di Vulcano*. Rend. Soc. It. Miner. Petr., **39** , 367-378.

Barberi F., Ferrara G., Taddeucci G. & Villa I.M. (1989) - *L'intrusione monzodioritica del sottosuolo della Fossa (Vulcano, Isole Eolie)*. Boll. Ann. G.N.V., **2** , 611-630.

Barberi F., Neri G., Valenza M. & Villari L. (1991) - *1987-1991 unrest at Vulcano*. Acta Vulcanol., **1** , 95-106.

Capasso G., Favara R., Francofonte F. & Romeo L. (1993) - *Water wells geochemistry survey*. Acta Vulcanol., **3** , 276-278.

Carapezza M.L. & Diliberto I.S. (1993) - *Helium and CO_2 soil degassing*. Acta Vulcanol., **3** , 273-276.

Chiodini G., Cioni R., Guidi M. & Marini L. (1991) - *Geochemical variations at Fossa Grande crater fumaroles (Vulcano Island, Italy) in summer 1988*. Acta Vulcanol., **1** , 179-192.

Faraone D., Molin G. & Zanazzi P.F. (1988) - *Clinopyroxenes from Vulcano (Aeolian Islands, Italy): crystal chemistry and cooling history*. Lithos, **22** , 113-126.

Gioncada A. & Sbrana A. (1991) - *"La Fossa caldera", Vulcano: inferences from deep drillings*. Acta Vulcanol., **1** , 115-125.

Martini M., Giannini L., Prati F., Cellini Legittimo P., Picardi G. & Capaccioni B. (1989) - *Vulcano 1977-1989: sintesi interpretativa delle osservazioni geochimiche*. Boll. Ann. G.N.V., 89-1, 405-414.

Panichi C. & Noto P. (1992) - *Isotopic and chemical composition of water, steam and gas samples of the natural manifestations of the island of Vulcano (Aeolian Arc, Italy)*. Acta Vulcanol., **2** , 297-312.

Pruess K. (1990) - *Modeling of geothermal reservoirs: fundamental processes, computer simulation and field applications*. Geothermics, **19** ,(1), 3-15.

Pruess K. (1991) - *TOUGH 2 - A general purpose numerical simulator for multiphase fluid and heat flow*. LBL Report 29400, Lawrence Berkeley Lab., Berkeley, CA.

Sommaruga C. (1984) - *Le ricerche geotermiche svolte a Vulcano negli anni '50*. Rend. Soc. It. Miner. Petr., **39** , 355-366.

Todesco M. (1994) - *Hydrothermal activity at Vulcano (Aeolian Islands, Italy): review of the volcanic system and physical modeling prospects*.. Subm. Earth-Science Rev.. Also VSG Report 94-1, Pisa, Italy.

Todesco M. (1995) - *Modeling of geothermal activity at Vulcano (Aeolian Islands, Italy)*. Proc. World Geothermal Congress,Firenze, Italy. Also VSG Report 94-8, Pisa, Italy.

TRIPLE-POROSITY/PERMEABILITY FLOW IN FAULTED GEOTHERMAL RESERVOIRS: TWO-DIMENSIONAL EFFECTS

Mario César Suárez Arriaga (@) and Fernando Samaniego Verduzco (*)

(@) Michoacán University & CFE, A.P. 7-31; 58290 Morelia, Mich., México, Fax: (43) 14 4735
(*) National Autonomous University of México, C.U., Coyoacán, México, D.F. Fax: (5) 616 1073

ABSTRACT

An essential characteristic of some fractured geothermal reservoirs is noticeable when the drilled wells intersect an open fault or macrofracture. Several evidences observed, suggest that the fluid transport into this type of systems, occurs at least in three stages: flow between rock matrix and microfractures, flow between fractures and faults and flow between faults and wells. This pattern flow could define, by analogy to the classical double-porosity model, a triple-porosity, triple-permeability concept. From a mathematical modeling point of view, the non-linearity of the heterogeneous transport processes, occurring with abrupt changes on the petrophysical properties of the rock, makes impossible their exact or analytic solution. To simulate this phenomenon, a detailed two-dimensional geometric model was developed representing the matrix-fracture-fault system. The model was solved numerically using MULKOM with a H_2O+CO_2 equation of state module. This approach helps to understand some real processes involved. Results obtained from this study, exhibit the importance of considering the triple porosity/permebility concept as a dominant mechanism producing, for example, strong pressure gradients between the reservoir and the bottom hole of some wells.

INTRODUCTION

For more than thirty years the naturally fractured media have been the object of multiple studies. Models of diverse complexity have been created to explain their behavior in different fields: groundwater, geothermal reservoirs and, above all, in petroleum engineering. The essential difficulty in the realistic modeling of fractured media continues to be the partial ignorance about the dimensions, spatial distribution and interconnections of the fractured network. Being even possible to write and solve transport equations into the matrix and in the fractures, there are many unknown parameters in any fractured region. From the fluid thermodynamics point of view, the fractures in the matrix blocks are rock discontinuities, while from a mass flow point of view, there are no discontinuities and the problem is essentially geometric.

Observations carried out in volcanic faulted reservoirs, (Los Azufres & Los Humeros, Mexico), showed singular behavior of wells intersecting open faults. Almost all producing wells crossed, at different depths, extremely high permeability zones (1-10 darcys,Suárez et al,1992), that does not correspond to fresh volcanic rock permeability ($\sim$1 microdarcy), neither to microfractures permeability ($\sim$100 milidarcys). This property, linked to other evidences observed, suggests that fluid and heat transport in such systems occurs in three stages: matrix-fractures-fault, implicating strong contrasts in the petrophysical parameters of each medium. Our purpose is to introduce some numerical results supported by real data, about what could happen in a medium of triple porosity and triple permeability flow at a detailed scale, representing real dimensions of faults and fractures. The focus of the proposed problem is essentially practical. We want to show some difficulties inherent to the understanding of real geothermal fractured reservoirs behavior with conductive faults, and the usefulness of its interpretation under the triple porosity/permeability concept.

DOUBLE POROSITY MEDIA

The media with double porosity behavior constitutes a classical topic in the literature on fractured reservoirs. The primal analytical and semianalytical models for flow of slightly compressible liquid emerged in the 60's. According to this idea, the matrix blocks surrounded by fractures, could be of any size, with scarce fractures or intensely fractured. The original concept of double porosity was stated for the first time by Barenblatt, Zheltov and Kochina (1960). Considering stationary flow in the matrix and ignoring storage in the fractures, those pioneers formulated a liquid flow equation in each medium. The interaction parameter between matrix and fractures was the mass flow passing at every second, per unit of volume of fractured rock. This term resulted to be proportional to density and to the pressure difference between both mediums and in inverse proportion to liquid viscosity: $q=\alpha\rho\ (p_m-p_f)\ /\mu$, where α was a dimensionless constant only relied to the geometry of the block-fracture boundary.

The model initially exposed by Warren & Root (1963) contains as essential parameters ω (quotient of fractures storativity with respect to total storage) and λ which is a resistance factor indicating the intensity of matrix-fractures interaction. These authors also considered a pseudostationary flow in the matrix, this hypothesis originates erroneous approaches for short simulation times. Nevertheless, this simplification conformed well to petroleum fields' data containing important differences between matrix and fracture permeabilities, because in those conditions there is a certain retard in matrix-fracture transfer. Subsequently, de Swaan (1976) considered the real transitory flow and, later, Cinco Ley & Meng (1988) included the effect of finite conductivity faults.

Similar double porosity problems were introduced in hydrothermal reservoir engineering (Cinco et al., 1979); but

the complex processes involved in phase change and the non-linearity of parameters in the basic equations, made the analytic solutions very scarce. The double porosity model in geothermal reservoirs was generalized by Pruess & Narasimhan (1985) and solved numerically by means of the Multiple Interacting Continua concept (MINC). A numerical model published recently (Zimmerman et al.,1993), treats matrix-fractures transient flow in semianalytical form.

TRIPLE POROSITY BACKGROUND

Closmann (1975) extended for the first time the double porosity concept, describing a fractured medium composed by two distinct types of matrix, one with lower permeability and minor porosity than the other, but considering only flow within the fractured network. Abdassah & Ershaghi (1986) used a model that they called of *triple porosity*, when remarking abnormal changes in the graphs of some well tests during the transitory period. Liu & Chen (1990) introduced an exact solution for an isothermal, cylindrical reservoir saturated with slightly compressible fluid, with a centered well in a multiple porosity, multiple permeability medium. Under this concept, N continua porous media interact between themselves; having each one its own pseudostationary interporosity flow and its own parameters. This model makes up the widest generalization of the original concept created by Barenblatt and coauthors.

In geothermal reservoirs with phase changes, the transitory period within the matrix cannot be neglected. Precisely, during the transfer between matrix and fractures, the medium's discontinuity causes abrupt changes in flow thermodynamics because geothermal fluid is extremely sensitive to geometrical changes of the flow conduits in the reservoir. The original idea of Barenblatt and coauthors, and the derived models, couldn't work fine for a fluid that changes from liquid to two-phase because density and viscosity are discontinue spatial functions.

In the aforementioned fields, we have observed wells that initially had a strong depression. When interrupting extraction during some period, and after reopening them, the production attained almost the same previous level after certain time. Thermal inversions also have been observed in some wells producing 100% steam from zones that correspond to compressed liquid conditions. For 12 years, some few wells maintained in permanent production, do not show any noticeable change in their thermodynamic characteristics. Zones of high permeability have been detected, coexisting with almost impervious close zones. The triple porosity/permeability concept unifies all these phenomenons.

GENERAL CONCEPTION OF THE TRIPLE POROSITY / PERMEABILITY MEDIUM

The triple porosity/permeability concept we are introducing, is based on experimental observation of fractured reservoirs traversed by big open faults or macrofractures, where the intensity of fissuring is high near to the fault, intermediate in the fractured network and where a remarkable permeability contrast exists between matrix blocks, microfractures and faults. Figure 1 is a photocopy of a 10 cm diameter core, cutting a 1.5 cm thickness fault of the Los Azufres geothermal field at 2680 m depth. In the picture is visible the intense network of fractures around the fault. The micro-fractures show an average opening of 0.1 cm. The behavior of some non producing wells suggest that fissuring decreases faraway from the faults at any depth (Suárez et al,1992). This observation implicates that after some distance to the fault, matrix blocks increase their size and only isolated sparse microfractures can be found.

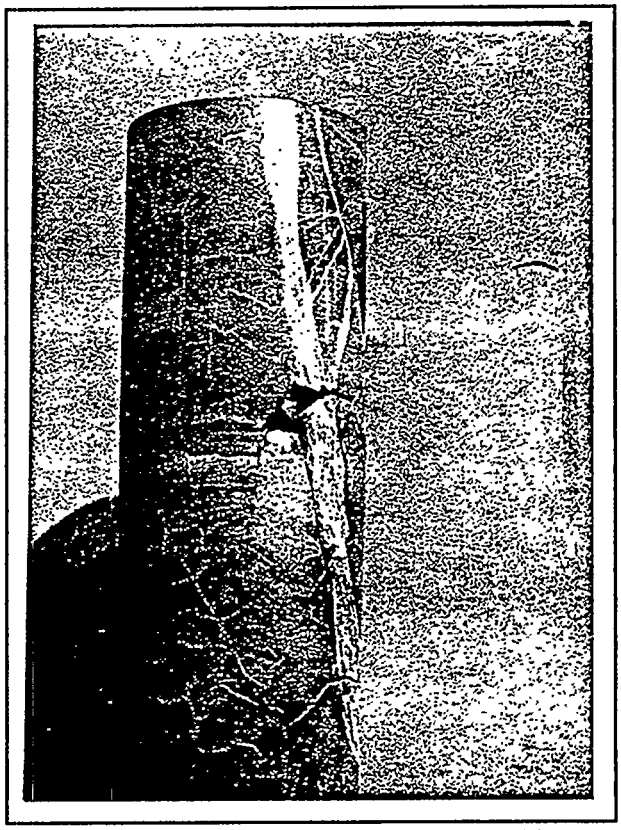

Fig. 1.- Core of andesite extracted from well Az-48 in Los Azufres geothermal field, at 2680 m depth.

From a practical point of view, is useful to consider the effect of the fissuring around the fault, only when the matrix blocks are sufficiently spaced between them, that is to say, when the middle distance between parallel fractures is greatter than a minimal value δ_m (Gringarten & Witherspoon, 1972). Otherwise it wouldn't be possible to distinguish between pressure/temperature averages in the fractured medium and those in the porous simple medium. The matrix-fractures interaction speed in mediums intensely fractured, with distances shorter than this minimal spacing compensates, in average, the effective pressure/temperature differences between both continua (Suárez,1990). Close to the fault, the medium could be considered of simple porosity with high permeability, constituting a transition

zone between blocks of fractured matrix and the fault.

The concept of "triple porosity" we are proposing, considers that diffusivity attains its largest values in the conductive fault and is much larger in the fractured network than in the matrix. Flow toward the wells occurs in such a way that the initial response in the extraction zone is immediately detected in the fault; then is noticed in the fractures and, much later in the matrix. The three mediums, matrix, fractures and fault are considered, under this concept, as three interacting continua exchanging mass and heat through special transport functions which depend on the form and size of blocks, on fissuring intensity and on the communication with the fault. The transfer among matrix-fractures-fault is transitory and must depend on many factors including tortuosity and mineralization. Our triple porosity medium is formed by three continua interconnected, having different petrophysic and thermodynamic characteristics, which coexist in a single physical space overlaid by the cartesian axis. A medium of triple porosity/permeability containing simple water, could be represented theoretically by two pseudo-vectorial equations:

$$\frac{\partial(\rho_j \phi_j)}{\partial t} + div(\rho_j \vec{v}_j) = q_{ij} \qquad [mass] \ldots (1)$$

$$\frac{\partial e_j}{\partial t} + div(\rho_j h_j \vec{v}_j - K_j \vec{\nabla} T_j) = q_{ij} h_j \quad [heat] \ldots (2)$$

Subindex j=m, f, F represents the respective medium's equation: matrix, fracture, Fault; thus a total of six scalar equations. The nomenclature is common: ρ_j is density, ϕ_j porosity, v_j speed of flow, e_j is the total energy rock+fluid, h_j means specific enthalpy of the fluid, K_j is thermal conductivity tensor and T_j ,the temperature in each medium. All terms are functions of time and space. Parameter q_{ij} represents mutual interchange among the three continua. The preceding equations are considerably simplified for a triple porosity reservoir initially saturated with liquid. Assuming petrophysical parameters approximately constant in each medium:

$$\frac{\partial \vec{p}}{\partial t} = \mathbb{N} \cdot \nabla^2 \vec{p} + \vec{q}; \quad \mathbb{N} = (\eta_{jk}) = \begin{pmatrix} \eta_m & 0 & 0 \\ 0 & \eta_f & 0 \\ 0 & 0 & \eta_F \end{pmatrix} \quad \ldots (3)$$

$$\vec{p} = (p_i); \left\{ \eta_i = \frac{k_i}{\phi_i C_i \mu_i} \right\}, \left\{ q_i = \frac{q_{ij}}{\phi_i C_i} \right\}; \; for \; i = m, f, F$$

∇^2 is the laplacian operator, p_i is fluid pressure in each medium, η_i is the diffusivity coefficient, k_i ,permeability, C_i , compressibility and μ_i , viscosity. Data measured in a fault zone of the Los Azufres geothermal field shows strong diffusivity contrast: $\eta_m \sim 0.003$, $\eta_f \sim 0.3$, $\eta_F \sim 1$ (m^2/s). These equations could be solved in some simplified cases. For example, in a very big reservoir with radial flow from the fractured net toward the fault, the general dimensionless equation which describes the flow motion is:

$$\omega \frac{\partial P_{fD}}{\partial t_D} = \frac{1}{r_D} \frac{\partial}{\partial r_D} \left(r_D \frac{\partial P_{fD}}{\partial r_D} \right) - \Omega \int_0^{t_D} \frac{\partial P_{fD}}{\partial \tau} \psi(t_D - \tau) \, d\tau \quad \ldots (4)$$

The flow function ψ ($t_D - \tau$) is attached to the geometry of flow between fractures and fault (or matrix and fractures). The variable Ω is a time independent, dimensionless coefficient that describes the geometric characteristics of fractures-fault contact. Similarly if a spherical, radial or linear flow is considered between matrix and fractures, another similar equation could be coupled for any of these flow geometries between matrix and fractures. Several analytic and semianalytic solutions can be found in the literature (see references). As a comparative illustration, the solution for equation 4 in Laplace space is:

$$\mathcal{L}[P_{fD}](r_D, s) = \frac{K_0(\sqrt{s\theta}\, r_D)}{s\sqrt{s\theta}\; K_1(\sqrt{s\theta})} \qquad \ldots\ldots \quad (5)$$

Where $\theta = \Omega\Psi(s) + \omega$ and $\Psi(s)$ is the Laplace transform of ψ (t_D), K_0 and K_1 are the modified second kind Bessel functions of 0th and 1st order respectively, s is the image in Laplace space of dimensionless time t_D. This formula can be numerically inverted to obtain, in real-time space, numerical values for dimensionless pressure (Cinco et al.,1979). As a general comment, it is remarked that pressure decrement in the fault, as calculated with this model, is much more smoother than that observed in real geothermal reservoirs. Thermodynamic properties may vary softly within the matrix; while in fractures variations are abrupt with discontinuities in the pressure/temperature gradients. These variations are emphasized into the faults being, in fact, open rough channels where, probably, Darcy's law is not valid. Because of lack of space we did not include a graphic comparison between this solution and the following approach.

NUMERICAL APPROXIMATION TO THE TRIPLE POROSITY/PERMEABILITY FLOW

General stated equations of mass and energy are contained in MULKOM's code (Pruess, 1988). The general ideas sketched before, were included in a two-dimensional model defining approximately the geometry of each continuum (Fig. 2). The model was solved numerically with MULKOM for an H_2O+CO_2 equation of state. We carried out the calculations for different initial states with fluid extraction in the fault and various boundary conditions. Fault thickness was simulated explicitly for an opening of 0.01 m (Fig. 1). The fractured network is heterogeneous and intense in the immediate vicinity of the fault within a radius of 5 meters. Close to the macrofracture there is a 10 meters transition zone with fewer fractures and lower permeability, connected to regular matrix blocks of increasing diameter, starting from 20 m until a distance of 100 m to the fault. In the fault's plane (X,Z) there are 43 elements in the X axis and 20 elements in the Z axis.

Distances between different elements forming the mesh, were constructed according to a normalized geometric succession: $d_N = d_{N-1}.\sqrt[5]{10}$, $d_1 = d_0.\sqrt[5]{10}$. Initial parameter d_0 is equal to 0.01 m in the fault, and 1.0 m in the fractured zone. In this way we could cover rapidly very short distances, passing to big distances without following a regular proportion. This technique influences positively the efficiency of the solution method. We perform several series of numeric experiments with the parameters indicated in table 1. With the purpose of forcing a rapid answer in the zone of extraction, there is no recharge of mass nor of heat through any boundary. Fluid was extracted supposing different initial states in the system: liquid and two-phase. The reservoir's portion around the fault is limited by two impervious boundaries located 100 m (right and left). A brief synthesis of results is described next.

EXTRACTION FROM A SINGLE VERTICAL FAULT

(a)- **Initial State: Liquid** (Figs.3,4,5,6).
Reservoir initial conditions correspond to compressed liquid, which is extracted in the fault. Depressions in fault and fractures are observed immediately; pressure decrement appears slowly in the matrix. During the short simulated time thermodynamic changes are isothermal in the matrix, starting at 15 m distance to the fault; consequently, single liquid remains as the dominant phase in the matrix blocks. Main changes are observed in the vicinity of the fault, where temperature and pressure draw down are homogeneous. Steam saturation and carbon dioxide partial pressure,change abruptly at matrix-fractures and fractures-fault interfaces after some days. Fluid expansion in the fractured network provokes the production of vapor within a limited radius up to 18 m distance. At matrixfractures interface, steam saturation reaches a maximum that goes falling down toward the fault. Such phenomena occur because the fault receives a liquid contribution from deeper zones. CO_2 partial pressure swoops rapidly inside the fault and fractures and remains constant in the matrix.

(b).- **Initial State: Two-Phase** (Figs. 7,8,9,10)
Initial steam saturation is 30%. The behavior of pressure and temperature is different from previous case. Depressions happen now faster but attenuate at less distance, while temperature decays up to 25 meters within the matrix, then it remains constant until the next impervious boundary. Steam saturation reaches 100% between the fractured zone and some near blocks; in the matrix vapor grows, but not so much between the boundary and this zone. CO_2 partial pressure falls rapidly and smoothly near the fractured network and increases abruptly in the fault, remaining almost constant in the matrix blocks near to the border. Triple porosity effect is appreciated in both variables. The fault and the fractured network are clearly distinguished. The lower quantity of vapor in the fault is explained the same as in the previous case.

Extracting fluid from two parallel faults presents combined effects, similarly to the cases previously discussed. Whether considering two faults inclined and parallel, intersected by the same well (Fig. 2), is equivalent to have two horizontal production zones of high permeability interacting through the well. In this case pressure fall off and temperature decrement occur precisely in the high permeability zone. When traversing a lower zone of high permeability, the temperature exhibits an inversion, that is to say, a sudden decrement at this depth; afterwards it increases again. Pure steam can coexist with a two - phase vertical zone or even with a compressed liquid region below or up to the production zone. Something similar occur with noncondensible gas. It can coexist with very low values in the zone of high permeability and higher values outside.

Fig2.-GEOMETRICAL MESH SHOWING CHARACTERISTICS OF: FAULTS, FRACTURED NETWORK AND MATRIX BLOCKS.

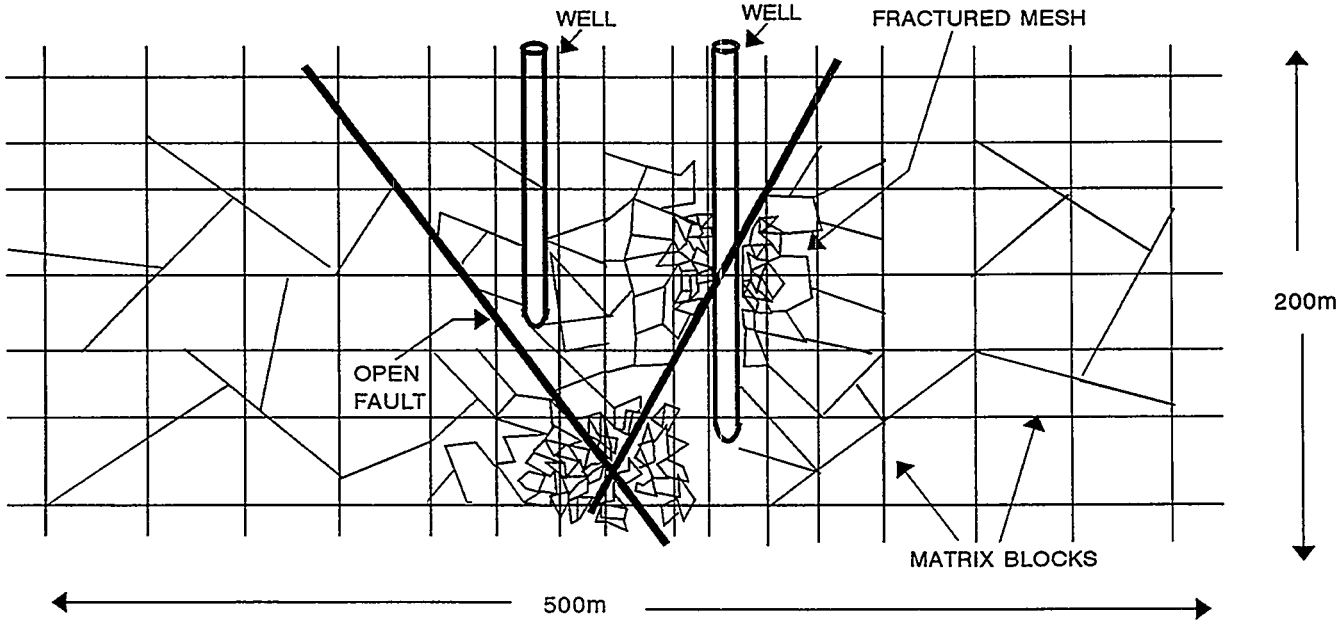

TABLE 1.- SOME PARAMETERS USED IN THE SIMULATIONS. {T_1 holds for initial liquid state; T_2 for two-phase. Initial vapor saturation is 0.3 and $P(CO_2)$=5 bar (all cases)}

Rock Type	ρ kg/m^3	ϕ	k_X (m^2)	k_Z (m^2)	K_T W/m/C	C_P J/kg/K	P bar	T_1 (°C)	T_2 (°C)	η_i m^2/s
FAULT	1355	0.75	10^{-11}	10^{-11}	0.62	3528	55	250	264	0.900
FRACT	2000	0.35	10^{-13}	10^{-13}	1.52	1992	55	250	264	0.300
MATRX	2251	0.01	10^{-16}	10^{-18}	2.00	1165	55	250	264	0.003

CONCLUSIONS

The main aim of this paper has been to present numerical results, obtained from a two-dimensional model, developed to simulate flow in a triple porosity/permeability faulted, naturally fractured geothermal reservoir. This work was motivated from the essential characteristic of some reservoirs where producing wells intersect a fault. From results of this study, the following conclusions can be made:

1.- Fluid transport from the formation to the wells occurs in three stages: flow between matrix and fractures, flow between fractures and fault, and last flow to the well mainly through the fault.

2.- Pressure and temperature measured in wells represent average values, resulting from multiple interactions among the macrofracture, the microfractures and the matrix.

3.- The effect of the fault presence results in important reservoir behavior differences with respect to conventional double porosity model behavior.

4.- These differences are emphasized with regard to the abrupt discontinuities in the gradient of thermodynamic properties, ocurring at the interfaces between the pairs of systems. These differences also include abrupt variations of the mass and energy production and of the spatial steam and CO_2 distribution in the reservoir. Total flow of heat is dominant in the faults and very poor in the matrix.

5.- The changes detected in the principal variables could have a wide variety of forms and behaviors. The effect of triple porosity is appreciated in the distribution of vapor and of carbon dioxide at fault's neighborhood.

6.- In fact what we are measuring in terms of "*reservoir pressure*" and "*temperature of the formation*", is an average value resulted from the multiple interaction between porous rock, microfractures and fault in the the zone immediately affected by extraction or by drilling and the word "*reservoir properties*" should be considered only as an ambitious euphemism in this class of systems.

REFERENCES

-**Abdassah, D. & Ershaghi, I.**; (1986). "*TRIPLE POROSITY SYSTEMS FOR REPRESENTING NATURALLY FRACTURED RESERVOIRS*". SPE Formation Evaluation, I(2), pp. 113-127.

-**Barenblatt, G., Zheltov, Y. & Kochina, I.**; (1960). "*BASIC CONCEPTS IN THE THEORY OF SEEPAGE OF HOMOGENEOUS LIQUIDS IN FISSURED ROCKS*". J.Appl.Math.Mech., No. 24, pp. 1286-1303.

-**Cinco Ley,H., Brigham,W., Economides,M., Miller,F., Ramey,H., Barelli,A. & Manetti,G.**; (1979). "*A PARALLELEPIPED MODEL TO ANALYZE THE PRESSURE BEHAVIOR OF GEOTHERMAL STEAM WELLS PENETRATING VERTICAL FRACTURES*". SPE 8231, 54th Annual Tech.Conf.

-Cinco Ley, H. & **Meng, H.Z.** (1988). "*PRESSURE TRANSIENT ANALYSIS OF WELLS WITH FINITE CONDUCTIVITY FRACTURES IN DOUBLE POROSITY RESERVOIRS*". SPE 18172.

-**Closmann, P.J.**; (1975). "*AN AQUIFER MODEL FOR FISSURED RESERVOIRS*". Soc. of Petroleum Engineers Journal, Vol. 15, No. 5, pp. 385-398.

-**De Swaan, A.**; (1976). "*ANALYTICAL SOLUTIONS FOR DETERMINING NATURALLY FRACTURED RESERVOIR PROPERTIES BY WELL TESTING*". SPE Journal, Vol. 16, pp. 117-122.

-**Gringarten, A. & Witherspoon, P.** (1972). "*A METHOD OF ANALYZING PUMP TEST DATA FROM FRACTURED AQUIFERS*".Proc. of the Symp. on Percolation Through Fissured rock. Stuttgart, Ger.

-**Liu, M.X. & Chen, Z.X.** (1990). "*EXACT SOLUTION FOR FLOW OF SLIGHTLY COMPRESSIBLE FLUIDS THROUGH MULTIPLE-POROSITY, MULTIPLE-PERMEABILITY MEDIA*". Water Res. Research, Vol. 26, No. 7, pp. 3393-1400.

-**Pruess, K. & Narasimhan, T.N.** (1985). "*A PRACTICAL METHOD FOR MODELING FLUID AND HEAT FLOW IN FRACTURED POROUS MEDIA*". SPE Journal pp. 14-26, February 1985.

-**Pruess, K.** (1988). "*SHAFT, MULKOM, TOUGH: A SET OF NUMERICAL SIMULATORS FOR MULTIPHASE FLUID AND HEAT FLOW*". GEOTERMIA - Revista Mexicana de Geonergía, Vol. 4, No. 1, pp. 185-202.

-**Suárez, M.C. & Mañón, A.; (1990).** "*INJECTION OF COLD WATER AND AIR INTO A TWO-PHASE VOLCANIC HYDROTHERMAL SYSTEM*". First TOUGH Workshop, Lawrence Berkeley Laboratory, Preprints, Sep. 13-14, Berkeley, California.

-**Warren, J.R. & Root, P.J.**; (1963). "*THE BEHAVIOR OF NATURALLY FRACTURED RESERVOIRS*". Soc. of Petroleum Engineers Journal, Vol. 3, No. 3.

-**Zimmerman, R.W., Chen, G., Hadgu, T. & Bodvarsson, G.S.** (1993). "*A NUMERICAL DUAL-POROSITY MODEL WITH SEMIANALYTICAL TREATMENT OF FRACTURE/MATRIX FLOW*". Water Resources Research, Vol. 29, No. 7, pp. 2127-2137. July 1993.

Fig. 3– PRESSURE EVOLUTION AT FAULT NEIGHBORHOOD (initial liquid)

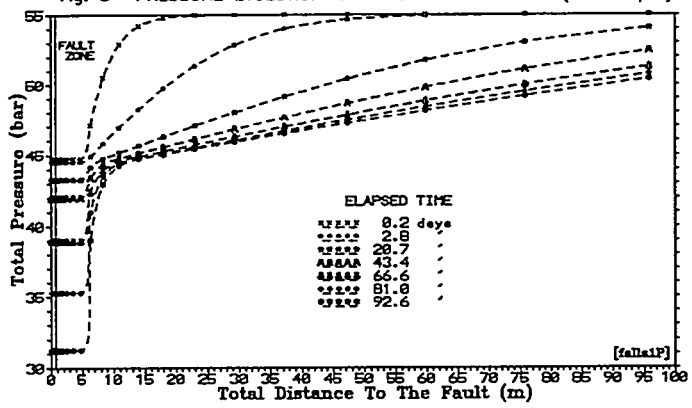

Fig. 7 – PRESSURE EVOLUTION AT FAULT NEIGHBORHOOD (initial 2–phase)

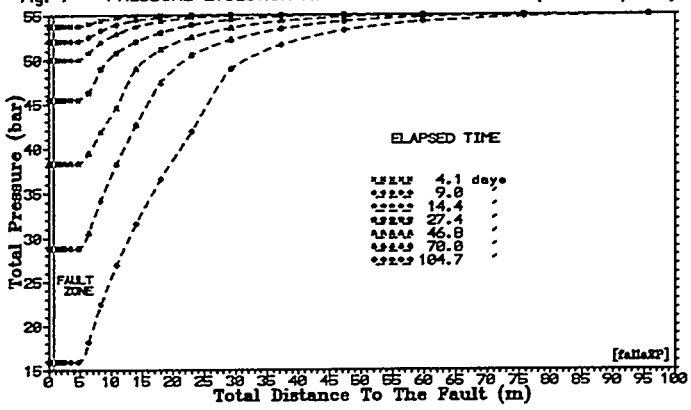

Fig. 4 – TEMPERATURE EVOLUTION AT FAULT NEIGHBORHOOD (initial liquid)

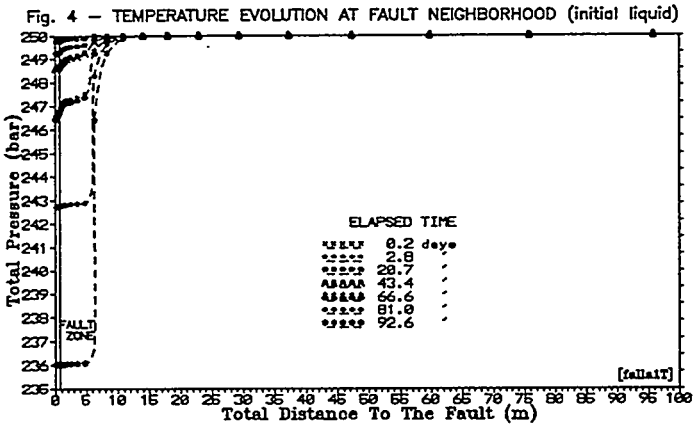

Fig.8 –TEMPERATURE EVOLUTION AT FAULT NEIGHBORHOOD (initial 2–phase)

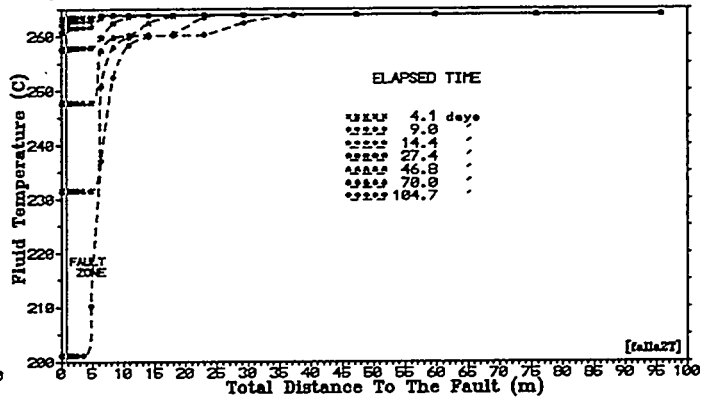

Fig. 5 – STEAM SATURATION AT FAULT NEIGHBORHOOD (initial liquid)

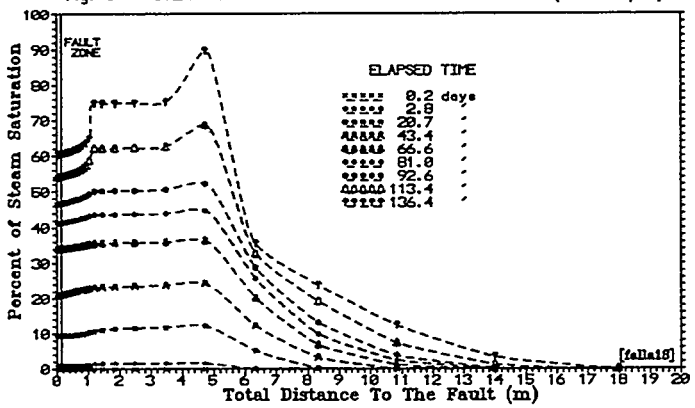

Fig. 9 – STEAM SATURATION AT FAULT NEIGHBORHOOD (initial Sv = 0.3)

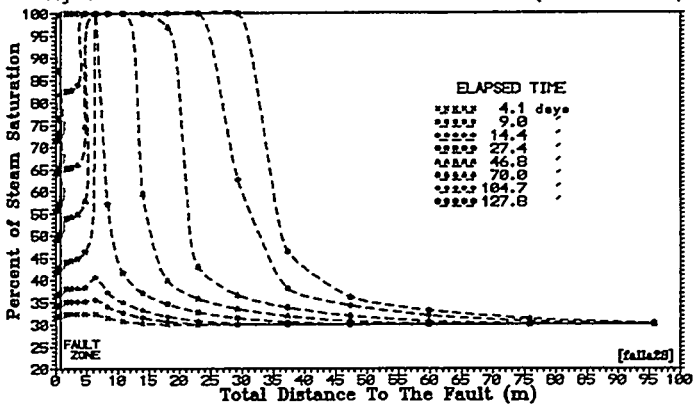

Fig.6–CO_2 PARTIAL PRESSURE AT FAULT NEIGHBORHOOD (initial liquid)

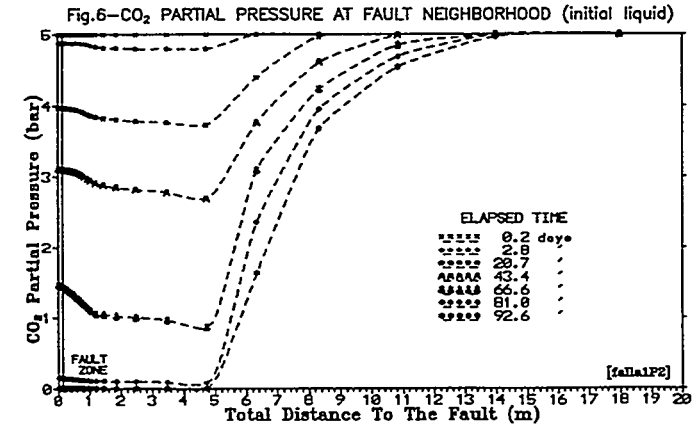

Fig.10– CO_2 PARTIAL PRESSURE AT FAULT NEIGHBORHOOD (initial 2–phase)

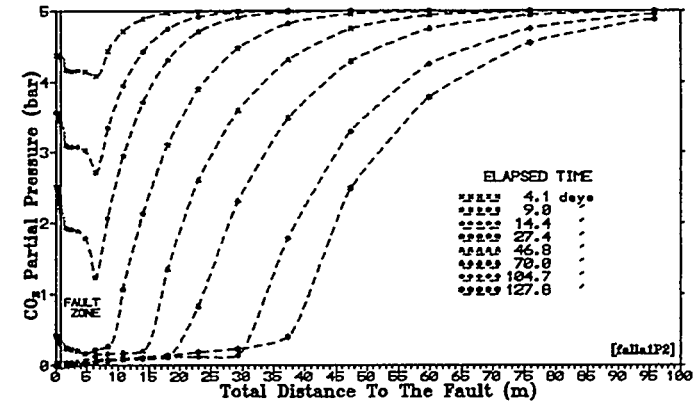

NUMERICAL SIMULATION OF CARBON DIOXIDE EFFECTS IN GEOTHERMAL RESERVOIRS

Sara L. Moya and Eduardo R. Iglesias

Instituto de Investigaciones Eléctricas
Departamento de Geotermia
Apartado Postal 475, 62000 Cuernavaca, Mor., México

ABSTRACT. We developed and coded a new equation of state (EOS) for water-carbon dioxide mixtures and coupled it to the TOUGH numerical simulator. This EOS is valid up to 350°C and 500 bar. Unlike previous thermodynamical models, it rigorously considers the non-ideal behavior of both components in the gaseous mixture and formally includes the effect of the compressibility of the liquid phase. We refer to the coupling of this EOS with TOUGH as TOUGH-DIOX. To complement this enhancement of TOUGH, we added indexed output files for easy selection and interpretation of results. We validated TOUGH-DIOX against published results. Furthermore we used TOUGH-DIOX to explore and compare mass and energy inflow performance relationships of geothermal wells with/without carbon dioxide (CO_2). Our results include the effects of a broad range of fluid and formation properties, initial conditions and history of reservoir production. This work contributes with generalized dimensionless inflow performance relationships appropiate for geothermal use.

INTRODUCTION

Many geothermal reservoirs contain considerable amounts of noncondensible gases, specially CO_2. A small fraction of this gas changes the thermodynamics and transport properties of the geothermal fluid. For this reason, is important to include in the geothermal simulators, a suitable Equation Of State (EOS) for the binary mixture H_2O-CO_2, in order to determine with confidence the mass and energy transport in the geothermal reservoirs. This in addition to the numerical qualities that the geothermal simulators must to have (e.g. Pruess, 1988; Pritchett, 1994).

We developed a new EOS for the binary mixture H_2O-CO_2 (Moya and Iglesias, 1992; Moya, 1994) valid up to 350°C and 500 bar. This new EOS is different that of O'Sullivan et al. (1985) and that one of Sutton (1976). Our EOS included the recent virial formulation of Spycher y Reed (1988) for the realistic determination of the fugacity coefficients of each component in the gaseous mixture. It also included the correlation of Andersen et al. (1992) for the evaluation of the enthalpy of the CO_2 gas.

Taking advantage of the efficiency and modular structure of the TOUGH geothermal simulator (Pruess, 1987) we coupled it our new EOS for the H_2O-CO_2 system. This coupling is refered as the TOUGH-DIOX simulator which included also index output files for easy selection and interpretation of the numerical results. We validated TOUGH-DIOX against published results.

As one applying of the TOUGH-DIOX simulator, we explored the

mass and energy productivities of the geothermal wells for a broad range of reservoir parameters, in order to obtain a dimensionless model of productivities. Various numerical studies have been published on the behavior of the flowing enthalpy in relation to the reservoir parameters (Sorey et al., 1980; Pritchett et al., 1981; Grant y Glover, 1984; Bodvarsson, 1984; O'Sullivan et al., 1985; Pruess et al., 1985; Lippmann et al., 1985; Gaulke, 1986; Bodvarsson y Gaulke, 1987; among others). However, up to now, there's no a numerical methodology in the geothermal literature which permits estimate the mass and energy productivities of geothermal wells, with independence of the transport and thermophysical parameters of the reservoir. In the petroleum industry this has been performed over twenty years ago through the use of dimensionless inflow performance relationships (IPR).

The IPR curves were suggested by Gilbert (1954) as an analysis method of oil wells. The pioneer work of Muskat (1937) and later on of Vogel (1968) gave a great impulse to the use of dimensionless IPR curves in order to estimate the mass productivity of oil wells. Vogel (1968) proposed his famous "reference curve" (dimensionless IPR curve) widely used in the oil industry since then. Our preliminary results for a case of pure water in a homogenous porous media (Iglesias y Moya, 1990) and even in a fracturated porous media (Iglesias y Moya, 1993) showed that this also is possible for geothermal wells.

Considering the effect of CO_2, in this work we presented IPR curves and GIPR curves (Geothermal Inflow Performance Relationships) inherents to geothermal reservoirs. Two dimensionless "reference curves" are proposed in order to estimate geothermal heat deliverability, one for mass productivity (dimensionless IPR curve) and another one for thermal productivity (dimensionless GIPR curve). These two reference curves are independent of the reservoir parameters, the initial conditions and stage of explotation of this.

EQUATION OF STATE

Figure 1 shows the values of Henry's constant obtained with our EOS (Moya e Iglesias, 1992) for the solubility of carbon dioxide in water, compared with those of previous thermodynamical models. It is seen that they differ for temperatures of geothermal interest. The main source of error for the earlier solubility models is the choice of the Lewis fugacity rule (values of Majumdar and Roy, 1956) which estimates the fugacity coefficient of a component in a gas mixture as the fugacity coefficient of the pure component at the same temperature and pressure of the mixture. This idealization is obviously inconvenient for geothermal systems due to the both components are present in significant amounts (Takenouchi and Kennedy, 1965). We chose the important and recent virial formulation of Spycher and Reed (1988) to compute reliable fugacity coefficients. The formulation of Spycher and Reed involves up to the third virial coefficient necessary at temperatures and pressures of geothermal interest. Another important improvement in our EOS is the rigorous consideration of the compressibility effect of the liquid phase named Poynting correction (Prauznitz, 1969) necessary for high pressures. Finally, our EOS doesn't present

the severe conflict between the linearity of the model and the lack of linearity of the experimental data, evident in previous thermodynamical models.

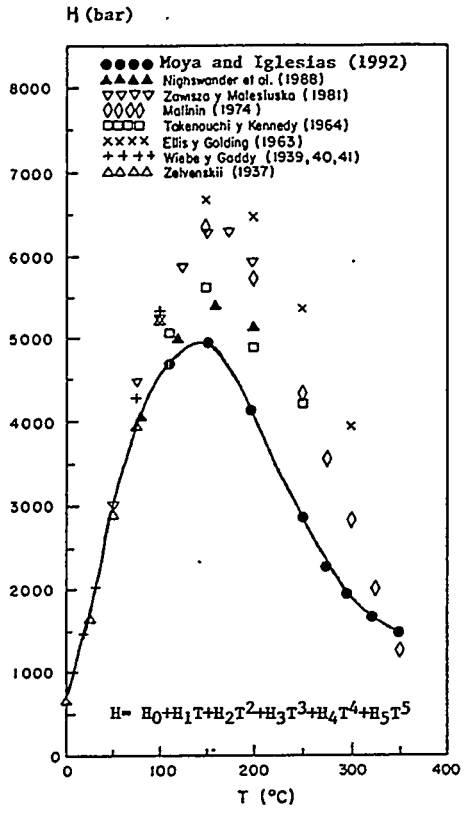

Fig. 1 Values of Henry's law constant by different authors. H_0=666.128, H_1=37.084, H_2=0.325, H_3=4.273x10^{-3}, H_4=1.344x10^{-5}, H_5=1.343x10^{-8}.

TOUGH-DIOX SIMULATOR

The TOUGH-DIOX simulator is the coupling of the TOUGH simulator (Pruess, 1987) and of a new equation of state (EOS) for H_2O-CO_2 mixtures (Moya e Iglesias, 1992), valid until 350°C and 500 bar. Furthermore, the TOUGH-DIOX simulator generates indexed output files that permit, through an interactive program (Moya, 1989), to process the required information by the user for a fast selection and interpretation of the numerical results. We validated TOUGH-DIOX against published results for two geothermal studies with CO_2. The comparison with one of this studies (Suárez et al., 1989) is detailed in Figure 2. It is seen that our results agree well with those of the MULKOM simulator (Pruess, 1988). Although we no know with detail the EOS employed in MULKOM, the range of pressures involved (up to 80 bar), doesn't require very strict considerations in the thermodynamic model. That's why we don't expect that the values obtained with both simulators be very different.

NUMERICAL METHODOLOGY

The radial inflow model is used. A cylindrical reservoir is considered with radio and width of approximately 1000 and 100 m, respectively, limited above and below by impermeable and adiabatic formations. In the center there is a fully penetrating well with constant rate production. The rock-fluid media is constituted of homogenous porous rock and two-phase water with CO_2 representing the effect of noncondensable gases. The fluid flow in the reservoir is governing under Darcy law without gravity effect (unidirectional radial flow). Local thermodynamical equilibrium is established. The numerical grid employed has a nodal distribution of $r_n=0.1(2)^{(n-1)/2}$ showing higher finesse in adjacent area of the well where strong pressure and temperature gradients are present.

The cases under study are summarized in Table 1 and the constant assumed formation properties in Table 2. Each case involves a range of accumulated produced mass between five and thirty-five per cent of the total mass of initial geothermal fluid (*in situ*). The residual saturations are the usual ones of 0.30 for the liquid and 0.05 for

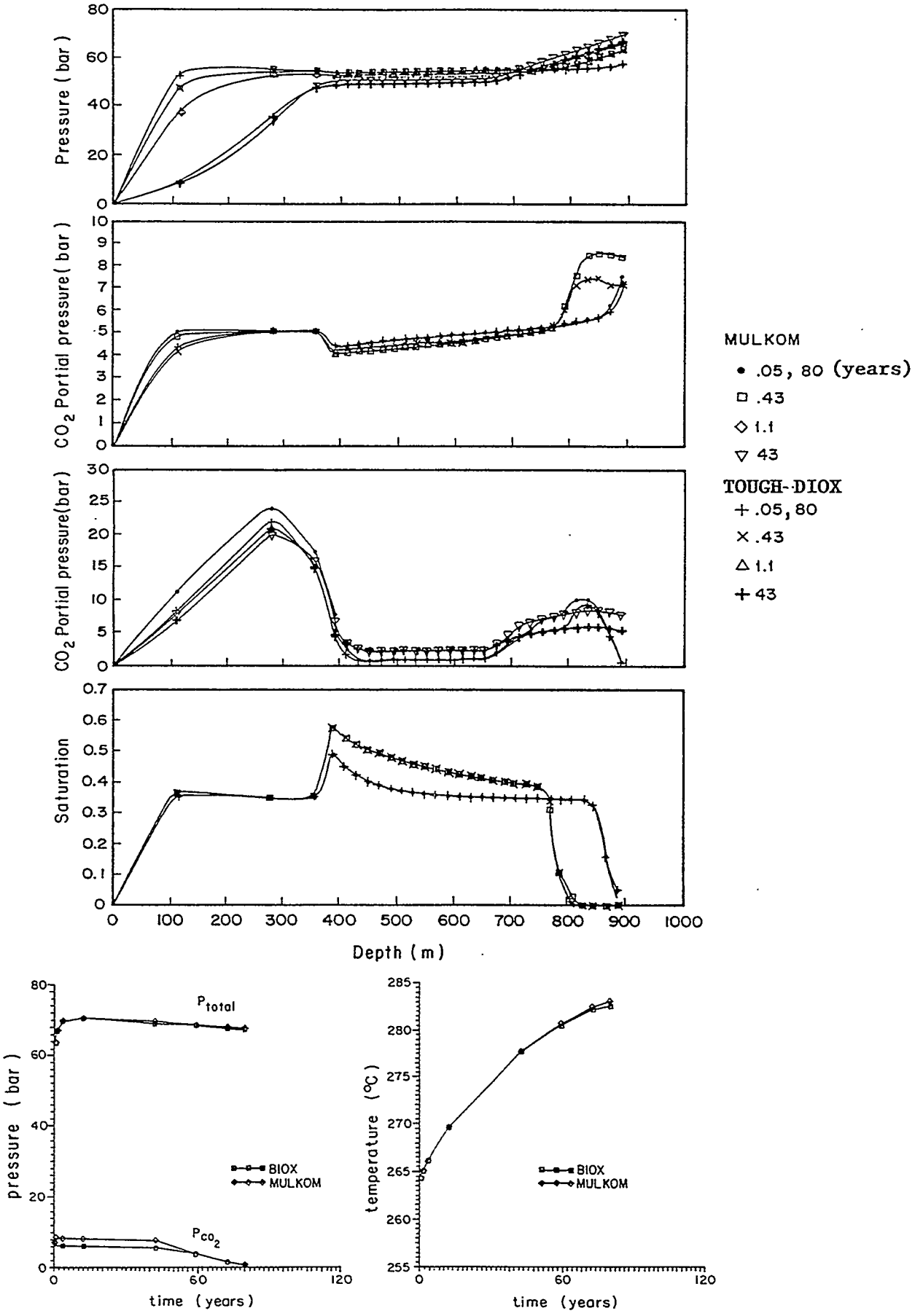

Figure. 2 Validation of the TOUGH- DIOX simulator.

the steam, as much as for the relative permeabilities of the Corey type as for those of the lineal type. The initial conditions correspond to a non-perturbed reservoir by the production under compressed liquid state almost boiling, containing 0.5% of CO_2 mass. Two initial temperatures are under analysis: 250 y 350°C that imply, at the beginning of production, partial pressures of CO_2 of 7 and 4 bar, respectively. The corresponding total pressures are of 50 and 170 bar, in accordance with the diagram of liquid-steam phases of a H_2O-CO_2 binary system containing 0.5% of CO_2 mass.

Each one of the indicated cases in Table 1 is numerically carried out to constant mass production until the quantity of accumulated produced mass reaches a thirty-five per cent of the initial total mass of the geothermal fluid *in situ*. During the transient simulation, the information of pressures is recorded in the reservoir-well interface as well as of the produced fluid enthalpy (flowing enthalpy). This, for the different percentages of accumulated produced mass. The procedure is repeated for other constant mass flows of the production, from the condition on non-perturbed reservoir for the production to the condition of maximum possible mass flow.

Table 1. Cases studied

Initial Temperature (°C)	Absolute Permeability (mD)	Relative Permeability	Cumulative mass produced %
250	10	Corey	5,10,15,20,25, 35
250	10	Lineal	idem
250	100	Corey	idem
250	100	Lineal	idem
350	10	Corey	idem
350	10	Lineal	idem
350	100	Corey	idem
350	100	Lineal	idem

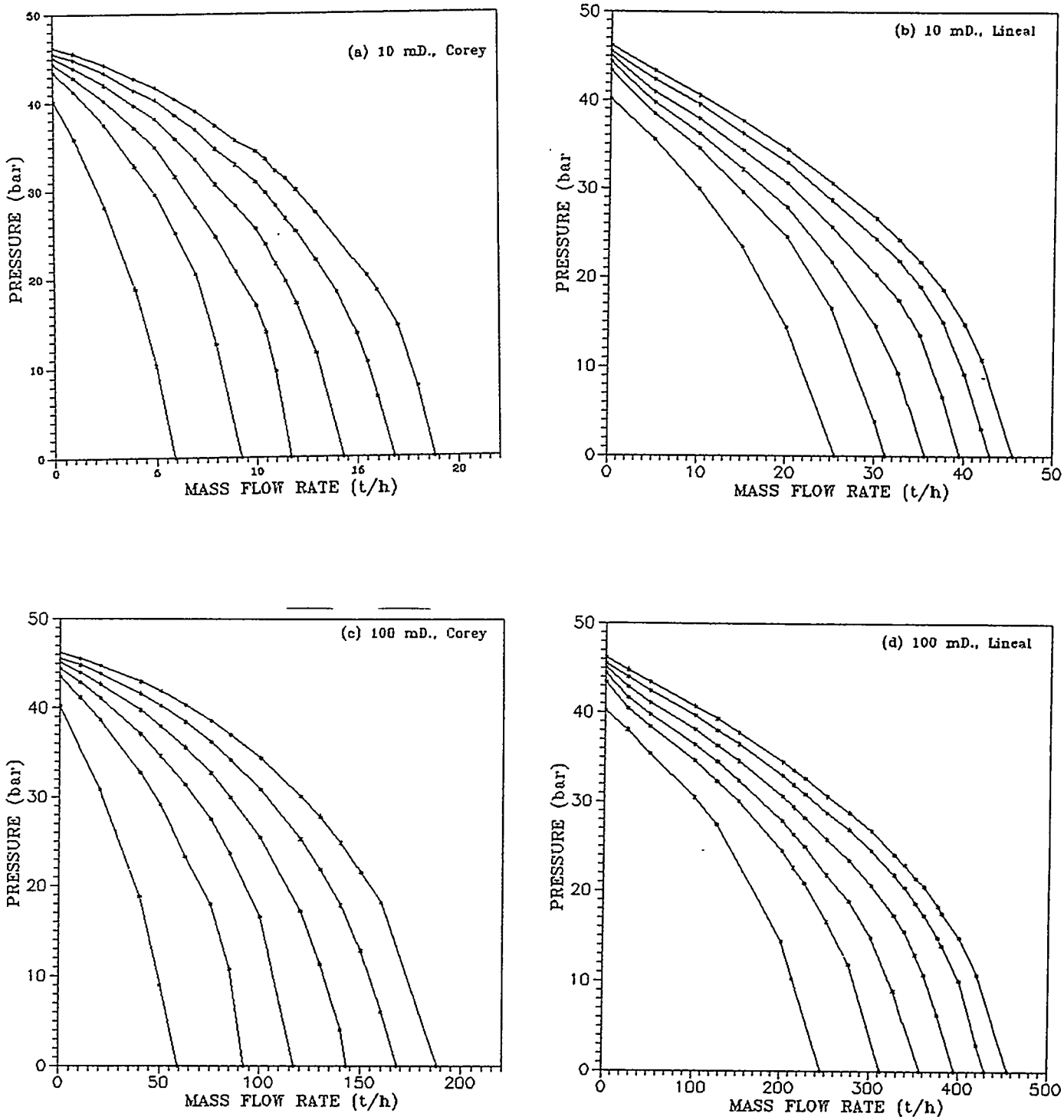

Fig. 3 Inflow performance relationships(IPR) for To=250°C, Po= 50 bar, 0.5% CO_2 initial mass.

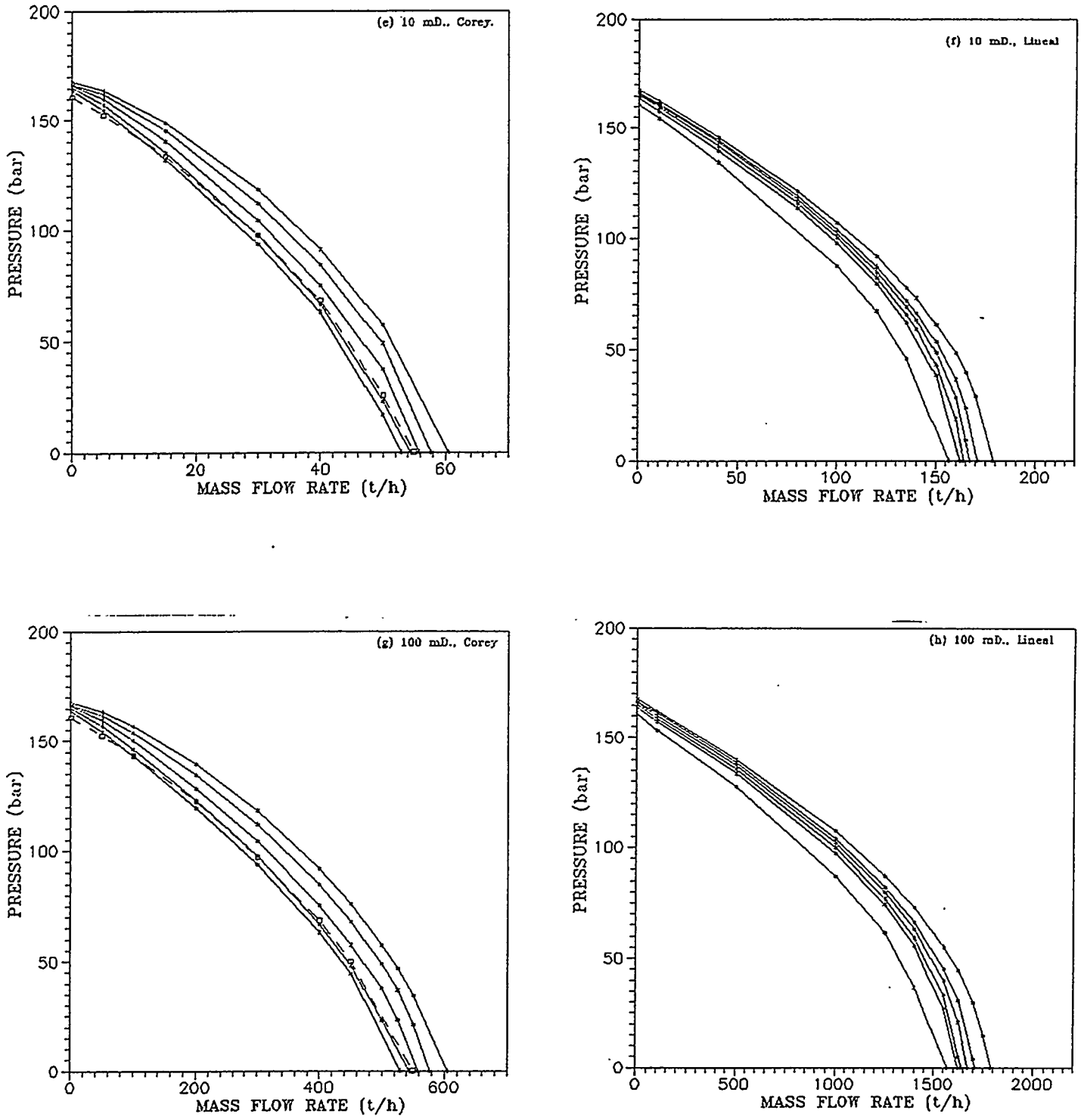

Fig. 3 Inflow performance relationships (IPR) for To=350°C, Po= 170 bar, 0.5% CO_2 initial mass.

Table 2. Formation properties

Porosity	0.10
Density	2,700 kg/cm²
Thermal conductivity	2.00 W/(m °C)
Specific heat	1,000 J/(kg °C)

RESULTS AND DISCUSSION

Reservoir contribution to the mass productivity

Figures 3(a-h) show IPR curves in the indicated order in Tabla 1. These denote the relation between the pressure in the reservoir-well interface and the produced mass flow for the different percentages of accumulated produced mass. The curves present a non-lineal behaviour as expected for 2-phase flows (Muskat, 1937). Some general conclusions can be established: a) the IPR curves for the 10 and 100 mD cases (keeping the other constant parameters) show self-similarity in scale of 10 in accordance with the Darcy law. b) The relative permeability cases of the lineal type allow higher mass flow with respect to the Corey type, between 2 and 3 times more, due to a smaller interference between the liquid and gaseus phases. c) The effect of a higher initial temperature is to permit higher mass flow and with less dependency of the accumulated produced mass.

Adimensional model of mass productivity

On normalizing each IPR curve with the corresponding maximum values of pressure and mass flow, we obtained the dimensionless values shown in figure 4 for all Table 1 cases. The narrow grouping of the dimensionless data outline one curve which we propose as "reference curve" in order to estimate the mass productivity of geothermal wells. This dimensionless reference curve is independent from thermophysical and transport parameters of the reservoir, of the initial conditions and of the grade of explotation of the same. This is the first one that is proposed for geothermal reservoirs containing CO_2.

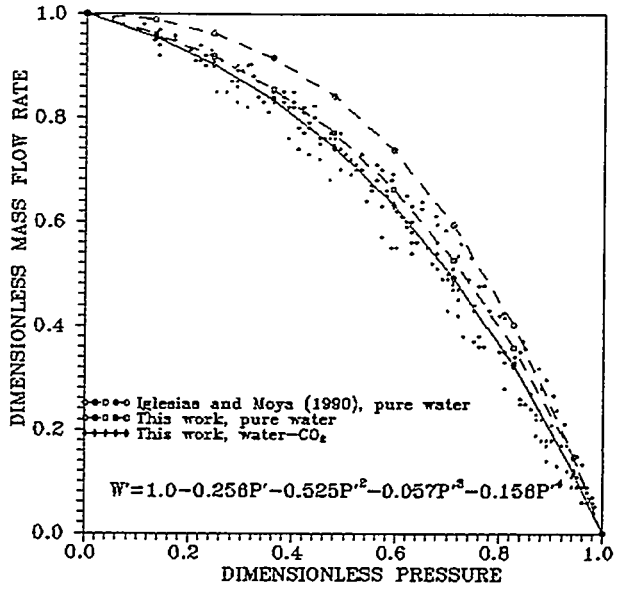

Fig. 4 Comparation of reference curves

Gunn and Freeston (1991) found a mistake of up to 30% on applying the former IPR (Iglesias and Moya, 1990), for the pure water system, to the Broadlands 13 well in New Zealand. This error could notoriously decrease if corresponding IPR to binary system would be applied. As it is wellknown, significative CO_2 amounts are found in Broadlands.

Reservoir contribution to the thermal productivity

Unlike the Oil Industry, the main geothermal recourse is the heat. The geothermal productivity is referred to the speed with which energy can be extracted as heat. It is necessary to produce fluid in order to extract heat. Consequently, heat and fluid productivities must be related with each other. The thermal power is the speed with which energy can be extracted as heat and it is the product of the specific enthalpy and the mass flow of the discharge. The Figure 5 shows, as an example, the GIPR curve corresponding to the IPR curve of the figure 3.a (for 250°C, 10 mD and relative permeability of Corey type). As it is seen, the thermal power is higher if mass flow is higher. On the other hand, the more advanced is the explotation range of the reservoir, the more effective is the thermal power obtained. This is as a consequence of the increase in the produced steam saturation and, consequently, of the flowing enthalpy. It must be reminded that no recharges are considered in this study. The GIPR curves reflect in general that the explotation of the geothermal energy is intimately linked with the extraction of the geothermal fluid.

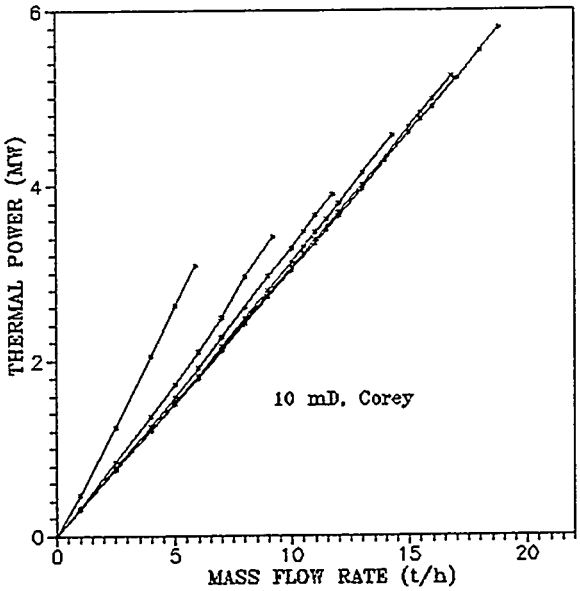

Fig. 5 Characteristics curves of thermal productivity for T_o=250°C, P_o=50 bar, and 0.5 CO_2 initial mass

Adimensional model of thermal productivity.

On normalizing each GIPR curve with the corresponding maximum values of thermal power and mass flow, we obtained the reference curve shown in Figure 6. The notable self-similarity of the dimensionless data reflects that heat deliverability in closed reservoirs is insensitive to undisturbed reservoir initial conditions, fluid and formation properties and history of reservoir production. This is due to the fact of that geothermal heat reserves residing overwhelmingly in the rock formation and not in the fluid.

Effect of CO_2 on mass and thermal productivities

In order to determinate the effect that the presence itself of CO_2 have on the productivities, the preceding study was conformed also for a pure water system. By comparation of the IPR and GIPR curves corresponding to binary system, with that corresponding to pure water system (no shown here),

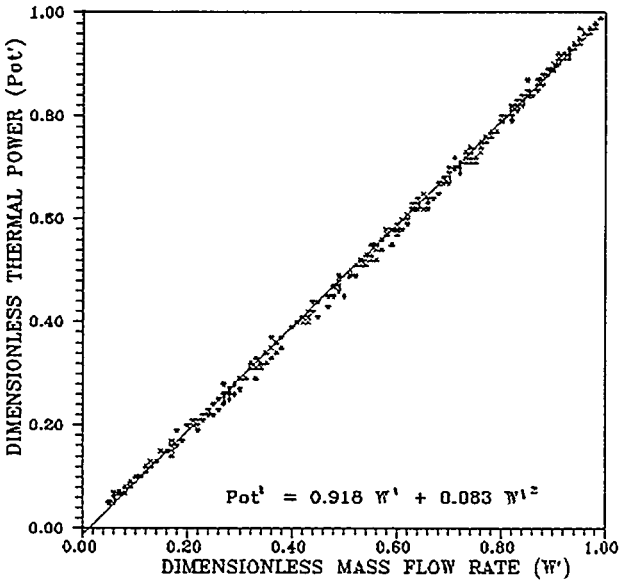

Fig. 6 Thermal productivity reference curve proposed for geothermal reservoir with CO_2.

it is conclude that the mass flows, and therefore the thermal powers, are higher for the binary system (up to 2 times more). This principally for the 250°C initial temperatura cases, at begining of the production, when the partial pressures of CO_2 are more important.

The Figure 4 includes the reference IPR curve obtained in this work for the pure water system. It is also compared with the one previously obtained (Iglesias y Moya, 1990) by means of another less adequate numerical methodology. By comparation of both curves for pure water with the obtained for the binary system, it is evident that the presence of CO_2 influences notoriously in the behaviour of the productivities, even though the initial concentration of CO_2 considered was scarcely of 0.5% in mass.

CONCLUSIONS

The numerical results presented under IPR and GIPR curves denote, respectively, the behaviour of mass and energy productivities of geothermal wells. This behaviour is a reflect of the properties of rock formation and of fluid, of the initial conditions and the history of the reservoir production.

The IPR and GIPR curves normalized with the corresponding maximum values of pressure, mass flow and thermal power, dimensionless curves, trend to collapse in relatively narrow zones, in spite of the wide ranges of properties of the rock-fluid media, of initial conditions and of the percentage of accumulated produced mass. Taking advantage of this self-similarity, two dimensionaless reference curves are proposed for the binary system H_2O-CO_2, one for mass productivity (figure 4) and another one for thermal productivity (figure 6). These curves, in conjunction with a few ground measurements (mass flow and discharge enthalpy, plus a determination of downhole pressure) allow to estimate the mass and energy productivities of geothermal wells for short, medium and long terms.

Nevertheless the presence of CO_2 in geothermal reservoirs affects negatively to the enthalpy content of the produced fluid, it helps to obtain higher mass flows and consequently, thermal powers also higher.

REFERENCES

Andersen G., Probst A., Murray L. and Buttler S., 1992. An accurate PVT model for geothermal fluids as represented by H_2O-CO_2-NaCl mixtures, Proceeding of the 18th Workshop on Geothermal Reservoir Engineering, Stanford CA.

Bodvarsson G.S., 1984. Numerical studies of enthalpy and CO_2 transients in two-phase wells, Geothermal Resources Council, TRANSACTIONS, Vol.8, 289-294.

Bodvarsson G.S., Gaulke S., 1987. Effects of noncondensible gases on fluid recovery in fractured geothermal reservoirs, SPE Reservoir Engineering, Agosto, 335-342.

Gaulke S.W., 1986. The effect of CO_2 on reservoir behavior for geothermal systems, Tesis de Maestría, LBL-22720.

Gilbert W.E., 1954. Flowing and gas-lift well performance, Drill. and Prod. Prac., API, 126-.

Grant M., Glover R., 1984. Two-phase heat and mass transfer experiment at well BR21 Broadlands, Geothermics, Vol.13, No.3, 193-213.

Iglesias E.R., Moya S.L., 1990. Geothermal inflow performance relationships, Geothermal Resources Council TRANSACTIONS, Vol.14, part II, 1201-1205.

Iglesias E.R., Moya S.L., 1993. Investigación de yacimientos geotérmicos fracturados, INFORME IIE/11/5014/I 01/F. 33 pp.

Lippman M.J., Bodvarsson G.S., Gaulke S.W., 1985. Enthalpy transients in fractured two-phase geothermal reservoirs, Geothermal Resources Council Transactions, 9.

Majumdar A.J., Roy R., 1956. Fugacities and free energies of CO_2 at high pressure and temperature, Geochim. Cosmochim. Acta, Vol.10, No.3, 311-315.

Moya S.L., 1989. Programa LAIGAG; INFORME IIE/11/2081/I 02/P, 35 pp.

Moya S.L., Iglesias E.R., 1992. Solubilidad del bióxido de carbono en agua en condiciones geotérmicas, Geofísica Internacional, Vol. 31, No. 3, 305-313.

Moya S.L., 1994. Efectos del bióxido de carbono sobre el transporte de masa y energía en yacimientos geotérmicos, Tesis Doctoral, DEPFI-UNAM.

Moya S.L., 1989. Programa LAIGAG, INFORME IIE/11/2081/I 02/P.

Muskat, 1937. Use of data on the build-up of bottom-hole pressures, Trans. AIME, Vol. 123, 44-48.

O'Sullivan M.J., Bodvarsson G.S., Pruess K., Blackeley M.R., 1985. Fluid and heat flow in gas-rich geothermal reservoirs, SPEJ 12102, 215-226.

Prausnitz J.M., 1969. Molecular thermodynamics of fluid-phase equilibria, Prentice Hall Inc.

Pritchett J.W., Rice M.H., Riney T.D., 1981. Equation of State for water-carbon dioxide mixtures: implications for Baca Reservoir, DOE/ET/27163-8.

Pritchett J.W., 1994. STAR-A general-purpose geothermal reservoir simulator, GRC BULLETIN, 139-141.

Pruess K., Celati R., Calore C., D'Amore F., 1985. CO_2 trends in the depletion of the Larderello vapor-dominated reservoir, Proc. Tenth Workshop on Geothermal

Reservoir Engineering, Stanford University, Stanford, California.

Pruess K., 1987. TOUGH User's Guide; REPORT LBL-20700, Lawrence Berkeley Laboratory, 78 pp.

Pruess K., 1988. SHAFT, MULKOM, TOUGH: A set of numerical simulator for multi-phase fluid and heat flow, Geotermia; Rev. Mex. de Geoenergía, Vol.4, 185-202.

Sorey M.L., Grant M.A., Bradford E., 1980. Nonlinear effects in two-phase flow to wells in geothermal reservoirs, Water Resources Research, Vol.16, No.4, 767-777.

Spycher N.F., Reed M.H., 1988. Fugacity coefficients of H_2, CO_2, CH_4, H_2O and of H_2O-CO_2-CH_4, mixtures: A virial equation treatment for moderate pressures and temperatures applicable to calculations of hydrothermal boiling, Geochim. Cosmochim. Acta, Vol.52, 739-749.

Suárez M.C., Pruess K., Lippman M., 1989. Preliminary modeling studies on Los Azufres Geothermal fields: Free convection in Tejamaniles, Workshop of Stanford Meeting, 161-172.

Sutton F.M., 1976. Pressure-temperature curves for a two-phase mixture of water and carbon dioxide, New Zealand Journal of Science, Vol.19, 297-301.

Takenouchi S., Kennedy G.C., 1964. The binary system H_2O-CO_2 at high temperatures and pressures, Am. J. Science, Vol.262, 333-337.

Vogel J.V., 1968. Inflow performance relationships for solution-gas drive wells, J. Pet. Tech., January, 83-92.

FOAM3D: A Numerical Simulator for Mechanistic Prediction of Foam Displacement in Multidimensions

A. R. Kovscek[1], T. W. Patzek[1,2], and C. J. Radke[1,3]

[1] Earth Sciences Division, Lawrence Berkeley Laboratory,
[2] Dept. of Materials Science and Mineral Engineering
[3] Dept. of Chemical Engineering
University of California, Berkeley, CA 94720

INTRODUCTION

Field application of foam is a technically viable enhanced oil recovery process (EOR) as demonstrated by recent steam-foam field studies [1,2]. Traditional gas-displacement processes, such as steam drive, are improved substantially by controlling gas mobility and thereby improving volumetric displacement efficiency. For instance, Patzek and Koinis [2] showed major oil-recovery response after about two years of foam injection in two different pilot studies at the Kern River field. They report increased production of 5.5 to 14% of the original oil in place over a five year period.

Because reservoir-scale simulation is a vital component of the engineering and economic evaluation of any EOR project, efficient application of foam as a displacement fluid requires a predictive numerical model of foam displacement. A mechanistic model would also expedite scale-up of the process from the laboratory to the field scale. No general, mechanistic, field-scale model for foam displacement is currently in use.

The population balance method for modeling foam in porous media [3] is mechanistic and incorporates foam into reservoir simulators in a manner that is analogous to energy and species mass balances. Accordingly, a separate conservation equation is written for the concentration of foam bubbles (i.e., texture). This simply adds another component to a standard compositional simulator.

This paper extends our one-dimensional foam displacement model [4,5] to multidimensional, compositional reservoir simulation. We have incorporated a conservation equation for the number density of foam bubbles into M2NOTS [6], a variant of TOUGH2. The foam conservation equation is treated with a fully implicit, backward differencing scheme, in analogy to the other component mass balances. The simulator employs saturation and surfactant-concentration-dependent rate expressions for lamella formation and destruction. Lamella mobilization is similarly included. To allow direct comparison with our previous one-dimensional results [4,5] , we discuss only isothermal and oil-free systems.

Foam in Porous Media

Foam microstructure in porous media is unique [7] and determines gas mobility within porous media. Accordingly, to model gas mobility it is important to understand foamed-gas microstructure. In water-wet porous media, the wetting surfactant solution remains continuous, fills the smallest pore spaces, coats pore walls in gas-occupied regions. Gas bubbles flow through the largest, least resistive pore space while significant bubble trapping occurs in the intermediate-sized pore channels where the local pressure gradient is insufficient to mobilize lamellae.

Foam reduces gas mobility in two manners. First, stationary or trapped foam blocks a large number of channels that otherwise carry gas. Gas tracer studies [8] show that the fraction of gas trapped within a foam at steady state in sandstones is quite large and lies between 85 and 99%. Second, bubble trains within the flowing fraction encounter significant drag because of the presence of pore walls and constrictions, and because the gas/liquid interfacial area of a flowing bubble is constantly altered by viscous and capillary forces. Hence, foam mobility depends strongly on the fraction of gas trapped and on the texture or number density of foam bubbles.

Bubble trains are in a constant state of rearrangement by varied foam generation and destruction mechanisms [7]. Individual foam bubbles are molded and shaped by pore-level making and breaking processes that depend strongly on the porous medium. More detailed summaries of the pore-level distribution of foam and of the mechanisms controlling texture are given in refs. [4] and [7].

FOAM DISPLACEMENT MODEL

The power of the population balance method lies in addressing directly the evolution of foam texture and, in turn, reductions in gas mobility. Gas mobility is assessed from the concentration of bubbles. Further, the method is mechanistic in that well-documented pore-level events are portrayed in foam generation, coalescence, and constitutive relations. Most importantly, the population balance method provides a general framework where all the relevant physics of foam generation and transport may be expressed. Only a brief summary of the method is given here as considerable details are available in the literature [4,5].

The requisite material balance equations for chemical species i during multiphase flow in porous media are written

$$\frac{\partial}{\partial t}\left[\phi\sum_j (S_j C_{i,j} + \Gamma_{i,j})\right] + \sum_j \nabla\bullet\vec{F}_{i,j} = \sum_j q_{i,j} \quad (1)$$

where S is the saturation of phase j, C is the molar concentration of species i in phase j, Γ is the absorption or partitioning losses of species i from phase j in units of moles per void volume, $\vec{F}$ is the vector of convective plus diffusive flux of species i in phase j, and q is a rate of generation of i in phase j per unit volume of porous medium. To obtain the total mass of species i, we sum over all phases j.

In the foam bubble population balance, $S_f n_f$ replaces $S_i C_{i,j}$ where n_f is the number concentration or number density of foam bubbles per unit volume of flowing gas, and S_f is the saturation of flowing gas. Hence, the first term of the time derivative is the rate at which flowing foam texture becomes finer or coarser per unit rock volume. Since foam partitions into flowing and stationary portions, Γ becomes $S_t n_t$ where S_t and n_t are the saturation of the stationary gas and the texture of the trapped foam per unit volume of trapped gas, respectively. Thus, the second term of the time derivative gives the net rate at which bubbles trap. Trapped and flowing foam saturation sum to the overall gas saturation, $S_g = S_f + S_g$. The second term on the left of Eq. (1) tracks the convection of foam bubbles where the flux, $\vec{F}$, is given by $\vec{u}_f n_f$, and $\vec{u}_f$ is the Darcy velocity of the flowing foam. Finally, q becomes the net rate of generation of foam bubbles. Because foam is present only in the gas phase, there is no need to sum over all phases. Within the above framework, foam is a component of the gas phase, and the physics of foam generation and transport become amenable to standard reservoir simulation practice.

The net rate of foam generation:

$$q_f = \phi S_g\left[k_1|\vec{v}_w||\vec{v}_f|^{1/3} - k_{-1}(P_c)|\vec{v}_f n_f|\right] \quad (2)$$

is written per unit volume of gas. In the simulations to follow, we do not inject pregenerated foam, and so, we do not require a source/sink term for bubbles. Interstitial velocities, *i.e.*, $\vec{v}_i = \vec{u}_i/\phi S_i$, are local vector quantities that depend on the local saturation and total potential gradient, including gravity and capillary pressure. Foam generation arises from snap-off of gas, and is expressed as a power-law relationship that is proportional to the magnitude of the flux of surfactant solution multiplied by the 1/3 power of the magnitude of the interstitial gas velocity [9]. The liquid-velocity dependence originates from the net imposed liquid flow through pores occupied by both gas and liquid, while the gas-velocity dependence arises from the time for a newly formed lens to exit a pore [9]. Snap-off is sensibly independent of surfactant properties consistent with its mechanical origin [7].

To prevent coalescence of newly formed gas bubbles, a surfactant must stabilize the thin-liquid films. Foam lamellae form given sufficient suction capillary pressure and a stabilizing surfactant. However, too high a suction-capillary pressure will collapse a lamella [7]. A flowing lamella is vulnerable to breakage in termination sites as it flows into a divergent pore space where it is stretched rapidly. If sufficient time does not elapse for surfactant solution to flow into a stretched lamella and heal it, coalescence ensues.

Equation (2) shows that foam lamellae are destroyed in proportion to the magnitude of their interstitial flux, $\vec{v}_f n_f$, into such termination sites. The coalescence rate constant, $k_{-1}(P_c)$, varies strongly with the local capillary pressure and surfactant formulation. It is given by

$$k_{-1}(P_c) = k^o_{-1}\left(\frac{P_c}{P_c^* - P_c}\right)^2, \quad (3),$$

where the scaling factor, k^o_{-1}, is taken as a constant and P_c^* is the limiting capillary pressure for foam coalescence [10].

The "limiting capillary pressure," P_c^*, as identified by Khatib *et al* [10] refers to the characteristic value of capillary pressure that a porous medium approaches during strong foam flow and is set primarily by surfactant formulation and concentration. Highly concentrated foamer solutions and robust surfactants lead to high a P_c^*. Equation (3) correctly predicts that at high capillary pressures or for ineffective foamer solutions, k_{-1} is quite high [10]. The foam coalescence rate approaches infinity as the porous medium capillary pressure approaches P_c^*.

In addition to bubble kinetic expressions, the mass balance statements for chemical species demand constitutive relationships for the convection of foam and wetting liquid phases. Darcy's law is retained, including standard multiphase relative permeability functions. However, for flowing foam, we replace the gas viscosity with an effective viscosity relation for foam. Since flowing gas bubbles deposit and slide over thin lubricating films of wetting liquid on pore walls, they do not exhibit a Newtonian viscosity. We adopt an effective viscosity relation that increases foam effective viscosity as texture increases, but is also shear thinning

$$\mu_f = \mu_g + \frac{\alpha n_f}{|\vec{v}_f|^{1/3}}. \quad (4),$$

where α is constant of proportionality dependent mainly upon the surfactant system. In the limit of no flowing foam, we recover the gas viscosity. This relation is consistent with the classical result of Bretherton [11] for slow bubble flow in capillary tubes .

Finally, stationary foam blocks large portions of the cross-sectional area available for gas flow and, thus, must be accounted for to determine gas flux. Since the portion of gas that actually flows partitions selectively into the largest, least resistive flow channels, we adopt a standard Stone-type model [12] for relative permeability that, along with effective viscosity, specifies gas-phase flow resistance. Because wetting aqueous liquid flows in the smallest pore space, its relative permeability is unaffected by the presence of flowing and stationary foam. Since flowing foam partitions selectively into the largest pore space, the relative permeability of the nonwetting flowing gas is a function of only S_f. Consequently, gas mobility is much reduced in comparison to an unfoamed gas propagating through a porous medium, because the fraction of gas flowing at any instant is quite small [8].

FOAM3D

We treat foam bubbles within FOAM3D as an insoluble, chemically inert component of the gas phase. Thus, the additional transport equation for foam bubble texture described above is added to the mass balances for water, gas, and n organic components. The discretized foam bubble equation is fully implicit with upstream weighting of the gas-phase mobility consistent with all other chemical species. In each grid block, the magnitude of the vectors representing the interstitial gas and liquid velocities are used to compute foam generation and coalescence rates from Eq. (2). The magnitude of each velocity is obtained by first summing the flow of each phase into and out of a grid block in the three orthogonal directions. Then the average flow in each direction is taken and the magnitude of the resultant vector used to calculate foam generation and coalescence rates.

Numerical values of the population balance simulation parameters are determined from only steady-state measurements in one-dimensional linear flow. Steady-state flow trends, saturation, and pressure drop profiles are matched. These can all be obtained within one experimental run. The suite of foam displacement parameters are not adjusted to accommodate different types of transient injection or initial conditions. Parameter values used here are taken from refs. [4,5] and apply specifically to very strong foams in the absence of oil.

NUMERICAL MODEL RESULTS

Because there are many initial conditions, types of injection, and multidimensional geometries of interest, we present the results from only two illustrative examples. First, we compare simulator predictions against experimental results for the simultaneous injection of nitrogen and foamer solution into a linear core saturated with surfactant. Second, foam displacement is simulated in a two-dimensional linear layer with gravity. To avoid confusion between foam formation, surfactant propagation and adsorption, foam-oil interaction, and partitioning of surfactant into the oil phase, we choose a porous medium that is fully saturated with surfactant solution as the initial condition. That is, $S_w = 1$, initially and rock adsorption of surfactant is satisfied. Nitrogen and foamer solution are coinjected simultaneously. Thus, we focus attention on foam formation, coalescence, transport, and reduction of gas mobility.

Linear Core

In the first example, nitrogen is injected continuously into a linear core of length 0.60 m at a rate of 0.43 m/day relative to the exit pressure of 4.8 MPa. Foamer solution is also injected continuously at 0.046 m/day to give a quality or gas fractional flow of 0.90 at the core exit. These flow rates and initial conditions correspond exactly to previous experiments conducted in a 1.3-μm^2 Boise sandstone [4,5] with a length of 0.60 m. The foamer was a saline solution (0.83 wt% NaCl) with 0.83 wt% active AOS 1416 (C_{14-16} alpha olefin sulfonate, Bioterg AS-40, Stepan).

Figures 1 and 2 display the transient experimental and simulated saturation and pressure profiles, respectively. Figure 3 displays the foam texture profiles generated by FOAM3D. Simulator results are represented by solid lines. Dashed lines simply connect the individual data points. Elapsed time is given as pore volumes of total fluid injected, that is, as the ratio of total volumetric flow rate at exit conditions multiplied by time and divided by the core void volume.

Steep saturation fronts are measured and predicted at all time levels in Fig. 1 whereby aqueous phase saturation upstream of the front is roughly 30% and downstream it is 100%. Model fronts are somewhat steeper and sharper than those measured experimentally, but the theoretical saturation profiles track experimental results very well. From the saturation profiles, it is apparaent that foam moves through the core in a piston-like fashion. Rapid foam generation and liquid desaturation occur at the core inlet, even though nitrogen and surfactant solution are injected separately. A region of net foam generation near the core inlet is evident in the transient pressure profiles of Fig. 2. Pressure gradients near the inlet are shallow, indicating that flow resistance is small and foam textures are coarse consistent with the injection of unfoamed gas. Figure 3 reports the predicted foam texture as a function of dimensionless distance and time. We find a coarsely textured foam near the inlet, but beyond the first fifth of the core, foam texture becomes very fine and nearly constant at each time level. High pressure gradients and fine foam textures are seen where liquid saturation is low and *vice versa*.

Figure 4 contrasts the highly efficient foam displacement above by displaying a simulated gas displacement. Initially the core is completely filled with aqueous liquid, but no stabilizing surfactant is present.

Whereas foam displacement is characterized by steep, sharp saturation fronts and long times to the first appearance of foam at the core outlet, gas displacement is characterized by the slow displacement of water and the early appearance of gas at the production end of the core. Obviously, foam increases gas displacement efficiency in linear core floods by several orders of magnitude.

Homogeneous Linear Layer with Gravity

The second example is foam generation in a linear, 1.3-μm^2, homogeneous layer where gravitational effects are appreciable. The layer is 0.6 m square with impermeable top and bottom boundaries. The y-axis corresponds to the vertical direction and the scale gives the distance from the origin in meters. Unfoamed gas and surfactant solution are injected in the lower quarter of the left boundary and production occurs at the right boundary against a constant pressure of 4.8 MPa. Injection rates are identical to the previous linear case: 0.43 m/day of gas and 0.046 m/day of foamer solution, where these superficial velocities are taken over the entire vertical interval.

To contrast foamed and unfoamed gas injection, Figure 5 displays the gas saturation contours after 0.10 PV of total injection in the complete absence of surfactant. The gray-scale shading of the figure illustrates the gas saturation. Unshaded portions of the figure refer to a gas saturation of zero and progressively darker shading refers to larger gas saturations. Black shading refers to a gas saturation of one. In Fig. 5, the areas contacted by gas are poorly swept as indicated by their light gray shading. Further, the unfoamed gas is quickly driven toward the top of the layer by buoyancy. A tongue of gas forms along the upper boundary due to gravity override that leaves areas along the lower horizontal boundary unswept by gas.

When surfactant solution initially saturates the homogeneous layer, foam generation is rapid and provides effective control of gravity override, as illustrated in Fig. 6. Figure 6a gives the gas saturation contours at 0.10 PV of total gas and foamer solution injection. This plot is dramatically different from Fig. 5. First, foam propagates spherically. Buoyancy-driven flow of gas upward causes foam generation and an increase in flow resistance that slows upward gas propagation. To balance flow resistance, foam generates almost equally in the horizontal and vertical directions, leading to spherical growth of the foam-filled zone. Additionally, the gas saturations in Figure 6a show that efficient displacement is occurring. The dark, nearly uniform shading of the foam-filled region corresponds to a gas saturation of roughly 0.70. The gas saturation falls off abruptly at the edges of the gas-filled region, indicating a sharp displacement front.

Figures 6b through 6d display the subsequent gas saturation contours at times of 0.20, 0.30, and 0.40 PV, respectively. Spherical growth of the foam zone and efficient displacement continue as illustrated by these figures. Foam, in this example, effectively negates gravity override. When foam reaches the upper boundary of the layer, displacement continues toward the right in the horizontal direction as a piston-like front that expels the surfactant-laden water.

SUMMARY

We have shown that it is possible to model foam displacement mechanistically in multidimensions. Beginning with M2NOTS, an n-component compositional simulator, the foam bubble population balance equations are successfully incorporated within the simulator's fully implicit framework. The mechanistic population balance approach allows us to insert the physics of foam displacement directly into a reservoir simulator. Foam is treated as a insoluble, chemically inert "component" of the gas phase and the evolution of foam texture is modeled explicitly through pore-level foam generation and coalescence equations. As foam mechanisms become better understood, this framework allows for their inclusion.

REFERENCES

1. Friedmann, F., M.E. Smith, W.R. Guice, J.M. Gump, and D.G. Nelson, *Soc. Pet. Eng. Res. Eng*, 9 (1994) 297-304.
2. Patzek, T.W. and M.T. Koinis, *J. Petr. Tech.*, 42 (1990) 496-503.
3. Falls, A.H., G.J. Hirasaki, T.W. Patzek, P.A. Gauglitz, D.D. Miller, and T. Ratulowski, *Soc. Pet. Eng. Res. Eng.*, 3 (1988) 884-892.
4. Kovscek, A.R. and C.J. Radke, in *Foams in the Petroleum Industry*, L.L. Schramm, (Ed.), American Chemical Society, Washington, D.C., 1994, 115-163.
5. Kovscek, A.R., T.W. Patzek, and C.J. Radke , SPE 26402, presented at the the 68th Annual Technical Conference of SPE, Houston, TX, October 1993.
6. Adenekan, A.E., T.W. Patzek, and K. Pruess, *Water Resources Research*, 29 (1993) 3727-3740.
7. Chambers, K.T. and C.J. Radke, in *Interfacial Phenomena in Petroleum Recovery*, N.R. Morrow, (Ed.), Marcel Dekker Inc., New York, 1991, 191-255.
8. Gillis, J.V. and C.J. Radke, SPE 20519, presented at the 65th SPE Annual Technical Conference, New Orleans, LA, September, 1990.
9. Kovscek, A.R., *Foam Displacement in Porous Media: Experiment and Mechanistic Prediction by the Population Balance Method,* Ph.D. Thesis, University of California, Berkeley, 1994.
10. Khatib, Z.I., G.J. Hirasaki, and A.H. Falls, *Soc. Pet. Eng. Res. Eng.*, 3 (1988) 919-926.
11. Bretherton, F.P., *J. Fluid Mech.*, 10 (1961) 166-188.
12. Stone, H.L., *J. Pet. Tech.*, 22 (1970) 214-218.

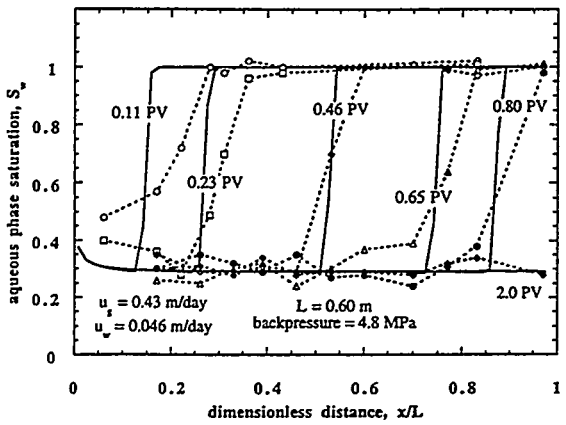

Figure1: Experimental and model transient aqueous-phase saturation profiles for the simultaneous injection of gas and foamer solution at fixed mass rates. The porous medium is presaturated with surfactant solution.

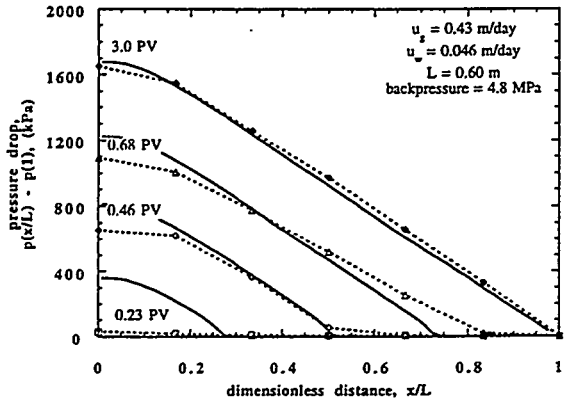

Figure 2: Experimental and model transient pressure profiles for the simultaneous injection of gas and foamer at fixed mass rates. The porous medium is presaturated with surfactant solution.

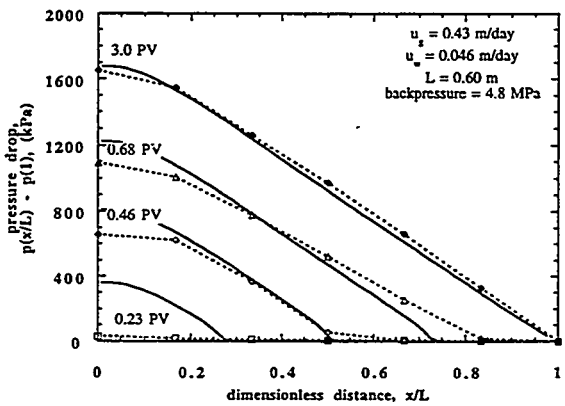

Figure 2: Experimental and model transient pressure profiles for the simultaneous injection of gas and foamer at fixed mass rates. The porous medium is presaturated with surfactant solution.

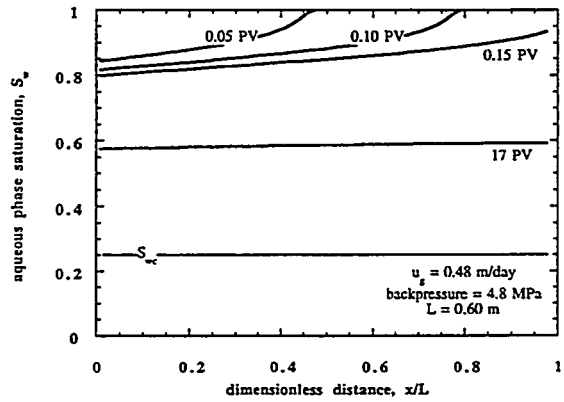

Figure 4: Transient aqueous-phase saturation profiles for the continuous injection of unfoamed gas.

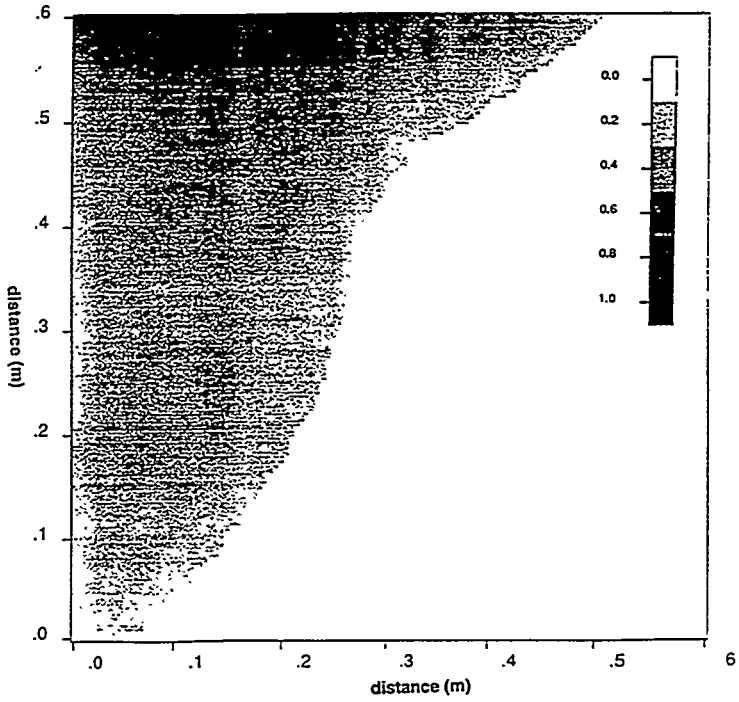

Figure 5: Gas saturation profile after 0.10 PV of unfoamed gas and liquid injection into a homogeneous linear layer.

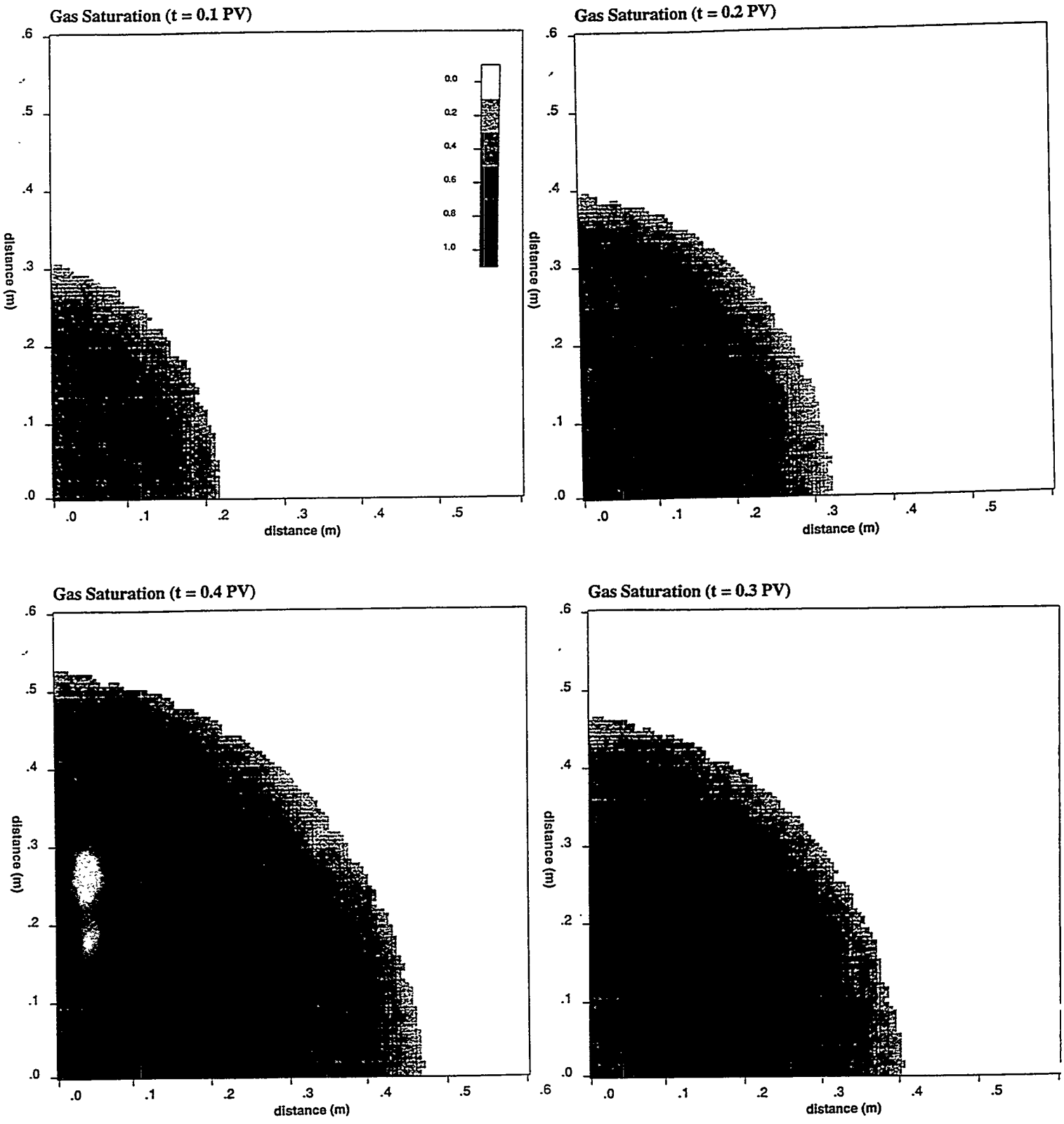

Figure 6: Gas saturation profile after (a) 0.10 PV, (b)0.20 PV, (c) 0.30 PV, and (d) 0.40 PVof foam injection into a homogeneous linear layer.

Three-Dimensional Multiphase Effects in Aquifer Gas Storage

by P. A. Witherspoon, P. Fuller and S. Finsterle
Earth Sciences Division, Lawrence Berkeley Laboratory,
University of California, Berkeley, CA 94720

Introduction

The underground storage of natural gas in the United States is one of the most widespread methods of storing energy in the United States. There are two main kinds of storage: (a) dry gas fields, and (b) aquifer storage fields. The storage of gas in dry gas fields involves the conversion of petroleum bearing reservoirs, usually after they have been depleted of any economic production, into a storage operation. An appropriate number of injection-withdrawal (I-W) wells are either drilled or converted from existing exploitation wells, and the storage operations begin by injecting gas to build up to some desired volume of gas in storage.

The storage of gas in aquifers involves finding a suitable anticlinal structure that contains permeable beds of sufficient thickness and areal extent with adequate closure to contain the desired storage volume. These beds are usually water-filled sandstone formations, 100 ft or more in thickness with an overlying relatively impermeable layer that serves as the "caprock" or barrier to vertical migration. Depths below the surface commonly range from 1,000 ft to 4,000 ft, and since the hydraulic heads in the aquifers are under normal hydrostatic control, the operating pressures for the gas "bubble", as it is termed, range from 500 psi to 2,000 psi.

The gas storage operation requires a certain number of I-W wells to be drilled at the crest of the anticline so that: (a) a relatively low rate of gas injection can be used to fill the structure at the end of each withdrawal period, and (b) an adequate number of wells is available to enable the field to deliver gas at a rate sufficient to meet the maximum anticipated demand. The initial development requires the injection of gas in only one or two I-W wells so that a gas saturated region can build at the crest and displace water down the flanks of the structure. As the bubble grows, additional I-W wells must be put in operation to hasten development. Normally, two to three years of uninterrupted injection are needed to grow the gas bubble to a desired total volume, which can range from 10 to 50 BCF (billion standard cubic feet) or more. Water observation wells are completed in the reservoir sand far enough out on the flanks of the structure to be beyond the maximum anticipated extent of the gas bubble. This provides a means of monitoring pressures in the water phase outside the gas bubble to correlate with those that are being measured in the gas bubble at the top of the structure.

Major development of aquifer gas storage started in the 1950's, and at the end of 1993, there were 45 storage projects in eight states with a total volume of 1,104 BCF of gas

in storage (AGA Statistics Task Group, 1993). The great bulk of this gas (95%) is being stored in just three states: Illinois, Indiana and Iowa. The value of this method of energy storage is evident from the fact that the demand for gas in the Chicago area during a severe cold period can increase in a matter of a few hours from a daily rate of about 2 BCF to 4 BCF. Some 15 gas storage projects have been developed in northern Illinois to serve this metropolitan area, and they can easily supply the gas volumes to meet such a demand.

One of the key problems in aquifer gas storage is to know where the gas bubble has developed as the water is displaced down structure. This is important because one needs an effective location for the I-W wells to maximize the efficiency of operation. The wells should be properly located on the structure and completed over a vertical interval of the reservoir sand so as to enable the desired rates of injection to be achieved, but more importantly to maximize the flow of gas and minimize the flow of water during the withdrawal period. This requires a detailed knowledge of how the injected gas invades the reservoir and develops into a man-made gas field. This, of course, is a three-dimensional problem, and after 40 years, it has not yet been solved satisfactorily, primarily because the technology to locate the gas phase away from the wellbore is still being developed.

We have been using the TOUGH2 code (Pruess, 1991) to investigate this problem because if the controlling parameters of the displacement process can be determined, one should be able to achieve an adequate description of the dynamics of the process and thus the geometry of the gas bubble. Field data from the Hillsboro aquifer gas storage project in Montgomery County, Illinois have been used in developing a numerical model. This project was developed in 1973 by the Illinois Power Company and currently has a total of 21.7 BCF in storage in the St. Peter sandstone of Ordovician age, at a depth of 3,100 ft. The storage structure is an asymmetric anticline about four miles north-south and two miles east-west with a relatively steep slope of 3 degrees on the west flank and an average of 0.6 degrees in other directions. Measurements on core samples of the storage sand, which has a thickness of about 110 ft, gave an average porosity of 17.2% and average values for the horizontal and vertical permeabilities of 323 md and 24 md, respectively.

The Model

The gridblock mesh used in TOUGH2 for the Hillsboro field is shown in Figure 1. The center of the mesh contains the smallest square elements with dimensions of 200 x 200 ft. These elements are increased in size four times by doubling to give the overall mesh shown. A total of 15 horizontal layers are provided, of which the top 9 layers are each 10 ft thick. The 6 layers beneath are 20 ft and 40 ft in thickness. The horizontal limits of each layer conform as closely as possible to the structural contours, and this provides a mesh with 8,362 elements.

The field contains 18 wells completed in the St. Peter sandstone aquifer whose locations are as shown on Figure 1. Fourteen of these wells are at the crest of the structure, of which one well (No. 15) is used to monitor reservoir gas pressures and the remaining 13 are used as I-W wells. Four down structure wells (Nos. 1, 12, 14, and 18) are used to monitor water levels.

The 200 x 200 ft gridblock locations of each of the 13 I-W wells can be remeshed as desired to refine the mesh around the wellbore. This is accomplished by dividing the gridblock into eight radial sectors, each covering 45° and centered on the wellbore. Each sector is further subdivided to provide elements that increase in size logarithmically from the center of the well to the outer boundary of the gridblock. Several of the 10-foot layers in a gridblock containing an I-W well can be remeshed, and depending on the number of gridblocks that are subdivided in this manner can increase the size of the model up to about 12,000 elements.

Model Parameters

One of the problems in developing a numerical model of an aquifer gas storage reservoir is the degree to which it is necessary to model the heterogeneity of the storage sand. Some modelers (Hower et al., 1993) have gone to the extent of developing a detailed description of three-dimensional variations in porosity and a correlation between porosity and permeability, from which they construct a complicated permeability map of the flow regime. Since it is well known that many geologic formations exhibit variations in permeability that are log-normally distributed, a question can be raised why the mean value for such a system is not equally applicable.

To investigate this point, we designed a simple model of one horizontal square layer that is 10 m thick and is subdivided into 99 x 99 gridblocks, each with dimensions of 200 m x 200 m. The outer boundaries of this square layer were closed and a well was placed in the center of the system so that water could be injected at 1 kg/s. This center gridblock was remeshed, as described above, so that the diameter of the wellbore was reduced to 2.5 mm. The pressure increases were recorded at several distances away from the well, and a typical result for a homogeneous system with a uniform permeability of 100 md (0.1E-12 m^2) is shown by the solid line on Figure 2.

We then changed to a heterogeneous system with a log normal distribution for the permeabilities, where the mean value is 100 md and $\sigma = 10$. The permeabilities were placed at random in the layer, and the frequency distribution for this system is shown by the narrow bell curve with open triangles in the inset on Figure 2. It can be seen that the results are essentially the same as was obtained with the homogeneous system. We repeated this exercise with a second heterogeneous system where the mean value is 100 md and $\sigma = 50$. As shown by the much wider bell curve with open squares in the inset on Figure 2, this produced a system with a much larger range in permeabilities.

Yet, it can be seen that the results are only slightly different from those of the homogeneous system.

These results indicate that an appropriate average value for the permeability of the storage reservoir may be justified in developing a numerical model. Another factor to consider is that if fracture conditions are present in the reservoir, an average value for the permeability derived from core data may be too low. There have been some instances where the permeability results derived from core data on gas storage projects had to be increased significantly before satisfactory history matches could be obtained (Rzepczynski et al., 1961; Hower et al., 1993).

It must also be kept in mind that in dealing with aquifer storage reservoirs, there will usually be a concentration of information at the crest of the structure where core data from the I-W wells has been gathered, and only limited information out on the flanks where a few water observation wells may have been drilled and cored. Thus, it can be argued that the available core data may only be primarily a reliable description of conditions in the vicinity of the I-W wells. Inasmuch as the area in which the I-W wells are located may only be 5-10 percent of the total area of the structure, one could just as well rely on average values for these parameters in developing the model.

With this in mind, we decided to construct an initial model of the Hillsboro field and use ITOUGH2 (Finsterle, 1993; Finsterle and Pruess, 1995) to search for the parameters that would lead to a satisfactory model of the performance of the field. We used pressure data measured in the five monitor wells mentioned above. These data were collected during an injection-withdrawal cycle, to perform a preliminary calibration of the three-dimensional model. In addition, a constraint was introduced that prevents excessive water production from wells during withdrawal. Finally, the permeability values obtained from core sample measurements were taken into account by assigning a certain weight to the estimates for the initial parameter.

ITOUGH2 can be used to estimate model-related formation parameters based on the maximum likelihood approach. During optimization, a sensitivity measure is calculated to select the parameters that determine the system behavior. It turned out that the horizontal and vertical permeabilities are the most sensitive parameters affecting pressure observations as well as the water production in the I-W wells. Adjusting these two parameters was sufficient to calibrate the TOUGH2 model of the Hillsboro field. The mean deviation between observed and calculated pressures is less than 10 psi, and water production is consistent with measured data.

The horizontal permeability was estimated to be 850 md, about 2.5 times larger than the result from core analysis. Vertical permeability, on the other hand, was estimated to be about 4 md, which is 6 times lower than the value determined in the laboratory. There are several reasons for these discrepancies.

First, there is a difference in scale. While the laboratory data represent point measurements, the estimates obtained using inverse modeling refer to effective parameters on a reservoir scale. The large-scale system behavior is controlled by highly permeable features affecting horizontal gas flow towards the wells. Conversely, the coning of water during withdrawal periods is limited by layers of low vertical permeability. These two effects explain why the model tends to favor large horizontal and low vertical permeabilities.

Second, the model was calibrated against a limited number of data at discrete points in space and time. Adding more sensitive data may help reduce parameter correlations, thus allowing for an independent and more accurate parameter determination.

Third, the estimated parameters refer to the given model structure, i.e. they are optimal for the specific numerical model that was developed to simulate gas storage at Hillsboro. It is important to realize that the model structure not only comprises the physical processes represented by a set of governing equations, but also includes the assumptions regarding initial and boundary conditions, the zonation pattern, the type of characteristic curves, and the degree of discretization. Since the model results are compared to borehole data, the discretization of the I-W wells is a key element of the model structure. The fact that calibration provides model-related parameters implies that they may not be valid for a model with a significantly different structure. On the other hand, inverse modeling insures that the estimated parameters represent the reservoir conditions on the scale of interest. Furthermore, they are tailored to the numerical model that is used for subsequent prediction runs. As a result, the use of inverse modeling techniques improves the reliability of the model predictions that will be performed to further optimize the operation of underground gas storage at Hillsboro.

Multiphase Effects

In the anticlinal structure at Hillsboro, the important part of the St. Peter sandstone is the top 90 ft where all the gas is stored; this section ranges from a depth of -2490 ft (below sea level) at the crest of the structure down to -2580 ft. The sandstone aquifer, of course, extends for hundreds of miles away from this local geologic feature. Details of the construction of the model have been presented above.

From 1973 through 1989, the Hillsboro field had an inventory of about 10 BCF of total gas in storage. In 1990, it was decided to enlarge the inventory and a program of growing the bubble began in May of that year. Gas injection continued through 1991, 1992 and into 1993. In September 1993, the total gas in storage was at the desired maximum of 21.7 BCF. It is of interest to investigate how the gas migration process evolved as the size of the gas bubble was increased.

In October 1989, when a total of 10.25 BCF of gas was in storage, an examination of the distribution of gas saturations with this volume in place seems to indicate that as

injection proceeds, the migration of gas moves down the slopes of the structure more readily than along the centerline of the structure. The path of this centerline is not vertical, and apparently as a result of the influence of the asymmetry of the structure, this path trends in an easterly direction with depth. Figure 3 shows the overall appearance of the gas bubble that developed from the top of the structure at elevation -2495 ft down to -2555 ft. Note that the vertical exaggeration is 50:1. A closeup view of the topmost part of the structure with a vertical exaggeration of only 20:1 is shown in Figure 4.

These results suggest that the gas bubble is 50 ft in thickness, but by removing appropriate sections of the model, as shown in Figure 5, this is not the case. Figure 5 shows a view of the horizontal plane at elevation -2545 ft where the gas saturations increase from minimum levels in the central part to higher saturations out around the edges of the structure. This movement down the flanks of the structure is evident from the shapes of the boundaries between gas saturations.

The four vertical sections on this figure enclose an area containing all but one of the 13 I-W wells so that one can relate the position of the injection area to the subsequent development of the gas bubble. Note on these vertical sections that the gas displacement process produces a gas-water transition zone that is near horizontal over most of the central region of the bubble. Note on the bar graph for the volume of gas in each 10-foot layer how the distribution of gas varies with depth. Potentially, the bottommost layers (-2545 ft and -2555 ft) can hold substantially more gas than is shown on this graph.

The bar graph also shows the distribution of mobile and immobile gas volumes in each layer. Gas is mobile when the saturation is at or above 40%. As a result, most of the mobile gas was present above an elevation of -2535 ft. Ten feet deeper at an elevation of -2545 ft, very low gas saturations were still present in the center of this horizontal plane, surrounded by a halo of much higher gas saturations out around the periphery of the structure. Evidently as the volume of the gas bubble increases, the I-W wells, which are at the highest locations near the crest of the structure, do not seem to have much influence on the directions of migration. The displacement process produces a gas-water transition zone that is near horizontal over most of the central region of the bubble, but out around the edges there is more of a downward movement of the gas and the transition zone is thicker.

In September 1993, with 21.7 BCF in storage, another examination of the distribution of gas saturations revealed that the expansion from 10.25 BCF to 21.7 BCF followed more or less the same pattern of development as described above. Figure 6 shows a closeup view of what the gas bubble looks like when the volume in storage had been increased from 10.25 BCF to 21.7 BCF. The bar graph on this figure shows how the distributions of mobile and immobile gas volumes vary with depth; it can be seen that the majority of the stored gas is in the layers above an elevation of -2565 ft.

A cutaway section at elevation -2545 ft (Fig. 7) shows how the gas saturations have increased significantly over what was present at this elevation with 10.25 BCF in storage (Fig. 5). With twice as much gas in place, one result is that the gas-water transition zone has moved downward to the interval between -2555 ft and -2565 ft (Fig. 6). The preferential migration of gas down the flanks of the structure is clearly evident.

With these results in mind, the next question to investigate was the multiphase effects during withdrawal. In the winter of 1993-94, a total of 7.6 BCF was produced which reduced the inventory to 14.1 BCF in March 1994. Figure 8 shows a closeup view, and the bar graph shows how much gas was removed from each layer. Figure 9 shows a cutaway section at elevation -2545 ft for comparison with the results for the same elevation on Figure 7 and illustrates how different the gas saturations are after withdrawal.

According to laboratory measurements on core samples, the gas is no longer mobile when its saturation falls below about 40%. This was used as the lower limit for the relative permeability to gas in the model, and as expected a large volume of the structure overlying the horizontal plane at -2565 ft retained gas at this immobile saturation. Note the large volume of rock (in medium gray color) on Figure 9 with gas saturations of 40% to 50% that are now located in the general area of the I-W wells. This is primarily the effect of the immobile saturations for gas and water, which were taken to be 40% and 32%, respectively. It appears that during injection, the gas moves preferentially down the flanks, and during withdrawal, the process is reversed with an even greater movement up the flanks of the structure. Note that there is still a significant volume of mobile gas in the top layers of the system.

A more recent development in the use of TOUGH2 has involved an attempt to investigate the displacement phenomena in the immediate vicinity of the borehole during injection and withdrawal. As discussed above, we have developed a subroutine to remesh any grid block that contains a well so that radial flow into the wellbore can be approximated.

Some preliminary results with this arrangement of a refined mesh around the wellbore indicate that the process of drying out the sand where gas first invades the reservoir can now be studied. The injection gas contains very little water vapor because its dew point is far below the reservoir temperature at Hillsboro (92° F). Therefore, after the water phase is reduced to its immobile saturation (32%) during gas injection, the vaporization of water will continue to take place as dry gas moves away from the wellbore, and the liquid water saturations will be further reduced.

An example of an east-west section through wells Nos. 9, 10, and 11 (see Fig. 1) is shown on Figure 10 with the inventory at 21.7 BCF. The model was run from a starting inventory of 12 BCF so that the addition of 9.7 BCF would reproduce the effects around the wellbore of injecting a significant volume of dry gas. Figure 11

shows how the drying out process had developed around the wellbore of Greenwood #1 (No. 10 on Fig. 1) when the gas volume had increased to 21.7 BCF. It can be seen that a dried out region extending out 10 - 18 ft from the center of the well was developed. The gas saturation exceeds 68% where the "Upper Limit of Mobile Water" is indicated on Figure 11, and the saturations increase up to 100% in the vicinity of the well. Figure 12 shows an interesting result for this drying out process in IPC #2 (No. 5 on Fig. 1), where there are two open intervals in the wellbore.

These results suggest that it should be possible to investigate how the dried out region around the wellbore affects the process of water coning during gas withdrawal. By controlling the injection of gas in appropriate sections of the completion interval and using this kind of modeling to get an idea of gas distributions, it should be possible to optimize the operation of I-W wells by creating saturations of gas around the wellbore that tend to reduce or eliminate water production during withdrawal.

References

Finsterle, S., "ITOUGH2 User's Guide Version 2.2," Lawrence Berkeley Laboratory Report, LBL-34581, Berkeley, CA, 1993.

Finsterle, S. and K. Pruess, "Solving the estimation-identification problem in two-phase flow modeling," Water Resources Res., v. 31, No. 4, 913-924, 1995.

Hower, T. L., M. W. Fugate, and R. W. Owens, "Improved performance in aquifer gas storage fields through reservoir management," paper SPE 26172 presented at the SPE Gas Technology Symposium held in Calgary, Alberta, Canada, June 28-30, 1993.

Pruess, K., "TOUGH2 - A general-purpose numerical simulator for multiphase fluid and heat flow," Lawrence Berkeley Laboratory Report, LBL-29400, Berkeley, CA, 1991.

Rzepczynski, W. M., D. L. Katz, M. R. Tek, and K. R. Coats, "How the Mount Simon gas-storage project was developed," Oil & Gas Journal, 86-91, June 19, 1961.

Statistics Task Group, Underground Storage Committee, "Survey of Underground Gas Storage Facilities in the United States and Canada, 1993," American Gas Association, 114 pp, 1993.

Figure 1. Gridblock mesh for model of Hillsboro gas storage field

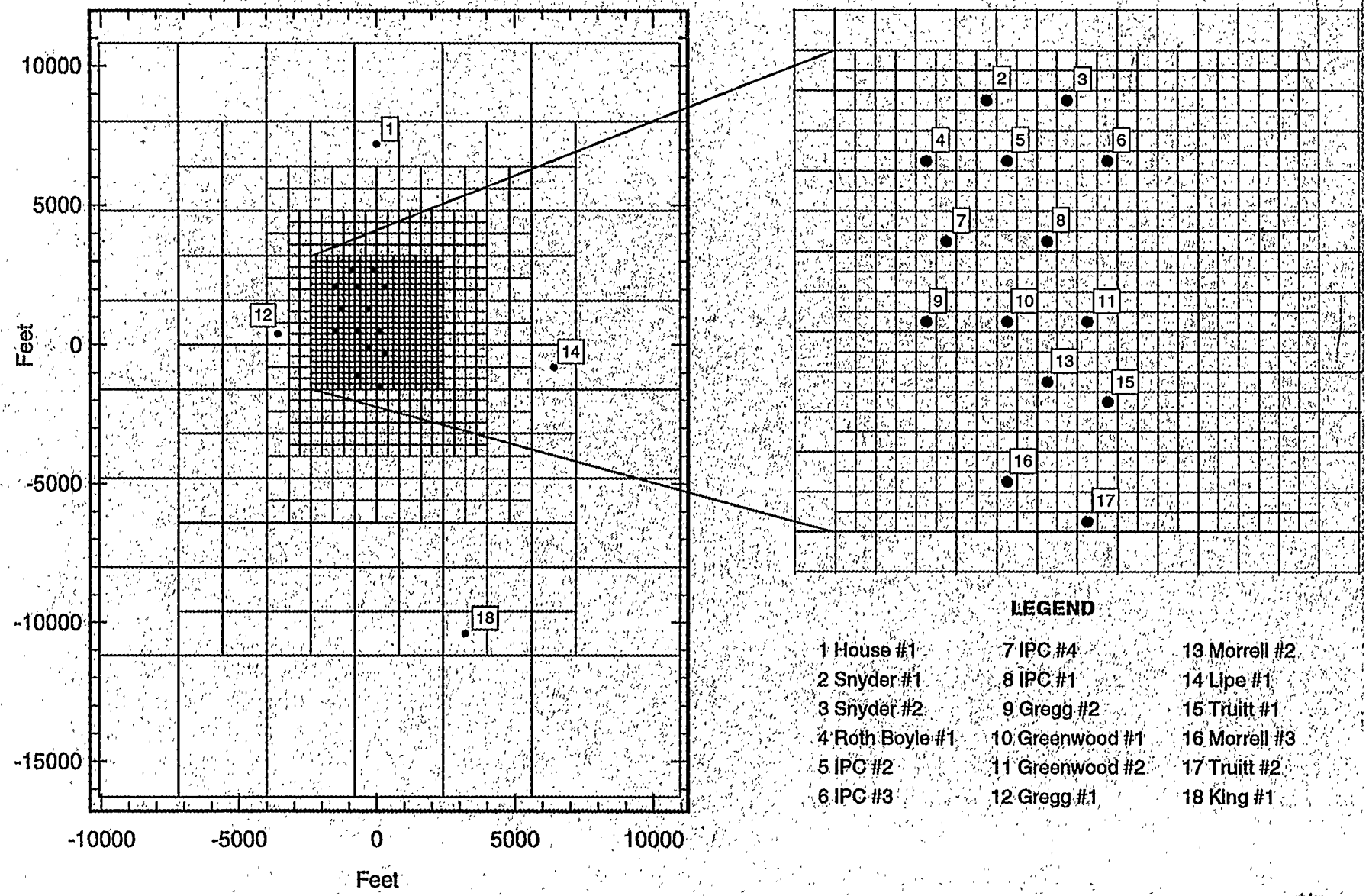

Figure 2. Pressure variations for homogeneous and heterogeneous systems

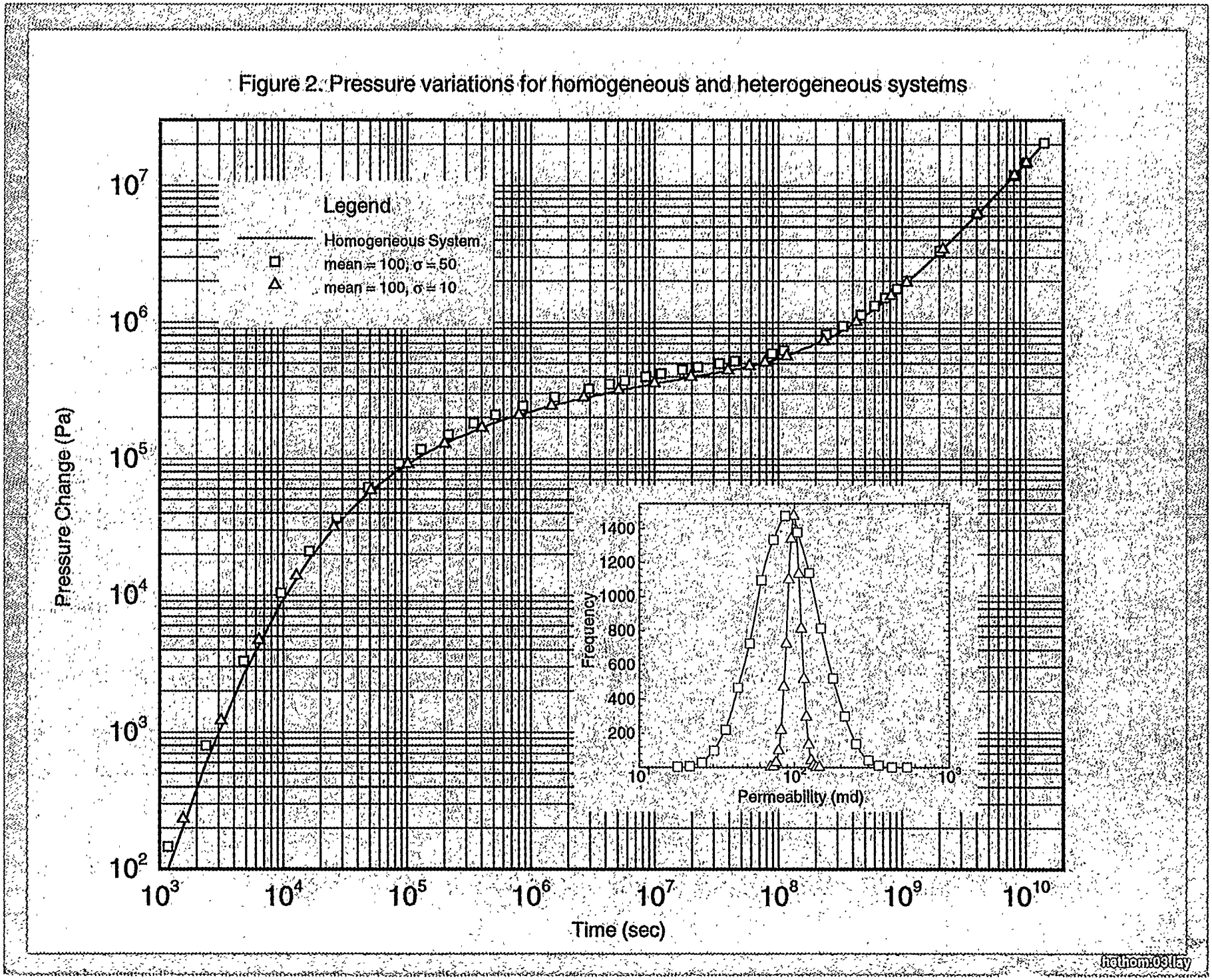

Figure 3. Hillsboro with 10.25 BCF in storage, October 1989. Looking down on gas bubble from northeast. Vertical exaggeration 50:1.

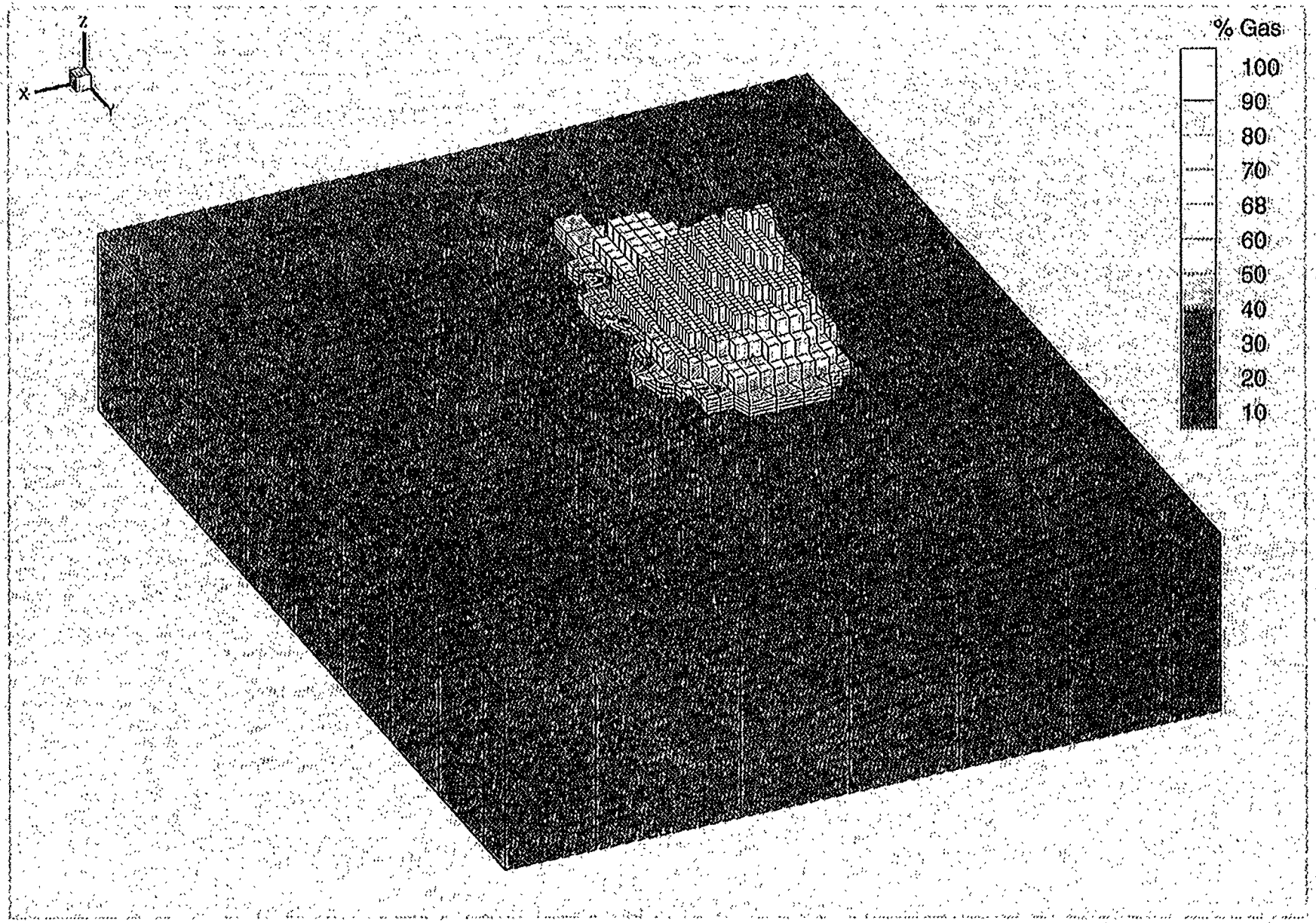

Figure 4. Hillsboro with 10.25 BCF of gas in storage, October 1989. Looking down on gas bubble from northeast. Vertical exaggeration 20:1.

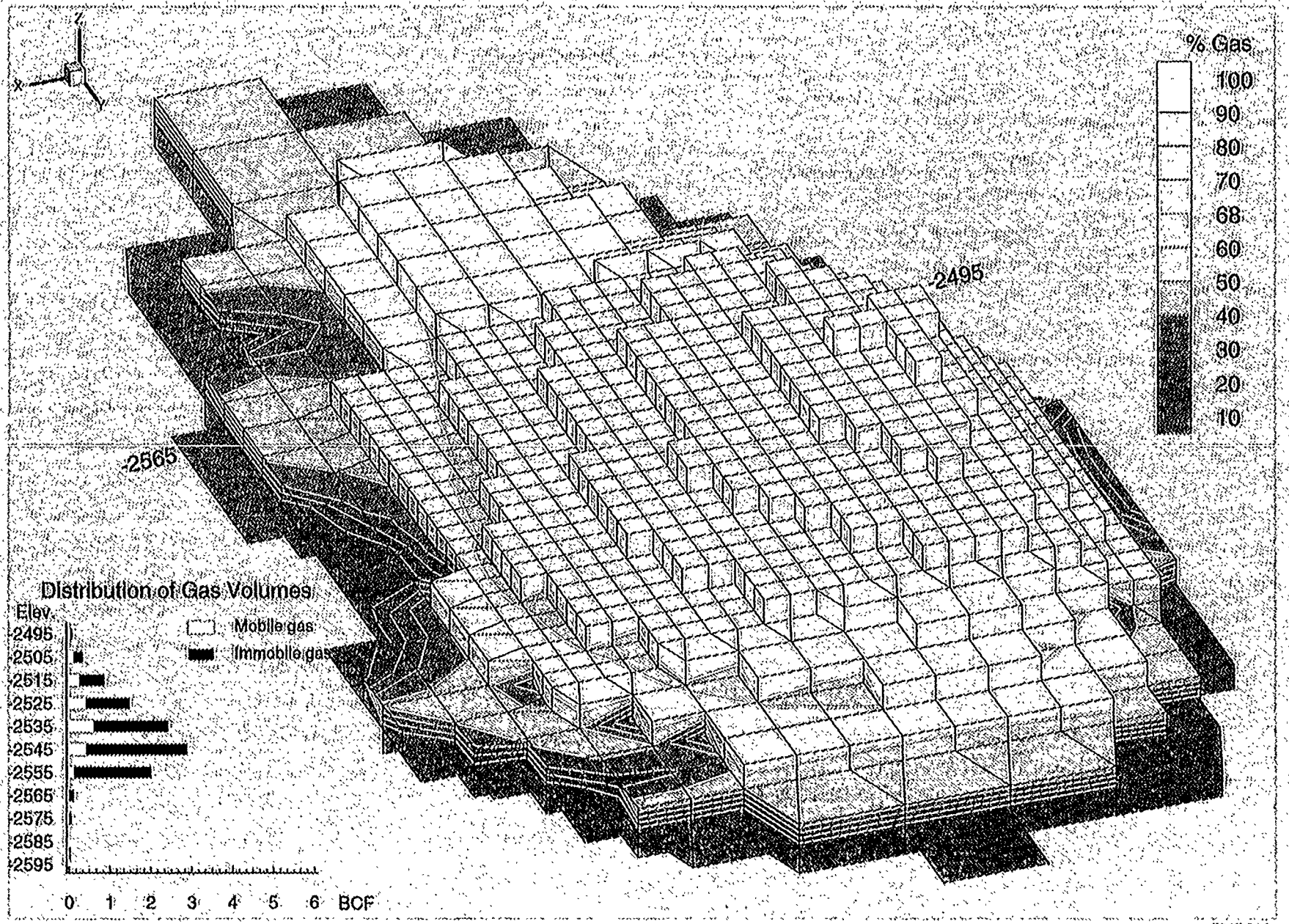

5916.01.lay

Figure 5. Hillsboro with 10.25 BCF of gas in storage, October 1989. Looking down on Elevation -2545 ft. Vertical exaggeration 20:1.

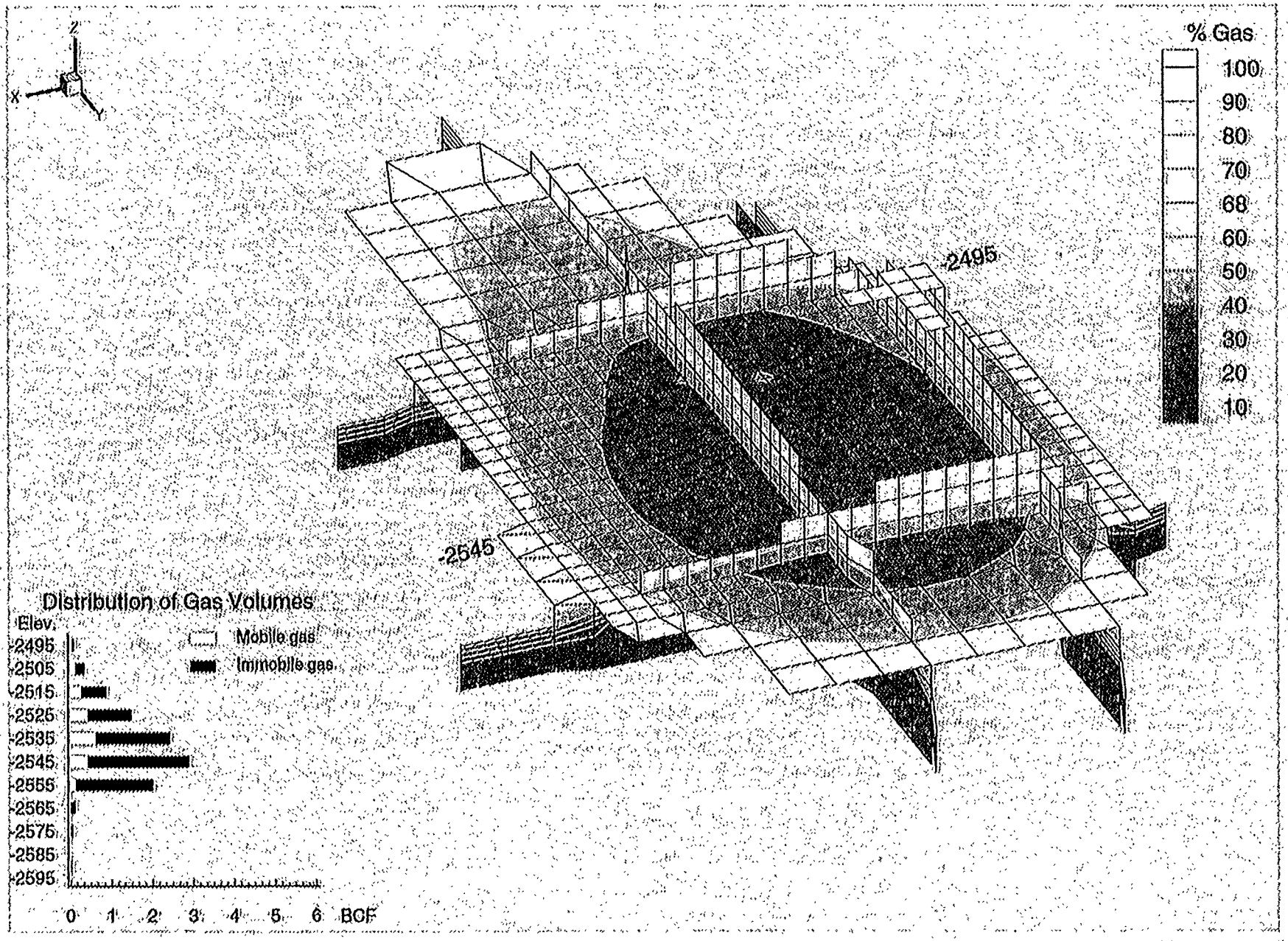

Mar2.5915.03.lay

Figure 6. Hillsboro with 21.7 BCF of gas in storage, September 1993. Looking down on gas bubble from northeast. Vertical exaggeration 20:1

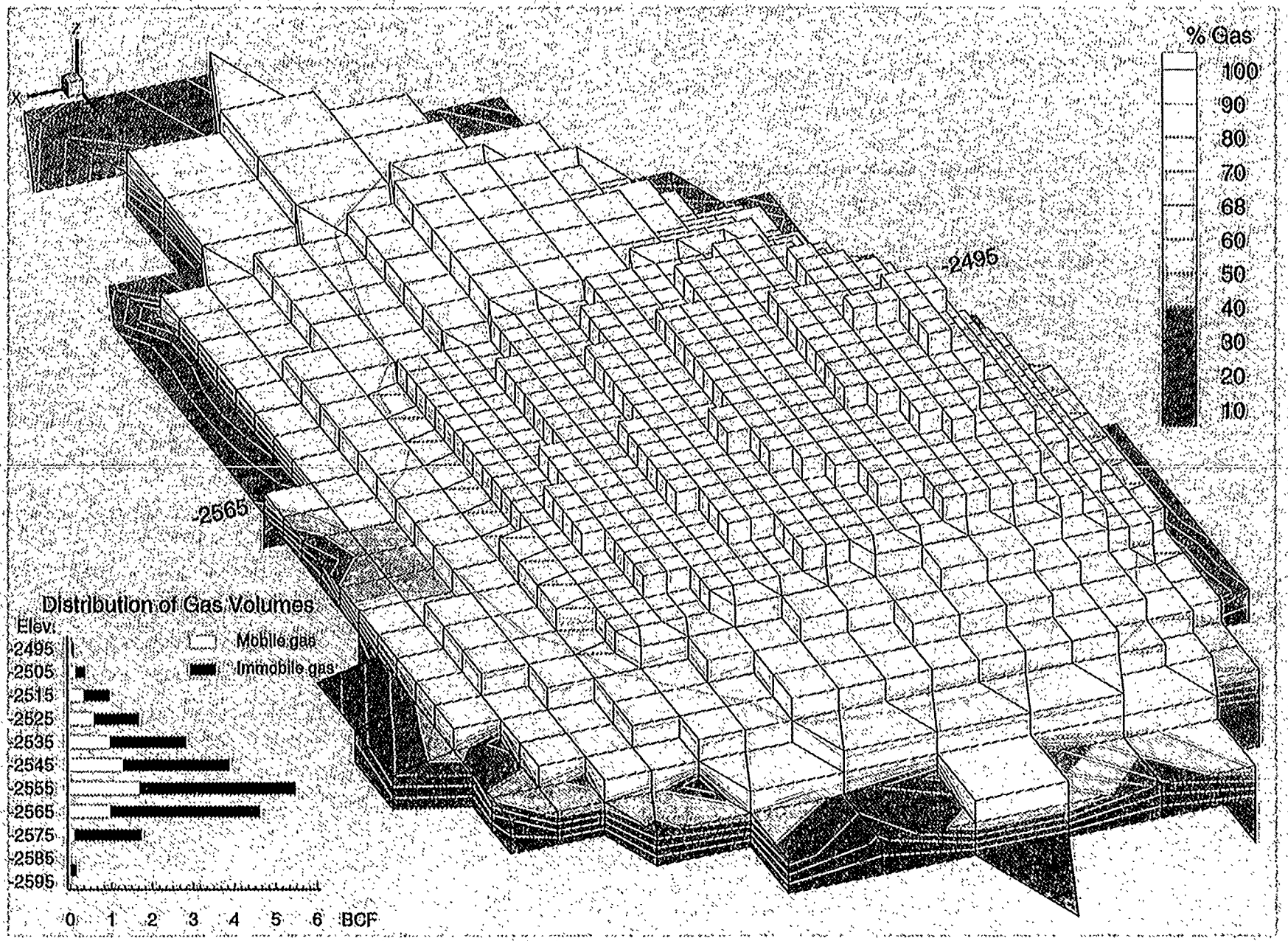

Figure 7. Hillsboro with 21.7 BCF of gas in storage, September 1993. Looking down on Elevation -2545 ft. Vertical exaggeration 20:1.

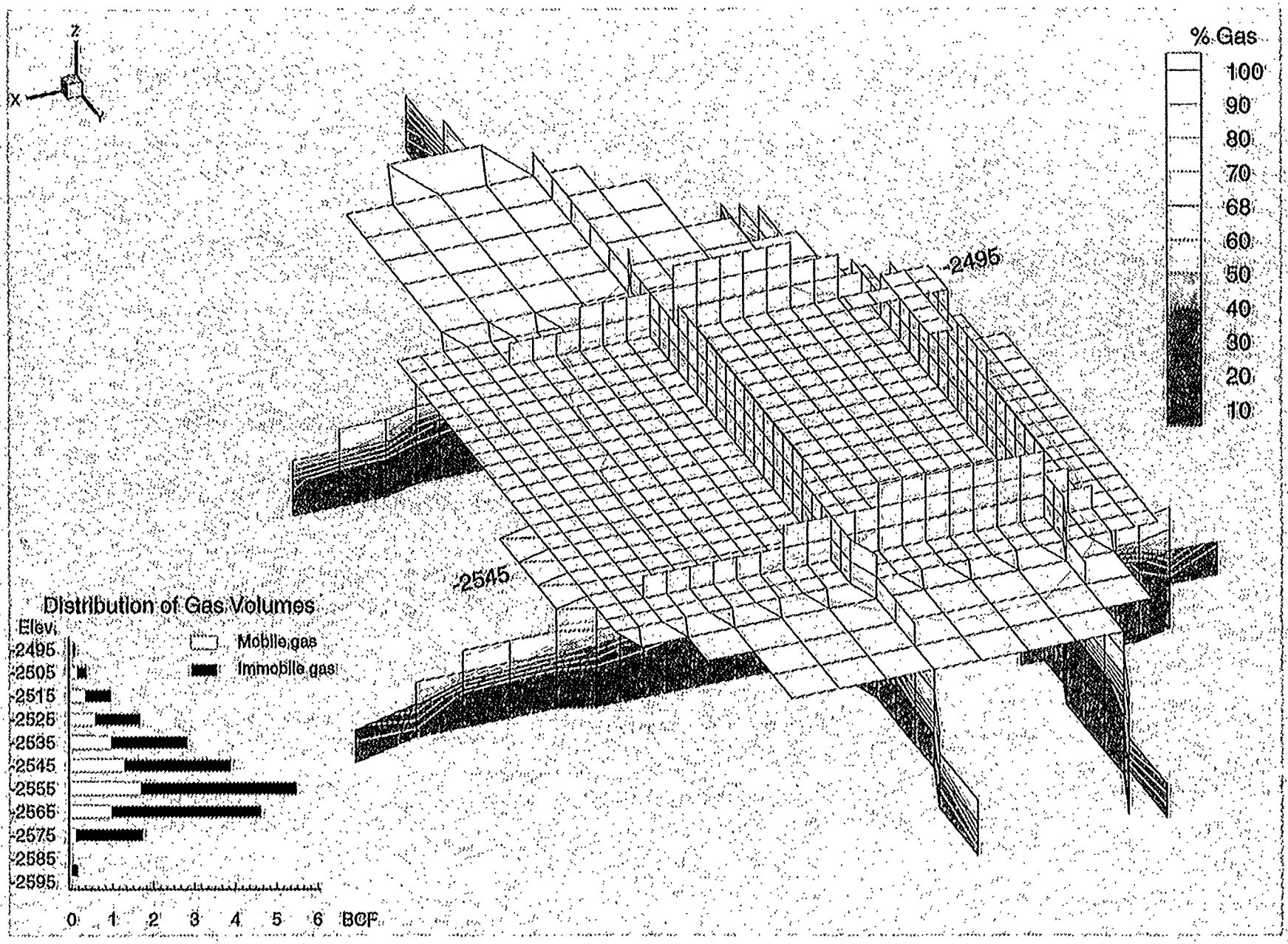

Figure 8. Hillsboro with 14.1 BCF of gas in storage, March 1994. Looking down on gas bubble from northeast. Vertical exaggeration 20:1.

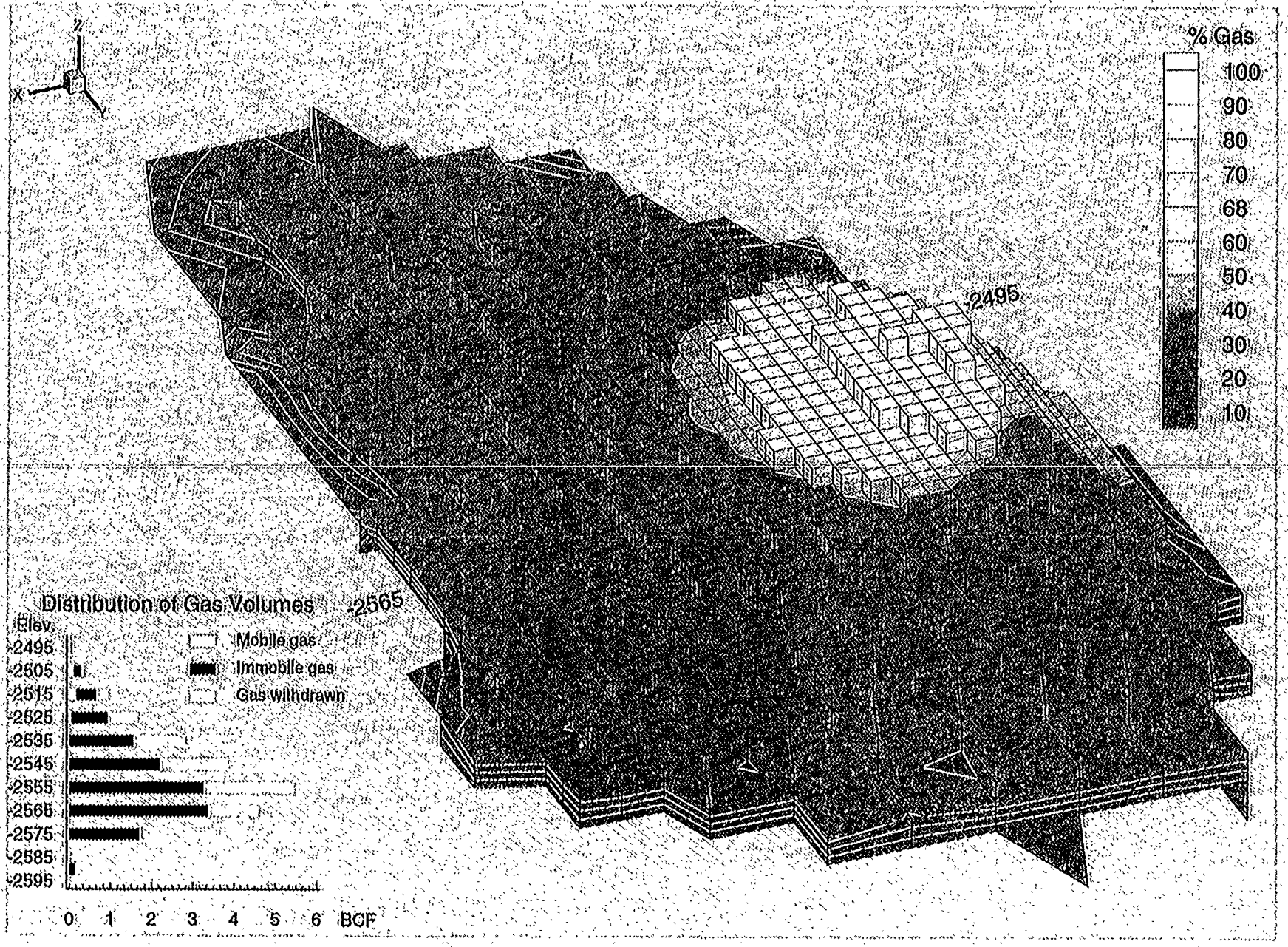

Mar2.7527.02.lay

Figure 9. Hillsboro with 14.1 BCF of gas in storage, March 1994. Looking down on Elevation -2545 ft. Vertical exaggeration 20:1.

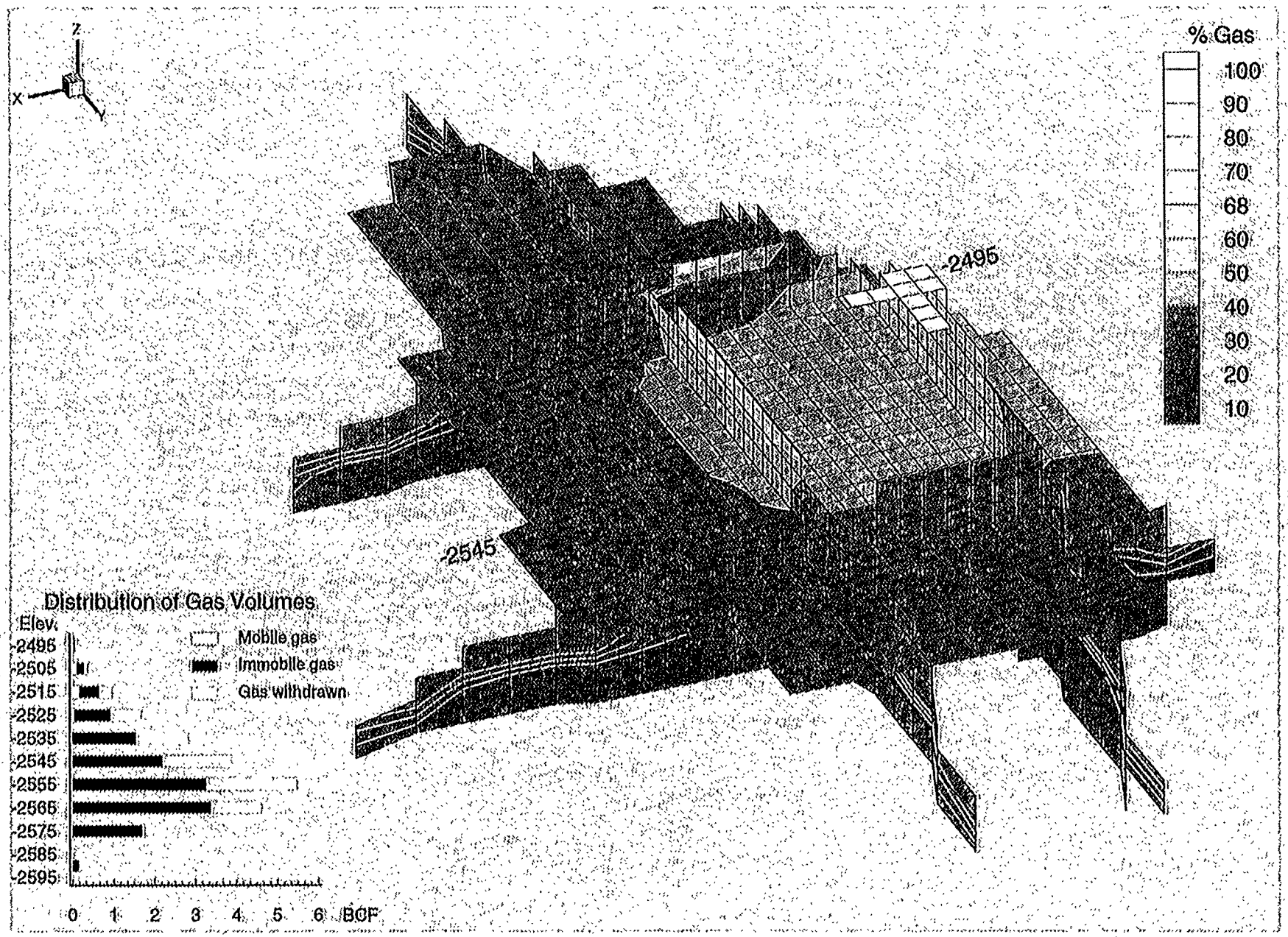

Figure 10. Hillsboro with 21.7 BCF of gas in storage, September 1993.
Vertical section, exaggeration 20:1.

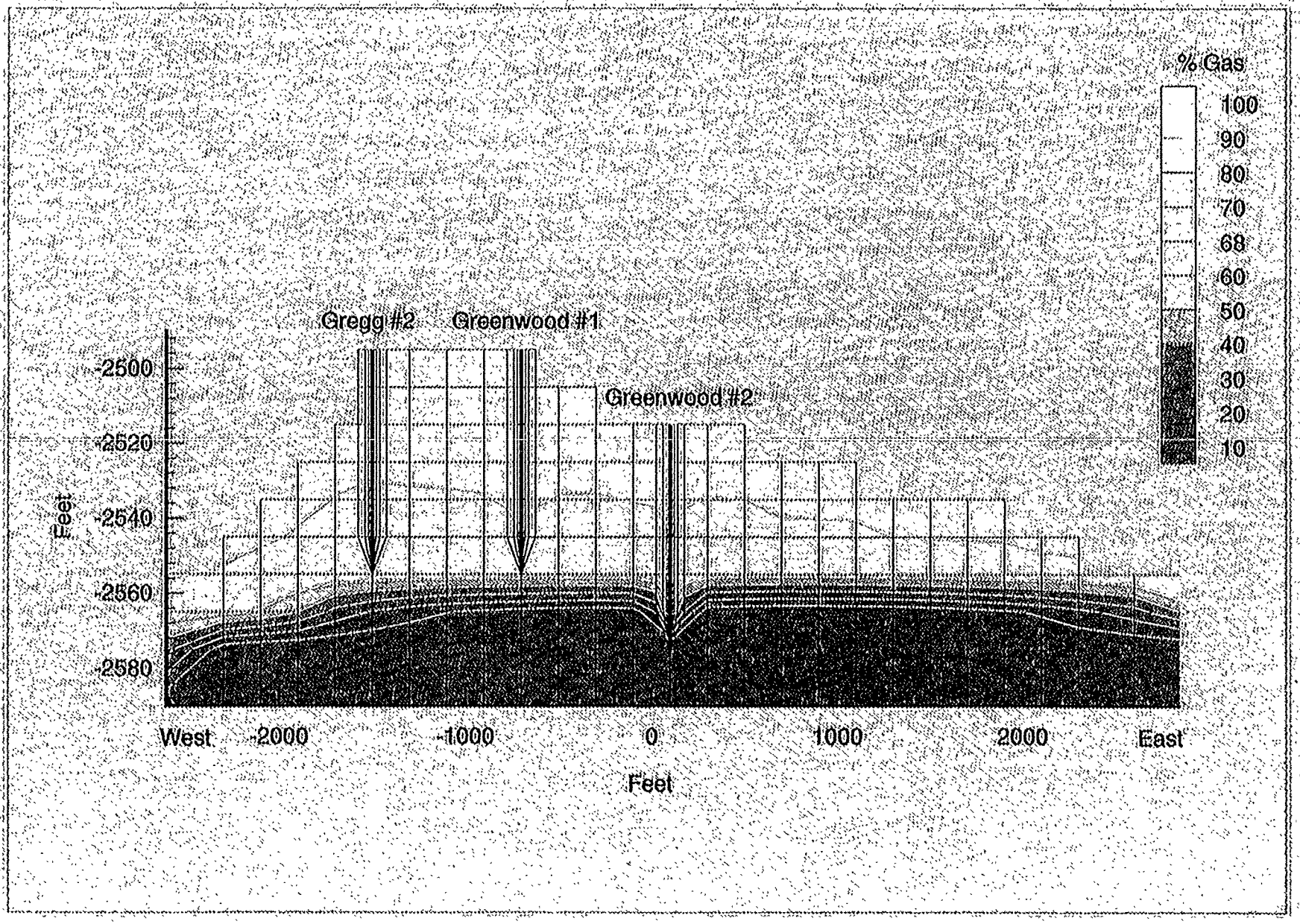

Mar9.7345.01:lay

Figure 11. Hillsboro with 21.7 BCF of gas in storage, September 1993. Vertical section through Greenwood #1 showing effects of drying around borehole.

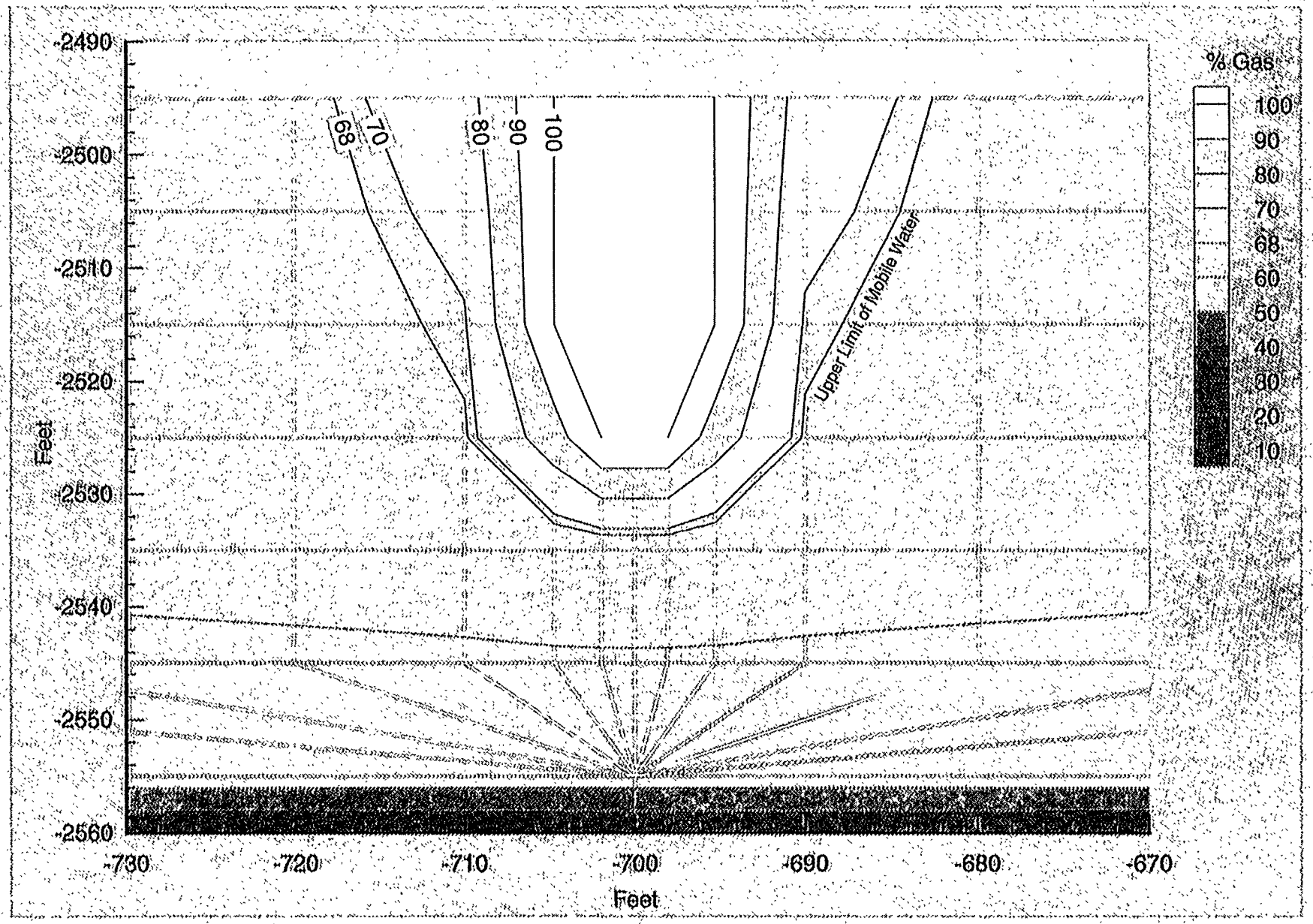

Figure 12. Hillsboro with 21.7 BCF of gas in storage, September 1993. Vertical section through IPC #2, showing effects of drying from two zones of injection.

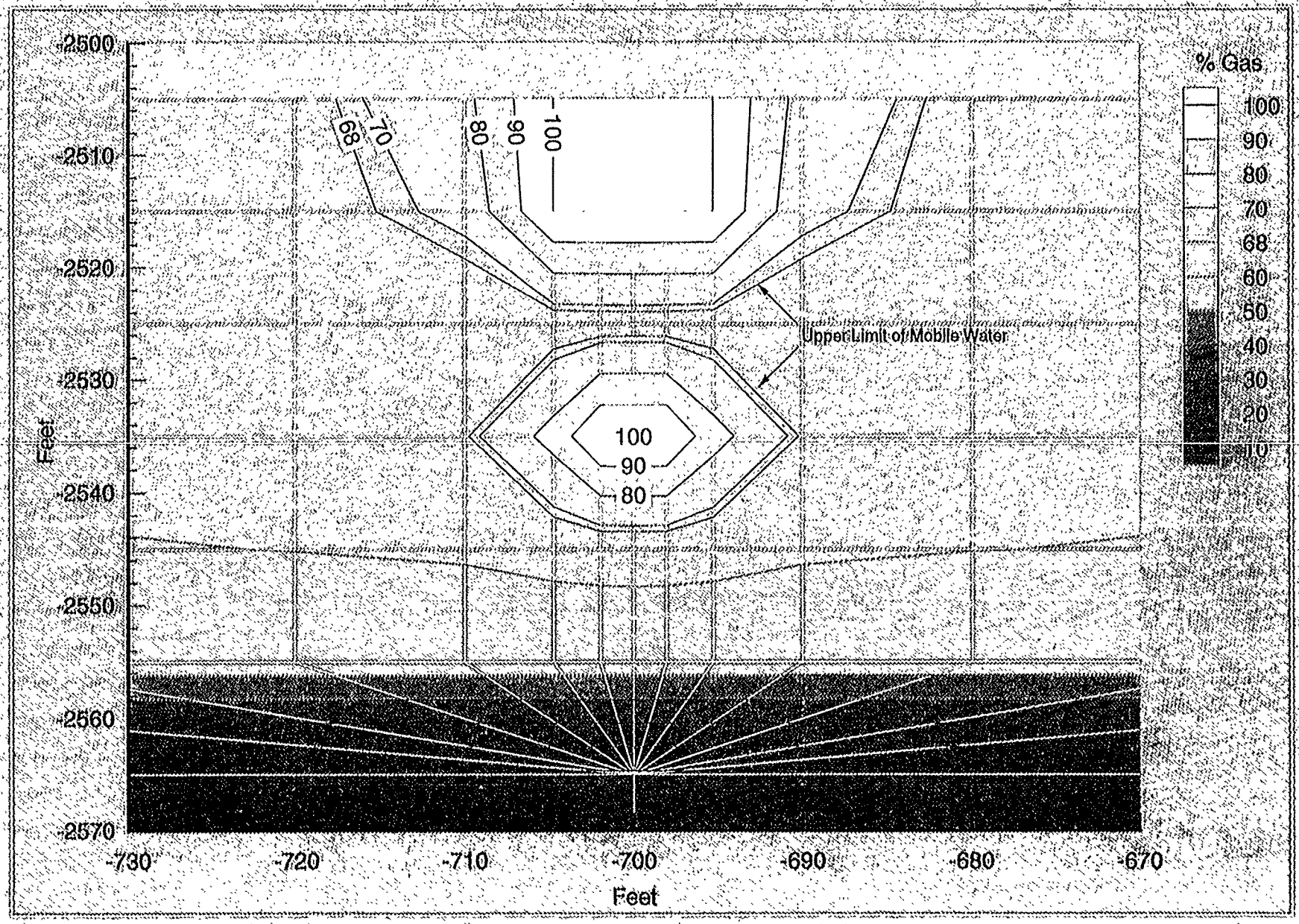

Analysis of Over-Pressure Mechanisms in the Uinta Basin, Utah

Brian McPherson and John Bredehoeft
U.S. Geological Survey, Menlo Park

Introduction

Extremely high pore fluid pressures exist in the area of the Altamont/Bluebell oil field in the Uinta basin, Utah. We discuss two possible mechanisms for the cause of these over-pressures in this paper: 1) compaction disequilibrium, and 2) conversion of kerogen to liquid hydrocarbon (oil). Compaction disequilibrium occurs during periods of rapid sedimentation. If the permeability of deeply buried strata is low, then connate water within the rock matrix does not escape rapidly enough as compaction occurs; as sedimentary deposition continues, high pore fluid pressures develop. Conversion of solid kerogen to a liquid generates both a liquid and additional pore space for the liquid to occupy. If the volume of the liquid generated is just sufficient to fill the pore space generated, then there will be no accompanying effect on the pore pressure. If the liquid is less dense than the solid it replaces, then there is more liquid than pore space created; pore pressure will increase, causing flow away from the area of the reaction (*Bredehoeft et al.*, 1994). Pore pressure is a sensitive measure of the balance between hydrocarbon generation and expulsion from the source into adjacent strata. If high pore pressures exist only where source rocks are thought to be generating oil, then kerogen conversion is a likely over-pressure mechanism. However, if over-pressures are found in low-permeability strata regardless of source rock proximity, then sedimentary compaction is probably a more dominant mechanism.

Maps of pore pressure gradients in the Uinta basin show some correlation between over-pressures and source rock occurrence. This is not sufficient evidence to conclude that over-pressures are a sole consequence of hydrocarbon generation. We examined the problem in more detail using numerical simulation. All of our simulations were performed using a modified version of TOUGH2.

The purpose of this paper is to provide an overview of how we adapted TOUGH2 as a basin analysis tool and to describe briefly the application of TOUGH2 for elucidating the causes of high pore pressure in the Uinta basin, Utah.

Basin Analysis Using TOUGH2

We used TOUGH2 to understand better the over-pressure mechanisms and the generation and migration of hydrocarbons within the Uinta basin. To improve TOUGH2 as a basin analysis tool, we added a compaction term to the governing equations. This allows strata to be deposited or exhumed and the model domain to be uplifted or subsided during model simulations of basin evolution. Layers of nodes are added during deposition and removed during erosion. The effective stress at each node in the solid skeleton is calculated at each time step, and the

compaction of each node is determined. An independent coordinate system is used to determine the movement of all nodes relative to each other.

Other critical aspects of the basin model include:

-All transient effects of sedimentation, uplift, erosion and oil generation on the hydrogeological and thermal aspects of the basin are considered.

-Elastic and plastic strain are represented by constitutive relations between porosity and effective stress. Changes in effective stress are explicitly accounted for and facilitated by calculating elastic (reversible expansivity/compressibility) and inelastic (non-reversible) porosity changes. We also tested assigning porosity from empirical porosity versus depth curves (e.g. *Sclater and Christie*, 1980), and from effective-stress versus porosity curves discussed in *Schneider et al.* (1993).

-Absolute permeability is assigned based on correlation of measurements of permeability and porosity for 223 samples and 78 drill stem tests taken from the Uinta basin. We also tested assigning permeability from the Kozeny-Carmen formulation for permeability versus porosity (*Bear*, 1972).

-Oil generation is kinetically controlled by a first order Arrhenius, parallel reaction, in which heat is the driving force. Because the reaction is driven purely by heat the thermal history is important for the analysis.

-The thermal history is constrained by the present day heat flow observations and by vitrinite reflectance data published for the basin.

-Relative permeabilities (of different fluid phases) assigned to source strata are different than the relative permeabilities assigned to reservoir rocks. Relative permeability curves for reservoir strata are usually measured experimentally, and numerous "typical" relative permeability curves for sandstone are published in the literature. However, experimental relative permeability data for shales and other tight-permeability source rocks are not available. *Burrus et al.* (1992), *Okui and Waples* (1993), and *Wendebourg* (1994) proposed different relative permeability functions for source rocks (than those for reservoir strata) to improve hydrocarbon expulsion aspects in their modeling studies. We elected to test various relative permeability curves for shale and sandstone proposed by these workers in an effort to improve our understanding of expulsion and migration in the Uinta basin.

-Capillary pressures of oil-water interfaces assigned to reservoir (sandstone) and source (shale) strata are also different. We used functional relationships for capillary pressure published by *Parker et al.* (1987) with experimental parameters for sandstone published by *Essaid et al.* (1993). *Burrus et al.* (1992) estimated the capillary pressures for oil-water interfaces in source shales with permeability ~ 10^{-21} m^2 to be ~100 bars (10 MPa). For shale we used the *Parker et al.* (1987) capillary functions scaled to a maximum of 10 MPa.

Over-pressures by Compaction Disequilibrium

We conducted a sensitivity analysis to determine whether compaction disequilibrium could cause significant over-pressures in the Uinta basin. In the basin evolution model, we used the same geometry and dimensions of the Uinta basin, but rather than using the estimated sedimentation rates and other known geologic information for the basin, we used effective stress - porosity functions for shale and sandstone (*Schneider et al.*, 1993) in conjunction with various sedimentation rates.

The effective stress - porosity relationship for sandstones did not produce significant over-pressures except with unreasonably high sedimentation rates. However, the results corresponding to a model using the shale effective stress - porosity function and the Kozeny-Carmen permeability-porosity formulation for shale (*Bear*, 1972) illustrate that for model sedimentation rates in the range of observed Uinta sedimentation rates, especially the higher sedimentation rates, significant over-pressures can develop.

Assuming that compaction disequilibrium is a possible cause of over-pressures, we attempted to ascertain what range of permeability is necessary to maintain high pore pressures for tens of millions of years after they have developed. Our model results suggest that permeabilities of less than 10^{-19} m^2 for most of the stratigraphic column above and adjacent to the over-pressure region are required to maintain over-pressures for time scales on the order of tens of millions of years.

Over-pressures by Oil Generation

A volumetric expansion accompanies the conversion of kerogen to oil. Fluid pressures increase when the oil generation rate exceeds the rate oil can readily flow away. This mechanism can create high pore pressure, pressures approaching lithostatic, in a low permeability environment. We used the basin evolution model to test whether this mechanism is responsible for over-pressures observed in the Uinta basin.

The first step in the process is to backstrip all sediments (e.g. see *Miall*, 1990) with an assumed porosity distribution and estimate sedimentation rates. The basin is then reconstructed through time with estimated timing and rates of uplift. Vitrinite reflectance data are used to estimate the maximum depth of strata during deposition and subsequent erosion (e.g. see *Johnson and Nuccio*, 1993). Additional information needed to parameterize the thermal properties and boundary conditions through time are the background heat flow and the thermal conductivity distribution (*Willett and Chapman*, 1987) and the estimated surface temperature history (adapted from *Wolfe*, 1978). The resulting thermal history determines the hydrocarbon generation history.

Our results suggest that after time of maximum burial until present, hydrocarbon generation in the source strata (oil shale) is the most likely cause of over-pressures in the region of the Altamont-Bluebell and Duchesne oilfields in the northern part of the basin. Minor

over-pressures due to compaction disequilibrium occur during periods of rapid deposition, but these over-pressures dissipate before significant oil generation begins.

The present day hydrodynamic state does not promote extensive regional migration. In our model, local migration of oil out of the Altamont-Bluebell and Duchesne fields occurs due to over-pressures. Fractures caused by over-pressures open higher permeability conduits in which oil moves. Our model suggests that most regional migration probably occurred prior to late Miocene time (before 10 Mya), which is when most uplift and erosion of the southern, western and eastern basin flanks began (*Johnson and Nuccio* (1993) and *Johnson and Finn* (1986). We found that both the over-pressures and migration are extremely sensitive to the permeability distribution and viscosity of the oil phase. For over-pressures to develop, marginal lacustrine and open lacustrine facies (source strata) must have very low permeability ($\sim 10^{-18}$ m^2 or lower). For regional migration to occur, at least portions of the alluvial facies (reservoir strata) must have permeability $\sim 10^{-15}$ m^2 or higher.

We also determined that diagenetic porosity loss may augment over-pressures; applying assumed porosity reduction rates associated with diagenesis increased over-pressures.

Summary

1. We used TOUGH2 to understand better the over-pressure mechanisms and the generation and migration of hydrocarbons (oil phase) within the Uinta basin, Utah.

2. To improve TOUGH2 as a basin analysis tool, we added compaction to the governing equations; strata can be deposited or exhumed and the model domain can be uplifted or subsided during model simulations of basin evolution. All transient effects of sedimentation, uplift, erosion and oil generation on the hydrogeologic and thermal aspects of the basin are considered. Elastic (reversible expansivity/compressibility) and plastic (non-reversible) strain are represented by constitutive relations between porosity and effective stress. Permeability in the basin evolution model is predicted by empirical correlations of permeability and porosity that are constrained by core and drill stem test data.

3. Basin history simulations suggest that compaction disequilibrium was likely a cause of over-pressure during periods of rapid deposition. Both analytical and numerical calculations suggest that, depending upon the permeability of the sediments, the over-pressure produced by sedimentary loading alone should dissipate within 10,000 to 1 million years following the maximum depth of burial. Hydrocarbon generation in the source strata (oil shale) is the most likely cause of current over-pressures observed in the area of the Altamont-Bluebell oilfields.

4. Model results suggest that the present-day hydrodynamic state does not promote extensive regional migration of hydrocarbons out of the Altamont-Duchesne source region. Model results also suggest that most migration of oil probably occurred prior to late Miocene time (before 10 Mya), when uplift and erosion of the basin flanks began.

5. We found that the over-pressure plus migration system is extremely sensitive to hydraulic conductivity. For over-pressures to develop, marginal and open lacustrine facies (source strata) must have very low permeability (~10^{-18} m^2 or lower). For regional migration to occur, at least portions of the alluvial facies (reservoir strata) must have permeability ~10^{-15} m^2 or higher.

6. We conclude that diagenetic porosity loss may augment over-pressures because applying assumed porosity reduction rates associated with diagenesis increased over-pressures.

REFERENCES

Bear, J., *Dynamics of Fluids in Porous Media*, Elsevier, New York, 1972.

Bredehoeft, J. D., J. B. Wesley, and T. D. Fouch, Simulations of the origin of fluid pressure, fracture generation, and the movement of fluids in the Uinta basin, Utah, *AAPG Bulletin, 78*, 1729-1747, 1994.

Burrus, J., A. Kuhfuss, B. Doligez, and P. Ungerer, Are numerical models useful in reconstructing the migration of hydrocarbons? A discussion based on the Northern Viking Graben, *in* W.A. England and A.J. Fleet, eds., *Petroleum Migration: Geological Society of London Special Publication, 59*, p. 89-109, 1992.

Essaid, H. I., W. N. Herkelrath, and K. M. Hess, Simulation of fluid distributions observed at a crude oil spill site incorporating hysteresis, oil entrapment, and spatial variabilitiy of hydraulic properties, *Water Resources Research, 29, no. 6*, 1753-1770, 1993.

Johnson, R. C., and V. F. Nuccio, Surface vitrinite reflectance study of the Uinta and Piceance basins and adjacent areas, eastern Utah and western Colorado--implications for the development of Laramide basins and uplifts, *U.S. Geological Survey Bulletin 1787-DD*, 1993.

Johnson, R. C., and T. M. Finn, Cretaceous through Holocene history of the Douglas Creek arch, Colorado and Utah, *in* Stone, D. S., editor, *New interpretations of northwest Colorado geology*, Rocky Mountain Association of Geologists, p. 77-95, 1986.

Miall, A. D., *Principles of Sedimentary Basin Analysis*, 2nd Edition, Springer-Verlag, New York, 1990.

Schneider, F., J. Burrus, and S. Wolf, Modelling over-pressures by effective-stress/porosity relationships in low permeability rocks: empirical artifice or physical reality?, *in* Dore, A. G., ed., Basin Modelling: Advances and Applications, *NPF Special Publication 3*, Elsevier, Amsterdam, 1993.

Okui, A. and D. W. Waples, Relative permeabilities and hydrocarbon expulsion from source rocks, *in* Dore, A. G., ed., Basin Modelling: Advances and Applications, *NPF Special Publication 3*, Elsevier, Amsterdam, 1993.

Parker, J. C., R. J. Lenhard, and T. Kuppusamy, A parametric model for constitutive properties governing multiphase flow in porous media, *Water Resources Research, 23, no. 4,* 618-624, 1987.

Sclater, J. C., and P. A. F. Christie, Continental stretching: an explanation of the post-mid-Cretaceous subsidence of the central North Sea basin, *J. Geophys. Res., 85,* 3711-3739, 1980.

Wendebourg, Johannes, *Simulating Hydrocarbon Migration and Stratigraphic Traps*, Ph. D. Dissertation, Stanford University, 1994.

Wolfe, J. A., A paleobotanical interpretation of Tertiary climates in the northern hemisphere, *American Scientist, 66,* 694-703, 1978.

Willett, S. D., and D. S. Chapman, Analysis of temperatures and thermal processes in the Uinta Basin, *in* Sedimentary Basins and Basin-Forming Mechanisms, *Can. Soc. Petrol. Geol. Memoir 12,* edited by C. Beaumont, and A. J. Tankard, pp. 447-461, 1987b.

Predicting the Distribution of Contamination from a Chlorinated Hydrocarbon Release

Mark J. Lupo

K. W. Brown Environmental Services
501 Graham Road, College Station, TX 77845

George J. Moridis

Earth Sciences Division, Lawrence Berkeley Laboratory
University of California, Berkeley, CA 94720

Introduction

The T2VOC model (Falta et al., 1995) with the T2CG1 conjugate gradient package (Moridis and Pruess, 1995) was used to simulate the motion of a dense chlorinated hydrocarbon plume released from an industrial plant. The release involved thousands of kilograms of trichloroethylene (TCE) and other chemicals that were disposed of onsite over a period of nearly twenty years. After the disposal practice ceased, an elongated plume was discovered. Because much of the plume underlies a developed area, it was of interest to study the migration history of the plume to determine the distribution of the contamination.

Procedure

The transport modeling approach in a typical environmental consulting firm would involve the use of a groundwater model to simulate the flow through the saturated zone. A vadose zone model could then be used to study the upward transport of contaminants into overlying buildings. However, the chemicals were poured into a well installed in the vadose zone. There have been field studies to demonstrate that the initial distribution of chlorinated hydrocarbons in the subsurface has a significant bearing on their transport and detectability in a soil-gas survey (Rivett, 1995). A source in the vadose zone, such as the one simulated by T2VOC in this study, and a source beneath the water table will yield very different transport histories and surface fluxes.

The sloped, coarse unsaturated material at the simulated site is underlain by highly fractured bedrock. The chlorinated chemicals released were dense but volatile, indicating that density driven vapor flow could be important. The release was of a great enough magnitude that dense nonaqueous phase liquids (DNAPLs) should be present. Field measurements showed that DNAPL did exist and that TCE was detectable at great depth in the underlying bedrock. This further suggested that the best approach would involve a multicomponent model capable of simulating the vadose zone as well as the saturated zone. In this way, a single code could be used to accurately simulate both the lateral and vertical transport of the TCE.

The plume of interest was several kilometers in length and up to 500 m wide. Contamination has been detected at depths greater than 100 m. The site is underlain by an unconfined aquifer. The surface topography can be approximated as a gentle slope, falling more than 13 m over a distance of 1.3 km. The release of volatile organic chemicals to the atmosphere from a coarse vadose zone can be significant. Locating the points of greatest vapor release was one of the objectives of the study. Thus, the top surface could not be modeled as a no-flow boundary. Boundary blocks representing the atmosphere were needed.

A 2,300-cell two-dimensional grid was developed that contained boundary blocks on the upgradient and downgradient sides, as well as large atmospheric blocks on the top boundary. The

bedrock and the alluvial soil were assumed to be uniform. The vadose zone grid blocks were assigned a thickness of 1 m. The length of the blocks was 20 m.

One key feature of the domain was the spatial variation in soil-bedrock contact. The porosity and permeability of the soil and bedrock were obtained from field measurements. Soil porosity was found to be a linear function of depth. Bedrock porosity was estimated from fracture spacing and permeability using the cubic law (Witherspoon and Gale, 1977; Witherspoon et al., 1980) and its refinements (Zimmerman et al., 1991; Zimmerman et al., 1992). Bedrock blocks were highly fractured; their permeability was not insignificant. Capillary pressure parameters were taken from laboratory measurements, modified to match field data, and used to obtain parameters for the functions of Parker et al. (1987). The relative permeability functions of Stone (1970) were used (IRP = 6).

Preliminary two-phase runs were conducted to reach steady state. These runs generated the initial conditions for subsequent runs. The first run concerned only the unsaturated blocks of the upgradient boundary. Above the column was a semi-infinite atmospheric boundary block, and below the column was a semi-infinite water table block (Figure 1a). The atmospheric block had a "rock grain specific heat" set 1,000 times higher than the soil formation, a permeability of 10^{-5} m^2, and a porosity of 1.0. The relative permeability of the block to air would be 1.0, and the permeability to water would be nearly zero. Thus, IRP was set to 2 and RP(1) was set to 20. The capillary pressure functions for the atmosphere were the "zero capillary pressure" functions, i.e., ICP = 9. The water table block had properties similar to the alluvial soil, except that the relative permeability was 1.0 in all phases (IRP = 5, "all perfectly mobile") and the zero capillary pressure functions were used (ICP = 9). Temperature, atmospheric pressure, and humidity data were obtained from government sources (Quayle and Presnell, 1991) and corrected as necessary. Pressure, for example, was corrected for elevation to the nearest pascal. Initial conditions for the capillary pressure in the vadose zone were precalculated using the model of van Genuchten (1980). Steady state was attained from the twentieth time step.

The determination of the pressure in the saturated portion of the upgradient boundary was computed separately, using the water table block described above as the upper boundary condition. The air pressure for the top boundary blocks was obtained by means of a horizontal one-dimensional run for the atmospheric blocks (Figure 1b). The boundary conditions were imposed on the system by the upgradient boundary block. The slope was simulated by means of the cosine parameter BETAX in the connections inputs. The initial pressures for the downgradient boundary were obtained in two steps following the method used for the upgradient side, using the properties of the most downgradient block of the horizontal run as a boundary condition.

With the boundary conditions established, it was possible to compute the steady-state pressures and saturations for the interior of the domain (Figure 2). Connecting semi-infinite atmospheric boundary blocks to the domain will result in desiccation unless recharge rates are provided for the surface blocks. There were four zones based on land use. The initial conditions for interior cells were determined from the van Genuchten (1980) model and the hydrostatic equation, based on the location of the water table and the bedrock-alluvium contact. About 500 time steps were needed to reach steady state. The steady-state run helped establish the location of the water table in the expanses between available data.

The T2VOC model was then run for three phases with a TCE source at the location of the release. Warm start simulations were then conducted for the period following the termination of the release. The properties of TCE were obtained from Reid et al. (1987).

Results

The model output gives a history of the flow. Figure 3 shows the TCE concentrations after 16 years. In the simulation, the dissolved-phase contamination arrived ahead of any DNAPL. TCE

vapor emanated from the water table. TCE vapor concentrations were highest just above the water table; this should be expected. Where density-driven flow is the dominant soil-vapor transport mechanism, dense TCE vapor will move along the water table. Where vapors move by a combination of dissolved-phase transport and Henry's Law partitioning, TCE concentrations will be highest near their source, the groundwater. Density-driven flow was favored nearer to the source of the release, and dissolved-phase transport further from the source.

The concentrations of TCE at the water table do not drop steadily as a function of horizontal distance from the source. In any given vertical cross section, there is a depth at which the maximum TCE groundwater concentration occurs. This maximum groundwater TCE concentration is progressively deeper as one moves downgradient. The TCE concentration at the water table is affected by the distance between the water table and the level of maximum concentration.

In the neighborhood of the source, the output shows how the DNAPL sinks to the less conductive bedrock. Although DNAPL penetrated the bedrock in places, a DNAPL pool formed at a local low in the soil-bedrock surface. The concentration of TCE gas was greatest just above the water table. An examination of TCE vapor concentrations along air-soil surface blocks shows that the highest concentrations were associated with the bedrock high, and the location directly above the point of the release. There was also a local maximum just upgradient of a high recharge zone.

One input parameter that has not been discussed so far is the width of the two-dimensional grid blocks. Clearly, concentrations are strongly affected by the volume of the formation into which it is assumed the contamination was released. In the above simulation, it was assumed that the blocks were 1 m wide. Since there is no force or structure corralling the contamination into a 1-m-wide corridor, this simulation can be taken to be a high transport end member. The simulation was repeated using a domain width of 300 m. This width is the approximate width of the 1,000 mg/m^3 contour. The significance of 1,000 mg/m^3 is that this is the concentration at the downgradient end of the domain. Figure 4 shows the modeled concentration of TCE in the groundwater after 16 years.

Discussion

The results of the second simulation were in better agreement with field data. However, near the source, this simulation failed to predict the DNAPL that has been found at depth. When very wide blocks are used in a two-dimensional simulation, the organic contaminant mass can be spread out to a point that it is difficult to attain concentrations in excess of the solubility necessary to produce the DNAPL that has been observed beneath the source. The proportion of TCE mass entering into the atmospheric blocks above the source is also increased by having wide blocks. The thermodynamic equations in T2VOC interpret the spreading out of the contaminant mass of a chemical such as TCE in terms of enhanced volatilization. Thus, widening the blocks yielded a mixed result in terms of the accuracy of the simulation: gains in accuracy downgradient from the source were achieved at a cost in accuracy closer to the source. The volume of DNAPL was underpredicted, and the rate of volatilization was overpredicted.

Conclusion

T2VOC model output is useful in simulating the transport of volatile chemicals in a realistic subsurface environment that includes the unsaturated zone. This is particularly true if the release occurred in the unsaturated zone, and when it is of interest to predict the release of soil gas into buildings. The contribution of soil-vapor transport to the spread of groundwater contamination was manifested by the arrival of detectable levels of TCE at the downgradient side of the domain seven years ahead of the time one would predict from its retarded velocity. However, density-driven flow was not exhibited in these simulations in every part of the domain with the chosen gridding scheme.

Two-dimensional simulations can overestimate the transport of the contaminant at great distance from the source if the domain thickness is too small. They can omit a free-phase liquid near the source and overestimate vapor flux near the source if the thickness is too great. Three-dimensional modeling avoids this difficulty. However, within the constraints many environmental problems must be solved, three-dimensional modeling can be inconvenient and its cost is prohibitive to many industrial clients. Thus, when T2VOC is used in a real-life industrial setting, careful choices must be made in determining the grid.

References

Falta, R. W., K. Pruess, S. Finsterle, and A. Battistelli, 1994, T2VOC User's Guide, Lawrence Berkeley Laboratory, Berkeley, CA, (LBL report number pending).

Moridis, G. J. and K. Pruess, 1995, T2CG1: A Package of Preconditioned Conjugate Gradient Solvers for the TOUGH2 Family of Codes, LBL Report Number 36235, Lawrence Berkeley Laboratory, Berkeley, CA.

Parker, J. C., R. J. Lenhard, and T. Kuppusamy, 1987, A Parametric Model for Constitutive Properties Governing Multiphase Flow in Porous Media, *Water Res. Res., 23*, (4), 618-624.

Quayle, R. and W. Presnell, 1991, Climatic Averages and Extremes for U.S. Cities, Historical Climatology Series 6-3, U.S. Department of Commerce, National Oceanic and Atmospheric Administration, Asheville, NC.

Reid, R. C., J. M. Prausnitz, and B. E. Poling, 1987, *The Properties of Gases and Liquids,* McGraw-Hill, New York.

Rivett, M. O., 1995, Soil-Gas Signatures from Volatile Chlorinated Solvents: Borden Field Experiments, *Ground Water 33*, (1), 84-98.

Stone, H. L., 1970, Probability Model for Estimating Three-Phase Relative Permeability, *J. Pet. Tech., 22*, (1), 214-218.

van Genuchten, M. Th., 1980, A Closed-Form Equation for Predicting the Hydraulic Conductivity of Unsaturated Soils, *Soil Sci. Soc. Am. J., 44*, 892-898.

Witherspoon, P. A. and J. E. Gale, 1977, Mechanical and Hydraulic Properties of Rocks Related to Induced Seismicity, *Eng. Geol. 11*, 23-57.

Witherspoon, P. A., J. S. Y. Wang, K. Iwai, and J. E. Gale, 1980, Validity of Cubic Law for Fluid Flow in a Deformable Rock Fracture, *Water Res. Res., 16*, (6), 1016-1024.

Zimmerman, R. W., S. Kumar, and G. S. Bodvarsson, 1991, Lubrication Theory Analysis of the Permeability of Rough-walled Fractures, *Int. J. Rock Mech. Min. Sci. & Geomech. Abstr. 28*, (4), 325-331.

Zimmerman, R. W., D.-W. Chen, and N. G. W. Cook, 1992, The Effect of Contact Area on the Permeability of Fractures, *J. Hydrol., 139*, 79-96.

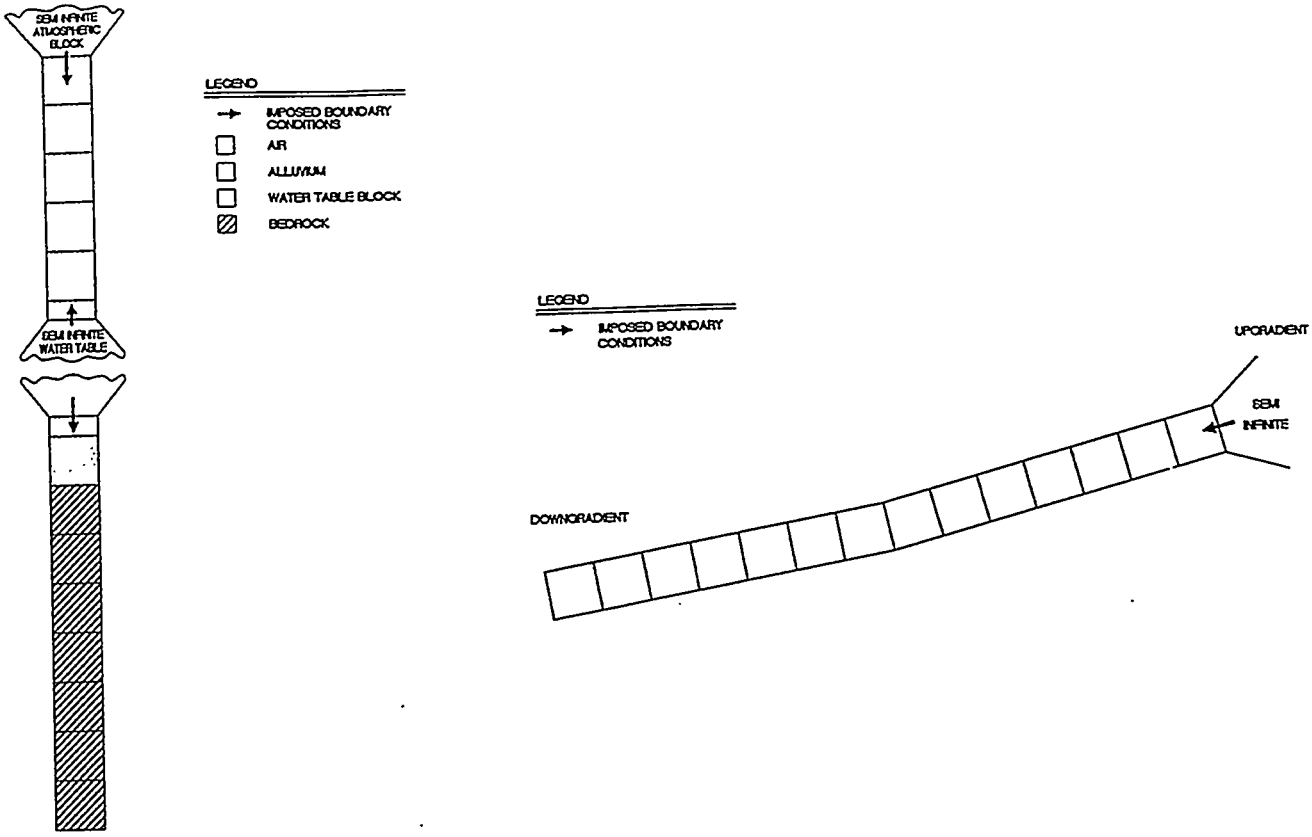

Figure 1. (a) Schematic representation of the upgradient boundary block calibration.
(b) Schematic representation of the atmospheric boundary block calibration.

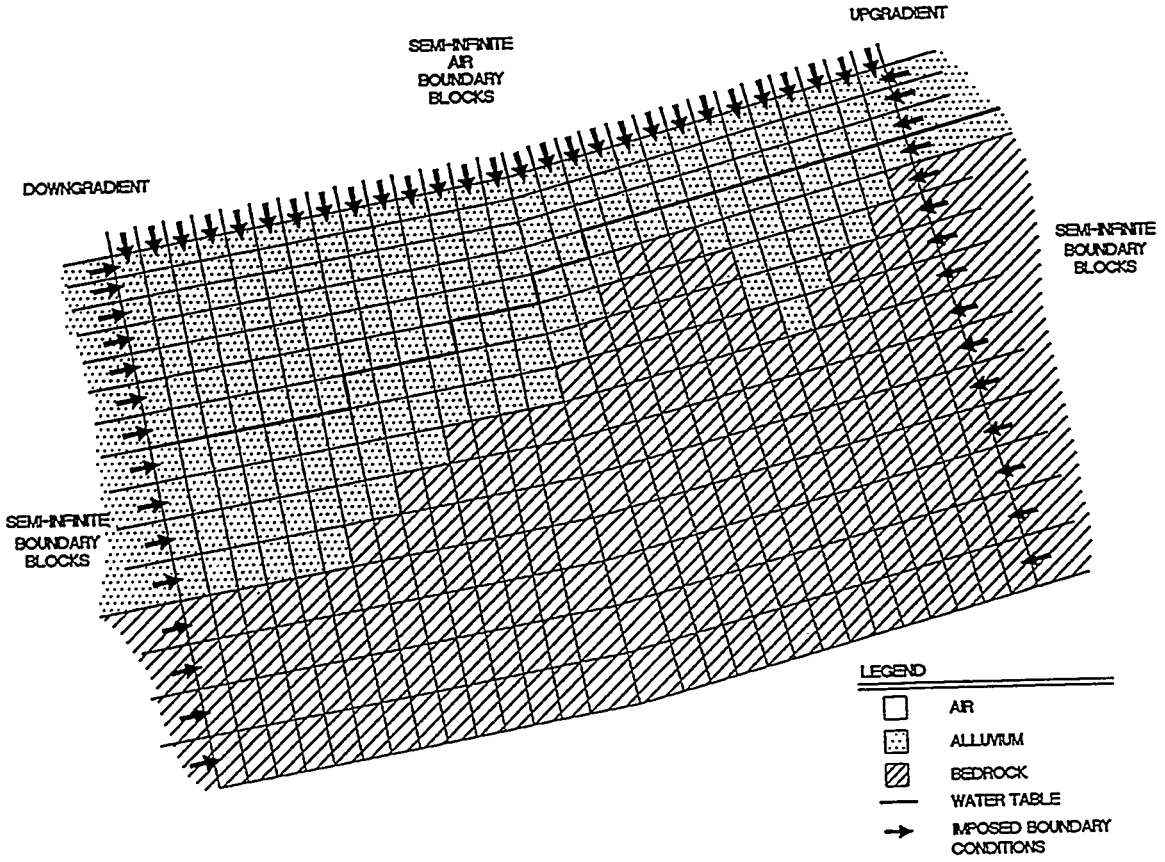

Figure 2. Schematic representation of the two-dimensional domain.

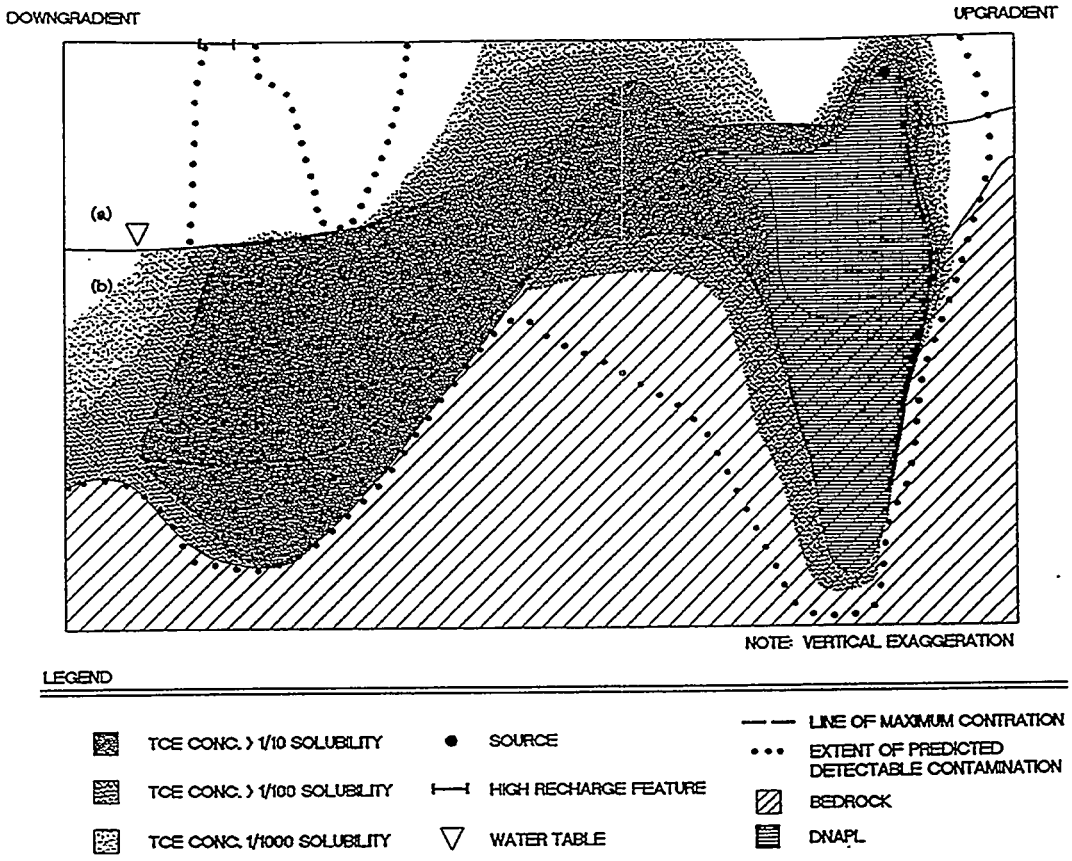

Figure 3. TCE concentrations after 16 years for the 1-m wide domain: (a) soil vapor in the vadose zone, (b) dissolved phase contamination in the groundwater.

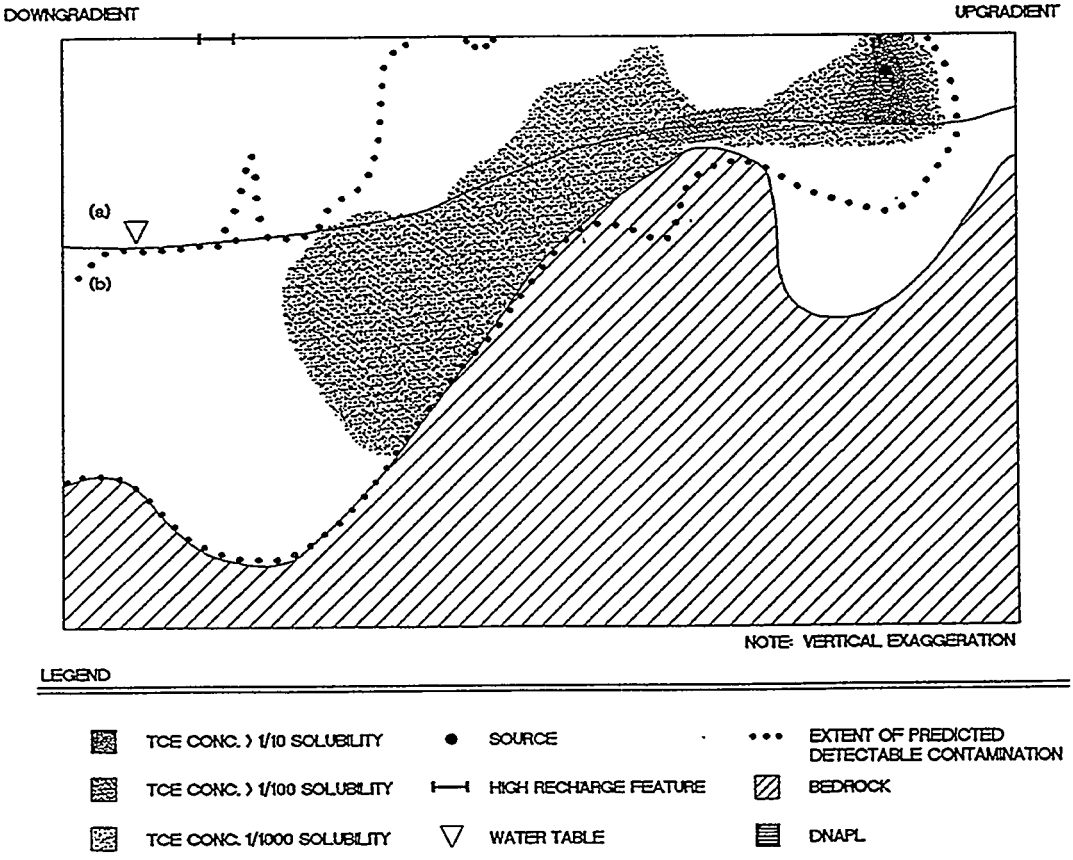

Figure 4. TCE concentrations after 16 years for the 300-m wide domain: (a) soil vapor in the vadose zone, (b) dissolved phase contamination in the groundwater.

LNAPL Infiltration in the Vadose Zone: Comparisons of Physical and Numerical Simulations

MARINA PANTAZIDOU
Department of Civil and Environmental Engineering, Carnegie Mellon University

ABSTRACT

The numerical model T2VOC was used to reproduce light, nonaqueous phase liquid (LNAPL) infiltration scenarios in the vadose zone. The numerical modeling results were compared to results from laboratory experiments simulating LNAPL spills in the vadose zone. Laboratory measurements included results from one-dimensional column and two-dimensional tank experiments using uniform sands of varying average grain sizes. The constitutive relationships for the sands were obtained from the one-dimensional experiments. The two-dimensional experiments simulated leakage of kerosene under constant head. The sensitivity of the numerical results to the constitutive relationships used and the specified boundary conditions was examined. For this purpose two different capillary pressure-saturation relationships were used for the same sand and both constant head and constant flux conditions were simulated. The constant head boundary conditions resulted in significantly greater contaminant front speeds than those observed experimentally. Within the contaminated area, different LNAPL saturations were obtained for the two capillary pressure curves used. The constant flux boundary conditions produced a much better prediction. At the initial stages of infiltration the results for both capillary pressure curves were similar and in good agreement with the experimental results. However, as the LNAPL front approaches the capillary fringe the choice of the capillary pressure curve was found to influence the results.

INTRODUCTION

Numerical models are indispensable in the study of immiscible fluid transport because the equations that describe multiphase fluid flow are strongly coupled and highly non-linear, and thus do not admit analytical solutions, except for specific problems in which simplifying assumptions are possible [e.g., one-dimensional displacement of oil by water (Buckley and Leverett, 1942)]. Modeling efforts include solutions for two-phase flow, i.e., water and NAPL (Hochmuth and Sunada, 1985; Osborne and Sykes, 1986; Kueper and Frind, 1991a,b) and for three-phase flow systems, i.e., water, NAPL, and air (Faust, 1985; Abriola and Pinder, 1985a,b; Kaluarachchi and Parker, 1989; Falta et al., 1992a). Validation of these codes, by comparison to field or laboratory data, has been very limited mainly due to the scarcity of such data (Lenhard et al., 1988; Faust et al., 1989; Falta et al., 1992b). In the absence of laboratory or field data, and given our present limited understanding of the migration potential of NAPLs, we can only hypothesize on the dimensional and time scales associated with NAPL transport processes. Examples of the questions we need to answer include: how long it will take an LNAPL to reach the water table? how far horizontally will the LNAPL spread? This paper investigates the effect of two factors, namely the boundary conditions specified and the constitutive relationships selected, on the answers that a numerical model might give to the aforementioned questions. The numerical code used, T2VOC (Falta et al., 1994), is an adaptation of the STMVOC simulator developed at Lawrence Berkeley Laboratory by R. Falta and K. Pruess (Falta and Pruess, 1991). The following sections describe briefly the experiments that are used for comparison and the results of the numerical simulations.

EXPERIMENTAL SIMULATIONS

One-dimensional drainage experiments were conducted in order to determine the constitutive relationships, which are required for numerical modeling of NAPL migration, using a procedure developed by Pantazidou (1991). Capillary pressure and relative permeability curves were determined for a fine and a coarse sand. The relative permeability curves obtained for the two sands were almost identical, confirming Wyckoff and Botset's (1936) early observation that relative permeability curves for sands are not affected by permeability magnitude. These relative permeability curves were also in good

agreement with Wyllie's (1962) formula, which expresses the relative permeability as a function of the third power of the scaled saturation (Pantazidou and Sitar, 1993). The capillary pressure curves were different for the two sands, as expected, since these curves reflect variations in particle or, equivalently, pore size distribution. Guided by these observations, the sensitivity of the numerical results to the input capillary pressure curves was examined in this study.

The two-dimensional experiments simulated LNAPL spills in unsaturated, two-dimensional domain above the water table. The procedure for the two-dimensional tests consisted of releasing red-dyed kerosene in the unsaturated zone, after a water table had been established within the sand sample. The dimensions of the sand sample were 61 cm by 61 cm by 5 cm. The evolution of the front was observed through the transparent side of the tank containing the sample and the contaminant front was traced at appropriate intervals. Visual observations were supplemented by pressure measurements of water and kerosene and by water saturation measurements. A total of fifteen tests was conducted to investigate the effects on NAPL transport of soil grain size, heterogeneities, and water table fluctuations. Detailed description of the materials used, the test procedures and the results is presented elsewhere (Pantazidou and Sitar, 1993). In this paper, one experiment on a uniform, fine sand sample was selected for comparison with the numerical results. The capillary pressure curve for this fine sand (measured points on Figure 1) was found to be approximated well by a van Genuchten type curve with α=3.157 and n=8.09 (curve C on Figure 1). Figure 2 shows contaminant front profiles at different times for this experiment. A total of 350 cm^3 of kerosene was allowed to infiltrate in the sand sample under a constant head of 4 cm of kerosene. Under this constant head, kerosene infiltration lasted for about 3 hours, corresponding to an average flux of 2.4 cm^3/min.

NUMERICAL SIMULATIONS

Four numerical simulations are selected for discussion in this paper reproducing constant head and constant flux boundary conditions for two different capillary pressure curves. The constant LNAPL head was specified to be the same as the constant kerosene head that was maintained in the physical simulations, i.e., 4 cm of kerosene. The constant LNAPL flux was calculated as an average of the actual flux that was observed in the experiments during kerosene infiltration under the 4-cm constant head, i.e., 2.4 cm^3 of kerosene per minute. The choice of the capillary pressure-saturation curve determines the volume of water retained in the pore space above the water table and is therefore expected to affect the LNAPL transport patterns in the unsaturated domain. Simulations using the best-fit van Genuchten capillary pressure curve ran into convergence problems associated with the steep rise in capillary pressure for saturations close to 100 percent (see curve C on Figure 1). Ongoing work is addressing these issues. In the meantime, simulations were performed with two alternative curves, A and B (see Figure 1). Curve A was selected because it produces an average water saturation (or water volume) above the water table that is comparable to the measured distribution (i.e., curve C on Figure 1). Curve B has been suggested in the literature (ES&T, Inc., 1990) for sands, and results in a very low water volume above the water table.

The constant head simulations, although better representing the experimental boundary conditions, resulted in very high contaminant front speeds. Figures 3a and 3b show LNAPL saturation profiles at 15 minutes after the beginning of infiltration; the experimentally observed contaminant front is also highlighted for comparison. It is interesting to note that the use of capillary curve B (lower water saturation above the water table) results in a deeper contaminated area (Figure 3b) and also in significantly higher LNAPL saturations within the contaminated area. Whereas the difference in saturation cannot be discerned from the black-and-white plots, inspection of the saturation output values shows a maximum LNAPL saturation beyond the leaking source of approximately 85 percent for the low water content case (curve B) compared to a maximum saturation of only 55 percent for the high water content case (curve A). As a result, the total volume of LNAPL in the sample is significantly larger for initial conditions of low water content, the difference increasing with time.

The constant flux simulations produced a much better agreement with the experimental results. Figures 4a and 4b show contaminant profiles after 30 minutes of kerosene infiltration. These figures show that the results for curves A and B do not differ significantly and are in good agreement with the observed contaminant fronts also shown on these figures. Output saturation values indicate that during the initial stages of infiltration, kerosene is mainly displacing air and, as a result, is not significantly affected by the contrast between the water saturation for the two cases. Upon careful inspection, a trend for lateral spreading can be discerned from the results obtained using curve A (higher water saturation above the water table).

The difference between the results obtained using the two curves increases at later stages of infiltration, as can be seen from Figures 5a and 5b, which present experimental and numerical results after 120 minutes of kerosene infiltration. The numerical simulations failed to accurately capture the horizontal spreading of the contaminant, the difference being more pronounced for the low initial water saturation case (Figure 5b). The dramatic contrast observed between calculated LNAPL saturations within the contaminated area for the curves A and B in the constant head simulations was not reproduced for the constant flux boundary conditions. However, the saturation distribution within the contaminated area exhibited different trends for the two cases. For the high water content initial conditions, the maximum saturations occupied a small portion of the contaminated area, close to the leaking source, whereas for the low water content condition, a significant portion of the affected area was contaminated at saturations close to the maximum value calculated. It is also interesting to note that the total contaminated area for the high initial water content was 20 percent larger compared to the low water content case. The predicted difference is in agreement with experimental results showing that during infiltration in the unsaturated zone, high initial water content conditions result in a larger contaminated area at lower LNAPL saturations compared to low initial water content conditions, for the same volume of contaminant release (Pantazidou and Sitar, 1993).

SUMMARY

These initial results indicate that the choice of boundary conditions can have a dramatic impact on the predicted mobility of NAPLs. In this study the constant head conditions failed to reproduce a realistic contaminant flux. Furthermore, the distribution of water in the unsaturated zone, as determined by the capillary pressure-saturation relationships, can affect significantly the results and therefore necessitates determination of the capillary pressure curve that corresponds to the soil type of interest. Perhaps the most important conclusion is that in the absence of experimental results, we may obtain several sets of numerical results that will look reasonable without having any way of telling which ones are realistic.

Acknowledgments. The unfailing assistance of Stefan Finsterle and Karsten Pruess of Lawrence Berkeley Laboratory and Jason Buesing of Carnegie Mellon University is greatly appreciated.

REFERENCES

Abriola, M., and G.F. Pinder, 1985a, A Multiphase Approach to the Modeling of Porous Media Contamination by Organic Compounds, 1, Equation Development, Water Resour. Res., 21:1:11-18.

Abriola, L.M., and G.F. Pinder, 1985b, A Multiphase Approach to the Modeling of Porous Media Contamination by Organic Compounds, 2, Numerical Simulation, Water Resour. Res., 21:1:19-26.

Buckley, S.E., and M.C. Leverett, 1942, Mechanism of Fluid Displacement in Sands, Trans. AIME, 146:107-116.

Environmental Systems & Technologies, Inc. (ES&T, Inc.), 1990, MOFAT: A Two Dimensional Finite Element Program for Multiphase Flow and Multicomponent Transport, Program Documentation - Version 2.0, Blacksburg, Virginia.

Falta, R.W., and K. Pruess, 1991, STMVOC User's Guide, Lawrence Berkeley Laboratory Report LBL-30758, Berkeley, CA.

Falta, R.W., K. Pruess, I. Javandel, and P.A. Witherspoon, 1992a, Numerical Modeling of Steam Injection for the Removal of Nonaqueous Phase Liquids From the Subsurface: 1. Numerical Formulation, Water Resour. Res. 28:2:433-449.

Falta, R.W., K. Pruess, I. Javandel, and P.A. Witherspoon, 1992b, Numerical Modeling of Steam Injection for the Removal of Nonaqueous Phase Liquids From the Subsurface: 2. Code Validation and Application, Water Resour. Res. 28:2:451-465.

Falta, R.W., K. Pruess, S. Finsterle, and A. Batistelli, T2VOC User's Guide, draft report, October 1994.

Faust, C.R., 1985, Transport of Immiscible Fluids Within and Below the Unsaturated Zone: A Numerical Model, Water Resour. Res., 21:4:587-596.

Faust, C.R., J.H. Guswa, and J.W. Mercer, 1989, Simulation of Three-phase Flow of Immiscible Fluids Within and Below the Unsaturated Zone, Water Resour. Res., 25:12:2449-2464.

Hochmuth, D.P., and D.K. Sunada, 1985, Ground-water Model of Two-phase Immiscible Flow in Coarse Material, Ground Water, 23:5:617-626.

Kaluarachchi, J.J., and J.C. Parker, 1989, An Efficient Finite Element Method for Modeling Multiphase Flow, Water Resour. Res., 25:1:43-54.

Kueper, B.H., and E.O. Frind, 1991a, Two-phase Flow in Heterogeneous Porous Media, 1, Model Development, Water Resour. Res., 27:6:1049-1057.

Kueper, B.H., and E.O. Frind, 1991b, Two-phase Flow in Heterogeneous Porous Media, 2, Model Application, Water Resour. Res., 27:6:1059-1070.

Lenhard, R.J., J.H. Dane, J.C. Parker, and J.J. Kaluarachchi, 1988, Measurement and Simulation of One-dimensional Transient Three-phase Flow for Monotonic Liquid Drainage, Water Resour. Res., 24:6:853-863.

Osborne, M., and J. Sykes, 1986, Numerical Modeling of Immiscible Organic Transport at the Hyde Park Landfill, Water Resour. Res., 22:1:25-33.

Pantazidou, M., 1991, Migration of Nonaqueous Liquids in Partly Saturated Granular Media, PhD Thesis, University of California, Berkeley.

Pantazidou, M., and N. Sitar, 1993, Emplacement of Nonaqueous Liquids in the Vadose Zone, Water Resour. Res., 29:3:705-722.

Wyckoff, R.D., and H.G. Botset, 1936, The Flow of Gas-Liquid Mixtures through Unconsolidated Sands, Physics, (J. Appl. Phys.), 7:9:325-345.

Wyllie, M.R.J., 1962, Relative Permeability, Chapter 25 of Vol.2 in: Petroleum Handbook, Frick, T.C. Ed., SPE of AIME, Dallas, Texas.

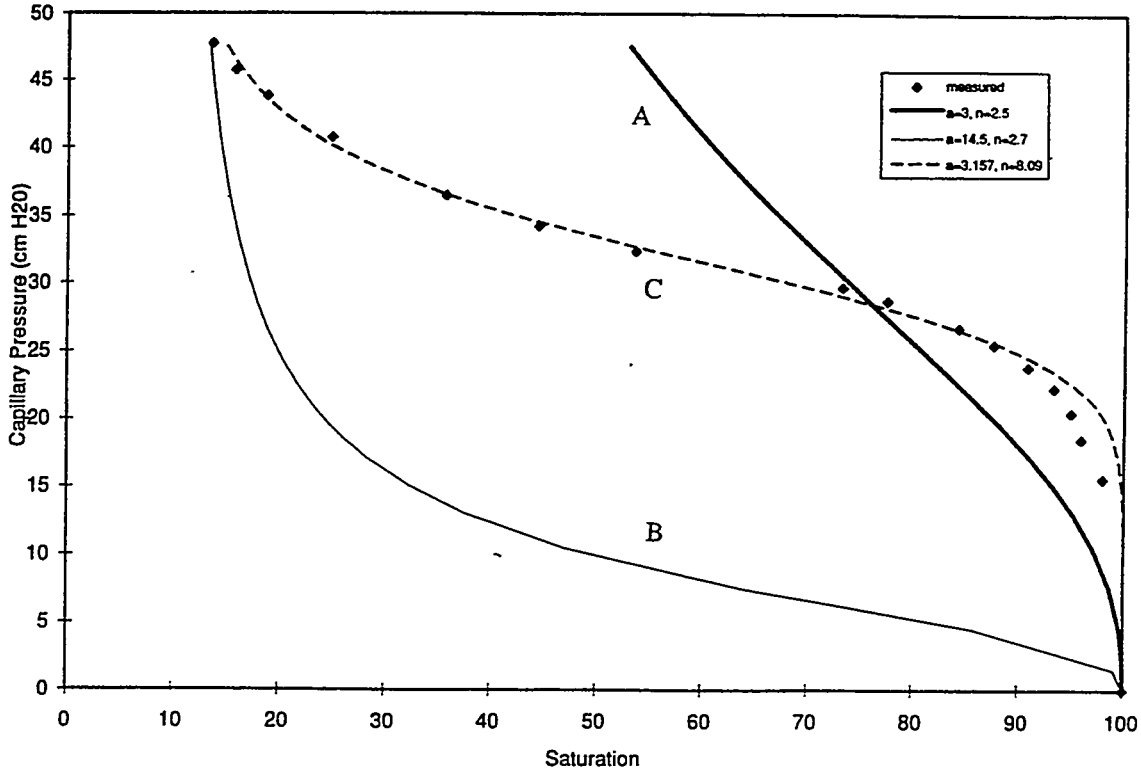

Fig. 1. Capillary pressure-saturation curves for different a and n parameters and measured values for fine sand.

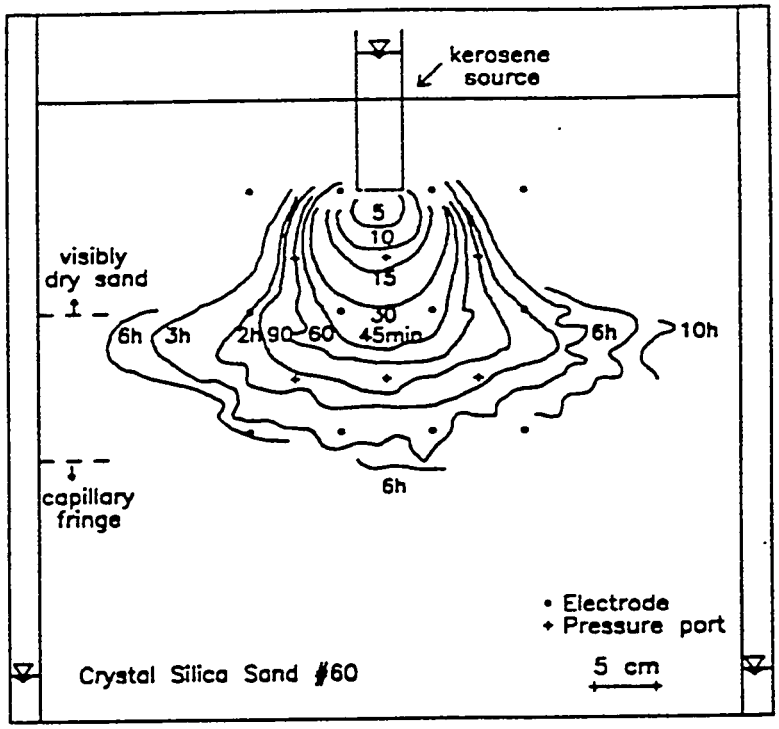

Fig. 2 . Observed kerosene front propagation for fine sand.

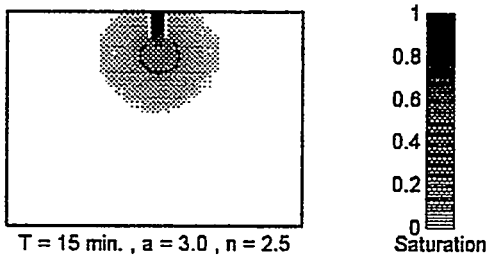

Figure 3a: Simulated kerosene front at 15 minutes using capillary pressure curve A and constant head.

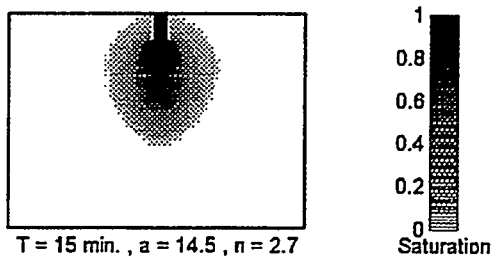

Figure 3b: Simulated kerosene front at 15 minutes using capillary pressure curve B and constant head.

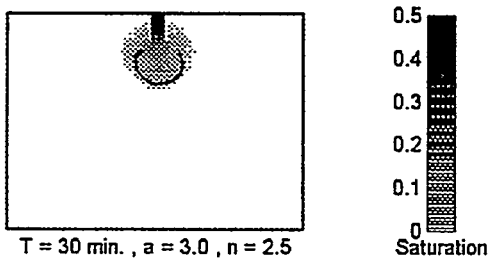

Figure 4a: Simulated kerosene front at 30 minutes using capillary pressure curve A and constant flux.

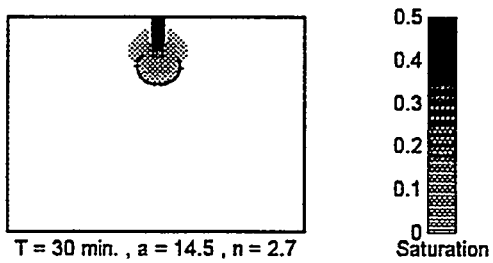

Figure 4b: Simulated kerosene front at 30 minutes using capillary pressure curve B and constant flux.

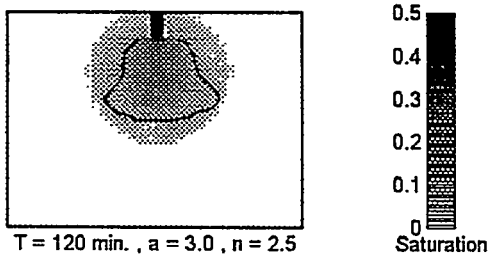

Figure 5a: Simulated kerosene front at 120 minutes using capillary pressure curve A and constant flux.

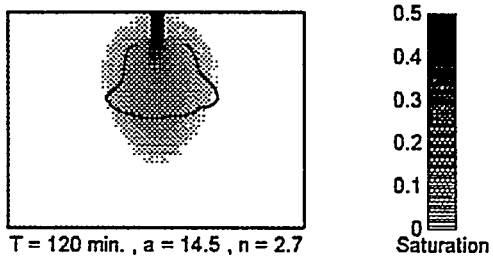

Figure 5b: Simulated kerosene front at 120 minutes using capillary pressure curve B and constant flux.

Presented at the TOUGH Workshop 95
Lawrence Berkeley Laboratory, Berkeley, CA 94720, March 20-22, 1995

AIR BARRIERS FOR WASTE CONTAINMENT IN THE SUBSURFACE

George J. Moridis and Karsten Pruess

Earth Sciences Division, Lawrence Berkeley Laboratory
University of California, Berkeley, CA 94720

Introduction

The increase of air saturation in a soil alters significantly its hydraulic characteristics by reducing its the relative permeability to liquids. This realization led to the concept that air injection could be used in the context of remedial strategies to create low permeability barriers to contaminated water and NAPL migration. Air offers a number of significant advantages as a barrier fluid: it is not a contaminant, already exists in the vadose zone, is abundant, easily available, free of charge, and has well-known thermodynamic properties. This report provides a brief summary of ait barrier modeling results to date.

Concept Description

The design discussed here involves a single layer of horizontal wells below the contamination in the vadoze zone. If the wells are numbered, the odd-numbered wells are used for air injection, and the even-numbered ones for gas removal. This system has a predominantly horizontal orientation of flow. This horizontal barrier is characterized by (1) a drier zone near the injection wells due to water displacement and evaporation, (2) a wetter zone near the removal wells due to recondensation, (3) a high gas pressure zone in the vicinity of injection, and (4) low gas pressure near the removal wells. In the vicinity of the injection wells, contaminated water and NAPLs cannot move downward because of a reduced NAPL relative permeability (caused by high gas saturation) and a pressure barrier to downward flow. In the vicinity of the removal wells, NAPLs and NAPL vapors cannot move downward due to a hydraulic gradient towards the wellbore.

In the vadose zone air injection not only displaces water, but also causes phase changes due to its drying effect. In the vicinity of the injection point, water and volatile NAPLs vaporize. The combination of displacement and drying drastically reduces the liquid relative permeability and creates a dry zone of high capillary suction from which liquid contaminants cannot escape. These effects may be significantly enhanced by increasing the temperature of the injected air. The vaporized water and NAPLs recondense away from the injection point, but their migration is controlled by the presence of the dry zone and the hydraulic impedance to flow between the injection and removal wells. In addition to containment, air barriers may also have a significant element of remediation because the vaporized NAPLs are removed from the subsurface through the gas removal well. These vapors will need to be treated before release to the atmosphere. Unlike other techniques, air barriers do not introduce a new liquid which can mobilize contaminants, and are easy to maintain.

Numerical Simulation

The problem under study involves numerous strongly non-linear complex processes: multi-phase (aqueous, gas, NAPL) multi-component flow, dissolution and advective transport, multicomponent diffusion, phase changes (evaporation and condensation) and heat transport. T2VOC [*Falta et al.*, 1995], a member of the TOUGH2 [*Pruess*, 1991] family of codes, was used for the simulation.

The computing platform was an IBM RS/6000 370 workstation. We used a typical Hanford soil and TCE as the contaminant. The soil was considered homogeneous and isotropic with a permeability $k = 1.6\times10^{-11}\ m^2$ and porosity $\phi = 0.385$. Relative permeability and capillary pressures were given by the *Parker et al.* [1987] 3-phase relationships, with $S_m = 0.13$, $n = 1.53$, $\alpha_{gn} = 13.15$, and $\alpha_{nw} = 15.47$ [*Falta et al.*, 1995]. The watertable was located 45 m from the surface. We modeled a section of the vadoze zone 40 m deep (from the surface) and 2 m wide.

The two-dimensional domain was discretized in 1720 gridblocks (20×86 in x,z). We made two runs. The first run (3 equations per cell, 5160 simultaneous equations) represented the reference case and involved continuous leakage of TCE at a rate q_o= 1.3 *kg/day* at z = 18.3 m from the top and $x = 1\ m$. The second run (4 equations per cell, 6880 equations) included the air barrier, with two wells located at ($x = 0\ m$, $z = 20\ m$) and ($x = 2\ m$, $z = 20\ m$). Air was injected into the first well at a rate of q_a = 1000 *kg/day* and an enthalpy of H_a = 101 *kJ/kg*, and gas was withdrawn from the second well at a rate of q_g = 1000 *kg/day*. For both runs t_{max} = 720 days.

Results and Discussion

The reference case required only 16,814 CPU sec to solve. The extreme non-linearities of the air barrier run necessitated rather small timesteps and required 138,118 CPU sec to cover t_{max} using the DSLUCS conjugate gradient solver of T2VOC. The results are presented in Figures 1 through 6. We reach the following conclusions:

1. From Figure 1, it is evident that the extent of free-phase TCE contamination is significantly smaller in the presence of the air barrier. As expected, the gas removal well attracts and vaporizes free-phase TCE. Note that the maximum TCE saturation with the air barrier is 0.22 (vs. 0.20 without), and is attributed to the focusing effect of the removal well.
2. Figure 2 shows that without the air barrier the soil gas contamination by TCE vapors is far more extensive than the TCE free-phase contamination, and poses a more serious problem because the TCE vapors are re-dissolved in the water (following Henry's law). The beneficial effect of the air barrier is more dramatic here: the extent of TCE gas contamination is dramatically smaller, localized, and limited to a narrow band which ends at the gas removal well. The maximum TCE concentration in the gas with the air barrier is 0.42 kg/m^3, almost twice as high as the 0.28 kg/m^3 observed without the barrier. The focusing action of the gas removal well seems to be responsible for the higher TCE concentration.
3. The air barrier is evident in Figure 3, which presents the gas saturation in the domain. We observe the emergence and evolution of a completely dry zone (with a gas saturation of 1), which is as much as 3 m thick. Due to practically zero liquid permeability, this zone is impermeable to NAPLs and/or contaminated water. This is evidenced by the fact that this zone is completely dry despite being overlain by the TCE free product in a very permeable medium.
4. The significant element of remediation (because the vaporized NAPLs are removed through the gas removal well) in air barriers is evident in Figures 4 and 5. The amount of TCE in the various phases (NAPL, gas, aqueous) is significantly lower with the air barrier (Figure 4). In Figure 5 the TCE mass ratio (defined as the ratio of TCE mass with and without the air barrier) in the NAPL, aqueous, and gas phases shows that the presence of the air barrier reduces the TCE amount by at least an order of magnitude over the reference case.
5. Without the air barrier, significant amounts of TCE contamination advance past the z = 20 m line, i.e. the line connecting the wells (Figure 6). The amount of TCE free product below the well line is 470 kg. However, no TCE in the gas, aqueous, or NAPL phases escapes past the dry zone established by the air barrier.

References

Falta, R.W., K. Pruess, S. Finsterle, and A. Battisteli, T2VOC User's Guide, LBL-30758, Earth Sciences Division, Lawrence Berkeley Laboratory, Berkeley, California, March 1995.

Pruess, K. (1991), TOUGH2 - A general-purpose numerical simulator for multiphase fluid and heat flow, Lawrence Berkeley Laboratory report LBL-29400.

Parker, J.C., R.J. Lenhard, and T. Kuppusamy, A parametric model for constitutive properties governing multiphase flow in porous media, Water Resour. Res., 23(4), 618-624, 1987.

Acknowledgement

This work was supported by the In Situ Remediation Technology Development Integrated Program, Office of Technology Development, Office of Environmental Restoration and Waste Management, U.S. Department of Energy, under contract DE-AC03-76SF00098. Drs. Curt Oldenburg and Stefan Finsterle are thanked for their helpful review comments.

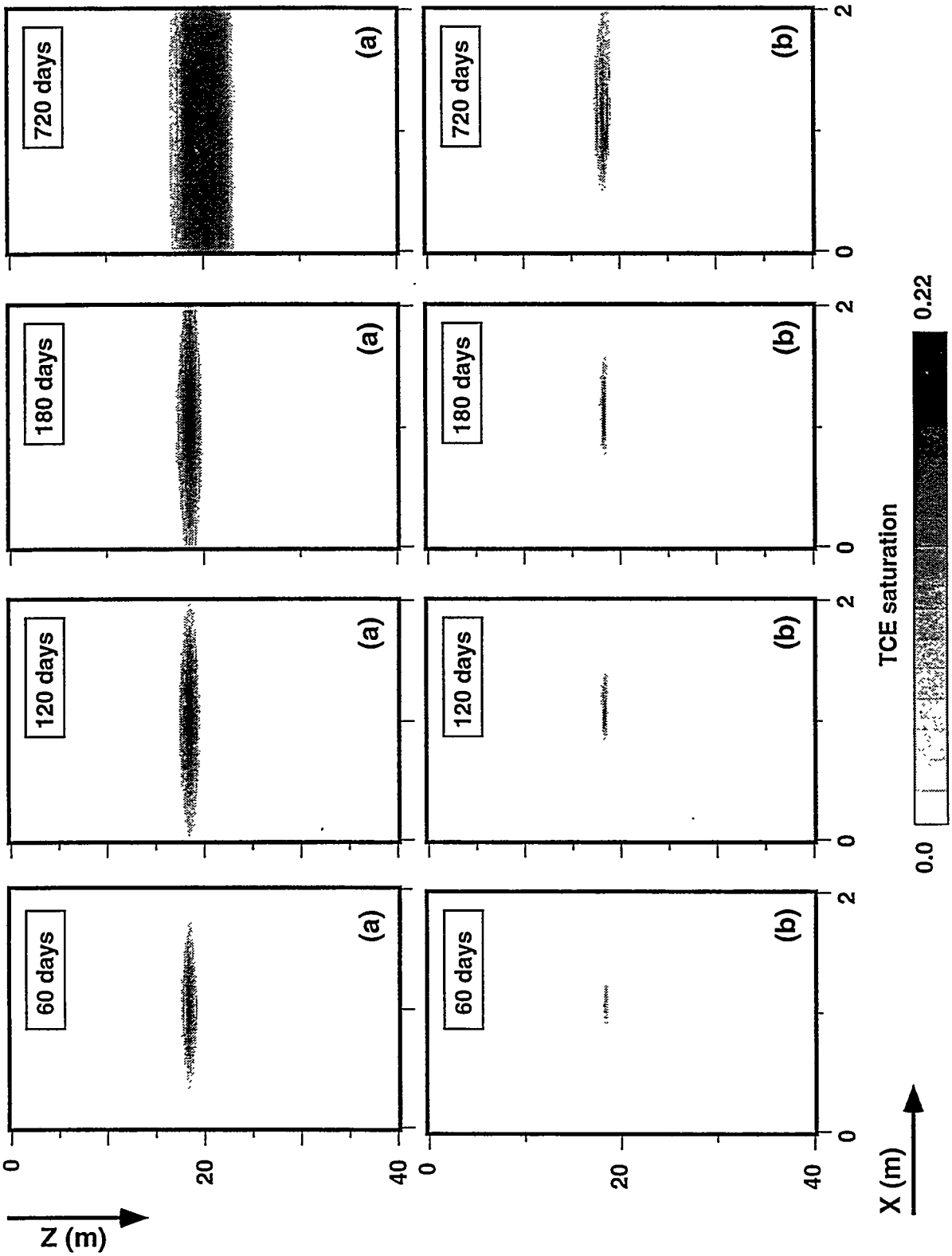

Figure 1. TCE saturation in the soil (a) without and (b) with the air barrier.

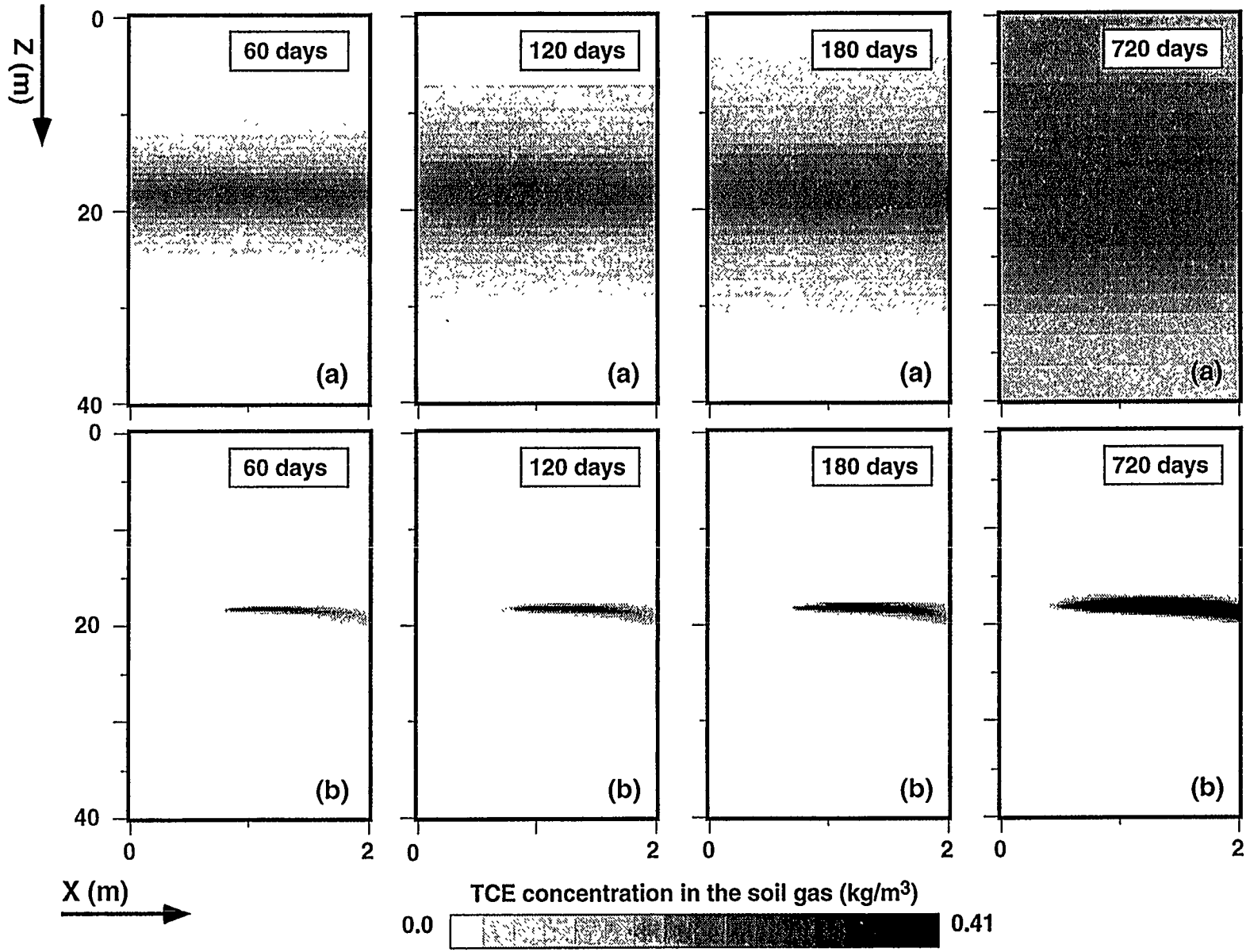

Figure 2. TCE concentration in the soil gas (a) without and (b) with the air barrier.

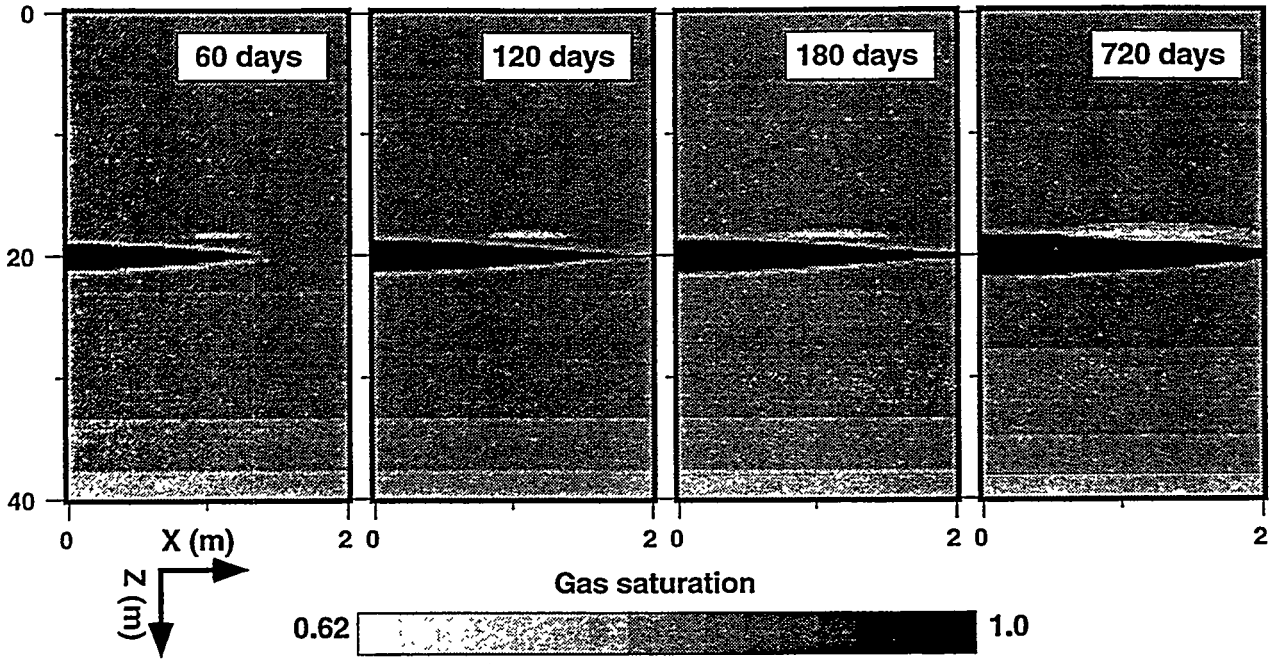

Figure 3. Gas saturation in the soil with an operating air barrier.

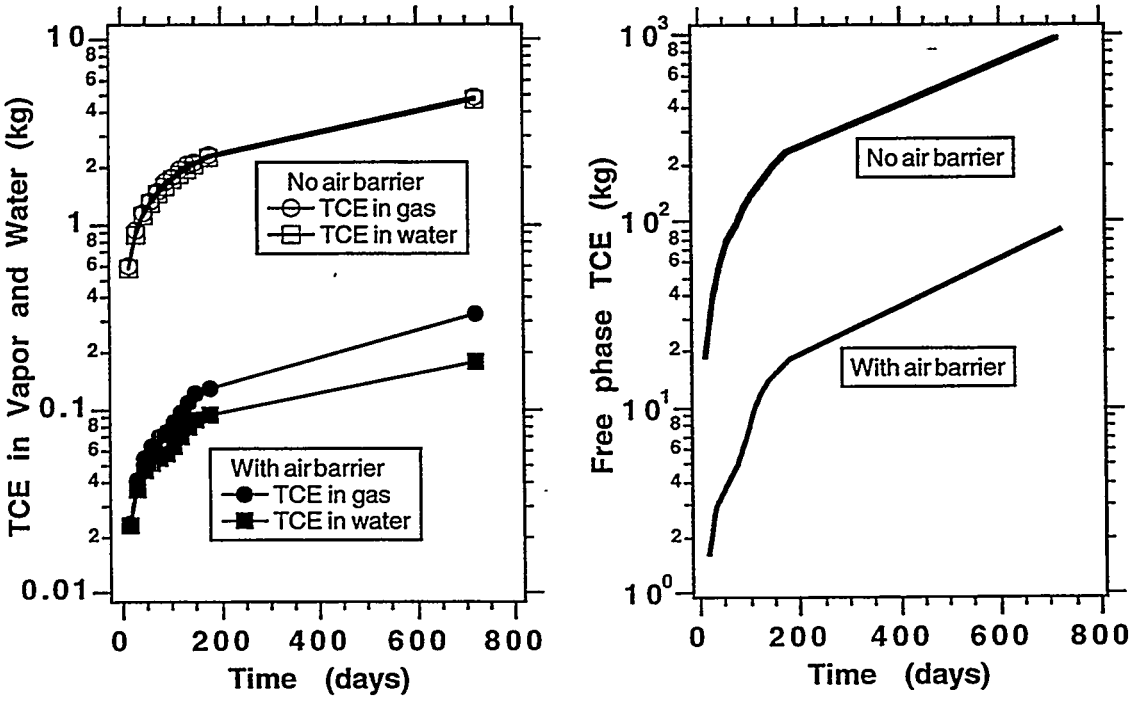

Figure 4. The amount of TCE in the vapor, liquid, and NAPL phases with and without the air barrier.

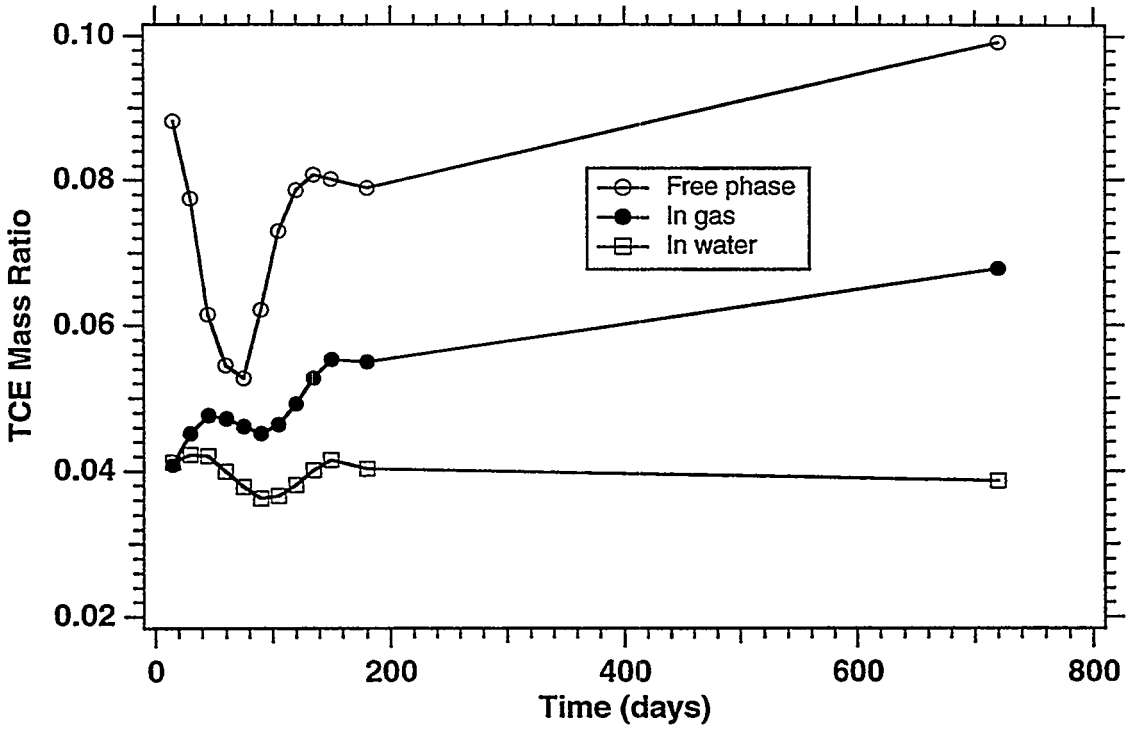

Figure 5. TCE mass ratio for the gas, aqueous, and NAPL phases.

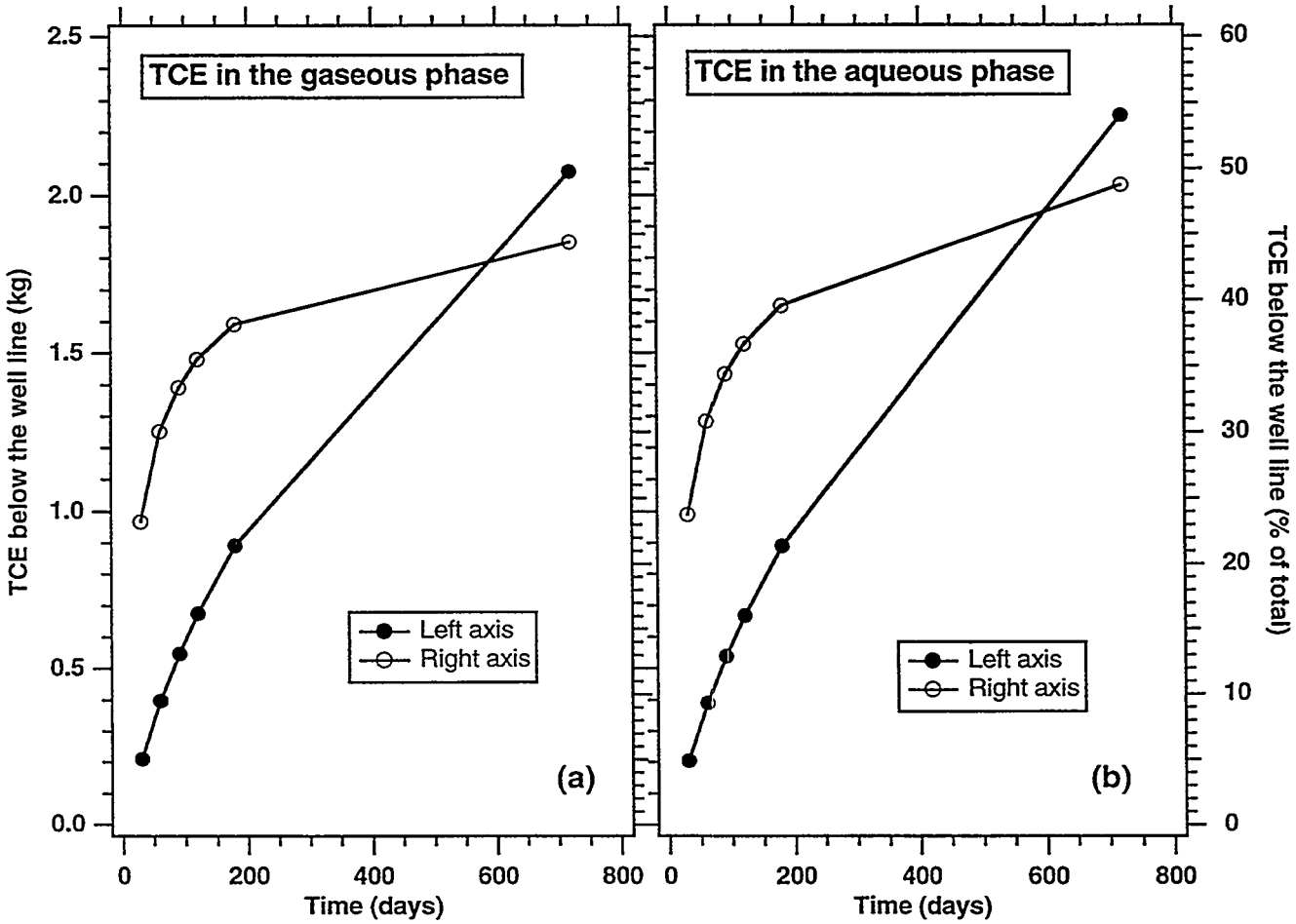

Figure 6. TCE mass below the level of the air wells without an air barrier. With an air barrier, no TCE advances below the well line.

Using Simulation-Optimization Techniques to Improve Multiphase Aquifer Remediation

Stefan Finsterle and Karsten Pruess

Earth Sciences Division
Lawrence Berkeley Laboratory
University of California
Berkeley, CA 94720
(510) 486-5205

Abstract

The T2VOC computer model for simulating the transport of organic chemical contaminants in non-isothermal multiphase systems has been coupled to the ITOUGH2 code which solves parameter optimization problems. This allows one to use linear programming and simulated annealing techniques to solve groundwater management problems, i.e. the optimization of operations for multiphase aquifer remediation. A cost function has to be defined, containing the actual and hypothetical expenses of a cleanup operation which depend - directly or indirectly - on the state variables calculated by T2VOC. Subsequently, the code iteratively determines a remediation strategy (e.g. pumping schedule) which minimizes, for instance, pumping and energy costs, the time for cleanup, and residual contamination. We discuss an illustrative sample problem to discuss potential applications of the code. The study shows that the techniques developed for estimating model parameters can be successfully applied to the solution of remediation management problems. The resulting optimum pumping scheme depends, however, on the formulation of the remediation goals and the relative weighting between individual terms of the cost function.

Introduction

The design of a cleanup operation for a contaminated aquifer comprises problems of a hydrological, technical, environmental, and economic nature. The main task is to select an effective and efficient remediation technology. The suitability of a proposed method depends on the chemical properties of the contaminant, the characteristics of the aquifer, and the overall remediation goals. Once a technology has been chosen, the operational scheme (e.g. pumping schedule) can be further optimized to reduce remediation costs.

Standard groundwater remediation operations include some form of pumping through extraction wells and subsequent treatment of the contaminated groundwater. Hazardous volatile nonaqueous phase liquids may be efficiently removed from contaminated soils and aquifers by injecting steam, thus vaporizing and displacing the contaminant toward the extraction wells. The use of numerical models to study different remediation designs requires simulating the transport of organic chemical contaminants in non-isothermal multiphase flow systems. In this study, we use the T2VOC code [*Falta et al.*, 1994], which is an adaptation of the STMVOC numerical simulator developed at Lawrence Berkeley Laboratory by R. Falta and K. Pruess [*Falta and Pruess*, 1991], for modeling contaminant transport.

The management of groundwater remediation by means of optimization techniques usually aims at maximizing contaminant removal by a minimum of capital, operating, and maintenance costs. Furthermore, technical constraints and regulatory cleanup standards have

to be observed. The purpose of this paper is to demonstrate how standard parameter estimation methods can be used to optimize remediation strategies. The ITOUGH2 code [*Finsterle*, 1993; *Finsterle and Pruess*, 1993, 1995] was originally developed for the estimation of hydrogeologic model parameters for the TOUGH2 code [*Pruess*, 1991] and some of its descendants, such as T2VOC. ITOUGH2 solves the inverse problem by automatic model calibration using non-linear optimization techniques. In principle, the same methodology can be applied to optimize remediation strategies by minimizing an appropriately defined objective (or cost) function. The example discussed in the paper examines the remediation of a large contaminant plume by an array of extraction wells. The pumping rate in each well is optimized to reduce cleanup costs.

Optimizing Pumping Schedule For Aquifer Cleanup Operation

Consider a confined aquifer of uniform thickness (10 m), contaminated by a spill of xylene. It is assumed that 3 years after release, the pollution is discovered, stopped, and the spatial distribution of the plume is determined. Subsequently, an array of wells is installed to extract the contaminated groundwater. The aquifer is assumed heterogeneous in hydraulic conductivity with a mean permeability of 10^{-11} m^2, a standard deviation of one order of magnitude, a correlation length of 100 m along the main west-east flow direction, and a correlation length of 20 m in the perpendicular direction. Effective porosity is 0.3. A natural hydraulic gradient of 0.01 is imposed across the model domain of 200 m length. There is no flow across the northern and southern boundaries. We realize that the unsaturated zone as well as density effects (concentration of low-density xylene near the top of the aquifer) are important aspects of plume migration which are not accounted for due to the two-dimensional nature of our schematic model.

The permeability field, the location of the contaminant source (square), and the pumping wells (circles) are shown in Figure 1. Superimposed are the contours of the contaminant plume after 3 years of continuous release.

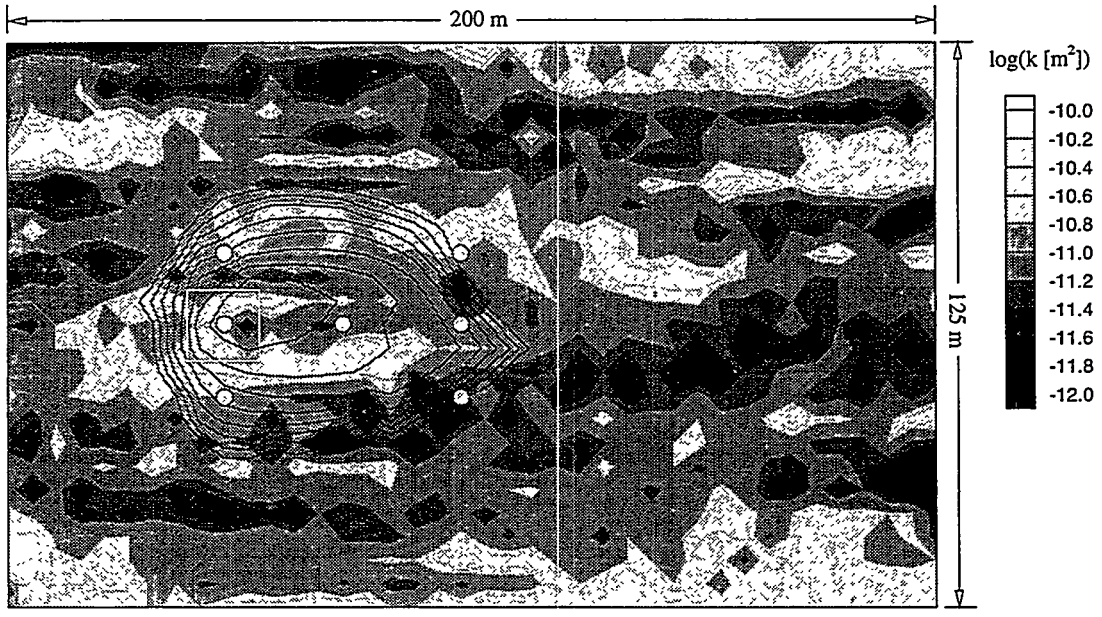

Figure 1: Log-permeability field of hypothetical contaminant site and NAPL saturation prior to remediation

The T2VOC code has been slightly modified so that the simulation automatically stops when the total amount of hydrocarbon in the system is lower than a certain predefined value (e.g. 70 % of the initial inventory). The actual cleanup time is then calculated by linear interpolation between the two last time steps. The cost function to be minimized is simply the total amount of fluid that needs to be pumped and treated, i.e. the product of pumping rate and cleanup time, totaled for all wells. Furthermore, each pump is assumed to have a maximum capacity of 4 kg/s which is the upper bound not to be exceeded during the optimization process.

The problem can now be formulated as follows: A set of pumping rates has to be determined that minimizes the total amount of contaminated groundwater extracted from the system. In inverse modeling terminology, the individual pumping rates are the unknown T2VOC input parameters to be determined, and the data point to be matched is a dummy measurement of zero, representing the desired cleanup costs.

We decided to determine three optimum pumping schedules for three phases of the cleanup operation. Since the location of the plume as well as its spreading changes with time, it is expected that the pumping rates have to be changed with time to achieve maximum aquifer remediation within a reasonable time frame. In this study we change the pumping schedule after 30 and 60 % of the contaminant has been removed.

The pumping schedule, cleanup time, and mean NAPL concentration of the extracted two-phase NAPL-groundwater mixture, as well as the total amount pumped are summarized in Table 1. The values for an alternative design which assumes pumping at a constant rate of 2 kg/s in each well is also included for comparison.

The location of the plume, i.e. the NAPL saturation, is shown in Figures 2, 3, and 4 after 30, 60, and 90 % of the original amount of contaminant is removed, respectively. Note that a relatively small percentage of the total contaminant inventory is dissolved in the water phase, flowing downstream at a higher velocity than the NAPL plume. Initially, most of the xylene is present as a free and mobile NAPL phase. The time required to remove the first 30 % of the total initial contaminant mass is calculated to be 20 days, whereas it takes more than 8 years to remove an additional 60 %. This is mainly due to the strongly reduced effective permeability at low NAPL saturations, i.e. the contaminant is removed basically by pumping groundwater, in which the chemical is dissolved.

Table 1: Optimum pumping schedule

	Pumping rate [kg/s]			
	optimized			not optim.
Contaminant removed	30 %	60 %	90 %	90 %
Well NW	1.9	0.1	0.0	2.0
Well NE	0.0	0.0	0.0	2.0
Well CW	4.0	0.9	0.6	2.0
Well CC	4.0	3.1	3.2	2.0
Well CE	4.0	3.9	3.0	2.0
Well SW	2.1	0.1	0.5	2.0
Well SE	0.2	0.6	0.0	2.0
Total pumping rate [kg/s]	16.3	8.7	7.3	14.0
Total cleanup time [day]	20	180	3110	3060
NAPL/water ratio at wells [gr/kg]	16.7	6.3	0.6	0.4
Total mass pumped [10^6 kg]	28	148	2270	3700

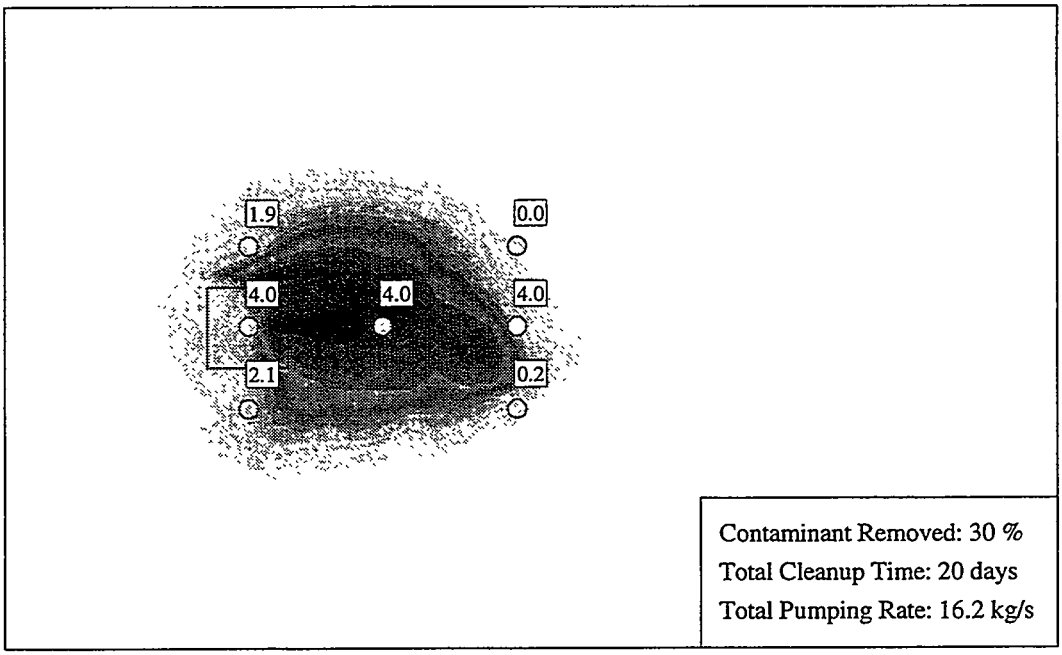

Figure 2: NAPL saturation after 30 % of the contaminant has been removed. Individual pumping rates are shown in boxes at wells.

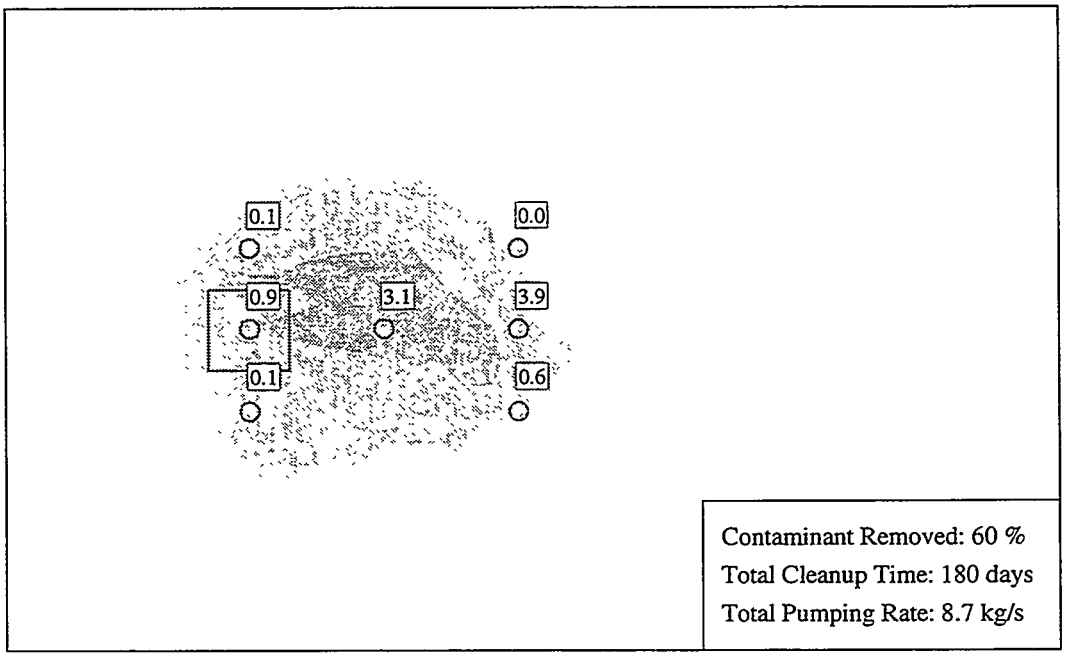

Figure 3: NAPL saturation after 60 % of the contaminant has been removed. Individual pumping rates are shown in boxes at wells.

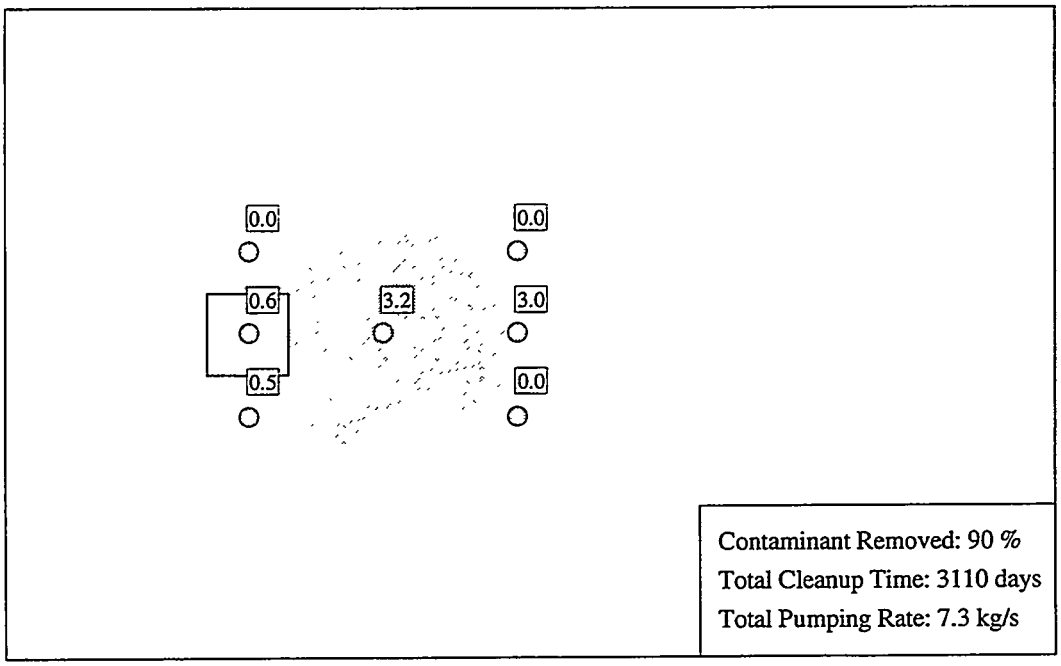

Figure 4: NAPL saturation after 90 % of the contaminant has been removed. Individual pumping rates are shown in boxes at wells.

For the initial period of the cleanup operation, the result of the optimization procedure suggests pumping the center wells at full capacity, and extracting contaminated groundwater also from the two wells on the west side of the field. The two wells to the east are almost shut down, because the water has low NAPL concentrations in that region.

During the second cleanup period, where the total contaminant content will be reduced from 70 to 40 % of the initial amount, the pumping rates in the western wells are lowered to avoid the formation of a stagnation zone. Part of the plume has moved east following the regional gradient, favoring extraction from wells center-east (CE) and south-east (SE) which are further downstream. Extracting an additional 30 % of the initial contaminant content requires pumping for a long period at a relatively low rate. Notice that the total duration of the cleanup operation is slightly longer than for the alternative design, but the total volume of removed groundwater is reduced by more than 50 %, leading to a higher contaminant concentration in the extracted fluid.

One might argue that the solution of the optimization is non-unique and strongly depends on the pumping rate initially assigned to each well. There is a hydrological reason for this unstable behavior. If a certain well starts out with a higher pumping rate than an adjacent well, the flow field and therefore the contaminant plume moves preferentially toward this well. This makes the neighboring well even less efficient because water of lower contaminant concentration is extracted. In addition, local heterogeneities may induce preferential flow of contaminant, thus influencing the selection of certain extraction wells for most effective remediation. Depending on the flow distances and the size and shape of the plume, it is often preferable to shut down peripheral wells, thus concentrating the remediation effort to a few wells in the center of the plume. It should be pointed out that a detailed site characterization study is required, and that the location of the plume has to be accurately determined, so that the effects discussed above are correctly accounted for.

Despite the problem of non-uniqueness, each proposed solution of similar efficiency is a valuable alternative which can help conceive of an improved remediation design. Given the optimum pumping schedule presented above, one might want to revise the number and location of the wells, thus reducing installation costs. The new well configuration can then be optimized in the same manner. Moreover, the long pumping period required to remove the contaminant suggests that another remediation technique may be more appropriate. For example, one might consider using air or steam injection to enhance the recovery of contaminant since the low mobility of the contaminant near residual saturation is the main reason for the inefficiency of the pump and treat method.

Concluding Remarks

The T2VOC numerical simulator has been linked to the ITOUGH2 code to optimize multiphase aquifer remediation operations. One simplified sample problem is discussed in this paper to demonstrate the methodology. More details can be found in *Finsterle and Pruess* [1994]. These studies show that the techniques developed for estimating model parameters can be successfully applied to solve remediation problems. A cost function has to be defined, representing the part of the management objective that is influenced by the hydrological properties of the aquifer. This means that optimization reduces the costs that depend - directly or indirectly - on state variables calculated by T2VOC. ITOUGH2 is flexible enough to handle complicated, discontinuous cost functions that may include pumping rates, energy costs, duration of total cleanup operation, capital costs for well installation, operational costs for the treatment of contaminated groundwater, etc. It is important to realize that the resulting optimum pumping scheme strongly depends on the formulation of the remediation goals, and the relative weighting between individual terms of the cost function. Nevertheless, the solution of the optimization process points towards alternative remediation schemes which have the potential to increase effectiveness with decreasing costs.

Acknowledgment This work was supported by the WIPP project, Sandia National Laboratories, under Document No. 129847, and by U.S. Department of Energy, under contract DE-AC03-76SF00098. We would like to thank Bruno Kälin for a helpful discussion of the cost functions.

References

Falta, R. W., and K. Pruess, STMVOC User's Guide, Lawrence Berkeley Laboratory Report LBL-30758, Berkeley, CA , 1991.

Falta, R. W., K. Pruess, S. Finsterle, and A. Battistelli, T2VOC User's Guide, Lawrence Berkeley Laboratory Report, Berkeley, CA, draft report October 1994.

Finsterle, S., ITOUGH2 User's Guide, Lawrence Berkeley Laboratory Report LBL-34581, Berkeley, CA , 1993.

Finsterle, S., and K. Pruess, Optimizing Multiphase Aquifer Remediation Using ITOUGH2, Lawrence Berkeley Laboratory Report LBL-36088, Berkeley, CA , 1994.

Finsterle, S., and K. Pruess, ITOUGH2: Solving TOUGH Inverse Problems, paper presented at the TOUGH '95 workshop, Berkeley, CA, March 20 - 22, 1995.

Pruess, K, TOUGH2 - A general-purpose numerical simulator for multiphase fluid and heat flow, Lawrence Berkeley Laboratory Report LBL-29400, Berkeley, CA, 1991.

SOIL REMEDIATON BY HEAT INJECTION: EXPERIMENTS AND NUMERICAL MODELLING

Poster presented by:
C. BETZ, M. EMMERT, A. FÄRBER, R. HELMIG, V. KALERIS and H. KOBUS
Institute for Hydraulics
University of Stuttgart
Germany

Abstract. In order to understand physical processes of thermally enhanced soil vapor extraction methods in porous media the isothermal, multiphase formulation of the numerical model MUFTE will be extended by a non-isothermal, multiphase-multicomponent formulation. In order to verify the numerical model, comparison with analytical solutions for well defined problems will be carried out. To identify relevant processes and their interactions, the results of the simulation will be compared with well controlled experiments with sophisticated measurement equipment in three different scales. The aim is to compare the different numerical solution techniques namely Finite Element versus Integral Finite Difference technique as implemented in MUFTE and TOUGH2 [9] respectively.

1 Introduction

During the last years, actual and potential contamination of air, soil and groundwater with organic substances became a field of increasing environmental interest in Germany. The focus is on the huge number of abandonned landfill sites, where organic liquid components often infiltrate the unsaturated zone. Since non-aqueous phase liquids (NAPL) - for example mineral oil or chlorinated hydrocarbons - are rather immobile if the NAPL-content of the soil is less than 10 % contaminant spills with NAPL stay as long term contaminant source. They evaporate in the soil air and will be transported by diffusion processes into the atmosphere, or they dissolve into the groundwater as organic solvents. For remediation the traditional "pump and treat" methods are inefficient because mass extraction depends on the solubility, sorption and vaporisation of the contaminant which can be rate limited processes.

To work on remediation technologies, the experimental hall VEGAS (research facility for subsurface remediation) [7] was built at the Institute for Hydraulics at University of Stuttgart/Germany. The aim of the investigations in VEGAS is to optimize existing and to develop new, improved technologies for in-situ remediation and exploration techniques by means of large scale laboratory experiments. One of the ongoing studies in VEGAS concerns soil venting, which is an established technology for the remediation of organic contaminants in the vadose zone. Additional injection of heat will enhance some physical processes, which are dominant for the remediation, e.g. increasing of vapor pressure and decreasing of capillary forces.

The aim of the study is to develop a better understanding of the physical processes in respect to the optimization of existing thermally enhanced methods. Therefore the study consists of two main parts. The experimental part investigates the remediation of contaminated soils in different scales. The numerical model would provide a quantitative description of the relevant processes and mechanisms based on the results of the experiments.

2 Experimental Setup

The experimental part consists of setups in three different scales, which represent 1-, 2- and 3-dimensional modes.

The 1-d-experimental column scale setup consists of a DURAN-glass column, 90 cm high

and 10 cm wide. The 2-d-setup, the so called bench scale experiment, measures 75 x 140 x 10 cm and is produced of TEMPAX-glass plates isolated with laminated wood and is fixed in a frame of stainless steel. These both laboratory setups are filled with quartz sand. The experiments will be conducted both in homogeneous and in distinct heterogeneous layers.

The laboratory offers many technical and methodical possibilities thus allowing to investigate the specific differences of hot air and steam as media carrying heat and of different contaminants. For these experiments a lot of measurement equipment is needed. The temperature and the fluid-phase saturation for two phase flow will be measured at five (for 1-d) respectively 52 (for 2-d) positions. At selected points the pressure will be recorded. The outflux of the extracted fluid phase as well as the fluxes of the injected and extracted gas will be recorded by integral measurement. The measurement of the saturation (principle: gammaabsorbtion), of temperatures (Pt-100), pressure (piezo-electrical sensor with numerical temperature-compensation) and bulk-flow (heated floating- body flow-meter with a magnetic servo system and a electropneumatical control-valve) requests an extended system of control and regulation. All signals from measuring and controling devices are recorded and evaluated with a data aquisition system via 4 interfaces with a total number of 66 channels.

In a first set experiments are conducted without contaminants, only with the components water and air. The aim is to develop a better understanding for the physical processes of flow and heat transport in this two phase system as well as to study the possibilities of process control and management. In a second set of experiments, contaminants and their material properties are included. In particular five different kinds of contaminants will be regarded: the pure compounds xylene, n-octan, dichlorobenzene and naphtalene. Kerosene, which often represents the main part of contaminations in air ports and gasoline-stations will be used as a mixture (C11-C13). The experiments focus particularly on understanding the physics of three phase flow including phase changes if steam is injected. Of special interest is the different behaviour of the five contaminants with respect to mass balance and mobility with respect to time.

The 3d-experiments will be performed in the large stainless steel VEGAS-container (h x b x l : 4.70 x 5.70 x 6.00 m). The experimental setup is shown schematicaly in Fig.1. The container is filled with well-defined homogeneous sand, later with several homogeneous layers of sand. For the remediation-experiments in the container kerosene will be used as contaminant. The media carrying heat will be injected into the porous media via six injection-wells arranged circularly around the contaminated area. From the central extraction well soil vapour is extracted so that the evaporating contaminants flow along the potential gradient towards the extraction well. In order to check the contaminant concentration in the saturated zone, groundwater will also be pumped for analysis. Temperatures will be recorded at about 200 selected positions to obtain the movement of the temperature front.

The comparison of the small-scale experiments conducted in the laboratory with the large-scale experiment in the VEGAS-container permits to understand possible scale-effects.

3 Numerical Model

A numerical model concept for simulating multiphase flow processes (MUFTE) [5] is presented. Up to now MUFTE is capable to simulate isothermal three phase flow (no partitioning of components from one phase in an other phase). Because the pressure formulation usually is unsuitable as a mathematical basis for investigating heterogeneous porous media because of negligably small capillary pressure, a pressure/saturation formulation involving the unknowns p_1, S_2, S_3, which is valid for an arbitrary capillary pressure, was chosen.

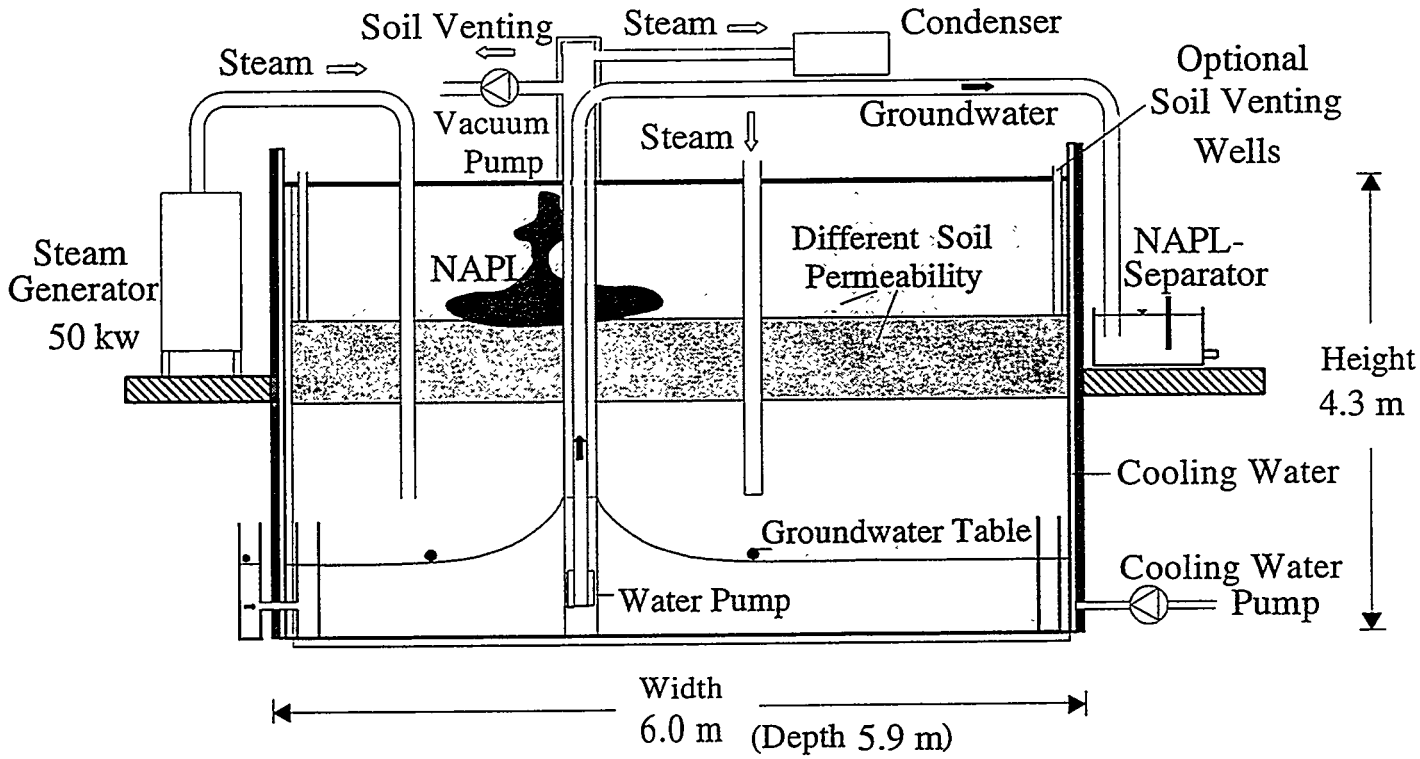

Fig. 1: Experimental setup for 3-D experiments

The system of equations presented is solved with the aid of a modified Petrov-Galerkin method. In discretizing the transient problem, it is appropriate to formulate the time discetization on the basis of an iterative concept. An implicit two-point algorithm developed for this purpose is incorporated into the Newton-type iterative concept for the consistent linearized multiphase problem. In order to describe various complicated geological structures (flow channels, fractures, rock matrix, highly heterogeneous media), it is necessary to employ arbitrary combinations of finite elements of different dimensions. Moreover, the finite elements must be capable of correctly describing the problem defined by the multiphase flow process.

Experience has shown ([10],[8]) that the following elements are especially suitable for modelling flow and transport processes in fractured porous media:

- isoparametric hexahedral elements;
  these may be applied to represent a continuum in three-dimensional models;

- plane isoparametric rectangular elements;
  these may be used to represent fractures in three-dimensional models and a continuum in two-dimensional models;

- line elements;
  these are suitable for representing well-defined flow channels or boreholes in three-dimensional models and for approximating fractures in two-dimensional models.

As the solutions are computed for each element in turn, the geological parameters may vary from one element to the next. The aforementioned combinations of different element types may be applied in a single model; the spatial orientation of the elements is arbitrary. By this means, it is possible to simulate complex geological structures [11].

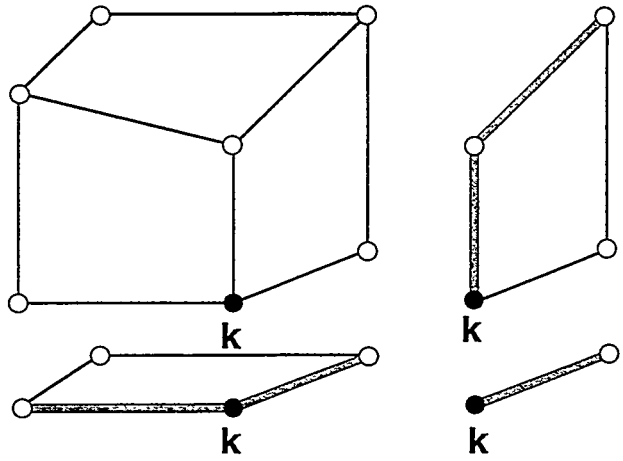

Fig. 2: Arbitrary coupling of 1-D, 2-D and 3-D elements

In order to ensure convergence of the numerical solution, a modified PETROV–GALERKIN method [4] was developed in which the test functions are up to two polynomial degrees higher than the base function (shape function). As a supplement to this, a lumped finite element formulation was also prepared. It should be noted that Hackbusch (1988) [3] was able to show that with regard to the conservation of mass for a patch, the PETROV–GALERKIN method in combination with the lumped finite difference formulation is equivalent to a finite volume formulation (e.g. TOUGH2).

Further development: Based on the isothermal part of MUFTE, the goal is to substitute the multiphase formulation by a multiphase-multicomponent formulation for the components air and water. In addition the energy equation has to be implemented to be able to simulate phase transitions from one phase to two phase and the opposite way. As primary variables, pressure, gas saturation and temperature were chosen for two phase conditions. When phase switching from two phase to one phase conditions occurs, the saturation is replaced by the air mass fraction as primary variable. The secondary variables like density, viscosity, enthalpy, internal energy and mass fractions are calculated from the primary variable set. For water and steam, all properties were calculated after International Formulation Committee [2]. For air ideal gas law was assumed. The governing equations for the conservation of mass of a component K and of energy in the gas and liquid phase ($\alpha = l, g$) are:

For component mass:

$$
\begin{aligned}
&L_{1,2}(p_g, S_g, T) := \\
&\quad n \sum_{\alpha=l,g} \frac{\partial(\varrho_\alpha X_\alpha^K S_\alpha)}{\partial t} \\
&\quad - \sum_{\alpha=l,g} \operatorname{div} \{\mathbf{K} \frac{k_{r\alpha}}{\mu_\alpha} \varrho_\alpha X_\alpha^K (\mathbf{grad}\, p_g - \varrho_\alpha \, \mathbf{g})\} \\
&\quad - \operatorname{div} \{\mathbf{K} \frac{k_{rl}}{\mu_l} \varrho_l X_l^K \frac{dp_c}{dS_l} \mathbf{grad}\, S_g\} \\
&\quad - \operatorname{div} \{ D_{AV}\, \varrho_g \mathbf{grad}\, X_g^K \} - m^K = 0
\end{aligned}
$$

For energy:

$$
\begin{aligned}
&L_3(p_g, S_g, T) := \\
&\qquad (1-n)\, \varrho_s c_s \frac{\partial T}{\partial t} + n \sum_{\alpha=l,g} \frac{\partial(\varrho_\alpha u_\alpha S_\alpha)}{\partial t} \\
&\quad - \sum_{\alpha=l,g} \operatorname{div} \{\mathbf{K} \frac{k_{r\alpha}}{\mu_\alpha} \varrho_\alpha h_\alpha (\mathbf{grad}\, p_g - \varrho_\alpha \, \mathbf{g})\} \\
&\quad - \operatorname{div} \{\mathbf{K} \frac{k_{rl}}{\mu_l} \varrho_l h_l \frac{dp_c}{dS_l} \mathbf{grad}\, S_g\} \\
&\quad - \operatorname{div} \{ D_{AV}\, \varrho_g (h_g^a - h_g^w) \mathbf{grad}\, X_g^a \} \\
&\quad - \operatorname{div} \{\mathbf{K}_E \mathbf{grad}\, T\} - m^E = 0
\end{aligned}
$$

The Jacobian matrix for the Newton-Raphson iteration scheme is calculated using thermodynamic relationships for the pressure-, saturation-, air mass fraction- and temperature-derivatives. To avoid excessive computing time, the implementation of the robust multigrid program "ug" [1] on unstructured grids on a parallel computer is planed. By the aid of the well controlled experiments a further goal is to compare this simulator

with TOUGH2 with respect to e.g. accuracy of the solution of isothermal/nonisothermal processes, numerical solution of sharp front problems, how fast convergence criteria can be achieved with FE/IFD methods and to verify and – if possible to validate – the program system by comparison with well controlled experiments, e.g. VEGAS (see fig. 2).

4 Joint Research

Presently no method is known or is likely to emerge in the near future, which could demonstrate the accuracy or validity of a numerical model in general final terms. This limitation calls for a cautious approach in model applications. Numerical modelling should be open to iterative refinement; models need to be complemented with engineering judgement, and provisions for monitoring and confirmation of system performance must be made. The test facility VEGAS [7] will provide new possibilities for extending the experimental data base for checking and validating multiphase flow and transport models (see Fig. 3).

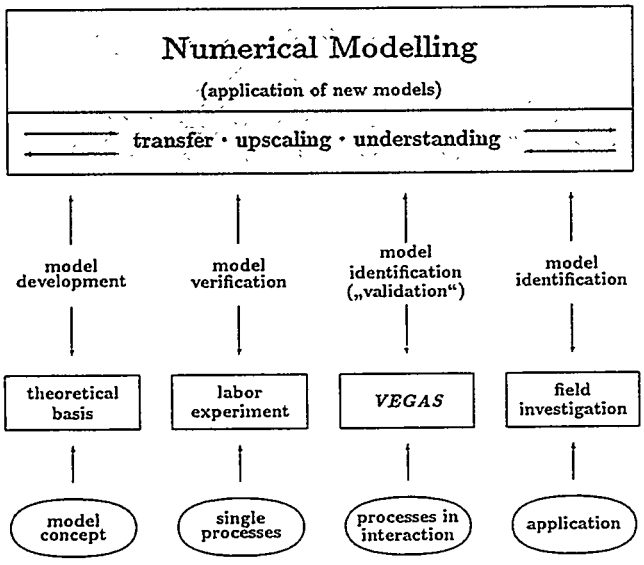

Fig. 3: Numerical modelling and upscaling [6]

The identification of processes will be achieved by the connection of physical and numerical experiments, whereby still a large amount of method- development is needed in both areas. For example from the physical point of view, this need will be covered by the introduction of innovative measurement methods like light fiber techniques and resistance tomography.

To reach this aim a joint research was founded in the framework of VEGAS. The participants and their projects follow. They are supposed to be completed in the future by basic-, technological- and use-orientated projects.

Dr. B. Barczewski, Institute for Hydraulics at University of Stuttgart: "Development of an *in-situ* method for local measurement of NAPLs in the underground": Modification and test of a fiber optical instrument for measurement of the concentration of organic substances in the subsurface. The advantage of an instrument like this compared to classical methods is the comparatively cheap measurement. The instrument will be used in other projects to measure the spatial– and time–changes of the substance concentration with high resolution.

Dr. C. Nitsche, Dresdner Grundwasserforschungszentrum: "Development of measurement– , investigation– and model–techniques for the evaluation of the status of soils, contaminated with mineraloil hydrocarbons" Modification of methods for the measurement of hysteresis state functions for the multiphase system solid–air, solid–water and hydrophobic liquid phase in small laboratory columns and use of these functions for the interpretation of an infiltration experiment on the upper next scale. The phase distribution will be measured by tomographical methods, which will be tested in a half–technical scale in this project. Such methods are quite attractive for the exploration at field scale (10 - 100 m).

Prof. Dr. K. Roth, University of Hohenheim: "Experimental pure research for the transport

of organic substances (CKW, ...) in different natural soils“ Experimental research of the multiphase transport in different natural structures on different scales by infiltration experiments in small (0.1 m) and big (1 m) undisturbed piles. The aim is to determine (i) the connection between processes on both scales and (ii) the distribution of the component's fluxes to the different phases. With this data, methods for upscaling and for the identification of parameters will be tested.

References

[1] Bastian, P., Wittum,G.: *Adaptivity and Robustness: The ug concept.* In: Hackbusch, W., Wittum, G. (eds.): Adaptive Methods P Algorithms, Theory and Applications. NNFM, Vieweg, Braunschweig, 1993.

[2] International Formulation Committee: *A formulation of the thermodynamic properties of ordinary water substance.* IFC Sekretariat, Düsseldorf, Germany, 1967.

[3] Hackbusch W.: *On First and Second Order Box Schemes.* Springer Verlag 1989.

[4] Helmig R.: *Theorie und Numerik der Mehrphasenströmungen in geklüftet-porösen Medien.* Bericht Nr.34, Institut für Strömungsmechanik und Elektron.Rechnen im Bauwesen, Universität Hannover, 1993.

[5] Helmig R., C.Braun, M.Emmert: *MUFTE - A numerical model for the simulation of multiphase flow processes in porous and fractured-porous media.* Programmdokumentation HG 208, Institut für Wasserbau, Universität Stuttgart, 1994

[6] Helmig R., H.Kobus, C.Braun: *Simulation and Interpretation of Multiphase Processes in Porous and Fractured-Porous Media.* Presented at X International Conference on Computatuonal Methods in Water Resources, Heidelberg/Germany, July 1994.

[7] Kobus H., O. Cirpka, B. Barczewski, H.-P. Koschitzky: *Versuchseinrichtung zur Grundwasser- und Altlastensanierung VEGAS - Konzeption und Programmrahmen.* Mitteilungsheft Nr. 82, Institut für Wasserbau, Universität Stuttgart, 1993.

[8] Kröhn K.–P.: *Simulation von Transportvorgängen im klüftigen Gestein mit der Methode der Finiten Elemente.* Bericht Nr.29, Institut für Strömungsmechanik und Elektron.Rechnen im Bauwesen, Universität Hannover, 1991.

[9] Pruess K.: *TOUGH2 — A General-Purpose Numerical Simulator for Multiphase Fluid and Heat Flow.* Lawrence Berkeley Laboratoy, University of California, 1991.

[10] Wollrath J.: *Ein Strömungs- und Transportmodell für klüftiges Gestein und Untersuchungen zu homogenen Ersatzsystemen.* Bericht Nr.28, Institut für Strömungsmechanik und Elektron.Rechnen im Bauwesen, Universität Hannover, 1990.

[11] Zielke W. und R. Helmig: Grundwasserströmung und Schadstofftransport — FE–Methoden für klüftiges Gestein. In Univ. Fredericiana Karlsruhe (TH), Editor, *Wissenschaftliche Tagung "Finite Elemente — Anwendung in der Baupraxis".* Verlag Ernst u. Sohn, Berlin, 1991.

Numerical Simulation of In-Situ DNAPL Remediation by Alcohol Flooding

Ron W. Falta and Scott E. Brame (Earth Science Department, Clemson, S.C. 29634)

ABSTRACT

The removal of residual saturations of dense non-aqueous phase liquids (DNAPLs) from below the water table using alcohol solutions is under investigation as a potential remediation tool. Alcohol flooding reduces the interfacial tension (IFT) and density difference between the aqueous and DNAPL phases, and increases the chemical solubility in the aqueous phase. Depending on the partitioning behavior of the alcohol/chemical system, DNAPL can be removed by either mobilization as a separate phase or through enhanced dissolution.

A new three dimensional multiphase numerical simulator has been developed for modeling this process. The code is based on the general TOUGH2 [Pruess, 1991] Integral Finite Difference formulation for multiphase transport with modifications to account for the complex behavior of an alcohol/water/ DNAPL system. The alcohol flood code uses a special equation of state module for computing phase compositions, IFT, saturations, densities, viscosities, relative permeabilities, and capillary pressures during each time step. This equation of state is based on a numerical interpolation of experimentally determined ternary phase data. The code was designed so that it can readily be applied to other three-component, two-phase problems such as surfactant and solvent floods given appropriate ternary data.

Comparisons of simulation results with column experiments performed at Clemson University [Brandes and Farley, 1992] were used to validate the simulator.

INTRODUCTION

Contamination of the saturated zone by dense nonaqueous phase liquids (DNAPLs) such as halogenated organic solvents has become a widespread problem in industrialized countries. These chemicals become trapped as blobs or ganglia in the pore spaces of the soil due to capillary forces. Reducing the residual saturations of the contaminants through conventional waterflooding (pump and treat) has proven to be an inefficient and uneconomical process. Alcohol flooding of these contaminated zones is a promising technology that is currently in the experimental stage. Recent laboratory-scale experiments [Boyd, 1991; Brandes, 1992] have demonstrated the effectiveness of this technology.

Characterizing the process of alcohol flooding is complicated by the unique and varied partitioning behavior of the injected alcohol between the aqueous and DNAPL phases. For this reason and because of the nonlinearity of the governing equations, the application of analytical solutions to multidimensional alcohol flooding problems is limited.

In the past decade, several numerical simulators have been developed and reported for use in environmental remediation which model NAPL transport in multiphase systems [Abriola and Pinder, 1985; Faust, 1985; Baehr and Corapcioglu, 1987; Falta et al., 1992]. None of these simulators contained the capability to handle an added miscible component.

In the petroleum industry, the desire to simulate the processes and mechanisms of tertiary oil recovery led to the development of simulators capable of modeling miscible displacement in the early 1960s. One-dimensional simulators for modeling the recovery of oil with alcohol solutions were reported by Donahue [1963] and by Farouq Ali and Stahl [1965]. The relative high cost of alcohol curtailed further development of solvent flooding simulators. Interest in the mechanisms of surfactant and chemical flooding led to the development of chemical flooding numerical simulators [Pope and Nelson, 1978; Thomas et al., 1984]. The two dimensional simulator for chemical flooding developed by Pope et al. [1981] was improved by Datta Gupta et al. [1986] for three-dimensional flow. This simulator, named UTCHEM, was recently used to simulate the three dimensional remediation of an aquifer contaminated with DNAPLs using surfactants [Pope et al, 1993].

NUMERICAL FORMULATION

Governing Equations

For an isothermal system containing three mass components, three mass balance equations are needed to fully describe the system. There is a mass balance performed on each of the three components: alcohol, water, and chemical. The governing transport equations follow Pruess [1987] with extensions to account for a NAPL phase and for the alcohol and chemical components. The three mass accumulation terms for the three components are based on a sum over the aqueous and NAPL phases. The three mass flux terms, like the mass accumulation terms, are summed over the aqueous and NAPL phases. The mass flux terms are calculated for each component in the aqueous and NAPL phases.

Equation of State

In order to describe the miscible behavior of an isothermal, three-component, two-phase system, three primary variables must be chosen. In this simulator, the primary variables used were pressure and the total chemical and alcohol mass fractions. In addition, a complete set of secondary variables must be calculated for the solution of the three coupled mass balance equations. These include mass fractions for the components of each phase, phase saturations, and phase densities. The mass fractions of the components in each phase and the interfacial tensions are numerically interpolated from the representative ternary diagram. For calculating the transport equations, additional parameters such as relative permeabilities, capillary pressures, and viscosities were determined at each time step.

The ternary diagram (shown, for example, in Figure 1) is represented by two data sets, one for the binodal curve and one for the tie lines. The area under the binodal curve represents the two-phase region with the area above the curve representing the single phase region. The slope of the tie lines in the two-phase region determines the alcohol partitioning behavior. An experimentally determined interfacial tension value is assigned to each tie line.

CODE VALIDATION AND APPLICATION

Simulation of Laboratory Column Experiments

Several laboratory-scale alcohol flooding experiments were performed by Brandes and Farley [1992] using columns packed with either glass beads or soil. Ternary diagrams were experimentally determined and constructed for each of the water/alcohol/chemical combinations being investigated [Bergelin et al., 1943; Brandes, 1992]. The experiments were conducted in vertical glass columns with a packing length of 60 cm and an inside diameter of 25 mm.

The columns were contaminated with DNAPL and then waterflooded until residual concentrations were achieved. One pore volume of an alcohol/water solution was then injected into the column in the upflow mode. Waterflooding in the upflow mode commenced immediately after the alcohol flood until the effluent concentrations of the DNAPL and alcohol had stabilized.

For the purpose of validating the ALCFLD simulator, several of the laboratory experiments were modeled numerically. Two simulations are discussed here. These two represented the two different mechanisms of DNAPL removal: enhanced dissolution and separate phase mobilization.

Enhanced dissolution was observed in the isopropyl alcohol (IPA) flood of perchloroethylene (PCE). The ternary diagram for the IPA/PCE/H2O system, converted to rectilinear coordinates, is shown in Figure 1. Since the tie lines are sloping toward the right, the alcohol will partition preferentially into the aqueous phase. Thus the DNAPL phase will not appreciably swell and will not be mobilized. As the aqueous phase becomes increasingly alcohol rich, any PCE liberated in the column will become dissolved in the aqueous phase.

Separate phase mobilization was observed in the tert-butyl alcohol (TBA) flood of trichloroethylene (TCE). The ternary diagram for the TBA/TCE/H2O system converted to rectilinear coordinates is also shown in Figure 1. The tie lines higher in the two phase region slope to the left, indicating preferential alcohol partitioning into the DNAPL phase at increasing alcohol concentrations. At lower alcohol levels, there is almost equal partitioning. As the DNAPL phase swells and the interfacial tension is reduced, the globules are mobilized and coalesce into a large bank.

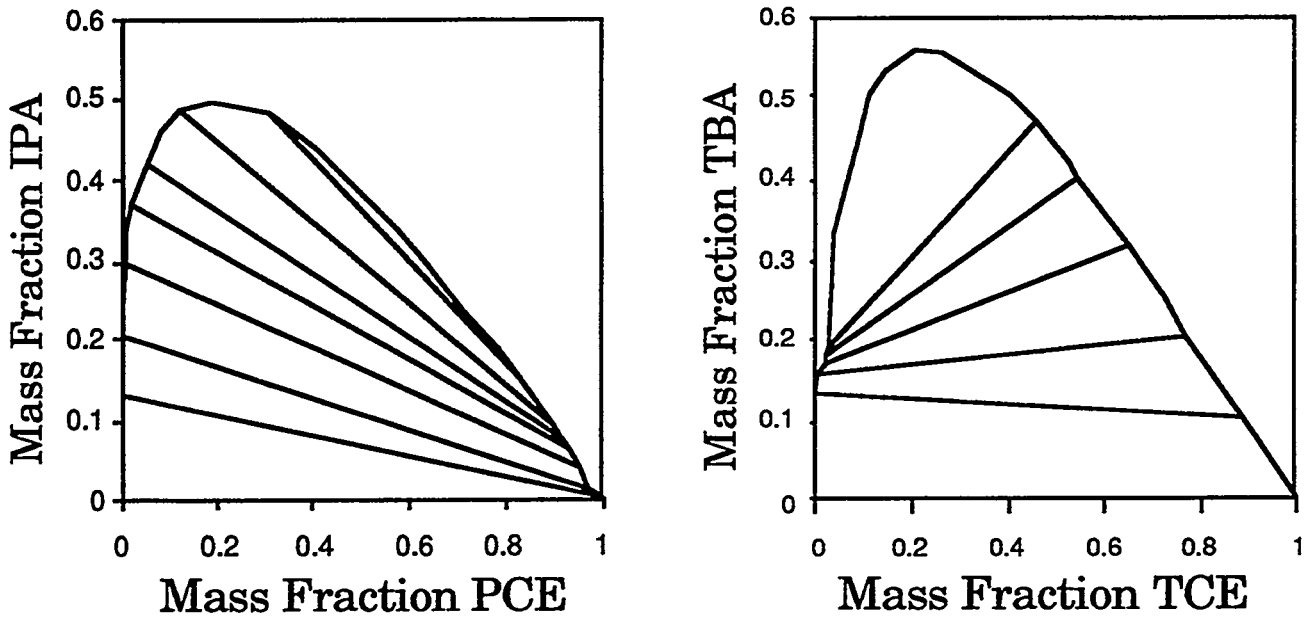

Figure 1. The ternary diagram for the IPA/PCE/H2O system and the TBA/TCE/H2O system converted to rectilinear coordinates.

Simulation of Enhanced Dissolution

Experiment one of Brandes [1992] was chosen for the simulation of enhanced dissolution. In this experiment, a 60% (by volume) isopropyl alcohol (IPA) solution was used to flood a column contaminated with residual saturations of PCE. In the experiment, no separate phase DNAPL was observed in the effluent. The saturation of PCE at the beginning of the alcohol flood was experimentally determined to be 16%. This was assumed to be uniformly distributed over the column for the simulation. The results of the simulation at different pore volumes are shown in Figure 2. The levels of NAPL saturation in Figure 2 show the distribution of the total amount of the PCE in *both* phases over the length of the column.

At 0.20 pore volumes (PV), the DNAPL phase was removed from about 3-4 cm of the column, as shown by the NAPL saturation curve in Figure 2. The single phase region continued to grow until reaching a maximum in the simulation at 1.5 PV. Thus, about one-third of the column was cleaned up with the one pore volume of alcohol flood.

At 0.20 PV, there is sharp rise in both the NAPL saturation and the total PCE up to the elevated levels, and then a more gradual return to the residual level. The elevated region delineates the zone of enhanced dissolution. At 0.50 PV, the elevated region has grown significantly and at 1.1 PV, the elevated region extends all the way from the sharp rise to the end of the column. Thus, at 1.1 PV, the maximum concentration of chemical is being produced as effluent. The NAPL saturation is elevated entirely from the slight amount of alcohol partitioning into the DNAPL phase.

At 1.5 PV, the NAPL saturation in the column rises sharply at the phase transition point, levels off at the old residual level and then rises gradually up to the enhanced dissolution region. At this point in the simulation, the follow-up waterflood was stripping the alcohol out of the NAPL and aqueous phases, thus decreasing the NAPL saturation and the corresponding enhanced solubility of chemical in the aqueous phase.

Comparisons of the simulated and observed effluent concentrations are shown in Figure 3. The chemical peaks are matched almost exactly and similar phase behavior is exhibited. In both cases, the alcohol front precedes the chemical front and is elevated over the maximum peak level of the chemical. The chemical front peaks just before one pore volume and maintains this level for almost one pore volume. Since the dissolution process was slow and the column was not fully decontaminated by the one pore volume alcohol flood, as shown by the chemical concentration returning to the residual concentration at 2.0 PV, the enhanced dissolution region was maintained until the waterflood removed

the remaining alcohol from the column. The irregularities in the observed curves after two pore volumes are considered to be artifacts of the experiment.

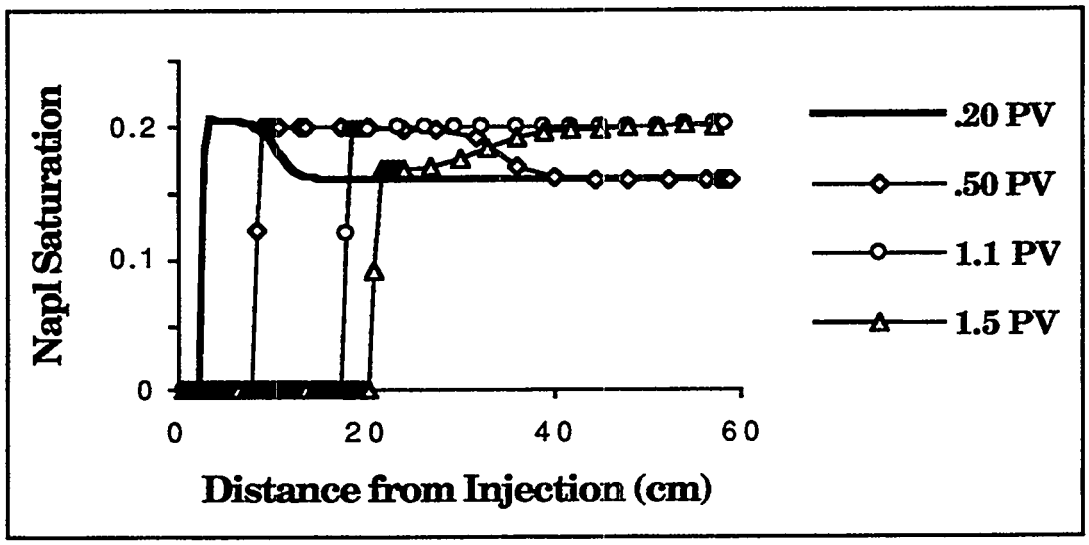

Figure 2. The NAPL saturations at different pore volumes for the simulation of a 60% IPA solution flood of a column contaminated with residual saturations of PCE.

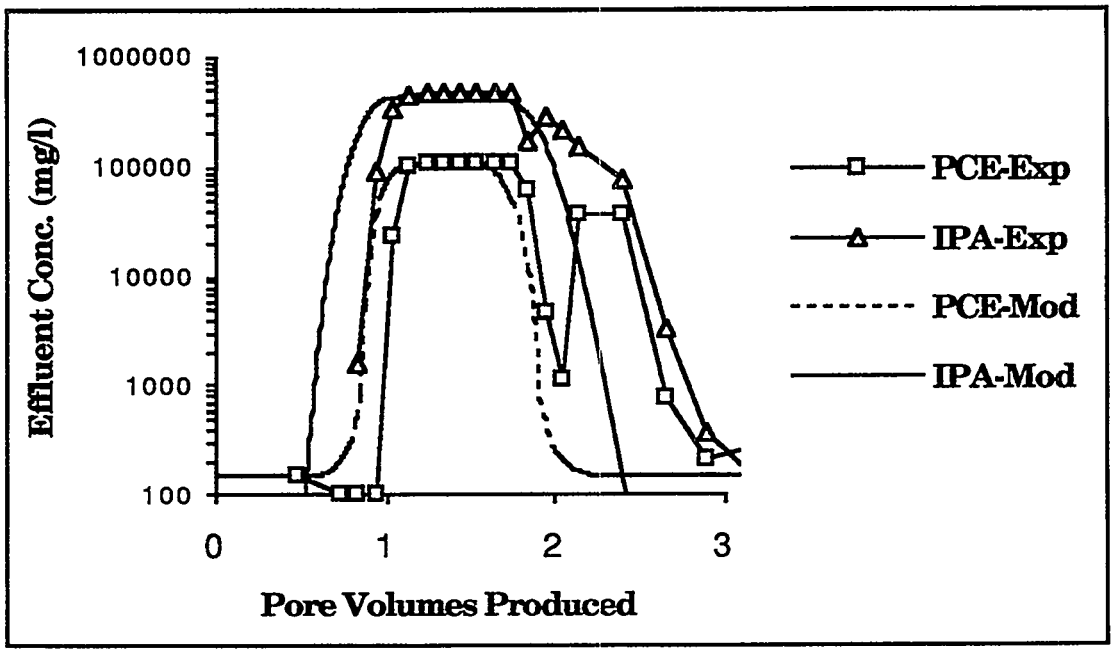

Figure 3. The simulated and observed effluent concentrations for a 60% IPA solution flood of a column contaminated with residual saturations of PCE.

Simulation of Separate Phase Mobilization

Experiment seven of Brandes [1992] was used as a comparison for the simulation of separate phase mobilization. In the experiment, a 70% (by volume) solution of tert-butanol (TBA) was injected upward into a fully saturated column contaminated with residual saturations of trichloroethylene (TCE). The saturation of TCE at the beginning of the alcohol flood was determined to be 15%. The experimental results indicated that large quantities of separate phase DNAPL were produced and that all the detectable chemical in the column was removed.

Figure 4 shows the trend of the NAPL saturations over the column at different pore volumes. This Figure demonstrates how the mobilized bank of DNAPL moves through the column over time and is eventually produced at high concentrations. Note at increasing pore volumes, the lateral width of the bank increases as the region affected by the alcohol flood grows. The saturations rise quite sharply at the point of the phase transition to a relatively high value, and maintain that level before dropping off fairly sharply near the front of the alcohol flood. The high value attained by the saturation in this simulation, compared to the height of the maximum NAPL saturation in Figure 2, shows that there is preferential partitioning of alcohol into the DNAPL phase. The rounding of the fronts at higher pore volumes results from dispersion of the alcohol flood.

At 0.25 PV, about 10 cm of the column had been converted to single phase conditions. Contrast this with the enhanced dissolution case in Figure 2, where only about 4 cm of the column was single phase at this point in the simulation. In the enhanced dissolution case, 0.75 PV of effluent had to be produced before 10 cm of the column was converted to single phase. The separate phase mobilization process is much more efficient at remediating contaminated soils. At one pore volume, high concentrations of chemical were being produced. After 1.5 PV, the simulator predicted total removal of the DNAPL phase from the column. There is still a slight amount of chemical left in the column at 1.5 PV, as shown in Figure 4, but it is dissolved in the aqueous phase and will be removed by the waterflood.

The overall behavior shown in Figure 4 is attributed to liberated chemical coalescing at the front of the DNAPL bank. This is in contrast with the enhanced dissolution case where the chemical was uniformly distributed over the alcohol swollen aqueous phase.

Figure 5 gives direct comparisons of the experimental and simulated effluent results. As shown, there is good correlation between the two figures. The TCE and alcohol are produced as sharp fronts at high concentrations as predicted. The simulated TBA effluent concentrations did not fall off after three pore volumes as was observed in the laboratory, but this can be attributed to the use of a log scale which accentuates the effects of numerical dispersion at higher pore volumes. The overall behavior is being modeled. Both curves show complete removal of TCE within two pore volumes.

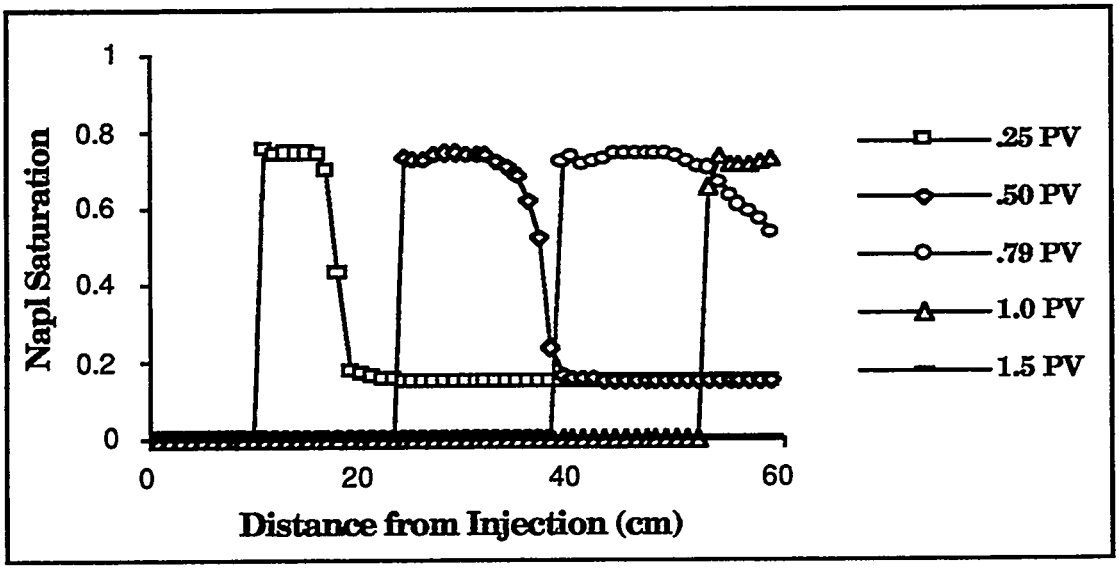

Figure 4. The NAPL saturations at different pore volumes for the simulation of a 70% TBA solution flood of a column contaminated with residual saturations of TCE.

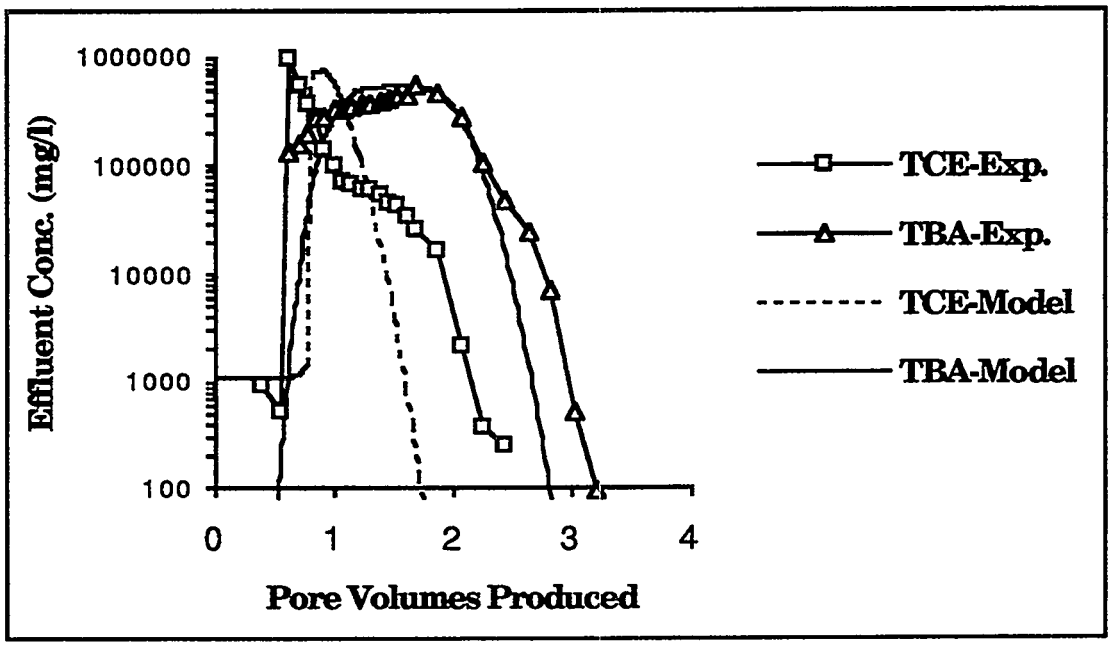

Figure 5. The simulated and observed effluent concentrations for a 70% TBA solution flood of a column contaminated with residual saturations of TCE.

REFERENCES

1. Boyd, G. R. 1991. Factors influencing nonaqueous phase liquid removal from groundwater by alcohol flooding. Ph.D. dissertation. Clemson University, Clemson, South Carolina.
2. Brandes, D. 1992. Effect of phase behavior on residual dense nonaqueous phase liquid displacement from porous media by alcohol flooding. MS thesis. Clemson University, Clemson, South Carolina.
3. Abriola, L.M. and G. F. Pinder. 1985. A multiphase approach to the modeling of porous media contamination by organic compounds, 2. Numerical simulation. *Water Resour. Res.* 21:19-26.
4. Faust, C.R. 1985. Transport of immiscible fluids within and below the unsaturated zone: A numerical model. *Water Resour. Res.* 21(4) 587-596.
5. Baehr, A.L. and Y.M. Corapcioglu. 1987. A compositional multiphase model for groundwater contamination by petroleum products 2. Numerical simulation. *Water Resour. Res.* 23:201-213.
6. Falta, R. W., Pruess, K., Javandel, I. and P.A. Witherspoon. 1992. Numerical modeling of steam injection of nonaqueous phase liquids from the subsurface 1. Numerical formulation. *Water Resour. Res.* 28(2) 433-449.
7. Donahue, D. A. T. 1963. A mathematical model to stimulate the recovery of oil and water from porous media by the injection of solvents. Ph.D. dissertation. Pennsylvania State University, University Park, Pennsylvania.
8. Ali, S.M. Farouq and C.D. Stahl. 1965. Computer models for stimulating alcohol displacement in porous media. *SPEJ* (March 1965) 89-99.
9. Pope, G.A. and R.C. Nelson. 1978. A chemical flooding compositional simulator. *SPEJ* (October 1978) 339-354.
10. Thomas, P. C., Fleming, P. D. and W. K. Winter. 1984. A ternary, two-phase, mathematical model of oil recovery with surfactant systems. *SPEJ* (Dec 1984) 606-616.
11. Pope, G.A., Hong, C.H., Sepehrnoori, K. and L. Lake. 1981. Two-dimensional simulation of chemical flooding. SPE 9939. Proceedings of SPE California Regional Meeting. Bakersfield, California.
12. Datta Gupta, A. 1985. Three dimensional simulation of chemical flooding. M.S. Thesis. The University of Texas, Austin, Texas.
13. Pope, G.A., Brown, C.L., Abriola, L.M. and K. Sepehrnoori. 1993. Simulation of surfactant enhanced aquifer remediation. *EOS Trans. AGU* 74(16):127.
14. Pruess, K. 1987. TOUGH user's guide. *NUREG/CR-4645*. Nucl. Regul. Comm. Washington, D.C.
15. Brandes, D. and K.J. Farley. 1992. Importance of phase behavior on the removal of residual DNAPLs from porous media by alcohol flooding. Accepted by Water Environ. Research.
16. Bergelin, O., F.J. Lockhart and G.G. Brown. 1943. Liquid-liquid extraction. *Trans. Am. Inst. Chem. Engrs.* 39:173-200

Presented at the TOUGH '95 Workshop, Lawrence Berkeley Laboratory, Berkeley, CA, March 20-22, 1995.

SAND95-0584C
Prediction of Single-Component NAPL Behavior for the TEVES Project Using T2VOC

Stephen W. Webb and James M. Phelan
Sandia National Laboratories
Albuquerque, NM 87185

Introduction

Soil heated vapor extraction is proposed as a process to remove solvents and chemicals from contaminated soils. In this process, the ground is heated electrically, and borehole(s) within the heated zone are maintained at a vacuum to draw air and evaporated contaminants into the borehole and a subsequent treatment facility. Sandia National Laboratories has designed a field demonstration of the process at the Chemical Waste Landfill at Sandia. The demonstration of the system, designated TEVES (Thermal Enhanced Vapor Extraction System), is currently underway. Additional details are given by Phelan and Webb (1994) and by Webb (in review).

As part of the evaluation process, detailed two-phase fluid flow and heat transfer simulations have been performed using the single-component NAPL version of the TOUGH2 computer code. The behavior of liquid water and contaminants will be influenced by a number of factors including soil heating rate and local temperature gradients, evaporation rate of the liquid water and contaminants, air flow rate, and borehole (vapor extraction) location(s). If the air flow rate is too small, the heating and evaporation processes may drive the contaminant vapors out of the heated zone and into the cooler unheated soil where they may condense, and contaminant migration into previously uncontaminated areas would occur. Figure 1 shows the general TEVES process setup. In this process, the ground is electrically heated, and borehole(s) within the heated zone are maintained at a vacuum to draw air and evaporated contaminants into the borehole and a subsequent treatment facility. The ground above the heated zone and beyond is insulated to minimize heat loss to the ambient environment. A vapor barrier is used over a yet larger area to provide for a more complete air sweep of the contaminated soil.

Model Development

Simulations of TEVES have been performed using the T2VOC version of TOUGH2, which includes the capability to simulate a single-component NAPL in addition to the water and air components already present (Finsterle and Pruess, 1993). The conjugate gradient solver package was also used to improve the numerical performance (Moridis and Pruess, 1993). The conceptual model and assumed parameters for these simulations are summarized below.

A three-dimensional TOUGH2 model with over 2200 elements was employed using quarter symmetry to simplify the model. Vapor extraction occurs through two vapor extraction wells located near the center of the heated zone. The nominal borehole vacuum is 2.5 kPa (10 inches of water). The borehole is specified as a constant pressure and temperature boundary element with no heat transfer between the soil and the borehole. The borehole vacuum is an

important parameter, because if the air sweep into the borehole is not sufficient, water vapor and VOCs generated by the heating process could migrate from the heated zone into the unheated soil resulting in a loss of containment.

Heat is added uniformly to the heated zone at the rate of 100 kW, or a volumetric heating rate of 190 W/m^3. If all the heat is assumed to go into evaporation of the initial water in the soil, approximately 0.044 kg/s of water vapor would be generated. The vapor barrier is assumed impermeable to flow. The permeability of the soil is assumed to be 50 darcies with a porosity of 0.333 and an initial liquid water saturation of 0.20, less than the liquid residual saturation. An initial o-xylene saturation of 0.05 in the entire heated zone is assumed to simulate an initial NAPL inventory. No NAPL is initially present in the unheated zone.

The soil is initially at ambient conditions, and heating and the venting occur simultaneously. As time proceeds, the soil heats up, and liquid water and NAPL are vaporized and generally transported toward the borehole. At 60 days, heating is stopped but venting continues. The soil cools down due to heat losses to the unheated soil and to the atmosphere.

The Parker et al. three-phase characteristic curves (Parker et al., 1987) have been used, although both liquid phases are initially immobile because the liquid residual saturation is greater than the initial value. Liquid transport only occurs due to evaporation and condensation phenomena, not due to transport of the liquid phase unless evaporation and condensation processes increase the local saturation sufficiently to mobilize the liquid.

The borehole vacuum was decreased from the nominal value of 2.5 kPa until NAPL migrated into the unheated soil surrounding the heated zone, which occurred at a borehole vacuum of 0.5 kPa. Webb (in review) presents the results for borehole vacuums of 2.5 kPa and 1.0 kPa. For 0.5 kPa vacuum, the NAPL migration percentage was small compared to the total inventory, and the NAPL quickly re-evaporated and was transported to the vapor extraction location as time went on. Nevertheless, migration into the unheated zone represents a loss of containment of the NAPL within the heated zone.

Simulation Results

The time variation of the soil temperature in the heated zone out to 60 days is shown in Figure 2 for a 0.5 kPa borehole vacuum; the time variation is very similar to other borehole vacuum cases. After 60 days, the heated zone average temperature is about 264°C with a range of 137 to 375 °C; these values are only about 15-20°C higher than for 2.5 kPa vacuum (Webb, in review) indicating minor heat losses to the air flow through the soil. A temperature contour plot looking from the side at 60 days is shown in Figure 3.

Figure 4a gives the time variation of the water and NAPL liquid masses in the heated zone. The NAPL mass in the heated zone is mostly gone within about 12 days; for a higher borehole vacuum of 2.5 kPa, the time is about 7 days. The increased time for the lower vacuum is due to the lower air flow rate through the soil. Figure 4b shows the NAPL

masses in the heated and unheated soil. At about 14 days, just before the last of the NAPL in the heated zone disappears, NAPL starts to migrate to the unheated soil. The NAPL in the unheated soil continues to increase until about 20 days. After this time, NAPL migration from the heated zone stops, and NAPL in the unheated soil starts to decrease as the unheated soil temperature increases and NAPL evaporates into the air flowing through the soil toward the extraction borehole. The maximum NAPL mass in the unheated soil is about 200 kg compared to an initial mass of almost 8000 kg in the heated zone, or less than 3% of the initial mass. While this migrated NAPL is eventually evaporated and transported to the borehole, the migration into the unheated soil represents undesirable contaminant migration caused by insufficient air sweep.

NAPL saturation contours are given in Figure 5 at 8 and 11.6 days. The saturation contours show a zone of NAPL which is left behind on the edges of the heated zone. Transport into the unheated zone is due to evaporation in the heated zone, flow into the unheated soil, and condensation in the cooler unheated soil. Liquid water saturation contours at 30 days, which are not shown, also indicate an insufficient air sweep. Water evaporates in the heated zone and is subsequently transported and condensed in the unheated soil as indicated by liquid saturations higher than 0.20 along some of the edges of the heated zone.

Figure 6 shows the various mass flow rates into the borehole. The total mass flow rate into the borehole increases in the early stages of heating due to the evaporation of the NAPL (VOC) component in the heated soil. For much of the simulation, the mass fraction is predominantly vapor. The vapor flow rate into the borehole peaks at a value of about 0.022 kg/s, or about 1/2 of the maximum vapor generation rate given earlier; this value is significantly lower than the 0.032 kg/s rate for 2.5 kPa borehole vacuum. However, the air flow rate into the borehole is dramatically reduced from the 2.5 kPa case, from a peak of 0.094 kg/s to a peak of 0.02 kg/s for 0.5 kPa. The vapor mass fraction into the borehole peaks at about 92% at 15 days, indicating little air flow through the heated zone. For the 0.5 kPa case, the borehole vacuum is not sufficient to capture all the vapor generated, and some flows into the unheated zone where it condenses. Some VOCs also flow along with the water vapor, condensing in the unheated soil. Obviously, a practical warning occurs when the vapor mass flow rate dominates the total mass flow rate into the borehole, indicating insufficient air flow and possible contaminant migration into the unheated soil.

Figure 7 shows details of the NAPL migration into the unheated soil; the results are given for 15 days, which is the maximum rate of NAPL inflow into the unheated zone. Figure 7a shows the pressure difference compared to the far-field value; dark areas indicate gas pressures less than the far-field, while light areas indicate higher gas pressures. At the top of the heated zone, the gas pressure is significantly higher than the far-field value. Figure 7b shows the resulting gas velocity vectors indicating significant gas flow from the heated zone into the unheated soil. As shown in Figure 7c, this region corresponds to NAPL migration into the unheated soil. If the borehole vacuum were higher, this pressure increase may not be sufficient to drive NAPLs out of the heated zone.

Summary and Conclusions

Detailed simulations have been performed for the TEVES Project using the TOUGH2 code considering air, water, and a single-component NAPL. A critical parameter varied in the simulations is the borehole vacuum which directly affects air flow through the system and indirectly influences soil temperatures and water and NAPL fluid masses. Contaminant migration from the heated zone into the unheated soil can occur if the borehole vacuum, or borehole flow rate, is not sufficient. Under these conditions, evaporation of liquids (water and NAPL) due to the heating can cause flow from the heated zone into the unheated soil. Insufficient air sweep may be indicated by a vapor dominated mass flow rate into the borehole, at least for the present configuration. Sufficient air flow through the heated zone must be provided to contain the contaminants within the heated zone.

Acknowledgment

This work was supported by the United States Department of Energy under Contract DE-AC04-94AL85000.

References

Finsterle, S. and K. Pruess (1993), *T2VOC, a 3-phase Water/Air/NAPL Module for TOUGH2*, Version 0.5, Lawrence Berkeley Laboratory.

Moridis, G.J., and K. Pruess (1993), *TOUGH2 Conjugate Gradient Package,* Lawrence Berkeley Laboratory.

Parker, J.C., R.J. Lenhard, and T. Kuppusamy (1987), "A Parametric Model for Constitutive Properties Regarding Multiphase Flow in Porous Media," Water Resour. Res., Vol. 23, No. 4, pp. 618-624.

Phelan, J.M., and S.W. Webb (1994), "Thermal Enhanced Vapor Extraction Systems - Design, Application, and Performance Prediction Including Contaminant Behavior," 33rd Hanford Symposium on Health and the Environment.

Webb, S.W. (in review), *TOUGH2 Simulations of the TEVES Project Including the Behavior of a Single-Component NAPL,* SAND94-1639, Sandia National Laboratories.

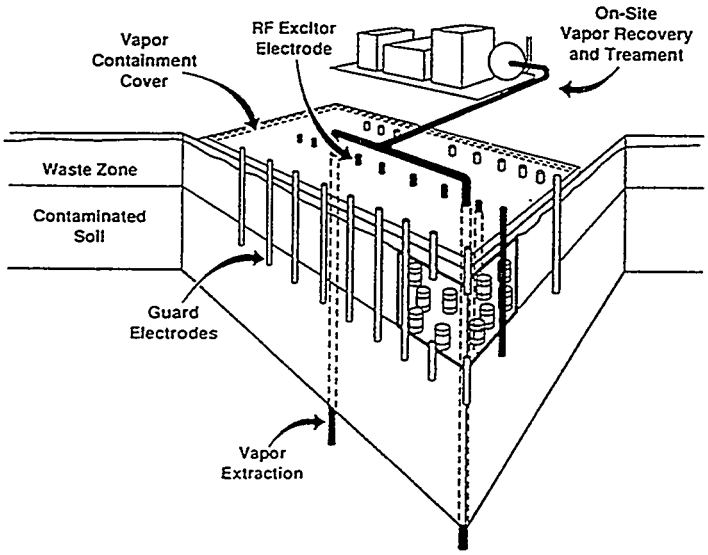

Figure 1
General TEVES Configuration

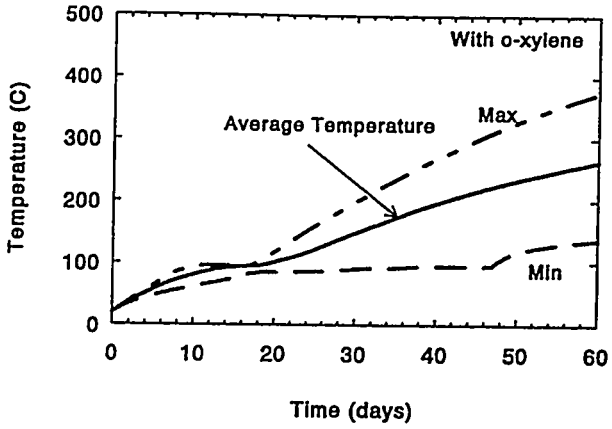

Figure 2
Heated Zone Temperatures

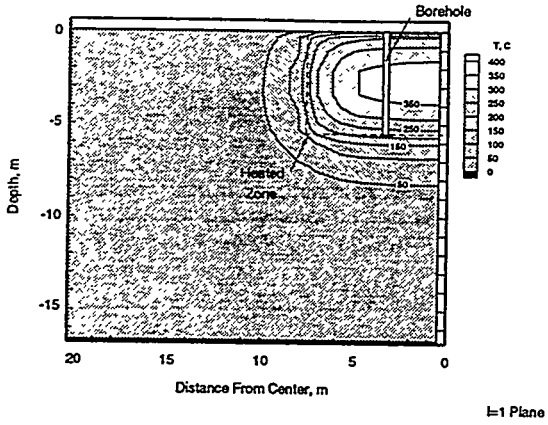

Figure 3
Temperature Contours at 60 Days

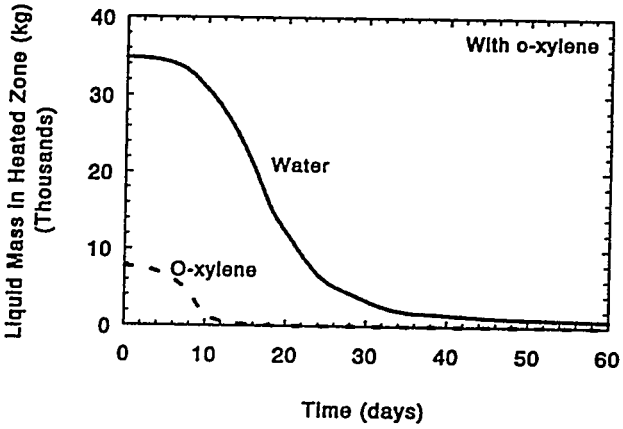

Figure 4a
Heated Zone Water and NAPL Masses

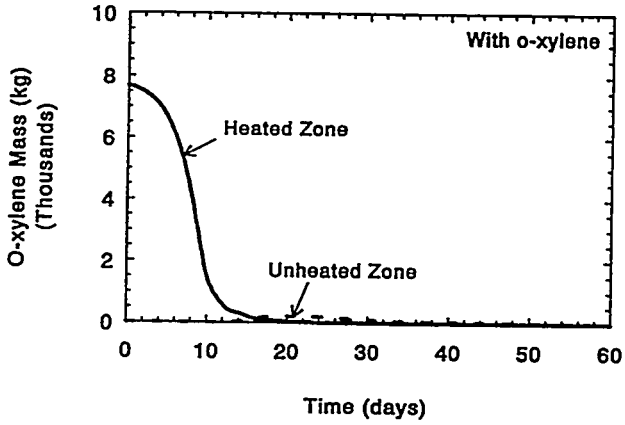

Figure 4b
Heated and Unheated Zone NAPL Masses

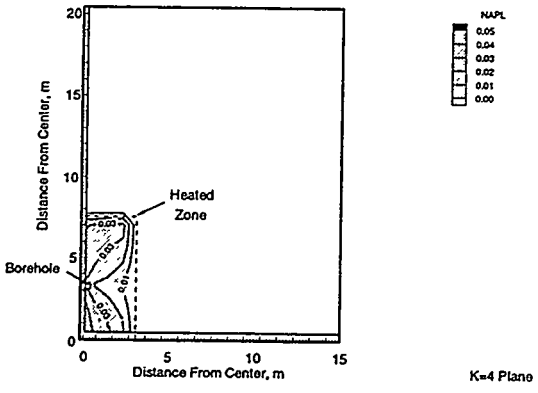

Figure 5a
NAPL Contours at 8 Days

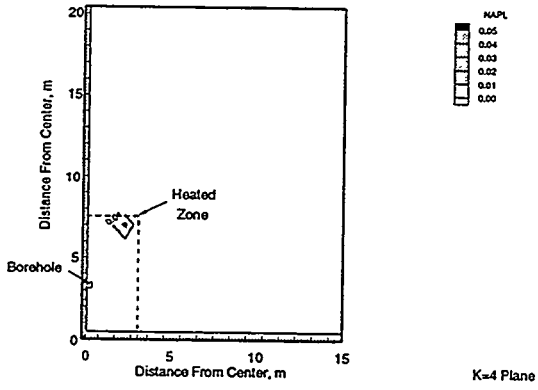

Figure 5b
NAPL Contours at 11.6 Days

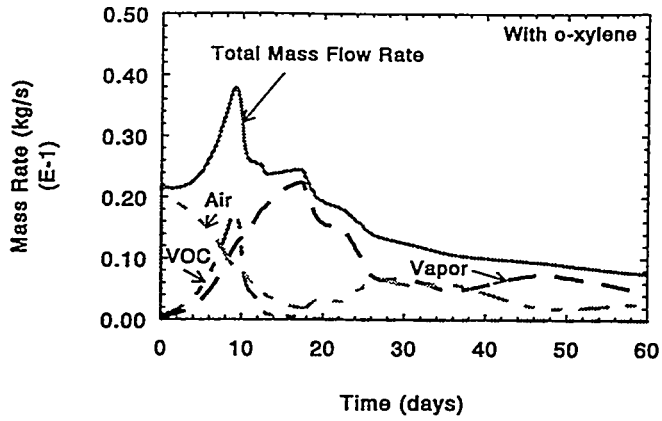

Figure 6
Mass Flow Rates Into Borehole

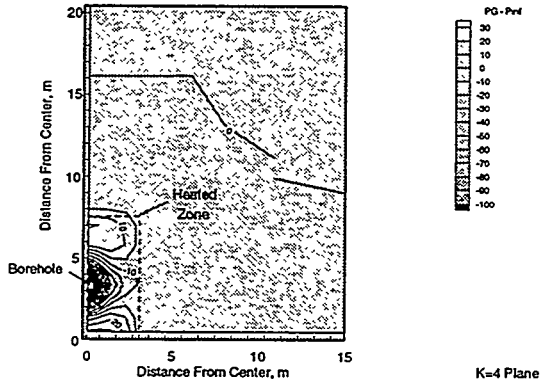

Figure 7a
Pressure Differential Contours at 15 Days

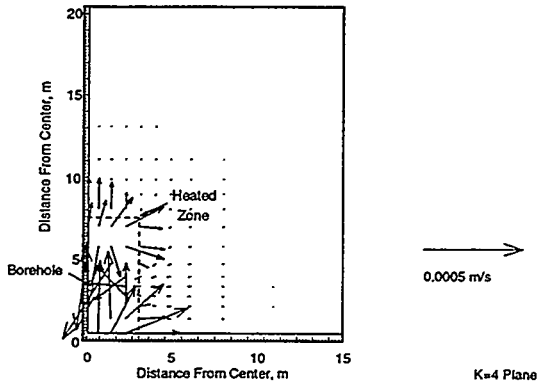

Figure 7b
Gas Velocity Vectors at 15 Days

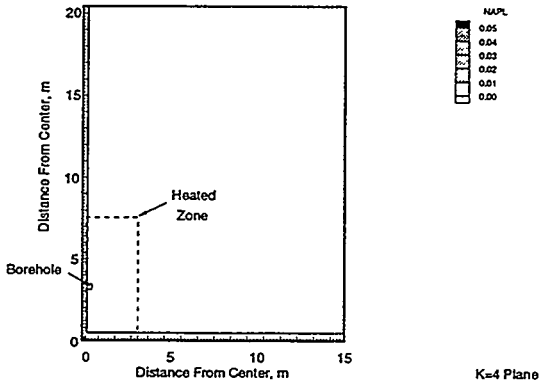

Figure 7c
NAPL Contours at 15 Days

Strongly Coupled Single-Phase Flow Problems: Effects of Density Variation, Hydrodynamic Dispersion, and First Order Decay

Curtis M. Oldenburg and Karsten Pruess

Earth Sciences Division, Lawrence Berkeley Laboratory
University of California, Berkeley, CA 94720

ABSTRACT

We have developed TOUGH2 modules for strongly coupled flow and transport that include full hydrodynamic dispersion. T2DM models two-dimensional flow and transport in systems with variable salinity, while T2DMR includes radionuclide transport with first-order decay of a parent-daughter chain of radionuclide components in variable salinity systems. T2DM has been applied to a variety of coupled flow problems including the pure solutal convection problem of Elder and the mixed free and forced convection salt-dome flow problem. In the Elder and salt-dome flow problems, density changes of up to 20% caused by brine concentration variations lead to strong coupling between the velocity and brine concentration fields. T2DM efficiently calculates flow and transport for these problems. We have applied T2DMR to the dispersive transport and decay of radionuclide tracers in flow fields with permeability heterogeneities and recirculating flows. Coupling in these problems occurs by velocity-dependent hydrodynamic dispersion. Our results show that the maximum daughter species concentration may occur fully within a recirculating or low-velocity region. In all of the problems, we observe very efficient handling of the strongly coupled flow and transport processes.

INTRODUCTION

TOUGH2 uses a residual-based convergence criterion and Newton-Raphson iteration to handle the non-linear equations for the changes in primary variables (Pruess, 1987; 1991). This formulation is efficient for handling the strong non-linearities of multiphase flow which enter, for example, through relative permeability, capillary pressure, and density effects. These same techniques also make possible the efficient solution of strongly coupled single-phase flow problems. In this paper, we show results of TOUGH2 calculations for two classic strongly coupled flow problems and we investigate radionuclide decay and hydrodynamic dispersion in a variable velocity flow field. The example problems are solved with T2DM, and T2DMR, the dispersion and radionuclide transport modules for TOUGH2. Complete details of the dispersion model and its implementation are presented in Oldenburg and Pruess (1993; 1994a). The focus of this paper is on model results and the handling of strongly coupled flow problems in the TOUGH2 simulator.

CONVERGENCE CRITERION

The example problems presented here are single-phase flow problems with coupled flow and transport. The coupling between the flow field and the transport equations arises through density effects, hydrodynamic dispersion, and a combination of the two. Coupling is handled in TOUGH2 by a residual-based formulation in which the discretized mass balance equations at each time step are solved simultaneously taking all coupling terms into account. For each grid block n and mass component κ, the residual is defined as $R_n^{(\kappa)}$ = {left-hand side} – {right-hand side} of the space-and-time discretized conservation equations. Specifically, the residual $R_n^{(\kappa)}$ at time step $k+1$ is written

$$R_n^{(\kappa)k+1} = M_n^{(\kappa)k+1} - M_n^{(\kappa)k} - \frac{\Delta t}{V_n}\left\{\sum_m A_{nm} F_{nm}^{(\kappa)k+1} + V_n\, q_n^{(\kappa)k+1}\right\} \quad (1),$$

where m labels the grid blocks that are connected to n, and $\Delta t = t(k+1) - t(k)$ is the time-step size. Using 2 components (water and brine) with isothermal conditions in EOS7, there are 2N residuals for a flow system with N grid blocks. These 2N residuals are generally non-linear functions of the 2N primary variables, namely, the set of pressures and brine mass fractions. The set of 2N non-linear discretized equations $R_n^{(\kappa)} = 0$ is solved by Newton-Raphson iteration. Expanding to first order in the primary variables and introducing an iteration index p, we have

$$R_n^{(\kappa)k+1}(x_{i,p+1}) = R_n^{(\kappa)k+1}(x_{i,p}) + \sum_i \left.\frac{\partial R_n^{(\kappa)k+1}}{\partial x_i}\right|_p (x_{i,p+1} - x_{i,p}) \doteq 0 \quad (2)$$

where $x_{i,p+1}$ is the set of unknown primary variables at time step $k+1$, iteration level $p+1$. Solution of Eq. 2 results in an updated estimate of the primary variables. Iteration continues until all residuals are reduced to a small fraction of the accumulation terms, i.e.,

$$\left|\frac{R_{n,p+1}^{(\kappa),k+1}}{M_n^{(\kappa),k+1}}\right| \le \varepsilon \quad (3).$$

The convergence criterion is set to a small number, typically $\varepsilon = 1.e\text{-}5$. When the accumulation term is very small, an absolute rather than a relative convergence criterion may be used.

The solution technique in TOUGH2 is efficient for strongly coupled flow problems for two reasons. First, both the flow and transport equations are solved simultaneously, with full coupling between the flow equations (through density), solute concentration, and solute dispersion. In this way, the numerical solution of flow and transport is coupled just as the physical flow and transport are coupled. Because the time-step size can be larger in this coupled solution technique, fewer time steps are needed. Second, reduction of residuals below a small fraction of the mass accumulation term ensures that the difference equations have in fact been solved; there is no possibility for "false" convergence. Other codes often used for coupled single and multiphase flow problems (e.g., FAST (Holzbecher, 1991), HST3D (Kipp, 1987), SUTRA (Voss, 1984), and SWIFT (Reeves et al., 1986)) use a criterion of "small" relative or absolute changes in primary variables to determine convergence. Such a criterion is dangerous in that small changes in primary variables during iteration do not necessarily indicate convergence, but may arise far from convergence when the convergence rate is slow.

DENSITY-COUPLED FLOW

Pure Solutal Free Convection

The Elder problem is a free-convection problem originally conceived as being pure thermal convection with heating from below

(Elder, 1967), but easily adapted for pure solutal convection with a salt source at the top. The large maximum density change (20%) makes this a strongly coupled flow problem. Consistent with the Elder pure thermal convection problem, which was performed in a Hele-Shaw cell, the emphasis in this problem is on the density coupling rather than coupling through hydrodynamic dispersion. Thus, transport is by advection and pure molecular diffusion. In the problem, a body of liquid-saturated porous media is juxtaposed against an infinite source of dense brine above. The domain, boundary conditions, and discretization for the problem are presented in Fig. 1, where symmetry about the line Y = 0 m has been assumed. The parameters for the problem are presented in Table 1.

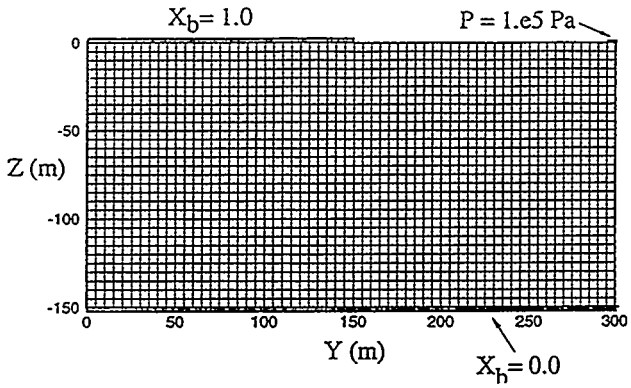

Fig. 1. Domain, boundary conditions, and discretization for the Elder (1967) pure solutal convection problem.

Table 1. Parameters for the Elder (1967) pure solutal convection problem.

symbol	quantity	value	units
ϕ	porosity	.1	–
k	permeability	4.845×10^{-13}	m^2
μ	viscosity	1.0×10^{-3}	Pa s
g.	gravity	9.81	$m\,s^{-2}$
α_T	transverse dispersivity	0.	m
α_L	longitudinal dispersivity	0.	m
d	molecular diffusivity	3.565×10^{-6}	$m^2\,s^{-1}$
τ	tortuosity	1.	–
ρ_0	density of pure water	1000.	$kg\,m^{-3}$
ρ_b	density of pure brine	1200.	$kg\,m^{-3}$

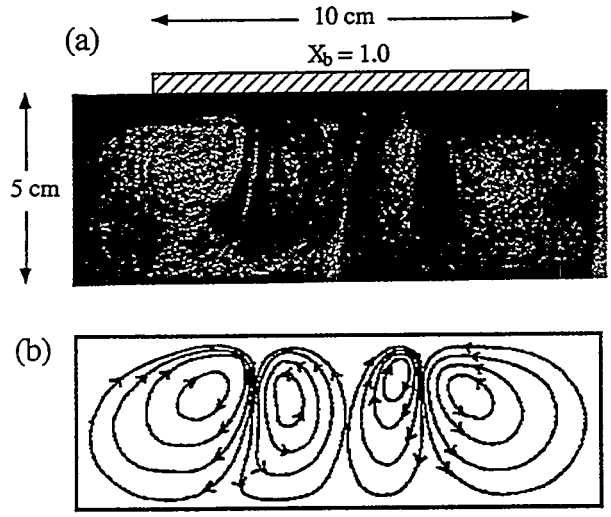

Fig. 2. Experimental results of Elder (1967): (a) flow visualization as presented by Elder (1967) and embellished with brine source boundary condition; (b) approximate streamlines made explicit for clarity.

We show in Fig. 2 a reproduction of a photo from Elder's paper (Elder, 1967), turned upside down to correspond to our solutal convection scenario and embellished with the boundary conditions and approximate streamlines. The photo clearly shows that Elder's laboratory result had the equivalent of central upflow. Fig. 3 shows our corresponding calculated results after 152 time steps at t = 20 years. Our calculated result agrees closely with Elder's experimental result. The convection process begins with downward flow near the right-hand edge of the dense brine region (Fig. 3) where the X_b = 1.0 boundary condition is maintained. Flow is upwards on both sides of this brine plume. With time, this region of downflow moves towards the center line (Y = 0). However, it does not actually reach the center line, and at later times in this transient flow there is upflow at the center line (Y = 0), which corresponds to central upwelling. For discussion and comparison of prior modeling efforts with current results, see Oldenburg and Pruess (1994b, 1995a).

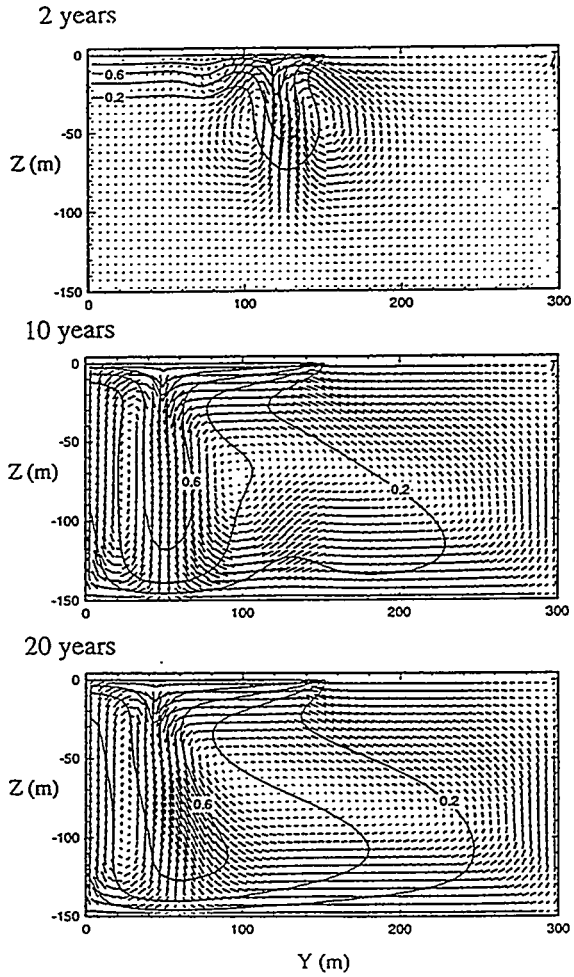

Fig. 3. Results for the Elder free-convection problem at t = 2, 10, and 20 years. Contours are labeled with mass fraction of maximum brine concentration ($X_{b,max}$ = 1.0). Flow field and concentration isopleths show agreement with the experimental results of Elder (1967) reproduced in Fig. 2.

Salt-Dome Flow

Patterned loosely after the hydrogeologic conditions at Gorleben, Germany, a site under consideration for use as a high-level nuclear waste repository (Langer et al., 1991), the salt-dome flow problem was set forth in the Hydrocoin code verification study (Andersson et al., 1986). In the problem, fresh water enters from the top boundary on the left-hand side of a two-dimensional domain, flows past a region of dense brine at the bottom, and then flows out through the top boundary on the right-hand side (Fig. 4). The in-flow and out-flow regions along the top boundary are not defined *a priori*, but must be determined as part of the solution. Transport of

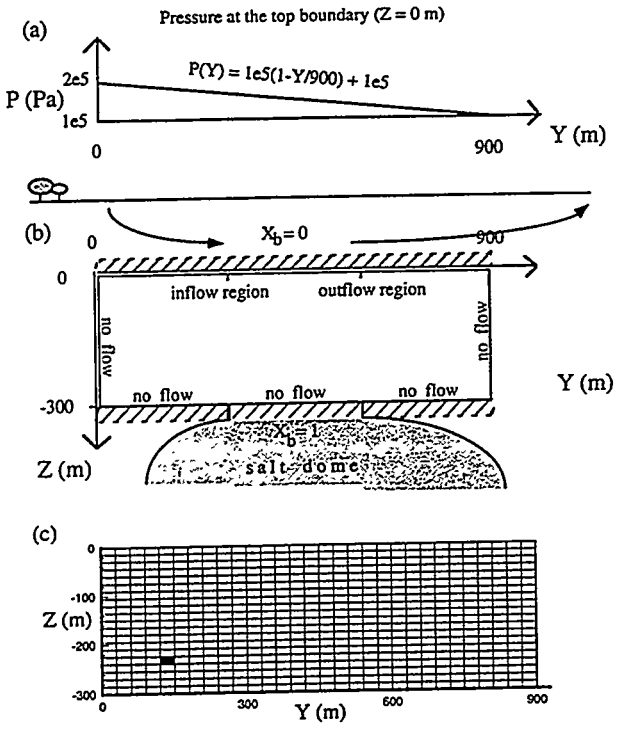

Fig 4. Domain and boundary conditions for the salt-dome flow problem. (a) Top pressure boundary condition. (b) Schematic and boundary conditions of the domain. (c) Discretization.

brine is by advection and hydrodynamic dispersion (no molecular diffusion). Strong coupling occurs through density variations of 20% and through hydrodynamic dispersion. Prior simulation results concluded that the steady-state flow field has a large recirculation in the bottom region, although the strong coupling in the problem has led to great difficulty in achieving steady state solutions (Andersson et al., 1986; Herbert et al., 1988).

Results for the problem calculated with T2DM are shown in Fig. 5. After approximately 100 time steps, these results are very close to steady state as evidenced by time steps on the order of 100 years. Further confirmation of the single steady-state solution was obtained by starting the simulation with different initial conditions and obtaining the same steady state. The calculated results show that fresh water picks up saline brine from the bottom brine boundary by hydrodynamic dispersion. Advection and dispersion then transport the plume of salty water generally from left to right. Our steady-state flow pattern is quite different from results presented by other workers, who obtained large recirculations in what was deemed to be a "steady" state. Based on our results we suggest that the recirculating state found by others is not "steady," but was mistaken as such because previous simulations had employed parameter stepping and a convergence criterion based on (small) changes in the primary variables rather than on residuals. A detailed discussion of these subtle issues is presented in Oldenburg and Pruess (1995a).

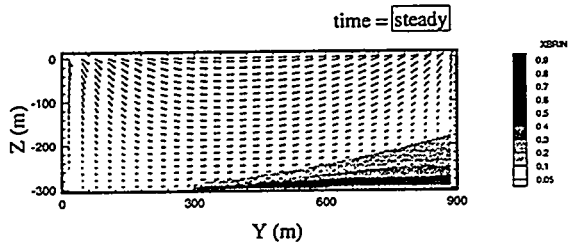

Fig. 5. Steady-state velocity and brine mass fraction for the salt-dome flow problem showing the swept-forward flow pattern. A weak recirculation occurs in the lower right-hand corner.

Table 2. Parameters for the salt-dome flow problem.

symbol	quantity	value	units
ϕ	porosity	.2	–
k	permeability	$1. \times 10^{-12}$	m^2
μ	viscosity	8.9×10^{-4}	Pa s
ρ	brine density	1.2×10^{3}	kg m^{-3}
g	gravity	9.80665	m s^{-2}
α_T	transverse dispersivity	2.	m
α_L	longitudinal dispersivity	20.	m
d	molecular diffusivity	0.	m^2 s^{-1}

FIRST-ORDER DECAY

Variable-Velocity Mixing

Next we apply T2DMR to a problem of dispersive mixing and radioactive decay of a passive tracer component in a flow field with a large-scale [O(100 m)] permeability heterogeneity located off-axis relative to the tracer source. The coupling in this problem is through hydrodynamic dispersion only. The permeability heterogeneity causes very slow velocities in the low-permeability region. These low velocities affect advective and dispersive mixing. The configuration is shown in Fig. 6, where the light stipple is the heterogeneity and the darker stipple is the region of injection of parent radionuclide. The heterogeneity is 100 times less permeable than the surrounding medium. With a pressure drop of $1. \times 10^5$ Pa across the 900-m wide domain, the average transit time across the domain is approximately 50 years. For this problem, we set the half-life of the parent to 500 years. The daughter is assumed stable. Parameters are presented in Table 3. In Fig. 7, we show the concentration of the parent at four times after injection. The parent is largely advected around the heterogeneity, but at steady state, clearly some parent has entered the low permeability heterogeneity. In Fig. 8, the daughter concentration at the same four times is shown. Daughter concentration is slow to build up in the low-permeability region but, remarkably, at steady state the maximum daughter concentration is located fully within the heterogeneity, completely off-axis from the parent maximum. It is apparent that over time, the parent component enters the heterogeneity by dispersion and advection. The residence time of the parent within the heterogeneity is relatively long; during this time, the parent decays to the daughter. The daughter is stable and does not decay, relying on dispersion and advection for its dilution. Only when the daughter concentration becomes quite large does its dispersive mixing balance its production by decay of parent. Details are presented in Oldenburg and Pruess (1995b).

Table 3. Parameters for the variable velocity radionuclide dispersion and decay problem.

symbol	quantity	value	units
ϕ	porosity	.2	–
k	permeability	$1. \times 10^{-12}$	m^2
μ	viscosity	8.9×10^{-4}	Pa s
α_T	transverse dispersivity	2.	m
α_L	longitudinal dispersivity	20.	m
d	molecular diffusivity	0.	m^2 s^{-1}
j	solute injection rate	1.6×10^{-6}	kg s^{-1}

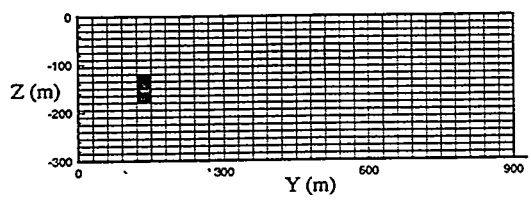

Fig. 6. Domain with permeability heterogeneity. Heavy stipple indicates the source grid blocks where parent is injected. Light stipple indicates the permeability heterogeneity where permeability is .01 of the background permeability.

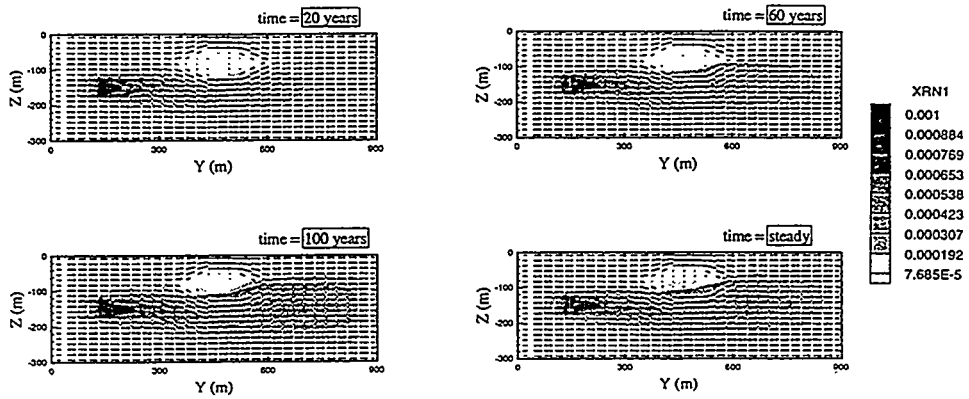

Fig. 7. Velocity and mass fraction of parent radionuclide component ($t_{1/2}$ = 500 years) in flow field with permeability heterogeneity at different times. Note the maximum concentration of parent occurs generally downstream from the grid blocks in which parent was injected.

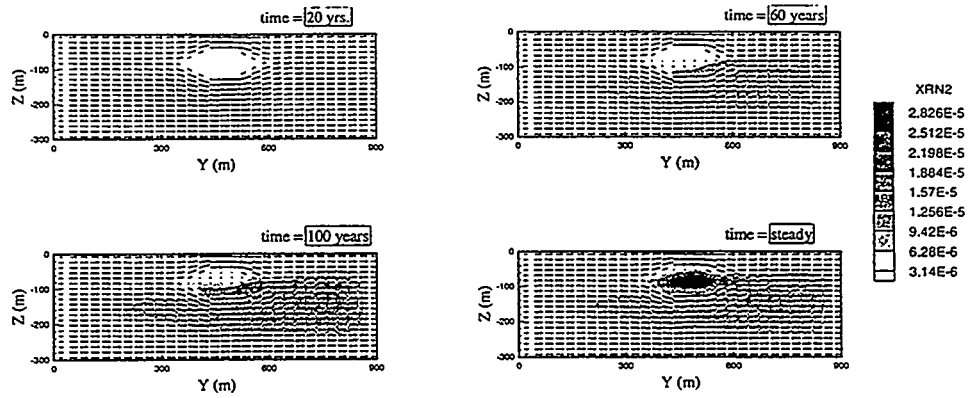

Fig. 8. Velocity and mass fraction of stable daughter radionuclide component in flow field with permeability heterogeneity at different times. Note the maximum concentration of daughter occurs within the permeability heterogeneity.

Salt-Dome Flow with First-Order Decay

Finally, we show an example calculation of the mixing of radioactive tracers in a more complicated flow field with a velocity gradient. The flow field itself comes from the strongly coupled salt-dome flow problem (Fig. 5). We inject passive radioactive components into the stippled grid block of Fig. 4c and we observe their distribution in time and space as they undergo decay and transport due to advection and hydrodynamic dispersion in the recirculating flow field.

In the steady-state salt-dome flow field, there is a weak recirculation near the right-hand wall caused by dense brine that has entered along the brine source but is too dense to be easily advected upward. Parent radionuclide is injected at a rate of 1.6e-6 kg/s in the grid block indicated in Fig. 9 by the stipple. The half-life is 50 years for the parent, and 250 years for the daughter. The concentration isopleths at t = 20, 60, 100, and 1400 years after injection are shown in Fig. 9. The daughter mass fraction is shown in Fig. 10. The maximum concentration of daughter shows a slight migration toward the lower boundary by t = 60 years. By t = 1400 years, the maximum daughter concentration lies in the weak recirculation in the lower right-hand corner. The maximum concentration of daughter has effectively moved down the velocity gradient and into the weak recirculation cell. The weak recirculation is a region of small advective velocity and long residence time analogous to the permeability heterogeneity of Fig. 8. Whereas one might expect the maximum daughter concentration to be found downstream from the maximum parent concentration, in fact the maximum daughter concentration lies within the recirculation.

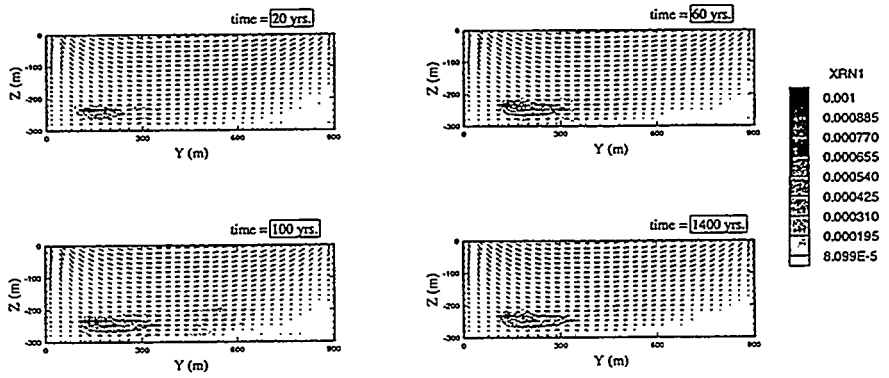

Fig. 9. Velocity and mass fraction of the parent ($t_{1/2}$ = 50 years) for salt-dome flow problem at different times.

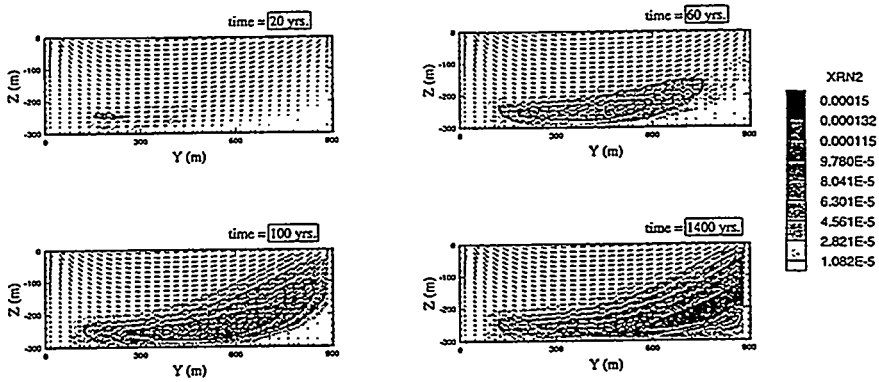

Fig. 10. Velocity and mass fraction of the daughter ($t_{1/2}$ = 250) years for salt-dome flow problem at different times. Note the maximum daughter concentration occurs within the weak recirculation in the lower right-hand corner.

CONCLUSIONS

Applications of T2DM and T2DMR to strongly coupled single-phase flow problems demonstrate the efficiency of the fully coupled solution technique in TOUGH2. For the Elder pure solutal convection problem, where strong coupling arises through density effects, T2DM is able to obtain answers similar to laboratory experimental results (Elder, 1967). For the salt-dome flow problem, where density and hydrodynamic dispersion couple the flow and transport, T2DM achieves verifiable steady-state answers that show a swept-forward flow field, a result fundamentally different from the best prior simulation results obtained using relative-change convergence criteria. T2MDR has been applied to coupled flow and transport of radioactive tracers undergoing decay in variable velocity flow fields. Our results indicate that daughter nuclides may reach their maximum concentrations not downstream from the parent source, but instead in regions of slow advective flow and corresponding long residence time.

Acknowledgments

This work was supported by the WIPP project, Sandia National Laboratories, and by the Office of Civilian Radioactive Waste Management, Yucca Mountain Site Characterization Project Office, U.S. Department of Energy, under contract No. DE–AC03–76SF00098. Computing support was provided by the Office of Basic Energy Sciences, U.S. DOE. We thank Stefan Finsterle and Yvonne Tsang for thoughtful reviews of an earlier draft.

Nomenclature

d	molecular diffusivity	$m^2\ s^{-1}$
g	acceleration of gravity	$m\ s^{-2}$
j	solute injection rate	$kg\ s^{-1}$
k	permeability	m^2
m	labels connected grid blocks	
M	mass accumulation term	$kg\ m^{-3}$
N	number of grid blocks	
NEQ	number of equations per grid block	
NK	number of mass components (species)	
NY	number of grid blocks in Y-direction	
NZ	number of grid blocks in Z-direction	
P	total pressure	Pa
q	source term	$kg\ m^{-3}\ s^{-1}$
R	residual	kg
t	time	years
V	volume	m^3
X	mass fraction	
Y	Y-coordinate	
Z	Z-coordinate (positive upward)	

Greek symbols

α	intrinsic dispersivity	m
ε	convergence criterion	
μ	dynamic viscosity	$kg\ m^{-1}\ s^{-1}$
ϕ	porosity	
ρ	density	$kg\ m^{-3}$
τ	tortuosity	

Subscripts and superscripts

b	brine
k	time-step index
L	longitudinal
m	indexes grid blocks connected to n
n	grid block index
p	Newton-Raphson iteration index
0	reference value
T	transverse
κ	mass components

References

Andersson, K., B. Grundfelt, D.P. Hodgkinson, B. Lindbom, and C.P. Jackson, *HYDROCOIN Level 1 Final Report: Verification of Groundwater Flow Models*, Swedish Nuclear Power Inspectorate (SKi), 1986.

Elder, J.W., Transient convection in a porous medium, *J. Fluid Mech.*,*27*(3), 609–623, 1967.

Herbert, A.W., Jackson, C.P., and Lever, D.A., Coupled groundwater flow and solute transport with fluid density strongly dependent on concentration, *Water Res. Res.*, *24* (10), 1781-1795, 1988.

Holzbecher, E., Numerische Modellierung von Dichteströmungen im porösen Medium, Technische Universität Berlin, *Mitteilung Nr. 117*, 1991.

Kipp, K.L., HST3D: A computer code for simulation of heat and solute transport in 3-D ground-water flow systems, *U.S. Geol. Surv., Water-resources Invest. Rep., 86-4095*, 1986.

Langer, M., Schneider, H., Kühn, K., The salt dome of Gorleben–target site for the German radioactive waste repository, pp. 57–66, in Witherspoon, P.A., *Proceedings of the Workshop W3B, 28th International Geological Congress*, Washington, D.C., July 1989, *Lawrence Berkeley Laboratory Report, LBL–29703*, January, 1991.

Oldenburg, C.M. and Pruess, K., A two-dimensional dispersion module for the TOUGH2 simulator, *Lawrence Berkeley Laboratory Report, LBL- 32505*, 1993.

Oldenburg, C.M. and Pruess, K., T2DMR: Radionuclide transport for TOUGH2, *Lawrence Berkeley Laboratory Report, LBL- 34868*, 1994a.

Oldenburg, C.M. and Pruess, K., Numerical simulation of coupled flow and transport with TOUGH2: A verification study, *Lawrence Berkeley Laboratory Report, LBL- 35273*, 1994b.

Oldenburg, C.M. and Pruess, K., Dispersive transport dynamics in a strongly coupled groundwater-brine flow system, *Water Res. Res, 31*(2), 289–302, 1995a.

Oldenburg, C.M. and Pruess, K., Mixing with First-Order Decay in Variable Velocity Porous Media Flow, *Transport in Porous Media*, submitted, 1995b.

Pruess, K., TOUGH User's Guide, Nuclear Regulatory Commission, Report NUREG/CR-4645, June 1987 (also *Lawrence Berkeley Laboratory Report, LBL-20700*, Berkeley, California, June 1987).

Pruess, K., TOUGH2 - A General Purpose Numerical Simulator for Multiphase Fluid and Heat Flow, *Lawrence Berkeley Laboratory Report, LBL-29400*, Berkeley, California, May 1991).

Reeves, M., Ward, D.S., Johns, N.D., and Cranwell, R.M., Theory and implementation of SWIFT II, the Sandia Waste-Isolation Flow and Transport Model for Fractured Media, *Report No. SAND83-1159*, Sandia National Laboratories, Albuquerque, N.M., 1986.

The International Hydrocoin Project, Level 1: Code Verification , Rep. 71617, Organization for economic cooperation and development (OECD), Paris, France, 1988.

Voss, C.I., SUTRA: A finite-element simulation model for saturated-unsaturated fluid-density-dependent ground-water flow with energy transport or chemically-reactive single-species solute transport, *U.S. Geol. Surv. Water-resour. Invest. Rep.*, 84-4369, 409 pp., 1984.

Voss, C.I., and Souza, W.R., Variable density flow and solute transport simulations of regional aquifers containing a narrow freshwater-saltwater transition zone, *Water Res. Res.*, *23*(10), 1851–1866, 1987.

Air Sparging for Subsurface Remediation: Numerical Analysis Using T2VOC

John E. McCray
Department of Environmental Systems Engineering, Clemson University, Clemson, SC 29634-0919
Currently at Department of Hydrology and Water Resources, Harshbarger Building 11, University of Arizona, Tucson, AZ 85721

Ronald W. Falta
Department of Earth Sciences, Clemson University, Clemson, SC 29634-1908

Abstract. Air sparging is under active investigation as a promising remediation technology for aquifers contaminated with volatile organic dense nonaqueous phase liquids (DNAPLs). A theoretical study for the removal of DNAPLs from the subsurface using this technology is presented. T2VOC is used to conduct multiphase numerical simulations of DNAPL removal utilizing a model aquifer with a radially-symmetric geometry. Both homogeneous and macroscale heterogeneous systems are considered. These simulations suggest that DNAPLs are efficiently removed in a zone of contaminant cleanup at relatively low gas saturations within the injected air plume. The zone of effective removal may be referred to as the radius of influence (ROI). The sparging-induced pressure increase below the water table, which may be measured in the field, is recommended as the best method for determining the ROI. Multiphase numerical simulations are used to support this recommendation, to relate the injected gas ROI to the zone of NAPL cleanup, and to illustrate the transient and steady-state aquifer behavior.

Introduction

DNAPLs are an increasingly common subsurface pollution problem. DNAPLs, which are denser than water, may act as a long-term source of ground water contamination in the saturated zone due to typically low aqueous solubilities. Air sparging is an innovative ground water remediation technology which shows promise in removing DNAPLs from the subsurface. Air sparging works on the principles of interphase mass transfer. Air is injected into the saturated zone below a contaminated area. As the air rises to the surface, dissolved and NAPL contaminant will partition into the gas phase when in contact with the air. Air sparging is typically coupled with a soil vapor extraction (SVE) system to collect the volatilized pollutant in the vadose zone. In some cases, sparging may be less costly and more effective than conventional pump-and-treat (Felten et al., 1992; Leonard and Brown, 1992; Loden, 1992).

Perhaps the most important parameter in an air sparging system design is the radius of influence (ROI) of the sparging well. Four methods currently used to estimate the sparge well ROI are: measuring the pressure response below the water table, measuring the increase in dissolved oxygen concentration in the ground water, measuring the mounding of the water table, and measuring increases in VOC vapor concentration in the unsaturated zone (Felten et al., 1992; Leonard and Brown, 1992; Loden, 1992). It is not clear, however, which of these methods best define the ROI. Ideally, the ROI should correspond to contaminant cleanup. Based on our numerical analysis, we recommend measurement of the pressure increase (above hydrostatic) in the sparge zone, or "positive pressure" as the most accurate method for ROI estimation. The numerical simulations presented here will demonstrate the utility of the recommended method, as well as show how the sparging ROI is related to NAPL cleanup under certain conditions. The simulations will also illustrate the significance of macro-scale heterogeneities (such as clay lenses) on sparging effectiveness. The transient and steady-state development of the injected gas plumes in our model systems is also discussed.

Adenekan et al. (1990) used STMVOC (see Falta et al. 1992a) to compare the effectiveness of air sparging, vapor extraction, and groundwater extraction for DNAPL removal. We use T2VOC (Pruess, 1991) for a detailed three-phase numerical study focused on air sparging in hopes that our study will contribute to the limited theoretical knowledge on the subject. The code has been validated with experimental data for several multiphase transport problems (Falta et al, 1992b; Falta, 1990, Seely et al, 1994). Recently, McCray (1994) used T2VOC to successfully model the air sparging experiment of Ji et al. (1993). The laboratory experiment demonstrated that air injected into a saturated medium of glass beads formed stable, parabolic-shaped plumes at steady state. While these plumes actually consisted of many discrete air channels, the average behavior on a larger scale appeared to be a stable, multiphase flow process. T2VOC simulated the shape and multiphase behavior of various plumes quite well under different flow conditions in both homogeneous and heterogeneous media.

Physical System and Model Representation

The physical system considered is a 20 m deep sandy aquifer, bounded on the bottom by an impervious barrier. The water table exists 10 m below the ground surface. The capillary fringe is about 0.5 m thick. The heterogeneous case contains a 3.5 meter radius, low permeability, high capillary "clay" disk of thickness 1 m located at mid-depth in the saturated zone. The radially-symmetric model is shown in Figure 1. The arrangement of sparging and SVE well screens is nested as shown, which is common in actual remediation scenarios (Loden, 1992). TCE is used as the pollutant. Physical and chemical data used for TCE is the same as in Falta et al. (1992b).

The top of the model aquifer is a constant, atmospheric pressure boundary, while the bottom is a "no-flow" boundary. The outer boundary, which is beyond the zone affected by sparging, is a static pressure, static fluid saturation, chemical-free boundary located 100 m from the center. For the homogeneous aquifer model, the numeric grid consists of 44 elements in the radial direction and 28 elements in the vertical direction. The numeric grid for the heterogeneous aquifer has 42 elements in the radial direction and 31 in the vertical direction. In general, the numeric mesh is finer near the well (0.25 m wide out to a 2 m radius) and within the clay disk (element height is 0.25 m) and becomes progressively coarser farther from the well and in the upper portions of the vadose zone. For example, in the heterogeneous case, the sparging influence is contained within a 20 m radius; at this radius the element width is 1 m. The well bore forms the centerline of the model grid. The sparge gridblock represents a 0.152 m (6 inch) diameter sparge well, screened 0.5 m high, one meter from the bottom. The SVE well screen is a 2 m high gridblock with the bottom placed 1.5 m above the water table. A constant SVE well vacuum pressure of 0.9 atmospheres is specified, which is typical for SVE/air sparging systems (Felten, et al., 1992; Leonard and Brown, 1992). The sparging system is simulated such that the volumetric flow ratio of extracted to injected air is about 6:1 for each case. Wisconsin requires at least a 4:1 ratio (Loden, 1992) to prevent vadose zone vapor migration. Ratios of over 10:1 are also common (Felten et al., 1992; Leonard and Brown, 1992; Loden, 1992).

Porous media parameters such as the intrinsic and relative permeabilities, capillary pressure, and porosity were chosen carefully. For this study, an intrinsic permeability of 10 darcys is used for the homogeneous, sandy medium. A permeability of 10^{-4} darcys is assumed for the clay. The three-phase NAPL permeability is calculated using Stone's first method (Stone, 1970). Parameters which determine the shape of the relative permeability curve are consistent with those given in Mercer and Cohen (1990) for water, TCE, and Xylene in sand and clay. For the three-phase capillary pressure relations, the formulation proposed by Parker et al. (1987) is adopted. The parameters which determine the shape of the capillary pressure for sand were derived from the experimental work of Lenhard and Parker (1987). For the clay, we felt it was important to obtain realistic numbers for breakthrough pressures. The breakthrough pressure is the capillary pressure which must be overcome for the non-wetting fluid (air or NAPL) to enter the largest pores in a water saturated medium. This pressure depends upon the radius of a representative water-filled pore resisting NAPL or air entry, the interfacial tension between the wetting and non-wetting phases, and the contact angles of the fluid-solid interfaces. Realistic values for these parameters were obtained from Mercer and Cohen (1990). Data from van Genuchten (1980) were used to determine the shape of the capillary curves for the clay. For a complete listing of the parameters used in these simulations, the reader is referred to McCray (1994).

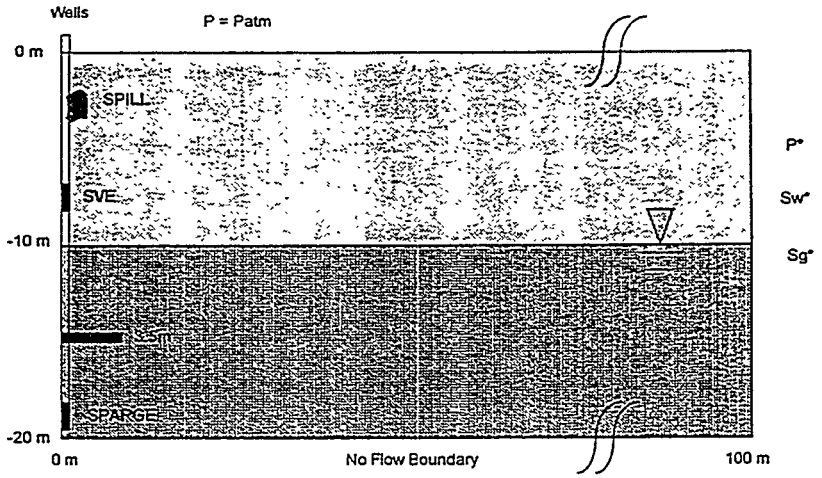

Figure 1. Model aquifer used for air sparging simulations.

Simulation of Sparging in a Homogeneous Medium

For the homogeneous TCE case, 2460 gallons (13602 kg) of liquid TCE is injected at the model grid centerline, 3 meters below the ground surface, at a rate of 50 gallons per day. The spill is allowed to pervade the subsurface for about 1 year prior to initiation of remediation. The initial distribution of TCE NAPL saturation (S_n) is shown in Figure 2a. The equilibrium air injection pressure for this simulation is 35 inches of water above hydrostatic. The volumetric sparge rate (Q_{spg}) is 8.6 scfm, and the volumetric flow for SVE (Q_{sve}) is 54 scfm. Air injection and SVE are begun simultaneously.

Upon the initiation of sparging, the injected gas plume is characterized by a transient period during which the gas plume first expands (causing mounding at the water table), and then collapses to form a steady-state plume. Figure 3 shows the gas plume after 4 hours of sparging and at steady state. At 4 hours, there is over 1 foot of significant mounding (70% water) directly above the sparge point. This mounding is due to a combination of the added air pressure and volume, and to density effects (Wisconsin Dept. of Natural Resources, 1993). Martinson and Linck (1993) observed in field pilot tests that 95% of the initial upwelling dissipated within 1 day. Our simulations also suggest that the mounding is transient. By shortly after 3 days, the plume has reached steady state.

Very little DNAPL is removed during the first several days. After 30 days (Figure 4a), NAPL within the higher gas saturations of the air plume are removed. After 1 year, all the NAPL plume above the air sparge point has been removed (Figure 4b). It is important to note that once the gas plume achieves steady state, the saturated zone DNAPL distribution above the sparge point lies almost entirely within the gas plume (defined by 0.1 gas saturation). Under these conditions, removal of the DNAPL by air sparging is quite effective. It may be very difficult to achieve this geometry in a field situation, however.

These simulations suggest that significant NAPL reduction occurs at relatively low gas saturations of less than 0.1. Previous numerical studies (McCray, 1994) also suggest that dissolved concentrations of TCE can be reduced to virtually zero at gas saturations less than 0.1. Apparently, gas saturation is a good measure of the sparging ROI.

Interestingly, the numerical simulations show that contours of steady-state positive pressure take on the same shape as the steady-state gas saturation profile. Figure 5 shows the positive pressure profile after 4 hours of sparging and at steady state. At steady state, the contour of about 3 inches of water pressure is in roughly the same location as the 0.1 gas saturation contour of Figure 3b. However, during the transient phase, the pressure contours do not resemble the gas saturation distribution. The simulations suggest that measurement of pressure response in monitoring wells below the water table after stabilization of the injected gas plume (as evidenced by the subsidence of water table mounding) may provide the best indication of the ROI.

For a multiphase system, this phenomena is due to capillary pressure effects. Once the gas plume geometry stabilizes, the ground water flow velocities become very small, and mainly consist of small convection currents at the edge of the gas plume (Wisconsin Dept. of Natural Resources, 1993). At this point, the ground water is nearly stagnant. Thus, the gage water pressure (P_w) at any location is equal to the hydrostatic pressure (P_{hyd}). Inside the sparge zone, multiphase conditions are present and the gas pressure is related to the gas-water capillary pressure (P_{cgw}) by

$$P_g = P_w + P_{cgw} \quad (1)$$

Since the ground water is at hydrostatic pressure, we propose that the increase in pressure above hydrostatic pressure (P_{pos}) measured in the sparge zone is a direct result of the capillary pressure between the gas and water phases:

$$P_{cgw} = P_g - P_{hyd} = P_{pos} \quad (2)$$

In the field, this pressure increase is easily measured using monitoring well points (Nyer and Sutherson, 1993). Monitoring points will measure the gas pressure rather than the water pressure or NAPL pressure because of the preferential flow of the nonwetting phase into the monitoring point due to capillary gradients. For a gas-aqueous system, and neglecting capillary pressure hysteresis, the capillary pressure given by (2) directly corresponds to some unique volumetric gas saturation, S_g. Most of the ground water cleanup will occur in the aerated zone (Angell, 1992; Leonard and Brown, 1992; McCray, 1994). Thus, assuming that contaminant cleanup occurs at low gas saturations around 0.1, the

positive pressure that corresponds to this gas saturation on a representative capillary pressure versus gas saturation curve for a field site may be used to define the ROI.

This relation is more complicated for the case where NAPL is present because the gas-water capillary pressure may not be easily measurable under three-phase conditions. In this case, the capillary pressure is not uniquely related to gas saturation but depend on all three phase saturations. Thus, there is no simple analytic expression to relate positive pressure to the ROI. However, Figures 6 and 7 illustrate that the positive pressure contours still mimic the gas saturation contours, even where NAPL is present. Again, positive pressure measurements appear to be a superior method for determination of the sparging ROI and for monitoring the shape of the gas plume. Although not shown here, this was also true for anisotropic systems with various permeability ratios (2:1 to 50:1).

Simulation of Sparging in Heterogeneous Media

For the heterogeneous TCE case, 8266 gallons (45747) kg of liquid TCE was injected at a rate of 50 gallons per day. More chemical was injected than in the homogeneous case to ensure that the DNAPL pooled on the bottom boundary. The TCE spill was allowed to move through the subsurface for nearly 6 months prior to the start of remediation. The initial distribution of NAPL saturation is shown in Figure 2b. The TCE pools on the disk surface since the weight of the DNAPL column is insufficient to overcome the breakthrough pressure.

The injection pressure and flow rates for this scenario are the same as for the homogeneous case. Figure 6 shows the transient and steady-state gas plumes. The clay also acts as a capillary barrier to the injected air for the given injection pressure. Thus, the air collects underneath the lens and eventually travels to the edge where it continues its upward movement.

Figure 7 illustrates the NAPL plume at 30 days and at 1 year (where the steady-state positive pressure distribution is superimposed over the NAPL plume to show its relation to the sparging ROI). Steady state is reached shortly after 3 days for both the gas plume and pressure. As in the homogeneous case, the transient pressure contours do not concur with the gas saturations (not shown), while at steady state, the positive pressure distribution mimics the shape of the gas plume. Note that the gas plume does not significantly contact the DNAPL plume above or below the clay lens except near the edge of the lens. For this reason, no DNAPL is removed directly above the clay. After a year, the vadose zone cleanup of the NAPL phase is complete, but in the saturated zone, only the chemical contained within the ROI is reduced. These simulations suggest that heterogeneities significantly impact sparging performance. Significant cleanup occurs within the injected air plume. Outside the plume, NAPL cleanup will be limited by diffusive and convective transport to the plume. Air sparging could still be effective in remediation for this case if additional wells were used. However, care must be taken in design to prevent migration of vaporous or dissolved contaminant.

Conclusions

Numerical modeling of the air sparging process is possible, even in heterogeneous media, but the distribution of capillarity and permeability must be well known. Gas flow patterns during sparging are strongly affected by heterogeneities, which may result in poor contact between the advective air phase and the pollutant chemical. Thus, sparging efficiency may be significantly degraded where the DNAPL is pooled on relatively impermeable barriers. Multiple sparging wells at various depths may be required to remove significant amounts of DNAPL in these cases.

The ability to make an accurate determination of the radius of cleanup is invaluable since the cost benefits of using air sparging for NAPL and dissolved cleanup will be greatly improved by matching the contaminant plume to this radius. Measurement of the steady-state pressure increase below the water table is recommended as the method of choice for determining the sparging ROI. Positive pressure measurements obtained prior to stabilization of the gas plume are not indicative of the ROI, but rather, reflect in part the transient ground water flow which occurs as the gas plume develops. Based on its transient nature, water table mounding is not a reliable indicator of the sparging radius of influence. The pressure increase present after gas plume steady state is achieved may be directly related to capillary pressure. When no NAPL is present, the ROI may be estimated by comparing the gas-water capillary pressure for a given gas saturation to field-measured positive pressure. When NAPL is present, the positive pressure distribution still mimics the gas saturation profile, and its measurement remains the best method to estimate the ROI.

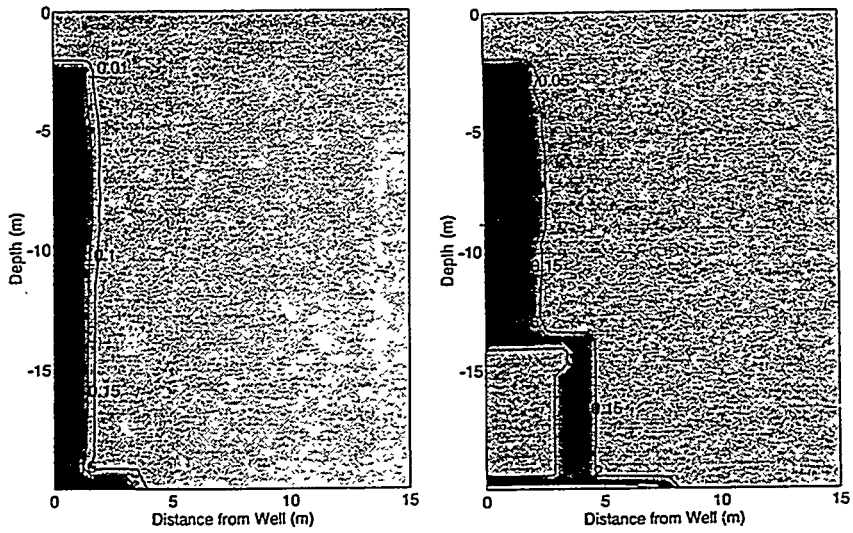

Figure 2. Initial NAPL saturation after the spill in the (a) homogeneous aquifer, and (b) the heterogeneous aquifer.

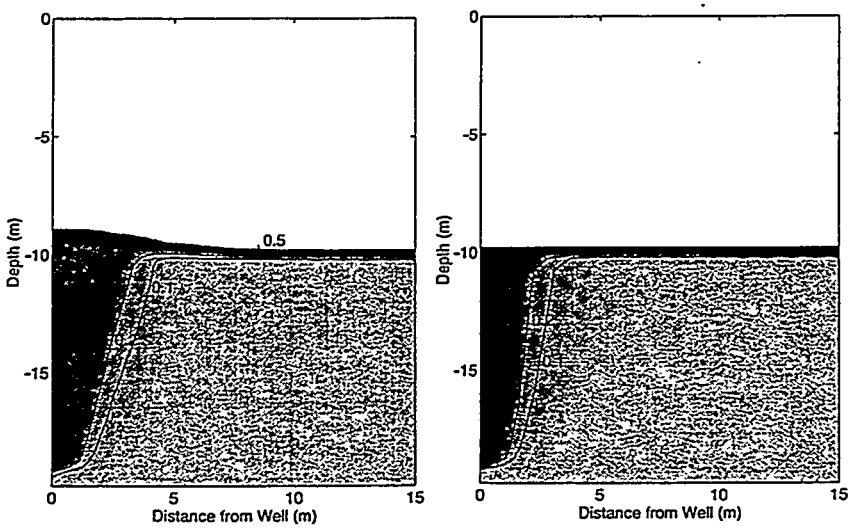

Figure 3. Gas saturation distribution at (a) 4 hours after the initiation of sparging, (b) steady-state in the homogeneous aquifer.

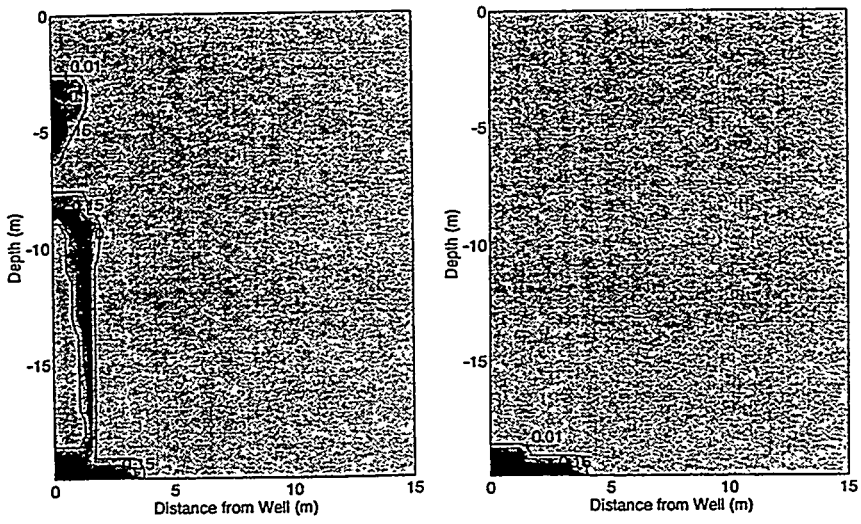

Figure 4. NAPL saturation distribution at (a) 30 days, (b) 1 year after the initation of sparging in the homogeneous aquifer.

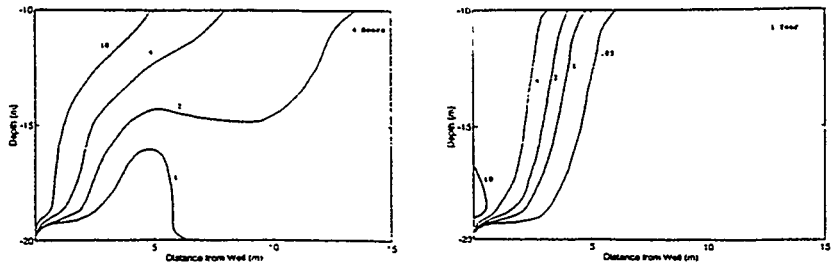

Figure 5. Positive pressure distribution (inches of water) at (a) 4 hours after the initiation of sparging, (b) at steady-state in the homogeneous aquifer.

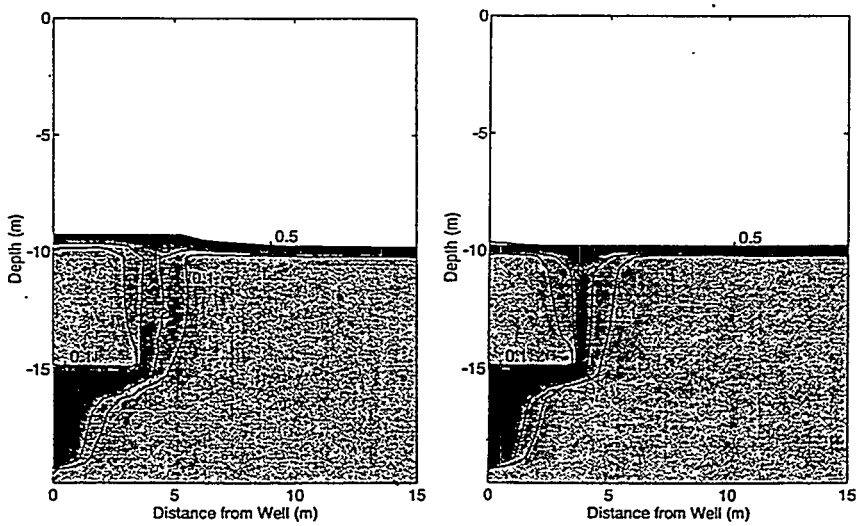

Figure 6. Gas saturation distribution at (a) 4 hours after the initiation of sparging, (b) steady-state in the hetergeneous aquifer.

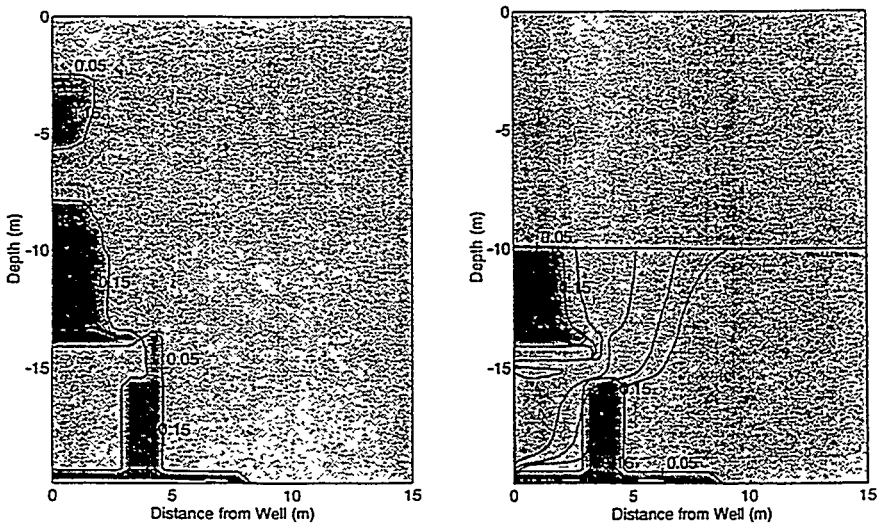

Figure 7. (a) NAPL saturation distribution at 30 days, and (b) at 1 year after the initiation of sparging in the hetergeneous aquifer.

References

Adenekan, A.E., Pruess, K. and Falta, R.W, 1990. Removal of Trichloroethylene contamination from the subsurface: A comparative evaluation of different remediation strategies by means of numerical simulation, Earth Sciences Division Report, Rpt. LBL-30273, Lawrence Berkeley Laboratory, Berkeley.

Angell, K.G., 1992. In situ remedial methods: Air sparging, The National Environmental J., January/February: 20-23.

Falta, R.W., 1990. Multiphase Transport of Organic Contaminants in the Subsurface, Ph.D. Dissertation, University of California at Berkeley, Berkeley.

Falta, R.W. , Pruess, K. Javandel, I., and Witherspoon, P.A., 1992a. Numerical modeling of steam injection for the removal of nonaqueous phase liquids from the subsurface, 1. Numerical formulation, Water Resour. Res., 28(2), 451-465.

Falta, R.W. , Pruess, K. Javandel, I., and Witherspoon, P.A., 1992b. Numerical modeling of steam injection for the removal of nonaqueous phase liquids from the subsurface, 2. Code validation, Water Resour. Res., 28(2): 466-476.

Felten, D.W., Leahy, M.C., Bealer, L.J., and Kline B.A., 1992. Case study: Site remediation using air sparging and soil vapor extraction, in Proceedings of the Petroleum Hydrocarbons and Organic Chemicals in Ground Water: Prevention, Detection, and Restoration Conference, 395-411, National Ground Water Association, Dublin, Ohio.

Ji, W., Dahmani, A., Ahlfeld, D.P., Lin, J.D., Hill, E.,1993. Laboratory study of air sparging: Air flow visualization, Ground Water Monitoring and Remediation, 13(4): 115-127.

Lenhard, R.J. and Parker, J.C., 1987. Measurement and prediction of saturation-pressure relationships in three-phase porous media systems, J. Contaminant Hydrol., 1: 407-424.

Leonard, W.C., and Brown, R.A., 1992. Air sparging: An optimal solution, in Proceedings of the Petroleum Hydrocarbons and Organic Chemicals in Ground Water: Prevention, Detection, and Restoration Conference, 349-363, National Ground Water Association, Dublin, Ohio.

Loden, M. E., 1992. A Technology Assessment of Soil Vapor Extraction and Air Sparging, U.S. EPA/600/R-92/173, U. S. EPA Office of Research and Development, Washington, D.C.

McCray, J.E., 1994. Numerical Analysis of Air Sparging for Subsurface Remediation, Master's. Thesis, Clemson University, Clemson, S.C.

Martinson, M. M., and Linck, J.A, 1993. Field pilot-testing for air sparging of hydrocarbon-contaminated ground water, Proceedings of the Sixteenth International Madison Waste Conference (in print), University of Wisconsin-Madison.

Mercer, J.W. and Cohen, R.M.,1990. A review of immiscible fluids in the subsurface: Properties, models, remediation, and characterization, J. Contaminant Hydrol., 6:107-163.

Nyer, E.K. and Sutherson, S.A. 1993. Air sparging: Savior of groundwater remediations or just blowing bubbles in the bath tub?, Ground Water Monitoring and Remediation 13(4): 87-91.

Parker, J.C., Lenhard, R.J., and Kuppusamy, T., 1987. A parametric model for constitutive properties governing multiphase flow in porous media, Water Resour. Res., 23(4): 618-624.

Pruess, K., 1991. TOUGH2-A general purpose numerical simulator for multiphase fluid and heat flow Rep. LBL-29400, Lawrence Berkeley Laboratory, Berkeley.

Seely, G.E., Falta, R.W., and Hunt, J.R., 1994. Buoyant advection of gases in unsaturated soil, ASCE J. Environmental Engineering, 120 (5).

Stone, H.L., 1970. Probability model for estimating three phase relative permeability, *J. Pet. Technol., 22*(1), 214-218.

van Genuchten, M.T., 1980. A closed form equation for predicting the hydraulic conductivity of unsaturated soils, Soil Sci. Soc. Am. J., 44: 892-898.

Wisconsin Department of Natural Resources, 1993. Guidance for the design, installation, and operation of in situ air sparging systems, Publication PBL-SW186-93.

Verification of T2VOC Using an Analytical Solution for VOC Transport in Vadose Zone

CHAO SHAN

Earth Science Division, Lawrence Berkeley Laboratory, University of California, Berkeley

T2VOC represents an adaption of the STMVOC [*Falta and Pruess*, 1991] to the TOUGH2 [*Pruess*, 1991] environment. In many contaminated sites, transport of volatile organic chemicals (VOC) is a serious problem which can be simulated by T2VOC. To demonstrate the accuracy and robustness of the code, we chose a practical problem of VOC transport as the test case, conducted T2VOC simulations, and compared the results of T2VOC with those of an analytical solution. The agreements between T2VOC and the analytical solutions are excellent. In addition, the numerical results of T2VOC are less sensitive to grid size and time step to a certain extent.

Problem of the Test Case

The problem of the test case is a one-dimensional vertical transport of VOC in a homogeneous vadose zone caused by an instant release of VOC in the soil. In this study, the ground-water table is assumed at a depth of $d_3=30m$, and at the depth interval of $d_1=9m$ to $d_2=10m$ there is trichloroethylene (TCE) contamination with an initial uniform total concentration of $C_0=100\mu g/cm^3$ (Figure 1). We have chosen a small value for the initial total concentration such that the non-aqueous phase liquid (NAPL) does not exist and such that the density-driven gas-phase advection is insignificant.

Some major transport mechanisms considered in the simulations are (a) the advection of dissolved TCE through the aqueous phase with a constant infiltration rate, (b) the diffusion of TCE vapor through the gas phase, and (c) the adsorption of dissolved TCE to the soil matrix. The soil properties used in the simulations are the saturated hydraulic conductivity of $K_s=0.001cm/s$, a porosity of $\phi=0.5$, the *van Genuchten* parameters $\alpha=0.05cm^{-1}$ and $n=2$, a residual volumetric moisture content of $\theta_r=0.05$, and the fraction organic carbon $f_{OC}=0.001$. The dry bulk density of the soil is $\rho_b=1.325g/cm^3$ which is calculated by using the porosity and a typical value of $2.65g/cm^3$ for the mass density. At the land surface, a constant infiltration with a Darcy velocity of $v_L=1cm/yr$ is assumed through the simulation time. Since an instant equilibrium between phases is assumed by both the analytical solution and the numerical code, we only need to examine the concentration profile in either phase, e.g., the aqueous phase in this study.

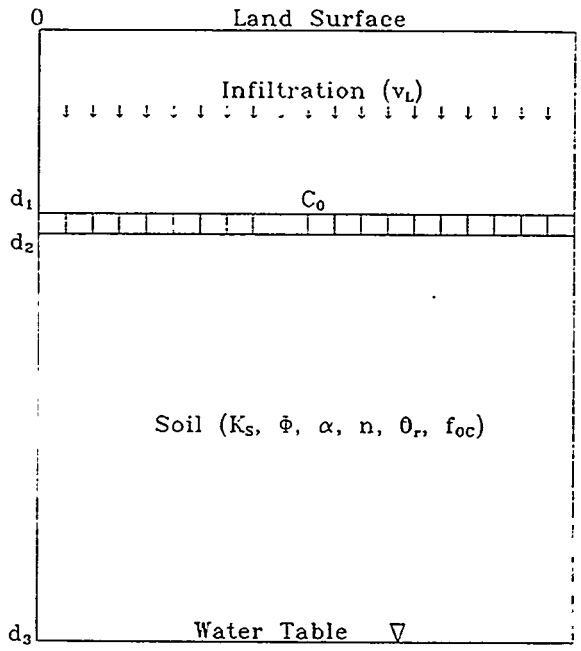

Fig. 1 Schematic view of the problem

The Steady-State Moisture Profile

Since we need to assume a steady-state moisture profile for the analytical solution [*Shan and Stephens*, 1994], it is necessary to generate such a moisture profile using either T2VOC or a simple analytical solution. The analytical solution for the one-dimensional vertical steady infiltration is simply the integration of the Darcy's equation

$$v_L = K\left(1 - \frac{d\psi}{dz}\right) \qquad (1)$$

where z is the vertical coordinates with the origin at the land surface, positive downwards; and K is the unsaturated hydraulic conductivity that is a function of the pressure head ψ via the *van Genuchten* [1980] model. Integrating the equation from the water table to an arbitrary depth, z, we obtain

$$z = d_3 + \int_0^{\psi} \left(1 - v_L/K\right)^{-1} d\psi \qquad (2)$$

which can be calculated by numerical integration. The calculated pressure head profile can be converted to a

moisture profile by further application of the *van Genuchten* model. The calculated steady-state moisture profile is represented by the solid line in Figure 2. We then used the same parameters and boundary conditions for two T2VOC flow simulations, one used a uniform grid size of $\Delta z=1m$ and the other used a uniform grid size of $\Delta z=0.1m$. The results are compared with the analytical solution in Figure 2. The agreements are excellent.

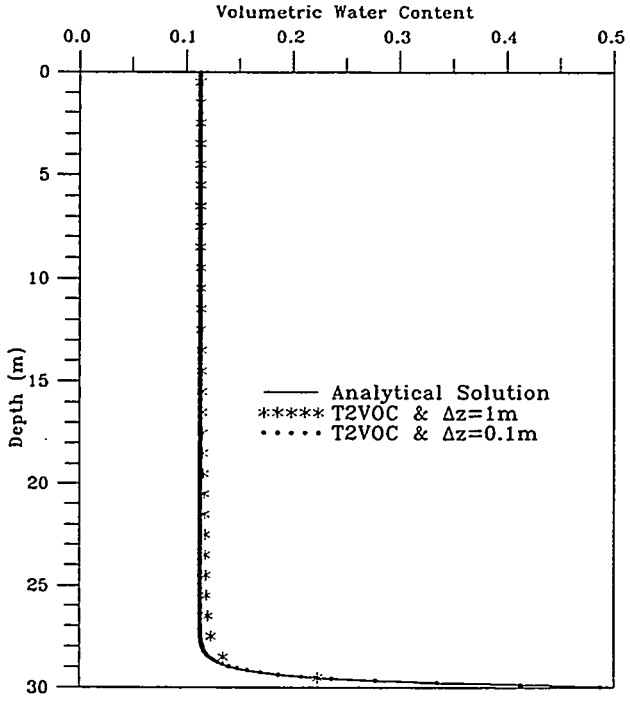

Fig. 2 Comparison of calculated steady-state moisture profiles

TCE Concentration in Water

The constant moisture content ($\theta=0.112$) on the upper part of the curve in Figure 2 is used for the concentration calculation using the analytical solution [*Shan and Stephens*, 1994]. In applying the analytical solution, we have neglected the gas phase advection and adsorption, the dispersion in both the aqueous and the gas phases, and the biodegradation. The TCE properties used for analytical solution are exactly the same as those used in T2VOC, e.g., the partition coefficient $K_{OC}=0.1m^3/kg$ (input data to T2VOC), the gas diffusion coefficient $D_g=7534cm^2/d$ (calculated using T2VOC model), and the dimensionless Henry's constant $K_H=0.2765$ (calculated from T2VOC). A constant temperature of 15°C was used for the T2VOC simulation.

The moisture profiles calculated by T2VOC using two different grid sizes were used as the initial conditions of flow for corresponding VOC transport simulations. For each grid size simulation, two runs

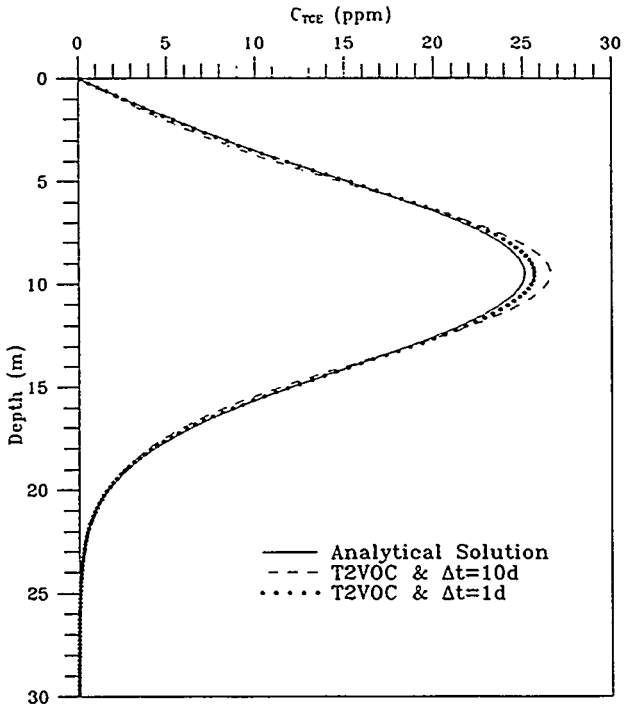

Fig. 3a Comparison of calculated TCE concentrations in the aqueous phase at $t=100d$ (constant $\Delta z=0.1m$)

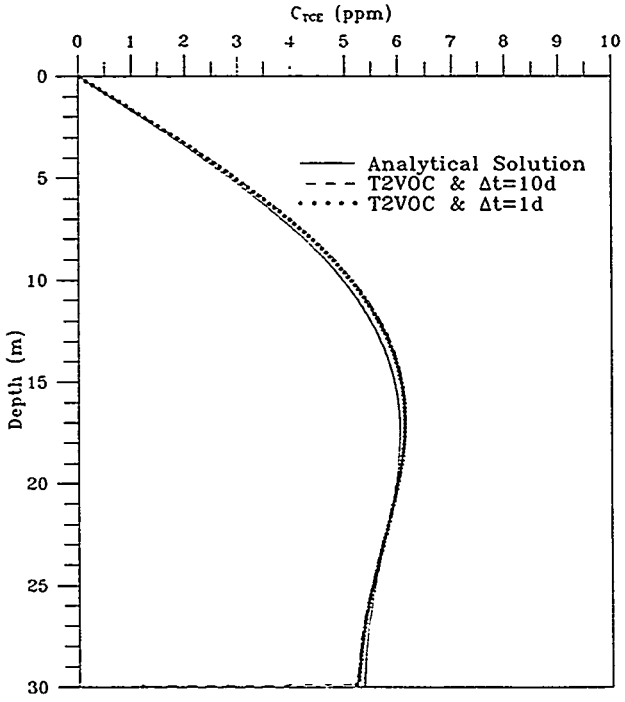

Fig. 3b Comparison of calculated TCE concentrations in the aqueous phase at $t=1000d$ (constant $\Delta z=0.1m$)

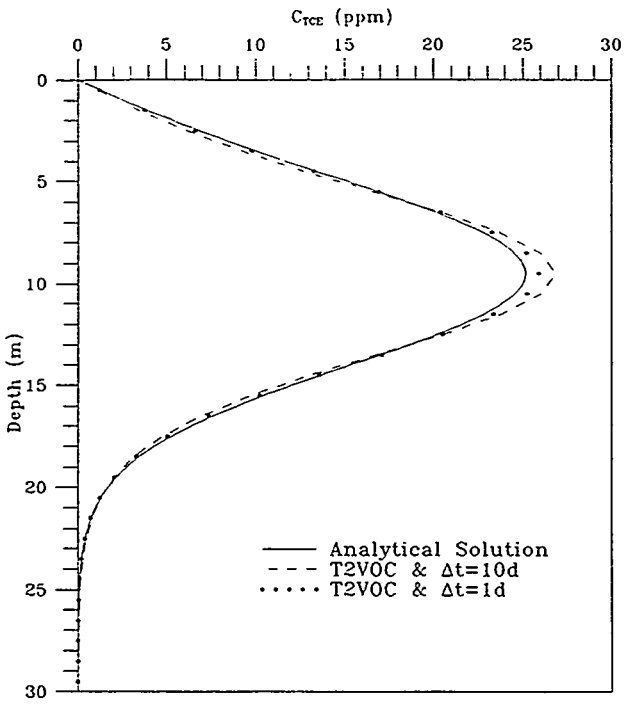

Fig. 4a Comparison of calculated TCE concentrations in the aqueous phase at t=100*d* (constant $\Delta z=1m$)

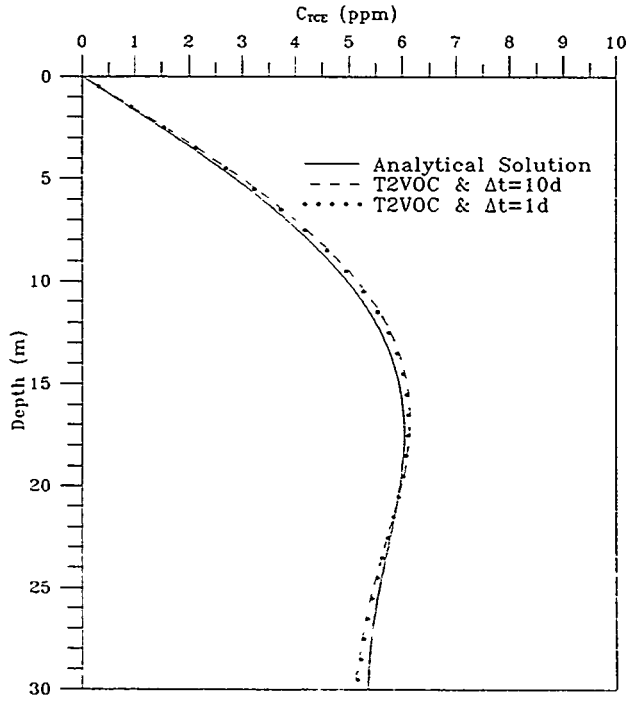

Fig. 4b Comparison of calculated TCE concentrations in the aqueous phase at t=1000*d* (constant $\Delta z=1m$)

were conducted using two different uniform time steps, i.e., $\Delta t=1d$ and $\Delta t=10d$. The TCE concentration in the aqueous phase at the end of 100*d* and 1000*d* for different cases are plotted in Figures 3a and 3b ($\Delta z=0.1m$), and Figures 4a and 4b ($\Delta z=1m$). These results are compared with the corresponding analytical solutions.

A thoughtful comparison among these figures gives us the following conclusions: (a) T2VOC results match the analytical solutions very well, (b) a reasonably large time step can give a result that is almost as good as that offered by a small time step, particularly as time increases, (c) a reasonably large grid size can give a result that is almost as good as that offered by a small grid size except for a possible loss of some detail information at places with big changes. Comparing Figures 4b with 3b, one could find that the discrepancy between the T2VOC solution and the analytical solution at the water table is missing from Figure 4b due to its large grid size. As previously mentioned, the large and non-uniform moisture content right above the water table (Figure 2) has been approximated to a small value in the analytical solution, which overestimates the gas-filled porosity and the gas diffusion above the water table. However, the large discrepancy appears only at times when the contamination front reaches the water table (e.g., at $t=1000d$ rather than $t=100d$). The interesting finding from Figure 3b is also an example demonstrating the strong capability of a numerical code such as T2VOC in modeling the real problem.

Acknowledgement

The author would like to thank S. Devine for editing the manuscript.

REFERENCES

Falta, R.W. and K. Pruess, 1991. STMVOC User's Guide, Lawrence Berkeley Laboratory Report LBL-30758, Berkeley, California.

Pruess, K., 1991. TOUGH2 - A General-Purpose Numerical Simulator for Multiphase Fluid and Heat Flow, Lawrence Berkeley Laboratory Report LBL-29400, Berkeley, California.

Shan, C. and D.B. Stephens, 1995. An analytical solution for vertical transport of volatile chemicals in the vadose zone, *J. Contam. Hydrol.*, accepted.

van Genuchten, M.T., 1980. A closed-form equation for predicting the hydraulic conductivity of unsaturated soils, *Soil Sci. Soc. Am. J. 44*, 892-898.

NUMERICAL SIMULATIONS OF MULTICOMPONENT EVAPORATION AND GAS-PHASE TRANSPORT USING M^{2}NOTS

Clifford K. Ho
Sandia National Laboratories
P.O. Box 5800, MS-1324
Albuquerque, NM 87185-1324
(505) 848-0712

Abstract

The multiphase, multicomponent, non-isothermal simulator M^{2}NOTS was tested against several one-dimensional experiments. The experiments represented a through-flow limiting condition of soil venting in which air flows through the contaminated region. Predictions using M^{2}NOTS of changing in situ compositions and effluent concentrations for toluene and o-xylene mixtures were compared to the observed results. Results showed that M^{2}NOTS was able to capture the salient trends and features of multicomponent through-flow venting processes.

Introduction

Soil vapor extraction is a technique that has been used widely in the remediation of subsurface sites contaminated with volatile organic compounds or NAPLs (non-aqueous phase liquids). In this process, liquid contaminants are volatilized and entrained into an advective air stream induced by a system of pumps and underground wells. The effectiveness of this method depends on how readily the contaminant vapors can be entrained into the advective flow.

Previous studies have provided experimental and theoretical evidence of significantly different contaminant removal rates for two limiting conditions of soil vapor extraction (Ho et al., 1994; Ho and Udell, 1993; Ho and Udell, 1992; Johnson et al., 1990). In the ideal through-flow case, air flows through the contaminated regions, causing higher volatility components to be removed preferentially. However, in diffusion-limited cases where the air stream bypasses the contaminated region, preferential recovery of the higher volatility components is not attained. As a preliminary assessment, the through-flow condition has been examined in this study.

The numerical code M^{2}NOTS (Multiphase Multicomponent Nonisothermal Organics Transport Simulator) developed by Adenekan (1992) was used to simulate laboratory experiments of multicomponent through-flow soil vapor extraction. Comparisons between the results of the numerical code and the experiments were made to verify the gas-NAPL formulation in M^{2}NOTS and to assess the performance of M^{2}NOTS in modeling multicomponent evaporation and gas-phase transport.

Experimental Approach

The one-dimensional experiments that were numerically simulated in this paper represented through-flow soil venting of liquid contaminant mixtures. Complete details of the experiments can be found in Ho and Udell (1993). Air at ambient conditions was blown from a compressor through activated carbon, a flowmeter, and then through a sand-filled glass tube (~2 cm diameter). The tube contained dry, machine sifted, 48-65 mesh Monterey sand (average particle diameter = 0.25 mm). The air then passed through a gas sampling bulb before being exhausted into a fume hood.

Prior to each experimental run, a mixture containing equal volumes of toluene and o-xylene was emplaced into the sand with a pipette at a rate of 1–2 ml/minute from the top end of the tube. The properties of toluene and o-xylene at 20 °C are given in Table 1 (Vargaftik, 1975). Approximately 3.6 ml of total liquid were emplaced in the sand. The tube was sealed and the liquid was allowed to drain under the forces of gravity and capillarity until visible movement ceased (~ 2 days). The airflow was then initiated through the apparatus.

The in situ liquid mole fractions were obtained by shutting the airflow off at a specified time. Then, the entire tube was sealed and placed into an ice bath to lower the vapor pressures of the liquid compounds remaining in the sand. Sections of the sand at various axial locations within the tube were then scooped out of the tube and placed into separate vials, which were analyzed by gas chromatography for liquid mole fractions. The liquid saturation of each sample was also determined by weighing the sample to determine the mass of liquid and sand present. Effluent gas concentrations were also recorded by using gas chromatography to analyze samples taken from the gas sampling bulb.

Table 1. Properties of toluene and o-xylene at 20 °C.

	Toluene	o-Xylene
molecular weight [kg/kgmol]	92.14	106.17
density [kg/m^3]	865	876
saturated vapor pressure [Pa]	2910	660
saturated vapor concentration [kg/m^3]	0.11	0.0288
binary diffusion coefficient of vapor in air [m^2/sec] (Fuller, Shettler, & Giddings, 1965)	7.9 x 10^{-6}	7.3 x 10^{-6}

Numerical Approach

The numerical code M^{2}NOTS was used to simulate the venting experiments described in the previous section under isothermal conditions. M^{2}NOTS is an extension of TOUGH2, which was developed by Pruess (1991) as a multiphase, multidimensional, nonisothermal code that simulates the transport of air, water, and heat in porous media. The unique feature of M^{2}NOTS is the additional capability to model the transport of any number of contaminant components in porous media. M^{2}NOTS contains balance laws for each component (air, water, heat, and N-contaminant components) in three phases: gas, aqueous, and NAPL. Each component can partition into all of the fluid phases that are present. In addition, each fluid phase can completely disappear or evolve in any part of the modeled domain. Complete mathematical details on the formulation of M^{2}NOTS can be found in Adenekan et al. (1993).

Major assumptions inherent in M^{2}NOTS include the assumption of local chemical and thermal equilibrium, the use of Darcy's law for all phase velocities, and the ideality of the NAPL and gas mixtures. Although these assumptions may be justified in many problems, the purpose of this study was to test the formulation and assumptions in M^{2}NOTS for a gas-NAPL system in which well-controlled experimental data could be obtained. One caveat of the gas-NAPL formulation that was identified even before the numerical simulations could be performed was the need for a fixed Henry's constant that relates the partial pressure of water vapor to the mole fraction of water in the NAPL phase. The original constant used in the code (4x10^7 Pa) yielded vapor mole fractions that were greater than one, which prevented the code from running properly. A smaller value of 1x10^5 Pa, which was used in this study, produced reasonable vapor mole fractions and solutions in the gas-NAPL system.

The M^{2}NOTS numerical model that was used to simulate the through-flow experiment is shown in Figure 1. In Figure 1, the numbered elements represent the sand where the liquid contaminants were emplaced. The "IN" and "OUT" elements are boundary elements that do not participate in the balance laws. The pressure of these elements was fixed to yield an inlet air flow rate of 1x10^{-5} m^3/sec that was observed for all the experiments. Element 18 was used to obtain effluent gas concentrations. The chemical parameters that were used in M^{2}NOTS were obtained from Reid et al. (1987). The initial and ambient (outlet) pressures were assumed to be 1.01x10^5 Pa for all cases.

The parameters that were used to calculate the gas-NAPL capillary pressures and relative permeabilities were based on values used in Adenekan (1992) for a generic sand (see Table 2). Although the Stone II model (1973) is used to calculate three-phase relative permeability to oil in M^{2}NOTS, the exponential equations of Corey (1954) are used to calculate two-phase relative permeabilities that were used in this study as follows:

$$k_{rog} = k_{rocw}\left[\frac{1-S_{org}-S_g}{1-S_{wir}-S_{org}}\right]^{n_{og}} \quad (1)$$

$$k_{rg} = k_{rgro}\left[\frac{S_g-S_{gr}}{1-S_{wir}-S_{org}-S_{gr}}\right]^{n_g} \quad (2)$$

where k_{rog} is the relative permeability of oil, k_{rg} is the

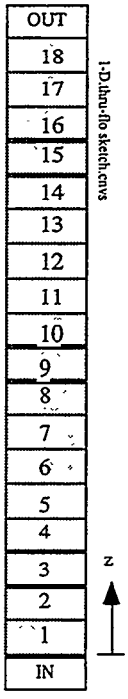

Element	z (cm)	Δ z (cm)	Volume (m^3)
1	0.5	1.0	3.4e-6
2	1.5	1.0	3.4e-6
3	2.5	1.0	3.4e-6
4	3.5	1.0	3.4e-6
5	4.5	1.0	3.4e-6
6	5.5	1.0	3.4e-6
7	6.5	1.0	3.4e-6
8	7.5	1.0	3.4e-6
9	8.5	1.0	3.4e-6
10	9.5	1.0	3.4e-6
11	10.5	1.0	3.4e-6
12	11.5	1.0	3.4e-6
13	12.5	1.0	3.4e-6
14	13.5	1.0	3.4e-6
15	14.5	1.0	3.4e-6
16	15.5	1.0	3.4e-6
17	16.5	1.0	3.4e-6
18	17.5	1.0	3.4e-6
In	—	—	0.0
Out	—	—	0.0

area of sand elements = 3.4e-4 m^2

Figure 1. Numerical model used in MNOTS.

relative permeability of gas, S_g is the gas saturation, and the other parameters are given in Table 2. The expressions of Parker et al. (1987) are used to calculate capillary pressures. For the gas-NAPL system studied here, the following equation was used to relate gas- and NAPL-phase pressures:

$$P_{cgo} = \frac{\rho_w g}{\alpha_{go}} \left\{ \left(\frac{S_w + S_o - S_m}{1 - S_m} \right)^{-1/m} - 1 \right\}^{1/n} \quad (3)$$

where P_{cgo} is the gas-NAPL capillary pressure (gas pressure minus the oil pressure), $\rho_w g$ is the specific gravity of water, S_w is the water saturation, S_o, is the oil saturation, and the other parameters are given in Table 2. Although the selection of the parameter values used in Equations (1)–(3) were fairly arbitrary, the mobility of the NAPL phase was expected to be small compared to the gas-phase transport. However, future assessment of these parameters may need to be considered.

Table 2. Sand parameters used in M^{2}NOTS.

Permeability (measured) [m^2]	8.4×10^{-11}
Porosity (measured)	see Table 2
Residual NAPL saturation, S_{org}	0.08
Irreducible water saturation, S_{wir}	0.1
k_{rocw}	1.0
k_{rgro}	1.0
n_{og}	1.8
n_g	1.2
S_m	0.1
α_{go} [1/m]	40
n	2

Results and Discussion

Figure 2 shows the experimentally determined liquid mole fraction distributions for toluene and o-xylene along with the liquid saturations after 15, 29, and 45 minutes (Runs 1, 2, and 3) of through-flow venting. The numerical predictions using M^{2}NOTS are also shown in Figure 2. The mole fractions and saturations are plotted as a function of position along the tube (note the orientation of the z-coordinate in Figure 1. An initial discussion of the experimental results will be followed by a comparison with the numerical predictions.

The initial liquid mole fractions of the emplaced mixture of toluene and o-xylene were 0.53 and 0.47, respectively. However, since toluene was more volatile, greater quantities of toluene were evaporated and entrained in the advective gas flow near the entrance (z=0 cm) where clean air initially swept through the contaminated region. This process continued until the experiment was stopped at 15 minutes (Run 1), at which time most of the toluene between z=0 cm and z=5 cm had already been removed. Between z=9 cm and z=18 cm, the remaining contaminant in situ contained toluene and o-xylene at the initial composition.

In Run 2 the liquid mole fractions were determined after 29 minutes of through-flow venting. At this time, Figure 2 shows that a nearly complete recovery of toluene existed upstream of z=12 cm. However, o-xylene still existed in-between z=5 cm and z=12 cm. This distribution indicates that the volatilization of the toluene and o-xylene behaved similarly to the propagation of separate evaporation fronts at different velocities (see Ho et al. (1994) for a detailed analysis of the propagation of evaporation fronts). At 29 minutes the o-xylene evaporation front was near z=5 cm while the toluene evaporation front was near 12 cm. Upstream of the o-xylene evaporation front nearly all of the contaminant had been recovered.

Run 3 was used to determine the liquid mole fraction distribution throughout the contaminated region at 45 minutes. At this time, the toluene mole fraction is shown in Figure 2 to be nearly zero everywhere, indicating that the evaporation front had propagated completely through the sand. However, significant amounts of o-xylene still remained downstream of the location of the o-xylene evaporation front at z=7 cm.

The results of M^{2}NOTS shown in Figure 2 are seen to behave very similarly to the experimental results. Although the liquid mole fraction distributions and liquid saturations appear to lag the experimental results, M^{2}NOTS seems to replicate the preferential evaporation of the toluene. The larger spread in the liquid mole fractions may be a result of the relatively coarse mesh used in the simulations. Nevertheless, the predictions shown in Figure 2 still give the appearance of evaporation fronts of toluene and o-xylene propagating downstream with time.

Figure 3 shows the results of Run 4 in which the effluent gas concentration of toluene and o-xylene were obtained from the through-flow venting experiment. These results are consistent with the results of the in situ mole fractions shown in Figure 2. Just after 30 minutes of venting, the toluene gas concentration drops to zero since the toluene was completely removed from the system (the toluene evaporation front had propagated through the entire system). As a result, the o-xylene liquid mole fraction jumped to one and the o-xylene effluent gas concentrations increased as shown in Figure 3. Finally, at 100 minutes, all of the o-xylene was removed from the system and the gas concentrations went to zero. The predictions of M^{2}NOTS are seen to correspond very closely to the experimentally observed results in Figure 3. This implies that for the flow rates used in the experimental study, the assumption of local chemical equilibrium was sufficient to describe the system.

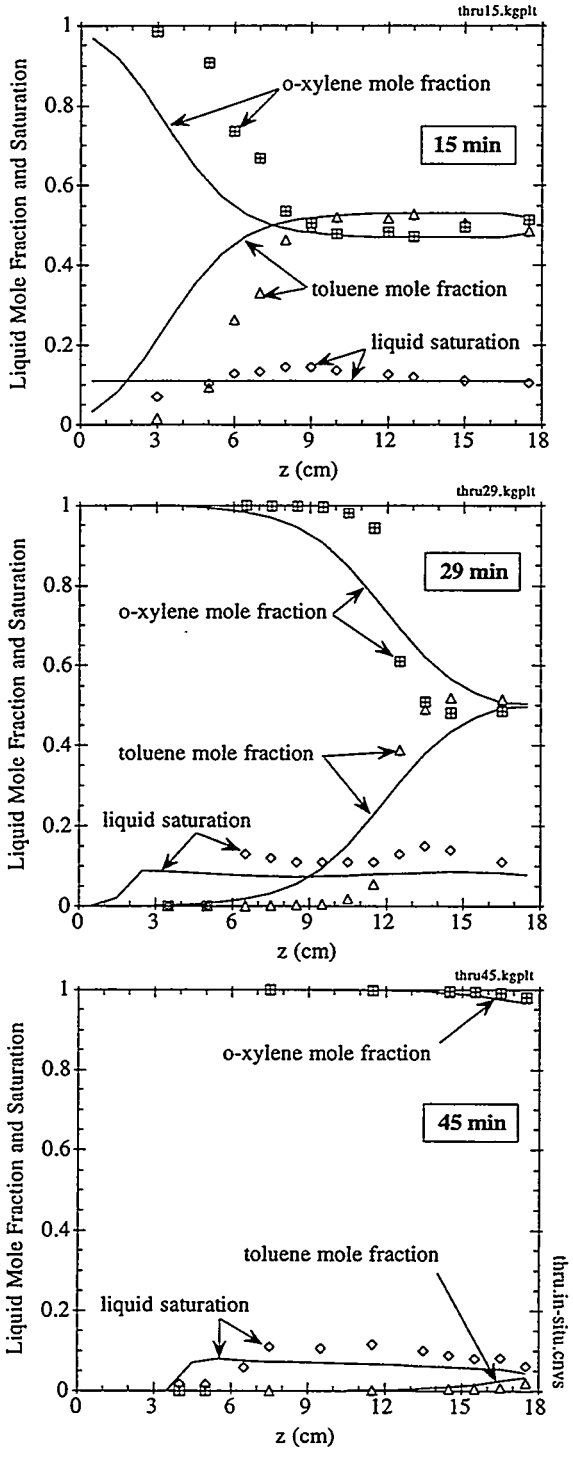

Figure 2. Liquid saturations and mole fractions of toluene and o-xylene after 15, 29, and 45 minutes of through-flow venting (Runs 1, 2, and 3). The solid lines are numerical predictions from M^{2}NOTS and the symbols are experimental results.

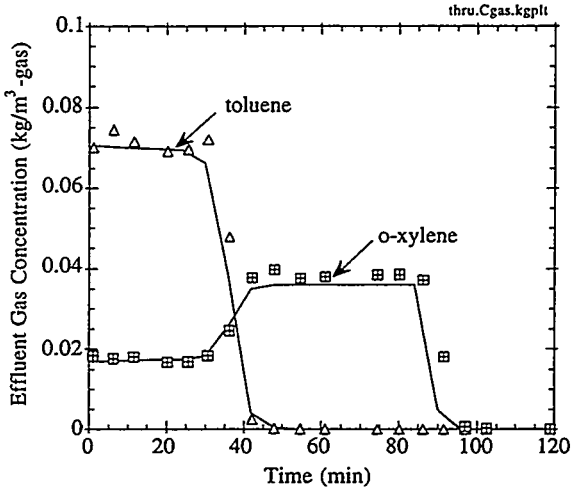

Figure 3. Effluent gas concentrations for toluene and o-xylene during through-flow venting (Run 4). The solid lines are numerical predictions from M^{2}NOTS and the symbols are experimental results.

Conclusions

The results of one-dimensional experiments simulating through-flow venting conditions were compared with numerical simulations using M^{2}NOTS. Based on these comparisons, several conclusions can be drawn:

- M^{2}NOTS was capable of simulating the selective evaporation of toluene during through-flow venting. Propagating evaporation fronts, corresponding to the location of volatilization of each compound, were observed in the simulations and in the experiments.
- Only the gas-NAPL formulation of M^{2}NOTS was tested in this study. Other phase combinations may need to be systematically tested against experiments or field studies to ensure robustness.
- Parameters controlling the mobility of the liquid phase (relative permeability and capillary pressure parameters) were uncertain and may need to be more rigorously assessed in problems where the liquid phase is mobile.
- Specified Henry's Constants in M^{2}NOTS may need to be altered to yield physically realistic results for specific multiphase problems.

Acknowledgments

This study was performed with financial support from the SNL LDRD project titled "Physical Simulation of Nonisothermal Multiphase Flow in Porous Media". Discussions with Mario Martinez, Ade Adenekan, and Steve Webb were greatly appreciated during the course of this study.

References

Adenekan, A.E. (1992). Numerical Modeling of Multiphase Transport of Multicomponent Organic Contaminants and Heat in the Subsurface, Ph.D. dissertation, Univ. of Calif., Berkeley.

Adenekan, A.E., T.W. Patzek, and K. Pruess (1993). Modeling of Multiphase Transport of Multicomponent Organic Contaminants and Heat in the Subsurface: Numerical Model Formulation, *Water Resources Research*, Vol. 29, No. 11, pp. 3727-3740.

Corey, A.T. (1954). The Interrelation Between Gas and Oil Relative Permeabilities, *Producers Month.*, **19**(1), 38-41.

Fuller, E. N., P. D. Schettler, and J. C. Giddings (1965). A Comparison of Methods for Predicting Gaseous Diffusion Coefficients, *J. Gas Chromatography,* 222-227.

Ho, C. K., S-W Liu, and K. S. Udell (1994). Propagation of Evaporation and Condensation Fronts During Multicomponent Soil Vapor Extraction, *J. Contam. Hydrol.,* **16**(4), 381-401.

Ho, C. K. and K. S. Udell (1992). An Experimental Investigation of Air Venting of Volatile Liquid Hydrocarbon Mixtures from Homogeneous and Heterogeneous Porous Media, *J. Contam. Hydrol.,* **11**(3), 291-316.

Ho, C. K. and K. S. Udell (1993). Mechanisms of Multicomponent Evaporation During Soil Venting, *ASME Multiphase Transport in Porous Media,* FED-Vol. 173/HTD-Vol. 265, pp. 83-92.

Johnson, P. C., C. C. Stanley, M. W. Kemblowski, D. L. Byers and J. D. Colthart (1990). A practical approach to the design, operation, and monitoring of in situ soil-venting systems, *Ground Water Monitoring Review,* **10**(2), 159-178.

Parker, J.C., R.J. Lenhard, and T. Kuppusamy (1987). A Parametric Model for Constitutive Properties Governing Multiphase Fluid Flow in Porous media, *Water Resour. Res.*, **23**(4), 618-624.

Pruess, K. (1991). TOUGH2–A General-Purpose Numerical Simulator for Multiphase Fluid and Heat Flow, LBL-29400, Lawrence Berkeley Laboratories.

Reid, R.C, J.M Prausnitz, and B.E. Poling (1987). The Properties of Gases & Liquids, Fourth Ed., McGraw-Hill Inc., New York.

Stone, H.L. (1973). Estimation of Three-Phase Relative Permeability and Residual Oil Data, *J. Can. Pet. Technol.*, 12, 53-61.

Vargaftik, N. B. (1975). *Tables on the Thermophysical Properties of Liquids and Gases*, 2nd ed., Hemisphere Publishing Corp.

The Effect of Vadose Zone Heterogeneities on Vapor Phase Migration and Aquifer Contamination by Volatile Organics

by Asitha Seneviratne and Angelos N. Findikakis
Bechtel Corporation, San Francisco

Organic vapors migrating through the vadose zone and inter-phase transfer can contribute to the contamination of larger portions of aquifers than estimated by accounting only for dissolved phase transport through the saturated zone. Proper understanding of vapor phase migration pathways is important for the characterization of the extent of both vadose zone and the saturated zone contamination.

The multiphase simulation code T2VOC is used to numerically investigate the effect of heterogeneties on the vapor phase migration of chlorobenzene at a hypothetical site where a vapor extraction system is used to remove contaminants. Different stratigraphies consisting of alternate layers of high and low permeability materials with soil properties representative of gravel, sandy silt and clays are evaluated. The effect of the extent and continuity of low permeability zones on vapor migration is evaluated. Numerical simulations are carried out for different soil properties and different boundary conditions.

T2VOC simulations with zones of higher permeability were made to assess the role of how such zones in providing enhanced migration pathways for organic vapors. Similarly, the effect of the degree of saturation of the porous medium on vapor migration was for a range of saturation values. Increased saturation reduces the pore volume of the medium available for vapor diffusion. Stratigraphic units with higher aqueous saturation can retard the vapor phase migration significantly.

Flow Reduction due to Degassing and Redissolution Phenomena

Christine Doughty
Earth Sciences Division
Lawrence Berkeley Laboratory

Introduction

At the Stripa mine in Sweden, flow and transport experiments in a water-saturated fractured granite were conducted to investigate techniques for site characterization for a geologic nuclear waste repository. In the Simulated Drift Experiment, measured water inflow to an excavated drift with pressure held at 1 bar was only 1/9th the value expected based on inflow to boreholes with pressure held at 2.7 bars [*Olsson*, 1992]. Several physical and chemical mechanisms were hypothesized to be responsible for this reduction in flow [*Long et al.*, 1992]. One possibility is that significant degassing of dissolved nitrogen takes place between 2.7 and 1 bars, creating a two-phase regime with an accompanying decrease in fluid mobility, resulting in a decrease in flow to the drift. To investigate this process, theoretical studies on degassing and redissolution phenomena have been carried out, beginning with an idealized model which yields a simple analytical solution, then relaxing some of the simplifying assumptions and using TOUGH2 to study the phenomena numerically. In conjunction with these theoretical studies, laboratory experiments on flow and degassing in transparent fracture replicas are being carried out [*Geller et al.*, 1995], and are being used to check the modeling approach. We need to develop a fundamental understanding of degassing and redissolution in particular and two-phase flow phenomena in general for flow in fractures and fracture networks, in order to successfully model conditions around a nuclear waste repository, where long time and large space scales may preclude conclusive field experiments.

Analytical Solution

For one-dimensional steady-state flow through a homogeneous medium, there is a simple analytical expression that gives an upper bound to the flow reduction that can be caused by degassing. Here one-dimensional means that there is only one spatial dimension in the problem, but the flow geometry can be linear ($n = 1$), radial ($n = 2$), spherical ($n = 3$), or the non-integral geometries characteristic of some fracture networks. The effect of gravity is neglected. Darcy's law governs fluid flow, and while the exact form of the characteristic curves need not be specified, there must be strong interference between phases. In general, strong interference is expected for flow through low-dimensional flow regimes (e.g., flow through highly channelized fractures would exhibit more interference than flow through an isotropic porous medium). Thermodynamic equilibrium between gas dissolved in the liquid phase and gas existing as a separate gas phase is assumed, and is governed by Henry's law. When pressure falls below the bubble pressure P_b, dissolved gas comes out of solution and forms a separate gas phase, whereas above P_b, gas remains in solution and single-phase liquid conditions prevail. According to Henry's law, P_b is directly proportional to gas content, defined as the mole fraction of gas dissolved in the liquid phase. Gas content can also be expressed as a mass fraction or as a volume percent at STP.

The pressure is assumed to be held fixed at both ends of a medium of length L, at one end below the bubble pressure (P_0), and at the other end above it (P_1). The upper frame of Figure 1 shows the pressure variation under degassing conditions schematically. For strongly interfering relative permeability curves, a steep pressure gradient is required to drive flow through the two-phase region, whose width l is rather small. The flow reduction due to degassing can be quantified by a normalized flow $\tilde{q}$, defined as the flow through the medium with gas present (q), divided by the flow through the medium under the same boundary conditions if no gas were present (q_0). According to Darcy's law, the normalized flow is simply the ratio of the slopes of the liquid-phase portion of the pressure curves:

$$\tilde{q} = \frac{q}{q_0} = \frac{(P_1 - P_b)/(L - l)}{(P_1 - P_0)/L} . \qquad (1)$$

In the limit $l \ll L$ this becomes

$$\tilde{q} \approx \frac{P_1 - P_b}{P_1 - P_0} . \qquad (2)$$

Figure 1 and Equation (2) illustrate how the interplay of gas content (as represented by P_b), and boundary conditions (P_1 and P_0) controls the flow reduction. In the context of the Stripa field experiment, P_1 is the far-field pressure, and P_0 is the pressure at the drift. The lower frame of Figure 1 shows the normalized flow as predicted by Equation (1) and the results for the Stripa Simulated Drift Experiment (SDE), and indicates that not nearly enough flow reduction is predicted by the analytical solution ($\tilde{q}_{an} = 0.92$ as opposed to $\tilde{q}_{obs} = 0.11$). The analytical solution was verified against numerical results using the TOUGH2 simulator [*Pruess*, 1987, 1991], and the effect of the choice of characteristic curves was studied numerically. Using relative permeability functions with weaker phase interference produced less flow reduction, as did the addition of capillary pressure. While expected on physical grounds, these findings did not improve the prediction of the Stripa SDE results or subsequent comparisons with laboratory results [*Geller et al.*, 1995], which were consistent with the Stripa SDE results. Therefore, a further examination of the assumptions used for the analytical solution was warranted, which required investigating the degassing and redissolution problem numerically.

Numerical Homogeneous Media Studies

By using TOUGH2 to examine the degassing problem numerically, both transient and steady-state conditions can be studied. In addition, the effect of the far-

field constant pressure boundary condition can be examined, by considering both finite and infinite systems. Under these conditions, the flow geometry has a tremendous effect not only on flow reduction, but on whether a steady-state develops at all. In a fractured rock mass the flow geometry is very complicated, as it depends on both the nature of the flow channels within a single fracture plane, and the connectivity of the network of fracture planes. However, simple models using either linear, cylindrical, or spherical flow geometries provide insight into limiting cases of possible flow geometries in a real rock mass. Figures 2, 3, and 4 show $\tilde{q}$ versus time for linear, radial, and spherical flow geometries, for finite and infinite systems. In all cases, the q_0 value used to normalize q is the steady-state value for a finite system. Time is normalized by t_{diff}, the time required for a pressure pulse to diffuse across the finite medium under liquid-phase conditions.

The $\tilde{q}$ value given by the analytical solution, shown as a symbol at the final time, agrees reasonably well with the numerically calculated values. The difference between finite and infinite systems decreases strikingly as flow dimension increases, because pressure changes become more localized around the borehole. For linear geometry, no steady state develops for an infinite system, whereas for radial geometry a quasi-steady state develops, and for spherical geometry there is no difference between finite and infinite systems. For linear geometry and an infinite medium (Figure 2), flow rates decline monotonically to zero. Because compressibility increases with gas content, the decline occurs at later times for greater gas contents. Thus at any given time, degassing causes a flow increase rather than reduction. For radial geometry (Figure 3) the difference between finite and infinite media is still apparent, but in both cases greater gas content causes greater flow reduction. The time required to reach steady state decreases as flow dimension increases, but increases strongly with gas content.

One of the powerful features of the integral finite difference method for spatial discretization which is employed in TOUGH2 is the ability to create efficient computational meshes for arbitrary flow geometries very easily. A mesh generator has been developed that creates a one-dimensional mesh with arbitrary flow dimension ranging from $n = 1$ (linear) to $n = 3$ (spherical). This mesh was used not only for the calculations illustrated above for $n = 1$, $n = 2$, and $n = 3$, but also to create meshes with non-integral flow dimensions of $n = 1.4$ and $n = 2.4$, which may be used to represent incompletely connected fracture networks. Figure 5 shows $\tilde{q}$ versus time for $n = 1.4$. As expected, the variation in $\tilde{q}$ is intermediate between that for $n = 1$ and $n = 2$, whereas the variation for $n = 2.4$ (not shown) is intermediate between $n = 2$ and $n = 3$.

In conclusion, relaxing the assumptions of the analytical solution did not improve the model's prediction of the Stripa SDE results or those of laboratory experiments. However, the numerical solution verified the essential features of the analytical solution. Firstly, if a steady-state value of $\tilde{q}$ exists (finite media for linear or radial flow geometries, finite or infinite media for spherical flow geometry), it is independent of flow dimension. Secondly, flow reduction increases as gas content increases. The steady-state flow reduction predicted by the numerical simulations generally agrees with the analytical solution, but as the amount of gas present increases, the analytical solution approximation gets worse.

Numerical Heterogeneous Media Studies

All the numerical simulations described above considered a homogeneous medium characterized by a single value of permeability. However, laboratory experiments being conducted with fracture replicas indicate that heterogeneity within the flow domain has an important effect on the magnitude of flow reduction [*Geller et al.*, 1995]. Therefore, a two-dimensional numerical model of a fracture replica was created in order to examine the effect of a heterogeneous medium on flow reduction. The fracture replica is about 74 mm on a side and the aperture distribution is given as a 369 by 369 array of aperture values, each representing a 0.02 mm by 0.02 mm square. Aperture values range from 0 (an asperity) to 240 microns. Using these values directly would result in a model with over 130,000 elements, which would be impractical for numerical simulation. After some study, it was decided to arithmetically average over 9 by 9 blocks of adjacent aperture values to obtain a 41 by 41 array of aperture values, each representing a 0.18 mm by 0.18 mm square. This results in a model with 1681 elements representing the fracture replica (Figure 6) and an additional 82 elements representing the constant-pressure boundaries. Doing harmonic or geometric averaging rather than arithmetic averaging did not make much difference in the averaged aperture distribution, and using a more finely discretized 123 by 123 array of apertures (averaging over 3 by 3 blocks) did not greatly alter the nature of the heterogeneity. The averaged aperture values were divided into eight ranges, and the element aperture value was assigned as the midpoint of the range minus 25 microns, a somewhat arbitrary value chosen to enhance the effects of asperities.

The cubic law was then used to determine the permeability of the element. Modified van Genuchten characteristic curves which exhibited strong phase interference ($\lambda = 0.4$) were employed, using the same relative permeability functions for each element and a capillary pressure strength inversely proportional to aperture.

A numerical simulation of flow from right to left through the model was done to compare with a laboratory experiment using the same flow geometry. Initial conditions consisted of a single-phase liquid at a uniform pressure of 5 bars, with a dissolved gas mass fraction of 7×10^{-5} (5% gas by volume at STP), which corresponds to a bubble pressure of 3.1 bars. The pressure was held fixed at 5 bars at the right side of the flow domain and 1 bar at the left side; the top and bottom boundaries were closed.

Figure 7 shows the variation of normalized flow $\tilde{q}$ with time for both the model with asperities and an earlier version of the model without asperities and less resolution of small apertures. Both simulations required over 800 time steps to reach steady state. The oscillation in

flow rate that is seen before steady-state conditions are reached suggests that there are multiple physical processes occurring on different time scales, which generally makes numerical simulation difficult. In particular, the use of strongly interfering relative permeability curves forces TOUGH2 to take small time steps in order for the Newton-Raphson iterations to converge. This occurs because a small increase in gas saturation due to degassing can cause a large decrease in fluid mobility, which results in a large decrease in flow rate, and hence a significant build-up of pressure up-gradient of the degassing location. When pressure increases above the bubble pressure, gas is redissolved, liquid relative permeability increases, fluid flow rate increases, and pressure decreases, setting the stage for degassing to resume, repeating the cycle. Thus, it is the intrinsic physics of the problem, which involves a subtle balance of forces, that makes the problem difficult to numerically simulate. Only the direct solver MA28, which is generally slower but more robust than the conjugate gradient solvers, could be used to reach steady state. Use of MA28 also limits the resolution of the fracture aperture distribution that may be achieved, as the maximum number of elements and connections is much smaller than for the conjugate gradient methods.

Figure 7 shows that the decrease in apertures which resulted from the addition of asperities decreases flow whether or not gas is present, as expected based on the cubic law. However, the steady-state normalized flow $\tilde{q}$ does not change. The final normalized flow value is slightly larger than the analytical solution, and not nearly as small as laboratory values using this fracture replica, indicating that simply adding heterogeneity to the model is insufficient to produce a significantly greater flow reduction.

The modeled steady-state pressure and gas-saturation distributions are shown in Figure 8. As expected, variations in the aperture distribution are manifested in the pressure distribution, such as the greater variability in aperture in the left half of the model resulting in greater irregularities in the pressure contours. Furthermore, there is a close correspondence between pressure and saturation distributions, with two-phase conditions occurring only below the bubble pressure. The gas saturation distribution shown in Figure 8 compares favorably with the experimental gas distribution, which is shown in Figure 9, indicating that some features of the actual fracture replica are being represented correctly in the numerical model, despite the incorrect prediction of $\tilde{q}$. The earlier version of the model, which did not resolve the small-aperture distribution, did not reproduce the observed saturation distribution nearly as well.

Several other variations on the numerical model of flow through the fracture replica were made, but none predicted a greater flow reduction than given by the analytical solution. These variations included using a different gas content, a uniform aperture distribution, a non-zero irreducible gas saturation, modeling flow in the opposite direction through the fracture replica, and varying the choice of characteristic curves.

Conclusions and Plans for Future Work

Our theoretical study began with a simple analytical solution for the flow reduction due to degassing under steady-state conditions in a finite one-dimensional homogeneous medium. When this solution did not predict laboratory or field conditions adequately, some the assumptions required for the analytical solution were relaxed and the problem was numerically simulated using TOUGH2. In particular, the model was extended from steady-state to transient conditions, finite to infinite media, from linear to radial, spherical, and non-integral flow geometries, and from a homogeneous medium to a heterogeneous medium. None of the extensions to the conceptual model has significantly increased the flow reduction due to degassing from that predicted by the analytical solution. Hence all the modeling studies significantly underpredict the effect of degassing on fluid flow measured in the laboratory and at the Stripa SDE. The next assumption to be investigated is that of equilibrium between degassing and redissolution. Adding non-equilibrium effects to TOUGH2 will be a significant effort, and three possible approaches are being considered. In order of increasing complexity (and rigor) they are: to consider degassing only, with no redissolution possible; to use a hysteretic form of Henry's law which makes degassing occur more readily than dissolution; and to use kinetic rate equations for both degassing and dissolution.

Acknowledgements

Thanks are due to Jil Geller, who conducted the laboratory experiments, for providing Figure 9 and also many useful discussions. The careful reviews of S. Finsterle and J.C.S. Long are also appreciated. The work was carried out under U.S. Department of Energy Contract No. DE-AC03-76SF00098, for the Director, Office of Civilian Radioactive Waste Management, Office of External Relations, administered by the Nevada Operations Office in cooperation with the Swedish Nuclear Fuel and Waste Management Company (SKB).

References

Geller, J.T., C. Doughty, R.J. Glass, and J.C.S. Long, Disturbed zone effects: two-phase flow, report to the international program under the cooperative agreement between SKB and U.S. DOE Radioactive Waste Management, *Rep. LBL-36848*, Lawrence Berkeley Laboratory, Berkeley, Calif, 1995.

Long, J.C.S., O. Olsson, S. Martel, J. Black, Effects of excavation on water inflow to a drift, in Proceedings of the U.S. Rock Mechanics Meeting, Lake Tahoe, Calif, 1992.

Olsson, O., ed, Site characterization and validation - final report, Stripa Project Technical Report 92-22, Swedish Nuclear Fuel and Waste Management Co., Stockholm Sweden, 364 pp., 1992.

Pruess, K., TOUGH user's guide, *Rep. LBL-20700*, Lawrence Berkeley Lab., Berkeley, Calif, 1987.

Pruess, K., TOUGH2 - A general-purpose numerical simulator for multiphase fluid and heat flow, *Rep. LBL-29400*, Lawrence Berkeley Lab., Berkeley, Calif, 1991.

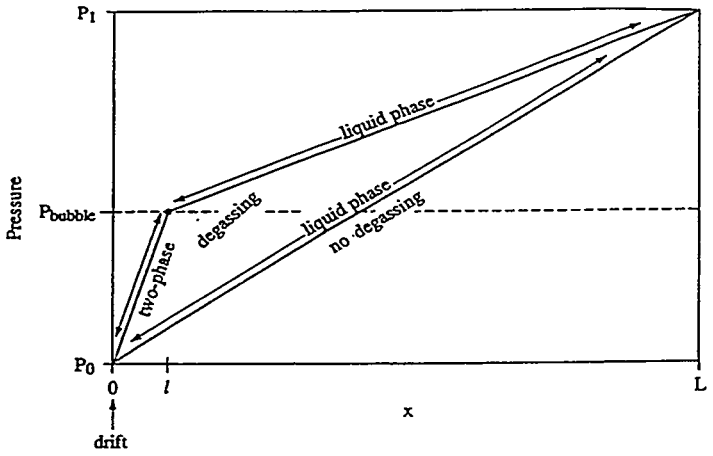

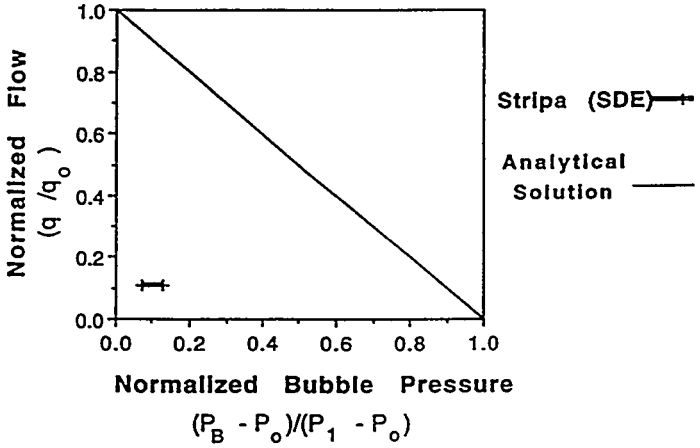

Figure 1. Top frame: conceptual model of flow reduction due to degassing for steady-state flow through a one-dimensional homogeneous medium with pressure held fixed at either end. Bottom frame: normalized flow versus normalized gas content for the analytical solution and the Stripa SDE result.

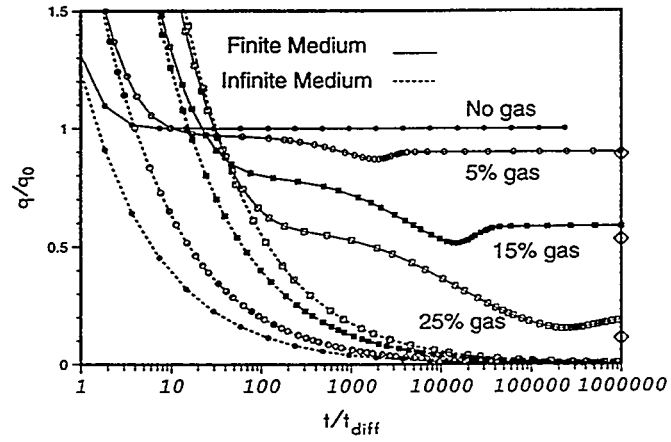

Figure 2. Normalized flow $\tilde{q}$ as a function of normalized time for linear flow geometry (n = 1), finite and infinite media, and various gas contents.

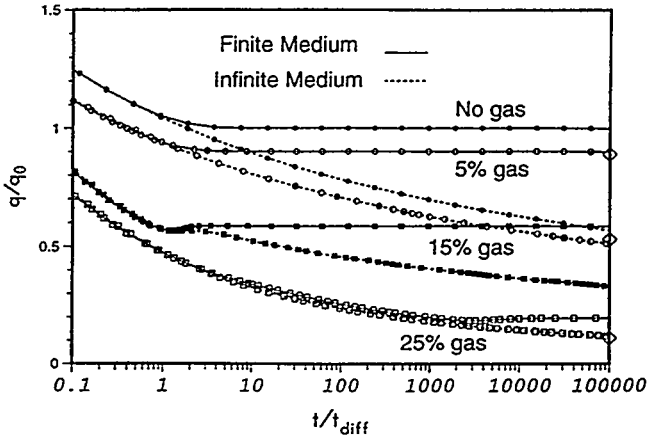

Figure 3. Normalized flow $\tilde{q}$ as a function of normalized time for radial flow geometry (n = 2), finite and infinite media, and various gas contents.

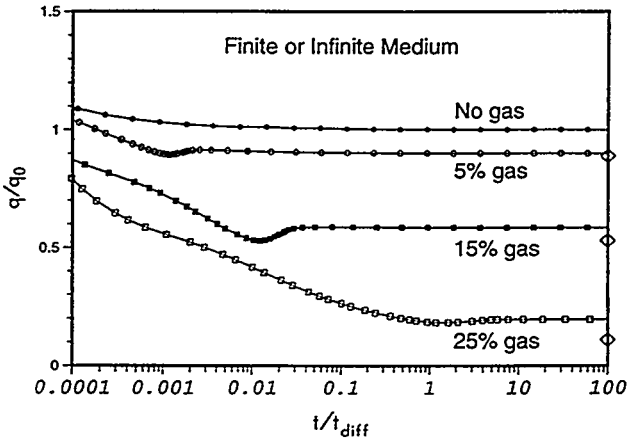

Figure 4. Normalized flow $\tilde{q}$ as a function of normalized time for spherical flow geometry (n = 3), finite and infinite media, and various gas contents.

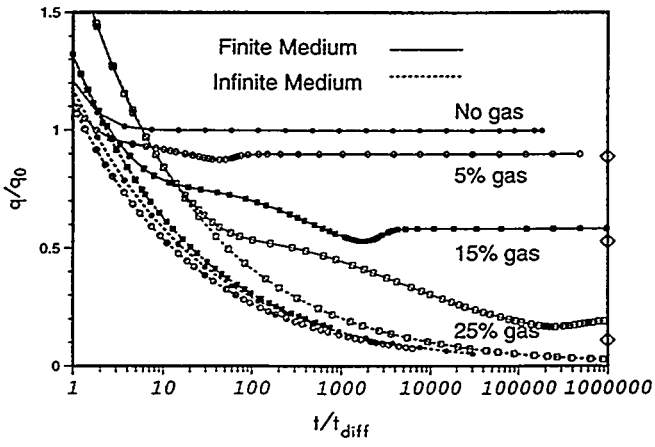

Figure 5. Normalized flow $\tilde{q}$ as a function of normalized time for non-integral flow geometry between linear and radial (n = 1.4), finite and infinite media, and various gas contents.

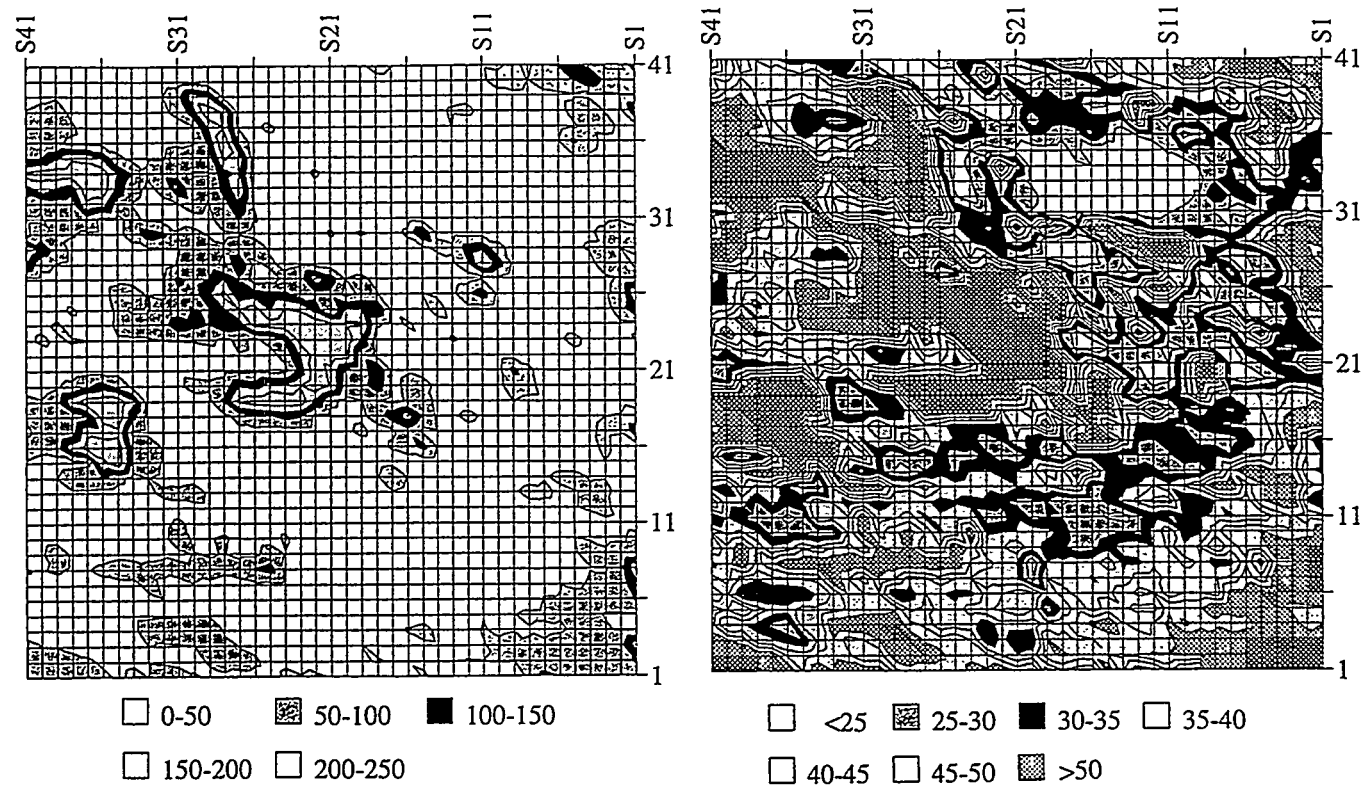

Figure 6. Aperture distribution for the Dixie Valley fracture. The left frame illustrates the overall aperture distribution, whereas the right frame focuses on the small-aperture distribution. For the numerical model, 25 microns were subtracted from each aperture value to enhance the effect of asperities. Flow is from right to left.

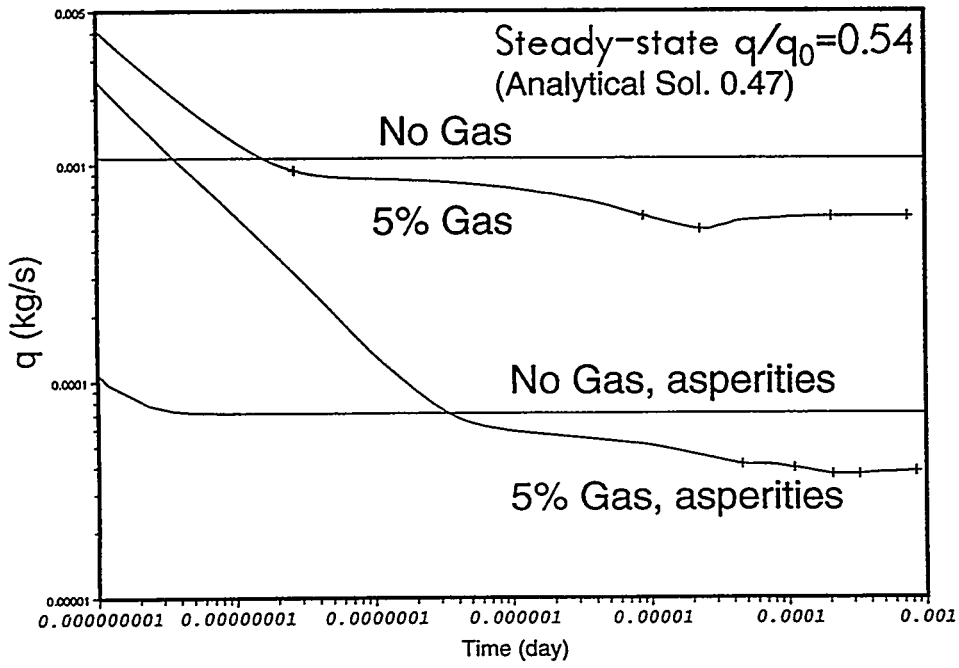

Figure 7. Flow rate as a function of time for two versions of the fracture model.

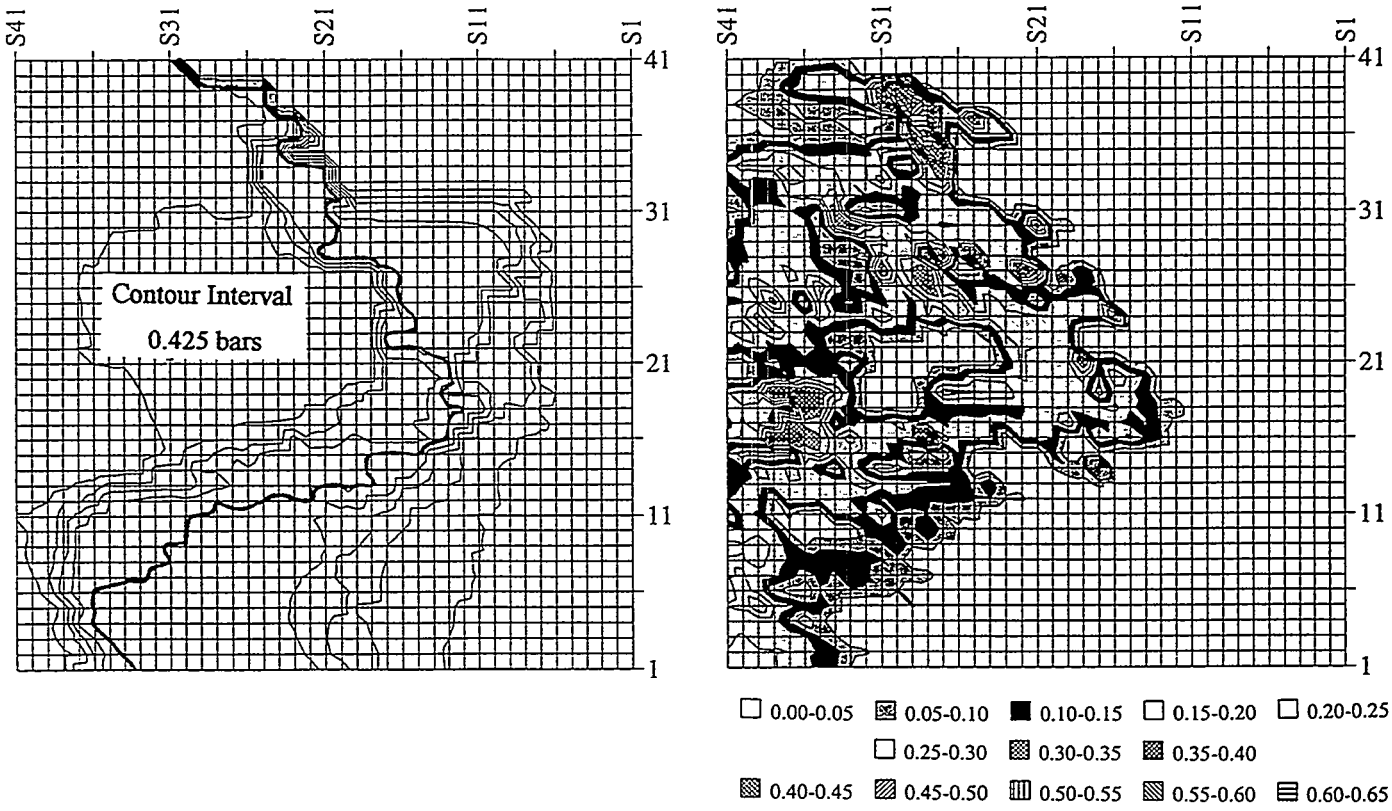

Figure 8. Modeled steady-state pressure (left) and gas saturation (right). Pressure is held fixed at 5 bars at the right edge and at 1 bar at the left edge. The bubble pressure is shown bold.

Figure 9. Observed steady-state gas distribution [white = gas, from *Geller et al.*, 1995].

RESERVOIR STORAGE AND CONTAINMENT OF GREENHOUSE GASES

G.J. WEIR, S.P. WHITE AND W.M. KISSLING

Applied Mathematics, Industrial Research Ltd., P.O. Box 31-310, Lower Hutt, New Zealand

Abstract This paper considers the injection of CO_2 into underground reservoirs. Computer models are used to investigate the disposal of CO_2 generated by an 800 MW power station. A number of scenarios are considered, some of which result in containment of the CO_2 over very long time scales and others result in the escape of the CO_2 after a few hundred years.

1 INTRODUCTION

If atmospheric concentrations of CO_2 are to stabilise without too large an impact on our industrialised lifestyle then novel storage sites for CO_2 are needed. Several researchers (e.g. [Steinburg *et al.*1985], [Ohgaki & Akano1992]) have considered the storage of CO_2 in the oceans, either as a liquid or as a hydrate (approximately $CO_2.6H_2O$). While this approach may be feasible for sources of CO_2 near the coast, costs will be higher for inland areas and an alternative storage technology may be more appropriate. We have investigated an alternative strategy, that of disposing of the CO_2 into deep aquifers within the earth. CO_2 has frequently been injected into petroleum reservoirs for at least two reasons. Some natural gas contains a high proportion of CO_2 and other light hydrocarbons. These may be stripped from the gas stream and reinjected into the reservoir in order to maintain reservoir pressures and to store the remnant hydrocarbons. Injected CO_2 has also been used to enhance oil recovery from low permeability oil reservoirs. The basis of the technology for the injection of CO_2 into aquifers already exists.

This paper describes a preliminary investigation into the storage of CO_2 in deep underground reservoirs. A similar scenario was investigated by [Hendriks *et al.*1991] who suggested the use of exhausted natural gas reservoirs for the storage of CO_2 from natural gas fired thermal power stations. Their paper concentrated on the technology and economics of the power station and recovery of CO_2 from the flue gases and did not examine the storage properties of the reservoir in detail. The emphasis of the current work is the behaviour of the injected CO_2 within the earth and establishing time scales for its return to the atmosphere. While the scenario we investigate is the injection into deep aquifers, the techniques developed would apply equally well if the injection were into a natural gas field. Injection rates considered are consistent with the disposal of the CO_2 generated by a 800 MW thermal power station.

2 MATHEMATICAL BACKGROUND

This section briefly reviews the mathematical equations that describe mass, heat and CO_2 flow in a porous aquifer. The conservation equations for heat, mass and CO_2 are of the form

$$\frac{\partial \rho_\beta}{\partial t} + \nabla . \mathbf{j}_\beta = Q_\beta \qquad \beta\text{=(Energy, Mass,}CO_2\text{)} \tag{1}$$

where the density terms and fluxes are given by

$$\begin{aligned} \rho_{CO_2} &= \phi X_l \rho_l S + \phi X_v \rho_v (1-S) \\ \rho_M &= \phi \rho_l S + \phi \rho_v (1-S) \\ \rho_E &= (1-\phi)\rho_m U_m + \phi \rho_l U_l S + \phi \rho_v U_v (1-S) \end{aligned} \tag{2}$$

$$\begin{aligned} \mathbf{j}_{CO_2} &= \rho_l X_l \mathbf{q}_l + \rho_v X_v \mathbf{q}_v \\ \mathbf{j}_m &= \rho_l \mathbf{q}_l + \rho_v \mathbf{q}_v \\ \mathbf{j}_e &= \rho_l h_l \mathbf{q}_l + \rho_v h_v \mathbf{q}_v - K \nabla T. \end{aligned} \tag{3}$$

In these equations ϕ is the porosity, K the rock matrix thermal conductivity, Q_β is a source term, X_α is the mass fraction of CO_2 in phase α =(liquid, vapour), ρ_α is the density of phase α, S is the liquid saturation, U_α is the internal energy of phase α, T is the temperature and P the pressure. The subscript $_m$ refers to the rock matrix.

The volume fluxes q_l and q_v are given by Darcy's equation $\mathbf{q}_\alpha = -k\frac{k_\alpha}{\mu_\alpha}(\nabla P - \rho_\alpha \mathbf{g})$ (α = (liquid, vapour))

Table 1: Coefficients of extended Redlick-Kwong EOS

i	1	2	3
c	2.39534×10^{1}	-4.55209×10^{-2}	3.65168×10^{-5}
d	4.09844×10^{-3}	1.23158×10^{-5}	8.99791×10^{-9}
e	2.89224×10^{-7}	8.02594×10^{-11}	7.30975×10^{-13}
f	-6.43556×10^{-12}	2.01284×10^{-14}	-2.17304×10^{-7}

Table 2: Permeabilities used in the simulations

Case	Region			
	Aquifer	Containment	Upper	
	k_h, k_v	k_h, k_v	k_h	k_v
1a	100 mD	0.01mD	10mD	10mD
1b	100 mD	1 mD	10mD	10mD
5a	100 mD	0.01mD	10mD	2mD
5b	100 mD	1mD	10mD	2mD

The solution of equations (1) is accomplished using a modified version of the computer program TOUGH2 developed at Lawrence Berkeley Laboratories by [Pruess1991].

3 THERMODYNAMIC PROPERTIES OF CO_2

In order to solve the equations of the previous section we need to be able to determine enthalpy, density and viscosity of water-CO_2 mixtures efficiently, for pressures up to 400 bars and temperatures up to 150°C. Equations describing the properties of water at these conditions are readily available (see, for example, [UK Steam Tables1970]).

Previous work on the transport of CO_2 in the earth has been carried out by researchers interested in the effects of non-condensible gases on geothermal fields (e.g. [O'Sullivan *et al.*1985], [Andersen *et al.*1992]). This work did not cover the full pressure range required for the current investigation and new formulae providing accurate approximations to the density, enthalpy and viscosity of CO_2 have either been derived or taken from the literature. These formulae are suitable for describing the properties of CO_2 to a depth of at least 5km. Thermodynamic properties of CO_2 are derived from an extended Redlich-Kwong (RK) equation of state (EOS) ([Kerrick & Jacobs1981]), which provides a good match to experimental values over a wide range of temperatures and pressures. Although it is not necessary for this work, the extended RK equation is easily modified to produce properties of CO_2/water vapour mixtures).

We begin with the extended RK equation of Kerrick and Jacobs and further extend this to provide a better match to properties below 50°C.

$$\frac{P}{\rho} = \frac{RT\left(1+\frac{b\rho}{4}+\left(\frac{b\rho}{4}\right)^2-\left(\frac{b\rho}{4}\right)^3\right)}{\left(1-\frac{b\rho}{4}\right)} - \frac{c(T)+d(T)\rho+e(T)\rho^2+f(T)\rho^3}{\sqrt{T}\,(b+\rho^{-1})} \tag{4}$$

where $b = 5.8\times10^{-5}\mathrm{m}^3/\mathrm{mole}$ and $c(T) = c_1 + c_2T + c_3T^2$. $d(T), e(T)$ and $f(T)$ are defined in a similar manner. Coefficients c_j etc. are given in table 1. The work of Kerrick and Jacobs does not have the f(T) term. Most of the required properties of CO_2 can be derived from the EOS given by equation (4).

Fugacity

The fugacity of CO_2 (f) can be derived from the EOS given in equation 4 by the expression ([Prausnitz1969])

$$RT\,log(f) = \int_v^\infty (P - \frac{RT}{v})dv - RT\,log(Z) + RT(Z-1) \tag{5}$$

Here Z is the compressibility factor given by $Z = \frac{RT}{PV}$. Evaluating equation (5) with the EOS given in equation (4) leads to

$$\begin{aligned}
\log(f) &= \frac{8y-9y^2+3y^3}{(1-y)^3} - \log(Z) \\
&- \frac{c(T)}{RT^{3/2}(v+b)} - \frac{d(T)}{RT^{3/2}v(v+b)} - \frac{e(T)}{RT^{3/2}v^2(v+b)} - \frac{f(T)}{RT^{3/2}v^3(v+b)} \\
&+ \frac{c(T)\log(v/(v+b))}{RT^{3/2}b} + \frac{d(T)\log((v+b)/v)}{RT^{3/2}b^2} - \frac{e(T)\log((v+b)/v)}{RT^{3/2}b^3} \\
&- \frac{f(T)\log(v/(v+b))}{RT^{3/2}b^4} - \frac{d(T)}{RT^{3/2}bv} - \frac{e(T)}{RT^{3/2}2bv^2} + \frac{e(T)}{RT^{3/2}b^2v} \\
&- \frac{f(T)}{RT^{3/2}3bv^3} + \frac{f(T)}{RT^{3/2}2b^2v^2} - \frac{f(T)}{RT^{3/2}b^3v}
\end{aligned} \tag{6}$$

where $y = \frac{b\rho}{4}$, $v = \frac{1}{\rho}$ and $c(T), d(T), e(T), f(T)$ are as defined in equation (4).

Enthalpy

The enthalpy of CO_2 is determined through the use of residual properties. A residual fluid property is defined as the difference between a real fluid property and the perfect gas state property value. We follow the procedure described in [Patel & Eubank1988]. The residual enthalpy is given by:

$$H - H^*_{ref} = H(T, \rho) - H^*\left(T_{ref}, P_{ref}/RT_{ref}\right)$$

where * indicates the perfect gas state.

Integration is done along the path

$$H\left(T, \rho_e\right) \rightarrow H^*(T, 0) \rightarrow H^*\left(T_{ref}, 0\right) \rightarrow H^*\left(T_{ref}, \frac{P_{ref}}{RT_{ref}}\right)$$

Starting with the thermodynamic identity

$$dU = C_v dT + R\left(\frac{\partial Z}{\partial(1/T)}\right)\frac{d\rho}{P\rho}$$

the residual internal energy is calculated using

$$\frac{U - U^*_{ref}}{RT} = \frac{1}{T}\int_0^\rho \left(\frac{\partial Z}{\partial(1/T)}\right)\frac{d\rho'}{\rho'} + \frac{1}{T}\int_{T_{ref}}^T \frac{C^*_v}{R}dT \tag{7}$$

This allows the residual enthalpy to be calculated as

$$\frac{H - H^*_{ref}}{RT} = \frac{U - U^*_{ref}}{RT} + Z - \frac{T_{ref}}{T}$$

We use the same reference state as in [Patel & Eubank1988]: $U^*_{ref} = -RT_{ref}$, $H_{ref} = 0$, $P_{ref} = 10^6$ Pa and $T_{ref} = 273.16$°K. The integrals in equation 7 require an integration of the perfect gas properties as well as integration of terms derived from the EOS given in equation (4). [Sweigert *et al.*1946] give the formula

$$C_p = 16.2 - \frac{6.53 \times 10^3}{T} + \frac{1.41 \times 10^6}{T^2}$$

for the specific heat at constant pressure (units are BTU/(lb-mole)/ °R) of CO_2 at zero pressure. Converting this to MKS units and noting that for a perfect gas $C_p = C_v + nR$, where n is the number of moles, allows us to write

$$\int_{T_{ref}}^T \frac{C^*_v}{R}dT = 59.315\left(T - T_{ref}\right) - 15139.5\left(\log\left(\frac{T}{T_{ref}}\right)\right) - 1808600\left(\frac{1}{T} - \frac{1}{T_{ref}}\right)$$

where T is in °K.

The first integral in equation 7 is rather long and has been evaluated using the symbolic algebra package MAPLE. For completeness we give the result here.

$$\begin{aligned}
\int_0^\rho \left(\tfrac{\partial Z}{\partial(1/T)}\right)\tfrac{d\rho'}{\rho'} &= (log(b\rho + 1)(b^3(18c_1 + 6c_2T - 6c_3T^2) + b^2(-18d_1 - 6d_2T + 6d_3T^2) \\
&+ b(18e_1 + 6e_2T - 6e_3T^2) + (-18f_1 - 6f_2T + 6f_3T^2)) \\
&+ b^3\rho^3(6f_1 + 2Tf_2 - 2T^2f_3) + b^3\rho^2(9e_1 + 3Te_2 - 3T^2e_3) \\
&+ b^2\rho^2(-9f_1 - 3Tf_2 + 3T^2f_3) + b^3\rho(18d_1 + 6Td_2 - 6T^2d_3) \\
&+ b^2\rho(-18e_1 - 6Te_2 + 6T^2e_3) + b\rho(18f_1 + 6f_2T - 6f_3T^2)) \\
&(12RT^{5/2}b^4)^{-1}
\end{aligned}$$

Fortunately MAPLE may also be used to generate FORTRAN (or C) code and this was done to produce subroutines to calculate the thermodynamic properties of CO_2.

4 Capillary Pressure

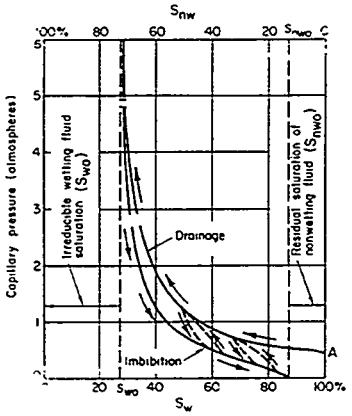

Figure 1. Typical capillary pressure - liquid saturation curves

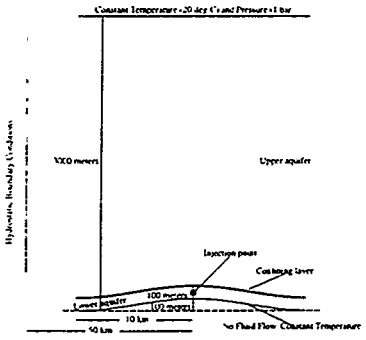

Figure 2: Portion of a generic reservoir used in modelling

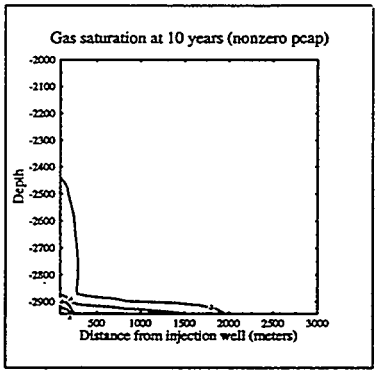

Figure 4: Gas saturation at 10 years, pcap=0

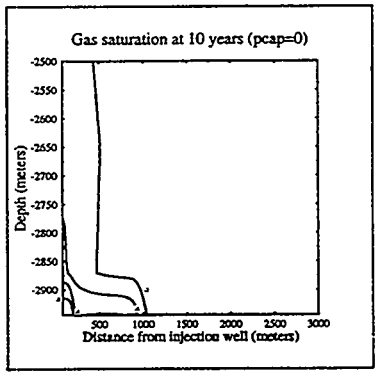

Figure 3: Gas saturation at 10 years, nonzero pcap

When considering the containment of a gas by a capping structure over a permeable reservoir an important property of the capping structure is the capillary pressure function. Experimentally, capillary pressure displays hysteretic behaviour such as that sketched in figure 1 (taken from Bear (1972)). The existence of a non-zero vapour entry pressure means that a capping structure can trap a layer of gas, typically a few tens of meters thick, beneath it. With a zero vapour entry pressure this trapping does not occur (although the escape of gas may be extremely slow when the capping structure has low permeability).

For the work described here we have ignored the hysteretic nature of capillary pressure but have included a non-zero vapour entry pressure. The functional form of capillary pressure chosen for this work is taken from Varva et al. (1992) and we have fitted a curve of the form $P_c = 1.08 \times 10^{-3}\sqrt{\frac{\phi}{k}}10^F$ where $F = 1.031(4.58 - 7.75S_l + 8.22S_l^2 - 3.40S_l^3)$. to the experimental data presented for "rock3" in figure 6 of [Varva *et al.*1992] (scaled to represent CO_2 - water rather than mercury - air).

5 PARAMETER SELECTION

The gross topography of subsurface layers of the earth is well known in many areas of the world. Seismic prospecting for petroleum reservoirs has resulted in reasonably detailed knowledge of the underground layered structure, especially in sedimentary basins. Regions where underground layering is convex upwards (anticlines) are natural sites for entrapment of petroleum products and these are also natural sites for storing greenhouse gases. The results of petroleum exploration, whether successful or not, provide a ready made database of suitable sites for the disposal of carbon dioxide. The type of trap modelled in this study consists of an almost impervious cover or cap rock overlying a permeable rock aquifer. A cross-section through the reservoir geometry considered in this paper is illustrated in figure 2.

We choose as an injection rate 100 kg/sec and assume this is all into a single well. This is representative of the CO_2 produced by a 800 MW thermal power station. Hendriks et.al. argue that an injection rate of about 10 kg/sec is a realistic average value for injection into depleted natural gas reservoirs. Experience in reinjecting waste water into geothermal fields suggests our higher value may be achievable in some aquifers.

6 SIMULATIONS AND RESULTS

All of the simulations performed in this report assumed an initial hydrostatic state consistent with the normal geophysical temperature gradient of 30°C/km. This initial condition was obtained by fixing the upper boundary (depth = 0) to "atmospheric" conditions of 1 bar pressure and 20° C. The lower boundary

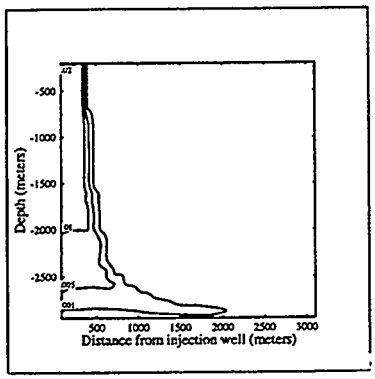

Figure 5: Gas saturation at 1000 years, pcap=0

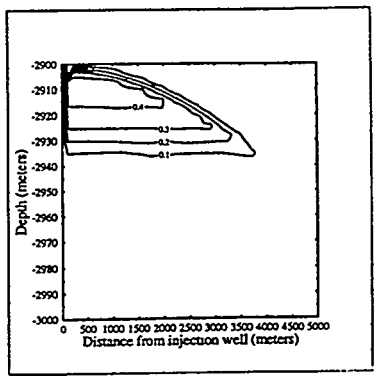

Figure 6: Gas saturation at 5000 years, nonzero pcap

for obtaining the initial conditions was set at 3100 m depth, to be below the undulating lower aquifer, and had a fixed temperature of 113° C. By permitting only heat flow (zero mass flow) across this lower boundary, and running the model for about 10^{13} seconds, a satisfactory quasi-steady state was obtained. This resulted in a pressure at the lower boundary of about 324 bars.

Four different permeability structures were assumed in the simulations. Table 2 lists the permeabilities used in the different simulations. Here k_h and k_v refer to the horizontal and vertical permeabilities. Corey (1977) relative permeability functions were used, with $S_{rg} = 0.05$, and $S_r = 0.3$. In all cases the rock porosity is taken as 0.1 in the upper and lower aquifers, and 0.04 in the confining layer. CO_2 is injected into the lower aquifer at 100 kg/s for 10 years and the simulation is continued to a total time of 5000 years.

We will consider the results of a single case (Case 1b) with and without capillary pressure effects in some detail, the results are similar to the other cases considered, although some CO_2 escapes to the atmosphere in Case 1b and it can be considered a "worst case " scenario.

Figures 3 (zero capillary pressure) and 4 (nonzero capillary pressure) show contours of gas saturation in a small section of the reservoir near the injection point immediately after injection has ceased. The differences in the saturation contours for these two cases can be quite clearly seen. When capillary pressure is included more gas is contained beneath the confining layer. This remains the case for the whole of the period of the simulation.

In figure 5 we show saturation contours after 1000 years for the case of ignoring capillary pressure and in figure 6 we show saturation contours after 5,000 years including capillary pressure. In the latter case most of the CO_2 is contained as a gas beneath the confining layer while in the former case the gas has reached the surface. This behaviour is also illustrated in figures 8 and 7.

The variation of location of CO_2 in these figures requires some explanation. The mechanism for the transport of CO_2 to the upper aquifer then back to the lower is the same in both cases. Initially as the gas is injected, a single phase bubble of gas forms. this is surrounded by a two-phase zone containing CO_2 and water saturated with CO_2. Buoyancy forces cause the bubble and surrounding two-phase zone to rise towards the surface. This upward movement towards the surface is delayed when capillary pressure is included until the gas pressure is sufficient to overcome the vapour entry pressure of the confining layer. Almost immediately injection is ceased the single phase gas bubble collapses into a two-phase area.

Liquid water saturated with CO_2 at reservoir conditions considered here is slightly more dense than pure water. The CO_2 saturated water sinks down towards the lower aquifer drawing more pure water towards the two-phase zone. Effectively CO_2 gas is washed from the two-phase zone and carried to the lower aquifer in the dense CO_2 saturated liquid. The liquid flows associated with this are shown in figure 9.

When capillary pressure is not included some gas does escape to the atmosphere, however most of the gas is contained dissolved in the liquid phase. This contrasts to the case when capillary pressure is included and almost all of the CO_2 is contained as a gas in a two-phase zone.

7 CONCLUSIONS

These research results show that underground storage of greenhouse gases is an attractive option, being:

- Self-containing. Results from the computer model show that provided the CO_2 is initially spread horizontally over about a kilometre from the injection site, then all of the upwardly migrating greenhouse vapour is eventually dissolved in the reservoir liquid, which then begins to descend under gravity. However, if the gas is not significantly spread laterally, then some gas can escape to the atmosphere.

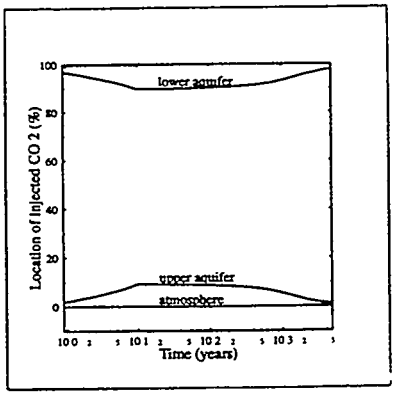

Figure 7: Disposition of CO_2 at 5000 years, nonzero pcap

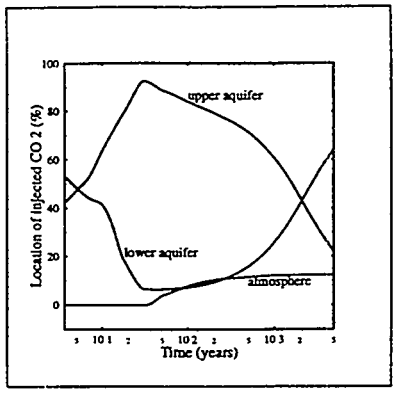

Figure 8: Disposition of CO_2 at 5000 years, pcap=0

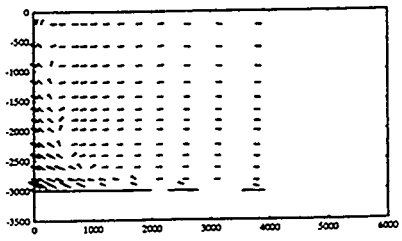

Figure 9: Liquid velocity vectors at 1000 years, pcap=0

- Volumetrically efficient. The greenhouse gases are stored at densities of hundreds of kilograms per cubic metre for several hundred years. Upward migration and dissolution reduces the storage density to about 40 kg/m^3 over about one thousand years. However, a non-zero vapour entry pressure term could significantly increase the density of the stored greenhouse gases.
- Viable. Aquifer permeabilities of 100 mD were assumed in our model calculations. Such permeabilities should exist within many geologic formations.

7 ACKNOWLEDGEMENT

This work was sponsored by New Energy and Industrial Technology Development Organisation (NEDO) / Research Institute of Innovative Technology for The Earth(RITE) of Japan.

*

References

Andersen, G. Probst, A. Murray, L. Butler, S., An Accurate PVT Model for Geothermal Fluids as Represented by $H_2O - CO_2 - NaCl$ Mixtures, *Proc. 17th Workshop on Geothermal Reservoir Engineering*, Stanford University, Jan 1992.

Bear, J., *Dynamics of fluids in porus media.* American Elseveir Publishing Company, Inc. 1972

C.A. Hendriks, K. Blok and W.C. Turkenburg, *Energy - The International Journal* 16,1277-1293 1991.

D.M. Kerrick and G.K. Jacobs, A Modified Redlich-Kwong Equation for H_2O, CO_2 and $H_2O - CO_2$ mixtures at Elevated Temperatures and Pressures, *Amer. J. Sci.* **281**, 1981.

K. Ohgaki and T. Akano, *Energy and Resources* 13,375-383, 1992.

O'Sullivan, M.J. Bodvarsson, G.S. Pruess, K. Blakeley, M.R. : 1985, Fluid and Heat Flow in Gas-rich Geothermal Reservoirs *Soc. Pet. Eng. J.* **Vol. 25** pp 215-225

Patel, M.R. Eubank, P.T. :1988, Experimental Densities and Derived Thermodynamic Properties for Carbon Dioxide-Water Mixtures *J. Chem. Eng. Data* **Vol. 33** pp 185-193

Prausnitz, J.M. :1969, *Molecular Thermodynamics of Fluid-Phase Equilibria* Englewood Cliffs, New Jersey, Prentice Hall Inc. p41

Pruess, K. (1991), TOUGH2 - A General-purpose numerical simulator for multiphase fluid and heat flow., *Report LBL-29400, Lawrence Berkeley Laboratory.*

M. Steinburg, H.C. Cheng and Horn, *A system study for the removal, recovery and dispossal of carbon dioxide from fossil fuel plants in the US*, Brookhaven National Laboratory 1985.

Sweigert, R.L. Weber, P. Allen, R.L. :1946, Thermodynamic Properties of Gases: Carbon Dioxide *Ind. & Eng. Chem.* **Vol 38**

UK Steam Tables in SI Units :1970, Edward Arnold London

Varva, C.L. Kaldi, J.G. Sneider, R.M., Geological Applications of Capillary Pressure: A Reveiw, *The Amer. Assn. Pet. Geol. Bull.*, **Vol 36** pp840-850 1992.

MODELING ACID MINE DRAINAGE IN WASTE ROCK DUMPS[1]

René Lefebvre[2]

Introduction

Acid mine drainage (AMD) results from the oxidation of sulfides present in mine wastes. The acidity generated by these reactions creates conditions under which metals can be leached and represent a threat for surface and ground waters. Even though leachate collection and neutralization are used to treat the problem, the industry is looking for methods to predict and prevent the generation of AMD at new sites and control methods for sites already producing AMD.

Waste rock dumps are generally very large accumulations of barren rocks extracted from open pits to access ore bodies. These rocks contain sulfides, most commonly pyrite, and often generate AMD at rates much higher than in mine tailings which are fine grained by-products of milling operations. Numerous coupled physical processes are involved in AMD production in waste rocks. Sulfide oxidation reactions are strongly exothermic and temperatures beyond 70 ºC have been mesured in some dumps. That heat is transfered by conduction and fluid advection. Dumps have thick partly saturated zones through which gases flow under thermal gradients and water infiltrates. Oxygen is required by the oxidation reactions and is supplied by diffusion and advection. The reaction products are carried in solution in very concentrated leachates.

Numerical modeling of AMD aims to 1) provide a better understanding of the physical processes involved in AMD, 2) allow the integration of available waste rock characterization data, 3) indicate new data or studies which are required to fill the gaps in our quantitative understanding of AMD processes, and 4) supply a tool for the prediction of AMD production, taking into account the impact of control methods. These objectives can only be met through sustained research efforts. This study is part of a wider research effort which as been on-going at La Mine Doyon since 1991 (Gélinas et al., 1994).

Reaction core model

In waste rock dumps, pyrite is contained in rock blocks and surrounded by other minerals and its oxidation proceeds from the surface of the blocks. As pyrite near the surface is oxidized, the oxidant must penetrate within the blocks to reach unreacted pyrite. A zonation appears within the blocks with an external zone in which pyrite is completely oxidized and an internal core where pyrite is unreacted. The whole of pyrite within a block is not oxidized simultaneously because the rate of oxygen consumption generally exceeds the rate of oxygen diffusion in the blocks. Our model uses features similar to those of Pantelis and Ritchie (1991), Cathles and Schlitt (1980), Jaynes (1983) and Levenspiel (1972). The volumetric oxidation rate Q_{Ox} (kg/m^3 s), observed in a unit volume of waste rocks, is related not only to surface oxidation but is also controlled by the oxygen diffusion rate in waste rock blocks:

$$Q_{Ox} = - K_{Ox} \cdot X_T \cdot X_{WO} \cdot \rho_{Ox}^{air} \cdot f(X) \ , \qquad (1)$$

where K_{Ox} is the global volumetric kinetic constant (s^{-1}), X_T and X_{WO} are kinetic factors related to temperature and oxygen partial density (0 to 1), ρ_{Ox}^{air} is the oxygen partial density in air (kg/m^3), and f(X) is the geometric factor which is a function of the proportion of pyrite remaining X.

---

[1]TOUGH Workshop '95, Lawrence Berkeley Laboratory, Berkeley, CA, March 20-22, 1995.
[2]INRS-Géoressources, 2700 Einstein, C.P. 7500, Sainte-Foy (Québec), Canada, G1V 4C7.

TOUGH AMD Capabilities

TOUGH AMD follows the same formulation as TOUGH2 (Pruess, 1991). However, the addition of a new component (oxygen) and a new primary thermodynamic variable (oxygen mass fraction in air) was required to represent AMD. Thus, in TOUGH AMD, there are three mass components (water, gases other than oxygen in air, oxygen) and one energy component (heat). Four equations, one for each component, have to be satisfied simultaneously to solve the system. Besides expanding components, other capabilities were added to represent AMD. Pyrite oxidation produces sinks for oxygen and sources of heat which are components of the system. Furthermore, that reaction consumes pyrite and produces sulfate, iron and acidity. The pyrite remaining has to be tracked since it affects the reaction rate and the production, accumulation and transport of sulfate is followed to represent AMD production outside the dump. The reaction core model is used to calculate the oxygen consumption rate Q_{Ox} (kg/m^3 s) to which the heat production rate is related. TOUGH AMD is thus adapted to the modeling of AMD and allows the representation of the main processes involved in waste rocks:

- Hydrology: Takes into account variable infiltration with time from the surface and represents unsaturated and saturated liquid flow within the dump.
- Gas transfer: Represents gas convection under pressure or temperature gradients as well as the diffusion of gas components, especially oxygen, under concentration gradients.
- Heat transfer: Includes the processes of conduction, fluid advection and gas diffusion. Takes into account the effect of phase changes on heat transfer and heat losses to confining beds.
- Geochemistry: Uses a reaction core model including the effects of surface reaction and diffusion on the volumetric oxidation rate. Computes the rates of consumption of pyrite and oxygen and the rates of heat and sulfate production.
- Mass transport: Uses sulfate to represent AMD production and tracks the production and advective transport of sulfate, its rate of mass accumulation and its release outside the dump.

Application of AMD numerical modeling

The first objective of numerical modeling is here to better understand the physical processes involved in AMD production in waste rocks. A general case is modeled to study the interaction of processes and identify the parameters having the greatest impact on the behavior of the system. The parameters and conditions used in the base case are representative of the South Dump at La Mine Doyon so that results may be compared to observations at this site (Gélinas et al., 1994). We are presenting here some of the findings of the modeling work for a base case. The application of the model to the evaluation of a control method, a border membrane, as well as a more detailled account of the modeling work is presented by Lefebvre (1994).

Model parameters and conditions

The base case is modeled for a period of 15 years and as such includes the period during which the dump has been in place (about 9 years) and provides a look at the potential future evolution of AMD production. It would be unrealistic to model the behavior of the dump for a longer period given the uncertainty in our knowledge of the site and in particular the absence of data on the evolution of physical properties with time which could affect significantly the behavior of the dump. This model actually supposes that physical properties remain constant even though we know from field observations that the material evolves and new minerals are formed and could alter the physical properties. Further studies are required to quantify the impact of this change in physical properties. The extensive characterization and monitoring program at La Mine Doyon allowed an evaluation of many physical properties of the waste rocks (Gélinas et al., 1994). Table I summarizes the physical parameters used in the model.

Table I - Physical properties of the base case.

Property	Symbol, value and units
Volumetric oxidation constant	$K_{ox} = 0.75 \times 10^{-6}$ s^{-1}
Diffusive / Chemical total times	$t_d/t_c = 2.5$
Pyrite mass fraction in solids	$w_{py} = 0.07$
Horizontal permeability	$k_h = 2.5 \times 10^{-9}$ m^2
Vertical permeability	$k_v = 1.0 \times 10^{-9}$ m^2
Porosity	$n = 0.33$
Solids density	$\rho_s = 2740$ kg/m^3
Dry thermal conductivity	$\lambda_d = 0.9$ W/m °C
Saturated thermal conductivity	$\lambda_w = 3.7$ W/m °C
Heat capacity of solids	$c_{ps} = 837$ J/kg °C
Thermal conductivity of the base	$\lambda = 1.55$ W/m °C
Global density of the base	$\rho_b = 2008.6$ kg/m^3
Heat capacity of the base	$c_p = 1504$ J/kg °C
Standard diffusion coefficient	$D_o = 2.13 \times 10^{-5}$ m^2/s
Temperature diffusion coef.	$\theta = 1.80$
Tortuosity factor	$\tau = 0.7$
van Genuchten "m" factor	$m = 0.23$
van Genuchten "α" factor	$\alpha = 0.504$ Pa^{-1}
Residual water saturation	$S_{wr} = 0.14$

The computation grid and limit conditions used in the base case are presented in figure 1. That grid represents a vertical half section within the dump and uses cartesian coordinates. The model has a 30 m thick unsaturated zone and a thin wedge-shaped saturated zone from zero to 1.5 m thick. Lateral dimensions are 87 m at the base and 57 m at the surface. The slope at the border is necessary to obtain representative air convection patterns (Pantelis and Ritchie, 1991). Since the internal boundary is a symmetry limit, the grid represents a system twice as wide. The limit conditions used are a water saturation of 0.42 generating an infiltration of about 35 cm per year, a temperature of 5 °C and atmospheric oxygen mass fraction (0.2315). Atmospheric pressure is set at 100 kPa at the surface whereas a hydrostatic pressure profile is used at the sloping border. The system is supposed homogeneous. The same parameters are used as initial conditions.

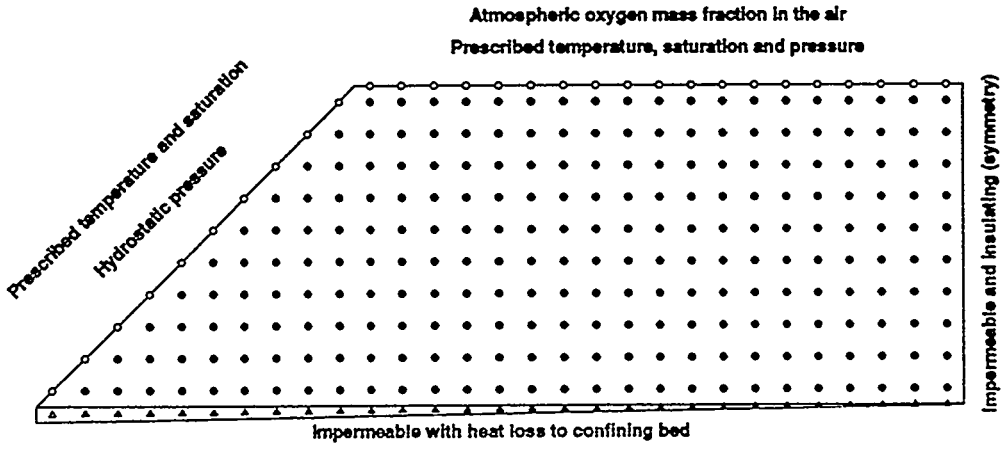

Figure 1 - Computation grid and limit conditions for the base case.

Physical conditions within the dump

Figure 2 shows the conditions prevailing in the dump after 9 years of AMD production: gas velocity and temperature, oxygen mass flux and relative concentration, and oxidation rate and remaining pyrite mass fraction. The key process in AMD production is oxygen supply to oxidation sites. Convection can provide oxygen in a much more efficient way than diffusion. Figure 2 (top) shows that air convection is controlled by temperature gradients. An increase in temperature reduces gas density and causes gas convection which is responsible for the supply of oxygen within the dump: figure 2 (middle) illustrates the oxygen mass flux and the relative oxygen concentration in the dump (with respect to atmospheric concentration). The oxygen flux is reduced along a given convection path within the dump because it is gradually consumed by the oxidation reaction. The oxygen concentration is thus maximum near air entry points and is gradually reduced within the dump. The central core of the dump is deprived of oxygen and does not produce much AMD. At this stage, the effect of diffusion is negligible compared with convection. Since pyrite oxidation is supposed to follow first order kinetics with respect to oxygen, its distribution has a direct impact on the oxidation rate. Figure 2 (bottom) shows the remaining pyrite mass fraction (contours) and the oxidation rate (circles). There is a sharp decrease in pyrite concentration at the border of the dump whereas the reduction is not as important near the surface. In the central part of the dump, very little pyrite is oxidized and a large potential for further AMD production remains.

Physical transfer processes

Transfer processes play an important role in AMD production. We will discuss the processes of heat transfer, water circulation and sulfate transport in waste rock dumps. Heat transfer in waste rock dumps occurs through the mechanisms of 1) conduction through the bulk of the material resulting from temperature gradients, 2) advection of fluids (liquid and gas) carrying heat and 3) diffusion of components in the gas phase. Figure 3 (top) shows the temperature distribution and the components of heat transfer. Three families of arrows represent respectively 1) the total heat flux, 2) the conductive heat flux (perpendicular to temperature contours) and 3) the diffusive heat flux. The difference between the total flux and the other components is the advective heat flux. At the outer limits of the dump, heat conduction is generally the dominant heat transfer mechanism. Conduction is also responsible for heating the center of the dump by carrying heat away from the zone of maximum temperature. Heat transfer by gas advection is dominant in the central hot zone where the gas phase contains more water vapor and carries a lot of heat. Water advection and its effect on heat transfer is very small in this case because of the low infiltration rate. However, this process can be significant in other cases. Heat transfer by diffusion in the gas phase is negligible because it is a binary process with diffusion and counterdiffusion of components with nearly equal heat capacity.

It is important to understand the modes of water circulation in a waste rock dump since the mass produced during AMD (sulfate, acidity, metals) is carried in solution. Figure 3 (middle) shows the distribution of water saturation and the mass fluxes of water in the liquid (downward pointing gray arrows) and vapor (black arrows) phases. Liquid water moves downward from the surface following infiltration in the unsaturated zone. Water is also transfered in the vapor phase by gas advection. Water transfer in the vapor phase is actually responsible for the redistribution of water within the dump. Relatively dry cold air entering the dump, mainly at the toe of the slope, acquires more and more water as it first moves horizontally and heats up. The gas phase carries the most water, as much as the liquid phase, as it moves upward through the hottest zone. Beyond that zone, in cooler areas near the surface, water vapor condenses and contributes to more infiltration. That process induces water saturation variations within the dump from 37.5% to 41.5%. The zone most influenced is near the toe of the slope at the base where water is withdrawn. Although important, the process of water vapor transfer by advection does not lead to important net water losses from the dump because most of the water withdrawn from the base recondenses near the top surface before the gas phase leaves the dump.

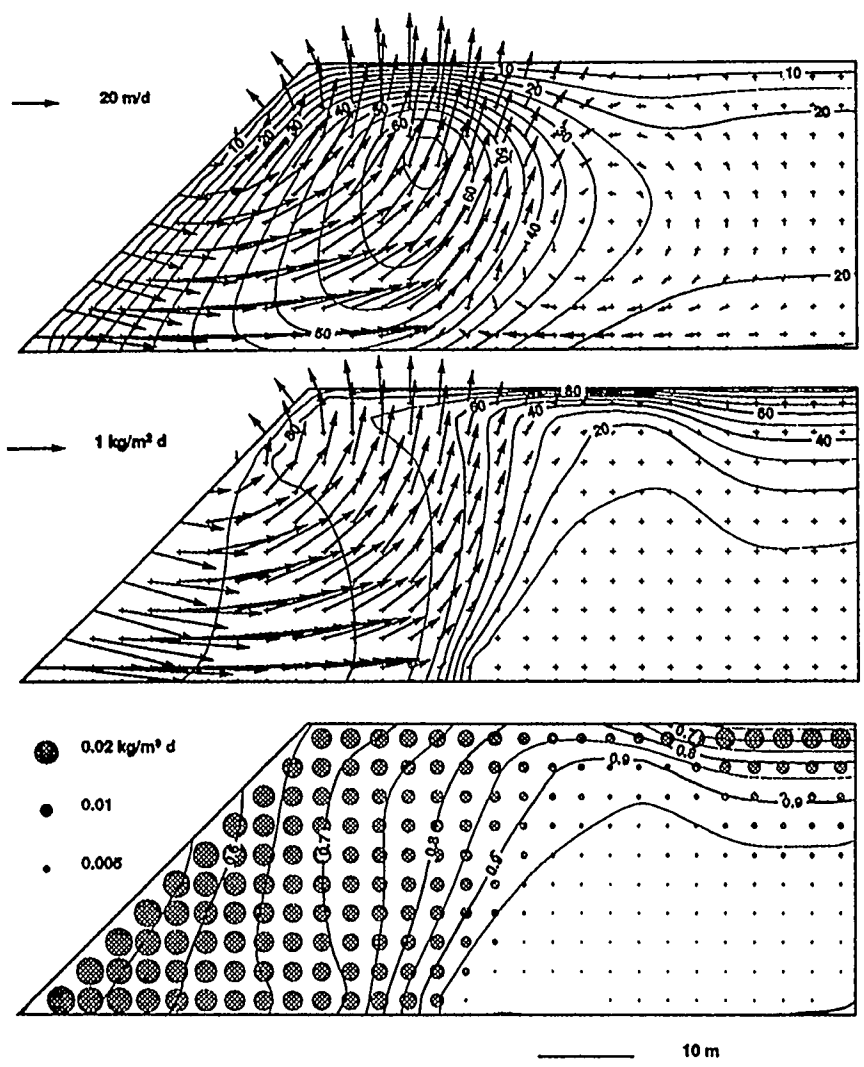

Figure 2 - Physical conditions (base case after 9 years).
Top: gas velocity (m/d) and temperature (ºC). Middle: oxygen mass flux (kg/m^2 d) and oxygen mass fraction in air with respect to atmospheric value (%). Bottom: unreacted pyrite mass fraction and oxidation rate (kg O_2/m^3 d).

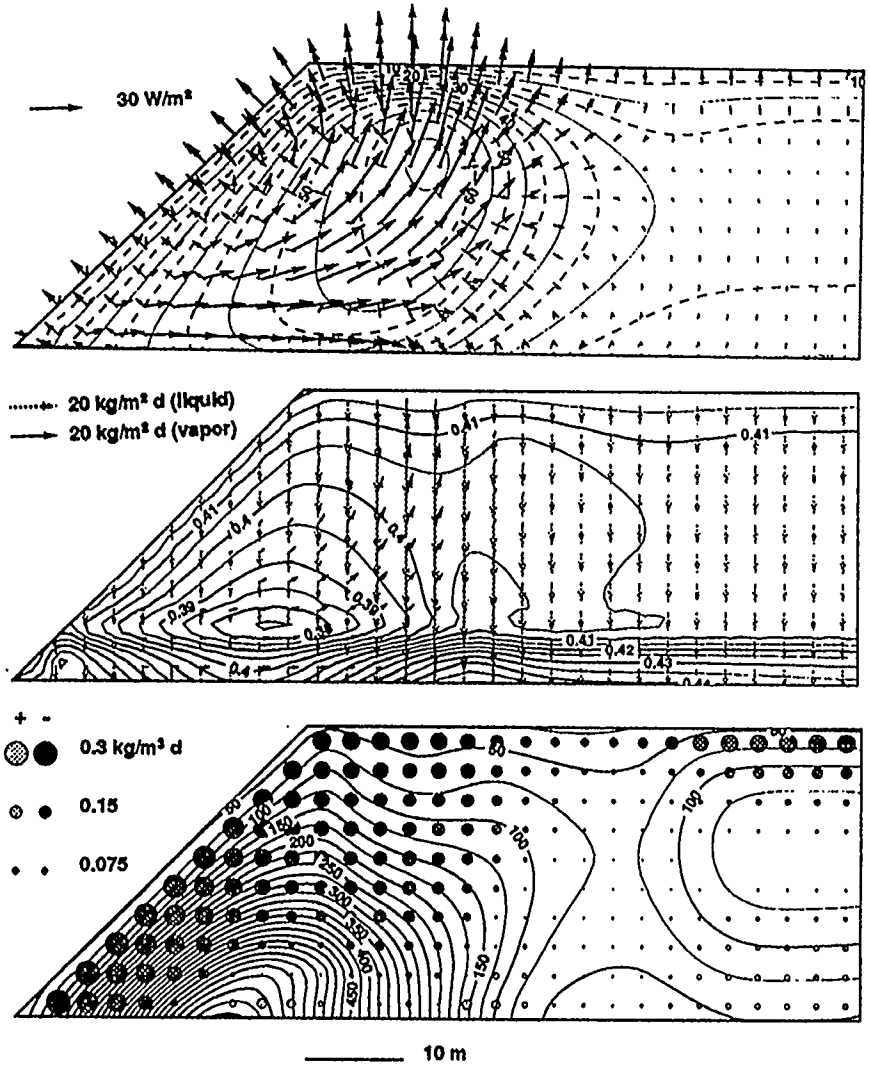

Figure 3 - Transfer processes (base case after 9 years).
Top: total, conductive and diffusive heat fluxes (W/m^2) and temperature (ºC). Middle: liquid (gray) and vapor (black) water mass fluxes (kg/m^2 d) and water saturation (-). Bottom: net sulfate flux (kg/d) and concentration (g/L).

AMD production is followed in the model by sulfate production, transport and release. Figure 3 (bottom) shows the distribution of sulfate concentration (contours) and the net sulfate flux in the grid elements. These net fluxes represent the difference in mass of sulfate entering and leaving an element. Net negative fluxes (dark circles) indicate that more mass exits the element than enters it whereas positive net fluxes (light circles) have an opposite meaning. Negative net fluxes occur in zones of high oxidation rate and consequently of high sulfate production. In these areas, more mass leaves the elements because internal production adds to the sulfate mass flux. Positive fluxes occur mainly at the core of the dump where sulfate mass production is low: in these areas, leachate of high concentration mixes with the leachate contained in the elements and comes out with less mass. This type of mass transport representation in the unsaturated zone supposes mixing of fluids instead of piston displacement and accounts for the limited leaching caused by small infiltration rates compared with the large volume of leachate stored in the unsaturated zone. This results in an increase in concentration and sulfate mass storage within the dump as more mass is produced than may be leached during the early years of AMD production. This representation of mass transport is simplistic and requires more work. Also, no account is taken in the model of mass loss due to new minerals precipitation (gypsum, jarosite). It is clear that the very high concentrations indicated by the model could not be reached in a real system because oversaturation and precipitation would occur to limit the concentration.

Conclusion

Further research is needed to develop the firm fundamental knowledge upon which applied numerical modeling must be based. Modeling is useful to better understand the coupled physical processes involved in AMD production in waste rocks. Also, modeling can be used to evaluate control methods mainly aimed at reducing air convection (Lefebvre, 1994). The processes of water infiltration in a coarse heterogeneous porous media, mass transport in the unsaturated zone, and the leachate geochemical behavior (interaction with rocks and mineral precipitation) need to be studied further both in the laboratory and in the field. The limited knowledge on these key processes limits further development of AMD modeling and our capability to predict the behavior of waste rock dumps. Further field studies are also required as we need more site characterization with integrated monitoring and modeling programs. For those sites, we have to develop methods to better characterize air permeability and its anisotropy as it affects both gas convection and water infiltration. We also have to be able to characterize, in the field and lab, the changes in physical properties of waste rocks through time and especially the effect of mineral precipitation.

References

Cathles, L.M., and Schlitt, W.J., 1980: A model of the dump leaching process that incorporates oxygen balance, heat balance, and two dimensional air convection. In Schlitt, W.J., ed., Leaching and recovering coper from as-mined materials. Proc. of the Las Vegas Symp., 26 Feb., 1980, Solution Mining Commitee, Soc. of Mining Eng. of AIME, pp. 9-27.

Gélinas, P., Lefebvre, R., Choquette, M., Isabel, D., Locat, J., and Guay, R., 1994: Monitoring and modeling of acid mine drainage from waste rocks dumps - La Mine Doyon case study. Report GREGI 1994-12 submitted to the MEND Prediction commitee, Sept. 1994.

Jaynes, D.B., 1983: Atmosphere and temperature within a reclaimed coal-stripmine and a numerical simulation of acid mine drainage from stripmined lands. Ph.D. Th., Penn. St., 198 p.

Lefebvre, R., 1994: Caractérisation et modélisation numérique du drainage minier acide dans les haldes de stériles. Ph.D. Thesis, Université Laval, 375 p.

Levenspiel, L., 1972: Chemical reaction engineering, 2nd ed. John Wiley & Sons, N.Y., 578 p.

Pantelis, G., and Ritchie, A.I.M., 1991: Macroscopic transport mechanisms as rate-limiting factor in dump leaching of pyritic ores. Appl. Math. Modeling, 15, March, pp. 136-143.

Pruess, K., 1991: TOUGH2 - A general-purpose numerical simulator for multiphase fluid and heat transfer. Lawrence Berkely Laboratory LBL-29400, 102 p.

Modeling the Response of the Geothermal System at Lihir Island, Papua New Guinea to Mine Dewatering

Anthony J. Menzies[1] and John L. Forth[2]

[1]GeothermEx, Inc., Richmond, California
[2]Lihir Management Company, Brisbane, Australia

INTRODUCTION

Lihir Gold, Ltd., with RTZ Corporation, Niugini Mining Ltd. and the Government of Papua New Guinea as major shareholders, plans to mine two contiguous gold orebodies (Leinetz and Minifie) located in the Luise Caldera, Lihir Island, Papua New Guinea; the location of Lihir Island is shown in figure 1. Niugini Mining Ltd. first discovered the deposit, which is believed to be the largest undeveloped gold deposit in the world, in 1982 and detailed exploration was later conducted by Kennecott Corporation (an RTZ subsidiary) who also prepared the plan for mining the deposit. The gold was deposited in the caldera breccias by rising hot fluids from a still active geothermal system to form the orebody which is to be mined in a 2 km x 1.5 km open pit that will ultimately reach a depth of about 220 m below sea level.

At the ground surface, fumaroles, hot springs and gas seeps define the present day 3 km^2 area of geothermal activity (figure 2); the northwestern half of the proposed mine lies within the area of surface geothermal activity. Characterization of the geothermal system in the sub-surface is based on data from over 300 drillholes and an extensive field investigation program conducted over a 6 year period. The geothermal system appears to be fed by upflowing, hot fluid with temperatures at depth ranging from 250°C to 270°C; in some areas of the caldera, temperatures exceed 200°C at depths as shallow as 200 m. The geothermal fluid contains approximately 80,000 mg/l total dissolved solids, with major concentrations of sodium, potassium, chloride and sulfate, is pH neutral and contains 0.8% by weight gas (at approximately 20:1 carbon dioxide:hydrogen sulfide).

The geothermal fluid mixes with infiltrating rainwater and discharges through permeable breccias to the sea; most of the discharge is believed to occur where permeable zones outcrop on the sea bed approximately 200 m off-shore near the southeast limit of the geothermal features (figure 2). The location and permeability of the outflow zone is based on the results from a pump-out test and data from monitoring of tidal responses in 40 wells. Additional discharge occurs at the surface thermal manifestations and at springs along the coast line.

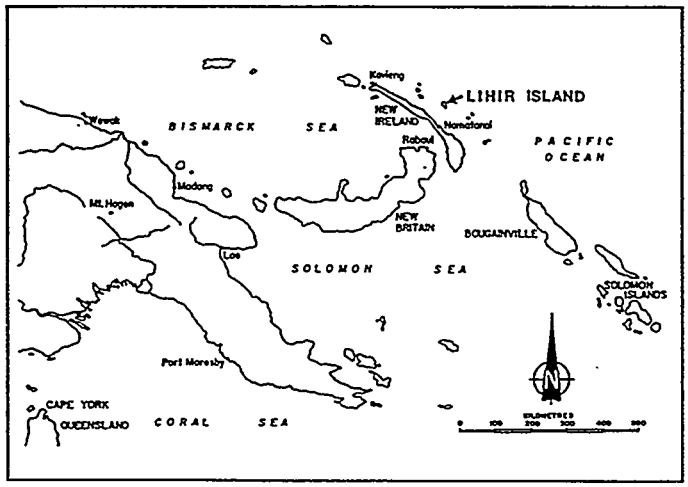

Figure 1: Location of Lihir Island

Results from a number of injection and pump-out tests show that the rocks within the defined pit area are generally very permeable to depths of about 250 m when compared with the surrounding unmineralized caldera wall rocks. This creates a permeable "bathtub" in the central part of Luise Caldera which is confined on three sides and at depth by relatively impermeable rocks. The "bathtub" is connected to the sea on the fourth side.

Because of the high permeabilities in the "bathtub", the water table through the ore zone is only slightly above sea level. Fluid pressures below the water table are generally hydrostatic, and no abnormally pressurized zones have been identified. Because of the lack of confining layers, no pressurized steam zones have been developed in the geothermal system, and the fluids present are predominantly in the liquid phase.

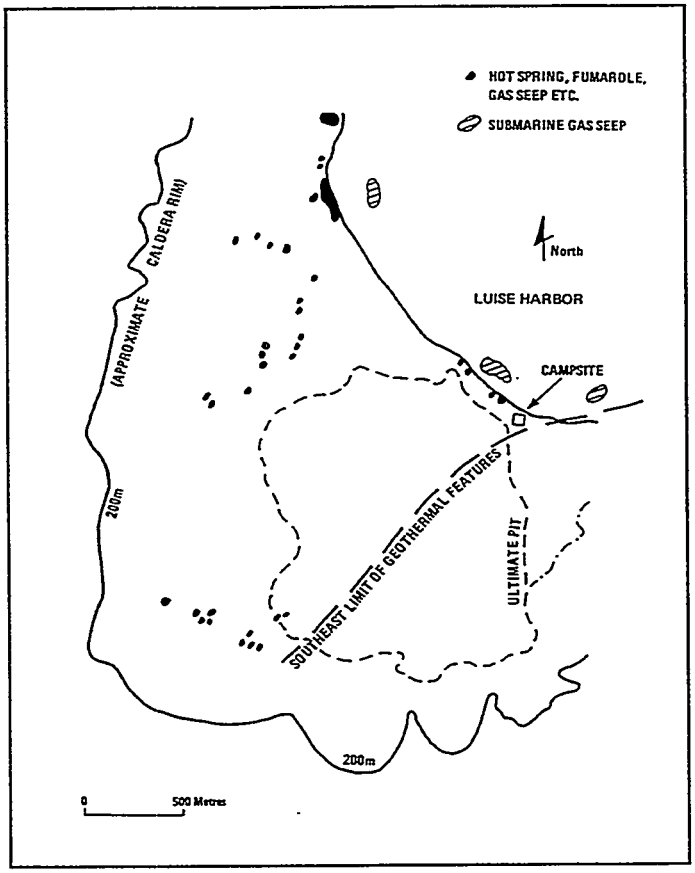

Figure 2: Surface geothermal features, Luise Caldera

The dewatering activities required to prevent sea water intrusion and to maintain "dry" conditions in the vicinity of the pit are expected to have a significant impact on the geothermal system. As pressures reduce, boiling will occur and steam will be formed. As a consequence, hot water and steam could flow toward the pit. If suitable geological conditions exist, pockets of pressurized steam could also form that will constitute a hazard if broached by mining.

MODEL DESCRIPTION

To investigate the impact of dewatering on the geothermal system, a numerical model of the Luise Caldera was constructed using a version of the TOUGH simulation code. The model was first calibrated by matching the initial state of the geothermal system (subsurface temperature and pressure distribution); it was then used to forecast the changes in pressure, temperature and steam saturation that will occur on a year by year basis in response to dewatering activities.

The model of the Lihir geothermal system contains a total of 561 grid blocks, including blocks used to define the various boundary conditions. The grid blocks are distributed over six layers which cover the depth interval from the ground surface down to -800 m, msl; the layer boundaries and node levels are summarized in table 1, while the grid

Layer	Top Boundary m, msl	Bottom Boundary m, msl	Node Level m, msl
1	topo	-100	-50
2	-100	-200	-150
3	-200	-250	-225
4	-250	-300	-275
5	-300	-500	-400
6	-500	-800	-750

Table 1: Layer boundaries and node levels used in TOUGH model

layout on layer 1 is shown in figure 3. Figure 3 also shows the major geographical areas included in the model. The grid layout on each layer was primarily determined by the shape of the measured subsurface temperature distribution and the general shape of the mine, with more blocks being used in the upper layers compared with the lower layers.

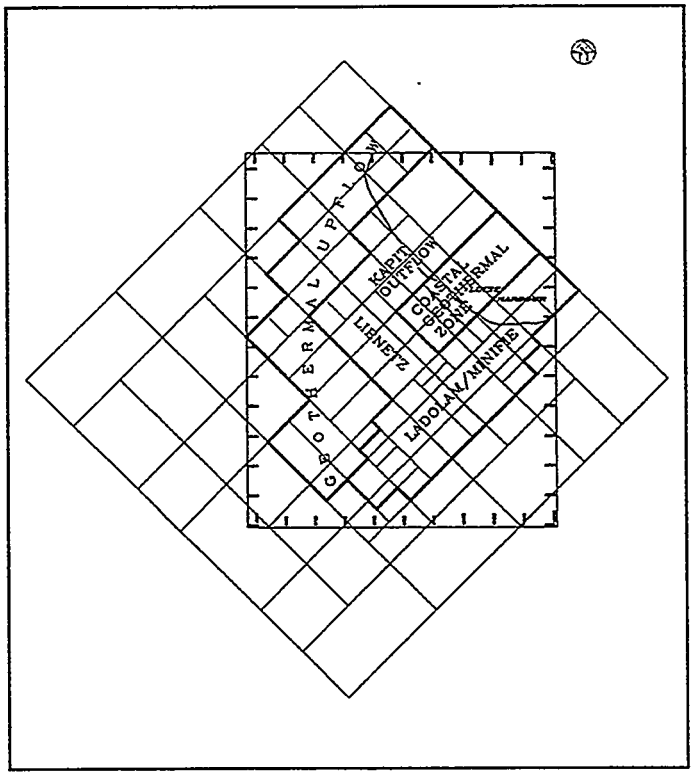

Figure 3: Model grid layout; top layer

Modeling of the geothermal system, including the geothermal upflow and interactions with the atmosphere, sea and infiltrating groundwater, required:

1. The use of the H_2O/CO_2 equation of state to allow the gas content (0.5 to 1.0 wt.-%) and thermodynamic conditions of the geothermal fluid to be more accurately modeled.

2. The use of constant pressure boundaries to model the interaction between the sea and the groundwater system.

3. The atmospheric boundary to be modeled as an open, constant pressure (100 kPa) boundary at constant temperature (30°C). The atmospheric boundary blocks are also

assumed to contain 100% CO_2 to approximate the properties of air. As dewatering proceeds, the CO_2 infilrates into the model, maintaining pressures at 100 kPa. In this way, the simulation model was used to approximate an unconfined system with a falling water table.

4. Constant rate point sources in selected blocks in the top layer to model infitration of meteoric water into the ore body.

5. The use of a constant pressure boundary at the base of the model to allow inflow of geothermal fluid at 240°C. Away from the upflow area, a conductive heat boundary with a temperature of 200°C was used.

6. Constant pressure boundaries on the sides of the top layer of the model to allow reasonable matches to be obtained to the measured pressure gradients within the system.

MODELING RESULTS

After specifying the model parameters and initial estimates of rock properties, the model was run and the results compared with the measured sub-surface distributions of temperature and pressure. After numerous runs, a reasonable match was obtained to the sub-surface temperature distribution and pressure gradients. The final rock types used in the model varied in permeability from 10^{-16} to $5x10^{-12}$ m^2; the lower permeabilities were mainly used on the sides of the model away from the geothermal upflow zone while the high permeabilities were used in the connection to the sea. The matching of the measured data required the inflows and outflows summarized in table 2.

After matching of the sub-surface data was successfully completed, the model was used to help develop the detailed groundwater (geothermal, stormwater and seawater inflow) management required for safe pit operation; the major elements of the plan are illustrated in figure 4. The principal operating element is a permanent wellfield of seawater interception wells to be located in Ladolam Valley, where ultimately an estimated 39 pump wells, averaging 250 m depth, are to be

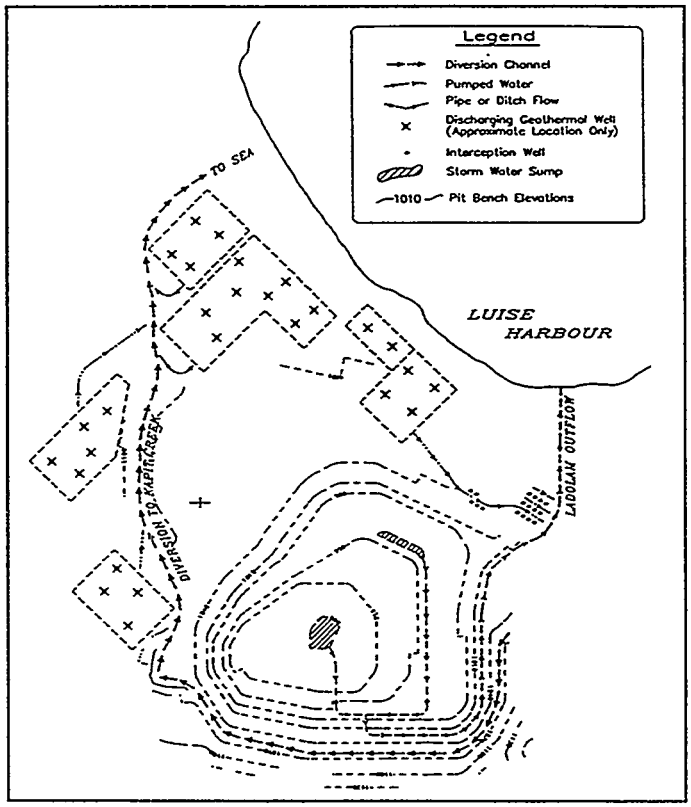

Figure 4: Conceptual water control management plan

Inflows to model		Outflows from model	
Geothermal upflow:	51.6 kg/s	Sea outflow:	98.3 kg/s
Infiltration:	37.9 kg/s	Atmospheric:	0.5 kg/s
Sides:	13.3 kg/s		
Total:	102.8 kg/s	Total:	98.8 kg/s

Table 2: Summary of mass balance required for initial state model

installed. These wells, each pumping at about 100 l/s, with an aggregate pumping of up to 1,300 l/s, will both dewater the pit area and intercept seawater being induced to flow toward the pit. Because of the very high permeabilities throughout the pit, it has been determined that by pumping from Ladolam Valley, the required pit dewatering through the life of mine can be accomplished from a single wellfield area sited outside of active working areas, an important consideration for a working mine.

Geothermal wells (totaling 70 in number through the 15 year mine life) are to be installed around the western and northern margins of the pit, outside working areas, as shown in figure 4. The geothermal wells will be sited about the pit to intercept and extract hot geothermal fluid, to enable monitoring of the geothermal system and to allow for the safe venting of steam and hot water should any build up of pressure occur.

The impact of depressurization will spread well beyond the pit limits and will induce boiling and steam formation within the strata surrounding the mine. Figures 5 and 6 show the impact on the geothermal system at the tenth year of mining and the locations of the pumped dewatering wells and geothermal wells. By this stage the mine is at its maximum areal extent and in some portions approaching maximum depth. As mentioned above, the simulations were conducted on a year-by-year basis to allow for the rapidly excavated mine. It was found that from Year 10 to the end of mining at Year 15, geothermal effects do not differ

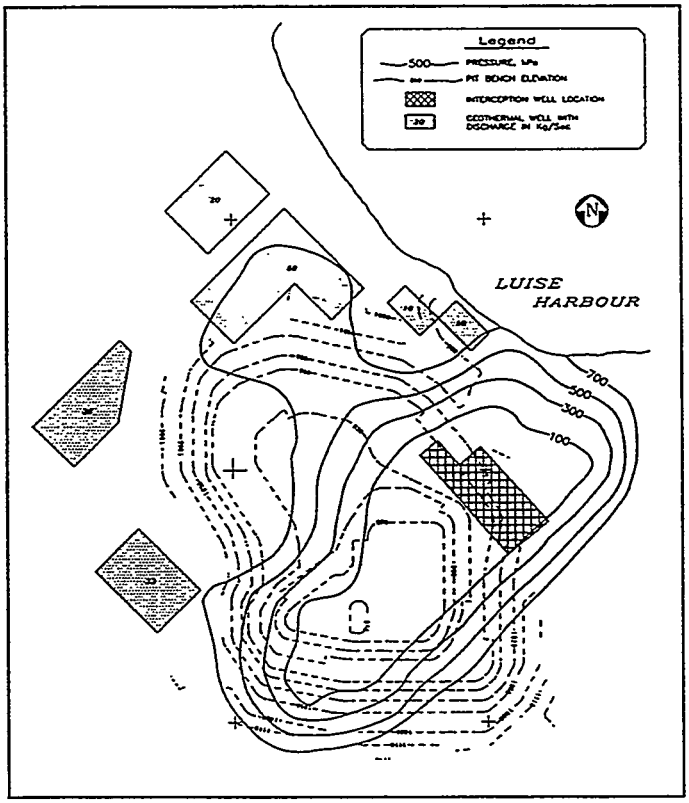

Figure 5: Calculated pressures (-150 m, msl); Year 10

significantly from those shown in figures 5 and 6.

Pressures within the geothermal system at Year 10 (figure 5) at -150 m, msl, correspond to a water level below the pit floor, except in the sump area. There are no indicated areas of excess pressure development which could drive hot fluids or steam toward the working pit. Depressurization will, however, result in the formation of shallow steam zones around the west margin of the mine and also in the coastal region. In the coastal area, steam saturation will exceed 40%; by Year 15 (the end on mining), computed steam saturations exceed 50% in some areas. The changes in sub-surface conditions, particularly the formation of steam, will be closely monitored during mine development using observation wells. If high pressures were to develop, these same wells would serve as vents to counteract the pressure increase. Additionally, these wells could be used for cold water injection to quench steam generation if such a need were perceived.

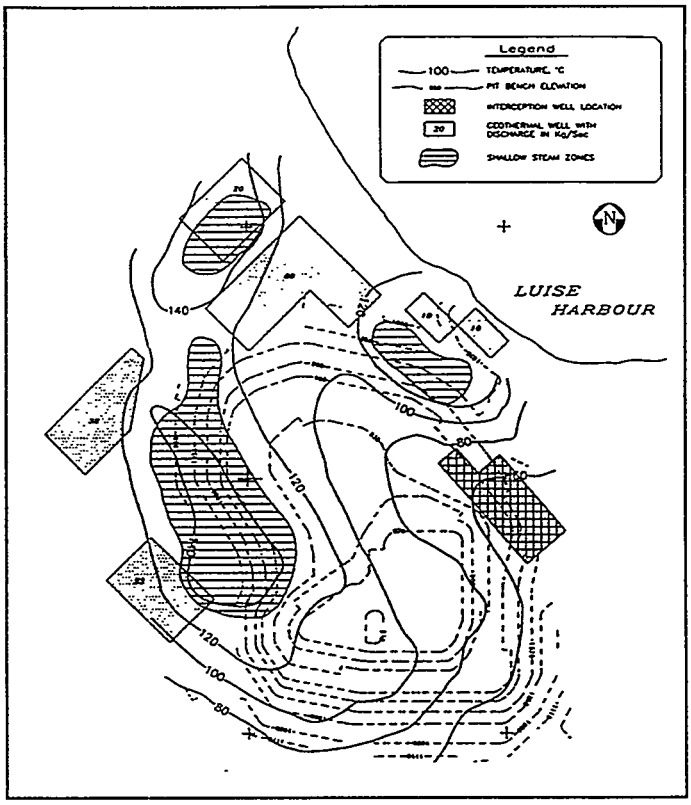

Figure 6: Areas of shallow steam formation and pit wall temperatures at Year 10

The estimated temperatures of rocks in the pit walls are shown on figure 6. Maximum near pit rock temperatures at Year 10 are anticipated to be about 120°C in the southwest. These temperatures are computed within the rock mass and do not represent skin temperatures which will be close to ambient temperature. It should also be noted that within the simulations no allowance was made for the cooling that will result from the annual rainfall of almost 4 m (on an average 230 raindays) which will enhance the wall cooling.

Dewatering will probably also result in an increase in the rate of upflow of hot geothermal fluid although the increase will be small, relative to the total water pumping requirement. It is not anticipated that the dewatering will cause the ascending geothermal upflow to migrate into different flow channels, nor is it expected that the temperature of the geothermal system will increase.

Some seeps and springs in the area west of the pit will probably dry up as a consequence of dewatering, and it is possible that geothermal activity could be instigated in some areas outside the pit perimeter that are presently geothermally inactive. Such activity is most likely to be seen as fumaroles, and low rate hot water seepages.

CONCLUSIONS

Computer simulations of a conceptual dewatering and geothermal management strategy indicate that it will be possible to construct and safely operate the proposed open cut pit in the Luise Caldera geothermal system at Lihir Island in Papua New Guinea.

The studies have shown that rock pre-cooling will not be necessary to allow safe mining, and that the required geothermal management, pit dewatering and seawater interception can all be accomplished with installations outside the actively working pit area, an important consideration for mine operation.

ACKNOWLEDGEMENTS

The permission to publish this paper given by the Lihir Management Company, the RTZ wholly owned subsidiary responsible for managing the Lihir Project, is gratefully acknowledged by the authors.

On the Development of MP-TOUGH2

C. M. Oldenburg, R. L. Hinkins*, G. J. Moridis, and K. Pruess

Earth Sciences Division
**Information and Computing Sciences Division*
Lawrence Berkeley Laboratory
University of California
Berkeley, CA 94720

ABSTRACT

We are developing MP-TOUGH2 for exploiting massively parallel computers. The goals of this effort are to (1) create a data-parallel subsurface transport code for solving larger problems than currently practical on workstations, (2) write portable code that can take advantage of scalability to run on machines with more processors, and (3) minimize the necessity for additional validation and verification of the resulting code. The initial strategy we have followed is to focus on optimizing the generic and time-consuming task of linear equation solution while leaving the bulk of TOUGH2 unmodified. In so doing, we have implemented a massively parallel direct solver (MPDS) that takes advantage of the banded structure of TOUGH2 Jacobian matrices. We have compared timings of the iterative conjugate gradient solvers DSLUBC, DSLUCS, and DSLUGM written in Fortran77 for the front end with the MPDS which uses the data parallel unit. The MPDS shows good performance relative to the iterative conjugate gradient solvers on our free-convection test problem. The robust direct solution provided by MPDS can be used to (1) check on the veracity of a given iterative conjugate gradient solution, or (2) be used on certain problems where iterative solvers fail to converge.

INTRODUCTION

One of the current challenges of scientific computing is the development of simulation codes that exploit massively parallel computers. Massively parallel computers have more than 1000 processors and are generally designed as single-instruction multiple data (SIMD) machines. Such computers can produce results faster and more efficiently using data-parallel methods supported by languages such as Fortran 90, where the same operations can be performed simultaneously on large arrays. Furthermore, Fortran 90 code is flexible because the same source code can be ported to other massively parallel computers with little or no modification. Given adequate memory resources, the maximum size of a tractable simulation problem scales with the number of processors on the available machine.

The promise of power and flexibility that data-parallel coding and massively parallel computers can theoretically bring to bear on simulation work must be tempered by the reality of the significant amounts of time and resources required to develop new simulation codes or rewrite existing codes. In the meantime, serial workstations and personal computers will become yet faster and cheaper, decreasing the potential return on investment in recoding. In addition, simulation codes such as TOUGH2 have received years of use and validation which have led to wide acceptance among users. New and rewritten code needs to be verified and validated and there is always considerable and justifiable resistance among users (and their customers) to use new codes.

The compelling potential of data-parallel coding coupled with the reality of scarce resources and uncertain return on investment has guided our initial development efforts. The strategy we have chosen to begin development of MP-TOUGH2, a massively-parallel version of TOUGH2, involves identifying time-consuming generic operations in TOUGH2 and exploiting optimized code to perform these tasks. The majority of computational effort in moderate- and large-size TOUGH2 problems goes to the solution of the system of linear equations involving a large, sparse, banded Jacobian matrix at each Newtonian iteration. This generic and time-consuming task is therefore the focus of our initial efforts.

In this report, we discuss our implementation of a massively parallel direct solver (MPDS) for the linear equation solution in TOUGH2. We use the 4096-processor MasPar MP-2204 at Lawrence Berkeley Laboratory, which consists of a front-end DEC Alpha 3000/300x and a 64 x 64 processor element array, also called the data-parallel unit (DPU). In keeping with the goal of minimizing recoding, we implemented MPDS as Fortran90 code that uses the DPU but is called from TOUGH2 compiled in Fortran77 on the front end. We compare timings of a two-dimensional natural convection test problem solved with MPDS running on the DPU and the same problem solved with iterative conjugate gradient solvers (Moridis and Pruess, 1995) running on the front end. We will show that the direct solver MPDS is competitive with the iterative conjugate gradient solvers on the test problem.

LINEAR EQUATION SOLUTION WITH MPDS

TOUGH2 generates a large and sparse banded Jacobian matrix at each Newtonian iteration which defines a set of linear equations to be solved for the changes in primary variables. Specifically, the equations

$$R_n^{(\kappa)k+1}(x_{i,p+1}) = R_n^{(\kappa)k+1}(x_{i,p}) + \sum_i \frac{\partial R_n^{(\kappa)k+1}}{\partial x_i}\Big|_p (x_{i,p+1} - x_{i,p}) \doteq 0 \qquad (1)$$

are solved where $R_n^{(\kappa)}$ is the residual for conservation of component κ in gridblock n, k is the time step index, x_i are the primary variables, and p is the index for the Newtonian iterations (Pruess, 1987; 1991). In a problem with NEL gridblocks and NEQ equations per gridblock, the Jacobian matrix $\{\partial R_n^{(\kappa)k+1}/\partial x_i\}$ is of order N = NEL x NEQ. It is this linear equation solution that consumes the majority of computation time for any moderate- or large-size TOUGH2 simulation.

We have implemented a banded direct solver provided to us by MasPar that takes advantage of library routines optimized for the DPU on the MP-2204. The MPDS is written in Fortran90 and uses the DPU. Meanwhile MP-TOUGH2 is compiled in Fortran77 to run on the DecAlpha 3000/300x front end, calling the Fortran90 MPDS for linear equation solution. In this way, neither TOUGH2 nor the iterative conjugate gradient solvers has been modified except for adding the option of calling the MPDS.

For simplicity in discussing the MPDS, we write the linear matrix equation (1) in the idealized form Ax = b, where A is the Jacobian matrix of order N, x is the vector containing the changes in primary variables, and b is the vector of residuals. The MPDS works by decomposing A into L(ower) and U(pper) where A = L U and then solving L (U x) = b. This decomposition and solution can be applied to any general matrix A. The Jacobian matrix in TOUGH2 is sparse and banded, with its non-zero elements near the

main diagonal, i.e. a(i,j) = 0 for abs(i - j) > m, where the bandwidth is 2m + 1. One can take advantage of this structure and modify the matrix storage scheme to achieve greater efficiency on a serial machine if m < N/3 (Dongarra et al., 1979). On a parallel SIMD machine with distributed memory, we can get parallel computation from the linear algebra library routines (MasPar Mathematics Library, 1993) by modifying the band storage scheme so that the non-zeroes in the band are submatrices of order N_S, where N_S is called the slab width. Each submatrix is distributed across the processors with one matrix element per processor. We choose N_S = 64 to optimize the mapping of the submatrices to the MP-2204 which has processor elements laid out on a 64 x 64 grid. The slab width parameter is generally chosen to match the processor array on the target machine, thus ensuring scalability for larger problems running on larger machines. The solve time depends on problem-dependent parameters including the matrix order and the bandwidth as well as the submatrix size.

RESULTS

The test problem used in this study is the Elder pure thermal convection problem (Elder, 1967). For generality, we use the TOUGH2 equation of state module EOS3 for water, air, and heat, although this particular problem is a single-phase flow problem. In prior work we used EOS7 and adapted the problem to pure solutal convection with a salt source at the top (Oldenburg and Pruess, 1994). Whether solutal or thermal convection is considered, the large maximum density change (20%) makes this a strongly coupled flow problem. Elder's actual laboratory apparatus was a Hele-Shaw cell 5 cm by 20 cm, but we use a two-dimensional porous medium with physical dimensions and parameters scaled for similarity to Elder's work. These parameters are presented in Table 1. Note that we have used heat capacity of zero for the matrix rock for similarity to pure solutal convection. The domain, boundary conditions, and coarsest discretization (60 x 32) for the problem are presented in Fig. 1. The flow and temperature fields at t = 2 yrs. are shown in Fig. 2. For a more complete discussion and analysis of the Elder free convection problems, see Oldenburg and Pruess (1994, 1995).

We have used 3 discretizations for the calculation time comparison of the various solvers. These were 60 x 32 gridblocks, 84 x 40 gridblocks, and 128 x 64 gridblocks in the Y- and Z-directions, respectively; NX is always 1 in this two-dimensional problem. With three equations per gridblock, these discretizations give rise to Jacobian matrices of order (N) equal to 5760, 10080, and 24576, respectively. Non-zero elements of the Jacobian matrix occur in bands of width 197, 245, and 389, for the three discretizations.

Given the many ways one can time multi-processor computations, we chose a simple method that we felt would make sense to users experienced with serial workstations. The timings presented are calculation times, as obtained by the TOUGH2 subroutine SECOND, divided by the number of linear equation solutions performed. Thus the time is an average time for one Newtonian iteration including the small overhead from other subroutines such as MULTI and EOS, among others. Timings of the solution of the Elder problem with three different two-dimensional discretizations are presented in Fig. 3.

We see in Fig. 3 that the MPDS running on the DPU is faster than the conjugate gradient solver DSLUGM running on the DecAlpha 3000/300x front end for all three discretizations. The performance of DSLUGM on this test problem degrades sharply as the order of the Jacobian matrix increases. The MPDS is about 30% slower than the conjugate gradient solvers DSLUBC and DSLUCS for the largest example problem. It is

important to emphasize that MPDS is a direct solver and is inherently more robust than iterative solvers. As such, it will be valuable as a tool to check upon the veracity of a given conjugate gradient solution, and may prove indispensible for certain difficult problems where the iterative conjugate gradient solvers may converge poorly.

Among the limitations of the MPDS on the MP-2204 are the memory restrictions of 64 kbytes per processor, and a 64 x 64 processor array. This memory limit affects calculation speed based upon both the bandwidth and the order of the matrix for a given problem. Another limitation is the relatively slow double-precision floating point operation on the MasPar processors. Communication between memory and processors is another factor affecting speed in parellel computing. For example, each processor element on the MP-2204 has its own local memory and sharing data between processors or between processors and the front end requires communication that can take considerable time. Nevertheless, the maximum size problem MPDS can handle will scale with the machine. MPDS will require no recoding to run larger problems on machines with more processors.

CONCLUSIONS

Guided by the considerable potential benefits and risks of developing a massively parallel subsurface simulation code, we have initiated development of a massively parallel version of TOUGH2 called MP-TOUGH2. We implemented the massively parallel direct solver MPDS to perform the generic and time-consuming task of linear equation solution in MP-TOUGH2. In this initial code, the essentially unmodified TOUGH2 is compiled in Fortran77 and runs on the front end. This code calls the MPDS which is written and compiled in Fortran90 and uses the DPU. We tested the MPDS on a strongly coupled two-dimensional pure thermal convection problem. Comparison of calculation times shows the MPDS to be competitive with the iterative conjugate gradient solvers on the front end. Because MPDS is a direct solver, it will be useful for establishing correct solutions and verifying conjugate gradient solver solutions. In addition, it may find application in solving problems where the iterative solvers coverge slowly, or fail. Future work will focus on testing and improving the MPDS as well as targeting other TOUGH2 tasks where data-parallelism can be exploited.

Acknowledgments

We thank the MasPar Computer Corporation for their generous contributions and continued support, and Frank Hale and Stefan Finsterle for reviews. This work was supported by the Assistant Secretary for Energy Efficiency and Renewable Energy, Geothermal Division, of the U.S. Department of Energy under Contract No. DE-AC03-76SF00098.

Nomenclature

C	heat capacity	$J\,kg^{-1}\,°C^{-1}$
g	gravitational acceleration	$m\,s^{-2}$
k	permeability	m^2
K	thermal conductivity	$J\,s^{-1}\,m^{-1}\,°C^{-1}$
N_S	slab width	
R	residual	kg

t	time	years
T	temperature	°C
X	X-coordinate	m
Y	Y-coordinate	m
Z	Z-coordinate (positive upward)	m

Greek symbols

μ	dynamic viscosity	kg m $^{-1}$ s $^{-1}$
ϕ	porosity	-
ρ	density	kg m $^{-3}$

Subscripts and superscripts

k	time step index
n	grid block index
p	Newtonian iteration index
κ	mass components

REFERENCES

Dongarra, J.J., C.B. Moler, J.R. Bunch, and G.W. Stewart, *LINPACK Users' Guide*, pg. 2.1, Society of Industrial and Applied Mathematics (SIAM), Philadelphia, 1979.

Elder, J.W., Transient convection in a porous medium, *J. Fluid Mech.*, *27*(3), 609–623, 1967.

MasPar Mathematics Library, *Document Part Number 9302-5001*, MasPar Computer Corporation, 749 North Mary Ave., Sunnyvale CA 94086, 1993.

Moridis, G.J., K. Pruess, T2CG1, A package of preconditioned conjugate gradient solvers for the TOUGH2 family of codes, Lawrence Berkeley *Laboratory Report, LBL-36235*, Berkeley, California, March 1995.

Oldenburg, C.M. and Pruess, K., Numerical simulation of coupled flow and transport with TOUGH2: A verifictation study, *Lawrence Berkeley Laboratory Report*, *LBL-35273*, Berkeley, California, October 1994).

Oldenburg, C.M. and Pruess, K., Dispersive transport dynamics in a strongly coupled groundwater-brine flow problem, *Water Res. Res, 31*(2), 289–302, 1995.

Pruess, K., TOUGH User's Guide, Nuclear Regulatory Commission, Report NUREG/CR-4645, June 1987 (also *Lawrence Berkeley Laboratory Report*, *LBL-20700*, Berkeley, California, June 1987).

Pruess, K., TOUGH2 - A General Purpose Numerical Simulator for Multiphase Fluid and Heat Flow, *Lawrence Berkeley Laboratory Report*, *LBL-29400*, Berkeley, California, May 1991).

Table 1. Parameters for the Elder (1967) pure thermal convection problem.

symbol	quantity	value	units
ϕ	porosity	.1	–
k	permeability	1.21×10^{-10}	m^2
μ	viscosity ($T = 20°C$)	1.0×10^{-3}	Pa s
K	thermal conductivity	1.49	$J\,kg^{-1}\,s^{-1}\,m^{-1}$
C	heat capacity of rock	0.	$J\,kg^{-1}\,°C^{-1}$
g	gravity	9.81	$m\,s^{-2}$
T_0	initial temperature	12.	°C

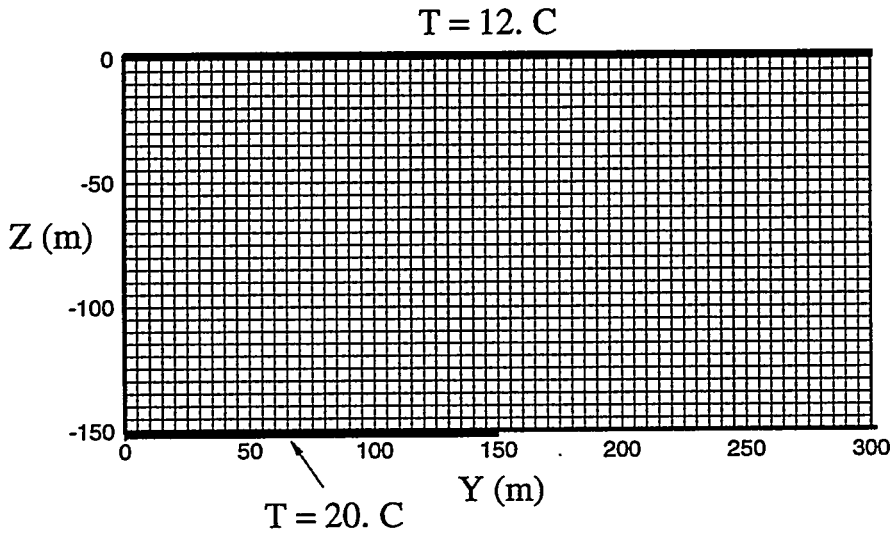

Figure 1. Domain and boundary conditions for the Elder pure thermal convection problem with the 60 x 32 gridblock mesh.

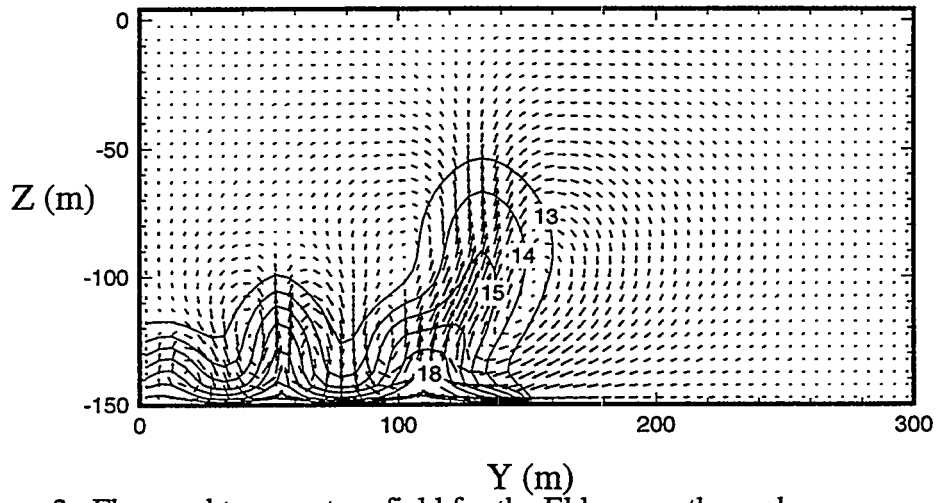

Figure 2. Flow and temperature field for the Elder pure thermal convection problem at $t = 2$ yrs.

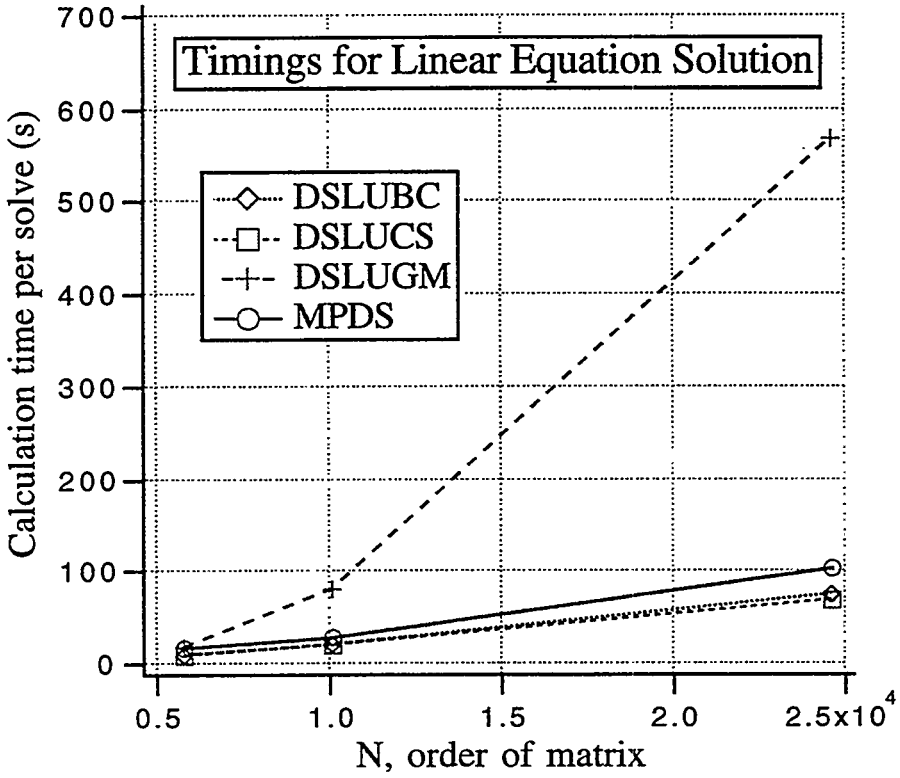

Figure 3. Calculation time plotted against N, the order of the Jacobian matrix, for three conjugate gradient solvers (DSLUBC, DSLUCS, DSLUGM) and for the massively parallel direct solver (MPDS).

A New Lumped-Parameter Approach to Simulating Flow Processes in Unsaturated Dual-Porosity Media

Robert W. Zimmerman, Teklu Hadgu, and Gudmundur S. Bodvarsson

Earth Sciences Division
Lawrence Berkeley Laboratory
University of California
Berkeley, CA 94720

Abstract: We have developed a new lumped-parameter dual-porosity approach to simulating unsaturated flow processes in fractured rocks. Fluid flow between the fracture network and the matrix blocks is described by a nonlinear equation that relates the imbibition rate to the local difference in liquid-phase pressure between the fractures and the matrix blocks. This equation is a generalization of the Warren-Root equation, but, unlike the Warren-Root equation, is accurate in both the early and late time regimes. The fracture/matrix interflow equation has been incorporated into a computational module, compatible with the TOUGH simulator, to serve as a source/sink term for fracture elements. The new approach achieves accuracy comparable to simulations in which the matrix blocks are discretized, but typically requires an order of magnitude less computational time.

Introduction

In a dual-porosity medium such as a fractured/porous rock mass, an interconnected network of fractures provides most of the global permeability, whereas most of the fluid storage takes place in the relatively low-permeability matrix blocks. In principle, one way to model flow in a fractured/porous rock mass would be to explicitly account for each fracture and each matrix block in the computational mesh. In practice this is rarely possible, due to the large number of gridblocks that would be needed, and to the difficulty in gathering the necessary information concerning the locations, lengths, and individual transmissivities of the fractures.

Another approach, which is more tractable, is the MINC method (Pruess and Narasimhan, 1985). In this approach, the fracture network is treated as a continuum, which is then discretized into fracture gridblocks. The matrix blocks that are located in the region occupied by each fracture gridblock are then represented by a single nested set of shell-like elements. This usually requires many fewer elements than would be needed in a discrete-fracture simulation, but still requires about 5-10 times as many matrix elements as fracture elements.

One way to eliminate the need for discretizing the matrix blocks is to treat them in a lumped-parameter manner, using only mean values of the pressure, saturation, etc. The matrix blocks then serve as source/sinks for the fracture elements. This approach was used by Barenblatt et al. (1960) and Warren and Root (1963), who assumed that the strength of the source/sink was proportional to the difference in potential between the fractures and matrix blocks. We have used a nonlinear modification of their approach, and implemented it into a computational module that is compatible with TOUGH. Our approach, which is summarized below, is also described in more detail by Zimmerman et al. (1995).

Warren-Root Method

In the traditional lumped-parameter approach (Barenblatt et al., 1960; Warren and Root, 1963) flow is assumed to take place through the fracture network, and also between the fractures and the matrix blocks. Each point in space has associated with it two sets of parameters, for the fractures and for the matrix blocks. The rate of flow between the fractures and matrix blocks must be expressed as some function of

the local fracture pressure, the local mean matrix pressure, and other properties such as the permeabilities, etc. In order to maintain the linearity of the equations, Barenblatt et al. (1960) and Warren and Root (1963) assumed that the volumetric flow rate of fluid from the fractures into the matrix blocks, per unit volume of matrix block, was governed by

$$q = \frac{\alpha k_m V_m}{\mu}(P_f - \bar{P}_m), \qquad (1)$$

where k_m is the permeability of the matrix block, μ is the viscosity of the fluid, P_f is the local pressure in the fractures, $\bar{P}_m$ is the mean pressure in the matrix block at a specified point in the fracture continuum, V_m is the volume of the matrix block, and α is a geometric factor that has dimensions of $[L^{-2}]$. The flowrate q given in eq. (1) therefore has dimensions of $[L^3 T^{-1}]$. The relationship between the numerical value of α and the size and shape of the matrix block is discussed by deSwaan (1990) and Zimmerman et al. (1993).

The flow of fluid into the matrix block causes the fluid pressure in the block to increase. If the fluid is a slightly-compressible liquid, this pressure increase is described by

$$\phi_m c_m V_m \frac{d\bar{P}_m}{dt} = q\,, \qquad (2)$$

where ϕ_m is the (dimensionless) porosity of the matrix block, and c_m, with dimensions of $[P^{-1}]$, is the combined compressibility of the pore fluid and the pore space of the matrix blocks. If eqs. (1) and (2) are combined, they yield the following equation that governs the fluid pressure in the matrix block:

$$\frac{d\bar{P}_m}{dt} = \frac{\alpha k_m}{\phi_m \mu c_m}(P_f - \bar{P}_m). \qquad (3)$$

For saturated flow of a slightly-compressible fluid, eq. (3) represents the most-slowly-decaying Fourier mode in the exact solution for infiltration into a matrix block (Zimmerman et al., 1993). As such, it correctly models the long-time, quasi-equilibrium regime of fracture/matrix interaction. However, as it does not contain any of the higher modes, it is not accurate at earlier stages of imbibition (deSwaan, 1990; Zimmerman et al., 1993). When incorporated into a dual-porosity model, the Warren-Root equation leads to qualitatively incorrect behavior during the transition between fracture-dominated and effective-continuum flow regimes (Najurieta, 1980).

Dykhuizen (1990) attempted to remedy this situation by essentially using two different equations for fracture/matrix flow, one in the early-time regime, and one in the late-time regime. Another related approach is that of Pruess and Wu (1993), who used the integral method to model flow in the matrix block using a polynomial pressure profile. This is not a lumped-parameter approach, but is similar in that only a small number of parameters are needed to account for the thermodynamic state of the matrix block, and the fracture/matrix flow interactions.

We use a variation of Dykhuizen's approach, wherein a single equation is found that seems to accurately represent the flowrate at both late and early times. This equation, which is derived from an approximate solution found by Vermeulen (1953) for diffusion into a spherical block, is

$$q = \frac{\alpha k_m V}{\mu} \frac{[(P_f - P_i)^2 - (\bar{P}_m - P_i)^2]}{2(\bar{P}_m - P_i)}, \qquad (4)$$

where P_i is the initial pressure in the matrix block, and α is the same shape factor that is used in the Warren-Root equation. When $\bar{P}_m$ is close to P_f, which is to say that the matrix and fractures are nearly in equilibrium with each other, eq. (4) reduces to eq. (1). However, eq. (4) is also accurate at early times, when the fracture pressure is varying rapidly and the matrix pressure has not yet had sufficient time to respond (see Zimmerman et al., 1993).

Unsaturated Flow Simulation Procedure

We have implemented a Vermeulen-type expression for fracture/matrix flow as part of a module of subroutines that is compatible with TOUGH (Pruess, 1987). The saturated flow version of this procedure is described by Zimmerman et al. (1993); here we focus on the unsaturated flow version.

TOUGH contains provisions for sources/sinks of mass and heat, which are calculated in the subroutine QU. The sources/sinks are typically used to account for fluid that is injected or withdrawn from a borehole that penetrates one of the gridblocks. We have modified this subroutine so as to include a new type of source/sink, which represents liquid water flowing into (or out of) the fracture gridblock from the matrix blocks

that are contained in a given fracture gridblock. The magnitude of the fracture/matrix flux for each fracture gridblock is computed using

$$q = \frac{\alpha V_m k_m k_r}{\mu} \frac{[(\psi_f - \psi_i)^2 - (\bar{\psi}_m - \psi_i)^2]}{2(\bar{\psi}_m - \psi_i)}, \quad (5)$$

where ψ is the capillary pressure, and k_r is the relative permeability of the matrix block. As the imbibition rate is primarily controlled by the hydraulic conductivity of the matrix block at the wetted boundary, we evaluate k_r at the capillary pressure that exists at the outer boundary of the matrix block, which is to say at the capillary pressure of the fracture. Note that the actual driving force for flow is the difference in liquid phase pressure; however, as the air phase pressure is assumed to be the same in the matrix and their adjacent fractures (i.e., the Richards approximation; see Zimmerman et al., 1995), the difference in liquid phase pressures is equivalent to the difference in capillary pressures. The volume V_m represents the total volume of matrix rock contained within the fracture gridblock; it is related to the volume of the fracture gridblock by $V_m = (1-\phi_f)V_f$, where $\phi_f \ll 1$ is the fracture porosity.

The generation term q represents the average instantaneous flux out of a given fracture gridblock, over the time interval $[t, t+\Delta t]$. To make the calculation fully implicit, the flux is computed using the values of the variables at time $t+\Delta t$. The new value of $\bar{\psi}_m$ that exists in the matrix block at time $t+\Delta t$ must be consistent with the new average saturation. From a mass balance in the matrix block, the new average saturation at time $t+\Delta t$ is given by

$$\bar{S}_m(t+\Delta t) = \bar{S}_m(t) + \frac{q\,\Delta t}{\phi_m V_m}. \quad (6)$$

The mean saturation $\bar{S}_m$ and the mean capillary pressure $\bar{\psi}_m$ are related to each other through the capillary pressure function of the matrix rock:

$$\bar{\psi}_m = f(\bar{S}_m), \quad (7)$$

where f is the capillary pressure function. At each TOUGH iteration, eqs. (5,6,7) are iterated (for each fracture gridblock) to find a consistent set of values of $\{\bar{\psi}_m, \bar{S}_m, q\}$. We must also calculate additional contributions to the Jacobian matrix, whose components are the partial derivatives of the energy, water and air residuals with respect to changes in the primary variables, which are the liquid saturation, the gas phase pressure, and the temperature. In our formulation, we neglect the possible presence of dissolved air in the water that flows between the fracture elements and their associated matrix blocks. However, we do include the latent heat that is transported with the liquid, which is calculated by multiplying the mass flux given by eq. (5) by the liquid phase enthalpy.

Example: Flow in a Leaky Fracture

As an example of the use of the new approach, consider the problem of water flowing along a single fracture imbedded in a porous matrix (Travis et al., 1984; Martinez, 1987; Nitao and Buscheck, 1991). Flow into the fracture is driven by the imposed potential at the inlet boundary, which we take to be zero in the following example. For the matrix blocks, we use the hydrological parameters that have been estimated for the Topopah Spring Member of the Paintbrush Tuff at Yucca Mountain (Rulon et al., 1986). In terms of the van Genuchten (1980) parameters, these properties are $k = 3.9\times10^{-18}\,\mathrm{m}^2$, $\phi = 0.14$, $n = 3.04$, $\alpha_{vg} = 1.147\times10^{-5}\,\mathrm{Pa}^{-1}$, $S_s = 0.984$, and $S_r = 0.318$. For the fracture, we use the properties that were derived by Pruess et al. (1988) using a mathematical model of a fracture as a rough-walled channel: $k = 5.5\times10^{-11}\,\mathrm{m}^3$ (per fracture), $n = 2.89$, $S_s = 1.0$, $S_r = 0.0$, and $\alpha_{vg} = 6.06\times10^{-4}\,\mathrm{Pa}^{-1}$. The volumes of the fracture elements were chosen to correspond to an aperture of 800 μm. This relatively large aperture was chosen so as to accentuate the early-time regime of the solution, in which matrix imbibition is not yet of much consequence, so as to clearly verify whether or not the new method is capable of capturing the transition between the two regimes.

The fracture was discretized into 45 elements, with the length of the n–th element given by $L_n = (1.2)^{n-1}\,\mathrm{m}$; *i.e.,* the element lengths were 1.0 m, 1.2 m, 1.44 m, etc. Relatively small fracture gridblocks are needed near the inlet in order to accurately model the diffusive front, particularly at small times. The temperature was taken to be 20°C, and the initial capillary pressure was taken to be 1.013×10^5 Pa. This capillary pressure corresponds, through the capillary pressure functions, to an initial matrix saturation of 0.6765, and an initial fracture saturation of 0.0004.

We have solved this problem using TOUGH with the new dual-porosity module to perform the fracture/matrix interaction calculations, and also using TOUGH without the source/sink expressions, but with explicit discretization of the matrix rock adjacent to the fracture. When solving the problem with explicit discretization of the fracture and matrix regions, the matrix elements must be extended sufficiently far into the the formation so as to effectively simulate a semi-infinite region. This distance will depend on the total elapsed time of the simulation. In the example simulation, which covered an elapsed time of 10^8 s (about 3 years), the matrix elements were extended about 20 m away from the fracture. This was achieved using 20 matrix gridblocks in the direction transverse to the fracture, with the thickness of the n–th gridblock given by $L_n = (2.0)^n \times 10^{-5}$ m. The total length of matrix gridblocks in the direction normal to the fracture was therefore equal to 21.97 m. Note that very small matrix gridblocks are needed near the fracture in order to accurately resolve the saturation fronts in the matrix at small times.

The instantaneous flowrate of liquid into the fracture at the inlet is shown in Fig. 1. At early times, no appreciable leakage has taken place into the relatively impermeable matrix, and the flow field is essentially that of diffusive flow along the fracture. In this regime the flux into the fracture at the inlet decays as $t^{-1/2}$. As time progresses, the wetted interface area between the fracture and the matrix rock increases, and the effect of leakage becomes more important. The overall flowrate into the fracture gradually changes from a $t^{-1/2}$ variation to a $t^{-1/4}$ variation, as was predicted theoretically by Nitao and Buscheck (1991). The saturation profiles in the fracture are plotted in Fig. 2, at elapsed times of 10^4 s, 10^6 s, and 10^8 s. At each time, there is close agreement between the saturation profile predicted by the new lumped-parameter method, and that predicted using a discretized matrix.

The amounts of CPU time needed for the simulations, which were performed on a Solbourne (Series 5) computer, are shown in Table 1. In each case the simulation was carried out to 10^8 s, starting with an initial timestep of 0.01 s, and with no restrictions placed on the timestep growth. The lumped-parameter approach required about 70% fewer timesteps than did the fully-discretized solution, which is to say it allowed, on the average, timesteps that were about 3.38 times larger. The total number of Newton-Raphson iterations needed by the fully-discretized simulation was about 3.04 times greater than that needed by the lumped-parameter method. The savings in CPU time for the new method was about 96%, which corresponds to a 25-fold increase in speed. This reflects both an increased speed per iteration, and a need for a fewer total number of iterations to reach the desired total simulation time of 10^8 s.

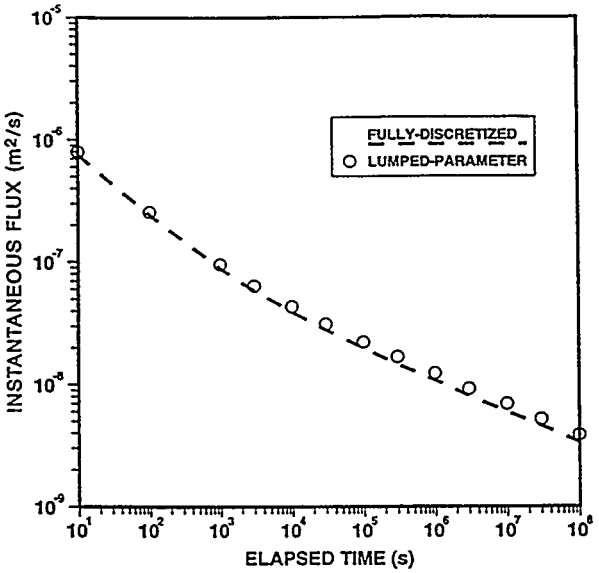

Fig. 1. Instantaneous flux into leaky fracture.

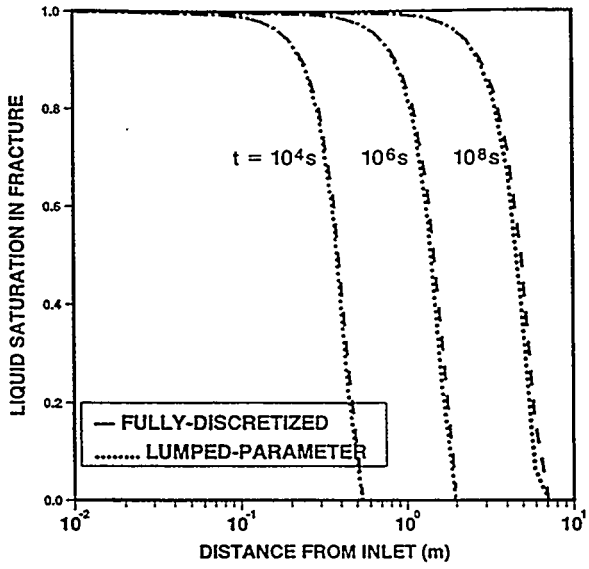

Fig. 2. Saturation profile in the fracture.

Table 1. CPU times for the problem of horizontal flow along a fracture located in a permeable formation. Both simulations were conducted with TOUGH running on a Solbourne (Series 5) computer.

	Fully-Discretized	Lumped-Parameter
# Fracture elements	45	45
# Matrix elements	45×20=900	0
Total # elements*	946	46
Timesteps	624	185
Iterations	3205	1053
CPU time (s)	20901	823

* Including one boundary element

Conclusions

A new lumped-parameter formulation has been developed for unsaturated flow in dual-porosity media. Fluid flow from the fracture network into the matrix blocks is modeled by a nonlinear equation, which can be thought of as a nonlinear extension of the Warren-Root equation. This expression for fracture/matrix flow has been incorporated into a module that is compatible with the TOUGH simulator, to act as a source/sink term for the fracture elements. The use of the modified code has been demonstrated on the problem of flow along a single horizontal fracture in a permeable rock, under constant-head boundary conditions. The new method gives very close agreement with simulations carried out by explicitly discretizing the matrix blocks, while yielding a substantial savings in CPU time. The new method also permits a simplification in the process of creating the mesh and the TOUGH input file. Other examples, and more details, can be found in Zimmerman et al. (1995).

Acknowledgments

This work was carried out under U.S. Department of Energy Contract No. DE-AC03-76SF00098, administered by the DOE Nevada Office, in cooperation with the U. S. Geological Survey, Denver. This work has benefited from the comments of our LBL colleagues Christine Doughty, Karsten Pruess, Yvonne Tsang and Joseph Wang.

References

Barenblatt, G. I., Zheltov, Y. P., and Kochina, I. N. (1960). Basic concepts in the theory of seepage of homogeneous liquids in fissured rocks, *J. Appl. Math. Mech., Engl. Transl.*, **24,** 1286-1303.

deSwaan, A. (1990). Influence of shape and skin of matrix-rock blocks on pressure transients in fractured reservoirs, *SPE Form. Eval.*, **5,** 344-352.

Dykhuizen, R. C. (1990). A new coupling term for dual-porosity models, *Water Resour. Res.*, **26,** 351-356.

Martinez, M. J. (1987). Capillary-driven flow in a fracture located in a porous medium, *Rep. SAND84-1697,* Sandia National Laboratory, Albuquerque, N.M.

Najurieta, H. L. (1980). Theory for pressure transient analysis of naturally fractured reservoirs, *J. Pet. Tech.*, **32,** 1241-1250.

Nitao, J. J., and Buscheck, T. A. (1991). Infiltration of a liquid front in an unsaturated, fractured porous medium, *Water Resour. Res.*, **27,** 2099-2112.

Pruess, K. (1987). TOUGH user's guide, *Report LBL-20700,* Lawrence Berkeley Laboratory, Berkeley, Calif.

Pruess, K., and Narasimhan, T. N. (1985). A practical method for modeling fluid and heat flow in fractured porous media, *SPE J.*, **25,** 14-26.

Pruess, K., and Wu, Y. S. (1993). A new semianalytical method for numerical simulation of fluid and heat flow in fractured reservoirs, *SPE Adv. Tech. Ser.*, **1,** 63-72.

Pruess, K., Wang, J. S. Y., and Tsang, Y. W. (1988). Effective continuum approximation for modeling fluid and heat flow in fractured porous tuff, *Report LBL-20778,* Lawrence Berkeley Laboratory, Berkeley, Calif.

Rulon, J., Bodvarsson, G. S., and Montazer, P. (1986). Preliminary numerical simulations of groundwater flow in the unsaturated zone, Yucca Mountain, Nevada, *Report LBL-20553,* Lawrence Berkeley Laboratory, Berkeley, Calif.

Travis, B. J., Hodson, S. W., Nuttall, H. E., Cook, T. L., and Rundberg, R. S. (1984). Preliminary estimates of water flow and radionuclide transport in Yucca Mountain, *Report LA-UR-84-40,* Los Alamos National Laboratory, Albuquerque, N.M.

van Genuchten, M. Th. (1980). A closed-form equation for predicting the hydraulic conductivity of unsaturated soils, *Soil Sci. Soc. Amer. J.,* **44,** 892-898.

Vermeulen, T. (1953). Theory of irreversible and constant-pattern solid diffusion, *Ind. Eng. Chem.,* **45,** 1664-1670.

Warren, J. E., and Root, P. J. (1963). The behavior of naturally fractured reservoirs, *SPE J.,* **3,** 245-255.

Zimmerman, R. W., Chen, G., Hadgu, T., and Bodvarsson, G. S. (1993). A numerical dual-porosity model with semi-analytical treatment of fracture/matrix flow, *Water Resour. Res.,* **29,** 2127-2137.

Zimmerman, R. W., Hadgu, T., and Bodvarsson, G. S. (1995). Transient dual-porosity simulations of unsaturated flow in fractured rocks *Report LBL-36807* Lawrence Berkeley Laboratory, Berkeley, Calif.

Extended abstract submitted to the TOUGH Workshop '95
Lawrence Berkeley Laboratory, Berkeley, CA, March 20-22, 1995

USE OF TOUGH2 ON SMALL COMPUTERS

Emilio Antúnez, Karsten Pruess, and George Moridis

Earth Sciences Division, Lawrence Berkeley Laboratory
University of California, Berkeley, CA 94720

ABSTRACT

TOUGH2/PC has been tested extensively on different PC platforms (486-33, 486-66, Pentium-90), with encouraging results. TOUGH2 performance has also been tested in other 32-bit computers as the MacIntosh Quadra 800, and a workstation IBM RISC 6000. Results obtained with these machines are compared with PCs' performance.

PC results for 3-D geothermal reservoir models are discussed, including: (a) a Cartesian; and (b) a geothermal reservoir model with 1,411 irregular grid blocks. Also discussed are the results of the TOUGH2-compiler performance tests conducted on small computer systems.

Code modifications required to operate on 32-bit computers and its setup in each machine environment are described.

It is concluded that in today's market PCs provide the best price/performance alternative to conduct TOUGH2 numerical simulations.

INTRODUCTION

The PC version of TOUGH2 [Pruess, 1991] was released to the Energy Sciences and Technology Software Center (ESTSC) in January 1995, for distribution. Prior to its release the code was extensively tested by LBL staff and selected Beta Testers. Because of the flexibility/price/performance of the PC environments, the applications and the demand for the TOUGH2/PC code have been steadily increasing.

The success of the PC version of the code has been mainly due to two factors: (a) the migration of applications from mainframes and workstations to PC platforms is completely transparent; and (b) to the addition of a set of three preconditioned conjugate gradient solvers[1] (CG) to TOUGH2 [Moridis *et al.*, 1995]. These solvers make a more

[1] Conjugate Gradient solvers are algorithms for the iterative solution of large sets of linear equations.

efficient use of memory and also provide matrix solutions faster than direct solvers, allowing the processing of larger simulation models in terms of number of grid elements and number of equations to solve. Models of 10,000+ grid elements have been processed successfully with TOUGH2 on PC type computers [Antúnez *et al.*, 1994, 1995]. All versions of TOUGH2 distributed by the ESTSC have been updated to include the CG solvers package to complement its standard direct solver MA28 [Duff, 1977].

Considering that current personal computers (PCs) have the same or more computational power than mainframes and minicomputers of a few years ago, it is not surprising that TOUGH2 applications traditionally executed on mainframes and minicomputers had started migrating towards the more cost-effective PC platforms. The PC code is currently being used at LBL in geothermal reservoir engineering, nuclear waste disposal, environmental restoration, and unsaturated groundwater hydrology.

PCs SETUP AND REQUIREMENTS

The TOUGH2 code requires 64-bit arithmetic. When using a 32-bit machine (i.e., machines with 386, 486 or higher processor and MacIntosh Quadra 800 68040 CPU), it is necessary to modify the code to declare all variables REAL*8 (or DOUBLE PRECISION), and to comply with the FORTRAN77 ANSI X-3.9-1978 standards, also all floating point constants must be converted from E##.# to D##.# format. The processing speed of the code will depend on the machine being used. The maximum size of computational grids will depend on the amount of extended memory (XMS) available on the machine[2]. A minimum configuration to run TOUGH2/PC (Antúnez *et al.*, 1994) would be a 386 PC equipped with 4 MB of RAM, an 80 MB hard drive and an optional (but recommended) numerical coprocessor (387). This configuration will allow to perform 3-D simulations[3] with grids of approximately 1,000 elements and 3,000 connections when using the CG solvers; or approximately 500 elements and 1,500 connections using the standard version of TOUGH2/PC with the direct matrix solver (MA28). The MacIntosh (Mac) memory requirements are similar to the PC's.

Very large models of up to 10,000 grid elements were run on a 486-DX2-66 MHz PC equipped with 32 MB of RAM and a 250 MB hard drive (Fig. 1). TOUGH2/PC was compiled and linked using Version 5.0 of the Lahey FORTRAN Compiler for 32-bit machines (Antúnez, *et al.* 1994). The study was limited to grids with a maximum of 10,000 elements; however, the previous configuration should be able to handle models with larger number of elements. Antúnez, et al (1994) concluded that the Lanczos-type Bi-Conjugate Gradient Squared [Sonneveld, 1989] was the fastest of the solvers and that it is the best choice on the basis of its performance efficiency, and its only slightly faster than linear growth of computation time and memory requirements with problem size. For

---

[2] Extended memory (XMS) is additional memory beyond the first MByte (MB) of random access memory (RAM). The first MB of RAM is usually occupied by the Disk Operating System (DOS), the 640 KB of DOS conventional memory and the Terminate and Stay Resident applications (TSR).

[3] 3-D simulations are the most memory demanding. 1-D and 2-D problems result in arrays of smaller size.

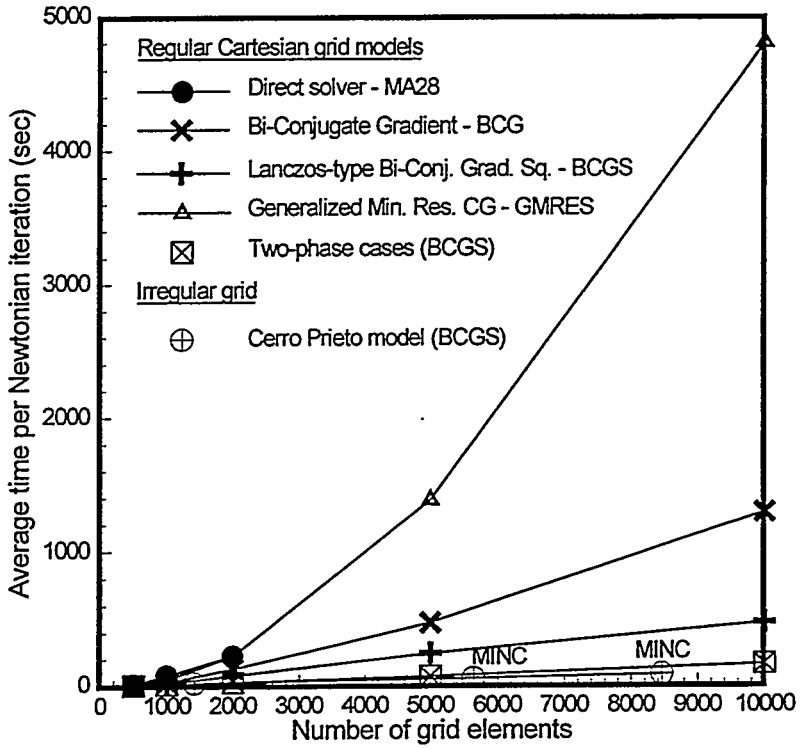

Fig. 1: Timing of Newtonian iterations for each of the analyzed matrix solvers as function of problem size [Antúnez *et al.*, 1994]

these reasons it was selected as the solver to use for the TOUGH2/machine's performance testing and became the default solver on the updated versions of TOUGH2.

DISCUSSION OF RESULTS

To compare the performance of the different solvers, the average timing of all Newtonian iterations[4] per run was plotted by Antúnez *et al.*, (1994) against the number of elements in the grid. Timing data of the various solvers are presented in Fig. 1.

[4] The testing was based on the average time it took each algorithm to complete a Newtonian iteration, which consists of: (a) Recalculating the terms of the Jacobian matrix that results from applying the mass and energy conservation equations at each grid element; (b) Preconditioning (except for the direct solver MA28) and solving the matrix using one of the CG solvers. The matrix solution provides the changes of all primary variables (pressure, temperature) for single-phase elements or (pressure, vapor saturation) for elements in two-phases; and (c) recalculating all the secondary variables (density, internal energy, viscosity, relative permeabilities, capillary pressure, phase saturation, mass fractions of each component) for all the elements of the grid.

For each Newtonian iteration, the CG solvers perform "internal" iterations of the CG algorithm (CG iterations) up to a hardcoded maximum (usually 10% of the number of elements times the number of equations per element). A closure (convergence) criterion of 10^{-6} was used in all three CG solvers.

Cartesian models and an irregular grid model developed for the Cerro Prieto geothermal field [Antúnez and Lippmann, 1993] were used to test the matrix solvers. The Cerro Prieto model was used for testing with: (a) a single porosity and (b) double-porosity formulations. The MINC method [Pruess, 1991] was used for the double-porosity calculations. From this study it was concluded that:

- Time comparisons for the different tested cases indicate that of the three CG tested, the BCGS solver showed the best performance, followed by BCG, MA28 and GMRES.
- The tested conjugate gradient solvers significantly reduced the execution time and storage requirements, making possible the execution of considerably larger problems (10,000+ grid blocks) on PCs.
- Memory requirements for TOUGH2/PC with the conjugate gradient solvers are approximately linear
- The Antúnez *et al.*, (1994) study demonstrates that the combination of the analyzed preconditioned conjugate gradient solvers and the current PCs (386 and higher) are a feasible, economical and efficient combination to conduct large-scale three-dimensional simulations that just a few years ago could only be executed on mainframe computers and high-end workstations.

It is important to emphasize that iterative methods are problem specific. A solver that showed good performance for a given problem is not guaranteed to work for all problems. Testing of the solvers with a specific problem is strongly recommended to determine which is the best for the task.

A comparison of the performance of TOUGH2 on different machines was conducted by Antúnez *et al.* (1995). The average timings of all Newtonian iterations per run were plotted against the machine type and are presented in Figure 2. Time comparisons for the different machines presented in this figure indicate that the three PCs showed performances very similar to the high-end workstation IBM RISC 6000 (model 320H-7012) and one of them, the PC Pentium 90, gave 50% faster performance than the workstation. At the current prices a well-equipped Pentium 90 - based PC costs three to five times less than a comparably equipped RISC 6000. The MacIntosh developed some roundup errors that did not allow the simulation to advance in time. The problem was solved by tightening the closure criteria for the conjugate gradient (from $1x10^{-6}$ to $1x10^{-8}$). This way the roundup errors did not continue increasing and the Mac was able to attain the same total simulation time as the other machines.

By the time this extended abstract was written Apple Computers made available the Power MacIntosh with a processor that uses RISC (Reduced Instruction Set Calculations) architecture and they claim that this machine runs two to six times faster than Quadras. If these specifications are correct, the Macs will be another small machine to consider to run large-scale geothermal simulations.

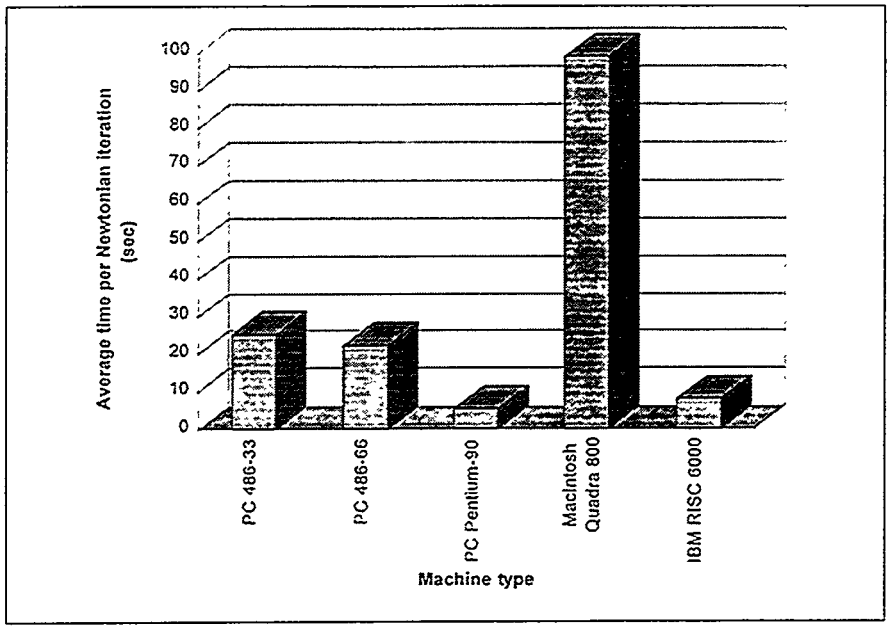

Fig. 2: Timing of Newtonian iterations for different machines using the Cerro Prieto model, the simulation code TOUGH2 and a Lanczos type biconjugate Gradient Squared solver [Antúnez *et al.*, 1995].

It is worth noticing that the results presented in Fig. 2 reflect not only the performance of the machine but also the efficiency of the executable code produced by its respective FORTRAN compiler. The details of the compilers used on each machine are given by Antúnez *et al.*, (1995). Each FORTRAN compiler was used on its respective computer system set to full optimization.

The discussed studies by Antúnez *et al.*, (1994 and 1995) demonstrate that the current PCs (386 and higher) are an economical and efficient platform to conduct large-scale three-dimensional simulations, and that they compare or surpass the performance of some of the most popular high-end workstations.

DISCLAIMER

ACKNOWLEDGMENTS

The authors want to express their gratitude to Marcelo Lippmann and Curt Oldenburg of LBL for reviewing this manuscript and for all their helpful suggestions. This work was supported by the Assistant Secretary for Energy Efficiency and Renewable Energy, Geothermal Division, of the U.S. Department of Energy under contract No. DE-AC03-76SF00098.

REFERENCES

Antúnez, E., and Lippmann, M. (1993) Numerical Study of the Effects of Brine Injection on the CP-1 Production Area of Cerro Prieto. Earth Sciences Division Annual Report 1992, Lawrence Berkeley Laboratory report LBID-33000, pp. 97-99.

Antúnez, E., Moridis, G., and Pruess, K. (1994) Large-Scale Three-Dimensional Geothermal Reservoir Simulation on PCs. Proceedings of the Nineteenth Workshop on Geothermal Reservoir Engineering, Stanford, CA, pp 99-106.

Antúnez, E., Moridis, G., and Pruess, K. (1995) Large-Scale Three-Dimensional Geothermal Reservoir Simulation on Small Computer Systems. Proceedings of the World Geothermal Congress, Florence, Italy, May 18-31, in press.

Duff, I. S. (1977) MA28 - A set of Fortran Subroutines for Sparse Unsymmetric Linear Equations. AERE Harwell Report R 8730.

Moridis, G and K. Pruess (1995) A Package of Preconditioned Conjugate Gradient Solvers for the TOUGH2 Family of Codes. Lawrence Berkeley Laboratory report LBL-36235.

Pruess, K. (1991) *TOUGH2* - A General-Purpose Numerical Simulator for Multiphase Fluid and Heat Flow. Lawrence Berkeley Laboratory report LBL-29400.

Sonneveld, P. (1989) CGS, A fast Lanczos-type solver for nonsymmetric linear systems. SIAM J. Sci. Stat. Comput., Vol. 10, No. 1, pp. 36-52.

Graphical User Interface for TOUGH/TOUGH2 - Development of Database, Pre-processor, and Post-processor

Tatsuya Sato, Takashi Okabe, Kazumi Osato, and Shinji Takasugi
Geothermal Energy Research and Development Co., Ltd., Tokyo 103, Japan

Abstract

One of the advantages of the TOUGH/TOUGH2 (Pruess, 1987 and 1991) is the modeling using "free shape" polygonal blocks. However, the treatment of three-dimensional information, particularly for TOUGH/TOUGH2 is not easy because of the "free shape" polygonal blocks. Therefore, we have developed a database named "GEOBASE" and a pre/post-processor named "GEOGRAPH" for TOUGH/TOUGH2 on engineering work station (EWS).

"GEOBASE" is based on the ORACLE[*1] relational database manager system to access data sets of surface exploration (geology, geophysics, geochemistry, etc.), drilling (well trajectory, geological column, logging, etc.), well testing (production test, injection test, interference test, tracer test, etc.) and production/injection history.

"GEOGRAPH" consists of "Pre-processor" that can construct the three-dimensional free shape reservoir modeling by mouse operation on X-window and "Post-processor" that can display several kinds of two/three-dimensional maps and X-Y plots to compile data on "GEOBASE" and result of TOUGH/TOUGH2 calculation.

This paper shows concept of the systems and examples of utilization.

1. Introduction

Processes of geothermal reservoir simulation are as follows; 1) construction of the conceptual hydrothermal model, 2) design of the grid block model, 3) natural state simulation, 4) history matching simulation, and 5) reservoir performance prediction.

On series of the numerical modeling, we have a few hundred to a few thousand of three-dimensional grid blocks. Therefore, we encounter many problems such as are:

1) It takes much time to generate the free shape polygonal blocks. 2) Outputs of TOUGH/TOUGH2 data (ex. P, T, SG, etc.) and observation data of wells (ex. P, T) are three-dimensional data. Therefore, two-dimensional interpolation is not exactly correct and three-dimensional interpolation is essential correctly. 3) It is very difficult to compare the calculated results with observation data. 4) Periodical modification of reservoir model using new data set may be required. Then, it is necessary for adequate reservoir simulations to have the database for managing existing data and new data that will be gotten in future.

We have developed a pre-processor and a post-processor, and a database named "GEOGRAPH" and "GEOBASE" respectively. Using these systems, we are aiming to conduct geothermal simulations efficiently. In this paper, we introduce summary of our systems as shown in Figure 1.

We have developed these systems on HP9000/755 (HP-UX9.03). And we use UNIRAS[*2] and PV-WAVE[*3] for mapping applications, and ORACLE for database platform.

[*1]Product of the Oracle Corporation

[*2]Product of the UNIRAS

[*3]Product of the Visual Numerics Inc.

2. Pre-processor

"Pre-processor" can construct the three-dimensional numerical models for TOUGH/TOUGH2 by mouse operation on X-window (X11R5). Since the program is based on GKS, this code does not depend on hardware so much.

2.1 Grid blocks and rock type definition

We define the grid blocks on the screen in graphics mode (see Figure 2).

1) We define the first element of the XY-plane structure in our grid. Next, we divide it to small blocks.
2) We define the layout of the grid in the z direction. First, we define it to occupy the area between z=zmin and z=zmax. Next, we copy our grid into other layers.
3) We add some regions defining the different rock type over our grid each layer.
4) We define the well blocks.

On these processes, ELEME and CONNE are made, and well block for GENER is defined.

2.2 Boundary and initial condition

We define the boundary and initial condition on the screen in graphics mode.

1) We set temperature and pressure on the top, bottom and side faces for initial condition. Or we can set pressure and temperature along the column of water at boiling point. These values are used to interpolate P and T over the whole face.
2) We set the boundary rocks connecting top, bottom and side faces (if necessary).

On these processes, INCON is made and information of boundary blocks is added to the ELEME and CONNE.

2.3 Parameters

We define the parameters (ROCKS, PARAMS, RPCAP, TIMES, GENER, etc.) on the screen in no graphics mode.

2.4 Generating the TOUGH/TOUGH2 input file

After finishing the above 2.1 to 2.3 stage, we compile each data set and make the input files using the generating input file program. In this stage, a file containing block names and the x, y, z coordinates of the center of the blocks is made.

3. Post-processor

"Post-processor" can display several kinds of two/three-dimensional maps and X-Y plots to compile data on the database and the calculation results of TOUGH/TOUGH2.

3.1 Three-dimensional contouring

Output files of TOUGH/TOUGH2 include each time step information from start to end of calculation. On the post-processor, we can select the data set for required time step using key word that is "TOTAL TIME =". Since the selected time-step data of TOUGH/TOUGH2 output (ex. P, T, SG, etc.) and observation data of wells (ex. P, T) have three-dimensional coordinate system, the cross point of both contour maps of horizontal distribution and the cross section based on two-dimensional data are not coincident exactly (see Figure 3).

Therefore, we use three-dimensional krigging for making contour maps on horizontal plane and vertical plane. On this process, the TOUGH/TOUGH2 output and observation data are used to interpolate each value over three-dimensional regular grid for mapping. After this, we can draw contour maps of horizontal plane and vertical plane.

Figure 4a is the example of contour map for horizontal plane, showing mismatching (residual) value of temperature between calculation and observation. We can know the meaningful matching area of the map by compiling the well pass points on each layer from "GEOBASE" (near well bore). Figure 4b shows the example of contour map for vertical plane. On these figures, the cross point of two contours is interpolated correctly.

And we can draw the three-dimensional bench-cut distribution maps as Figure 5a.

3.2 Three-dimensional flow vector map

Selected data set on the above 3.1 include flow vector information (ex. FLOF, FLOH, etc.). In this stage, we can draw the three-dimensional flow vector map.

Firstly, we pick up the data (ex. FLOF, FLOH, etc.) from TOUGH/TOUGH2 output file. Next, flow vector on each grid block is calculated using CONNE, and plotted on the three-dimensional space.

3.3 x-y graph

On history matching simulation, we have to compare the TOUGH/TOUGH2 outputs with well testing and production/injection data.

Firstly, we select the well blocks. Next, we pick up the data set (ex. T, P, SG, SL, ENTHALPY, etc.) of all time steps. And, we draw calculated results and observation data on the x-y graph.

Figure 6 shows example of matching operation.

4. Database

The data used for construction of conceptual model and the data for matching are stored on database which is based on the ORACLE relational database manager system.

The following data are stored; 1) well depth versus observation data, 2) time versus observation data, 3) two- or three-dimensional coordinate versus observation data. For example, 1) are well trajectory and well log data, 2) are well test and production/injection data, and 3) are distribution of temperature, pressure and geophysical data.

Each data set has header information table and ID code. At first, we search the header table and get the ID code. Then, we get the data set using ID code. And we send the data set to post-processor (see Figure 1).

5. Summary

TOUGH/TOUGH2 is trusted for geothermal simulator. But, we know it is time consuming process to generate model and it is difficult to compare calculated results with observation data. Also, even two-dimensional contouring of the TOUGH/TOUGH2 outputs should be made with three-dimensional interpolation technique, theoretically.

Therefore, we have developed pre-processor, post-processor and database for TOUGH/TOUGH2. We have confirmed using this system that we can make models efficiently and exactly, in addition we can show the performance of reservoir visually.

Reference

Pruess, K., 1987, *TOUGH User's Guide*, Earth Sciences Division, Lawrence Berkeley Laboratory, Univ. of California.

Pruess, K., 1991, *TOUGH2 - A General Purpose Numerical Simulator for Multi Phase Fluid and Heat Flow*, Earth Sciences Division, Lawrence Berkeley Laboratory, Univ. of California.

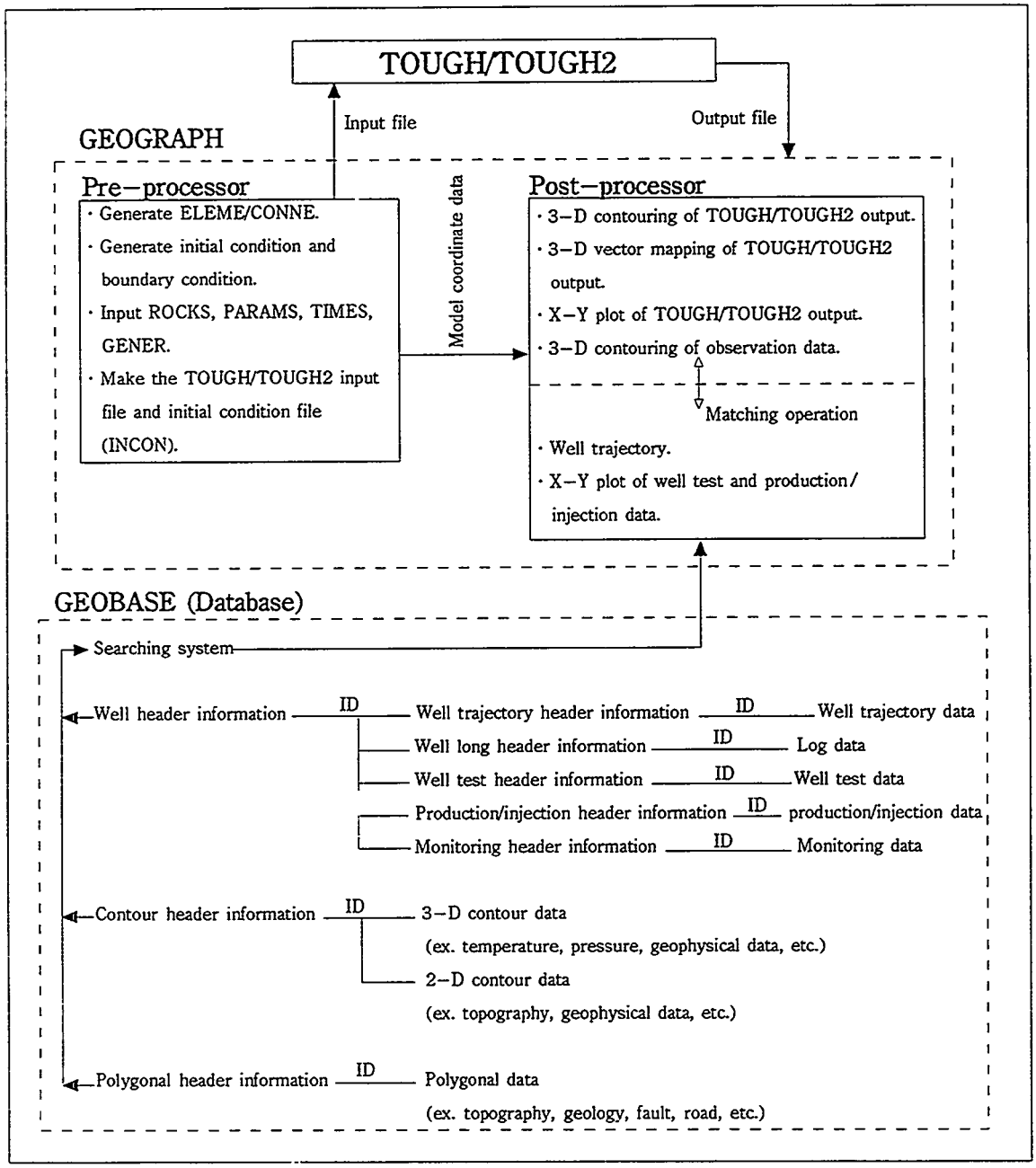

Figure 1. Summary of GEOGRAPH (pre/post−processor) and GEOBASE (database) for TOUGH/TOUGH2.

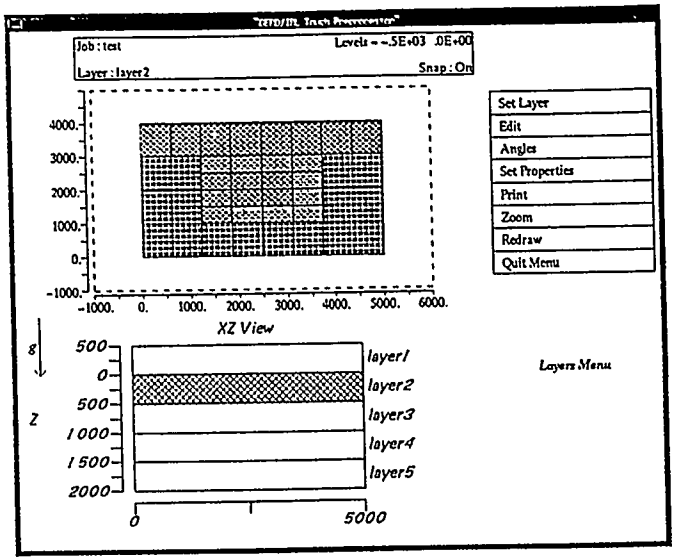

Figure 2. Example of grid blocks and rock type definition on pre-processor.

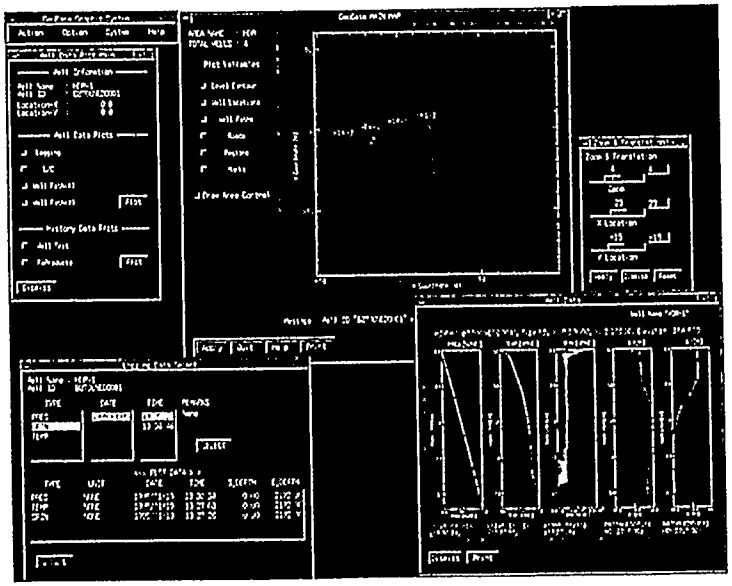

Figure 6. Example of database operation. The display shows searching well log data.

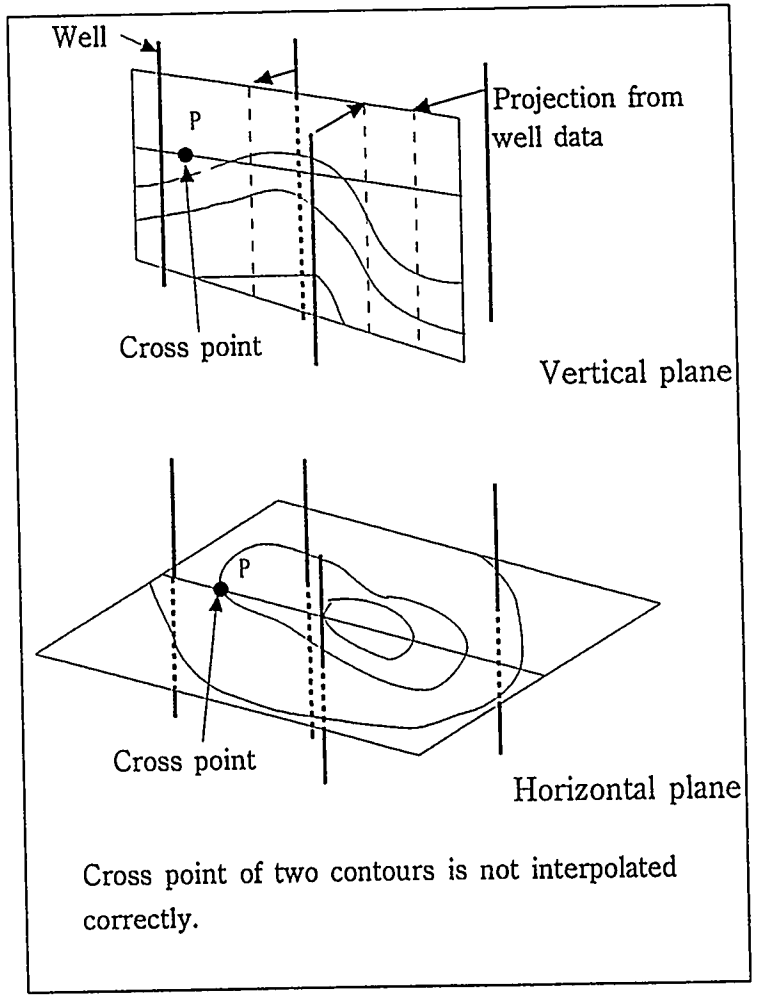

Figure 3. Mismatching of two-dimensional interpolation using three-dimensional data.

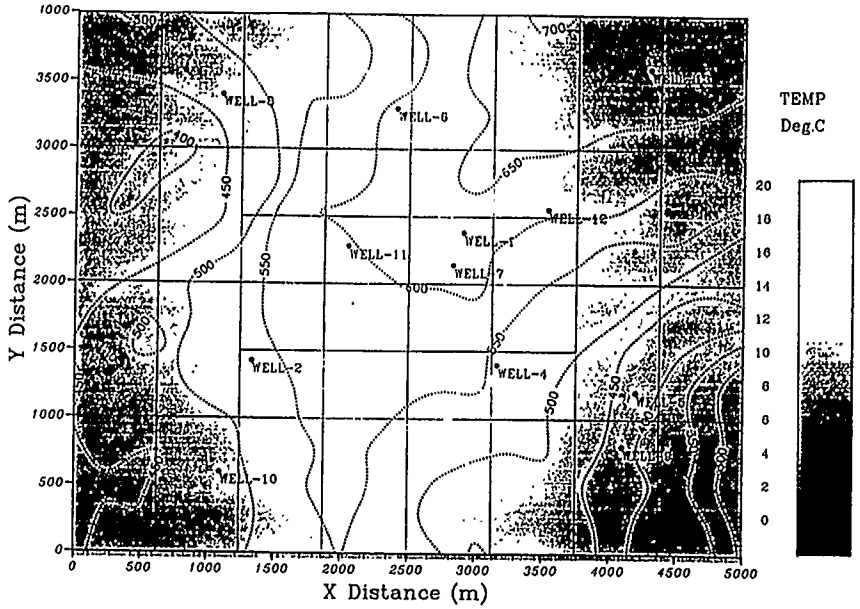

Figure 4a. Example of post-processor contour map (horizontal plane). The contour shows mismatching (residual) value of temperature between calculation and observation.

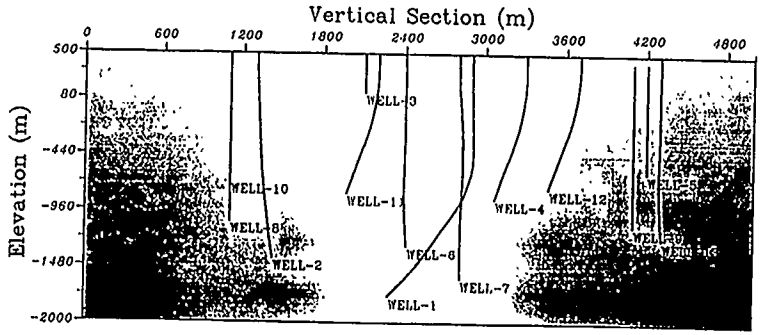

Figure 4b. Example of post-processor contour map (vertical plane). The contour shows mismatching (residual) value of temperature between calculation and observation.

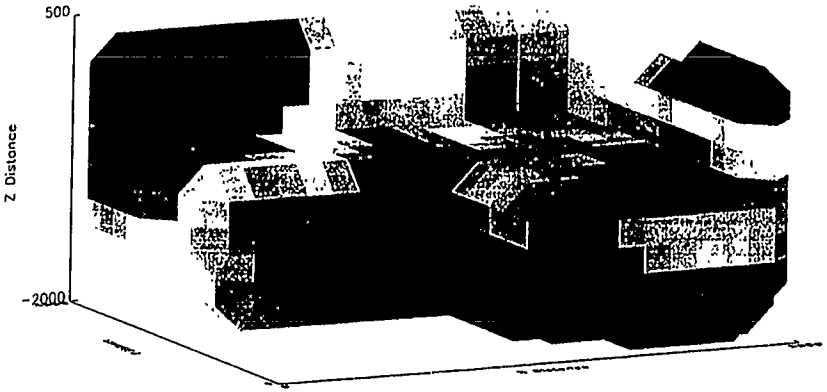

Figure 5a. Example of three-dimensional block map. The block map shows the three-dimensional bench-cut distribution of temperature.

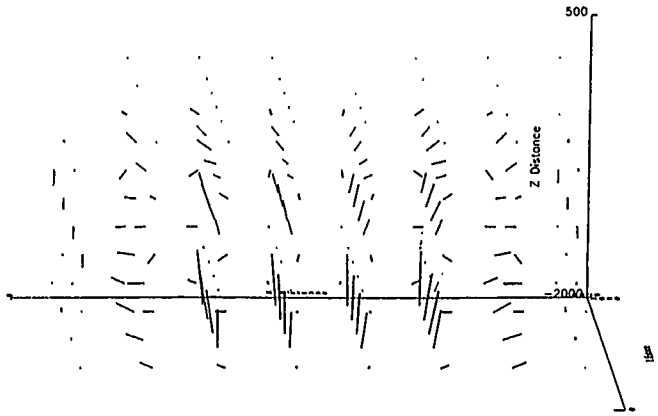

Figure 5b. Example of three-dimensional vector map. The vector map shows fluid flow vector of TOUGH/ TOUGH2 output.

ENERGY SCIENCE AND TECHNOLOGY SOFTWARE CENTER

Edwin M. Kidd, Director

The Energy Science and Technology Software Center (ESTSC), is the U.S. Department of Energy's (DOE) centralized software management facility. It is operated under contract for the DOE Office of Scientific and Technical Information (OSTI) and is located in Oak Ridge, Tennessee. The ESTSC is authorized by DOE and the U.S. Nuclear Regulatory Commission (NRC) to license and distribute DOE- and NRC-sponsored software developed by national laboratories and other facilities and by contractors of DOE and NRC. ESTSC also has selected software from the Nuclear Energy Agency (NEA) of the Organisation for Economic Cooperation and Development (OECD) through a software exchange agreement that DOE has with the agency.

The ESTSC collection consists of almost 900 software packages ready for distribution, and the Center has several hundred older packages that can be made ready on request. The packages available from the Center are applicable to solving many problems in energy, science, environment, administration, mathematics, and computing. Software packages are primarily applications-oriented and developed to run on personal computers, workstations, mainframes, and supercomputers. Packages are also available where the same source code can be loaded on different types of computers. These are defined as multi-platform and are treated as a fifth platform type in the Center rate structure. The Center with copies of TOUGH for three different platforms (Cray, DEC, and SUN) parallels the multiple-version availability of many of the packages. TOUGH2 for the PC, which will soon be available from ESTSC, is a multi-platform package.

Through an agreement with the Radiation Shielding Information Center (RSIC) at the Oak Ridge National Laboratory, DOE-sponsored, unlimited software that falls within the RSIC scope is announced by the ESTSC but is distributed by RSIC. Software packages and inquiries relating to those packages are forwarded to RSIC. ESTSC is designated by NRC as the primary source for their packages regardless of scope.

The ESTSC has agreements for joint activities with the Computer Software Technology Transfer Center (COSMIC), which distributes software sponsored by the National Aeronautic and Space Administration. These activities include announcements of software availability via a joint newsletter, shared conference exhibits, and a combined catalog on diskette. The agreements also include discounts for sponsoring organizations.

Unlimited software (not copyrighted by the developer) is available for general distribution by ESTSC. Copyrighted software is, in general, made available for government related usage by distribution to DOE, DOE contractors, and other federal agencies. In some cases it may also be distributed to other federal agency contractors.

Requests from organizations wishing to use copyrighted software for nongovernment purposes are referred to the copyright holder except for cases where the copyright holder has approved distribution by ESTSC. Unlimited (noncopyrighted) software is available to the public but is withheld by DOE from foreign dissemination for two years after licensing. Exceptions may be made if the sponsoring DOE office approves the dissemination prior to the end of the two-year withholding period and verifies that U.S. competitiveness will not be adversely impacted by foreign dissemination of the software.

The centralized management of DOE software was done at the National Energy Software Center (NESC), Argonne National Laboratory, from about 1965 until December 1991 at which time the collection was moved to the ESTSC in Oak Ridge. The move of about 2000 packages included TOUGH and the first release of TOUGH2. NESC distributed 27 copies of the software during the time period of 1988 through 1991.

The NESC rights to distribute the Harwell MA28 mathematical routines used in the TOUGH and TOUGH2 packages were in a license that NESC obtained from Harwell. It was determined that the license did not transfer to ESTSC with the move of the software. The distribution of the TOUGH/TOUGH2 software by ESTSC was delayed for a period of time to establish an agreement with Harwell that recognizes the transfer of the rights to ESTSC. From the first part of 1992 until late in 1994, ESTSC has distributed 48 copies of TOUGH and TOUGH2.

Following receipt of the preconditioned conjugate gradient solvers in November 1994 their availability was announced to all recipients of TOUGH and TOUGH2 and distributed to those responding to the announcement. Inquiries are still being received. This distribution of an addendum to a package is a departure from the ESTSC operating policy. The preconditioned conjugate gradient solvers have been added to all ready versions of TOUGH2 offered by ESTSC.

The PC-version of TOUGH2 was received in January 1995 and is expected to be screened and available for distribution before the end of February 1995. Its availability will be announced to all who have made inquiries and to previous recipients of the TOUGH and TOUGH2. This version of TOUGH2 is being offered as a multi-platform code, a platform category now being used by ESTSC for several packages.

Primary Center functions include software package receipt, review, screening, and in some cases testing; responding to inquiries and orders received via phone, fax, mail, and E-mail; dissemination of general Center information, specific package information, and software packages; and reporting to the agencies on overall Center operation. Other Center functions include interfacing with the agencies on operating

and policy questions and with Center partners on various agreements; working with package developers to resolve questions relating to submitted or requested packages; and announcing and exhibiting the Center software.

DOE expects the ESTSC to recover from package fees all operating costs related to processing DOE-sponsored packages. NRC supports part of the cost relating to Center processing of their packages and expects the balance to be recovered from fees charged for the packages. As DOE-sponsored software, processing costs related to TOUGH and TOUGH2 are to be recovered from fees charged for package distributions.

Pricing of software packages is determined on the basis of customer category: DOE (includes DOE offices, DOE contractors, other Federal agencies, U.S. educational institutions, and Cooperative Agreement Partners), public, or foreign. Platforms include personal computers (PC), workstations (WS), mainframes (MF), supercomputers (S), and multi-platform (MP).

Customer Category	PC	WS	MF	S	MP
DOE	$ 250	$ 400	$ 500	$ 1,200	$ 600
PUBLIC	510	1,305	1,835	4,560	2,200
FOREIGN	940	2,000	2,715	6,700	3,300

General information items available on request include a brochure (ESTSC-B1) that contains general information about the Center, the ESTSC Software Listing (ESTSC-2/Rev.3) that provides a listing and brief description of software packages in paper copy, and a joint ESTSC/COSMIC catalog on diskette. Internet users can access the file through the DOE Home Page as shown below and can contact ESTSC via E-mail or other methods as listed below.

U.S. Mail: Energy Science and Technology Software Center
P.O. Box 1020
Oak Ridge, TN 37831-1020

Commercial Carrier: 175 Oak Ridge Turnpike
Oak Ridge, TN 37830

Phone: 615/576-2606

Fax: 615/576-2865

Internet E-mail: estsc@adonis.osti.gov

World Wide Web (WWW) server: Use one of the following Uniform Resource Locators.

http://www.doe.gov

Accesses the DOE Home Page.

http://www.doe.gov/html/osti/estsc/estsc.html

Accesses general ESTSC information including the software catalog.

http://www.doe.gov/waisgate/estsc.html

Accesses the ESTSC software catalog.

Experiences using multigrid for geothermal simulation

D.P. Bullivant, M.J. O'Sullivan
Department of Engineering Science
University of Auckland
New Zealand

Z. Yang
Centre for Petroleum Engineering
University of New South Wales
Australia

Abstract

Experiences of applying multigrid to the calculation of natural states for geothermal simulations are discussed. The modelling of natural states was chosen for this study because they can take a long time to compute and the computation is often dominated by the development of phase change boundaries that take up a small region in the simulation. For the first part of this work a modified version of TOUGH was used for 2-D vertical problems. A "test-bed" program is now being used to investigate some of the problems encountered with implementing multigrid. This is ongoing work. To date, there have been some encouraging but not startling results.

1 Introduction

This work is motivated by the desire to speed up the calculation of natural states in geothermal reservoir simulation. It was noticed that during these calculations, the time step size is limited by phase changes in just a few blocks. This observation suggests that improvements could be made if the computational effort was directed towards these few blocks. Yang [5] looked at a number of ways for doing this, one of which was multigrid.

A brief introduction to multigrid is given in the following section. In the third section the feasibility study of multigrid for geothermal simulation, carried out by Yang [5], is summarized. The fourth section describes the work in progress to solve some of the problems identified by the feasibility study. The final section is a summary.

2 What is multigrid ?

Multigrid is a numerical method for solving differential equations, which uses two or more levels of discretization. It can reduce the time needed to solve the problem because a full solution is only required on the coarsest level. At the other levels, "smoothing" is carried out before the error is transferred to the next coarsest level or the correction is transferred to the next finest level. The sequence of levels the method goes through is called a cycle. Briggs [2] gives a good introduction to the multigrid method.

For a linear differential equation

$$\mathcal{L}(\mathbf{u}) = \mathbf{g} \tag{1}$$

the discretization at level h can be written as

$$\mathcal{L}^h(\mathbf{u}^\mathbf{h}) = \mathbf{r}^\mathbf{h} \tag{2}$$

where at the finest level $\mathbf{r}^\mathbf{h} = \mathbf{g}^\mathbf{h}$. Then the multigrid V-cycle algorithm can be written as

1. While not at the coarsest level do
   (a) "Smooth" the solution at the current level (h)
   (b) Transfer the error to the next coarsest level ($2h$) using the restriction operator I_h^{2h},
   $$\mathbf{r^{2h}} = I_h^{2h}(\mathbf{r^h} - \mathcal{L}^h(\mathbf{u^h})) \tag{3}$$
   (c) Move to the next coarsest level
   $$\mathcal{L}^{2h}(\mathbf{u^{2h}}) = \mathbf{r^{2h}}, \text{ with initial estimate } \mathbf{u^{2h}} = \mathbf{0} \tag{4}$$
2. Solve the differential equation at the coarsest level
3. While not at the finest level do
   (a) Transfer the solution to the next finest level ($h/2$) using the interpolation operator $I_h^{h/2}$,
   $$\mathbf{u^{h/2}} = \mathbf{u^{h/2}} + I_h^{h/2}(\mathbf{u^{h/2}}) \tag{5}$$
   (b) Move to the next finest level
   $$\mathcal{L}^{h/2}(\mathbf{u^{h/2}}) = \mathbf{r^{h/2}} \tag{6}$$
   (c) "Smooth" the solution at the current level ($h/2$)

This is called a V-cycle because of the pattern it makes moving through the levels (see Figure 1). To converge to a solution this is repeated several times. In our latest work, we are using a full multigrid V-cycle (see Figure 1).

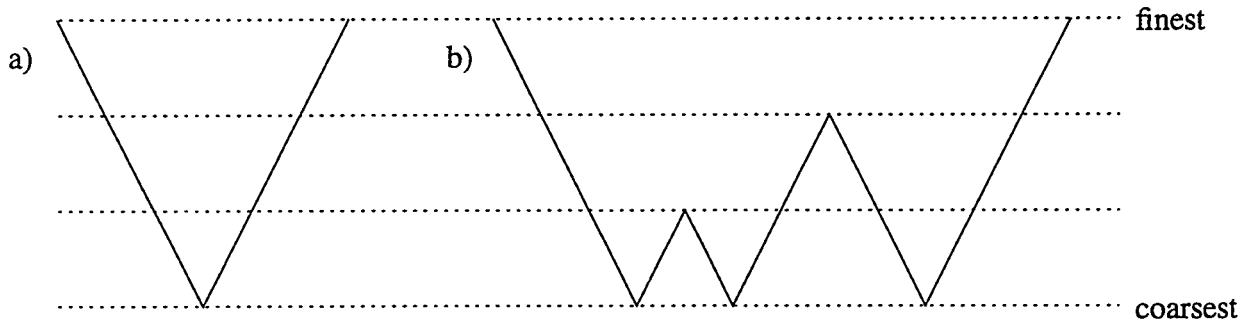

Figure 1: Multigrid cycles. a) V-cycle, b) full multigrid V-cycle

A "smoothing" sweep involves stepping through the solution vector $\mathbf{v^h}$ and solving for each value with the other values fixed. For a linear system of equations, this is the Gauss-Seidel method. A common strategy is to carry out two smoothing sweeps before transferring from fine to coarse and one smoothing sweep after transferring from coarse to fine.

For nonlinear differential differential equations, such as those solved by TOUGH, the multigrid method needs to be modified. We are using the full approximation storage method McCormick [3]. For this method the transfer of the error from fine to coarse is modified as follows:

$$\mathbf{r^{2h}} = I_h^{2h}(\mathbf{r^h}) + \mathcal{L}^{2h}(I_h^{2h}(\mathbf{u^h})) - I_h^{2h}(\mathcal{L}^h(\mathbf{u^h})) \tag{7}$$

The initial estimate on the coarse grid is the restriction of the fine grid solution

$$\mathbf{u^{2h}} = I_h^{2h}(\mathbf{u^h}) \tag{8}$$

and the transfer of the correction from coarse to fine is also modified:

$$\mathbf{v^{h/2}} = \mathbf{v^{h/2}} + I_h^{h/2}(\mathbf{v^h} - I_{h/2}^h(\mathbf{v^{h/2}})) \tag{9}$$

In the following sections, the interpolation and restriction operators used will be discussed.

3 Feasibility study

Part of the work by Yang [5] is concerned with improving the computational efficiency of steady state simulations of geothermal reservoirs. One method that was considered was multigrid. This section summarizes Yang's work on multigrid.

Multigrid was implemented by modifying MULKOM. The test problem for this work was a 2-D vertical square (1km side) with heat input over a fifth of the base, atmospheric conditions at the top and no flow through the rest of the boundary (see Figure 2). Two grids were used - a coarse 5 by 5 grid and a fine 10 by 10 grid. The normal MULKOM/TOUGH solution routine was used to solve on the coarse grid.

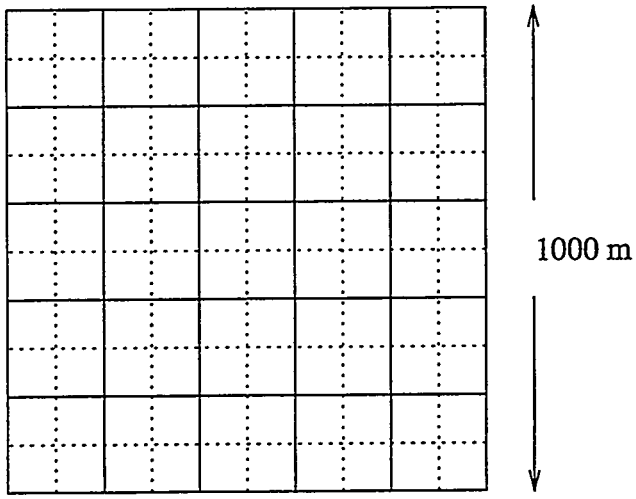

Figure 2: Test problems

When implementing multigrid, choices have to be made for the restriction operator, the interpolation operator and the smoothing method. For this feasibility study the best results were obtained by:

- Transferring the right hand side from fine to coarse, I_f^c, by averaging over the four fine blocks that make up the coarse block and multiplying by a damping factor ω ($0 <= \omega <= 1$)

$$r^c_{i,j} = \omega * (r^f_{2i-1,2j-1} + r^f_{2i-1,2j} + r^f_{2i,2j-1} + r^f_{2i,2j})/4 \tag{10}$$

  For strongly two-phase flow, values of ω less than 0.5 were found to be necessary to ensure stability.

- Always using the MULKOM solution to the unmodified problem (r^c not modified by fine grid) on the coarse grid, u^c, as the initial estimate rather than the restricted pressure and temperature or saturation from the fine grid. The restriction that was used was to convert from pressure and temperature or saturation to pressure and enthalpy for each of the four fine blocks, average these pressures and enthalpies to get a pressure and enthalpy for the coarse block, and convert this pressure and enthalpy to a pressure and temperature or saturation. This was found to sometimes give an initial estimate for which MULKOM did not converge.

- Transferring the estimate from the coarse grid to the fine grid by converting the pressure and temperature or saturation estimates on the coarse grid into pressures and enthalpies, computing the changes in pressure and enthalpy from u^c, linearly interpolating these changes multiplied by another damping factor on to the fine grid, and converting the updated pressures and enthalpies on the fine grid into pressures and temperatures or saturations.

- Smoothing using box Gauss-Seidel (see Brandt [1]). Standard Gauss-Seidel involves sweeps through all the blocks in the grid fixing the pressure and temperature or saturation in all but the current block and solving for the pressure and temperature or saturation in the current block using Newton-Raphson. For box Gauss-Seidel, Newton-Raphson is used to solve for the current block and some of its neighbours. As the number of neighbours in the box goes up, the smoothing gets better, but the computational cost goes up.

For the test problem, four different inputs - 1 MW, 2 MW, 4 MW and 6 MW - were used. For 1 MW there is no two-phase zone. For 6 MW there is a large two-phase zone running from the base of the model, above the heat source, to the top of the model and halfway across the top of the model.

The multigrid implementation described above is able to solve the test problem with the four different heat inputs, but is slower than standard MULKOM. As the heat input is increased, multigrid has more difficulty in solving the problem (as does MULKOM).

4 Ironing out the wrinkles

In Yang's preliminary implementation, only two levels were used and changes to the way that standard multigrid transfers between levels were made because of the MULKOM/TOUGH choice of primary variables (pressure and temperature or saturation). To remove these limitations and investigate multigrid further, a "test-bed" program is being written. It is intended to solve the steady-state geothermal equations (as formulated for TOUGH, Pruess [4]) on a square or a cube, with an arbitrary number of multigrid levels, using integrated finite differences (like MULKOM/TOUGH) and with pressure and enthalpy as the primary variables (unlike MULKOM/TOUGH). Our development schedule is:

1. Use integrated finite differences and multigrid to solve Poison's equation. This will check that the outer multigrid loop is working.

2. Develop a single block solver for the steady-state geothermal equations. This will solve for the pressure and enthalpy in a single block with the pressures and enthalpies in the neighbouring blocks fixed. It is the fundamental part of the Gauss-Seidel smoother.

3. Implement standard restriction and interpolation operators. The restriction operator, to transfer values from the fine grid to the coarse grid, will average the values in the fine grid blocks that make up the coarse grid block. The interpolation operator, to transfer values from the coarse grid to the fine grid, will use the value in the coarse grid block in all the fine grid blocks contained in the coarse grid block. These will be easier to implement than in the feasibility study because it will not be necessary to convert between pressure and enthalpy and pressure and temperature or saturation.

4. Investigate the performance of the method on the test problems from the feasibility study.

The implementation of integrated finite differences and multigrid to solve Poison's equation was relatively straight forward and the expected multigrid convergence rate, the ratio of the error at the end of the V-cycle to the error at the beginning of the V-cycle, of 0.1 was achieved. In the implementation, care had to be taken with the boundary conditions.

At present we are working on the single block solver. This is proving difficult. The following subsection discusses the single block solver.

4.1 Single block solver

The single block solver should be able to solve for the pressure and enthalpy in a block when the pressures and enthalpies in the neighbouring four, in 2-D, or six, in 3-D, blocks are specified and fixed. The solver needs to work even when the initial guesses are poor, because it was noticed in the preliminary implementation that poor estimates were sometimes obtained when restricting from the coarse grid to the fine grid, especially on the boundary of two-phase zones.

Our current solver uses Newton-Raphson with time stepping and care when crossing the phase change boundaries. This is the same method as in TOUGH, but it is using different primary variables.

To test the solver, problems in 2-D with no flow through three sides and the pressure and enthalpy specified for the fourth. With all combinations of boundary orientation (specified pressure and enthalpy either on top or to the side), initial estimate (liquid, two-phase or vapour) and boundary conditions (liquid, two-phase or vapour), there are 18 test problems.

TOUGH converges for all the test problems, but in some problems to the wrong answer -

- For two-phase boundary conditions on the side, the block converges to same pressure and temperature as on the boundary, but has a different saturation (enthalpy).
- For vapour boundary conditions on the top, the block converges to liquid conditions, but for some initial estimates the pressure gradient is liquid-static (correct) and for other initial estimates the pressure gradient is vapour-static (incorrect).

We believe that these errors can be corrected by -

- Using liquid pressures

$$p_l = p + g(d/2)(1 - s_l)(1 - s_l) * (\rho_v - \rho_l) \tag{11}$$

for calculating the liquid flux and vapour pressures

$$p_v = p + g(d/2)s_l s_l(\rho_v - \rho l) \tag{12}$$

for calculating the vapour flux. The concept of liquid and vapour pressures is similar to capillarity pressure, but is independent of rock properties. The pressures at the top and bottom of the block were estimated by assuming that the block is hydrostatic with vapour over liquid and that the block pressure is the average of the pressure with depth. The liquid pressure at the centre of the block, p_l, was calculated by assuming liquid-static from the bottom to the centre. The vapour pressure at the centre of the block, p_v, was calculated by assuming vapour-static from the top to the centre.

- Modifying the gravity correction for the liquid flux from

$$gsin(\beta)(\rho_{l1} + \rho_{l2})/2 \tag{13}$$

and the gravity correction for the vapour flux from

$$gsin(\beta) * (\rho_{v1} + \rho_{v2})/2 \tag{14}$$

to both be

$$gsin(\beta)(d_1(s_{l1}r_{l1} + (1 - s_{l1})\rho_{v1}) + d_2(s_{l2}\rho_{l2} + (1 - s_{l2})\rho_{v2})/(2 * (d_1 + d_2)) \tag{15}$$

Our single block solver with the above modifications does not converge for some of the test problems. We think that the convergence problems are due to the discretized equations not being smooth. There are discontinuities in the slopes of the residuals across the phase change boundaries which both TOUGH and our block solver take care over, but there are also discontinuities in the slopes across any of the lines where a flux changes sign because of the upwinding. TOUGH does not suffer as badly as our single block solver and this may be due to the choice of primary variables. We are now considering making the above modifications to TOUGH to see if it can then solve all the test problems correctly.

5 Summary

A feasibility study of applying multigrid to geothermal reservoir simulation has been carried out and showed that the method could solve the equations but the implementation was slower than standard TOUGH. This study identified a number of problems in implementing multigrid and these are currently being investigated.

A major problem is how to solve for the pressure and enthalpy in a single block with pressures and enthalpies specified on the boundaries. There are difficulties with the formulation of the "capillary" pressure and also because the residuals are not smooth across phase changes and when flows change direction (due to upwinding).

Acknowledgement

This work has benefitted from many discussions with Stephen F. McCormick, University of Colorado, Boulder.

References

[1] A. Brandt. Guide to multigrid development. In W. Hackbusch and U. Trottenberg, editors, *Multigrid Methods, Proceedings of Conference at Koln-Porz, November 23-27, 1981*. Springer-Verlag, 1982.

[2] William L. Briggs. *A multigrid tutorial.* Society for Industrial and Applied Mathematics, 1987.

[3] Stephen F. McCormick. *Multilevel adaptive methods for partial differential equations*, volume 6 of *Frontiers in Applied Mathematics*. Society for Industrial and Applied Mathematics, 1989.

[4] Karsten Pruess. TOUGH2. A general-purpose numerical simulator for multiphase fluid and heat flow. Technical Report LBL-29400, Earth Sciences Division, Lawrence Berkeley Laboratory, 1 Cyclotron Road, Berkeley, CA94720, May 1991.

[5] Zhongke Yang. *Numerical simulations of geothermal systems with an unsaturated zone.* PhD thesis, University of Auckland, 1994.

ITOUGH2: Solving TOUGH Inverse Problems

Stefan Finsterle and Karsten Pruess

Earth Sciences Division
Lawrence Berkeley Laboratory
University of California
Berkeley, CA 94720
(510) 486-5205

Abstract

ITOUGH2 is a program that provides inverse modeling capabilities for the TOUGH2 code. While the main purpose of ITOUGH2 is to estimate two-phase hydraulic properties by calibrating a TOUGH2 model to laboratory or field data, the information obtained by evaluating parameter sensitivities can also be used to optimize the design of an experiment, and to analyze the uncertainty of model predictions. ITOUGH2 has been applied to a number of laboratory and field experiments on different scales. Three examples are discussed in this paper, demonstrating the code's capability to support test design, data analysis, and model predictions for a variety of TOUGH problems.

Introduction

Simulating multiphase fluid flow in porous or fractured media using TOUGH2 requires specifying a number of parameters that are difficult to determine. Parameters measured in the laboratory may significantly differ from their model counterparts both conceptually and numerically mainly because of scale effects. Calibration of a TOUGH2 model against a test response that is relevant to the ultimate application, is a strategy to obtain model-related formation parameters. These parameter estimates represent effective properties at the scale of interest, thus greatly improving the reliability of the subsequent model predictions.

ITOUGH2 is a program that provides inverse modeling capabilities for the TOUGH2 simulator. The core of the program contains an algorithm that examines the impact of model parameters on the simulation results by repeatedly solving the flow problem using TOUGH2. The information about parameter sensitivities, combined with an efficient and robust optimization technique and a detailed error analysis, makes ITOUGH2 a powerful tool not only for parameter estimation, but also for the optimization of test designs and the analysis of prediction uncertainties.

ITOUGH2 solves the inverse problem by automatic model calibration based on the maximum likelihood approach. All TOUGH2 input parameters including initial and boundary conditions as well as geometrical features such as fracture spacing can be considered unknown or uncertain. The parameters can be estimated based on any type of observations for which a corresponding TOUGH2 output is available. Furthermore, user-specified parameters and observations can be introduced. The user can select from a number of different objective functions and minimization algorithms. One of the key features of ITOUGH2 is its extensive error analysis which provides statistical information about final residuals, estimation uncertainties, and the ability to discriminate among model alternatives. The theoretical background as well as the usage of the hierarchically structured command language are documented in *Finsterle* [1993]. Three examples are discussed in this paper,

demonstrating the capability of ITOUGH2 to support test design, data analysis, and model predictions.

Test Design

Design of a laboratory or field test can be optimized, so that the uncertainty of the estimated parameters is as small as possible. The basic idea supported by ITOUGH2 is the following:

- Conceive a test design, i.e. sequence of test events, type of data to be collected, location of sensors, number and type of parameters to be identified, etc.
- Generate synthetic data using TOUGH2. A random noise can be added to represent measurement errors.
- Solve the inverse problem for all unknown or uncertain parameters using ITOUGH2.
- Analyze sensitivity matrix. Revise test design to improve sensitivity of data .
- Analyze covariance matrix. Optimize test design to reduce parameter correlation and estimation uncertainty.
- Examine impact of conceptual model on parameter estimates. Check whether the data are selective with respect to competing model alternatives.

As an example, we simulated the response to a series of standard borehole tests, including pulse withdrawal (PW) and pulse injection (PI) tests, a constant rate pumping (RW) - recovery (RWS) test, as well as injection of water (RI) and gas (GRI) at a constant rate, followed by shut-in recovery periods (RIS, GRIS). A synthetic inverse problem is first solved under the assumption that only data from test sequence 1 are available (Figure 1). The covariance matrix of 10 unknown parameters is calculated, and the standard deviations and correlation coefficients are analyzed. Table 1 demonstrates that performing test sequence 1 alone is insufficient to identify a number of two-phase flow parameters. Adding test sequences 2 and 3 considerably improves the ability to determine parameter values by reducing both the estimation error and the correlations between the parameters. Details can be found in *Finsterle* [1995].

Table 1: Reduction of estimation error and parameter correlation as a result of adding test sequences 2 and 3, van Genuchten model

van Genuchten						
Parameter	Sequence 1 only		Sequence 1 and 2		Sequence 1, 2 and 3	
	σ	χ	σ	χ	σ	χ
log (k [m^2])	0.32	0.04	0.03	0.26	0.03	0.27
p_i [bar]	N/D	0.01	0.64	0.19	0.21	0.50
S_{gi} [-]	N/D	0.03	0.03	0.12	0.02	0.14
AEP $1/\alpha$ [bar]	N/D	0.02	0.52	0.14	0.26	0.27
PSDI n [-]	N/D	0.01	0.87	0.05	0.43	0.09
S_{lr} [-]	N/D	0.02	0.16	0.06	0.10	0.10
S_{gr} [-]	N/D	0.02	0.01	0.06	0.01	0.07
ϕ [-]	N/D	0.01	0.01	0.07	0.01	0.11
log (c_{tz} [Pa^{-1}])	N/D	0.29	0.19	0.09	0.19	0.09
p_{bh} [bar]	0.62	0.19	0.25	0.45	0.22	0.51

σ : standard deviation from joint probability density function
χ : ratio of conditional and joint standard deviation; low value indicates high correlation
N/D : not determinable, i.e. standard deviation much larger than parameter value

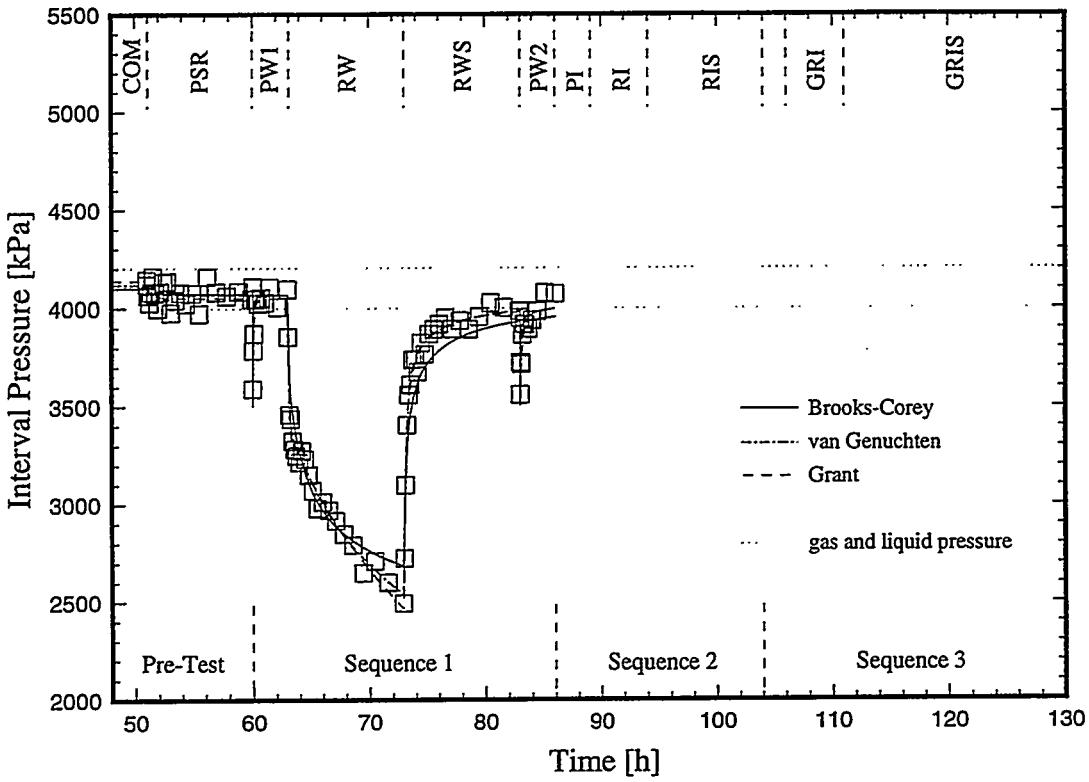

Figure 1: Fitting alternative models to data synthetically generated for test sequence 1

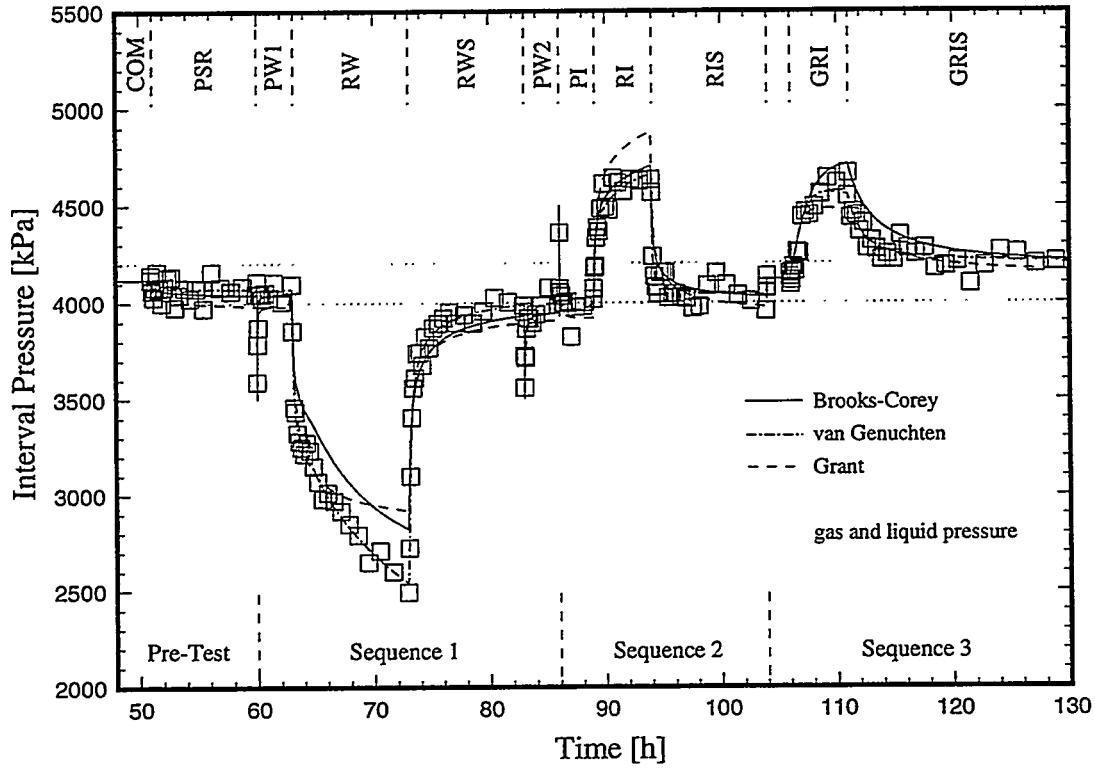

Figure 2: Fitting alternative models to data generated for test sequences 1, 2, and 3

Table 2: Estimated error variances using different characteristic curves; data are generated using the van Genuchten model, perturbed by a normally distributed noise with $\sigma_0 = 50$ kPa.

Estimated Error Variance s_0^2/σ_0^2			
Model	Sequence 1 only	Sequence 1 and 2	Sequence 1, 2 and 3
data (van Genuchten)	1.00	1.00	1.00
van Genuchten	0.92	0.99	1.06
Brooks-Corey	0.89	*2.81*	*4.39*
Grant	0.95	*5.77*	*4.78*
s_0^2 : estimated error variance = *a posteriori* error variance of residuals; if s_0^2/σ_0^2 is greater than $F_{0.95}$=1.35 (*italic*), the model is unlikely to explain the data			

The synthetic data for each test design are inverted using three different characteristic curves (Brooks-Corey, van Genuchten, and Grant). The goodness-of-fit can be used to examine the capability of the test design to discriminate among alternative conceptual models.

It can be seen (Table 2, Figure 1) that each model explains the flow system equally well if only data from test sequence 1 are available. If data from sequences 2 and 3 are added (Figure 2), however, one of the models performs significantly better, and provides a basis for rejecting the competing alternatives. In conclusion, the extended test design has the potential of identifying a model that is more likely to represent field conditions.

Model Calibration

The main purpose of the ITOUGH2 code is to estimate model-related parameters by automatically calibrating an appropriate TOUGH2 model to laboratory or field data. The indirect approach to calibration provides great flexibility in choosing scale and layout of an experiment that can be analyzed to determine two-phase hydraulic properties.

Analysis of a ventilation test performed by *Gimmi et al.* [1992] at the Grimsel Rock Laboratory is shown here. A TOUGH2 model that simulates evaporation at a ventilated drift surface and propagation of a drying zone into the initially fully saturated rock matrix was calibrated against transient water potential measurements at six different depths. Pressure data in two boreholes as well as estimates of evaporation rates at the drift surface were also considered. Absolute permeability and the parameters of van Genuchten's characteristic curves were determined. Figure 3 shows the comparison between observed and calculated water potentials. Minimization was started from different initial parameter sets. All inverse runs resulted in parameter sets that are almost identical, suggesting that the solution is unique within the parameter space of interest.

The predicted water potentials, plotted as solid lines in Figure 3, are close to the measured values. The calculated flow rate of 0.31 mg m^{-2} s^{-1} compares very well to the observed value of 0.3 mg m^{-2} s^{-1}. The difference between measured and calculated gas pressures in the two boreholes is less than 0.01MPa. This example shows that inverse modeling of the ventilation experiment provides reliable estimates of model-related formation parameters affecting two-phase flow. It requires, however, a high model sophistication to simulate the physical processes relevant to desaturation of a granitic rock matrix. The error analysis indicates that if the absolute permeability can be determined independently, the parameters of van Genuchten's characteristic curves are estimated with less uncertainty because of a more favorable correlation structure. Details can be found in *Finsterle and Pruess* [1995].

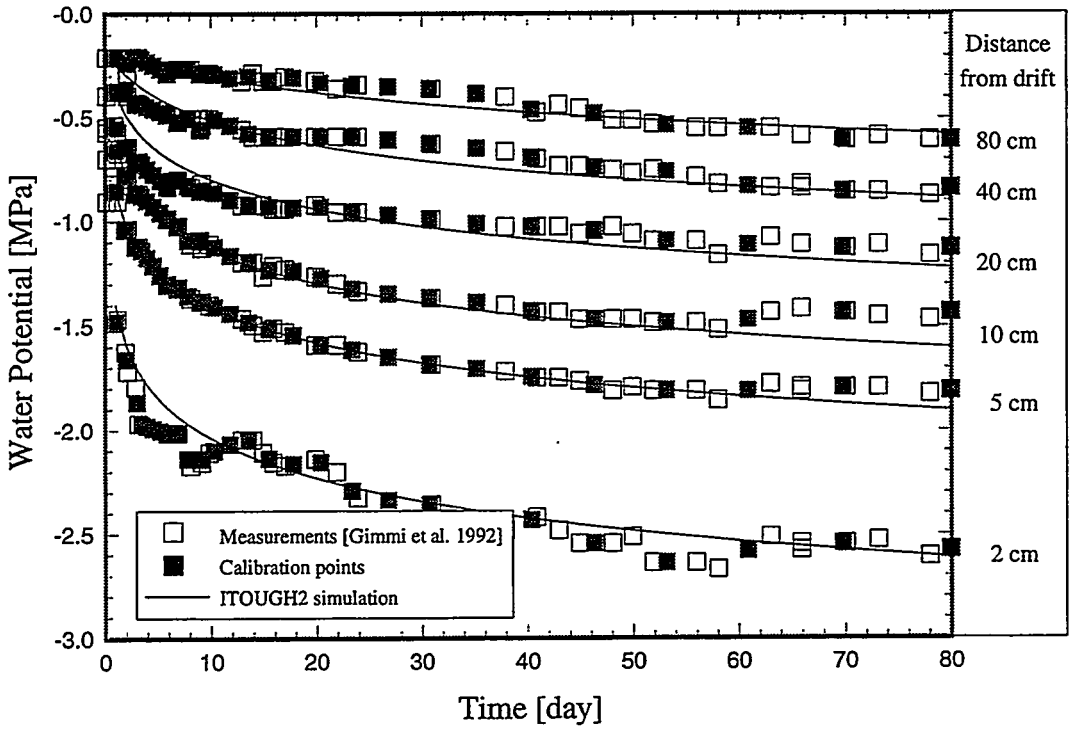

Figure 3: Comparison between calculated and measured water potentials during a ventilation period of 80 days. Data from six tensiometers at different depths are available. Calibration points are linearly interpolated between actual data points. Data from *Gimmi et al.* [1992].

Uncertainty Analysis for Model Predictions

Model predictions using TOUGH2 are uncertain due to the uncertainty associated with the input parameters. ITOUGH2 provides two options to analyze prediction errors. The variance of a model output can be calculated using standard First Order Second Moment error analysis which may take into account the correlations between the parameters. This method results in normally distributed prediction errors. It assumes, however, that the model is linear in the parameters, and that the probability density function of the input parameters is close to Gaussian. The strong nonlinearities inherent in multiphase flow modeling may require performing Monte Carlo simulations. The probability density function of the prediction error is then obtained by statistically analyzing a large number of TOUGH2 realizations.

The difference between the two methods is demonstrated for a synthetic laboratory experiment, in which the outflow of water at the bottom of a column is measured during injection of gas at a constant pressure from the top. The flow rate initially increases as a result of increasing total mobility. Once the gas has reached the outlet, the flow rate drops sharply due to the reduced relative permeability and water content. Values for absolute permeability and three parameters of the characteristic curves are sampled from a normal distribution, and 100 Monte Carlo simulations are performed. The results indicate (Figure 4) that the prediction errors are not symmetrical around the mean, i.e. that the linearity assumption is violated. Nevertheless, the simple First Order Second Moment error analysis provides a reasonable estimate of prediction uncertainties during the initial and final stages of the experiment.

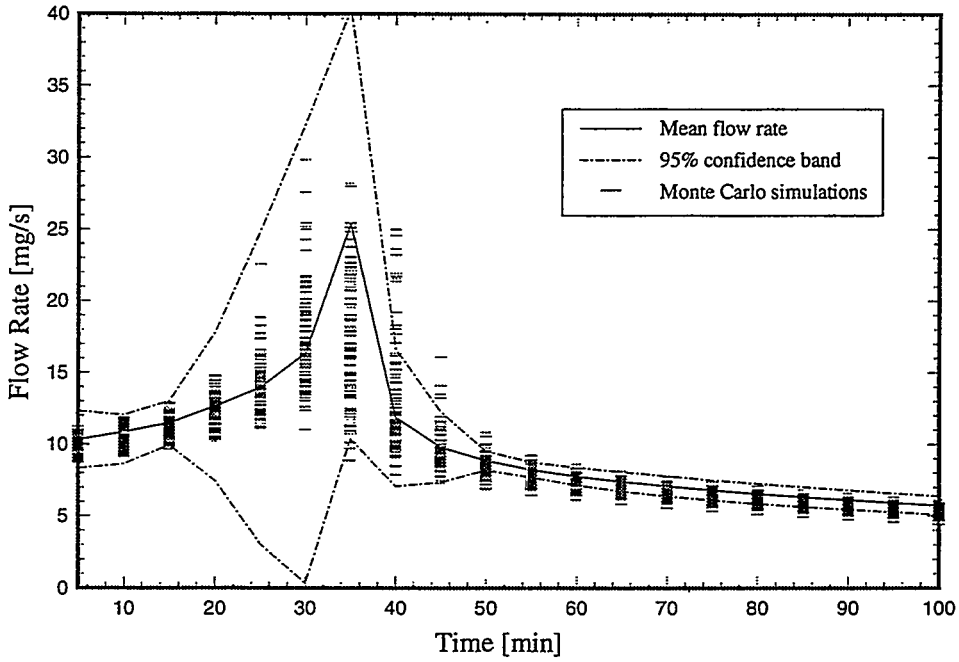

Figure 4: Uncertainty of model prediction for synthetic laboratory experiment. The results of 100 Monte Carlo simulations represent the probability density function of the model output. The uncertainty is fairly well reproduced by a First Order Second Moment error analysis.

Concluding Remarks

Inverse modeling provides an appealing technique to obtain model-related TOUGH2 parameters by calibrating the numerical model against sensitive observations of the system state. The combination of sophisticated process description (TOUGH2) and a flexible and robust inverse approach with detailed error analysis (ITOUGH2) yields a powerful tool for test analysis under two-phase flow conditions. The design of an experiment can be optimized prior to testing in order to improve the subsequent estimation of parameter values. Finally, the impact of parameter uncertainties on model predictions can be studied using ITOUGH2.

Acknowledgment This work was carried out under U.S. Department of Energy Contract No. DE-AC03-76SF00098 for the Director, Office of Civilian Radioactive Waste Management, Office of External Relations, and was administered by the Nevada Operations Office, U.S. Department of Energy, in cooperation with the Swiss National Cooperative for the Disposal of Radioactive Waste (Nagra).

References

Finsterle, S., ITOUGH2 User's Guide Version 2.2, Lawrence Berkeley Laboratory Report LBL-34581, Berkeley, CA, August 1993.

Finsterle, S., Test Design for Determining Two-Phase Hydraulic Properties at the Wellenberg Site, Lawrence Berkeley Laboratory Report, Berkeley, CA, February 1995.

Finsterle, S., and K. Pruess, Solving the Estimation-Identification Problem in Two-Phase Flow Modeling, paper accepted for publication in *Water Resources Research*, 1995.

Gimmi, T., H. Wydler, T. Baer, H. Abplanalp, H. Flühler, Near field desaturation experiment at the Grimsel Test Site (FLG), Nagra Internal Report, Wettingen, Switzerland, 1992.

Presented at the TOUGH Workshop 95
Lawrence Berkeley Laboratory, Berkeley, CA 94720, March 20-22, 1995

LBL-37066

A NEW SET OF DIRECT AND ITERATIVE SOLVERS FOR THE TOUGH2 FAMILY OF CODES

George J. Moridis

Earth Sciences Division, Lawrence Berkeley Laboratory
University of California, Berkeley, CA 94720

ABSTRACT

Two new solvers are discussed. LUBAND, the first routine is a direct solver for banded systems and is based on a LU decomposition with partial pivoting and row interchange. BCGSTB, the second routine, is a Preconditioned Conjugate Gradient (PCG) solver with improved speed and convergence characteristics. Bandwidth minimization and gridblock ordering schemes are also introduced into TOUGH2 to improve speed and accuracy.

Introduction

Most of the computational work in the numerical simulations of fluid and heat flows in permeable media arises from the solution of large systems of linear equations $\mathbf{Ax} = \mathbf{b}$, where $\mathbf{A}$ is a banded matrix of order N, $\mathbf{x}$ is the vector of the unknowns, and $\mathbf{b}$ the right-hand side. These are solved using either direct or iterative methods. The most reliable (and often the simplest) solvers are based on direct methods. The robustness of direct solvers comes at the expense of large storage requirements and execution times. Iterative techniques exhibit problem-specific performance and lack the generality, predictability and reliability of direct solvers. These disadvantages are outweighed by their low computer memory requirements and their substantial speed especially in the solution of very large matrices.

In TOUGH2 the matrix $\mathbf{A}$ is a Jacobian with certain consistent characteristics. In systems with regular geometry, $\mathbf{A}$ has a known block structure with well defined sparsity patterns. In general, $\mathbf{A}$ matrices arising in TOUGH2 simulations are non-symmetric with typically no diagonal dominance. Although $\mathbf{A}$ can be positive definite in regular systems with homogeneous property distributions, it usually is not, and ill-conditioning is expected in realistic heterogeneous large systems. Due to the fact that $\mathbf{A}$ is a Jacobian, the elements of $\mathbf{A}$ in a single row may vary by several orders of magnitude. In TOUGH2 simulations it is possible to encounter a large number of zeros on the main diagonal of $\mathbf{A}$, making central $S = NB$ pivoting impossible and resulting in very ill-conditioned matrices. TOUGH2 creates matrices which are among the most challenging, with all the features that cause most iterative techniques to fail. In addition, the general-purpose nature of TOUGH2 means that different matrix characteristics may arise for different types of problems. This explains the past heavy reliance of TOUGH2 on the direct solver MA28 [*Duff*, 1977].

The LUBAND Solver

LUBAND is a direct solver intended to replace the MA28 solver currently used in the TOUGH2 family of codes. It is derived from routines in the LAPACK [1993] package, which have been enhanced and extensively modified to conform to the TOUGH2 architecture. It is based on a LU decomposition with partial pivoting and row interchange, and allows the solution of systems with a large number of zeros on the main diagonal. Unlike MA28 (which is a general solver), LUBAND is a banded matrix solver, and as such it capitalizes on the significantly lower and well defined memory requirements of these solvers. A pseudo-banded matrix structure is automatically created by LUBAND for systems with irregular grids.

Although LUBAND can be applied without any problem in the current TOUGH2 version, a new MESHMAKER routine was also developed to minimize the bandwidth of matrix $\mathbf{A}$ and maximize the benefits of LUBAND. This was prompted by the heavy penalty which non-

optimization of the bandwidth exacts. Defining *work* W as the number of multiplications and divisions necessary to convert the full matrix to an upper triangular form and to perform back substitution, *Price and Coats* [1974] showed that for direct solvers

$$W \propto NM^2 \qquad \text{and} \qquad S = NB \tag{1}$$

and S is the minimum storage requirement, N is the order of the matrix and M its half-bandwidth, the full bandwidth B being

$$B = 2M + 1. \tag{2}$$

The form of the matrix depends upon the ordering of equations. For a given problem size N, work and storage are minimized when M is minimized. If I, J, K are the number of subdivisions in the x-, y- and z-directions respectively, the shortest half-bandwidth is $M = JK$ when $I > J > K$. This is called *standard* ordering [*Aziz and Settari,* 1979], and the resulting matrices are banded. As W increases with the square of M, it is obvious that the penalty for non-optimization of the ordering of equations may be substantial. Note that it is possible to use the new MESHMAKER with MA28.

A further substantial improvement was added to the new MESHMAKER, which features as an option the implementation of the Alternating Diagonal Scheme (D4) for gridblock ordering. D4 is a direct solution technique belonging to the matrix-banding class, which derives its benefits from the numbering of the grid points. More details can be found in *Price and Coats* [1974]. D4 ordering partitions the matrix into four distinct entities. This structure allows forward elimination through the equations in the lower half of $\mathbf{A}$, which zeroes all original entries in the lower left quadrant of $\mathbf{A}$ and transforms it into a null matrix, while creating non-zero entries in the submatrix $\mathbf{A_{LR}}$ in the lower right quadrant of $\mathbf{A}$. The submatrix $\mathbf{A_{LR}}$ is of order $N/2$, and allows the calculation of the lower half of $\mathbf{x}$, from which the upper half is obtained by simple substitution. Depending on the grid geometry, D4 makes possible execution speed improvement by a factor ranging between a minimum of 2 and a maximum of 5.85 [*Price and Coats,* 1974] over standard ordering. Moreover, it reduces storage requirements by a factor of 2.

LUBAND makes possible the solution of large multi-dimensional problems. The maximum benefits of LUBAND are realized when used within the context of D4, i.e. to solve the submatrix $\mathbf{A_{LR}}$. However, D4 can only be used with regular grids. Although it is theoretically possible to solve $\mathbf{A_{LR}}$ using MA28, the user is strongly advised against for two reasons: the uncertainty over the storage requirements of MA28 and the known rapid deterioration of the MA28 performance as the matrix fill-in increases (e.g. in 3-D problems). The user has also the option of solving $\mathbf{A_{LR}}$ using the package of Preconditioned Conjugate Gradient (PCG) solvers available in TOUGH2 [*Moridis and Pruess*, 1995].

The BCGSTB Solver

BCGSTB, the second solver, belongs to the PCG family, and complements T2CG1 [*Moridis and Pruess,* 1995], the existing suite of iterative solvers in TOUGH2. It was developed based on the BiCGSTAB(ℓ) algorithm [*Sleijpen and Fokkema*, 1993], which is a recent extension of the more traditional BiCGSTAB algorithm of *van der Vorst* [1992]. It was developed to address the problem of irregular convergence behavior of the PCG solvers in T2CG1 in situations where the iterations are started close to the solution (e.g. when approaching steady state). This is a weakness which afflicts most PCG solvers, and may lead to severe residual cancellation and errors in the solution. BiCGSTAB(ℓ) alleviates the irregular (oscillatory) convergence common to the Bi-Conjugate Gradient (Bi-CG) [*Fletcher*, 1976] and Conjugate Gradient Squared (CGS) [*Sonneveld*, 1989] methods in T2CG1, thus improving the speed of

convergence. Finally, it alleviates potential stagnation or even breakdown problems which may be encountered in traditional BiCGSTAB. According to *Sleijpen and Fokkema* [1993], BiCGSTAB(ℓ) combines the speed of Bi-CG with the monotonic residual reduction in the Generalized Minimum Residual (GMRES) method, while being faster than both. Theoretical analysis of the underlying concepts also indicates that the BiCGSTAB(ℓ) algorithm is especially well-suited to the solution of very large (i.e. N > 50 000) problems [*van der Vorst*, 1992].

BCGSTB uses the Boeing-Harwell matrix storage scheme of TOUGH2, and has the same architecture as the other routines in T2CG1. It uses a modified LU decomposition for preconditioning, as well as ILU and MILU preconditioners with various levels of fill. Its memory requirements increase linearly with the order ℓ of the Minimal Residual polynomial. For ℓ = 4, it requires twice the memory of Bi-CG or CGS, which is half the GMRES requirement.

Examples

The solvers were tested in four test problems. Test problem 1 involves a laboratory convection cell experiment. A porous medium consisting of glass beads fills the annular region between the two vertical concentric cylinders. Application of heat generates a thermal buoyancy force, giving rise to the development of convection cells. This problem has been discussed in detail by *Moridis and Pruess* [1992]. The EOS1 module is used. The domain consists of 16x26 = 416 gridblocks in (r,z), with NK = 1 and NEQ = 2, resulting in a total of N = 832 equations.

Test problem 2 examines flow as it reaches steady state in a simple two-dimensional model of a heterogeneous porous medium. The basic computational grid is composed of 80 × 120 = 9600 grid blocks in (x,y). Impermeable obstacles with lengths uniformly distributed in the range of *2 - 4 m* are placed in the domain. These blocks are removed from the mesh, leaving a total of 8003 grid blocks. EOS1 is used, and NK = NEQ = 1. *Moridis and Pruess* [1995] present a thorough discussion of the problem.

Test problem 3 describes the WIPP (**W**aste **I**solation **P**ilot **P**lant) repository, which is planned for the disposal of transuranic wastes. It is located in a bedded salt formation, is brine saturated and consists of a large number of beds with thin interbeds. The layer permeabilities vary by four or five orders of magnitude. The purpose of the model is to evaluate effects of gas generation and two-phase flow on repository performance within a complex stratigraphy. The simulated domain consists of 1200 elements in a 2-D vertical grid. EOS3 is used in this isothermal (NK = NEQ = 2) problem, which results in a total of N = 2400 equations. More details can be found in *Moridis and Pruess* [1995].

Test problem 4 describes the TEVES (**T**hermal **E**nhanced **V**apor **E**xtraction **S**ystem) process, which is designed to extract solvents and chemicals contained in the Chemical Waste Landfill at Sandia National Laboratories. In this process the ground is electrically heated, and boreholes at the center of the heated zone are maintained at a vacuum to draw air and vaporized contaminants into the borehole and to a subsequent treatment facility. The 3-D grid consists of 1300 gridblocks. EOS3 is used (NK = 2, NEQ = 3), and N = 3900 equations are solved. Additional information can be found in *Moridis and Pruess* [1995].

Results and Conclusions

The results are presented in Tables 1 through 4 and Figures 1 and 2. In all the simulations a modified LDU preconditioner was used with no fill-up of the resulting LU preconditioned matrices. The following conclusions can be drawn:

(1) The LUBAND routine is a fast and efficient solver with modest memory requirements, and can solve large problems previously untractable with the MA28 solver.

(2) Bandwidth minimization significantly improves the LUBAND performance.

(3) Coupling D4 with LUBAND increases the solver speed by at least a factor of 2, and makes it competitive with iterative solvers in small and medium-sized matrices. However, the speed advantage of the PCG solvers becomes apparent in three-dimensional problems.

(4) BCGSTB is very competitive, and outperforms the T2CG1 iterative solvers in almost all cases. There seems to be no measurable difference in performance for $\ell = 2$ and $\ell = 4$.
(5) BCGSTB does not exhibit oscillatory behavior, and does not suffer from instability as it approaches the steady-state condition.

Acknowledgement

This work was supported by the Director, Office of Civilian Radioactive Waste Managenent, Yucca Mountain Site Characterization Project Office, under U.S. Department of Energy contract No. DE-AC03-76SF00098. Drs. Curt Oldenburg and Stefan Finsterle are thanked for their helpful review comments.

References

Aziz, K. and A. Settari (1979), Petroleum Reservoir Simulation, Elsevier, London and New York.
Duff, I. S. (1977) MA28 - A set of Fortran Subroutines for Sparse Unsymmetric Linear Equations, AERE Harwell Report R 8730.
Fletcher, R. (1976) Conjugate gradient methods for indefinite systems. Numerical Analysis, Lecture Notes in Mathematics 506, Springer-Verlag, New York.
LAPACK (1993), Univ. of Tennessee, Univ. of California at Berkeley, NAG ltd., Courant Institute, Argonne National Lab., and Rice University, Version 1.1.
Moridis, G.J., and K. Pruess (1992), TOUGH simulations of Updegraff's set of fluid and heat flow problem, Lawrence Berkeley Laboratory report LBL-32611.
Moridis, G.J., and K. Pruess (1995), T2CG1: A package of preconditioned conjugate gradient solvers for the TOUGH2 family of codes, Lawrence Berkeley Laboratory report LBL-36235.
Price, H. S., and K. H. Coats (1974), Direct methods in reservoir simulation, Trans. SPE of AIME (SPEJ), 257, 295-308.
Sleijpen, G.L.G., and D. Fokkema (1993), BICGSTAB(l) for linear equations involving unsymmetric matrices with complex spectrum, Electronic Transcations on Numerical Analysis, 1, 11-32.
Sonneveld, P. (1989) CGS, A fast Lanczos-type solver for nonsymmetric linear systems. SIAM J. Sci. Stat. Comput., 10(1), 36-52.
van der Vorst, H.A. (1992), Bi-CGSTAB: A fast and smoothly converging variant of Bi-CG in the presence of rounding errors, SIAM J. Sci. Statist. Comput., 13, 631-644.

Table 1. Solver Performance in Test Problem 1

Number of Equations: 832 (2-D)			Apple Macintosh QUADRA 800		
SOLVER	Number of Δt's	Newtonian Iterations	Maximum N_{CG}	Minimum N_{CG}	CPU Time (sec)
MA28	26	91	-	-	331
DSLUBC	26	91	31	2	321
DSLUCS	26	91	35	2	295
DSLUGM	26	91	41	11	299
LUBAND	26	91	-	-	246
LUBAND/D4	26	91	-	-	98
BCGSTB(2)	26	91	36	4	301
BCGSTB(4)	26	91	32	8	300

Table 2. Solver Performance in Test Problem 2					
Number of Equations: 8,003 (2-D)			IBM RS/6000 370		
SOLVER	Number of Δt's	Newtonian Iterations	Maximum N_{CG}	Minimum N_{CG}	CPU Time (sec)
MA28	Could not solve the problem due to insufficient memory.				
DSLUBC	10	17	225	172	158
DSLUCS	10	17	173	154	86
DSLUGM	10	19	316	810	379
LUBAND	10	17	-	-	55
LUBAND/D4	10	17	-	-	26
BCGSTB(2)	10	17	64	16	40
BCGSTB(4)	10	17	64	24	33

Table 3. Solver Performance in Test Problem 3					
Number of Equations: 2400 (2-D)			IBM RS/6000 370		
SOLVER	Number of Δt's	Newtonian Iterations	Maximum N_{CG}	Minimum N_{CG}	CPU Time (sec)
MA28	97	521	-	-	450
DSLUBC	102	554	45	9	593
DSLUCS	110	594	45	6	408
DSLUGM	125	673	179	8	478
LUBAND	97	521	-	-	946
LUBAND(opt)	97	521	-	-	376
LUBAND/D4	97	521	-	-	168
BCGSTB(2)	106	531	40	4	388
BCGSTB(4)	104	529	40	8	399

Table 4. Solver Performance in Test Problem 4					
Number of Equations: 3,900 (3-D)			IBM RS/6000 370		
SOLVER	Number of Δt's	Newtonian Iterations	Maximum N_{CG}	Minimum N_{CG}	CPU Time (sec)
MA28	Could not solve the problem due to insufficient memory.				
DSLUBC	50	249	36	8	619
DSLUCS	50	239	20	4	462
DSLUGM	50	250	28	7	451
LUBAND	50	232	-	-	6412
LUBAND(opt)	50	232	-	-	4228
LUBAND/D4	50	232	-	-	1683
BCGSTB(2)	50	236	16	8	439
BCGSTB(4)	50	235	32	8	453

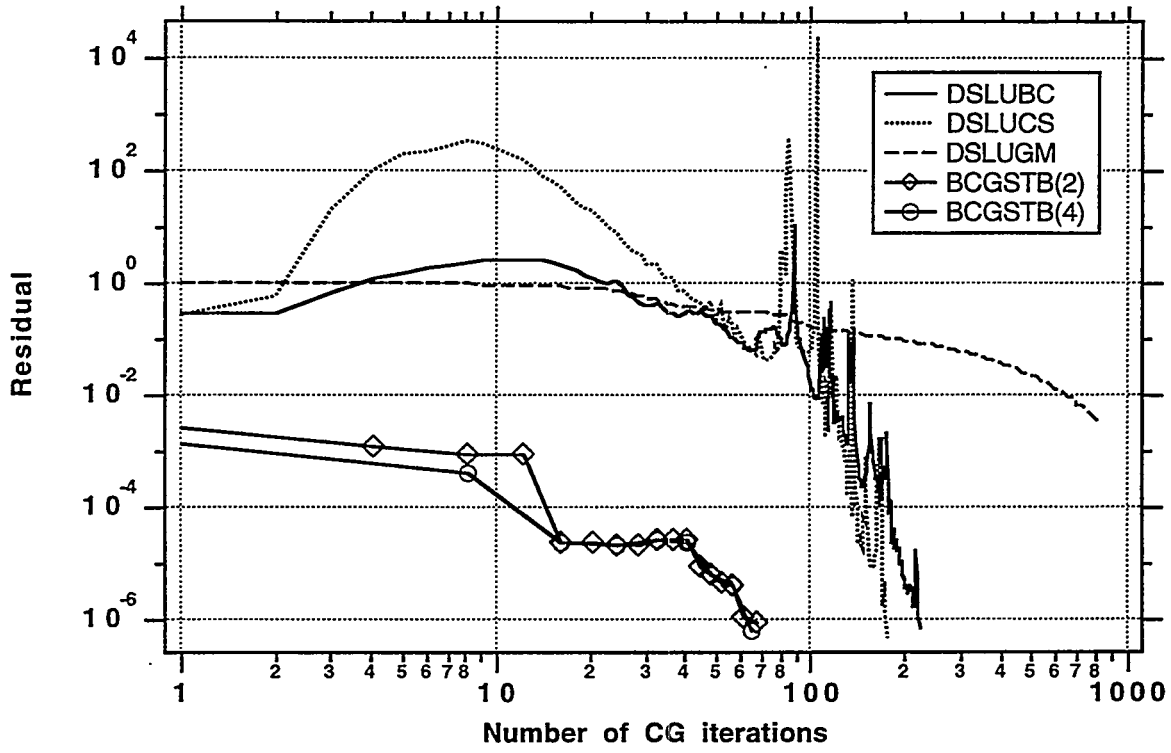

Figure 1. CG solver performance in the first Newtonian iteration of the 10th timestep in Test Problem 2.

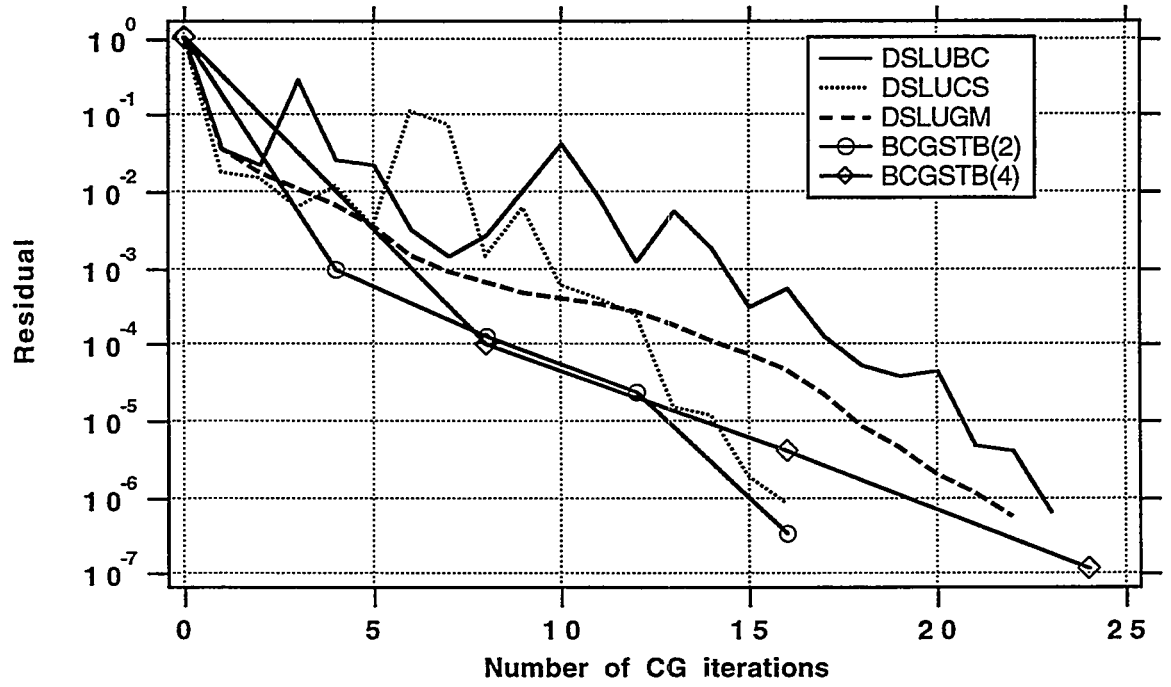

Figure 2. CG solver performance in the first Newtonian iteration of the 50th timestep in Test Problem 2.

DIOMRES (k, m): AN EFFICIENT METHOD BASED ON KRYLOV SUBSPACES TO SOLVE BIG, DISPERSED, UNSYMMETRICAL LINEAR SYSTEMS

Eli de la Torre Vega * & Mario César Suárez Arriaga **

* Instituto de Investigaciones Eléctricas, Int.Ap. Palmira, Cuernavaca, Mor., México
** Universidad Michoacana SNH, 58090 Morelia, Michoacán, México. Fax (43) 14 4735

ABSTRACT

In geothermal simulation processes, MULKOM uses Integrated Finite Differences to solve the corresponding partial differential equations. This method requires to resolve efficiently big linear dispersed systems of non-symmetrical nature on each temporal iteration. The order of the system is usually greater than one thousand and its solution could represent around 80% of CPU total calculation time. If the elapsed time solving this class of linear systems is reduced, the duration of numerical simulation decreases notably. When the matrix is big ($N \geq 500$) and with holes, it is inefficient to handle all the system's elements, because it is perfectly figured out by its elements distinct of zero, quantity greatly minor than N^2. In this area, iteration methods introduce advantages with respect to gaussian elimination methods, because these last replenish matrices not having any special distribution of their non-zero elements and because they do not make use of the available solution estimations. The iterating methods of the Conjugated Gradient family, based on the subspaces of Krylov, possess the advantage of improving the convergence speed by means of preconditioning techniques. The creation of DIOMRES(k,m) method guarantees the continuous descent of the residual norm, without incurring in division by zero. This technique converges at most in N iterations if the system's matrix is symmetrical, it does not employ too much memory to converge and updates immediately the approximation by using incomplete orthogonalization and adequate restarting. A preconditioned version of DIOMRES was applied to problems related to unsymmetrical systems with 1000 unknowns and less than five terms per equation. We found that this technique could reduce notably the time needful to find the solution without requiring memory increment. The coupling of this method to geothermal versions of MULKOM is in process.

INTRODUCTION

The MULKOM family of computer modules for simulating the flow of mass and heat in reservoirs (Pruess, 1988), uses a numerical method that generates big systems of algebraic linear equations. These systems could have some few elements different from zero irregularly distributed in the corresponding matrix. The resolution of such sparse unsymmetrical large systems represents typically 80% of the total CPU time in any simulation, which could last from some minutes to some days, depending on the computer and on the class of problem. Some years ago the linear systems were resolved by gaussian elimination or by factorization. But in this type of dispersed systems, the necessary memory increases a lot, without taking advantage of available knowledge about the possible solution's location. The Jacobi and Seidel iterating methods do not have this inconvenient, but they can only improve one variable simultaneously at each iteration.

The Conjugate Gradient iterating procedures vary all the variables at the same time, seeking the best directions of change and the best longitude of movement. The method we are introducing resolves approximately linear systems of the form: $\mathbf{A}\,\mathbf{x} = \mathbf{b}$, where $\mathbf{A}$ is the matrix of coefficients, $\mathbf{x}$ is the unknown vector and $\mathbf{b}$, the information vector.

Let $\mathbf{x}^*$ be the exact solution; for an approximation $\mathbf{x}_n$ corresponding to the n^{th} iteration, the error is given by the vectorial equation $\epsilon_n = \mathbf{x}^* - \mathbf{x}_n$. The residual is defined by $\mathbf{r}_n = \mathbf{b} - \mathbf{A}\,\mathbf{x}_n$. Both become zero when the approximation attains the exact solution: $\mathbf{x}_n = \mathbf{x}^*$. The methods of the Conjugate Gradient family (Reid, 1971), which contributed with several ideas to the construction of our method, are: ORTHOMIN (Eisenstat, 1983), DIOM (Saad, 1984) and GMRES (Saad, 1986).

THE DIOMRES (k, m) METHOD

DIOMRES generates approximations that take advantage of an initial value ($\mathbf{x}_0$), combining a set of linearly independent vectors ($\mathbf{v}_1$, $\mathbf{v}_2$, ..., $\mathbf{v}_n$), in a similar way as in the Conjugated Gradient method:

$$x_n = x_0 + \sum_{j=1}^{n} v_j y_j = x_0 + V_n Y_n \quad \ldots\ldots\ldots\ldots \quad (1) \ ,$$

where the columns of matrix $\mathbf{V}_n$ are the searching directions $\mathbf{v}_j$ and the coordinates y_j are chosen by minimizing the residual's squared norm $R_m = r_m^T r_m$ instead of the error's A-norm $\| \varepsilon \|_A^2 = \varepsilon^T A \varepsilon$ which requires that $\mathbf{A}$ be symmetrical and definite positive to converge. Including the advantages of two well-known techniques, DIOMRES(k,m)

was developed, by modifying the method GMRES(m) with ideas from DIOM(k). Following the Conjugate Gradient technique, which produces orthogonal residuals with respect to the basis: ($\mathbf{V}_n^T\, \mathbf{r}_n = \mathbf{0}$), the method DIOM(k) finds the coordinates solving the system:

$$H_n Y_n = V_n^T A\, V_n Y_n = V_n^T r_0 \quad \ldots\ldots\ldots\ldots \quad (2)\ ,$$

where the elements $h_{i,n} = \mathbf{v}_i^T\, (\mathbf{A}\, \mathbf{v}_n)$ are the required factors to orthogonalize $\mathbf{Av}_n$ with the previous vectorial basis and $h_{n+1,n}$ is needed to normalize:

$$v_{n+1} = (A v_n - \sum v_i h_{i,n}) / h_{n+1,n} \quad \ldots\ldots\ldots\ldots \quad (3)$$

The initial vector $\mathbf{v}_1$ is taken normalizing the initial residual: $v_1 = r_0 / \| r_0 \|$ and arriving to:

$$V_n = V_n H_n^* \qquad V_n^T r_0 = \| r_0 \| \quad \ldots\ldots\ldots\ldots \quad (4)\ ,$$

where $\mathbf{e}_1$ has an element equal to one in the first component and zeros in all the others. $\mathbf{H}^*_n$ is a matrix formed by the first n columns of matrix $\mathbf{H}_{n+1}$. Generating the basis in this way, $\mathbf{H}_n$ has null all its elements below the first inferior diagonal ($h_{i,j}=0$, if $i>j+1$) and if the matrix $\mathbf{A}$ is symmetrical, $\mathbf{H}_n$ also will be; this means that only is necessary to orthogonalize $\mathbf{Av}_n$ with the two previous vectors ($\mathbf{v}_n$ and $\mathbf{v}_{n-1}$) in order to get the same outcomes.

DIOMRES (k,m) also uses this basis but, minimizing the norm of the residual, obtains always better approximations than the foregoing. In this way, this technique could arrive to be as exact as is allowed by the computer's rounding error. Provided that vectors $\mathbf{v}_{j+1}$ are obtained as combinations of $\{\mathbf{v}_1, \mathbf{v}_2, \ldots \mathbf{v}_j, \mathbf{Av}_j\}$, the technic originates that the subspace generated by the basis $\{\mathbf{v}_1, \mathbf{v}_2, \ldots \mathbf{v}_{n+1}\}$ be the same as the space generated by $\{\mathbf{v}_1, \mathbf{Av}_1, \mathbf{A}^2\mathbf{v}_1, \ldots \mathbf{A}^n\mathbf{v}_1\}$, which is known as a **Krylov** subspace of order n+1. These last vectorial generators have the property of being linearly independent when the matrix A is non singular.

GMRES(m) contributed with the factorization: $H^*_m = Q_m U^*_m$ where $\mathbf{Q}_m$ is an adequate orthogonal matrix ($Q_m^T Q_m = I$). $\mathbf{U}^*_m$ is a matrix composed by a superior triangular matrix $\mathbf{U}_m$,; its line $(m+1)^{th}$ contains only zeros, in order to conceive the squared norm of the residual before calculating the new vectorial residual. Substituting the definition of the residual, equations 1 and 4, together with the orthogonality of the basis, plus this factorization and the orthogonality of $\mathbf{Q}_n$, we arrive to:

$$R_n = r_n^T r_n = Z_n^T Z_n + z_n^{*2} - 2 Y_n^T U_n^T Z_n + Y_n^T U_n^T U_n Y_n \quad \ldots (5)$$

whose minimal is obtained from: $\mathbf{Y}_m = \mathbf{U}_m^{-1}\, \mathbf{Z}_m$ where:

$$Q_m^T \| r_0 \| e_1 = \left[Z_m^T \mid z_m^* \right]^T$$

DIOMRES(k,m) also uses this factorization, but utilizing an incomplete orthogonalization; the way to update the solution is also different. In GMRES(m):

$$x_n = x_0 + V_n (U_n^{-1} Z_n) = x_0 + V_n Y_n \quad \ldots\ldots\ldots \quad (6)\ ;$$

this requires to wait for the m^{th} iteration to accomplish the backward substitution and resolve $\mathbf{Y}_n$; and then update the solution; this needs to stock the m vectors of the basis $\mathbf{v}_j$. Whereas, DIOMRES(k,m) performs:

$$x_n = x_0 + (V_n U_n^{-1}) Z_n = x_0 + W_n Z_n = x_{n-1} + w_n z_n \quad \ldots (7);$$

where vectors $\mathbf{w}_j$ are solved by means of a forward substitution when calculating the columns of $\mathbf{U}_n$. These vectors no longer change, allowing to update the solution immediately.

Among the analysed methods to solve several kinds of linear problems, the most rapid was GMRES(m) in some unsymmetrical cases, and ORTHOMIN (k) for the indefinite symmetric and the other non-symmetric cases. Both methods minimize the squared norm of the residual. GMRES(m) solved the memory problem using frequent restarts, and ORTHOMIN(k) using incomplete orthogonalization, which is exact in the symmetric case. However, indefinite matrix systems exist where ORTHOMIN(k) incurs in a division by zero before arriving to the solution and could lose its convergence speed if an inferior value for k is used. DIOMRES(k,m) doesn't have this risk. This technique solves the memory problem choosing a small value for k and the loss of speed is prevented by restarting the process in an opportune moment. If the matrix is symmetric, k =2 and m =N are always used.

DIOMRES(k,m) ALGORITHM

Data needed by DIOMRES are: matrix of coefficients (A), vector (b), an initial approximation ($\mathbf{x}_0$), maximum number of iterations, an acceptable error's norm (tolerance), number (k) of orthogonalizations to do and a restart period (m). The initial residual and its norm are calculated first:

$$r_0 = b - A x_0\ ; \quad z_1^* = \| r_0 \| \quad \ldots\ldots\ldots \quad (8)\ .$$

If its value is sufficiently accurate, $\mathbf{x}_0$ is accepted as the solution. Else, the residual is normalized to get the first vector of the basis: $v_1 = r_0 / \| r_0 \|$ ... (9) .

From this moment, at every m^{th} iteration of this cycle, the following steps are carried out:

a) the n^{th} column of $\mathbf{H}^*_m$ and the new basis are calculated:

$$h_{i,n} = \begin{cases} 0, & i \le n-k \qquad \bar{v}_{n+1} = A v_n - \sum_{i=1}^{n} v_i h_{i,n} \\ v_i^T A v_n, & n-k < i < n \\ \| \bar{v}_n \|, & i = n+1 \qquad v_{n+1} = \bar{v}_{n+1} / h_{n+1,n} \end{cases} \qquad (10)$$

b) The rotations detected before are applied to the new column of $\mathbf{H}_m^*$; for j=1,2, ... , n-1, and $h^*_{1,n} = h_{1,n}$:

$$\begin{bmatrix} u_{j,n} \\ h^*_{j+1,n} \end{bmatrix} = \begin{bmatrix} q_{1,j} & q_{2,j} \\ -q_{2,j} & q_{1,j} \end{bmatrix} \begin{bmatrix} h^*_{j,n} \\ h_{j+1,n} \end{bmatrix} \quad \text{..... (11)}$$

c) The new rotation data are found:

$$u_{n,n} = \sqrt{h^2_{n,n} + h^2_{n+1,n}}; \quad q_{1,n} = \frac{h_{n,n}}{u_{n,n}}; \quad q_{2,n} = \frac{h_{n+1,n}}{u_{n,n}} \quad \text{... (12)}$$

d) This last rotation is applied to the right side of the system $\mathbf{H}^*$:

$$\begin{bmatrix} z_n \\ z^*_n \end{bmatrix} = \begin{bmatrix} q_{1,n} & q_{2,n} \\ -q_{2,n} & q_{1,n} \end{bmatrix} \begin{bmatrix} z^*_{n-1} \\ 0 \end{bmatrix} \quad \text{... (13)}$$

e) A new vector w_n is found and the solution is updated:

$$w_n = \frac{(v_n - \sum_{j=1}^{n-1} w_j u_{j,n})}{u_{n,n}}; \quad x_n = x_{n-1} + w_n z_n \quad \text{... (14)}$$

f) If available iterations were finished or if desired accuracy ($|z^*_n| \leq Tol$) was reached, x_n is accepted as the solution.

g) If the cycle of m iterations was completed, the initial value becomes $x_0 = x_m$ and the algorithm is restarted.

More details about this algorithm are given in de la Torre (1990). Information on the previous methods and the manner of using preconditioning system techniques to accelerate convergence are also found in the cited document.

PROPERTIES OF DIOMRES(k,m)

The principal properties of this method are:

i) DIOMRES(m,m) produces the same approximations as GMRES(m).
ii) DIOMRES(k, ∞) produces the same approximations as ORTHOMIN(k-1).
iii) The termination in no more than N iterations is guaranteed using k =N when the matrix is symmetric.
iv) Every approximation minimizes the squared norm of the residual into the subspace generated by the last k vectors of the basis and transferred by the latest approximation. This allows to attain the maximum accuracy permitted by computer's rounding.
v) Although, for a same value of k, DIOMRES(k,m) could be in disadvantage in front to another methods (table 1), using an adequate restart period (m), generally allows to reduce the needful value of k achieving a minor requirement of auxiliary memory and time.
vi) DIOMRES(k, ∞) and DIOM(k) have the same time and memory requirements but, as long as DIOMRES(k,m) minimizes the residual, it always generates improved approaches and finishes swifter.
vii) Approximations are updated in each iteration.
viii) It is applicable to both symmetric (and takes advantage of it) and unsymmetric systems.

NUMERICAL EXPERIMENTS

In the following experiments the convergence speed of the aforementioned techniques will be compared and the results illustrated in log-linear graphs. All numerical experiments were performed in a Micro VAX 11/730 employing a rounding unit of 1.39×10^{-17} approximately, in double precision. The vector zero was always taken as the initial approached value.

1.- The first test was carried out with a linear system arisen when resolving numerically the equation of Laplace in two dimensions $\nabla^2 F(x,y) = 0$, using finite differences in a plane region with 30 divisions in the X axis and 50 in the Y axis. The matrix is of order 1500, symmetric and definite positive. Figure 1 shows the graphs obtained during the solution of this system. For this problem, the most rapid method is Conjugate Gradient, (this type of matrix is its specialty). However, DIOMRES(2,N) doesn't stay so far. GMRES(5) resulted to be the worst technique for this type of problems.

2.- The second experiment was taken from a problem proposed by Saad (1984); it corresponds to finite differences solution of the equation: $-\nabla^2 f(x,y) + c\partial f/\partial x + bf(x,y) = g(x,y)$, on a plane with 10 divisions in X and 20 in Y. The resultant system, of order 200, is unsymmetric and indefinite. Figure 2 shows that ORTHOMIN(14) takes a long time to converge and requires much memory. Conjugate Gradient shoots up, then converges in penultimate place. DIOMRES(5,66) results the fastest method, followed very close by DIOM(5) and GMRES(9).

3.- The third test was fulfilled with a linear system arose in a real application, when solving a non linear partial differential equation, from the Electrical Research Institute of Mexico (de la Torre, 1990). This is the type of system that introduces more difficulties and is a good example where Conjugate Gradient diverges and DIOM (k) requires much time and memory to converge. The corresponding matrix is unsymmetrical, indefinite, highly dispersed (5 terms per equation) and of order 961. The methods were proven first without preconditioning. Figure 3 demonstrates that unsymmetrical cases exist where Conjugate Gradient diverges without hope whatever. DIOM(4) fluctuates and is the slowest, while the other techniques differ little in speed.

TABLE 1.- COMPARISON OF TIME AND MEMORY REQUIREMENTS IN DIFFERENT METHODS.

Method	No. Products / Iteration (@)	Memory	Ref.
CONJUGATE GRADIENT	$MT+5N$	4N	Hestenes,1952 Reid, 1971
ORTHOMIN(k)	$MT+(3k+4)N$	(2k+3) N	Stanley, 1983
GMRES (k)	$MT+(k+3+\frac{1}{k})N$	(k+2) N	Saad, 1986
DIOM(k)	$MT+(3k+2)N$	(2k+3) N	Saad, 1984
DIOMRES(k,m)	$\frac{m+1}{m}MT+(3k+2-\frac{k(3k-1)}{2m})N$	(2k+3) N	De la Torre, 1990

(@) N is the number of equations; MT indicates the number of non-zero matrix elements.

4.- The same previous problem was solved in the fourth experiment, but now with preconditioning. All the methods improve their speed, however DIOMRES(2,4) results unquestionably, the fastest and with its superior convergence speed, it didn't require more memory than the rest.

CONCLUSIONS

We introduced a brief description and some numerical results showing the typical behavior of DIOMRES(k, m) when confronted to Conjugate Gradient, GMRES(k), DIOM(k) and ORTHOMIN(k), under different conditions of symmetry, spectrum (set of eigenvalues) and preconditioning. As is appreciated in the graphs, the adequate preconditioning election, the restart period and the number of orthogonalizations, allows us to solve big, unsymmetrical, sparse linear systems fast and with few memory. The method presented herein takes advantage of the available estimates of the solution avoiding the stalemate provoked by insufficient orthogonalization and taking the advantage, with symmetric matrices, of $\mathbf{Av}_n$ orthogonalization with the two more recent vectors. The adequate preconditioning technic generally diminishes the time required to find the solution in all methods. Linear systems exist where DIOMRES is flagrantly faster than the best tested methods. Being a method that minimizes the norm of the residual in each iteration, it is possible to reach all the exactness permitted by the computer's processor. The coupling of this method to MULKOM simulator is in process.

REFERENCES

-**Arnoldi, W.E.**; 1951. "*THE PRINCIPLE OF MINIMIZED ITERATION IN THE SOLUTION OF THE MATRIX EIGENVALUE PROBLEM*".Quart. Appl. Math., 9, (pp.17-29).

-**De la Torre V., E.** 1990. "*SOLUCION DE SISTEMAS LINEALES GRANDES Y HUECOS MEDIANTE MÈTODOS ITERATIVOS BASADOS EN LOS ESPACIOS DE KRYLOV*". Bc.Sc.Thesis on Mathematical Physics, Michoacán University, Morelia, Mich.; México (156 p.). This work was supported by the National Council of Science and Technology.

-**Golub,G.H. & Van Loan,C.**1983. "*MATRIX COMPUTATIONS*". The John Hopkins U.Press Baltimore Maryland, (pp.362-379).

-**Hestenes,M. & Stiefel,E.**; 1952. "*METHODS OF CONJUGATE GRADIENTS FOR SOLVING LINEAR SYSTEMS*". J. Res. Nat. Bur. Standards, 49, (pp. 409-436).

-**Lanczos,C.**1950. "*AN ITERATION METHOD FOR THE SOLUTION OF THE EIGENVALUE PROBLEM OF LINEAR DIFFERENTIAL AND INTEGRAL OPERATORS*". J. Res. Nat. Bur. Standards, 45, (pp. 255-282).

-**Paige,C. & Saunders,M.A.** 1975. "*SOLUTION OF SPARSE INDEFINITE SYSTEMS OF LINEAR EQUATIONS*". SIAM J. Anal., Vol. 12, Num. 4, (pp. 617-629).

-**Pruess, K.** (1988). "*SHAFT, MULKOM, TOUGH: A SET OF NUMERICAL SIMULATORS FOR MULTIPHASE FLUID AND HEAT FLOW* GEOTERMIA - Rev.Mex.de Geo.,Vol. 4, No.1, pp. 185-202.

-**Reid,J.** "*ON THE METHOD OF CONJUGATE GRADIENTS FOR THE SOLUTION OF LARGE SPARSE SYSTEMS OF LINEAR EQUATIONS*". Proc. Conf. on Large Sparse Sets of Linear Equations, Academic Press, New York, 1971, (pp. 231 - 254).

-**Saad,Y.**1981. "*KRYLOV SUBSPACE METHODS FOR SOLVING LARGE UNSYMMETRIC LINEAR SYSTEMS*".Math.Compt.,37,(pp.105-126).

-**Saad.Y.**; 1984. "*PRACTICAL USE OF SOME KRYLOV SUBSPACE METHODS FOR SOLVING INDEFINITE AND NONSYMMETRIC LINEAR SYSTEMS*". SIAM J. Numer. Anal., 5, (pp 203-227).

-**Saad,Y. & Schults,M.**1986. "*GMRES: A GENERALIZED MINIMAL RESIDUAL ALGORITHM FOR SOLVING NONSYMMETRIC LINEAR SYSTEMS*". SIAM J.Scl.Stat.Com., Vol.7,Num.3,(pp.856-869).

-**Stanley,C.,Eisenstat,H.,ELman,C.,& Shultz, M.** 1983. "*VARIATIONAL ITERATIVE METHODS FOR NONSYMMETRIC SYSTEMS OF LINEAR EQUATIONS*"., SIAM J. Numer Anal. Vol. 20 No.2.

-**Young,D. M.**; 1971. "*ITERATIVE SOLUTION OF LARGE LINEAR SYSTEMS*". Academic Press.

Fig. 1.- Computational Work Vs. Residual For a Symmetric, Definite Positive Linear System with 1500 equations.

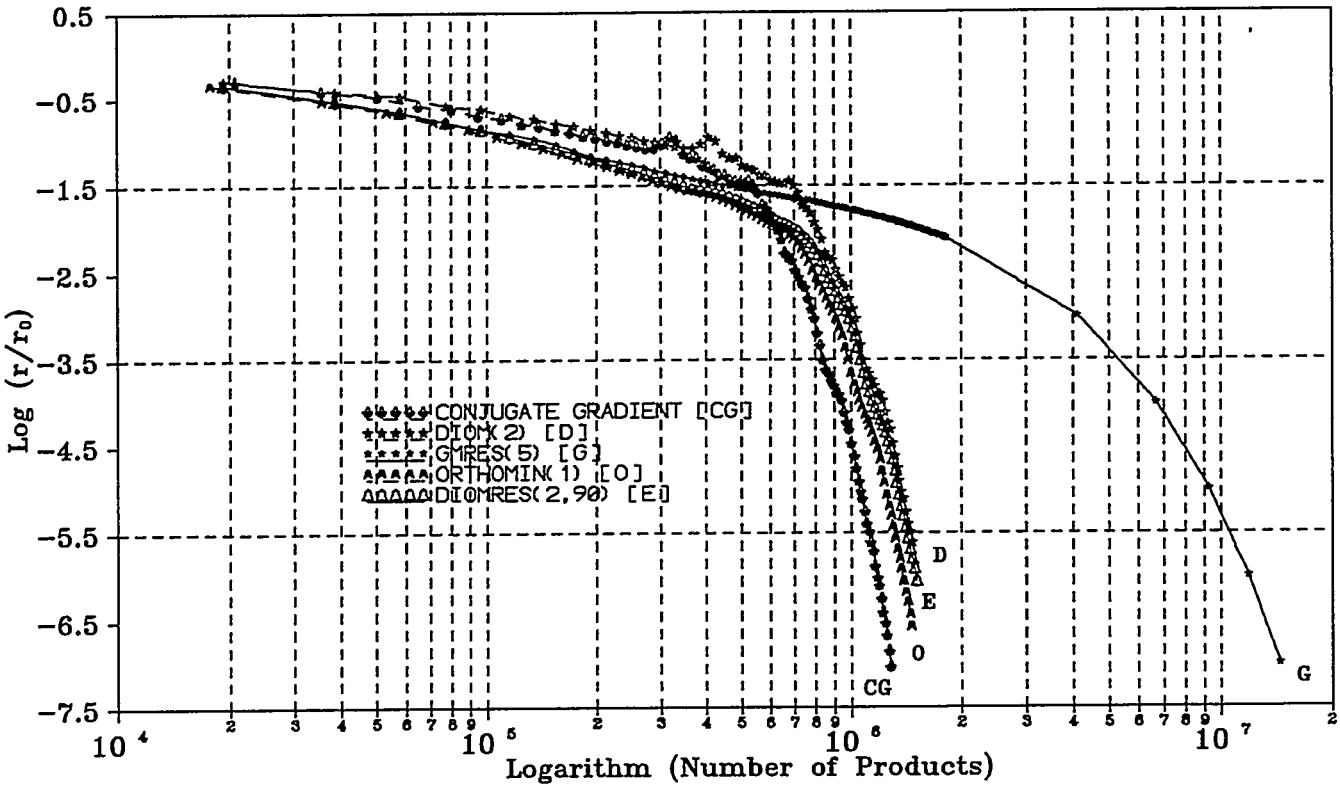

Fig. 2.- Computational Work Vs. Residual For an Unsymmetric, Indefinite Linear System with 200 equations.

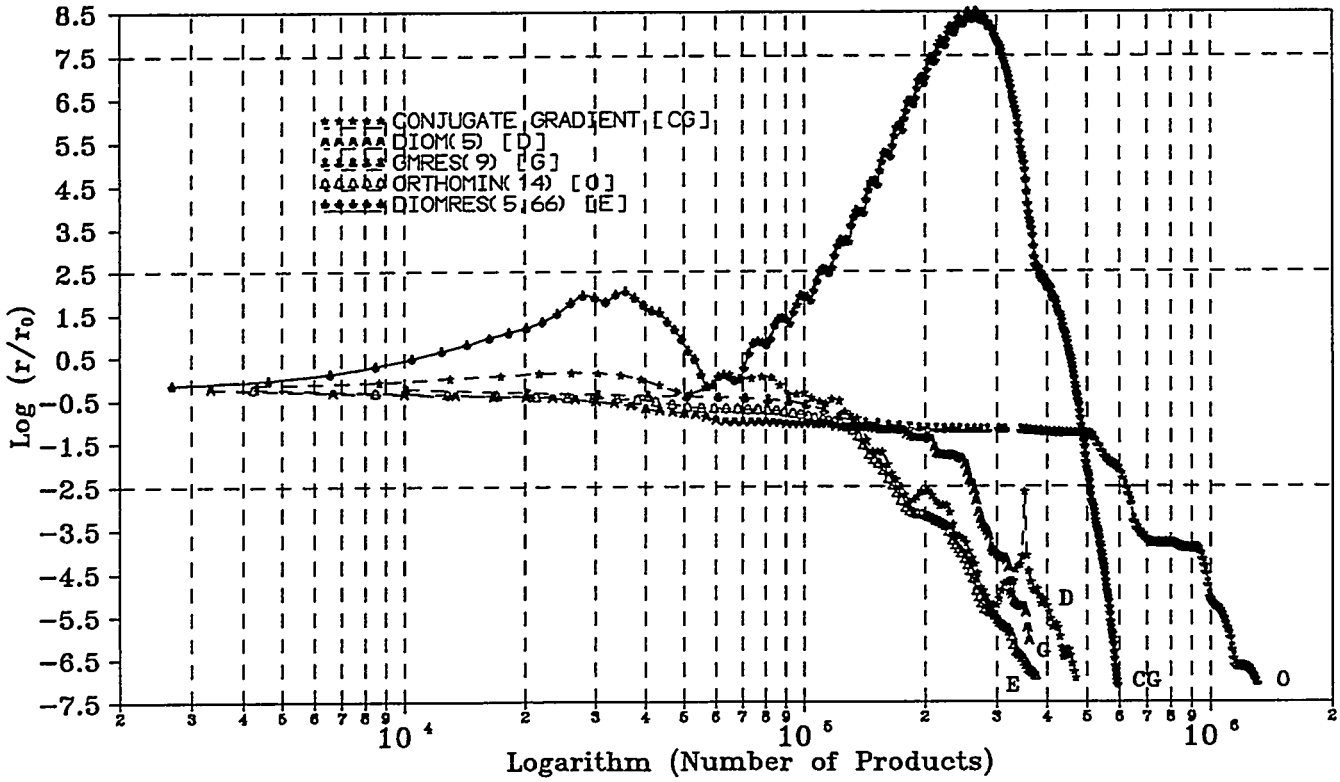

Fig. 3.- Computational Work Vs. Residual For an Unsymmetric, Indefinite Linear System with 961 equations, without Preconditioning.

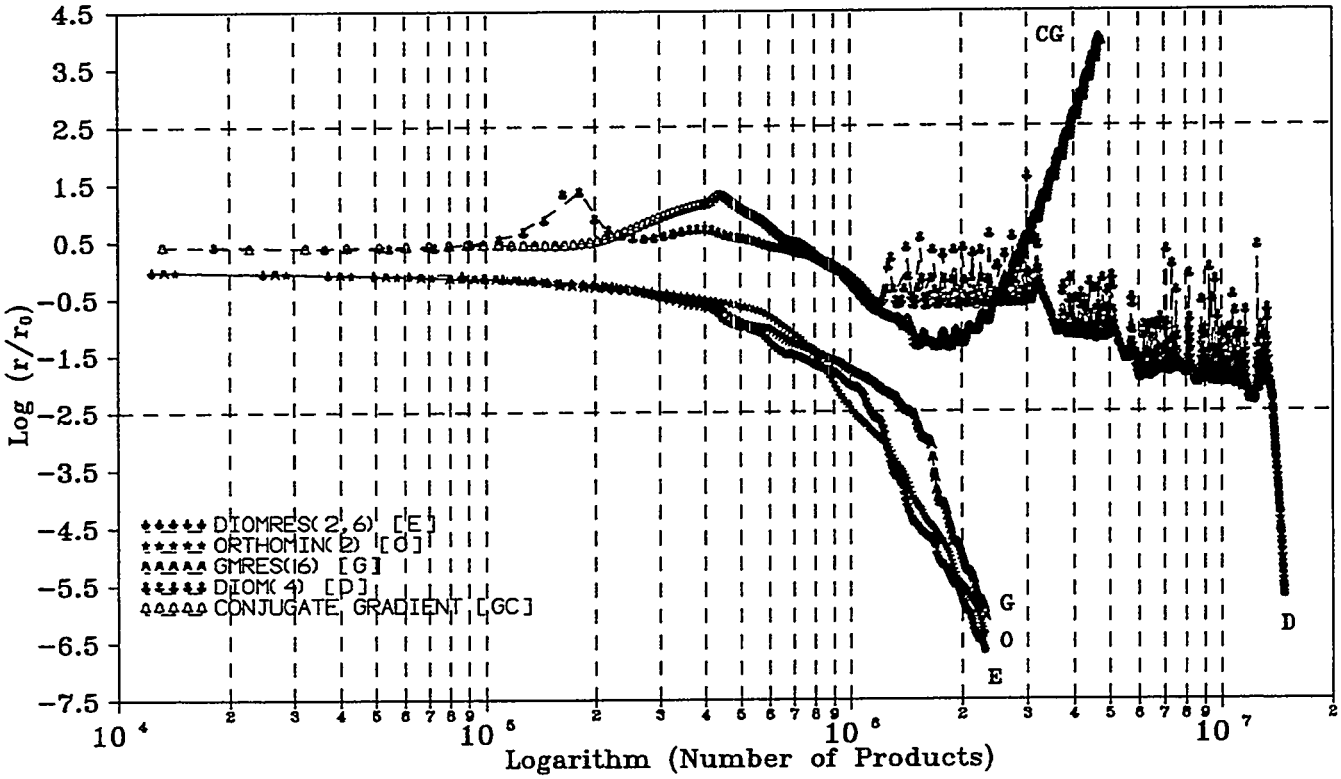

Fig. 4.- Computational Work Vs. Residual For an Unsymmetric, Indefinite Linear System with 961 equations, with Preconditioning.

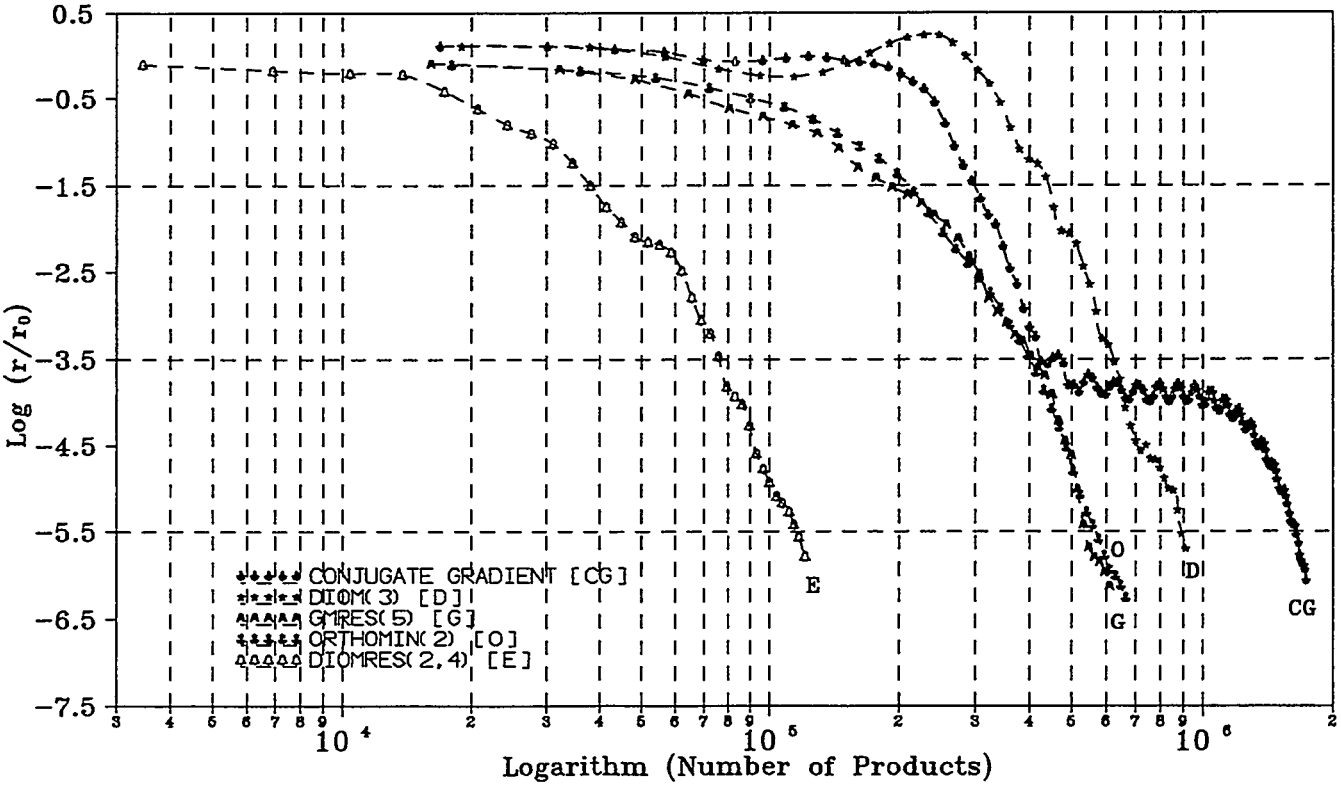

EVEGAS Project

(European Validation Exercise of **GAS** Migration Model)

T. Manai

Géostock S.A., Immeuble Sedgwick, 7, rue E. et A. Peugeot
92563 Rueil-Malmaison, Cedex, FRANCE

EVEGAS PROJECT

Title:	**EVEGAS (European Validation Exercise of GAS migration model through porous media**
Contractors:	**GEOSTOCK (France)**
Major Subcontractor:	**Bertin & Compagnies (France)**
Associated Contractors :	**ANDRA (France),CIMNE (Spain),ARMINES (France), INTERA(UK), CEN (Belgium), SIMOCO (UK)**
Other Participants:	**GRS (Germany)**
Contract Number:	**FI2W-CT93-0125**
Duration of Contarct:	**January 1994 to December 1995**
Period Covered:	**January 1994 to December 1994**
Project Leader :	**T. MANAI (GEOSTOCK (France))**
Support:	**CEC DGXII/F5 WSME R&D Programme on Management and storage of Radiactive Waste disposal of the European Commision**

A. OBJECTIVES AND SCOPES

The EVEGAS project aims at the verification and validation of numerical codes suitable for simulating gas flow phenomenon in low permeability porous media.
Physical phenomena involved in gas generation and gas flow are numerous, often complex, and may not be very well described.
The existing numerical codes cannot represent all the occurring possible phenomena, but allow a good trade-off between simplicity and representativity of such phenomena.
Two phase flow (Gas and Water) appear to be the most consequential phenomena in gas migration and pressure sizing.
The project is organised in three major steps:

1)A simple problem with analytical solutions

This is a necessary first step which allows assessing the accuracy of numerical solutions in function of given parameters. Such a quantitative evaluation of the numerical codes, will be useful to interpret deviations that might occur in simulating more realistic test cases.

2)A few problems based on laboratory or in-situ experiments

Such tests will aim access to the following information:

- the accuracy of the numerical solutions (**assuming the existing of good and representative experimental data**).

3)A 3-D repository scenario involving the following aspects

- a repository design
- a source of gas
- rock characteristics
- fluid characteristics.

B. WORK PROGRAM

The project is divided into five work packages (denoted WP) each of them involving one or several tasks.
The first work package (WP1) is dedicated to the analysis of selected numerical codes. Such analysis will be of paramount importance in describing test cases.
It includes examination of the problems that can be simulated and of the numerical schemes and solving methods used.
The next work packages (WP2, WP3, WP4) are related to the three levels of test cases. Each work packages includes four tasks as follows:

- T1: general and detailed specification (GDS) of the test cases
- T2: general and detailed definition (GDD) of the test cases
- T3: simulation of the test cases by participants
- T4: analysis of results and reporting.

C. PROGRESS OF WORKS AND RESULTS

State of advancement

The last year was dedicated to the following work packages and tasks :

-Code analysis (WP1)
-First level test cases specification and definition (WP2T1, WP2T2)
-First level test cases simulation by participants (WP2T3)
-First level test cases simulation results analysis and reporting (WP2T4)
-Second level test cases specification and definition (WP3T1, WP3T2)

WP1,WP2T1,WP2T2,WP2T3,WP2T4,WP3T1 and WP3T2 was accomplished

Progress and results

C1. CODE ANALYSIS(WP1)
C1.1.Comments

C.1.1.1.Codes objectives

The six considered codes have been initially designed for different purposes, and then extended in order to take into account new problems. This initial design or main scope appears in the documentation, and also explains that a number of features only appear into one or two of them.

This paragraph presents the vocation of the codes, but this should not be interpreted as limitations of the ability of each of them to treat the problems addressed to in the EVEGAS project.
Only the two codes SUNIDJ and BRIGHT are dedicated to the problem under concern, namely gas migration related to radioactive waste disposal, and they are also the most recent among the six analysed codes.
For SUNIDJ the problem is that of the migration of a gas (H_2) produced at one location (point or finite volume) of a porous medium saturated by a liquid, and with the assumption that the overall problem is an isothermal one.
It can be noticed that this code explicitly tries to apply petroleum engineering based approaches to solve this actual problem.
For BRIGHT the point dealt with, is that of the sealing joints of repository wells dug in salty formations. As the joints are filled by compacted salt aggregates, the problem is to ensure that no migration may occur, neither toward the atmosphere nor toward the surrounding water, due to some thermal (not gas) release at the repository location.
GENESYS and ECLIPSE have been initially designed to study gaseous and liquid petroleum production, with some emphasis put on phase changes, miscibility phenomena, and on the fractured nature of the porous media. They of course consider multispecies and heat transport.
TOUGHII and PROFLOW are generic codes, i.e. not really dedicated to some specific problem, the former, whose name is an acronym of "Transport of Unsaturated Groundwater and Heat" has been mainly used for hydrogeology studies including some phase changes and multispecies considerations, the latter, as also indicated by its name, aims general fluids transports in porous media.
The high degree of generality of a code like PORFLOW, makes it a multipurpose tool which can deal with various physical problems, with the drawback that the description of the problem remains to be done.
In the same way, the codes issuing from petroleum engineering, and which as such have been highly developed, are now also multipurpose tools (for example even gas-storage problems can be treated by option modules), having their own language.

C1.1.2.Entrance levels

This paragraph presents at which level of the modelisation process, is defined the documentation of each code, as indeed a code results from the modelisation of a class of problems.

The terms of the problem consist, firstly in the description of the whole set of taken into account phenomena, this defining the physical modelisation or set of physical hypotheses, and secondly in the set of questions concerning the studied process.
This is ***the first entrance level*** of a given problem.
BRIGHT is the only code to start from this first level, this making easier the search of the used physical hypotheses. SUNIDJ partly starts from this level but the asked questions, i.e. the quantities to be defined, are not clearly presented.
Once the physical problem is well and completely posed, it has to be translated mathematically; this leads to express equations: definition equations for the quantities, equations translating the used general physical principles, and some equations representing specific phenomena.
This is ***the second entrance level.***
At this level, the equations are written directly together with the boundary conditions (BC) and the system state equations at some initial time (IC). This implies that a first selection has been made among the various quantities, to define those which are considered as unknowns and those which are considered as parameters. By many aspects SUNIDJ is defined at this level.
In order to go towards the problem resolution, the former equations, BC and IC are most often mathematically transformed by substitution, addition and so on, to achieve a restricted set of equations and principal unknowns completed by compatible BC and IC, and to which are joined secondary equations and unknowns.
This is ***the third entrance level***, at this third level, the objective is to solve a mathematically well posed problem rather than to deal with physical interpretation.
Three of the studied codes use this entrance level:

- this level is natural for PORFLOW with respect to its generic vocation
- and as regards TOUGHII and GENESYS, it is probably because they are under development for a longer time and that the two first levels must have been published earlier.

Finally, as the equations are solved numerically, they have to be discretized, and often linearized, in a way which takes into account algorithms and computers constraints.
This is ***the fourth entrance level***, which is the only one used in the supplied ECLIPSE's documentation.

C1.1.3.Main physical hypotheses

The analysed codes are related to:

- flows, therefore to fluids displacements and to migrations when relative displacements occur
- in a porous unsaturated medium, therefore containing somewhere a minimum amount of at least two fluids
- with mass and thermal transfers
- with time dependency
- in a limited spatial domain.

In this spatial domain, Newtonian mechanics and ordinary thermodynamical principles are applied, hence the necessary conservation of mass, momentum and energy.
These quite general hypotheses are as hidden as are those which concern the macroscopic continuity of the media, which is necessary to define thermodynamical quantities, or the continuity of movements which allow to define partial and total derivatives. In a way or another, all the codes deal with multiphase flows.
The studied flowing fluids either are each considered as a specific fluid like in PORFLOW, or can be most often considered as fluids having two phases (liquid and vapour).
It must be noticed that for petroleum engineering originated codes, only the main fluid can have two phases.
As these flows take place in a porous material, there are indeed three phases.
All the codes consider at least one solid phase (porous material), and at least two different fluids, therefore they are multispecies.
All the codes can also treat imbibition and drainage problems with at least one wetting fluid (or phase) and at least one non-wetting fluid (or phase).

But for BRIGHT, which studies the complete medium i.e. the porous material plus the fluids, the porous material is assumed to be perfectly rigid, with usually isotropic and locally homogeneous properties.
PORFLOW, GENESYS and ECLIPSE have options for some non-isotropic properties like permeabilities.
The heterogeneity linked to fractured porous material can be taken into account by GENESYS and ECLIPSE.
The mass transfers are taken into account for phase changes, and species displacements.
The thermal transfers generally occur via the solid phase, but can also concern the primary fluid, though it is limited by the hypothesis of local thermal equilibrium.

Two exceptions must be outlined:

- on one side SUNIDJ considers no thermal transfer
- at the opposite side BRIGHT studies the local thermo-hydro-mechanics interdependencies.

For all the codes, at least the principal unknowns are assumed to vary in space and time, therefore all of them can treat unsteady problems.
The spatial domain is rather poorly defined, it is more or less assumed to be infinite, with specific areas for gas sources (but for BRIGHT), or for liquid sources (but for BRIGHT and SUNIDJ), or for thermal sources (but for SUNIDJ).

C1.1.4.Hypotheses related to the porous medium

A porous medium is characterised by:

- a geometrical quantity (porosity)
- a behaviour law with respect to local constraints (rheological law)
- and a quantity which defines the interactions between solid and fluid phases (permeability).

This last quantity implies the selection of a law of flow in the porous medium.

It can be noticed that other characterisations of the porous medium could have been done, like those based on fractal approaches.
Only BRIGHT offers a geometrical model for the porosity; an idealised geometry of salt grains and open pores is characterised by three parameters, the total porosity of the open pores is computed locally, and can vary in time and space.
Generally, the porosity is defined by a single parameter, constant in time, and which may vary in space inside the studied domain.
In order to have this scalar quantity everywhere defined, the concepts of homogenisation, representative elementary volume or effective quantity, are used. All these concepts consist in computing a local mean value, which will be all the more precise as the medium will be homogeneous.
Petroleum engineering originated codes also define a **dual porosity in order to represent (to model) the fractures**, therefore at each point two porosities are defined, and through an option these can be used to build an average value or pseudo-porosity.
The porous medium is generally assumed to be rigid; BRIGHT is the only code to really take into account the deformability of the medium with respect to local constraints, temperature and geometrical definition of the medium.
The permeability concept can only be defined with respect to the law of flow in porous medium, generally Darcy's law. But as this law is used independently for each fluid or phase, this requires to introduce concepts of intrinsic permeability (related to the porous medium alone) and of relative permeabilities (related to the different fluids or phases).
It must be pointed out that for very little porous media, the independent use of Darcy's law for each fluid may be doubtful, as some effects like Knundsen's ones are not described, though they may be important in this case.
The intrinsic permeability is usually represented by a scalar quantity, which is an average over values in several directions or values in the vicinity. In fact it is an effective permeability.

For PORFLOW the permeabilities can be defined with respect to the three main directions, and for ECLIPSE one permeability is considered along the main flow direction, and another one is considered orthogonal to it.
ECLIPSE and GENESYS consider one permeability for the matrix and another one for the fractures, with an option to deduce from them an average value, which defines an effective intrinsic permeability.
The relative permeabilities are assumed to be functions of the saturations in all the codes, with several available selections for these functions which can be derived from arrays of value or from empirical laws. These relative permeabilities are usually the one of the main source of non-linearity in the equations.
For example, in TOUGHII, some available functions are: linear law, power law, Brook-Corey's curves, Grant's curves, functions of Flatt-Klikoff, Sandia, Vermia...
The associated phenomena such as residual saturation of the wetting phase, hysteresis are also dealt with but the way it is done is not documented.
The Klinkenberg, i.e. the dependency of the relative permeability with respect to the local pressure level, may also be taken into account in all the codes.
The global permeabilities (intrinsic permeability x relative permeability) are therefore also dependent of the saturations and of the capillary pressure.
This capillary pressure, which is well defined only in the case of one solid phase, one non-wetting phase and one single wetting phase, is a function of the characteristics of the porous medium (porosity), of the permeabilities and of the saturations.
As for relative permeabilities, several empirical laws can be used to define the capillary pressure.
For example, in TOUGHII, some available laws are: linear law, Dickens's function, Trust model, functions of Milly, Leverett, Sandia, or Brooks-Corey's relationships.
It must be outlined that, everything related to relative permeabilities and capillary pressures, in a porous medium with numerous fluid components, is still to be studied, and therefore that only a priori models can be used for such cases. Moreover available data concern almost exclusively, either the couple water-air or the couple liquid-gas for the petroleum.
And last, it can be noticed that the saturation vapour pressure of a fluid is not the same in a free open space that in a porous medium. **This effect is taken into account by TOUGHII (Kelvin's law) and by BRIGHT.**

C2.FIRST LEVEL TEST CASES(WP2T1,WP2T2)

C2.1.Objectives

The prediction of gas migration in the context of radioactive waste disposal requires to take into account quite a lot of simultaneous phenomena, such as interactions of gas with liquids, thermal transfers, capillary pressure effects..., all of these phenomena occurring in a more or less known porous media, which may present gradients of properties.
In order to have realistic predictions of gas migration, it is essential to have a good physical knowledge of all these phenomena, and it is also essential to use numerical schemes able to deal with the mathematical modelling of these phenomena, with the maximum accuracy and with as small side-effects as possible.
For example when physical diffusion is an important phenomenon, it is essential that the so-called numerical diffusion is negligible with respect to the physical one.
On another hand, to be effective, the numerical prediction has to use reasonable computing resources on current computers, and in fact computational modelling is always a trade-off between available resources and some desired accuracy.
Therefore, to establish these compromises users have to get some insight of how the accuracy evolves as a function of the used computational resources.

C2.2.Detailed objectives

Once the physical model has been established, i.e. the set of equations is defined, the user which faces an existing tool can only act on the following features:

- mesh definition
- time step choice
- numerical scheme selection if several of them are available.

It is the objective of these tests specifications to get some insight of how costs, accuracy and side-effects evolve with respect to these features, avoiding the intrinsic difficulties of physical modelling which has to be addressed by another set of test cases.

C2.3.Test cases selection

C2.3.1.Numerical difficulties

To select significant test cases, one has to consider the main numerical difficulties related to gas migration modelling, which apart from boundaries conditions, are:

- no linearities related to relative permeabilities and capillary pressure evolutions with respect to saturations
- large gradients like in the vicinity of saturation fronts
- coupling of equations.

Another difficulty, at least for finite differences approximations, is the fact that, for fully 3-D flows, it is impossible to have meshes aligned with the flow characteristics, and that this leads to a loss of accuracy called axes effects.
It must also be stressed that, in order to have reasonable computational costs, it is necessary to use implicit solvers which use to smear solutions (numerical diffusion) especially in the case of non-linear equations.
Significant test cases have to address these difficulties.

C2.3.2.Constraints

The constraints which have been taken into account to select these level one test cases are:

- compatibility with all the numerical tools used in the project
- no physical modelling difficulties
- availability of analytical solutions in order to have a firm basis for accuracy assessment.

C2.3.3.Selection

The basic test case which has been selected, is the 1-D immiscible displacement of one fluid by another one with the following assumptions:

- uniform and constant densities
- uniform permeability
- analytical properties.

This case is well known as the **Buckley Leverett** case and it exhibits several interesting features:

- as far as the capillary pressure is neglected there is an analytical transient solution
- there is a discontinuity of the saturation profile, i.e. an infinite gradient.

In order to address the objectives presented in § 2.2, computations will be performed on several 2-D meshes with several time steps.

C3 Result simulation analysis(WP3T4)

C3.1 Mesh size effect

This effect is to be analysed by comparing the results of the cases:

- 1.01 (dx = L/10)
- 1.02 (dx = L/20)
- 1.03 (dx = L/40),

or

- 1.08 (dx = L/10)
- 1.09 (dx = L/20)
- 1.10 (dx = L/40).

C3.2 Irregular mesh effect

This effect is to be analysed by comparing the results of the cases:

- 1.03 (dx = L/40)
- 1.04 (dx = L/10 for x < 0.4 L and dx = L/40 for x > 0.4 L),

or

- 1.10 (dx = L/40)
- 1.11 (dx = L/10 for x < 0.4 L and dx = L/40 for x > 0.4 L).

For the chosen parameters, the saturation front is located in the region x > 0.4 L where the mesh spacing is L/40.

C3.3 Mesh orientation effect

This effect is to be analysed by comparing the results of the cases:

- 1.02 (dx = L/20)
- 1.05 (dx = L/20 ,the mesh lines at 45 degrees from the front propagation direction)

or

- 1.08 (dx = L/20)
- 1.12 (dx = L/20 with the mesh lines at 45 degrees from the front propagation direction).

C3.4 Time step effect

This effect is to be analysed by comparing the results of the cases:

- 1.02 (dx = L/20 dt = t0/15)
- 1.06 (dx = L/20 dt = t0/30)
- 1.07 (dx = L/20 dt = t0/60),

or

- 1.08 (dx = L/20 dt = t0/15)
- 1.13 (dx = L/20 dt = t0/30)
- 1.14 (dx = L/20 dt = t0/60).

The value of t0 is such that the front is approximately located at x = 0.6 L, and is the reference time at which all the results are analysed.

C3.5 Capillary pressure effect

This effect is to be analysed by comparing the results of the cases 1.01 to 1.07 with the results of the cases 1.08 to 1.14.

C3.6. Criteria

C3.6.1 Front location

The front location can be classically defined by three points:

- the point where a value close to the front top is reached
- the point where a value close to the front foot is reached
- the point where the mid height value is reached.

The later definition, has been chosen as it doesn't depend too much on the front spreading. It is built from the supplied results by linear interpolation.

C3.6.2 Front spreading

As numerical models use discretised representations, the saturation front spreading has been defined by the number of cells on which it is spread, and also by the distance between the points corresponding to saturation levels
s1 and s2 defined by :

$$\begin{cases} S_1 = S^f_{min} + 0.1(S^f_{max} - S^f_{min}) \\ S_2 = S^f_{min} + 0.9(S^f_{max} - S^f_{min}) \end{cases}$$

where S^f_{min} is the minimum (initial) saturation, and S^f_{max} the saturation value at the front.

C3.6.3 CPU evolution

The tests have been performed on different computers having different architectures, moreover as the objective related to this criterion is mainly to define whether the CPU cost is proportional to the number of nodes or grows faster, the raw CPU cost have been normalised by the CPU cost of the test case 1.01, for each software.

C3.6.4 Memory evolution

The memory requirements are not very much dependant on the computers, so the memory sizes are absolute values.

C3.7. Presentation of the results

C3.7.1 Status of cases

The table below shows the status of the cases with the following conventions:

- D stands for Done
- F stands for done but obviously False
- C stands for done but not converged.

TOUGH corresponds to the use of TOUGH by ANDRA and TOUGH.b by GRS.

Tableau 1.

case	TOUGH	TOUGH.b	ECLIPSE	SUNIDJ	PORFLOW	GENESYS	BRIGHT
1.01	D	D	D	D	F	D	N
1.02	D	D	D	D	F	D	N
1.03	D	F	D	D	F	D	N
1.04	D	D	D	D	F	D	N
1.05	N	N	N	N	N	N	N
1.06	D	D	D	D	F	D	N
1.07	D	D	D	D	F	D	N
1.08	D	D	D	D	F	D	D
1.09	D	D	D	D	F	D	D
1.10	D	N	D	D	F	D	D
1.11	D	D	D	C	F	D	D
1.12	N	N	N	N	N	N	D
1.13	D	N	N	D	F	D	D
1.14	D	D	D	D	F	D	D

C3.7.2 Comments on the cases

As it can be seen from table 1, there are no results for the case 1.05 and only one for the case 1.12, so these cases are not taken into account for the analysis.

Generally speaking the specified time steps have not been used as such, they have instead been used as maximum time steps together with some automatic time step control, and it seems that these 'maximum' time steps have not been reached in any test cases.

C3.7.2.1 TOUGH

It has appeared that TOUGH cannot deal with arbitrary fluids and properties in fact it can only take into account predefined standard fluids like air and water together with their usual properties, and moreover only one single liquid phase can be computed at a time.

These restrictions of use have lead to the definition of specific physical values input, compatible with the objectives of the test cases, but inducing different results. For the analysis, the main difference is that for the basic cases the saturation front height is about 0.1 and is about 0.95 for the test performed using TOUGH, and also that there are no gradients near the input side at the opposite of the basic case.

The specific input parameters are:

- permeability 3.10^{-12} m^2
- water viscosity 1.10^{-3} $kg/m.s$
- air viscosity 1.810^{-5} $kg/m.s$
- filtration velocity 1.10^{-8} m/s

These features must be kept in mind, when looking at the results.

C.3.7.2.2 TOUGH.b

See previous paragraph for the test cases definition. The case 1.03 is obviously false, probably because of a bad input value. For unknown reasons there are two missing cases : 1.10 and 1.13.

C.3.7.2.3 ECLIPSE

For unknown reasons one case is missing : 1.13. The cases with capillary pressure (1.08 to 1.14) look strange, this may be due to some mistake in the boundary conditions.

C3.7.2.4 SUNIDJ

Some computations have been performed several times, using different numerical options, especially some test cases have been performed using one or two (left and right) saturation value per node. Only the cases with two saturations per node have been analysed.
The case 1.11 failed to converge for unknown numerical reasons.

C.3.7.2.5 PORFLOW

All the cases are obviously false because there is no front in the computational domain, this may be due to some mistake in the input values.

C3.7.2.6 GENESYS

No remarks.

C3.7.2.7 BRIGHT

The cases without capillary pressure (or with a neglectible one) have not been done.
The cases with capillary pressure have been done using an initial water saturation value which is not neglectible, i.e. 0.03 for a front height of about 0.1. The corresponding theoretical saturation profile has been taken into account for the analysis.

C3.8. Analysis

For this global analysis, the cases which can be considered as false are not taken into account.

C3.8.1 Front location

The front is rather well located for most cases. For the cases without capillary pressure the discrepancy between the numerical values and the theoretical ones are always smaller than half a cell.

For the cases with capillary pressure the discrepancy between the numerical values and the theoretical ones are larger ,but for TOUGH (and TOUGH.b) for which the results are almost identical to those without capillary pressure because of its specific test cases definition. The effect of mesh size can mostly be seen for cases 1.08 1.09 and 1.10, for which it is clear that the finer the mesh the better the results.

The influence of a coarse upstream mesh can be seen by comparing the results of the case 1.04 (resp 1.11) with those of the case 1.03 (resp 1.10). All these cases having the same fine spatial discretization in the neighbourhood of the front ($x > 400$), the discrepancies only come from the fact that the front has been travelling in a coarse mesh before arriving in the fine one.

C3.8.2 Front spreading

All the numerical tools spread the front over approximately 2 to 3 cells,this being a classical range.

•the first order improvement of the results versus the spatial discretization (cases 1.01 1.02 1.03 and cases 1.08 1.09 1.10)

•the relatively small influence of a coarse upstream mesh.

C3.8.3 CPU evolution

The CPU cost evolution is classically $C = N^P$,where C is the CPU cost, N the number of cells and p an exponent.

Table 2

Software	Exponent P
TOUGH	1
SUNIDJ	3
ECLIPSE	1
PORFLOW	1
GENESYS	2
BRIGHT	2.5

It must be noticed that these values combine the direct effect of computing more nodes, and the induced effect of computing more time steps because usually the finer the mesh the smaller the time step.

When the exponent value is 1., it means that the number of time steps remains unchanged.

C3.8.4 Memory requirements

The memory evolution, is classically $C = N^q$,where M is the memory requirement, N the number of cells and q an exponent.

the values of q **are all close to 1**., this means that the memory requirements are proportional to the number of cells, i.e. that there is no matrix storage.

C3.8.5 Time steps

As explained above, automatic time step control has been used for almost all cases.

The main conclusion which can be derived from the results is that all the used time steps are all smaller than the specified ones. More precisely, the fact that the results of cases 1.02 1.06 and 1.07 (or 1.09 1.13 and 1.14) are identical implies that the effective time steps are smaller than the specified minimum one.

The minimum specified time step (150 days) corresponds to a displacement of 0.88 m ,i.e. 1/28 the cell size for these cases.

C3.9 Analysis of the softwares

This paragraph presents some provisional conclusions about the use of the tested softwares.

TOUGH and GENESYS produced satisfactory results for all cases, taking in mind the restrictions presented above for TOUGH.

ECLIPSE and SUNIDJ produced satisfactory results only for the cases without capillary pressure. For the cases with capillary pressure, it is not possible to know whether their bad results come from mistakes in input data or from the numerical approach.

BRIGHT produced some satisfactory results only for the cases with capillary pressure (with some numerical instability in the vicinity of the front for one case), it would be interesting to know its behaviour for cases with a neglectible capillary pressure.

PORFLOW did not produce any results comparable with the reference solution, hopefully because of mistakes on input data. The only remarks that can be done are that the results are relatively dispersed, and that there are non neglectible numerical instabilities for all the cases with capillary pressure.

It can be noticed that GENESYS and ECLIPSE predict saturation values higher than the theoretical ones in a quite large domain upstream the front and also at the front location.

C4 Second level test case definition and specification (WP3T1,WP3T2)

EVEGAS second level test cases based on laboratory experimental result. A heterogeneous plug made by eight rocks samples (whose length is L_i from different rocks) is maintained in a vertical position and was saturated with water at the initial time and the bottom plug pressure is maintained at 20 bar. The air was injected downward at the plug top at a constant flow rate (150 cm^3/h). The produced gas and water at the plug bottom are monitored by a flash device. The whole experiment apparatus is maintained at a constant temperature (20 °C).

The aim of the second test cases is to simulate the laboratory experiment ,at the above described conditions and configuration, in order to predict water production versus time and water saturation profiles and pressure profiles at some relevant times. Some data related to computing aspect are required.

This second level test cases in the frame of the EVEGAS project should contribute to get information on the predictive numerical model capabilities faced experimental result.

Presented at the TOUGH '95 Workshop, Lawrence Berkeley Laboratory, Berkeley, CA, March 20-22, 1995.

Modeling of Capillary Barriers and Comparison to Data

Stephen W. Webb and John C. Stormont
Sandia National Laboratories
Albuquerque, NM 87185

Measurements of capillary barrier performance have been conducted in above-grade wooden structures (boxes) configured to measure the water balance as shown in Figure 1. The capillary-barrier portion of the boxes is 6.0 m long, 2.0 m wide, and 1.2 m high with a slope of 5%. A coarse-grained material was placed in the bottom 25-cm of the box with a 90-cm deep fine-grained material (local soil) on top. A region for laterally diverted water to accumulate and drain was created in the last 1.0 m of the box. The soil at the top is terraced into five, 1.4 m long, level intervals to prevent runoff when adding water. Water is added uniformly to the entire top of the box at a rate of about 66 l/day, or an infiltration rate of 1.7 m/year. The top of the box is covered with fiber-reinforced plastic to minimize evaporation of water, discourage plant growth, and prevent rainfall from contacting the soil. Five drains are spaced along the bottom of the coarse layer. These drains discretize the coarse layer into five collection regions to provide a means of identifying the breakthrough location into the coarse layer. A drain is also located in the downdip collection region of the box. Soil moisture changes were measured in the fine-grained material with a frequency-domain reflectometry (FDR) probe, which was calibrated using soil from the field site at a known moisture content and density. The location of the vertical and horizontal access pipes for the probe is given in Figure 1.

Vertical moisture content data as a function of time and location are shown in Figure 2 for the first (#1) and last (#5) vertical FDR locations. Early-time data for the soil-wetting phase are shown out to 43 days. After this time, the moisture content profiles change very little. In addition to the data shown, measurements were also made within a few centimeters of the top of the soil. However, the FDR access pipes vibrated due to the wind, creating a small open annulus around the access tubes near the surface. This open annulus, and the possibility of preferred infiltration around the access tubes near the surface, interfered with the measurement, so these near-surface data are not included. Horizontal moisture content data were also obtained but are not shown because some measured values were influenced by a pipe coupling around the tubes.

In addition to moisture content data, drainage data for the six drains were obtained. The initial water flow from the drains occurred at drain 6, downstream of the capillary barrier at about 44 days followed quickly by the rest of the drains except drain 1, which never had water flow. As expected, the drainage rate increases from drain 2 to drain 5. These data are not shown in this paper since the present analysis is concerned with the soil-wetting phase and prediction of the saturation profiles with time. Consideration of the drainage data will be addressed after the soil-wetting phase analysis is complete.

Properties of the local soil were measured including unsaturated properties, while properties of the underlying coarse-grained material, which is a poorly-graded round stone, have been estimated from the literature; the appropriate values are listed in Table 1. The van Genuchten (van Genuchten, 1978, 1980) two-phase characteristic curves were used to fit the data.

Table 1
Material properties

	Fine (measured)	Coarse (estimated)
Porosity	0.394	0.42
Permeability (m^2)	1.23×10^{-13}	3.5×10^{-8}
S_{lr}	0.213	0.012
S_{ls}	0.99	0.99
m	0.465	0.543
α (Pa^{-1})	1.86×10^{-4}	5.03×10^{-2}

Data-Model Comparison

It was assumed that a capillary barrier numerical model could be developed with TOUGH2 and, using the above soil properties, that the model predictions would be reasonably similar to the measurements. Such was the case for the lab-scale infiltration data of Vauclin et al. (1979) which was successfully analyzed by Moridis and Pruess (1992) using TOUGH. Based on this belief, a detailed two-dimensional model of the capillary barrier geometry was developed consisting of over 1800 elements. The initial liquid saturation of the fine layer was estimated as 40 percent, or an initial moisture content of just under 16 percent, based on moisture in the original soil and water added to the soil during construction of the boxes. Water was added to the top of the model at a constant rate corresponding to the average value from the tests, and the soil-wetting phase and water drainage were calculated.

As shown in Figure 3 for FDR locations 1 and 5, however, the predicted moisture content profiles are significantly different than the data, especially at later times. Both the predicted moisture content values are greater and the predicted profiles are much steeper than the data. The significant differences between the numerical and experimental results have resulted in plans to conduct a numerical sensitivity study to evaluate the important soil properties that could cause such large differences. This study is currently in process and is not reported here.

One of the most significant differences between the numerical predictions and the data is the range of moisture content values. While the long-term data seem to be clustered around moisture contents varying between 20 and 40 percent, the predictions are limited to values between 30 and 40 percent.

As clearly seen from the model results in Figure 3, transient flow in capillary barriers can be broken into two distinct regimes, a suction regime or soil-wetting phase, and a flow regime. The suction regime occurs early on when the infiltration rate is higher than the local liquid-phase permeability (intrinsic permeability times relative permeability) such that the excess infiltrated water goes to increasing the local moisture content (and the relative permeability) until the local permeability is high enough to readily transmit water at the given infiltration rate. In the flow

regime, the local permeability is equal to or higher than the flow rate and the additional water flows through the system. The moisture content may be constant or increase with depth depending on the characteristic curves. The transition between these two flow regimes occurs when the local permeability is just equal to the infiltration rate. If one measures or assumes water relative permeability expressions and appropriate constants, the wetting-phase saturation or moisture content for this transition can be calculated.

For example, the model predictions are based on an infiltration rate of 1.7 m/year (5.6×10^{-15} m^2), while the soil intrinsic permeability is 1.23×10^{-13} m^2, or about 37 m/year. Therefore, the relative permeability is equal to 0.046 for the transition between the suction and the flow regimes. Based on the assumed soil properties and the van Genuchten wetting-phase relative permeability expressions:

$$S_e = \frac{S - S_{lr}}{S_{ls} - S_{lr}} \tag{1}$$

$$k_{r,w} = S_e^{1/2} \left(1 - \left(1 - S_e^{1/m}\right)^m\right)^2 , \tag{2}$$

the relative permeability equals 0.046 at an effective saturation of about 0.68 or a moisture content of 29 percent (saturation of 0.74), consistent with the model predictions shown earlier.

Sensitivity studies are underway varying the intrinsic permeability, relative permeability, and residual saturations in order to evaluate the influence on the profiles. The general influence on the range of saturation or moisture content values can be estimated by the above expressions. In addition, the shape of the saturation profiles is dependent on the capillary pressure and the two-phase characteristic curves. Therefore, the use of ITOUGH2 (Finsterle, 1992) is being considered for further evaluation of the data-model comparison.

Conclusions

Capillary barrier data have been obtained in above-grade wooden structures (boxes) configured to measure the water balance. Simulations of the capillary barrier performance have been conducted with TOUGH2 based on measured and assumed soil properties. The predicted moisture content profiles in the soil-wetting phase for the soil are significantly different than the measured values. A numerical sensitivity study to evaluate the important soil properties that could cause such large differences is currently underway.

Additional future work on capillary barrier performance prediction will evaluate the performance of a new EOS module being developed by Karsten Pruess based on Richards' equation. In some preliminary tests, the numerical performance of TOUGH2 for applications similar to capillary barriers was improved tremendously. Further evaluation of this new module is underway.

Acknowledgment

This work was supported by the United States Department of Energy under Contract DE-AC04-94AL85000.

References

Finsterle, S. (1993), ITOUGH2 User's Guide, Version 2.2, LBL-34581, Lawrence Berkeley Laboratory, August 1993.

Moridis, G.J, and K. Pruess (1992), TOUGH Simulations of Updegraff's Set of Fluid and Heat Flow Problems, LBL-32611, Lawrence Berkeley Laboratory.

van Genuchten, R. (1978), Calculating The Unsaturated Hydraulic Conductivity With a New Closed-Form Analytical Model, Research Report 78-WR-08, Department of Civil Engineering, Princeton University, September 1978.

van Genuchten, M.Th. (1980), "A Closed-form Equation for Predicting the Hydraulic Conductivity of Unsaturated Soils," Soil Sci. Soc. Am. J., Vol. 44, pp. 892-898, 1980.

Vauclin, M., D. Khanji, and G. Vachaud (1979), "Experimental and Numerical Study of a Transient Two-Dimensional Unsaturated-Saturated Water Table Recharge Problem," Water Resour. Res., Vol. 15, pp 1089-1101.

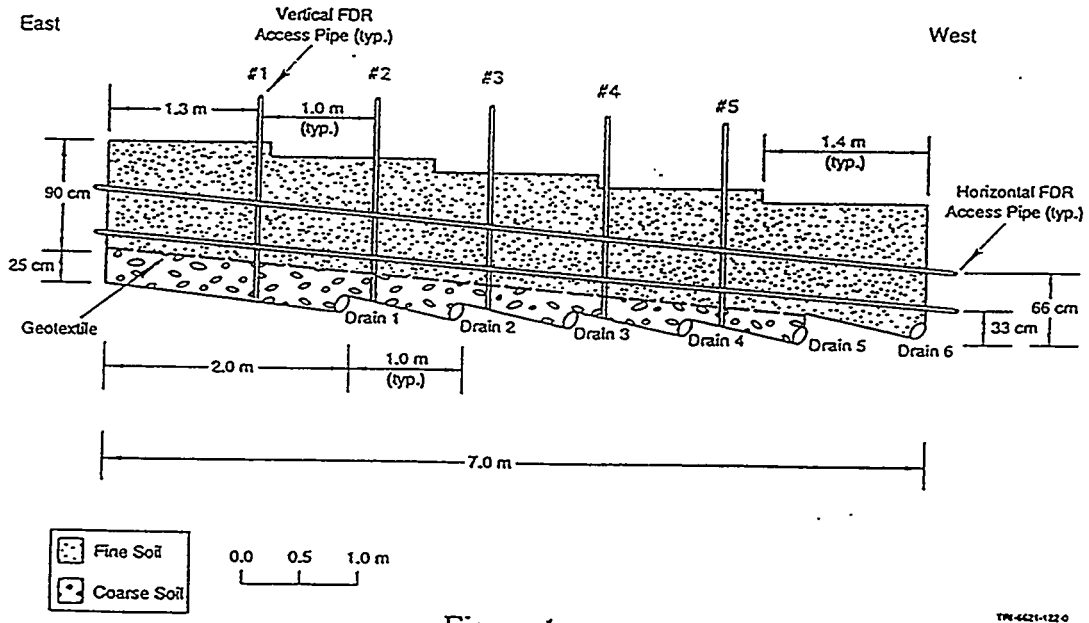

Figure 1
Capillary Barrier Box Experiment

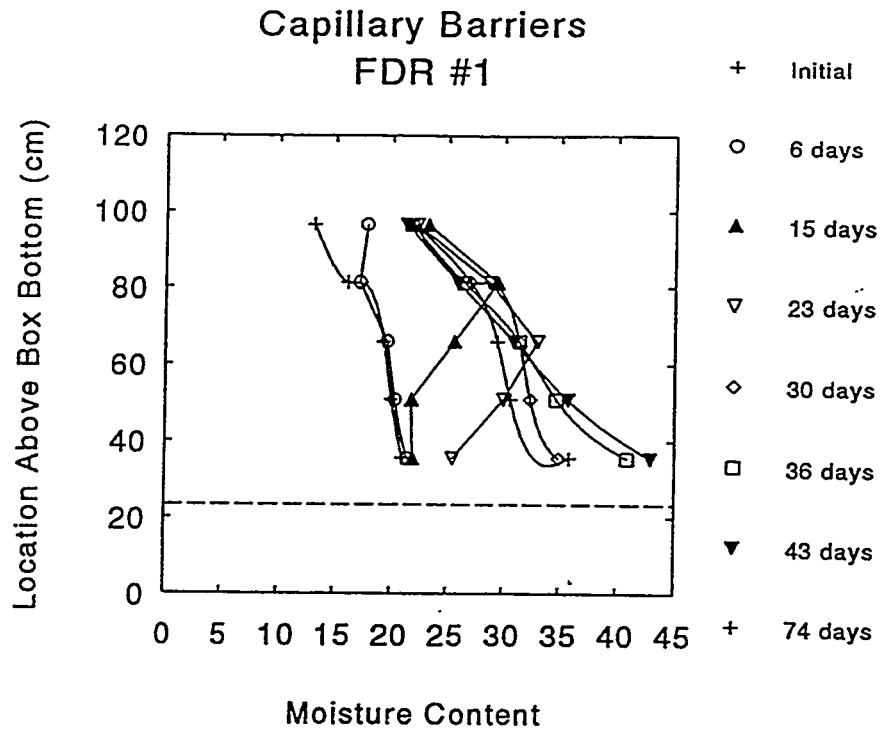

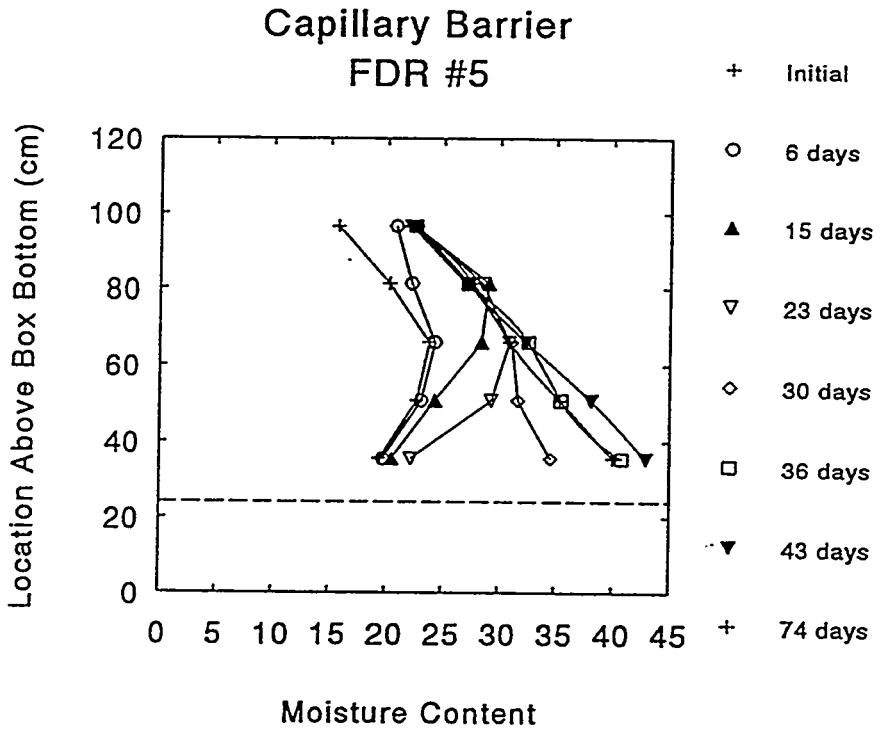

Figure 2
Moisture Content Data

TOUGH2 Results Using
Measured Soil Properties

FDR #1

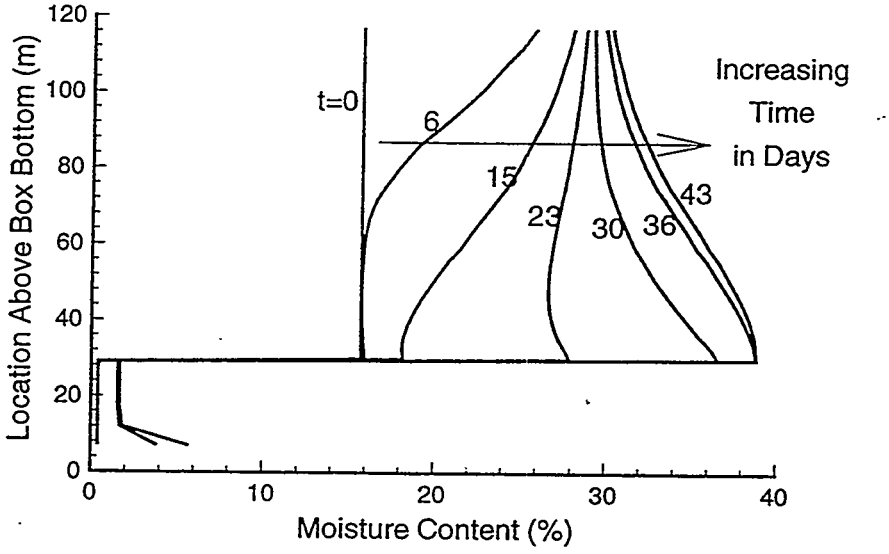

TOUGH2 Results Using
Measured Soil Properties

FDR #5

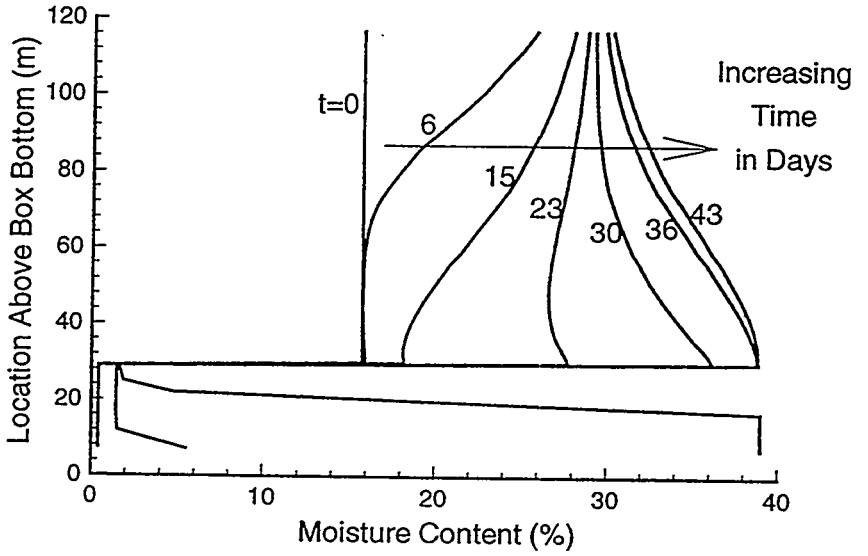

Figure 3
TOUGH2 Predictions Using Measured Soil Properties

SAND95-0324C
Presented at the TOUGH Workshop '95 held at Lawrence Berkeley Laboratory, Berkeley, CA, March 20-22, 1995

ASSESSING ALTERNATIVE CONCEPTUAL MODELS OF FRACTURE FLOW

Clifford K. Ho
Sandia National Laboratories
P.O. Box 5800, MS-1324
Albuquerque, NM 87185-1324
(505) 848-0712

Abstract

The numerical code TOUGH2 was used to assess alternative conceptual models of fracture flow. The models that were considered included the equivalent continuum model (ECM) and the dual permeability (DK) model. A one-dimensional, layered, unsaturated domain was studied with a saturated bottom boundary and a constant infiltration at the top boundary. Two different infiltration rates were used in the studies. In addition, the connection areas between the fracture and matrix elements in the dual permeability model were varied. Results showed that the two conceptual models of fracture flow produced different saturation and velocity profiles—even under steady-state conditions. The magnitudes of the discrepancies were sensitive to two parameters that affected the flux between the fractures and matrix in the dual permeability model: 1) the fracture-matrix connection areas and 2) the capillary pressure gradients between the fracture and matrix elements.

Introduction

The possibility of fast-flow pathways in fractured unsaturated rock has received much attention lately, especially in nuclear waste management. The transport of radionuclides from buried nuclear waste packages can be enhanced if fast-flow paths exist in the surrounding environment. Such conditions may exist in the variably welded tuff units at the potential repository site at Yucca Mountain, Nevada. The ability to model the flow and transport in these systems is necessary to accurately assess the performance of the potential repository. However, the inability to accurately characterize fracture networks in situ and the lack of rigorous discrete fracture flow models has prompted the need for alternative conceptual models of fracture flow. Two of these models include the equivalent continuum model (ECM) and the dual permeability (DK) model.

The equivalent continuum model has been described in detail by Klavetter and Peters (1986) and Dudley et al. (1988). This model has been used extensively in describing flow through fractured rock as a result of its relative simplicity and ease of computational implementation. In this model, the pressures in the matrix and fractures are assumed equal. As a result, the flow through this fracture-matrix system is equivalent to flow through a composite porous medium, which has hydraulic properties comprised of both fractures and matrix properties. Dudley et al. express that for conditions similar to those found at Yucca Mountain (i.e. low infiltration rates and good coupling between the fracture and matrix), the equivalent continuum model provides a reasonable approximation to fracture-matrix flow. However, recent studies have shown that flow processes such as fingering in fractures (Glass and Tidwell, 1991) and mechanical aspects such as fracture coatings may effectively reduce the coupling between the fractures and matrix. This may cause pressure disequilibrium between the fractures and matrix, even under low infiltration rates.

If pressure equilibrium cannot be assumed, other models such as the dual permeability model must be used. Details of the dual permeability model can be found in Pruess and Narasimhan (1985) and Pruess (1983). Unlike the equivalent continuum model, the dual permeability model represents the fractures and matrix as separate continua. As a result, different pressures can exist in the fractures and matrix, which allows flow to occur between the two continua. Propagation of flow in fractures is more likely to be observed in these models, depending on such parameters as fracture-matrix conductance and capillary pressure gradients between the fractures and matrix. However, relatively few analyses have been performed with the dual permeability model in conjunction with analyzing fast flow paths for the assessment of a potential nuclear waste repository.

The purpose of this report is to compare the dual permeability and equivalent continuum models by simulating infiltration and flow through a one-dimensional, unsaturated, heterogeneous, fractured rock (the context being relevant to the potential

nuclear waste repository at Yucca Mountain). Saturations and velocities resulting from the two models are compared, and sensitivity analyses are performed. Parameters such as the infiltration rate and the connection area between the fractures and matrix are varied to demonstrate the importance of specific variables on the resulting saturation and velocity profiles.

Numerical Approach

In order to compare the equivalent continuum and dual permeability models, infiltration into a hypothetical one-dimensional vertical transect of Yucca Mountain was investigated. Figure 1 shows a sketch of the domain that was modeled using TOUGH2 (1991). A saturated boundary condition was assumed at the bottom, and a constant infiltration rate was assumed at the top boundary. In the equivalent continuum model, 106 elements were used as shown in Figure 1. In the dual permeability model, an additional set of elements was created using MINC (Pruess, 1983) so that both the fracture and matrix continua could be modeled discretely. As a result, twice as many elements were used in the dual permeability model. In addition, the constant infiltration rate was applied only to the top of the fracture continuum in the dual permeability model. The material properties that were used for both models were taken from TSPA-93 (Wilson et al., 1994) and are summarized in Table 1. The van Genuchten (1980) capillary pressure and relative permeability curves were used for all calculations, and the initial saturation of all domain elements was set to 0.85. Isothermal conditions were assumed to exist, and the single-phase EOS9 module (Richard's equation) of TOUGH2 was used.

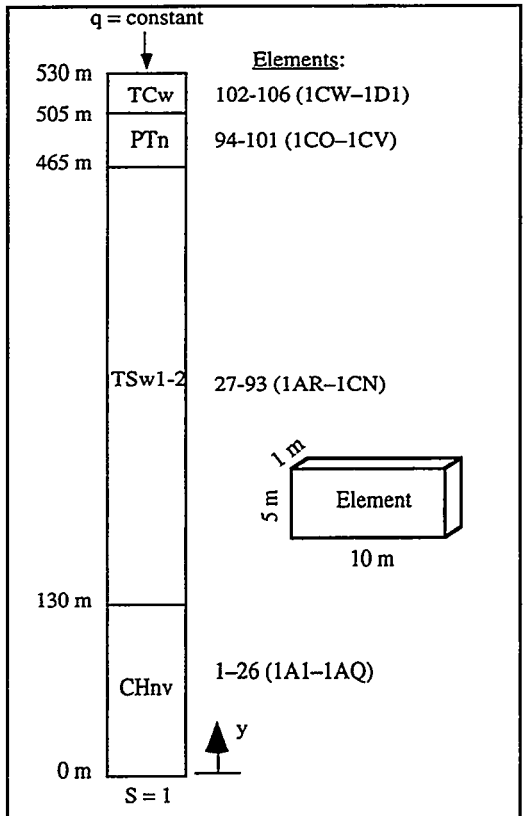

Figure 1. One-dimensional layered model used in TOUGH2 simulations. The initial saturation of all the elements was set to 0.85.

Parameters such as the fracture-matrix connection areas and the distances between the fractures and matrix that were used in the dual permeability model were calculated in MINC, part of the TOUGH2 code. Table 2 summarizes the important mesh-related parameters that were used in the dual permeability model for this study. Since MINC, in general, calculates these parameters based on the geometry of an idealized set of fractures and matrix blocks, non-ideal physical features and processes such as fracture coatings and fingering may alter the value of these parameters. As a sensitivity analysis, the connection areas between the fracture and matrix elements ($A_{f\text{-}m}$)were reduced by two orders of magnitude from the MINC-calculated values in some of the dual permeability simulations. Other parameters, such as the distance between the fracture and matrix elements, could also have been varied, but the desired effect of reducing the conductance between the fracture and matrix elements would have been the same. The TOUGH2 simulations that were performed are summarized in Table 3. Each of the simulations was run until steady-state conditions were achieved. The runs were stopped at either a simulation time of one billion years or 4000 time steps, whichever came first.

Results

Infiltration Rate, q = 0.1 mm/year (Runs 1,2, and 3)

Figure 2 shows the steady-state matrix saturations for the equivalent continuum and dual permeability models using an infiltration rate of 0.1 mm/year (3.16e-8 kg/sec). At this infiltration rate, the matrix elements were capable of conducting the entire flow. As a result, the saturations were less than one everywhere, and the saturations decreased in the non-welded units where the porosity was greater. The dual permeability model that used the MINC-calculated fracture-matrix connection areas produced saturations that were nearly identical to the saturations of the equivalent continuum model. This implies that the conductance between the fractures and matrix elements in the dual permeability model was sufficient to allow most of the liquid to be imbibed into the matrix where it was conducted through the matrix continuum. This is also shown in Figure 3(a), in which the fracture and matrix pore velocities are plotted. For reference, the composite pore velocity of the equivalent continuum model is also plotted. The matrix velocity is seen to be over six orders of magnitude larger than the fracture velocity for the MINC-calculated dual permeability model.

Table 1. TSPA93 (Wilson et al., 1994) parameters used in the TOUGH2 calculations.

	TCw	PTn†	TSw1-2	CHnv
Matrix				
porosity (m^3-p/m^3-m)	0.087	0.421	0.139	0.331
permeability (m^2)	2.04e-18	2.51e-14	2.09e-18	1.10e-16
α (1/Pa)	7.91e-7	3.78e-5	1.36e-6	2.79e-6
$\lambda=1-1/\beta$	0.383	0.578	0.444	0.594
S_r	0.0212	0.154	0.0453	0.0968
S_s	1.0	1.0	1.0	1.0
Fracture				
porosity††	2.93e-4	9.27e-5	2.43e-4	1.11e-4
intrinsic perm. (m^2)	4.06e-9	7.14e-9	4.57e-9	6.53e-9
fracture spacing (m)	0.618	2.22	0.74	1.62
fracture aperture (m)	1.81e-4	2.06e-4	1.80e-4	1.79e-4
scaled perm. (m^2)	1.19e-12	6.62e-13	1.11e-12	7.23e-13
α (1/Pa)	1.23e-3	1.4e-3	1.22e-3	1.22e-3
$\lambda=1-1/\beta$	0.667	0.667	0.667	0.667
S_r†††	0.0	0.0	0.0	0.0
S_s	1.0	1.0	1.0	1.0
Composite				
porosity	0.0873	0.421	0.139	0.331
permeability (m^2)	1.19e-12	6.87e-13	1.11e-12	7.23e-13

†The matrix permeability and α of the PTn were bi-modal, so the area weighted average was used for those parameters.

††The fracture porosity was calculated as the fracture aperture divided by the fracture spacing.

†††The residual fracture saturation was changed to 0.03 in the 0.1 mm/year infiltration cases because Run 2 could not reach steady-state within 4000 time steps using S_r=0.

Table 2. MINC (Pruess, 1983) input and output parameters for a 1-D dual permeability model with two interacting continua (fracture and 1 matrix continua).

	TCw	PTn	TSw1-2	CHnv
Aperture, b (m)	1.81e-4	2.06e-4	1.80e-4	1.79e-4
Fracture spacing, D (m^3)	0.62	2.2	0.74	1.6
Volume of grid block, V (m^3)	50	50	50	50
Fracture porosity, ϕ_f (b/D)	2.93e-4	9.27e-5	2.43e-4	1.11e-4
Fracture volume in grid block ($V*\phi_f$) (m^3)	1.46e-2	4.68e-3	1.22e-2	5.59e-3
Matrix volume in grid block ($V*(1-\phi_f)$) (m^3)	49.9854	49.9953	49.9878	49.9944
Distance between fracture and matrix, d=(D-b)/6 (m)	0.1033	0.3667	0.1233	0.2667
No. of matrix blocks per grid block, σ (V/D^3)	210	4.70	123	12.2
Fracture-matrix connection area on matrix block scale, $A'_{f\text{-}m}=2*(D-b)^2$ (m^2)	0.768	0.968	1.09	5.12
Fracture-matrix connection area on grid block scale, $A_{f\text{-}m}=A'_{f\text{-}m}*\sigma$ (m^2)	161	45.5	135	62.5

Table 3. Summary of TOUGH2 runs using the effective continuum model (ECM) and the dual permeability (DK) model.

Run	q (mm/year)	model	comments
1	0.1	ECM	—
2	0.1	DK	—
3	0.1	DK	$A_{f\text{-}m}$ reduced by 2 orders of magnitude
4	4.0	ECM	—
5	4.0	DK	—
6	4.0	DK	$A_{f\text{-}m}$ reduced by 2 orders of magnitude

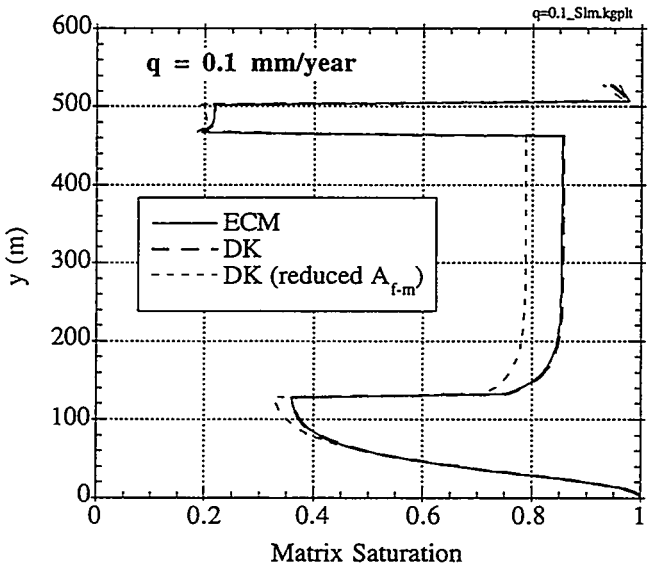

Figure 2. Steady-state matrix saturations for the equivalent continuum model (ECM), the dual permeability (DK) model as calculated by MINC, and a modified dual permeability model in which the fracture-matrix connection area was reduced by two orders of magnitude. The infiltration rate is 0.1 mm/year (3.16e-8 kg/sec).

However, when the connection area between the fractures and matrix (A_{f-m}) was reduced by two orders of magnitude, drastic changes were observed. Figure 2 shows that the matrix saturations for the modified dual permeability model were lower than the saturations of the previous models. The reduced conductance between the fractures and matrix reduced the flow to the matrix elements. The reduced flow through the matrix elements resulted in a decrease in the matrix saturations, which in turn increased the matrix capillary pressures. Although this caused an increase in the capillary pressure gradient between the fractures and matrix, the decreased fracture-matrix connection area offset the increased capillary pressure gradient. The end result was a larger portion of liquid flowing through the fractures. Figure 3(b) shows that the fracture pore velocities increased over six orders of magnitude from the previous dual permeability calculation, exceeding the matrix pore velocities.

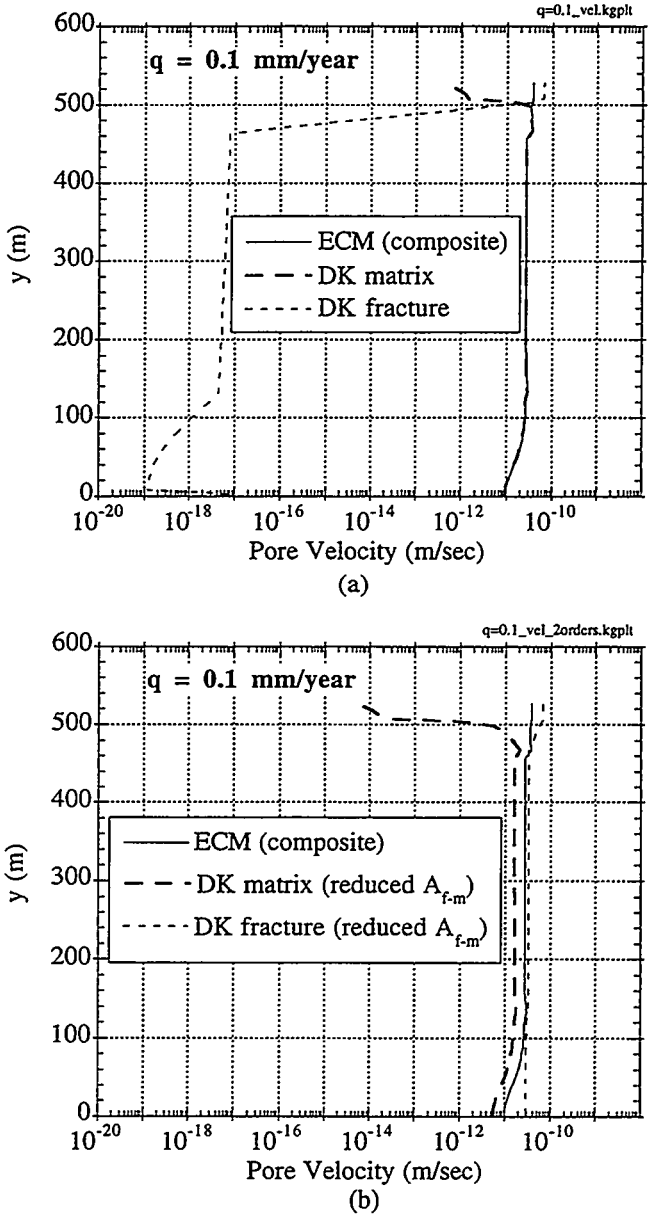

Figure 3. Steady-state pore velocities in the fractures and matrix: a) MINC-calculated dual permeability model; b) modified dual permeability model where the fracture-matrix area was reduced by two orders of magnitude. The composite ECM velocity is shown for reference. The infiltration rate is 0.1 mm/year (3.16e-8 kg/sec).

Infiltration Rate, q = 4.0 mm/year (Runs 4, 5, and 6)

At an infiltration rate of 4.0 mm/year, the saturated conductivities of the welded units (TCw and TSw1-2) were exceeded. As a result, Figure 4 shows that the steady-state saturations in the matrix of the welded units were nearly saturated for all the models. In the non-welded units (PTn and CHnv), the modified dual permeability model (in which the fracture-matrix connection area was reduced by two orders of magnitude) showed a decrease in the saturations. Note also that the MINC-calculated dual permeability model produced discrepancies from the equivalent continuum saturations at the top of the CHnv (y ~ 130 m). Since the flow was predominantly in the fractures through the welded TSw1-2 unit, the flow continued through the fractures even as it entered the non-welded CHnv unit.

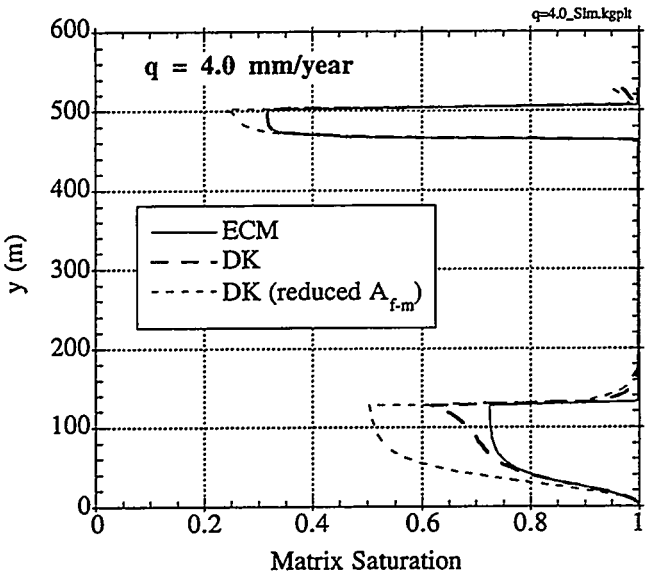

Figure 4. Steady-state matrix saturations for the equivalent continuum model (ECM), the dual permeability (DK) model as calculated by MINC, and a modified dual permeability model in which the fracture-matrix connection area was reduced by two orders of magnitude. The infiltration rate is 4.0 mm/year (1.266e-6 kg/sec).

Figure 5(a) shows the fracture and matrix pore velocities for the MINC-calculated dual permeability model. The fracture velocities were higher than the matrix velocities in the welded TCw and TSw1-2 units, but the opposite was true in the non-welded PTn and CHnv units. Again, in this model the conductance between the fractures and matrix was large enough so that in regions where the matrix was not saturated (i.e. in units where the infiltration rate did not exceed the saturated conductivity), the flow was imbibed and subsequently carried by the matrix. However, the modified dual permeability model showed that by reducing the conductance between the fractures and matrix, the flow could remain in the fractures in regions where the matrix saturations were less than one. Figure 5(b) shows that in the modified dual permeability model the fracture velocities increased in regions where matrix flow dominated prior to the reduction in the fracture-matrix connection area. However, in the welded TCw and TSw1-2 units, where the matrix was saturated and fracture flow dominated from the onset, no changes in the velocity profiles were observed.

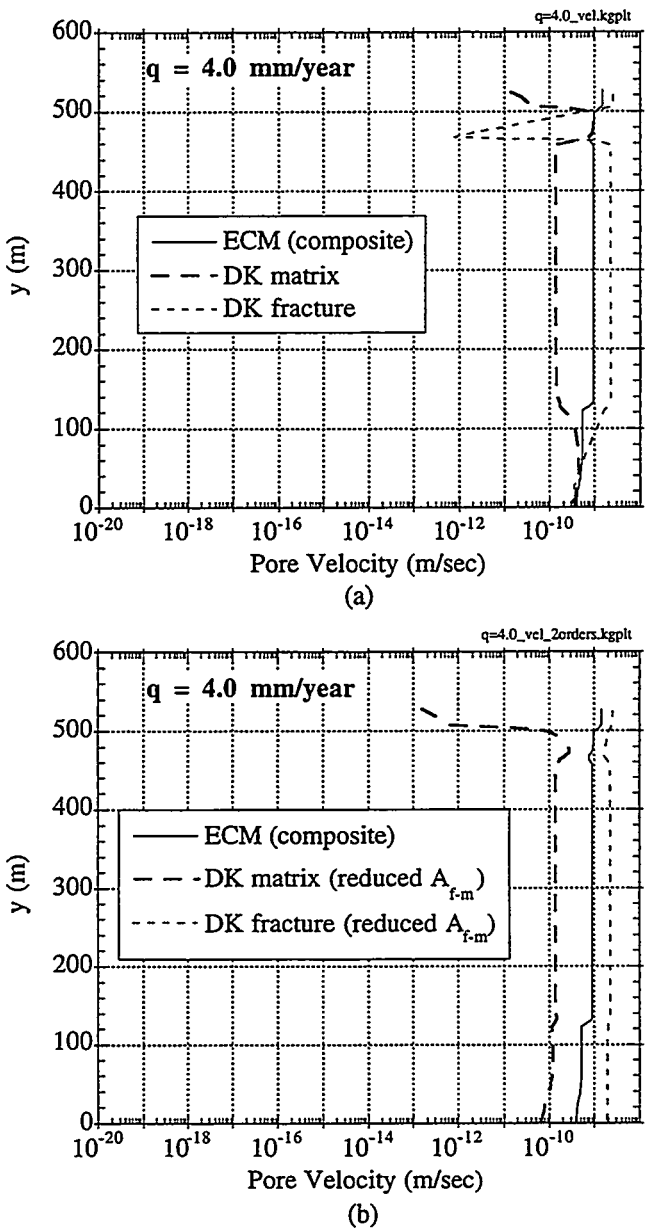

Figure 5. Steady-state pore velocities in the fractures and matrix: a) MINC-calculated dual permeability model; b) modified dual permeability model where the fracture-matrix area was reduced by two orders of magnitude. The composite ECM velocity is shown for reference. The infiltration rate is 4.0 mm/year (1.266e-6 kg/sec).

Discussion

In these numerical simulations, the dual permeability model was seen to produce similar results to the equivalent continuum model when the conductance between the fractures and matrix was sufficiently large. Since the MINC calculations were based on idealized geometric configurations of fracture and matrix blocks, the calculated conductance could be significantly different from that of actual systems. When this conductance was reduced by two orders of magnitude, the dual permeability model showed significant differences in the fracture and matrix velocities—even at steady-state. Intuitively, it

makes sense that *transient* responses to an infiltration event would be different if the fracture-matrix conductivity is altered, but the behavior of dual permeability systems under steady-state conditions is perhaps not so intuitive. Figure 6 shows a few elements from the one-dimensional dual permeability model used in this study. Figure 6 also shows Darcy's law as applied to the flow between a fracture and a matrix element. At steady-state, the mass flow into any element must equal the mass flow out of that element. If the connection area between the fracture and matrix (or any other parameters related to the conductance) is reduced, the mass flow rate into the matrix is also lowered. As long as this reduced mass flow into the matrix element equals the mass flow out of that element, steady-state conditions can be maintained. The result is a larger mass flow rate through the fractures.

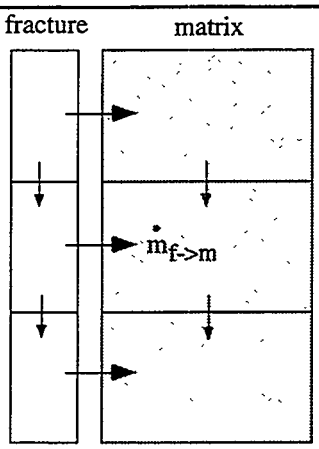

$$\dot{m}_{f->m} = \rho A_{f-m} \frac{k_m k_{rm}}{\mu} \frac{P_{l,f} - P_{l,m}}{d}$$

Since $P_c = P_g - P_l$, and for P_g constant:

$$\dot{m}_{f->m} = \rho A_{f-m} \frac{k_m k_{rm}}{\mu} \frac{P_{c,m} - P_{c,f}}{d}$$

conductance — capillary pressure gradient

Figure 6. Fracture and matrix elements in a one-dimensional dual permeability model showing the mass flow into and out of each element.

Note that in addition to the conductance terms of Darcy's law, the capillary pressure gradient between the fracture and matrix element also contributes to the mass flow into the matrix element. This explains why the 4.0 mm/year infiltration cases did not result in a change in the matrix saturations or velocities for the different models. At that infiltration rate, the capillary pressure of the fracture elements remained small due to higher fracture saturations. As a result of the large capillary pressure gradient, imbibition into the matrix elements continued until the matrix was nearly filled. In the 0.1 mm/year infiltration case, however, lower fracture saturations resulted in higher fracture capillary pressures, which reduced the capillary pressure gradient between the fractures and matrix. In both cases, the end result was based on the steady-state condition that the mass flow into an element equaled the mass flow out, where the mass flow rates between the fractures and matrix depended on both the conductance terms (e.g. fracture-matrix connection area) and the capillary pressure gradient.

Although the reduction in the connection area between the fracture and matrix elements seems arbitrary, physical processes and features observed in laboratory and field studies support this assumption in actual systems. Commonly observed flow channeling (or fingering) in fractures (Glass and Tidwell, 1991) and fracture coatings can act to effectively reduce the conductance between a fracture and matrix. When this occurs, both the physical observations and the numerical studies presented here show that the flow velocities through the fracture network can be significantly higher than the velocities that would be observed through either an effective continuum model or a dual permeability model based on idealized geometric configurations.

Finally, Table 4 shows the calculation times for each of the runs. The equivalent continuum simulations ran the fastest. Of the dual permeability runs, the ones with the reduced fracture-matrix connection area reached steady-state considerably faster than the MINC-calculated dual permeability models.

Table 4. Calculation times for TOUGH2 runs.

Run	No. of time steps	Simulated time (sec)	Calculation time (sec)
1	473	3.1536e16	89.8
2	4000	3.84e14	1615
3	393	3.1536e16	142
4	439	3.1536e16	87.1
5	4000	4.92e15	1772
6	981	3.1536e16	386

Conclusions

The equivalent continuum and dual permeability models were compared using TOUGH2. Infiltration into a one-dimensional, layered, unsaturated domain was investigated. The connection areas between the fractures and matrix were reduced by two orders of magnitude in some of the dual permeability runs as sensitivity analyses. Two different infiltration rates (0.1 mm/year and 4.0 mm/year) were used. Based on the results of these simulations, the following conclusions were drawn:

- The MINC-calculated dual permeability model (based on an ideal fracture-matrix geometry) produced similar results to those of the equivalent continuum model for both infiltration rates under steady-state conditions. For the 0.1 mm/year infiltration rate, the matrix was able to carry the entire flow. The 4.0 mm/year infiltration rate was greater than the saturated conductivity of the welded TCw and TSw1-2 units, which resulted in significant fracture flow in those regions.

- Reducing the conductance by two orders of magnitude between the fractures and matrix in the dual permeability model resulted in significantly higher fracture pore velocities where the matrix was unsaturated. Thus, depending on the fracture-matrix conductance, the dual permeability model is capable of modeling significant fracture propagation even when the matrix is unsaturated.

- The steady-state saturations and velocity profiles in the dual permeability model are sensitive to the fracture-matrix interaction. The fracture-matrix interaction depends on both the conductance terms between the fractures and matrix (e.g. the fracture-matrix connection area) and the capillary pressure gradient (which, in this study, was affected by the infiltration rates).

- The effective area (conductance) between fractures and matrix needs to be quantified and assessed through laboratory or field studies to provide reasonable estimates for use with the dual permeability model.

Nomenclature

$A_{f\text{-}m}$	connection area between the fracture and matrix elements
CHnv	Calico Hills non-welded vitric unit at Yucca Mountain
d	distance used to calculate fracture-matrix pressure gradients
DK	dual permeability
ECM	equivalent continuum model
k	permeability (m^2)
k_r	relative permeability
$m_{f->m}$	mass flow from the fracture to the matrix (kg/sec)
MINC	Multiple INteracting Continua (part of TOUGH2 code to generate dual permeability models)
P_c	capillary pressure (Pa)
P_g	gas pressure (Pa)
P_l	liquid pressure (Pa)
PTn	Paintbrush non-welded unit at Yucca Mountain
q	infiltration rate (mm/year)
S	liquid saturation
S_r	residual liquid saturation
S_s	full liquid saturation
TCw	Tiva Canyon welded unit at Yucca Mountain
TSw1-2	Topopah Springs welded units at Yucca Mountain
α	van Genuchten fitting parameter (1/Pa)
β	van Genuchten fitting parameter
ρ	liquid density (kg/m^3)
μ	dynamic liquid viscosity (kg/m-sec)

Subscripts:

f	fracture
m	matrix

Acknowledgments

This study was performed under WA-0192, W.B.S. 1.2.5.4.4 PACS OS544S30 (case# 2378.238). This work was supported by the United States Department of Energy under contract DE-AC04-94AL85000.

References

Dudley, A.L., R.R. Peters, J.H. Gauthier, M.L. Wilson, M.S. Tierney, and E.A. Klavetter (1988). Total System Performance Assessment Code (TOSPAC) Volume 1: Physical and Mathematical Bases, SAND85-0002, Sandia National Laboratories, Albuquerque, NM.

Glass, R.J. and V.C. Tidwell (1991). Research Program to Develop and Validate Conceptual Models for Flow and Transport Through Unsaturated, Fractured Rock, SAND90-2261, Sandia National Laboratories, Albuquerque, NM.

Klavetter, E.A. and R.R. Peters (1986) Estimation of Hydrologic Properties of an Unsaturated, Fractured Rock Mass, SAND84-2642, Sandia National Laboratories, Albuquerque, NM.

Pruess, K. (1991). TOUGH2–A General-Purpose Numerical Simulator for Multiphase Fluid and Heat Flow, LBL-29400, Lawrence Berkeley Laboratories.

Pruess, K. and T.N. Narasimhan (1985). A Practical Method for Modeling Fluid and Heat Flow in Fractured Porous Media, *Society of Petroleum Engineers Journal*, **25**, pp. 14–26.

Pruess, K. (1983). GMINC—A Mesh Generator for Flow Simulations in Fractured Reservoirs, LBL-15227, Lawrence Berkeley Laboratory, Berkeley, CA.

van Genuchten, M.Th. (1980). A Closed-Form Equation for Predicting the Hydraulic Conductivity of Unsaturated Soils, *Soil Sci. Soc. Am. J.*, Vol 44, pp. 892-898.

Wilson, M.L., J.H. Gauthier, R.W. Barnard, G.E. Barr, H.A. Dockery, E. Dunn, R.R. Eaton, D.C. Guerin, N. Lu, M.J. Martinez, R. Nilson, C.A. Rautman, T.H. Robey, B. Ross, E.E. Ryder, A.R. Schenker, S.A. Shannon, L.H. Skinner, W.G. Halsey, J. Gansemer, L.C. Lewis, A.D. Lamont, I.R. Triay, A. Meijer, and D.E. Morris (1994). Total-System Performance Assessment for Yucca Mountain—SNL Second Iteration (TSPA-1993), SAND93-2675, Sandia National Laboratories, Albuquerque, NM.

AIR-TOUGH: A FULLY 3-DIMENSIONAL LINKING OF ATMOSPHERE WITH SOIL USING EDDY DIFFUSIVITY CONCEPT AND V-TOUGH

Parviz Montazer
Multimedia Environmental Technology, Inc.
3990 Westerly Place, Suite 200
Newport Beach, California 92660
(714) 852-9767

ABSTRACT

In arid climates, evapotranspiration is a strongly-coupled thermodynamic process that is controlled by the interaction of the atmospheric boundary layer and the upper soil surface. Simulation of this process requires a fully-coupled thermodynamic multi-phase fluid-flow and energy-transport code. Such a code was developed in a previous investigation using V-TOUGH. The resulting efficient computer code, A-TOUGH, simulates the effect of dynamic atmospheric fluctuations on vapor movement between the soil and the atmosphere and the resulting moisture movement in the soil. However, the coupling between the atmosphere and soil employed eddy diffusivity which was only a function of time and not a function of space. In the present study the code is extended to allow spatial as well as temporal variation of eddy diffusivity.

I. INTRODUCTION

The problem of interfacing the atmosphere with the surface soil layer is that the flow of air in the atmosphere is turbulent even during the calmest days [2,5]. The transport of vapor in the atmospheric boundary layer near the ground surface is very fast and can be simulated with eddy diffusion. Eddy diffusion is the mixing process between adjacent layers of the air stream with different velocities. The mathematical description of the transport of vapor and other compounds across layers of fluid under turbulent conditions has been the subject of studies in chemical engineering for a number of years[1]. Exact mathematical models of such systems require solution of the Navier-Stokes and material/energy balance equations. Solving these equations is a very difficult task even for simple systems. Numerical solutions are implemented in the atmospheric sciences; however, they are not practical for application to simple evaporation from the soil due to extensive computer requirements. The eddy diffusivity simplification has been used instead to describe the mass and energy transfer across the boundary layers in turbulent conditions[1,2,5]. The transport of vapor from the molecular sublayer to the atmosphere is a function of

surface roughness, wind shear, and thermal stratification as well as the humidity (or vapor concentration) gradient. Therefore, the rate of vertical vapor transfer (or evaporative flux) is given by:

$$q_{evap} = -D^*_{atm} \left.\frac{\partial \rho}{\partial z}\right|_{z_0} \qquad (1)$$

and

$$\rho(z) = \rho^*(z) h(z) \qquad (2)$$

where ρ is vapor density, ρ^* is saturated-vapor density, and h is humidity. Eqn. 1 is similar to Fick's law except that the molecular diffusion coefficient is replaced with D^*_{atm}, the eddy diffusivity. Eddy diffusivity varies with time as temperature and wind speed change with time. Therefore, in order to couple soil processes with atmospheric processes, the eddy diffusivity and the thermal diffusivity parameters must be varied dynamically in addition to the soil boundary conditions.

The principles described above can also be used to approximate transfer of heat across atmospheric layers with turbulent flow[5]:

$$F_{SH}(z) = K_H \rho c_p \frac{\partial T}{\partial z} \qquad (3)$$

where K_H is the eddy diffusion coefficient for heat (which in this case is set equal to D^*_{atm}), ρ is the density of air, c_p is the atmospheric specific heat at constant pressure, T is the temperature, and z is the vertical distance above the ground surface. Therefore, thermal conductivity is calculated for the atmospheric layers as:

$$K_{atm} = D^*_{atm} \rho c_p \qquad (4)$$

II. DESCRIPTION OF THE MODEL

A-TOUGH (Atmospheric TOUGH) was based on V-TOUGH (the Vectorized-version of TOUGH, Transport Of Unsaturated Ground water and Heat). TOUGH was originally developed by Pruess[4] and vectorized by Nitao[4]. A-TOUGH can simulate the 3-dimensional transport of air, vapor, and heat through an atmospheric media which can be directly coupled with the transport of moisture, an air-vapor mixture, and heat through porous and/or fractured media. However, it is limited in variation of the eddy diffusivity in space. This is an important limitation for application to sites such as Yucca Mountain where mountainous terrain results in substantial spatial variation of eddy diffusivity.

The resulting code was tested with many simple and some relatively complicated problem sets, including a two-dimensional low-level radioactive waste trench with a layered cap. In addition, the code was verified against the U.S. Geological Surveys code VS2D[3]. The three-dimensional nature of the code could not be tested due to unavailability of data at time of this publication.

III. RESULTS AND CONCLUSIONS

The long-term effect of changes in atmospheric climatological conditions on subsurface hydrological conditions in the unsaturated zone in arid environments is an important factor in determining the performance of a high-level and low-level radioactive waste repositories in geological environment. Computer simulation coupled with paleohydrological studies can be used to understand and quantify the potential impact of future climatological conditions on repository performance. Air-TOUGH efficiently simulates (given current state-of-the-art technology) the physical processes involved in the near-surface atmosphere and its effect on subsurface conditions. This efficiency is due to the numerical techniques used in TOUGH and the efficient computational techniques used in V-TOUGH to solve non-linear thermodynamic equations that govern the flux of vapor and energy within subsurface porous and fractured media and between these media and the atmosphere.

REFERENCES

1. Bird, R.B., Stewart W.E., and E.N. Lightfoot (1965): Transport phenomena; John Wiley & Sons, New York, New York; 780 pp.

2. Brutsaert, W. H. (1982): Evaporation into the atmosphere: Theory, history, and applications; D. Reidel Publishing Company, London, England; 299 pp.

3. Lappala, E.G., Healy, R.W., and E.P. Weeks (1987): Documentation of computer program VS2D to solve the equations of fluid flow in variably saturated porous media; United States Geological Survey - Water Resources Investigation Report 83-4099, Denver, Colorado; 184 pp.

4. Nitao, J. J. (1989): V-TOUGH - An enhanced version of the TOUGH code for the thermal and hydrologic simulation of large-scale problems in nuclear waste isolation; Earth Sciences Department, Lawrence Livermore National Laboratory, Draft 1.1, November 18; 24 pp.

5. Peixoto, J.P. and A.H. Oort (1992): Physics of climate; American Institute of Physics, New York, New York; 520 pp.

6. Pruess, K. (1987): TOUGH user's guide; Earth Sciences Division, Lawrence Berkeley Laboratory, University of California, Berkeley, California, LBL-20700; 78 pp.

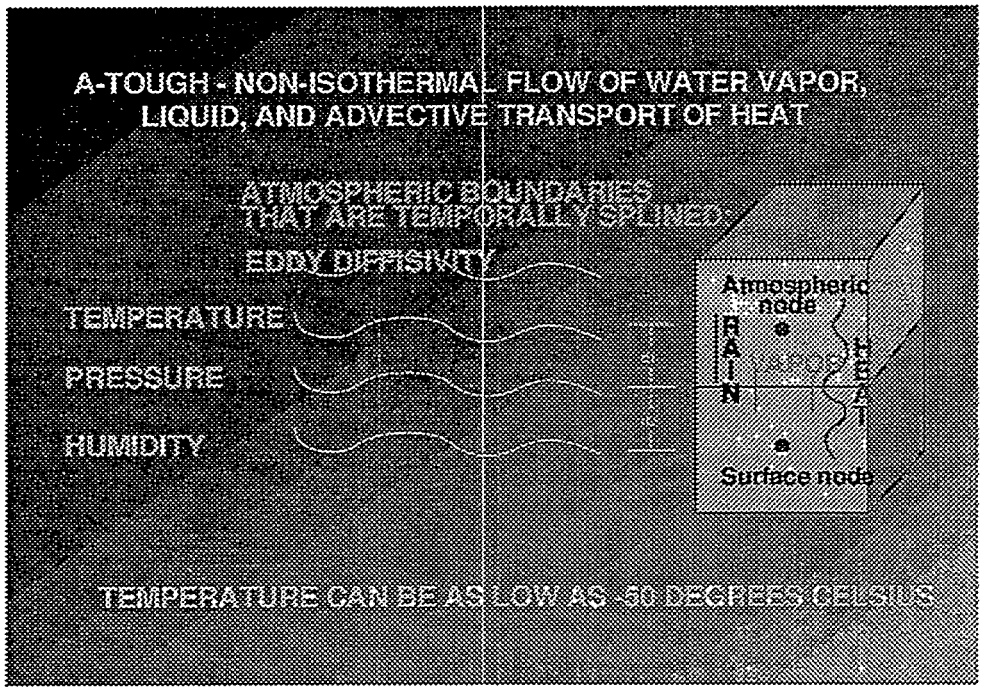
A-TOUGH - NON-ISOTHERMAL FLOW OF WATER VAPOR, LIQUID, AND ADVECTIVE TRANSPORT OF HEAT
ATMOSPHERIC BOUNDARIES THAT ARE TEMPORALLY SPLINED
EDDY DIFFUSIVITY
TEMPERATURE
PRESSURE
HUMIDITY
Atmospheric node
RAIN
HEAT
Surface node
TEMPERATURE CAN BE AS LOW AS -50 DEGREES CELSIUS

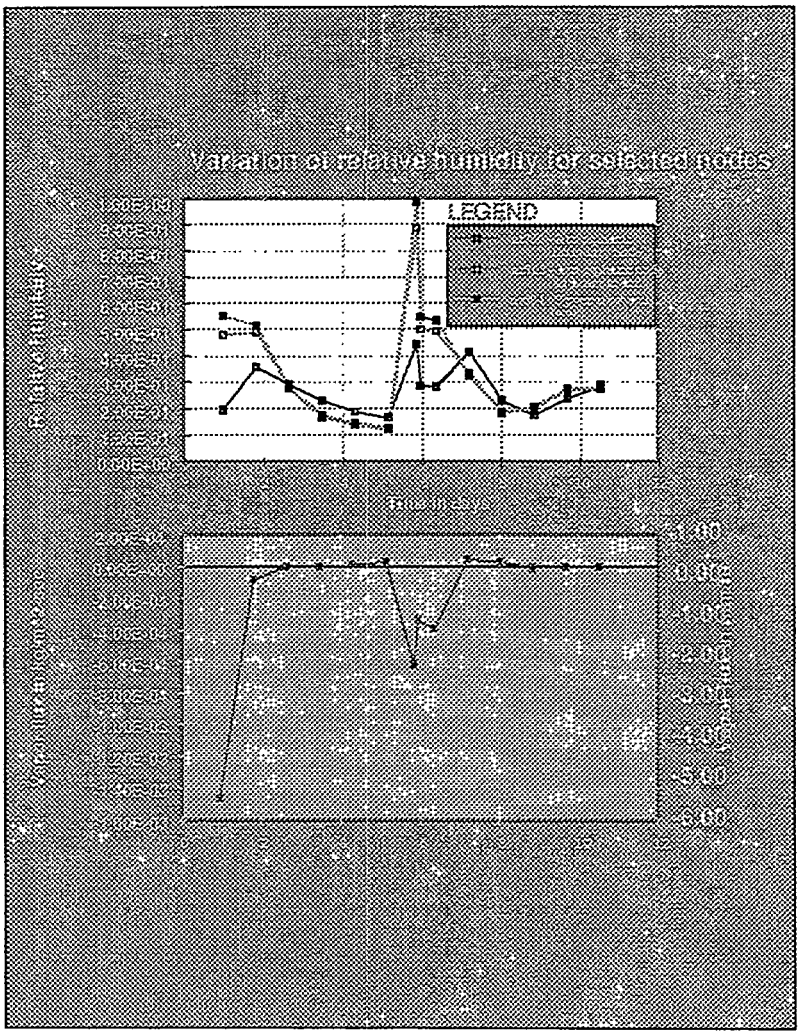
Variation of relative humidity for selected nodes
LEGEND

APPLICATION OF TOUGH TO HYDROLOGIC PROBLEMS RELATED TO THE UNSATURATED ZONE SITE INVESTIGATION AT YUCCA MOUNTAIN, NEVADA

by Edward M. Kwicklis[1], Richard W. Healy[1], G.S. Bodvarsson[2], and Ning Lu[3]

[1]U.S. Geological Survey
[2]Lawrence Berkeley Laboratory
[3]Foothills Engineering/U.S. Geological Survey

ABSTRACT

To date, TOUGH and TOUGH2 have been the principal codes used by the U.S. Geological Survey in their investigation of the hydrology of the unsaturated zone at Yucca Mountain. As illustrated by the range of particular studies to which they have been applied, these codes have proven very versatile and robust, and, when necessary, adaptable for applications not originally envisioned during their development.

Examples of some applications of the TOUGH and TOUGH2 codes to flow and transport problems related to the Yucca Mountain site investigation are presented, and the slight modifications made to the codes to implement them are discussed. These examples include: (1) The use of TOUGH in a simple fracture network model, with a discussion of an approach to calculate directional relative permeabilities at computational cells located at fracture intersections. These simulations illustrated that, under unsaturated conditions, the locations of dominant pathways for flow through fracture networks are sensitive to imposed boundary conditions; (2) The application of TOUGH to investigate the possible hydrothermal effects of waste-generated heat at Yucca Mountain using a dual-porosity, dual-permeability treatment to better characterize fracture-matrix interactions. Associated modifications to TOUGH for this application included implementation of a lookup table that can express relative permeabilities parallel and transverse to the fracture plane independently. These simulations supported the continued use of an effective media approach in analyses of the hydrologic effects of waste-generated heat; and (3) An investigation of flow and tracer movement beneath a wash at Yucca Mountain in which a particle tracker was used as a post-processor. As part of this study, TOUGH2 was modified to calculate and output the x-,y- and z-components of fluid fluxes and pore velocities as input into the particle tracker. This study suggested that contrasts in hydrologic properties of a layered sequence of tuffs overlying the potential repository site will result in the formation of capillary barriers that locally promote considerable lateral flow, thereby significantly decreasing the magnitude of fluxes from peak values at the ground surface and delaying the arrival of surface-derived moisture at the potential repository horizon.

INTRODUCTION

Yucca Mountain, Nevada, is being investigated as a potential location for a high-level nuclear waste repository. If the site is found suitable, the repository would be located in the unsaturated zone, approximately 250-350m below ground surface, depending on local topography, and 225m above the regional water table. The hydrogeologic environment in which the waste would be placed consists primarily of ash flow and ash-fall tuffs, which have been welded and fractured to varying degrees. In general, the more densely welded tuffs possess lower porosity and primary permeability than the nonwelded or moderately welded tuffs, but are more intensely fractured. The secondary permeability of densely welded tuffs may be six orders of magnitude or more greater than their primary permeability, and several orders of magnitude larger than the primary permeability of the less welded tuffs. As with other arid zone sites where annual precipitation is much less than potential evapotranspiration, the areally-averaged annual flux is believed to be a small fraction of annual precipitation, although net infiltration may be locally large following rainstorms or snowmelt, particulary when infiltration occurs in fractures and can move rapidly away from the ground surface where it might otherwise be removed by evapotranspiration. Because the areally-averaged flux is believed to be small and fractures are probably drained most of the time, the movement of water as vapor is potentially an important component of the overall moisture balance, especially following waste emplacement when a large volume of in situ pore

water is likely to be vaporized by waste-generated heat.

The geometric flexibility offered by TOUGH and TOUGH2 has permitted their application to hydrologic problems involving fracture networks, and to mulitphase problems that require consideration of dual-porosity, dual-permeability effects. Their numerical robustness has also allowed their use in numerical investigations of the dynamics of water movment in layered, variably fractured tuff sequences subjected to abrupt changes in boundary conditions.. These applications and the modifications to the TOUGH and TOUGH2 codes that allowed their implementation are described below.

APPLICATIONS

Water Movement in a Variably Saturated Fracture Network

Interest in the mechanisms of water movement in thick, fractured unsaturated zones has occurred only relatively recently, primarily as a result of the possibility of nuclear waste isolation in such environments. Therefore, understanding of the hydrologic behavior of variably saturated fractured rock is not as fully developed as for other hydrogeologic environments. To gain insight into the possible behavior of variably-saturated fractured rock , a numerical study was conducted of water movement through a simple fracture network using TOUGH. Of particular interest was the potential for water flow through the network to become concentrated along specific pathways, and the conditions under which flow behavior was similar to, or deviated strongly from, behavior believed typical of porous media. The intent was that the insight gained would result in better strategies for physically testing or monitoring such media..

A TOUGH compatible integrated finite difference mesh was created for a simple fracture network using FMMG (Okusu et al., 1989), and eliminating the matrix elements, which were assumed impermeable. The network included two fracture sets: a subvertical set containing five fractures and a subhorizontal set containing four fractures. Three sets of simulations were conducted, including: (1) a "mixed" network with subvertical and subhorizontal fractures having average physical apertures of 125 and 25μm, respectively; (2) a geometrically similar network in which all fractures had physical apertures of 125μm; and (3) a network in which fractures had physical apertures of 25μm. The lengths and locations of the fractures were arbitrary and are not

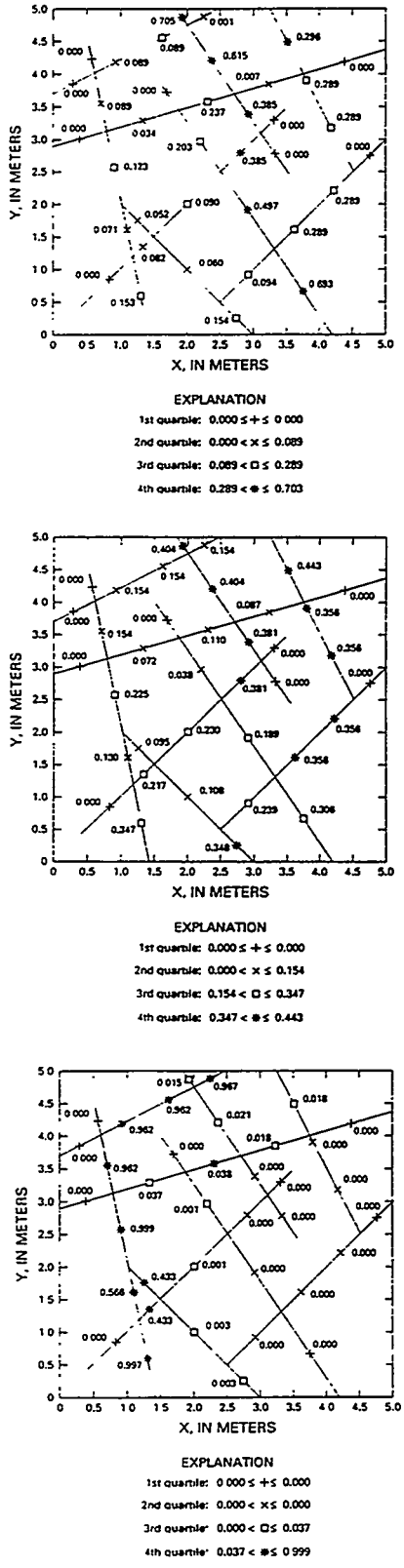

Figure 1. Distribution of fractional flux in the "mixed" network for prescribed boundary pressure heads of (a) 0.0m (b) -0.10m, and (c) -0.25m.

intended to reflect any specific geologic environment. The fracture apertures were within the range of values reported for Yucca Mountain. Unsaturated properties , including effective permeability to water and saturation as functions of pressure head, were determined by a separate numerical model VSFRAC (Kwicklis and Healy, 1993) that considered aperture variability within individual fractures having the cited mean apertures. Average unsaturated hydrologic properties for 10 stochastic realizations of each fracture size were fit with functional forms for ease of incorporation into TOUGH. Water flow under the influence of gravity was simulated for each of the three networks for prescribed upper and lower boundary pressure heads ranging from 0 to -0.25m, in increments of 0.05m.

In performing these simulations, the critical modeling issue was the manner in which the relative permeabilities were determined at cells representing fracture intersections. Directional relative permeabilities were assumed for these cells, with relative permeabilities at each interface calculated on the basis of the capillary pressure of the cell and on the properties assigned to the adjacent fracture segment. A small subroutine was added that expressed relative permeability as a function of capillary pressure. Upstream weighting was used for numerical stability. For numerical stability, it was also necessary that each fracture element along the inflow or outflow boundaries was assigned its own boundary element.

For each boundary condition, the steady-state distributions of water flow and pressure heads were recorded, along with variability in flow and pressure head within the network. Figure 1 shows how the principal flowpaths through the "mixed" network change as a function of the boundary pressure heads. Listed adjacent to each fracture element in Figure 1 is the fractional flux, which is defined as the liquid water flux passing through that element divided by the total flux carried by the network. From these results it can be observed that both the location of the dominant pathways and the variability in normalized flux change with relatively small changes in boundary pressure. The variability in normalized flux (figure 2) reflects the degree to which the flux is either concentrated along specific paths or spread among many pathways in the network. The constant, but nonzero, standard deviations shown in figure 2 for the uniform 25 and 125 µm fracture networks reflect the variability in flux caused by differences in orientation of the elements with respect to gravity. Similar analyses were done for pressure heads within the network. Plots of the variability in flux and pressure

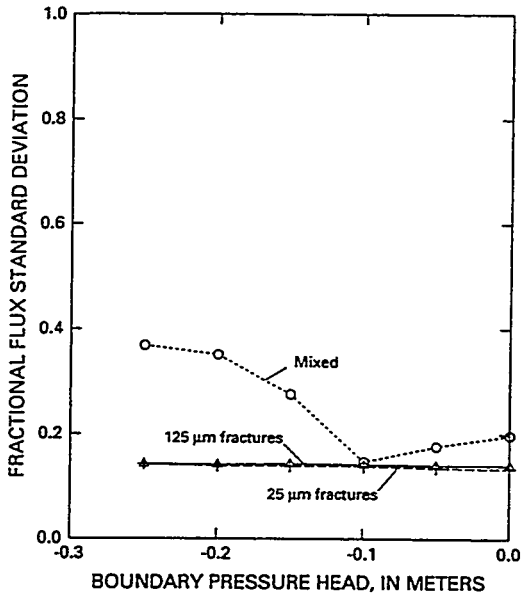

Figure 2. Standard deviation of fractional flux as a function of boundary pressure head for the three fracture networks.

head as a function of boundary pressure head implied that the network behaved more like porous media for some pressure heads, but less so at others.

These results also implied that the locations of dominant flow paths through the fracture network within the unsaturated zone at Yucca Mountain might be quite dynamic and depend on climate-induced changes in boundary conditions at the ground surface. Therefore, observations of the present-day distribution of seeps in tunnels may bear an uncertain relation to the future distribution of seeps.

Dual Porosity - Dual Permeability Simulation of the Hydrologic Effects of Waste-Generated Heat.

With notable exceptions (Pruess et al., 1990a,b), numerical simulations of repository dry-out due to thermal loads generated by radioactive decay of nuclear waste have typically assumed that the use of the equivalent continuum model (ECM) results in negligible error. The ECM assumes that when the temperature at a given location in space has been raised above the boiling point, water at that location can immediately move as vapor within drained portions of the fracture network. The time required for water to move from the central parts of each matrix block to the fracture face (where it is

vaporized) is not considered by the ECM. Hence, the extent of the dry-out zone coincides closely with the boiling front (e.g. Buscheck and Nitao, 1993), even when matrix blocks are very large, matrix permeability is very low, and thermal loads and conductivity are very large. Intuitively, one would expect that where matrix block sizes are large, or when matrix permeability is small (due to natural variability or desaturation), the assumption of instantaneous transfer of liquid to the fracture face would be increasingly in error, especially at high thermal loads.. In these cases, both the rate of dry-out and the rate of condensate generation (and, hence, of reflux) would be overestimated by the ECM. This overestimation, if it occurs, may be important because previous studies employing the ECM have concluded that the refluxing of condensate would overwhelm the natural recharge, even for pluvial conditions. The purpose of this study was to compare rates of dry-out and condensate generation predicted from two different models: the equivalent continuum model (ECM) and a true double porosity approach.

The study employs a highly simplified stratigraphy consisting of a single unit with matrix properties thought to be representative of the densely welded Topopah Spring Member. The simplied stratigraphy is justified because the concern here is principally with differences that result from the modeling approach employed, and not in predicting the actual response of Yucca Mountain to thermal loading. The simplified stratigraphy permits these differences to be seen more clearly. Boundary conditions imposed were gas pressure=86,000 Pa, temperature=13 °C, and liquid flux=0.0 at the ground surface, and gas pressure=91,822 Pa, temperature=31 °C, and liquid saturation=1.0 at the water table. These boundary conditions resulted in essentially static equilibrium conditions for both the liquid and gas phases. Simulations employing these boundary conditions were run to long times to establish the initial conditions for the thermal loading calculations.

Hydrologic properties for the ECM model were derived by assuming there are 3 orthogonal fracture sets with 1-m spacing, resulting in matrix blocks that are 1-m^3. Each fracture set was assumed to consist exclusively of fractures with average physical apertures of 25 microns. Moisture characteristic and effective permeability curves for single fractures having average physical apertures of 25 microns were estimated using a numerical model (VSFRAC) which considers aperture variability at the pore-scale. Calculated results that were averages of 10 different realizations of the aperture field were smoothed and extrapolated by fitting closed-form functions. ECM properties were entered in tabular form into TOUGH as a function of gas saturation.

The double-porosity calculations employed the Multiple Interacting Continuum (MINC) approach of Pruess and Narasimhan (1985). Most applications of the MINC method do not allow for block-to-block flow within the matrix continuum. However, it was clearly necessary to consider this process to allow for the possiblity that some or even most of the condensate might reflux back toward the repository through the matrix. Furthermore, the calculations of Buscheck and Nitao (1993) indicated that heat flow was dominated by conduction through the rock matrix, rather than by convection through the fracture system. Therefore, for each fracture continuum cell, the associated lumped matrix block that resulted from application of the MINC approach was connected to similar blocks centered on cells above and below it. Similarly nested shells of these lumped matrix blocks were connected across areas that were determined from the intercell area of the fracture continuum, and the fractional volume of the lumped matrix blocks contained by those shells. By connecting similarly located shells of adjacent matrix blocks in this manner, identical darcy fluxes and head changes within all shells of a given matrix block could, theoretically, be obtained for one-dimensional flow in the absence of interaction with the fracture continuum.

Wet and dry thermal conductivity of the matrix blocks were the same as for the ECM continuum. "Effective" fractures in the fracture continuum were defined as including matrix extending to 0.5 mm from the center plane through the 25 micron fractures. The inclusion of a small amount of matrix into the fracture continuum results in new effective continuum hydraulic conductivity and capillary pressure curves. Similarly, the thermal conductivity and heat capacity of the fracture continuum were calculated as weighted fractions of the analogous matrix quantities. Almost all the thermal conductivity and heat capacity are associated with the matrix continuum, as one would expect given its larger cross-sectional area and volume. The inclusion of some small amount of matrix material in the fracture continuum was done to facilitate the numerical computations by providing additional heat capacity and fluid storage, controlling temperature and saturation changes and thereby permitting larger time steps to be taken than would otherwise be possible (Pruess et al., 1990a,b). Although the small addition of matrix may have dampened the response of the fractures to flow to a small degree, over 99% of the rock mass remained in the matrix continuum, free to

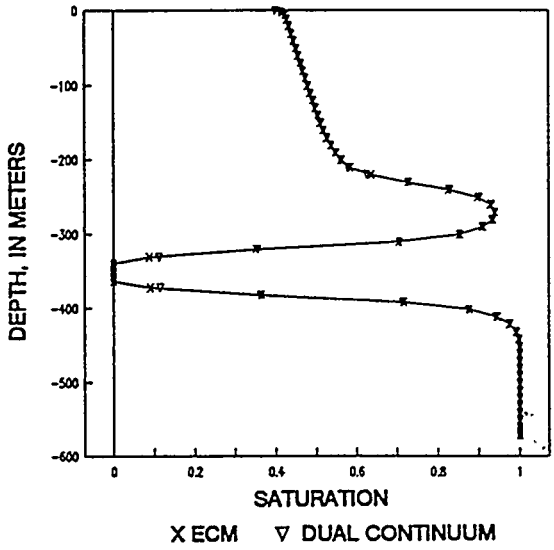

Figure 3. Comparison of the saturation versus depth profiles at 500 years following waste emplacement for the ECM and dual-continuum models.

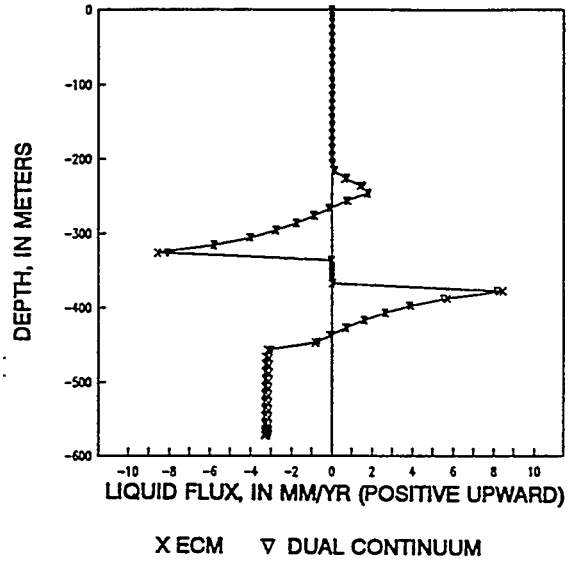

Figure 4. Comparison of the liquid flux versus depth profiles at 500 years following waste emplacement for the ECM and dual-continuum models.

remain in disequilibrium with the fracture continuum.

A modeling issue that has had potentially large influence on the rate of fluid exchange between the fracture and matrix continua is the definition of hydraulic properties of the fracture in a direction perpendicular to the fracture plane. It has been suggested (Wang and Narasimhan, 1985) that the appropriate relative permeability in this direction is the fractional wetted area, that is, the fraction of the fracture plane that is water-filled. The assumption of water potential equilibrium between fractures and the 0.5 mm of adjacent matrix allows these conceptual difficulties to be sidestepped. The fracture continuum contains matrix material immediately adjacent to the fractures and water must pass through this adjacent material to get from the fractures to the matrix continuum. Therefore, to remain internally consistent, the most appropriate fracture continuum properties to use in modeling its interaction with the matrix continuum are the welded tuff matrix intrinsic and relative permeabilities.

Heat generation curves for 8-year old spent nuclear fuel taken from Tsang and Pruess (1987) were used to represent the thermal loads caused by radioactive decay of the waste. Thermal properties for the Topopah Springs unit were also taken from the work by Tsang and Pruess (1987). An initial thermal loading of 114 kw/acre was assumed.

The ECM and dual-porosity models were compared for times ranging from 100 to 5000 years, which encompassed periods during which the dry-out zone was rapidly expanding and during which time the boiling isotherm had collapsed. Over this range of times, the results obtained by the ECM and dual-porosity methods for temperature, gas and capillary pressure, saturation, and vapor and liquid water fluxes were nearly identical. Figure 3 shows the bulk-rock saturation profiles at 500 years and figure 4 shows the liquid water fluxes for the same time. Both models predict complete dryout for several tens of meters above and below the repository located at about a 350m depth (figure 3). Superposition of the temperature profile at 500 years on these figures would show that vapor is condensing near the 100 °C isotherms at depths of approximately 250 and 450m. Figure 4 shows that water moves upward and downward away from these condensation zones located both above and below the repository. Maximum liquid fluxes of about 8 to 9 mm/yr are flowing back toward the repository. Downward drainage to the water table is about 3.4mm/yr at this time. The dual porosity model allows the component of the flux carried by the fracture continuum to be identified explicitly (figure 5). Surprisingly, due to the strong capillary pressure gradients, nearly all of the water refluxing back toward the repository is being carried by the matrix. This occurred even at 100 years when the maximum rate of refluxing toward the repository was between 25 and 30 mm/yr. Figure 5 also shows that, below the repository, an

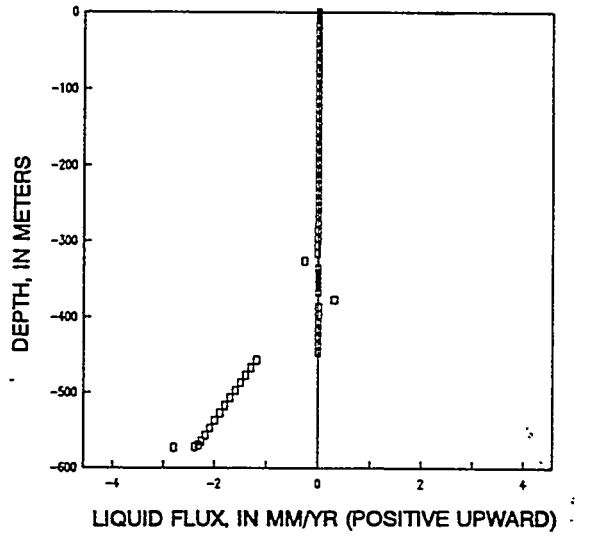

Figure 5. Liquid water flux versus depth for the fracture continuum at 500 years following waste emplacement, as calculated by the dual continuum model.

increasing amount of drainage is occurring through the fracture network as a result of the weak capillary pressure near the water table.

While the accuracy of the effective continuum model will degenerate eventually for decreasing matrix permeabilities and larger fracture spacings, this comparison showed it performed surprisingly well for fracture spacings and matrix permeabilities thought to be representative of the Topopah Spring unit. It should be kept in mind, however, that even the dual continuum approach represents only the average behavior of the fracture network. The absence of heterogeneity in fracture, as well as matrix properties, may underestimate the degree to which flow might become focussed in specific fractures or faults. Additionally, the effective permeability assumed for the fracture continuum was on the order of 10^{-15} m^2, which is approximately two orders of magnitude smaller than what has recently been measured for the Topopah Spring unit (LeCain and Walker, 1994).

Transient Water and Particle Movement Beneath an Alluvial Wash

The purpose of this study was to analyze the movement of water in the upper 120m beneath Pagany Wash, located on the eastern slope of Yucca Mountain, and thereby gain insight into the possible behavior of several similar washes that exist at the site. More specifically, the objectives of the numerical model were to (1) interpret the observed saturation, water potential and isotope data to infer the magnitude and direction of past and present-day water movement, (2) investigate the system dynamics, including identification of the controlling processes and features, and (3) develop an understanding of how the hydrologic system might respond to possible future climates.

Available data included porosity, saturation, water potential, stratigraphic and isotope (^3H, ^{14}C) data from two approximately 110m deep boreholes: UE-25 UZ#4, located in the center of the alluvial wash, and UE-25 UZ#5, located on a bedrock sideslope 38m to the southwest of UZ#4. To account for the heterogeneity reflected in the porosity profiles, each 1-m depth interval in the upper 120m at each hole was assigned to one of twelve porosity classes ranging from 0.05 to 0.60. The properties of each class were determined from correlations derived from a pre-existing data set between hydraulic conductivity, parameters that characterize the unsaturated moisture characteristic and hydraulic conductivity functions, and porosity (Kwicklis et al., 1993). Densely to moderately welded tuffs were assigned to the 0.05 to 0.30 porosity classes and given fracture porosity and permeability. However, based on their estimated capillary and hydraulic characteristics, the fractures were relatively nontrasmissive to water at water-potentials less than -1m.

The simulation domain extended 250m in a lateral direction, and 472m in depth to take advantage of known boundary conditions at the water table. The wash, conceptually located along the upper boundary within the central 10m, was assigned an infiltration rate of 20mm/yr, and the adjacent bedrock outcrop was assigned 0.1mm/yr. Initial conditions resulted from a uniform steady flow rate of 0.1 mm/yr throughout the entire domain. These boundary and initial conditions were suggested by 1-d simulations which determined that large fluxes were required to reproduce the observed saturation and water potentials profiles in the upper part of the boreholes, and conversely, the lower parts of the profiles were consistent with much smaller fluxes. Results are shown for the upper 120m, or elevations from 352 to 472m above the water table.

Many of the trends as well as values of the observed saturation and water potential profiles were reproduced by the numerical model, although some discrepencies remain due to uncertainties in hydrologic properties, assumptions concerning fracture-matrix potential equilibrium, and the

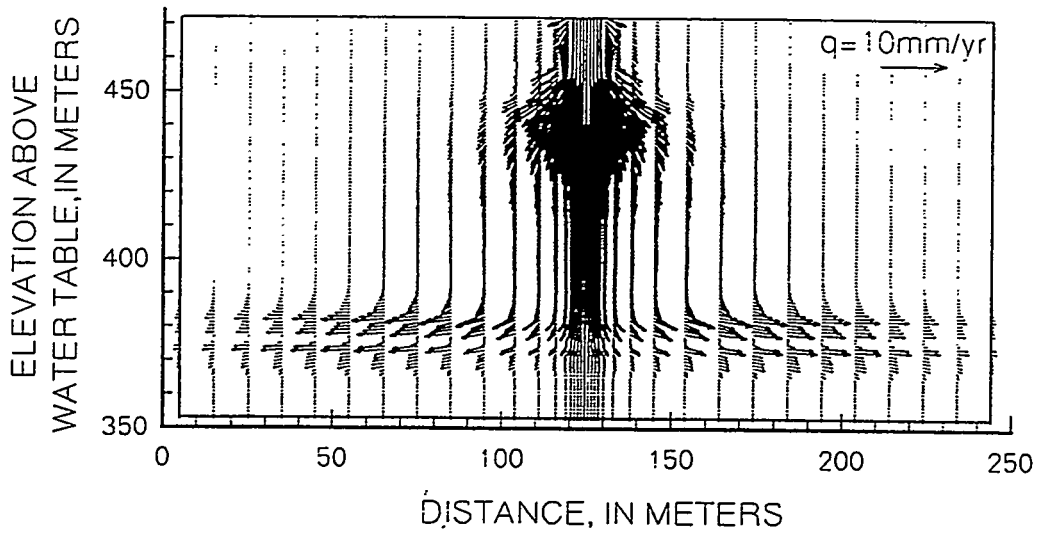

Figure 6. Water flux distribution beneath the wash at 10,000 years after the onset of increased flux in the wash.

conceptual model of infiltration. Additionally, the model results indicate the relative importance of various stratigraphic layers in promoting lateral spreading of focussed infiltration, thereby decreasing fluxes from peak values (figure 6). One such zone occurs in the nonwelded, relatively unfractured base of the Tiva Canyon Member between elevations of 430 to 450m (depths of 25 to 40m), where, due to a relatively abrupt change in degree of welding, porosity increases from 0.1 to 0.5, fractures terminate, and flow beneath the wash makes a transition from fracture to matrix dominated. A second significant interval in which lateral flow occurs is just above a low porosity vitrophyre at an approximately 360m elevation (110m depth). Lateral flow above this interval occurs partially in response to capillary barrier effects which occur at the interface between the rock pores of the nonwelded tuffs and the relatively larger openings of the fractures in the underlying densely welded tuffs. Water accumulates above this interface until it becomes sufficiently wet that fractures accept the water being delivered by the overlying rock matrix. As this water accumulates beneath the wash, it also flows laterally due to water potential gradients. Oldenburg and Pruess (1993) discuss modeling issues relevant the to investigation of capillary barriers with integrated finite difference codes such as TOUGH and TOUGH2..

A plot of steady-state vertical fluxes as a function of depth for the left half of the flow system (figure 7) shows that, by a 40m depth, peak fluxes beneath the wash have decreased to less than 5mm/yr, and that, at a 110m depth, fluxes are uniform and less than 1mm/yr. Thus, at least in the absence of faults, these layered sequences are predicted to play a key role in decreasing the amplitude of peak surface fluxes, and in delaying the arrival of surface derived moisture at the repository horizon.

To help assess the implications of the isotope data, the semianalytical particle tracking method developed by Lu (1994) was employed as a post processor to calculate particle movement under unsteady flow conditions. Velocities output from TOUGH for various elapsed simulation times were reformatted and used as input to the particle tracker, which traced particles applied along the upper boundary. The positions of those particles at various times after their release at t=1000yrs define the isochrons of figure 8. At an approximately 100m

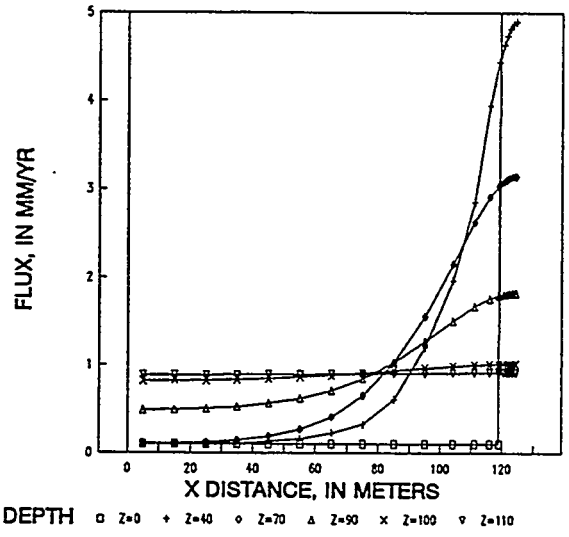

Figure 7. Steady-state vertical components of water flux across planes located at various depths beneath the wash.

depth in UZ#4, the model predicted a travel time of about 2,700 years, compared with the 1,000 year age date based on ^{14}C. At UZ#5, an age of approximately 5,100 years was predicted, compared with an age of 4900 years based on ^{14}C. The trend from younger water beneath the wash to older water with increasing distance from the wash, indicated by both the model results and the ^{14}C data, provide support for the argument that over millennia-long time scales, Pagany Wash has been an important source of recharge, despite evidence that that it has not been an important contributor over the last decade or longer (Hevesi and Flint, 1993). However, at locations where bomb-pulse ^{3}H has been found, the model predicts significantly longer advective travel times. Overprediction of travel times may have resulted because, in contrast to the model assumptions, much of the pore space in the densely welded tuffs in the Tiva Canyon Member is inaccessible to infiltrating water, which probably flows episodically but at high rates through near-surface fractures.

Since this application, TOUGH2 has been modified to output the x-, y- and z-components of liquid and gas fluxes and pore velocities, thereby greatly facilitating the application of particle tracking codes as post processors. That version of TOUGH2 requires, as user-supplied input, the x, y and z coordinate of the nodes associated with each cell. Fluid fluxes crossing the cell interfaces are resolved into their x-, y-, and z-components based on the coordinate information and the sign and magnitude of the flux, and assigned to the nodal points of the cell from which the flow is originating. Three-dimensional, nonorthogonal meshes are permitted, as long as standard integrated-finite difference assumptions have been adhered to in the mesh design.

SUMMARY

This paper describes three very different applications of the TOUGH code to hydrologic problems associated with the characterization of Yucca Mountain as a potential repository site. These included: (1) an investigation of steady water movement through a variably-saturated fracture network which suggested that flow path locations in natural systems may be quite dynamic and climate sensitive; (2) a dual continuum model of the hydrologic effects of waste-generated heat which supported the continued use of simpler, more computationally efficient effective continuum models in these types of analyses; and (3) an investigation of transient water and particle movement beneath an alluvial wash, which illustrated that contrasts in hydrologic properties of tuffs overlying the potential repository horizon could result in the formation of capillary barriers that would significantly decrease the amplitude of peak surface fluxes and delay the arrival of surface-derived moisture at the potential repository horizon.. Modeling issues and code modifications associated with these applications were discussed.

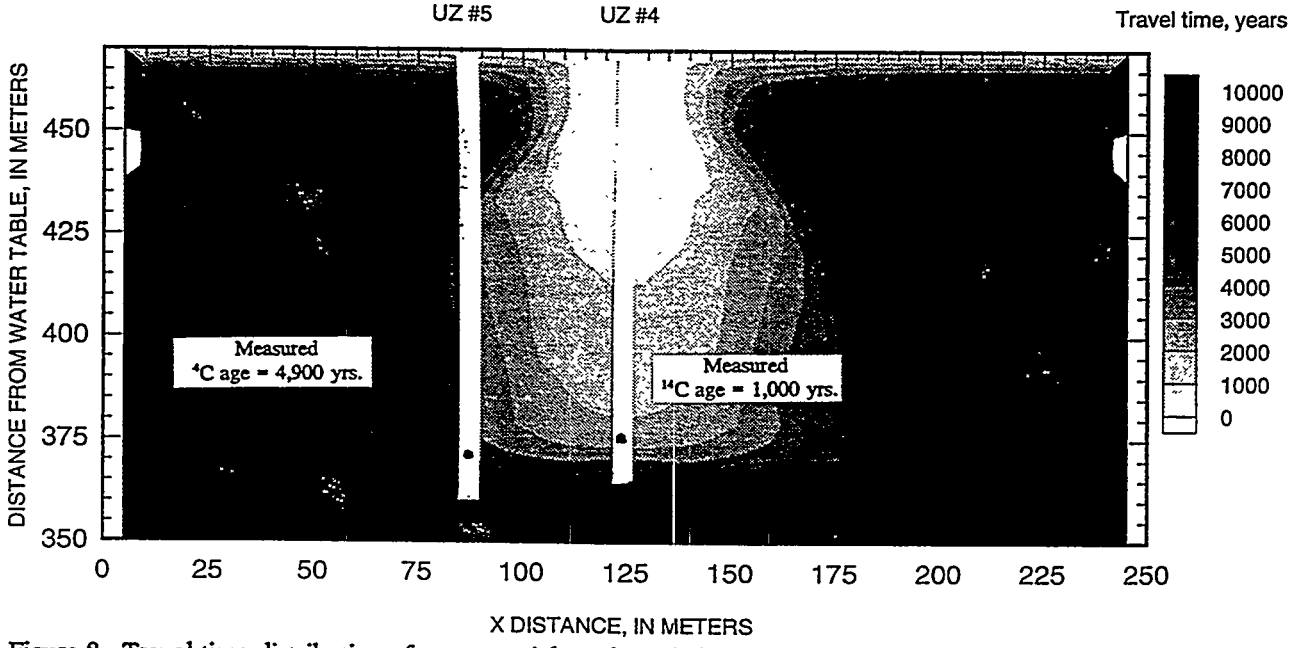

Figure 8. Travel time distribution of water particles released along the upper surface of the simulation region 1,000 years after the onset of increased flux in the wash.

REFERENCES

Buscheck, T.A., and J.J. Nitao, The analysis of repository-heat-driven hydrothermal flow at Yucca Mountain, in High-Level Radioactive Waste Management, Proceedings of the Fourth International Conference, Vol. 1, p. 847-867, American Nuclear Society, La Grange Park, Ill, 1993.

Hevesi, J.A., and A.L. Flint, The influence of seasonal climatic variability on shallow infiltration at Yucca Mountain, in High-Level Radioactive Waste Management, Proceedings of the Fourth International Conference, Vol. 1, p. 122-131, American Nuclear Society, La Grange Park, Ill, 1993.

Kwicklis, E.M., and R.W. Healy, Numerical investigation of steady liquid water flow in a variably saturated fracture network, Water Resources Research, vol. 29, no. 12, p. 4091-4102, 1993.

Kwicklis, E.M., A.L., Flint, and R.W. Healy, Estimation of unsaturated zone liquid water flux at boreholes UZ#4, UZ#5, UZ#7 and UZ#13, Yucca Mountain, Nevada, from saturation and water potential profiles, in Proceedings of the Topical Meeting on Site Characterization and Model Validation: Focus '93, p. 39-57, American Nuclear Society, La Grange Park, Ill., 1993.

LeCain, G.D., and J.N. Walker, Results of air-permeability testing in a vertical borehole at Yucca Mountain, Nevada, in High-Level Radioactive Waste Management, Proceedings of the Fourth International Conference, Vol. 4, p.2782-2788, American Nuclear Society, La Grange Park, Ill, 1994.

Lu, N., A semianalytical method of path line computation for transient finite-difference groundwater flow models, Water Resources Research, vol. 30, no. 8, p. 2449-2459, 1994.

Okusu, N.M., K. Karasaki, J.C.S. Long, and G.S. Bodvarsson, FMMG: A program for discretizing two-dimensional fracture/matrix systems, User's manual and listing, report, Lawrence Berkeley Lab., Berkeley, Calif., 1989.

Oldenburg, C.M., and K. Pruess, On numerical modeling of capillary barriers, Water Resources Research, vol., 29, no. 4, p. 1045-1056, 1993.

Pruess, K., and T.N. Narasimhan, A practical method for modeling fluid and heat flow in fractured porous media, Soc. Pet. Eng. J., 25(1), p. 14-26, 1985.

Pruess, K, J.S.Y. Wang, and Y.W. Tsang, On thermohydrologic conditions near high-level nuclear wastes emplaced in partially saturated fractured tuff: 1. Simulation studies with explicit consideration of fracture effects, Water Resources Research, vol. 26, no. 6., p. 1235-1248, 1990.

Pruess, K, J.S.Y. Wang, and Y.W. Tsang, On thermohydrologic conditions near high-level nuclear wastes emplaced in partially saturated fractured tuff: 2. Effective continuum approximation, Water Resources Research, vol. 26, no. 6., p. 1249-1261, 1990.

Tsang, Y.W., and K. Pruess, A study of thermally induced convection near a high-level nuclear waste repository in partially saturated fractured tuff, Water Resources Research., vol. 23, no. 10, 1958-1966, 1987.

Wang, J.S.Y. and T.N. Narasimhan, Hydrologic mechanisms governing fluid flow in a partially saturated, fractured, porous medium, Water Resources Research, vol. 21, no.12, p. 1861-1874, 1985.

Acknowledgement

This work was supported, in part, by the Director, Office of Civilian Radioactive Waste Management, Yucca Mountain Site Characterization Project Office, Regulatory and Site Evaluation Division, and by the Assistant Secretary for Energy Efficiency and Renewable Energy, Geothermal Division, of the U.S. Department of Energy under Contract No. DE-AC03-76SF00098.

Appendix A. Author Index

Appendix B. Registered Participants

Michael C. Adams
Earth Sciences & Res. Institute
391 Chipeta Way, Suite C
Salt Lake City, UT 84108
(801) 584-4435
(801) 584-4453
madams@rock-doc.uuri.utah.edu

Adeyinka E. Adenekan
Exxon Production Research Co.
P. O. Box 2189
Houston, TX 77252
(713) 965-7943
(713) 965-7579
aadenekan@aol.com

Rick Ahlers
Nuclear Waste Department
Lawrence Berkeley Laboratory
1 Cyclotron Road, 50E
Berkeley, CA 94720
(510) 486-7341
(510) 486-5686
ahlers@jard.lbl.gov

Susan J. Altman
Sandia National Laboratories
P. O. Box 5800
Dept. 6312/MS 1326
Albuquerque, NM 87185
(505) 848-0893
(505) 848-0739
sjaltma@nwer.sandia.gov

Emilio U. Antúnez
Lawrence Berkeley Laboratory
1 Cyclotron Road
Berkeley, CA 94720
(510) 486-5866
(510) 486-4159
emilio@jard.lbl.gov

Michio Aoki
Sunshinego 29P
NEDO
3-1-1, Higashi-Ikebukuro
Toshima-ku
Tokyo, Japan 170
81-3-3987-9455
81-3-3986-8197

Georg Arens
Bundesamt für Strahlenschutz
Postfach 10 01 49
38201Salzgitter
Germany
49-531-592-7694
49-531-592-7674

Mark Bandurraga
Lawrence Berkeley Laboratory
1 Cyclotron Road
Berkeley, CA 94720

Alfredo Battistelli
Aquater S.p.A.
Via Miralbello
San Lorenzo in Campo
Pesaro, Italy 61047
39-721-731-326
39-721-731-308

Jens T. Birkhoelzer
Lawrence Berkeley Laboratory
1 Cyclotron Road
Berkeley,CA 94720
(510) 486-7118
(510) 486-5686
jensbirk@ux5.lbl.gov

K. Kit Bloomfield
Pacific Gas & Electric Company
P. O. Box 456
Healdsburg, CA 95448
(707) 431-6235
(707) 431-6187
kkb2@pge.com

Gudmundur S. Bodvarsson
Earth Sciences Division
Lawrence Berkeley Laboratory
1 Cyclotron Road, 50E
Berkeley, CA 94720
(510) 486-4789
(510) 486-5686

John Bredehoeft
Hydrodynamics Group
P. O. Box 291
La Honda, CA 94020
(415) 747-0441
(415) 747-0273
jdbrede@aol.com

David P. Bullivant
Dept. of Engineering Science
University of Auckland
Private Bag 92019
Auckland 1, New Zealand
64-9 3737599, x5807
64-9 3737468
d.bullivant@auckland.ac.nz

John G. Burnell
Industrial Research Limited
P. O. Box 31-310
Lower Hutt, New Zealand
(64) 4-569-0000
(64) 4-569-0003
j.burnell@irl.cri.nz

Pablo Ramón Calvo
Dep. Math. Aplicada
Universidad de Zaragoza
Zaragoza, Spain 50009
34-76-356617
34-76-356244
fpetriz@mcps.unizar.cs

Gang Chen
Earth Science Division
Lawrence Berkeley Laboratory
1 Cyclotron Road, 50E
Berkeley, CA 94720
(510) 486-7107
(510) 486-5686
gchen@jard.lbl.gov

Tracy L. Christian-Frear
RE/SPEC, Inc.
Suite 300
4774 Indian School Rd NE
Albuquerque, NM 87110
(505) 268-2661
(505) 268-0040
tlchris@respec.com

Leslie A. Dillard
U.S. Geological Survey/Stanford U.
345 Middlefield Rd., MS 496
Menlo Park, CA 94025
(415) 354-3171
(415) 354-3363
leslie@pangea.stanford.edu

Christine Doughty
Lawrence Berkeley Laboratory
1 Cyclotron Road, 50C-106
Berkeley, CA 94720
(510) 486-6453
(510) 486-4159
cadoughty@lbl.gov

Roger R. Eaton
Sandia National Laboratories
Albuquerque, NM 87185
(505) 844-4063
(505) 844-8251
rreaton@engsci.sandia.gov

Martin Emmert
Univ. of Stuttgart
Pfaffenwaldring 61
D-70550 Stuttgart
Germany
49-711-685-7013
49-711-685-7020

Margaret A. Ennis
University of California, Berkeley
440 David Hall
Berkeley, CA 94720
(510) 642-9005
(510) 525-6490
mguell@ce.berkeley.edu

Stefan M. Eugster
ETH, Zürich
VAW-DOL
CH-8092Zuerich
Switzerland
41-1-6325103
41-1-2520147
eugster@vaw.ethz.ch

Jerry P. Fairley
M&O/WCFS
101 Convention Ctr. Dr., P-110
Las Vegas, NV 89109
(702) 794-7461
fairleys@ymv5.ymp.gov

Geoff A. Freeze
INTERA, Inc.
1650 University Blvd. Ste. 300
Albuquerque, NM 87102
(505) 246-1600
(505) 246-2600
interags@nmia.com

Ronald W. Falta
College of Sciences
Clemson University
340 Brackett Hall, Rm 339
P. O. Box 341908
Clemson, SC 29634
(803) 656-0125
(803) 656-1041
ron@geology.clemson.edu

Peter Fuller
Lawrence Berkeley Laboratory
1 Cyclotron Road
Berkeley, CA 94720
(510) 486-5026
(510) 486-5686

Merton E. Fewell
Sandia National Laboratories
P. O. Box 5800
Albuquerque, NM 87185

Jil Geller
Lawrence Berkeley Laboratory
1 Cyclotron Road
Berkeley, CA 94720
(510) 486-7313

Angelos N. Findikakis
Bechtel Environmental, Inc.
45 Fremont Street
San Francisco, CA 44119
(415) 768-8550
(415) 768-4898

Peter Gribi
Colenco Power Consulting, Ltd.
Mellingerstrasse 207
CH-5405Baden
Switzerland
41-56-77-12-12
41-56-83-73-57

Stefan Finsterle
Earth Sciences Division
Lawrence Berkeley Laboratory
1 Cyclotron Road, 50E
Berkeley, CA 94720
(510) 486-5205
(510) 486-5686
finster@lbl.gov

Boliang Gu
Earth Sciences Division
Lawrence Berkeley Laboratory
1 Cyclotron Road, 50E
Berkeley, CA 94720

Shaun D. Fitzgerald
Petroleum Engineering Dept.
Stanford University
Stanford Geothermal Program
Stanford, CA 94305
(415) 725-2728
(415) 725-2099
shaun@pangea.stanford.edu

Teklu Hadgu
Earth Science Division
Lawrence Berkeley Laboratory
1 Cyclotron Road
Berkeley, CA 94720
(510) 486-6474
(510) 486-5686

Rainer Helmig
Univ. of Stuttgart
Pfaffenwaldring 61
D-70550Stuttgart
Germany
49-711-685-7016
49-711-685-7020
rainer@iws.uni-stuttgart.de

Clifford K. Ho
Sandia National Laboratories
P. O. Box 5800, MS-1324
Albuquerque, NM 87185
(505) 848-0712
(505) 848-0605
ckho@nwer.sandia.gov

April L. James
Earth Sciences Division
Lawrence Berkeley Laboratory
1 Cyclotron Road
Berkeley, CA 94720
(510) 486-7214
(510) 486-5686
april@telos.lbl.gov

Jerker Jarsjo
Lawrence Berkeley Laboratory
1 Cyclotron Road, 50C
Berkeley, CA 94720
(510) 486-6770
(510) 486-4159
jerker@ifs.lbl.gov

Vijen Javeri
Gesellschaft f. Reaktorsicherheit
Schwertnergasse 1
50667 Köln
Germany
0221-2068291
0221-2068442

John H. Kessler
Electric Power Research Inst.
3412 Hillview Avenue
Palo Alto, CA 94304
(415) 855-2069
(415) 855-2774
jkessler@paloalto.epri.com

M. Ali Khan
Department of Conservation
State of California
Div. of Oil, Gas & Geothermal Res.
50 "D" Street #300
Santa Rosa, CA 95405
(707) 576-2385
(707) 576-2611

Edwin M. Kidd
Energy Science and Technology
Software Center
P. O. Box 1020
Oak Ridge,TN 37831
(615) 576-1037
(615) 576-2865
ed.kidd@ccmail.osti.gov

M. Kathryn Knowles
Sandia National Laboratories
P. O. Box 5800, MS 1322
Albuquerque, NM 87185
(505) 848-0611
(505) 848-0605
mkpicke@nw.sandia.gov

Lin Kong
University of California, Berkeley
Berkeley, CA 94720

Anthony R. Kovscek
Lawrence Berkeley Laboratory
1 Cyclotron Road, 50E
Berkeley, CA 94720
(510) 486-5926
(510) 486-3805
kovscek@garnet.berkeley.edu

Edward M. Kwicklis
U.S. Geological Survey
Box 25046, MS 421
Den. Federal Center
Lakewood, CO 80225
(303) 236-6228
(303) 236-5047

Kenrick Lee
Lawrence Livermore National Lab.
P. O. Box 808, L-206
Livermore, CA 94550
(510) 423-8492
(510) 422-3118
lee@s89.es.llnl.gov

Mark J. Lupo
K. W. Brown Environmental Svcs.
501 Graham Road
College Station, TX 77845
(409) 690-9280
(409) 690-7310

René Lefebvre
INRS-Géoressources
2700 Einstein, C.P. 7500
Sainte-Foy,Quebec
Canada G1V 4C7
(418) 654-2651
(418) 654-2615
rlefebvre@gsc.emr.ca

T. Manai
Géostock
Immeuble Sedgwick
7, rue E. et A. Peugeot
92563 Rueil-Malmaison
France
47-08-7300
47-08-7373

Suresh Lingineni
CRWMS/M&O
101 Convention Center Dr.
Las Vegas, NV 89109

Mario J. Martinez
Sandia National Laboratories
MS 0827, Dept. 1511
Albuquerque, NM 87122
(505) 844-8729
(505) 844-4523
mjmarti@sandia.gov

Francisco Javier Lisbona
Dept. Math Aplicada
Universidad de Zaragoza
Plaza de San Francisco S/N
Zaragoza, Spain 50009
34-76-356617
34-176-356244
lisbona@cc.unizar.es

John E. McCray
University of Arizona
Harshbarger Bldg. 11
Tucson, AZ 85710
(602) 621-1195
(602) 621-1422
jem@hwr.arizona.edu

Ning Lu
USGS
P. O. Box 25046, MS 421
Denver Federal Center
Lakewood, CO 80225

Brian McPherson
USGS, Menlo Park
345 Middlefield Road
Menlo Park, CA 94025

Tex Lu
Dames & Moore
8801 Folsom Blvd. #200
Sacramento, CA 95826
(916) 387-8800
(916) 387-0802
sactl@dames.com

Anthony J. Menzies
Geothermex, Inc.
5221 Central Ave., Suite 201
Richmond, CA 94804
(510) 527-9876
(510) 527-8164

Srikanta Mishra
INTERA
101 Convention Ctr. Dr, Ste. 110
Las Vegas, NV 89109

Curt M. Oldenburg
Earth Sciences Division
Lawrence Berkeley Laboratory
1 Cyclotron Road
Berkeley, CA 94720
(510) 486-7419
(510) 486-5686
cmoldenburg@lbl.gov

Parviz Montazer
Multimedia Environmental Tech.
3990 Westerly Pl., Suite 200
Newport Beach, CA 92660
(714) 852-9767
(714) 852-8434
montazar@mic.cerf.net

Victor V. Palciauskas
U.S. Nuclear Waste Tech. Rev. Bd.
1100 Wilson Blvd., #910
Arlington, VA 22209
(703) 235-4473
(703) 235-4495
nwtrb@gmu.edu

George J. Moridis
Earth Science Division
Lawrence Berkeley Laboratory
1 Cyclotron Road, 50E
Berkeley, CA 94720
(510) 486-4746
(510) 486-5686
gjmoridis@lbl.gov

Marina Pantazidou
Dept. of Civil & Environ. Eng.
Carnegie Mellon University
5000 Forbes Avenue
Pittsburgh, PA 15213
(412) 268-2943
(412) 268-7813
marina+@andrew.cmu.edu

R. William Nelson
INTERA-PMO
TRW Environmental Safety Sys.
101 Convention Center Dr. MS 425
Las Vegas, NV 89109
(702) 794-1880
(702) 295-9664

Jens R. Pedersen
Unocal
3576 Unocal Place
Santa Rosa, CA 95403
(707) 545-7600
(705) 544-6855

Jahan Noorishad
Lawrence Berkeley Laboratory
1 Cyclotron Road
Berkeley, CA 94720
(510) 486-4905
(510) 486-4159
shiva@csa.lbl.gov

Minh Pham
Geothermex, Inc.
5221 Central Ave., Suite 201
Richmond, CA 94804
(510) 527-9876
(510) 527-8164

Michael J. O'Sullivan
University of Auckland
Private Bag 92019
Auckland, New Zealand
64-9-373 7599, x8393
64-9-373 7468
osullivan@auckland.ac.nz

Mel G. Piepho
Daniel B. Stephens & Assoc., Inc.
1845 Terminal Dr., Ste. 200
Richland, WA 99352
(509) 946-6627
(509) 946-6712

Karsten Pruess
Earth Sciences Division
Lawrence Berkeley Laboratory
1 Cyclotron Road, 50E
Berkeley, CA 94720
(510) 486-6732
(510) 486-5686
pruess @ lbl.gov

Mark Reeves
INTERA, Inc.
6850 Austin Ctr. Blvd., Ste. 300
Austin, TX 78731
(512) 346-2000
(512) 346-9436

Avelino G. Roching
Waste Isolation Division
Westinghouse Electric Corp.
P. O. Box 2078
Carlsbad, NM 88221
(505) 234-8736
(505) 234-8854
rochino@wipp.carlsbad.nm.us

Peter E. Rose
Earth Sciences & Res. Institute
391 Chipeta Way, Suite A
Salt Lake City, UT 84108
(801) 584-4430
(801) 584-4453
prose@uuri.utah.edu

Steven F. Saterlie
TRW
101 Convention Ctr. Dr, Ste. 110
Las Vegas, NV 89109
(702) 794-5376
(702) 794-7445

Tatsuya Sato
Geothermal Energy R & D Co.,Ltd.
Kyodo Bldg., 11-7, Kabuto-cho
Nihonbashi, Chuo-ku
Tokyo, Japan 103
81-3-3666-5822
81-3-3666-5289
kyc04752@niftyserve.or.jp

S. David Sevougian
INTERA
101 Convention Ctr. Dr., Ste. P-110
Las Vegas, NV 89109
(702) 295-9626
(702) 294-1822
david_sevougian@notes.ymp.gov

Chao Shan
Lawrence Berkeley Laboratory
1 Cyclotron Road, 50E
Berkeley, CA 94720
(510) 486-5718
(510) 486-5686

Don L. Shettel
Geoscience Management Inst. Inc.
1000 Nevada Hwy, Ste. 106
Boulder City, NV 89005
(702) 294-3064
(702) 294-3065
dshettel@delphi.com

G. Michael Shook
Idaho National Engineering Lab.
P. O. Box 1625, MS 2107
Idaho Falls, ID 83415
(208) 526-6945
(208) 526-0875
ook@inel.gov

Steven R. Sobolik
Sandia National Laboratory
Albuquerque, NM 87185
(505) 848-0777
(505) 848-0739
srsobol@nwer.sandia.gov

Lorenz R. Spangler
Benchmark Environmental Corp.
4501 Indian School Rd., NE Ste. 105
Albuquerque, NM 87110
(505) 262-2694
(505) 262-2698

J. R. Stroble
Waste Isolation Division
Westinghouse Electric Corp.
P. O. Box 2078
Carlsbad, NM 88221
(505) 234-8256
(505) 234-8854

Micol Todesco
University of Pisa
Dip. Scienze dello Terra
v.s. Maria, 53
I-56126Pisa, Italy
39 (50) 568273
39 (50) 500675
todesco@dst.unipi.it

Alex H. Treadway
Sandia National Laboratories
MS 1328, Org. 6749
Albuquerque, NM 87185
(505) 848-0367
(505) 848-0705
ahtread@nwer.sandia.gov

Yvonne Y.W. Tsang
Earth Sciences Division
Lawrence Berkeley Laboratory
1 Cyclotron Road, 50E
Berkeley, CA 94720
(510) 486-7047
(510) 486-5686
ytsang@csa.lbl.gov

Helga Tulinius
Orkustofnun
Grensasvegur 9
Reykjavik, Iceland 109
354-5-696065
354-5-688896
hlul@os.is

Stephen W. Webb
Sandia National Laboratories
Geohydrology Dept. 6115/MS 1324
Albuquerque, NM 87195
(505) 848-0623
(505) 848-0605
swwebb@nwer.sandia.gov

Stephen P. White
Industrial Research Limited
P. O. Box 31-310
Lower Hutt, New Zealand
(64) 4-569-0000
(64) 4-569-0003
s.white@irl.cri.nz

Paul A. Witherspoon
Lawrence Berkeley Laboratory
1 Cyclotron Road, 50E
Berkeley, CA 94720
(510) 486-5082
(510) 527-1336

Andrew V. Wolfsberg
Los Alamos National Laboratory
MS C400
Los Alamos, NM 87544
(505) 667-3599
(505) 665-8244
awolf@lanl.gov

Yu-shu Wu
Lawrence Berkeley Laboratory
1 Cyclotron Road
Berkeley, CA 94720
(510) 486-5686 FAX

Yanyong Xiang
INTERA, Inc.
TRW Environmental Safety Sys. Inc.
101 Convention Ctr. Dr., Suite 110
Las Vegas, NM 89109
(702) 794-7331
(702) 794-1822

Gemei Yang
Nuclear Engineering Department
Univ. of California, Berkeley & LBL
Etcheverry Hall, Room 1110C
Berkeley, CA 94720
(510) 642-5213

Winnie Zhang
Earth Science Division
Lawrence Berkeley Laboratory
1 Cyclotron Road, 50E
Berkeley, CA 94720
(510) 486-5570
(510) 486-5686

Robert W. Zimmerman
Lawrence Berkeley Laboratory
1 Cyclotron Road
Berkeley, CA 94720
(510) 486-7106
(510) 486-5686
rwzimmerman@lbl.gov

Appendix C. Technical Program

TOUGH Workshop '95

March 20 - 22, 1995

Lawrence Berkeley Laboratory (LBL)
Berkeley, California USA 94720

TECHNICAL PROGRAM (as presented)

Monday, March 20, 1995

A.M.

7:30 Registration: Lobby, Auditorium, Building 50

8:30 Welcome and Introduction (Karsten Pruess, LBL)

8:45 **Session 1: *Nuclear Waste Isolation* I**
(chairman: Ron Falta, Clemson University)

M. Reeves and S. Lingineni, M&O/Intera, Inc., Las Vegas, NV. "Drift-Scale Thermo-Hydrologic Analyses for the Proposed Repository at Yucca Mountain, Nevada"

V. Javeri, GRS, Köln, GERMANY. "Analysis of Nuclide Transport under Natural Convection and Time Dependent Boundary Condition using TOUGH2"

S.M. Eugster and R.K. Senger, ETH/Intera, SWITZERLAND. "Investigation of Potential Water Inflow into a Ventilated Tunnel of the Proposed Low/Intermediate-Level Waste Repository in Switzerland"

G.S. Bodvarsson, G. Chen, C. Haukwa, and E. Kwicklis, LBL/USGS. "The Use of TOUGH2 for the LBL/USGS 3-Dimensional Site Scale Model of Yucca Mountain, Nevada"

10:25 Coffee Break

10:55 **Session 2: *Geothermal Reservoir Enginering* I**
(chairman: Tony Menzies, Geothermex, Inc.)

A. Battistelli, C. Calore, and K. Pruess, Aquater S.p.A., San Lorenzo in Campo, ITALY. "Vapor Pressure Lowering Effects due to Salinity and Suction Pressure in the Depletion of Vapor-Dominated Geothermal Reservoirs"

T. Hadgu, R. Zimmerman, and G.S. Bodvarsson, LBL. "Coupling of the Reservoir Simulator TOUGH and the Wellbore Simulator WFSA"

M.J. O'Sullivan and D.P. Bullivant, Dept. of Engineering Science, U. of Auckland, NEW ZEALAND. "A Graphical Interface to the TOUGH Family of Flow Simulators"

P.M.

12:10 Lunch Break

1:30 **Session 3: *Oil and Gas***
(chairman: Ade Adenekan, Exxon Production Research Co.)

A.R. Kovscek, T.W. Patzek, and C.J. Radke, LBL/UCB. "FOAM3D: A Numerical Simulator for Mechanistic Prediction of Foam Displacement in Multidimensions"

P. Witherspoon, P. Fuller, and S. Finsterle, LBL. "Three-Dimensional Multiphase Effects in Aquifer Gas Storage"

B. McPherson and J. Bredehoeft, USGS/Hydrodynamics Group, Menlo Park, CA. "Analysis of Over-Pressure Mechanisms in the Uinta Basin, Utah"

Monday, March 20, 1995 (continued)

P.M.

2:45 Adjourn for Poster Setup

4:00 **Poster Session** (LBL Cafeteria)

S.W. Webb and K.W. Larson, Sandia, Albuquerque, NM. "The Effect of Stratigraphic Dip on Multiphase Flow at the Waste Isolation Pilot Plant"

T.L. Christian-Frear and S.W. Webb, Sandia, Albuquerque, NM. "Modification and Application of TOUGH2 as a Variable-Density, Saturated Flow Code and Comparison to SWIFT II Results"

G.A. Freeze, K.W. Larson, P.B. Davies, and S.W. Webb, INTERA, Inc./Sandia, Albuquerque, NM. "Using TOUGH2 to Model the Coupled Effects of Gas Generation, Repository Consolidation, and Multiphase Brine and Gas Flow at the Waste Isolation Pilot Plant"

M.G. Piepho, Daniel B. Stephens & Assoc., Inc., Richland, WA. "Preliminary Analysis of Tank 241-C-106 Dryout due to Large Postulated Leak and Vaporization"

M.J. Lupo and G.J. Moridis, K.W. Brown Environmental Services/LBL. "Predicting the Distribution of Contamination from a Chlorinated Hydrocarbon Release"

M. Pantazidou, Carnegie-Mellon University, Pittsburgh, PA. "LNAPL Infiltration in the Vadose Zone: Comparisons of Physical and Numerical Simulations"

G.J. Moridis and K. Pruess, LBL. "Air Barriers for Waste Containment in the Subsurface"

S. Finsterle and K. Pruess, LBL. "Using Simulation-Optimization Techniques to Improve Multiphase Aquifer Remediation"

S.W. Webb and J.C. Stormont, Sandia, Albuquerque, NM. "Modeling of Capillary Barriers and Comparison to Data"

C.K. Ho, Sandia, Albuquerque, NM. "Assessing Alternative Conceptual Models of Fracture Flow"

C.M. Oldenburg, R.L. Hinkins, G.J. Moridis, and K. Pruess, LBL. "On the Development of MP-TOUGH2"

R. Zimmerman, T. Hadgu, and G.S. Bodvarsson, LBL. "A New Lumped-Parameter Approach to Simulating Flow Processes in Unsaturated Dual-Porosity Media"

J. Poppei and D. Fischer, Geothermie Neubrandenburg, GERMANY. "Prognostic Simulation of Reinjection - Research Project Geothermal Site Neustadt-Glewe, Germany"

E. Antunez, K. Pruess, and G. Moridis, LBL. "Use of TOUGH2 on Small Computers"

T. Sato, T. Okabe K. Osato, and S. Takasugi, GERD, Tokyo, JAPAN. "Graphical User Interface for TOUGH/TOUGH2 - Development of Database, Pre-processor, and Post-processor"

C. Doughty, LBL. "Flow Reduction due to Degassing and Redissolution Phenomena"

E. Kidd, ESTSC, Oak Ridge, TN. "Energy Science and Technoloy Software Center"

C. Betz, M. Emmert, A. Färber, R. Helmig, V. Kaleris, and H. Kobus, Institute for Hydraulics, University of Stuttgart, GERMANY. "Soil Remediation by Heat Injection: Experiments and Numerical Modeling"

P. Witherspoon, P. Fuller, and S. Finsterle, LBL. "Three-Dimensional Multiphase Effects in Aquifer Gas Storage"

6:00 Buffet Dinner (LBL Cafeteria)

7:30 Adjourn

Tuesday, March 21, 1995

A.M.

8:45 **Session 4: *Environmental Remediation* I**
(chairman: Angelos Findikakis, Bechtel Co.)

R.W. Falta and S. Brame, Clemson University, Clemson, South Carolina. "Numerical Simulation of in-situ DNAPL Remediation by Alcohol Flooding"

S.W. Webb and J.M. Phelan, Sandia, Albuquerque, NM. "Prediction of Single-Component NAPL Behavior for the TEVES Project Using T2VOC"

C.M. Oldenburg and K. Pruess, LBL. "Strongly Coupled Single-Phase Flow Problems: Effects of Density Variation, Hydrodynamic Dispersion, and First Order Decay"

10:00 Coffee Break

10:40 **Session 5: *Mining Engineering***
(chairman: George Moridis, LBL)

G.J. Weir, S.P. White, and W.M. Kissling, Industrial Research, Ltd., Lower Hutt, NEW ZEALAND. "Reservoir Storage and Containment of Greenhouse Gases"

R. Lefebvre, INRS-Géoressources, Québec, CANADA. "Modeling Acid Mine Drainage in Waste Rock Dumps"

A.J. Menzies and J.L. Forth, Geothermex, Inc./Kennecott Co., Richmond, CA. "Modeling the Response of the Geothermal System at Lihir Island, Papua New Guinea, to Mine Dewatering"

11:55 Lunch Break

P.M.

1:20 **Session 6: *Simulation Methods***
(chairman: Alfredo Battistelli, AQUATER S.p.A.)

D.P Bullivant, M.J. O'Sullivan, and Z. Yang, Dept. of Engineering Science, U. of Auckland, NEW ZEALAND. "Experiences Using Multigrid for Geothermal Simulation"

S. Finsterle and K. Pruess, LBL. "ITOUGH2: Solving TOUGH Inverse Problems"

G.J. Moridis, LBL. "A New Set of Direct and Iterative Solvers for the TOUGH2 Family of Codes"

E. de la Torre and M.C. Suarez, IIE, Cuernevaca, MEXICO. "DIOMRES(k,m): An Efficient Method Based on Krylov Subspaces to Solve Big, Dispersed, Unsymmetrical Linear Systems" (no oral presentation)

T. Manai, Géostock, Rueil-Malmaison, FRANCE. "EVEGAS (European Validation Exercise of Gas Migration Model)"

3:00 Coffee Break

3:30 **Session 7: *Nuclear Waste Isolation* II**
(chairman: Rainer Helmig, University of Stuttgart)

S.W. Webb, K.W. Larson, G.A. Freeze, and T.L. Christian-Frear, Sandia, Albuquerque, NM. "Summary of Applications of TOUGH2 to the Evaluation of Multiphase Flow Processes at the WIPP"

G. Arens, L. Höglund, and M. Wiborgh, Bundesamt für Strahlenschutz/Kemakta, Salzgitter, GERMANY. "Requirements on Sealing Measures Due to Gas Production"

Y. Xiang, S. Mishra, and B. Dunlap, Intera, Las Vegas, NV. "Parametric Analysis of a Two-Dimensional Groundwater Flow Model of the Unsaturated Zone at Yucca Mountain"

K. Pruess and E. Antunez, LBL. "Applications of TOUGH2 to Infiltration of Liquids in Media with Strong Heterogeneity"

5:10 Adjourn

7:00 Banquet

Speaker: John Bredehoeft, Consultant

Wednesday, March 22, 1995

A.M.

8:30 **Session 8: *Environmental Remediation* II**
(chairman: Ed Kidd, Energy Science and Technology Software Center)

J.E. McCray and R.W. Falta, University of Arizona/Clemson University, Tucson, Arizona. "Air Sparging for Subsurface Remediation: Numerical Analysis Using T2VOC"

C. Shan, LBL. "Verification of T2VOC Using an Analytical Solution for VOC Transport in Vadose Zone"

C.K. Ho, Sandia, Albuquerque, NM. "Numerical Simulation of Multicomponent Evaporation and Gas-Phase Transport Using M2NOTS"

A. Seneviratne and A.N. Findikakis, Bechtel Corp., San Francisco, CA. "The Effect of Vadose Zone Heterogeneities on Vapor Phase Migration and Aquifer Contamination by Volatile Organics"

10:10 Coffee Break

10:40 **Session 9: *Vadose Zone Hydrology***
(chairman: David Bullivant, University of Auckland)

P. Montazer, Multimedia Environmental Technology, Inc., Newport Beach, California. "Air-TOUGH, A Fully 3-Dimensional Linking of Atmosphere with Soil Using Eddy Diffusivity Concept and V-TOUGH"

E. Kwicklis, R.W. Healy, G.S. Bodvarsson, and N. Lu, U.S.G.S., Denver, CO. "Application of TOUGH to Hydrologic Problems Related to the Unsaturated Zone Site Investigation at Yucca Mountain, Nevada"

11:55 Lunch Break

P.M.

1:20 **Session 10: *Geothermal Reservoir Enginering* II**
(chairman: Steve Webb, Sandia)

E. Antunez, M. Lippmann, M. Ali-Khan, and T. Boardman, LBL/California Department of Conservation, Division of Oil and Gas. "Simulation of the Heber Geothermal Field, a TOUGH2/PC Application"

M. Todesco, Universita degli Studi di Pisa, Pisa, ITALY. "Modeling of Hydrothermal Circulation Applied to Active Volcanic Areas. The Case of Vulcano (Italy)"

M.C. Suarez and F. Samaniego, CFE, Morelia, MEXICO. "Triple-Porosity/Permeability Flow in Faulted Geothermal Reservoirs: Two-Dimensional Effects" (no oral presentation)

S.L. Moya and E.R. Iglesias, IIE, Cuernevaca, MEXICO. "Numerical Simulation of Carbon Dioxide Effects in Geothermal Reservoirs" (no oral presentation)

2:10 Coffee Break

2:40 **Session 11: Open Discussion: Future Developments and Exchanges of the TOUGH/MULKOM Family of Codes**
(chairman and moderator: Michael O'Sullivan, University of Auckland)

5:00 Workshop ends

Appendix D. Mailing List for Yucca Mountain Site Characterization Project

D. A. Dreyfus (RW-1) [1]
Director
Office of Civilian Radioactive Waste Management
U.S. Department of Energy
1000 Independence Avenue, S.W.
Washington, DC 20585

L. H. Barrett (RW-2) [1]
Acting Deputy Director
Office of Civilian Radioactive Waste Management
U.S. Department of Energy
1000 Independence Avenue, S.W.
Washington, DC 20585

J. D. Saltzman (RW-10) [1]
Office of Human Resources and Administration
OCRWM
U.S. Department of Energy
1000 Independence Avenue, S.W.
Washington, DC 20585

J. C. Bresee (RW-10) [1]
Office of Human Resources and Administration
OCRWM
U.S. Department of Energy
1000 Independence Avenue, S.W.
Washington, DC 20585

T. Wood (RW-14) [1]
Contract Management Division
OCRWM
U.S. Department of Energy
1000 Independence Avenue, S.W.
Washington, DC 20585

R. A. Milner (RW-30) [1]
Office of Program Management and Integration
OCRWM
U.S. Department of Energy
1000 Independence Avenue, S.W.
Washington, DC 20585

C. A. Kouts (RW-36) [1]
Regulatory Integration Division
OCRWM
U.S. Department of Energy
1000 Independence Avenue, S.W.
Washington, DC 20585

S. Rousso, (RW-40) [1]
Office of Waste Acceptance, Storage and Transportation
OCRWM
U.S. Department of Energy
1000 Independence Avenue, S.W.
Washington, DC 20585

Victoria F. Reich, Librarian [4]
Nuclear Waste Technical Review Board
1100 Wilson Blvd., Suite 910
Arlington, VA 22209

R. M. Nelson, Jr., Acting Project Manager [5]
Yucca Mountain Site Characterization Office
U.S. Department of Energy
P.O. Box 98608--MS 523
Las Vegas, NV 89193-8608

Office of the Director [1]
Office of External Affairs
DOE Nevada Operations Office, Nevada
U.S. Department of Energy
P.O. Box 98518
Las Vegas, NV 89193-8518

Technical Information Officer [8]
DOE Nevada Operations Office
U.S. Department of Energy
P.O. Box 98518
Las Vegas, NV 89193-8518

P. K. Fitzsimmons, Technical Advisor [1]
Office of Assistant Manager for
Environmental Safety and Health
U.S. DOE/Nevada Operations Office
P.O. Box 98518
Las Vegas, NV 89193-8518

E. P. Binnall [1]
Field Systems Group Leader
Building 50B/4235
Lawrence Berkeley Laboratory
Berkeley, CA 94720

D. R. Elle, Director [1]
Environmental Protection Division
DOE Nevada Operations Office
U.S. Department of Energy
P.O. Box 98518
Las Vegas, NV 89193-8518

Center for Nuclear Waste Regulatory Analyses [1]
6220 Culebra Road
Drawer 28510
San Antonio, TX 78284

Repository Licensing & Quality
Assurance [1]
Project Directorate
Division of Waste Management
U.S. Nuclear Regulatory Commission
Washington, DC 20555

W. L. Clarke [3]
Technical Project Officer for YMP
Attn: YMP/LRC
Lawrence Livermore National Laboratory
P.O. Box 5514
Livermore, CA 94551

Senior Project Manager for Yucca
Mountain [1]
Repository Project Branch
Division of Waste Management
U.S. Nuclear Regulatory Commission
Washington, DC 20555

J. A. Blink [1]
Deputy Project Leader
Lawrence Livermore National Laboratory
101 Convention Center Drive, Suite 820, MS 527
Las Vegas, NV 89109

NRC Document Control Desk [1]
Division of Waste Management
U.S. Nuclear Regulatory Commission
Washington, DC 20555

J. A. Canepa [4]
Technical Project Officer for YMP
N-5, Mail Stop J521
Los Alamos National Laboratory
P.O. Box 1663
Los Alamos, NM 87545

Philip S. Justus [1]
NRC Site Representative
301 E. Stewart Ave., Room 203
Las Vegas, NV 89101

H. N. Kalia [1]
Project Leader for ESF Test Coordination
Los Alamos National Laboratory
Mail Stop 527
101 Convention Center Drive, Suite 820
Las Vegas, NV 89101

N. Z. Elkins [1]
Deputy Technical Project Officer
Los Alamos National Laboratory
Mail Stop 527
101 Convention Center Drive, Suite 820
Las Vegas, NV 89101

L. E. Shephard [5]
Technical Project Officer for YMP
Sandia National Laboratories
Organization 6310
P.O. Box 5800
Albuquerque, NM 87185

J. F. Devine [1]
Assistant Director for Engineering
Geology
U.S. Geological Survey
106 National Center
12201 Sunrise Valley Drive
Reston, VA 22092

L. R. Hayes [1]
Technical Project Officer
Yucca Mountain Project Branch--MS 425
U.S. Geological Survey
P.O. Box 25046
Denver, CO 80225

R. E. Lewis [1]
Yucca Mountain Project Branch--MS 425
U.S. Geological Survey
P.O. Box 25046
Denver, CO 80225

V. R. Schneider [1]
Asst. Chief Hydrologist--MS 414
Office of Program Coordination &
Technical Support
U.S. Geological Survey
12201 Sunrise Valley Drive
Reston, VA 22092

J. S. Stuckless [1]
Chief, Geologic Studies Program--MS 425
Yucca Mountain Project Branch
U.S. Geological Survey
P.O. Box 25046
Denver, CO 80225

D. H. Appel, Chief [1]
Hydrologic Investigations Program--MS 421
U.S. Geological Survey
P.O. Box 25046
Denver, CO 80225

R. W. Craig, Chief [1]
Nevada Operations Program
U.S. Geological Survey
101 Convention Center Drive
Suite 860, MS 509
Las Vegas, NV 89109

A. L. Flint [1]
U.S. Geological Survey
MS 721
P.O. Box 327
Mercury, NV 89023

D. A. Beck [1]
Water Resources Division
U.S. Geological Survey
6770 So. Paradise Road
Las Vegas, NV 89119

B. T. Brady [1]
Records Specialist
U.S. Geological Survey--MS 421
P.O. Box 25046
Denver, CO 80225

M. D. Voegele [1]
Technical Project Officer for YMP
Science Applications International Corp.
101 Convention Center Dr., Suite 407
Las Vegas, NV 89109

L. D. Foust [2]
Nevada Site Manager
TRW Environmental Safety Systems
101 Convention Center Drive
Suite P-110, MS 423
Las Vegas, NV 89109

C. E. Ezra [1]
YMP Support Office Manager
EG&G Energy Measurements, Inc.
MS V-02
P.O. Box 1912
Las Vegas, NV 89125

E. L. Snow, Program Manager [1]
Roy F. Weston, Inc.
955 L'Enfant Plaza, S.W.
Washington, DC 20024

Technical Information Center [1]
Roy F. Weston, Inc.
955 L'Enfant Plaza, S.W.
Washington, DC 20024

D. Hedges, Vice President, Quality
Assurance [1]
Roy F. Weston, Inc.
4425 Spring Mountain Road, Suite 300
Las Vegas, Nevada 89102

D. L. Fraser, General Manager [1]
Reynolds Electrical & Engineering Co., Inc.
MS 555
P.O. Box 98521
Las Vegas, NV 89193-8521

D. L. Koss [1]
Technical Project Officer for YMP
Reynolds Electrical & Engineering Co., Inc.
MS 408
P.O. Box 98521
Las Vegas, NV 89193-8521

B. W. Colston, President/General Manager [1]
Las Vegas Branch
Raytheon Services Nevada
MS 416
P.O. Box 95487
Las Vegas, NV 89193-5487

W. P. Kopatich [1]
Technical Project Officer for YMP
Raytheon Services Nevada
Suite P-230, MS 403
101 Convention Center Dr.
Las Vegas, NV 89109

Paul Eslinger, Manager [1]
PASS Program
Pacific Northwest Laboratories
P.O. Box 999
Richland, WA 99352

A. T. Tamura [1]
Science and Technology Division
Office of Scientific and Technical Information
U.S. Department of Energy
P.O. Box 62
Oak Ridge, TN 37831

Carlos G. Bell, Jr. [1]
Professor of Civil Engineering
Civil and Mechanical Engineering Dept.
University of Nevada, Las Vegas
4505 So. Maryland Parkway
Las Vegas, NV 89154

P. J. Weeden, Acting Director [1]
Nuclear Radiation Assessment Division
U.S. Environmental Protection Agency
Environmental Monitoring Systems Laboratory
P.O. Box 93478
Las Vegas, NV 89193-3478

ONWI Library [1]
Battelle Columbus Laboratory
Office of Nuclear Waste Isolation
505 King Ave.
Columbus, OH 43201

T. Hay, Executive Assistant [1]
Office of the Governor
State of Nevada
Capitol Complex
Carson City, NV 89710

R. R. Loux [3]
Executive Director
Agency for Nuclear Projects
State of Nevada
Evergreen Center, Suite 252
1802 N. Carson St.
Carson City, NV 89710

C. H. Johnson [1]
Technical Program Manager
Agency for Nuclear Projects
State of Nevada
Evergreen Center, Suite 252
1802 N. Carson St.
Carson City, NV 89710

John Fordham [1]
Water Resources Center
Desert Research Institute
P.O. Box 60220
Reno, NV 89506

David Rhode [1]
Desert Research Institute
P.O. Box 60220
Reno, NV 89506

John Fordham [1]
Water Resources Center
Desert Research Institute
P.O. Box 60220
Reno, NV 89506

Eric Anderson [1]
Mountain West Research-Southwest, Inc.
2901 N. Central Ave., #1000
Phoenix, AZ 85012-2730

The Honorable Cyril Schank [1]
Chairman
Churchill County Board of Commissioners
190 W. First St.
Fallon, NV 89406

Dennis A. Bechtel, Coordinator [1]
Nuclear Waste Division
Clark County Department of Comprehensive Planning
301 E. Clark Ave., Suite 570
Las Vegas, NV 89101

Juanita D. Hoffman [1]
Nuclear Waste Repository
Oversight Program
Esmeralda County
P.O. Box 490
Goldfield, NV 89013

Eureka County Board of
Commissioners [1]
Yucca Mountain Information Office
P.O. Box 714
Eureka, NV 89316

Brad R. Mettam [1]
Inyo County Yucca Mountain
Repository Assessment Office
P.O. Drawer L
Independence, CA 93526

Lander County Board of
Commissioners [1]
315 South Humboldt St.
Battle Mountain, NV 89820

Jason Pitts [1]
Lincoln County Nuclear Waste
Project Office
P.O. Box 90
Pioche, NV 89043

Judy Foremaster [1]
City of Caliente Nuclear Waste
Project Office
P.O. Box 158
Caliente, NV 89008

Vernon E. Poe [1]
Office of Nuclear Projects
Mineral County
P.O. Box 1600
Hawthorne, NV 89415

Les W. Bradshaw [1]
Program Manager
Nye County Nuclear Waste Repository Project
Office
P.O. Box 1767
Tonopah, NV 89049

William Offutt [1]
Nye County Manager
P.O. Box 153
Tonopah, NV 89049

Phillip. A. Niedzielski-Eichner [1]
Nye County Nuclear Waste Repository Project
Office
P.O. Box 221274
Chantilly, VA 22022-1274

Florindo Mariani [1]
White Pine County Coordinator
P.O. Box 135
Ely, NV 89301

Glenn Van Roekel [1]
Director of Community Development
City of Caliente
P.O. Box 158
Caliente, NV 89008

Ray Williams, Jr. [1]
P.O. Box 10
Austin, NV 89310

Charles Thistlethwaite, AICP [1]
Associate Planner
Inyo County Planning Department
Drawer L
Independence, CA 93526

Nye County District Attorney [1]
P.O. Box 593
Tonopah, NV 89049

Economic Development Department [1]
City of Las Vegas
400 E. Stewart Ave.
Las Vegas, NV 89101

Community Planning and
Development [1]
City of North Las Vegas
P.O. Box 4086
North Las Vegas, NV 89030

Community Development and
Planning [1]
City of Boulder City
P.O. Box 61350
Boulder City, NV 89006

Commission of the European Communities [1]
200 Rue de la Loi
B-1049 Brussells
BELGIUM

M. J. Dorsey, Librarian [2]
YMP Research and Study Center
Reynolds Electrical & Engineering Co., Inc.
MS 407
P.O. Box 98521
Las Vegas, NV 89193-8521

Amy Anderson [1]
Argonne National Laboratory
Building 362
9700 So. Cass Ave.
Argonne, IL 60439

Steve Bradhurst [1]
P.O. Box 1510
Reno, NV 89505

Michael L. Baughman [1]
Intertech Services Corp.
P.O. Box 93537
Las Vegas, NV 89193

Dr. Moses Karakouzian [1]
1751 E. Reno, #125
Las Vegas, NV 89119